Combined measures of oxygenation, haemodynamics and metabolism to understand neural responses in infants

Maheen Faisal Siddiqui

A thesis presented for the degree of

Doctor of Philosophy (Ph.D)

University of London

2018

Birkbeck, University of London, Malet Street, London, WC1E 7HX

Originality Statement

'I hereby declare that this submission is my own work and to the best of my knowledge it contains no materials previously published or written by another person, or substantial proportions of material which have been accepted for the award of any other degree or diploma at the University of London or any other educational institution, except where due acknowledgment is made in the thesis. Any contribution made to the research by others, with whom I have worked at University of London or elsewhere, is explicitly acknowledged in the thesis.'

The following research thesis includes work that appears in the following articles;

- **Siddiqui, M.F.**, Elwell, C.E. & Johnson, M.H. (2016) Mitochondrial Dysfunction in Autism Spectrum Disorders. *Autism Open Access*, 6(5): 1000190

- **Siddiqui, M.F.**, Lloyd-Fox, S.F., Kaynezhad, P., Tachtsidis, I., Johnson, M.H. & Elwell, C.E. (2017) Non-invasive measurement of a metabolic marker of infant brain function. *Scientific Reports*, 7:1330

- **Siddiqui, M.F.**, Lloyd-Fox, S.F., Kaynezhad, P., Tachtsidis, I., Johnson, M.H. & Elwell, C.E. (2018) Changes in Cytochrome-C-Oxidase Account for Changes in Attenuation of Near-Infrared Light in the Healthy Infant Brain. In: Thews, O., LaManna J., Harrison D. (eds) Oxygen Transport to Tissue XL. *Advances in Experimental Medicine and Biology*, vol 1072. Springer, Cham

Abstract

fNIRS is an established research tool used to investigate typical and atypical brain development. Primarily, it provides measures of haemodynamic changes that are used to indirectly infer neural activity. Broadband NIRS provides a more direct marker of neuronal activation through measurement of changes in cytochrome-c-oxidase (CCO). As a cellular measure, CCO can be used as a bridge to improve our understanding of the link between neural and haemodynamic activity or "neurovascular coupling".

Study 1 demonstrated that changes in mitochondrial activity could be measured alongside haemodynamics during functional activation, over the temporal cortex, using a miniature system in four-to-six-month-old infants. In order to investigate the spatial specificity of CCO, its relation to haemodynamics and to build upon our understanding of neurovascular coupling mechanisms, multi-channel broadband NIRS was used alongside EEG in Study 2 where responses were measured over the visual cortex. Study 2 was performed in adults as the development of a concurrent NIRS and EEG protocol was methodologically challenging. Following this, Study 3 extended on experimental paradigms from Studies 1 and 2 to measure changes in metabolic activity and haemodynamics over the temporal and visual cortices, in four-to-seven-month-old infants. This study demonstrated simultaneous broadband NIRS and EEG use in infants for the first time. The results provided evidence of underdeveloped coupling of cerebral blood flow changes and mitochondrial activity in early infancy. Finally, Study 4 extended the protocol to investigate underlying biological mechanisms that may be altered in neurovascular coupling in autism, by studying infants at high familial risk for the disorder. The findings demonstrated that the combined protocol was not only feasible for use to study atypical brain development but also provided preliminary evidence of altered coupling between cerebral energy metabolism and haemodynamics.

Taken together, this work illuminates hitherto undocumented evidence of neurovascular coupling during brain development and highlights the potential of using broadband NIRS with EEG for future neurodevelopmental research in typical and atypical populations.

Acknowledgements

I would like to thank my supervisors; Professor Mark Johnson, Professor Clare Elwell, Dr Sarah Lloyd-Fox and Dr Emily Jones for their constant, invaluable support and encouragement over the last three years. Mark, thank you for providing me with the opportunity to work in such a rich collaborative research environment and for allowing me the freedom to learn and grow as a researcher. Clare, thank you for your constant encouragement and for always being available to provide advice (not just about my PhD). Your supervision has allowed me to enhance my knowledge as well as develop personally. Thank you to Sarah and Emily for firstly being great sources of inspiration and secondly for constantly being available to guide and support me as I learned.

I am especially grateful for the collaboration of Dr Ilias Tachtsidis who very kindly provided the systems that were needed to carry out the studies presented in this thesis. Also many thanks to many members of his group; Phong Phan, Pardis Kaynezhad, Gemma Bale, Isabel de Roever and Paola Pinti for always being available to help me with my engineering-related queries. Many thanks to Martyn Carter from UCL B-Made for always providing useful advice about 3-D printed headgear designs. Thanks also to George and Romain and the incredibly helpful staff at the UCL Institute of Making who were not always extremely helpful and kind but provided me with the opportunity to use their printers to experiment with materials for headgear development. Thank you to Andrew Levy for his collaboration, wit and intellect and for embarking on a stressful (and slightly crazy journey) developing headgear together.

I would especially like to thank Leslie Tucker, the Research Coordinator at the CBCD. Leslie, you have always been immensely helpful in providing advice and navigating difficult situations. I have always felt supported and taken care of at the CBCD and much of that has been down to you. I will always be extremely grateful for all your support over the last 3 years.

To the wonderful friends and colleagues that I have made during my time at the CBCD

Contents

List of Figures

14

22

31

List of Tables

List of Abbreviations

3-D   3-dimensional

AA   arachidonic acid

ACA   anterior cerebral artery

AMPA α-amino-3-hydroxy-5-methyl-4-isoxazolepropionic acid

APT   avalance photodiode

ASD   autism spectrum disorders

BBB   blood brain barrier

BOLD   blood oxygen level dependent

BORL   Biomedical Optics Research Laboratory

Ca^{2+} calcium ion

CBCD   Centre for Brain and Cognitive Development

CCD   charge-coupling devices

CCO   cytochrome-c-oxidase

Cl^{-} chloride ion

CMRG   cerebral metabolic rate of glucose uptake

$CMRO_2$ cerebral metabolic rate of oxygen consumption

CW   continuous wave

DCM   dynamic causal modelling

DFT   discrete fourier transform

DOT   diffuse optical tomography

DPF   differential pathlength factor

DSM-V   Diagnostic and Statistical Manual of Mental Disorders

E/I   excitation inhibition balance

EEG   electroencephalography

EET   epoxyeicosatrienoic acid

ELC   early learning composite score

EMG   electromyography

eNOS   endothelial nitric oxide synthase

EPSP   excitatory postsynaptic potential

ERP   event related potential

ERSP   event-related spectral perturbation

ETC   electron transport chain

FADH$_2$ flavin adenine dinucleotide

FD   frequency domain

FDM   fuse deposition modelling

FDR   false discovery rate

FFT   fast fourier transform

fMRI   functional magnetic resonance imaging

fNIRS   functional near-infrared spectroscopy

FT	fourier transform
GABA	gamma amino butyric acid
GLM	general linear modelling
HbO_2	oxygenated haemoglobin
HC	high contrast
HHb	deoxygenated haemoglobin
HIE	hypoxia ischaemia encephalopathy
HR	high risk
HRF	haemodynamic response function
H^+	hydrogen ions
IFG	inferior frontal gyrus
IPSP	inhibitory postsynaptic potential
K^+	potassium ion
K_{ir}	inward rectifier potassium ion channels
LC	low contrast
LD	laser diode
LED	light emitting diode
LFP	local field potential
LGN	lateral geniculate nucleus
MBLL	modified beer-lambert law
MCA	middle cerebral artery
mGluR	metabotropic glutamate receptors

Mini-CYRIL miniature cytochrome research instrument and application

MSEL   mullen scores of early learning

NADH   nicotinamide adenine dinucleotide

Na^+ sodium ion

NE   neonatal encephalopathy

NIC   neuroelectrics instrument controller

NIR   near-infrared region

NMDA   N-methyl-D-aspartate

nNOS   nitric oxide synthase

NO   nitric oxide

NVU   neurovascular unit

oxCCO   oxidation status of cytochrome-c-oxidase

PCA   posterior cerebral artery

PCTPE   plasticized copolyamide thermoplastic elastomer

PD   photodiode

PET   positron-emission tomography

PG   prostaglandins

PLA_2 phospholipase A_2

PMT   photo-multiplier tube

PPI   psycho-physiological interaction model

PSD   power spectral density

rCBF   regional cerebral blood flow

rCMRO$_2$ regional cerebral metabolic rate of oxygen consumption

rOEF   regional oxygen extraction fraction

SLS   selective laser sintering

SMA   subminiature version A

SO$_2$ oxygen saturation

SPECT   single-photon emission computed tomography

STFT   short-time fourier transform

STS-TPJ   superior temporal sulcus - temporo-parietal junction

TCA   tricarboxylic acid cycle

TOI   tissue oxygenation index

TR   time-resolved

TTP   time to peak

Δ[HbO$_2$]   change in concentration of oxygenated haemoglobin

Δ[HHb]   change in concentration of deoxygenated haemoglobin

Δ[oxCCO]   change in concentration of oxidation status of cytochrome-c-oxidase

^{1}H MRS   Proton Magnetic Resonance Spectroscopy

Chapter 1

INTRODUCTION

1.1 Motivations and objectives

Over the past twenty years, there has been an increase in the use of Functional Near-Infrared Spectroscopy (fNIRS) in the field of neurodevelopmental research to investigate human infant brain development; from language processing (Minagawa-Kawai et al., 2008; Homae et al., 2006; Abboub et al., 2016; Issard and Gervain, 2017; Minagawa-Kawai et al., 2007) to social perception (Wilcox et al., 2013; Ichikawa et al., 2013; Grossmann et al., 2008; Hyde et al., 2010; Lloyd-Fox et al., 2009) and object processing (Wilcox et al., 2005a), to understanding the development of visual pathways in early infancy (Taga et al., 2004; Meek et al., 1998; Watanabe et al., 2008). fNIRS has also been employed more recently to study atypical brain development in neurodevelopmental disorders such as autism spectrum disorders (ASD) (Lloyd-Fox et al., 2013, 2018; Braukmann et al., 2018). While these studies yield invaluable insight into human brain development, less work has focused on understanding underlying metabolic pathways in early infancy. This is primarily due to the lack of available techniques to investigate these processes in awake infants non-invasively. Broadband near-infrared spectroscopy (NIRS), is a technique that allows measurement of cellular oxygen consumption and energy metabolism non-invasively through measurement of changes in the oxidation state of mitochondrial respiratory chain enzyme cytochrome-c-oxidase (CCO), which has been shown to be a unique marker of brain activity (de Roever et al., 2016; Bainbridge et al., 2014) and may be more closely linked to neural activity as it informs on cellular changes that occur within the neurovascular cou-

pling pathway in comparison to measures of blood oxygenation which primarily inform on the oxygen delivery component. The motivation underlying the work presented in this thesis therefore, was to use broadband NIRS simultaneously with electroencephalography (EEG) in order to investigate neurovascular related metabolic pathways in human brain development in infants at low and high risk of autism. At the onset of this PhD work, there was only one published developmental neuroimaging study utilising broadband NIRS to measure cellular changes (Zaramella et al., 2001b) and only one study employing the use of fNIRS simultaneously with EEG during functional activation in infants (Telkemeyer et al., 2011). Moreover, as evidence emerges of potential neurophysiological differences between ASD individuals and controls (Belger et al., 2011a; Harris et al., 2011; Chauhan et al., 2011; Gu et al., 2013), as well as atypical processing of social stimuli in infants at high familial risk for autism (Lloyd-Fox et al., 2013; Braukmann et al., 2018; Jones et al., 2016a; Lloyd-Fox et al., 2018), broadband NIRS (in particular simultaneously with EEG) presents a unique opportunity to non-invasively explore irregularities in metabolic pathways in atypical brain development. Therefore, broadband NIRS and EEG were used to also investigate brain activity in infants at high-risk for autism. The thesis aimed to address the following questions:

- *Can broadband NIRS be used to measure changes in cellular oxygen consumption and energy metabolism during functional activation in infancy?*

- *Can multi-channel broadband NIRS be used in conjunction with EEG successfully to improve our understanding of the status of neurovascular coupling in the infant brain?*

- *If this is possible, then can the technique be used to help explore the relationship between neuronal activity and cerebral blood oxygenation changes and how does measuring changes in CCO shed a light on this relationship?*

- *Can differences in regional cortical development be inferred?*

- *Can this method be applied to understand atypical brain development?*

At the onset of this PhD work, we were at the advent of two novel applications to investigate human brain development. First, the application of broadband NIRS to infant and

second, its use simultaneously with EEG. There were several methodological challenges to be overcome, one of the major ones being the development of appropriate headgear that allowed integration of NIRS optodes with EEG electrodes on the head. Therefore, the work in this thesis also involved a methodological component that aimed to develop suitable headgear for multi-channel broadband NIRS as well as headgear for simultaneous NIRS and EEG studies.

The remainder of this chapter first provides a background on neuronal processes that occur in the brain and details neurovascular coupling, the vascular part of which is interrogated using fNIRS and the neural activity component is studied using using EEG. Then, evidence of development of cerebral vasculature and neural circuitry is reviewed in both typical and atypical brain development and limitations from previous infant work that motivated the current research are discussed. Lastly, studies that have thus far utilised broadband NIRS to investigate brain function are reviewed.

1.2   Neuronal processes

1.2.1   Neuronal structure

The brain is a complex organ in the human body that constantly requires energy. There are several mechanisms in place that fulfill the metabolic demands of the brain by supplying oxygen and nutrients via blood. These were first described by Roy and Sherrington (1890) and are referred to as (i) cerebral autoregulation and (ii) neurovascular coupling. Autoregulation is the mechanism that is responsible for maintaining constant blood flow to the brain (Iadecola, 1993) while neurovascular coupling, also referred to as functional hyperemia, is the process that occurs only during functional activation. Functional activation is defined as the neuronal activation of specific cortical areas of the brain in response to stimuli. During functional activation, neural activity in specific regions of the brain increases (Kim and Filosa, 2012) and due to this, there is an increase in oxygen demand. The increase in neuronal demand of oxygen and nutrients causes a group vascular and neural cells, referred to as the neurovascular unit (NVU), to act on blood vessels in the brain by either increasing their intraluminal diameter (vasodilation) or decreasing their

intraluminal diameter (vasoconstriction) (Peppiatt et al., 2006a). Vasodilation leads to an overcompensatory increase in oxygen supply to the specific brain region which then allows the measurement of haemodynamic changes. This action is performed mainly due to the production of vasoactive mediators and metabolites (Iadecola et al., 1995). The following section describes the NVU in detail.

1.2.1.1 Neurovascular unit

The neurovascular unit has been described previously as the coupling between neural activity and cerebral blood flow. The NVU is composed of neurons, astrocytes, endothelial cells, myocytes, pericytes and extracellular matrix components. It is the anatomical and chemical relationship between these cells that detects the metabolic demands of nearby neurons and then triggers the required responses in order to meet these demands. On one end, neurons and astrocytes facilitate synaptic transmission while at the other end astrocytes work closely with endothelial cells at the blood-brain barrier (BBB), which is a selective barrier formed by the endothelial cells that line cerebral microvessels to regulate movement of molecules (Abbott et al., 2006). Figure 1.1 shows a simplified illustration of the NVU.
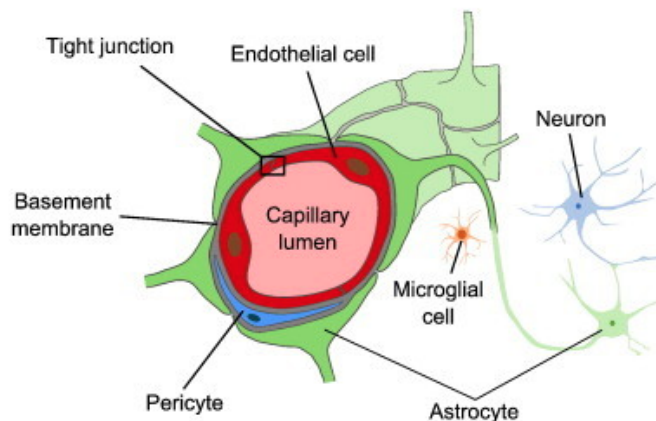
Figure 1.1: Simplified illustration of the NVU, this image was reproduced from (Heye et al., 2014) with permission.

Neurons   The basic structure of a neuron is composed of a cell body, dendrites and an axon. Neurons communicate with other neurons, glial cells (which are cells that surround neurons) and muscle cells by means of electrochemical processes. Dendrites are thin structures arising from the cell body that receive signals from the axons of other neurons via synapses and an axon is the extension of the cell body that transmits the electrical signal. Neurons form the basic building block of the NVU as they are able to detect small variations in the availability of oxygen, energy and nutrients and communicate with other cells in in order to meet metabolic requirements (Figley and Stroman, 2011). There a number of different types of neurons which include sensory neurons, motor neurons and interneurons (which are neurons that act as relay neurons). Figure 1.2 shows the basic structure of a neuron.
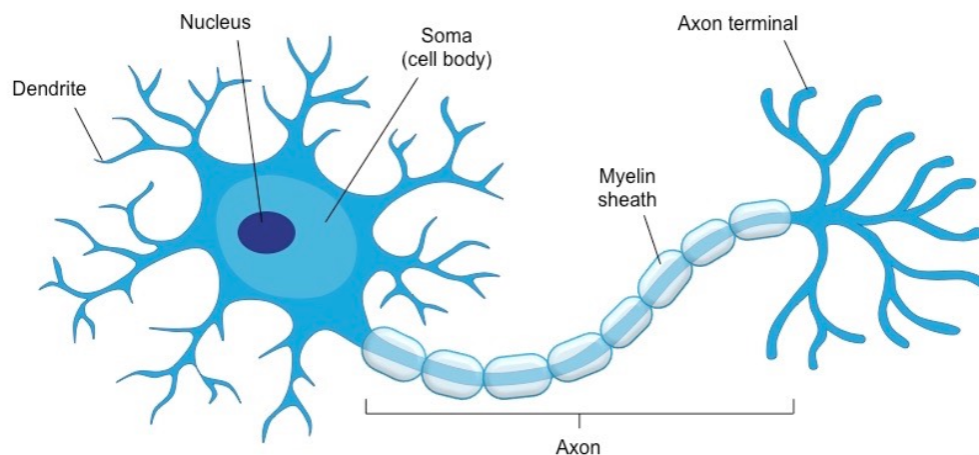
Figure 1.2:   Illustration of the basic structure of a neuron, this image was adapted from (Arizona Board of Regents, 2012)

Astrocytes   Astrocytes are a type of glial cell that mediate the coupling between neuronal activity and the subsequent change in cerebral blood flow thereby providing the link between neurons and vasculature. They have end-feet that are in close connection with walls of cerebral microvessels and support the endothelial cells in forming the BBB and are therefore deemed an important part of the NVU.

Endothelial cells   Endothelial cells are another important component of the NVU that form the BBB between the blood stream and brain tissue. They are squamous cells that line blood vessels and form tight junctions to strictly regulate the movement of substances to brain tissue. Endothelial cells also aid neurovascular coupling by being in constant communication with astrocytes in order to regulate cerebral blood flow via the release of vasoactive mediators which act on the blood vessels by causing vasoconstriction or vasodilation, thereby leading to an increase or decrease in cerebral blood flow.

Pericytes   Pericytes are contractile cells that are located at intervals along capillary walls and are important for the maintenance of the BBB. Recent studies have demonstrated that they are important regulators of blood flow and can dilate capillaries (Attwell et al., 2016; Hall et al., 2014).

Astrocytes, pericytes and endothelial cells are all indicated in Figure 1.1.

1.2.2   Cellular mechanisms

Electrical signals are propagated from one neuron to another by means of action potentials and synaptic transmission, also referred to as neurotransmission. Both of these processes are strongly interlinked and are described in the following section.

1.2.2.1   Action potentials and synapses

As mentioned previously, neurons have dendrites and axons; dendrites receive electrical impulses from other neurons while axons transmit them. The point where the axon terminal of the transmitting neuron meets the dendrites of the receiving neuron is referred to as the synaptic cleft or synapse. An electrical impulse can be classed either as excitatory or inhibitory, with an excitatory impulse causing the neuron to fire/be in an excitable state while an inhibitory impulse prevents the neuron from firing. A neuron is connected to numerous other neighbouring neurons and electrical impulses and constantly receives electrical impulses that are summated at the axon hillock. This means that if a neuron receives many excitatory impulses which, when summated, exceed the resting potential of the cell (-70mV), an action potential is generated which is then propagated along the

axon to the axon terminal for transmission to another neuron by means of a synapse. If the neuron receives multiple excitatory and inhibitory impulses, then these may cancel each other out and no action potential is generated. When an excitatory action potential is propagated to the axon terminal, it causes the membrane to become depolarised which leads to the influx of Ca^{2+} from voltage gated calcium channels. This causes synaptic vessels in the presynaptic terminal to release neurotransmitters which travel across the synaptic cleft and bind to receptor proteins in the postsynaptic terminal causing the membrane either become depolarised (as a result of an excitatory potential) or hyperpolarised (asa result of an inhibitory potential). Depolarisation of the postsynaptic terminal causes an influx of Ca^{2+} and Na^+ ions from ion channels, leading to a localised change in the membrane potential and thereby causing the neuron to generate its own action potential, which is then propagated to the axon terminal. Figure 1.3 depicts the process of a synapse.

At the synaptic cleft, the chemical neurotransmitter is rapidly removed in anticipation of the arrival other action potentials and this can be achieved in a number of ways: (i) enzymatic degradation, (ii) re-uptake by the presynaptic neuron, (iii) diffusing away from the synapse or (iv) removal by nearby glial cells.
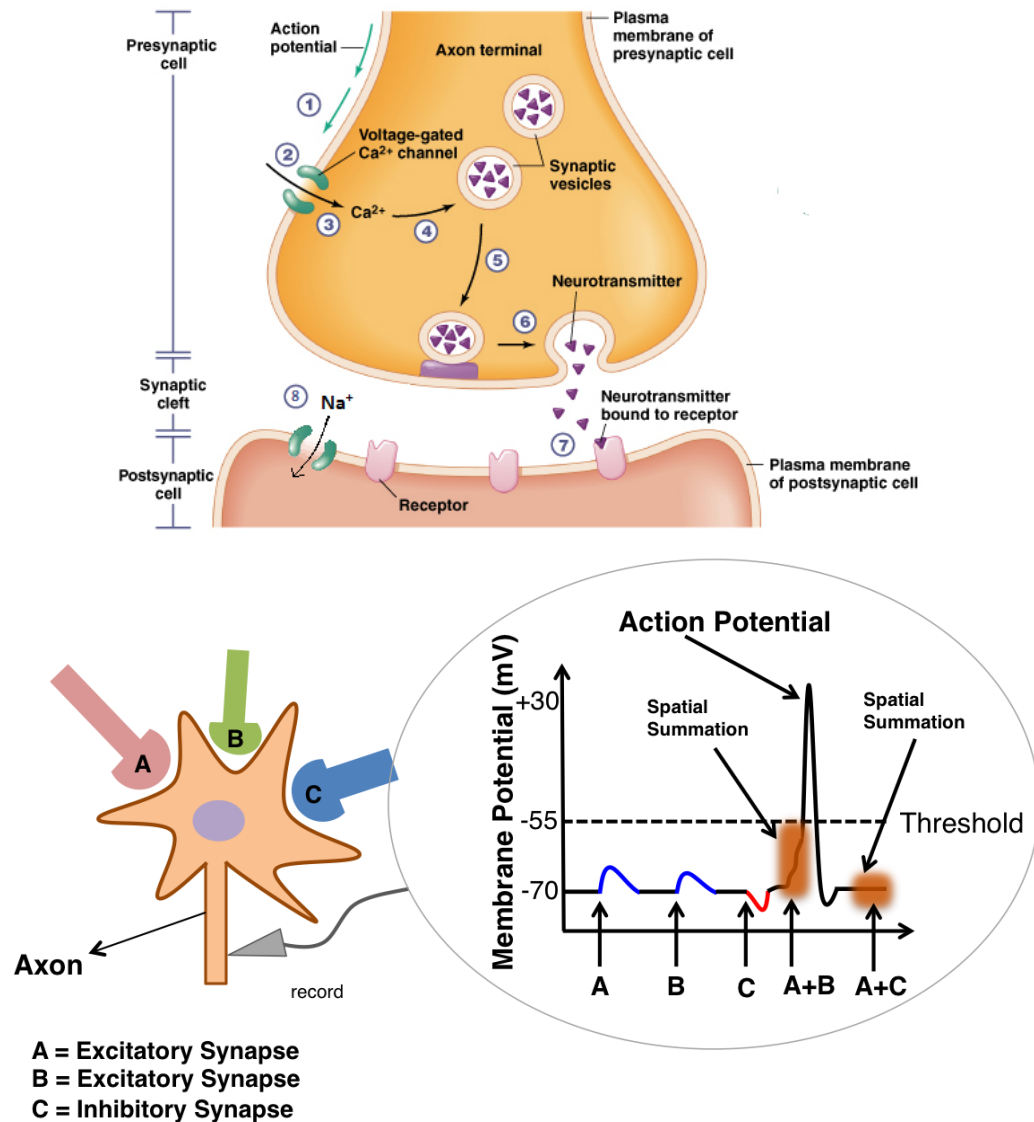
Figure 1.3: (Top) Illustration of the synaptic cleft and pre- and postsynaptic cells (this figure was reproduced from (Biology, 2016)) (Bottom) Illustration of the generation of a excitatory postsynaptic potential (EPSP) as a result of the summation of all presynaptic inputs

Synapses   Synapses may be broadly classes into two types:

1. An electrical synapse whereby the impulse is transmitted directly from the presynaptic to the postsynaptic neuron without neurotransmitters, by means of a gap junction. This allows the direct flow of ions from one neuron to the other.

2. A chemical synapse which employs the use of neurotransmitters and voltage gated channels for the transmission of the synapse from the presynaptic to postsynaptic

neuron.

There are a number of different types of neurotransmitters and each neurotransmitter has a specific receptor protein that it can act on. Broadly, there are two types of receptor proteins:

1. Ligand-activated ion channels known as *ionotropic receptors*. These are large protein complexes that act as (a) binding sites for neurotransmitters and (b) undergo a conformational change once the neurotransmitter has bound, in order to act as channels to allow ions to pass through.

2. *Metabotropic receptors* which use do not act as channels but upon binding of the neurotransmitter, employ the use of a secondary signaling pathway that causes the subsequent opening and closing of nearby ion channels to allow influx of ions.

There are a number of different types of neurotransmitters which can be classified according to their composition. These include glutamate, gamma amino butyric acid (GABA) and glycine, which are all small molecule neurotransmitters made up of amino acids. Dopamine, norepinephrine, serotonin and histamine, which are all biogenic amines made of amino acid precursors. Adenosine triphosphate and adenosine, which are nucleotides and nucleosides and lastly acetylcholine. The list of neurotransmitters is non-exhaustive and there are many others which I have not mentioned. The two main ones that I am interested in discussing are glutamate and GABA.

Glutamate is one of the primary excitatory neurotransmitters and has both ionotropic and metabotropic receptors. The ionotropic receptors are *α-amino-3-hydroxy-5-methyl-4-isoxazolepropionic acid* (AMPA), *N-methyl-D-aspartate* (NMDA) and *kainic acid.* The metabotropic receptors are referred to as metabotropic glutamate receptors (mGluRs).

GABA is an inhibitory neurotransmitter that causes hyperpolarisation of the membrane of postsynaptic neuron by causing an influx of Cl- ions. It also has both ionotropic and metabotropic receptors which are referred to as $GABA_A$ and $GABA_B$ respectively.

1.2.2.2 Energy metabolism

One component of the neurovascular coupling mechanism is neural and synaptic activity, which was just described in the previous section. Another important component is the

uptake of oxygen and glucose in order to meet the metabolic demands of the neurons. Here, the processes involved in energy generation are described.

Glycolysis   Glycolysis is the first step in the generation of energy and takes place in the cytoplasm. This process converts glucose into two pyruvate molecules and generates two ATP and two nicotinamide adenine dinucleotide (NADH).

Krebs Cycle   Pyruvate molecules that are generated in glycolysis enter the Krebs Cycle or tricarboxylic acid (TCA) cycle which further generates ATP and NADH and flavin adenine dinucleotide ($FADH_2$). These act as electron donors to the electron transport chain (ETC) which is the final stage of energy generation.

Oxidative phosphorylation   The ETC or the process of oxidative phosphorylation occurs in the inner mitochondrial membrane and accounts for most of the ATP production in cells. The ETC consists of a number of protein complexes (Complex I, Complex II, Co-enzyme Q, Complex III, Cytochrome-c and Complex IV also known as Cytochrome-c-oxidase or CCO) that are embedded in the inner mitochondrial membrane. Energy is generated in a series of oxidation and reduction (or redox) reactions whereby electrons are transferred from electron donors NADH and $FADH_2$ to electron acceptors. Coupled with this process is the transfer of H^+ ions across the mitochondrial membrane in order to generate an electrochemical proton gradient which leads to the synthesis of ATP through the activity of ATP synthase. Figure 1.4 shows the ETC (along with the other stages of energy metabolism) and the complexes involved and the arrows indicate the flow of electrons. The terminal electron acceptor is CCO which is responsible for 95% of oxygen metabolism.
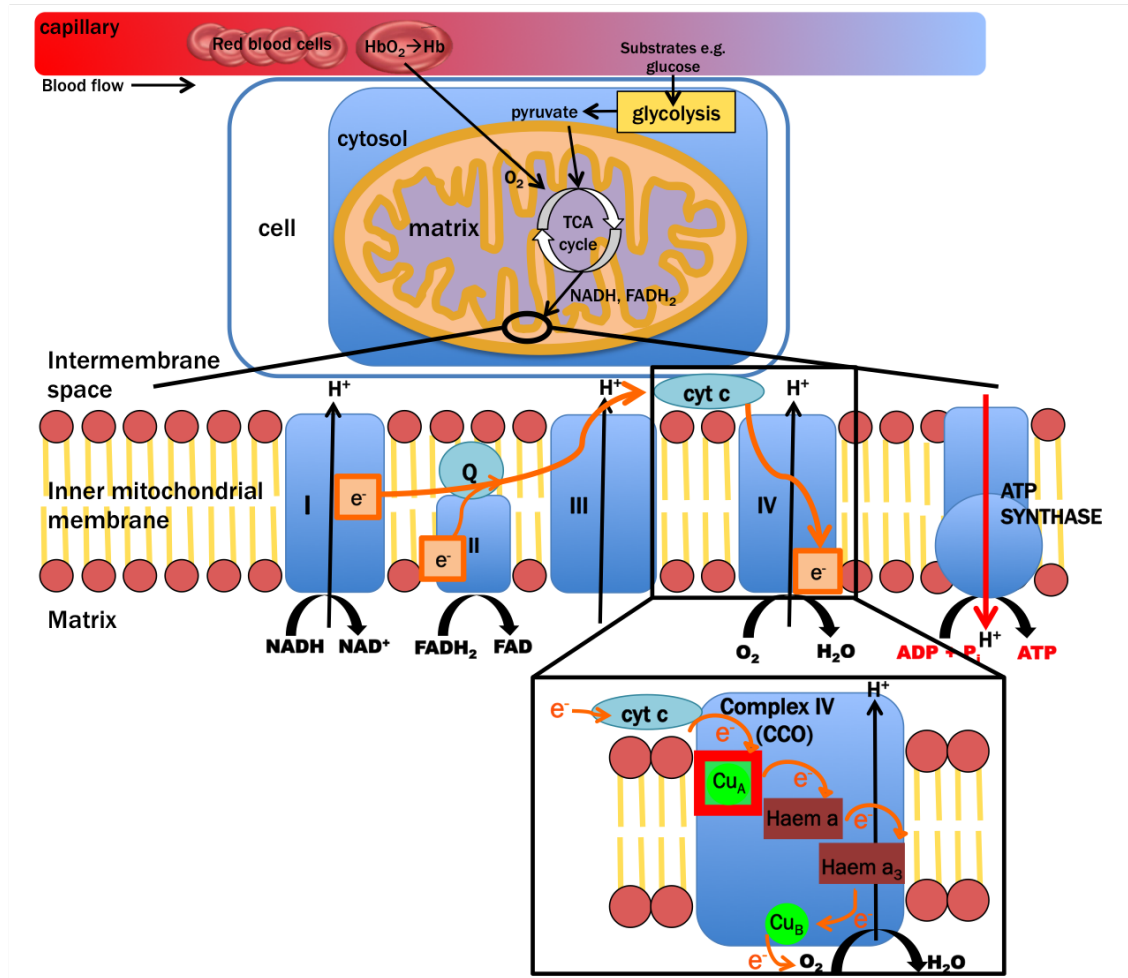
Figure 1.4: Illustration of the stages involved in energy generation which include glycolysis, the TCA cycle and the electron transport chain (ETC). This figure is my own.

The basic biological processes involved in different parts of the neurovascular coupling pathway have been discussed, providing the background to understanding the actual coupling mechanisms in play that lead to an increase in cerebral blood flow as a result of neuronal activation. While these coupling mechanisms are highly complex and not entirely understood, recent findings provide evidence implicating the roles of different components of the NVU in the process (Attwell et al., 2010a; Iadecola, 2017; Attwell and Iadecola, 2002; Cauli and Hamel, 2010a; Hamel, 2006) and the general consensus is discussed in the next section.

1.2.3 Neurovascular coupling

Traditionally, the negative feedback hypothesis was held in popular opinion to explain how neural activity controlled the vascular supply of oxygen, glucose and nutrients. This hypothesis proposes that neurons generate a metabolic signal when there is either a decrease in oxygen levels, a decrease in the concentration of glucose or an increase in the concentration of carbon dioxide which leads to an increase in blood flow. This implied that cerebral blood flow was mediated by energy demand. Recent research however, have provided evidence of a feed-forward mechanism of neurovascular coupling which proposes that cerebral blood flow is largely controlled by neurotransmitter-mediated signaling where glutamate has a major role and neurons, astrocytes and pericytes all play important roles. The feed-forward mechanism is discussed here in further detail.

Feed-forward mechanisms involve two modes of signaling:

1. **Neuronal signaling to blood vessels:** Neuronal signaling involves the release of glutamate which causes activation of the NMDA receptor site and leads to the influx of Ca^{2+} ions and the activation of the enzyme that synthesises nitric oxide (nNOS). This triggers the release of vasoactive mediator nitric oxide (NO) which acts on blood vessels causing vasodilation and leading to an increase in vascular flow (Busija et al., 2008; Attwell et al., 2010a; Lindauer et al., 1999). Another mechanism by which neurons are thought to signal to blood vessels is through neurotransmitter GABA whereby the ionotropic receptor $GABA_A$ becomes activated which mediates a component of vasodilation however its effects are not entirely understood (Kocharyan et al., 2008).

2. **Astrocyte signaling to blood vessels:** Astrocytes are conveniently located close to neurons and can therefore be influenced by neural activity and their end-foot processes envelop blood vessels which are able to control the diameter of blood vessels through the use of two mechanisms. The first of these are K^+ mechanisms, studies have suggested that when glutamate is released at a synapse, some of it travels from the synaptic cleft to the mGluR receptors that are positioned on astrocytes, thereby leading to an increase in Ca^{2+} in the astrocytes (Porter and McCarthy, 1996; Attwell

et al., 2010a). The increase in Ca^{2+} has been reported (Filosa et al., 2006) to trigger the opening of Ca^{2+} activated K^+ channels by the astrocyte end-feet, leading to a release of K^+ ions which can dilate vessels through the hyperpolarisation of smooth muscle cells that line blood vessels. Another mechanism that astrocytes may potentially employ is by the influx of Ca^{2+} that is caused by the activation of mGluR receptors on astrocytes activates a compound known as phospholipase A_2 (PLA_2) which leads to the production of arachidonic acid (AA) by membrane phospholipids. The build up of AA triggers the production of different types of metabolites - prostaglandins (PGs) and epoxyeicosatrienoic acids (EETs) which cause dilation of nearby arterioles (Metea, 2006; Gordon et al., 2008; Peng et al., 2004, 2002; Zonta et al., 2003).

These processes are summarised in Figure 1.5.
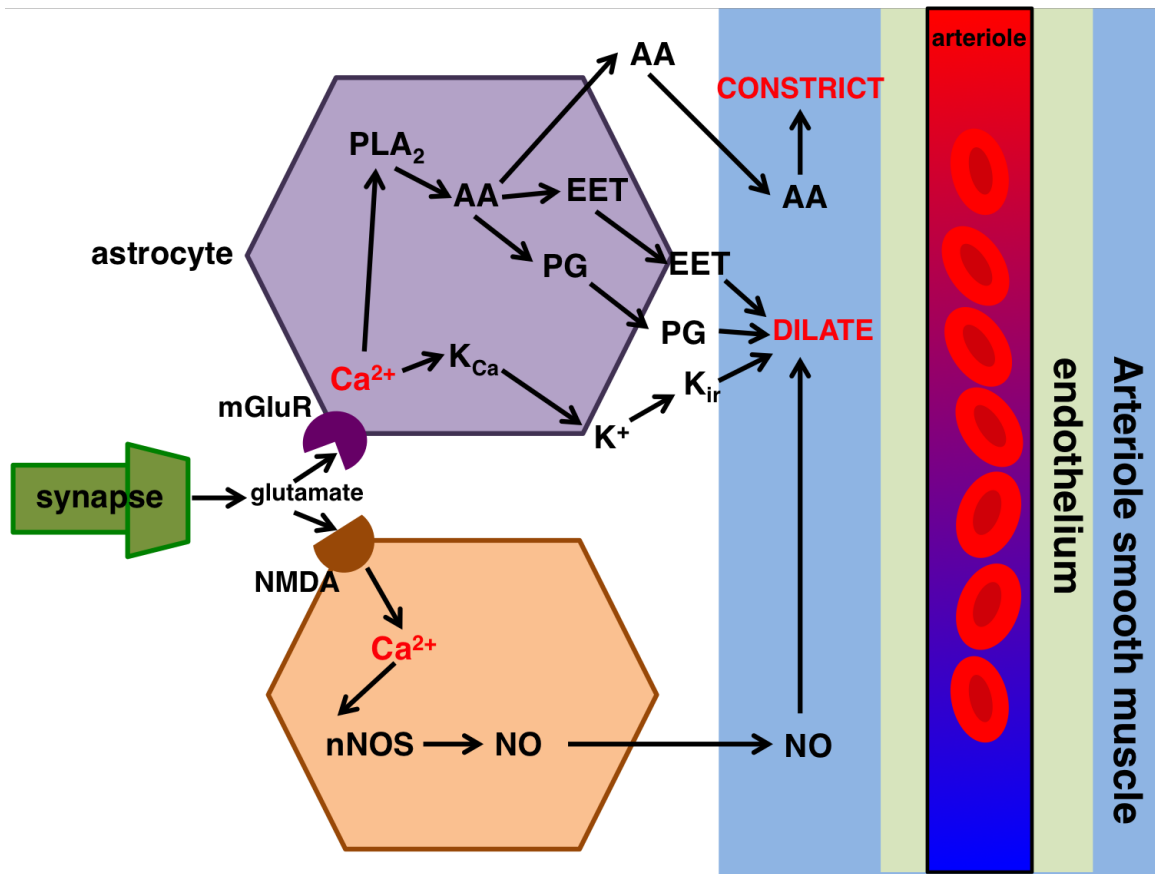
Figure 1.5: Illustration of the signalling pathways that mediate neurovascular coupling. This figure was adapted from (Harris et al., 2011). When neurons are active they release the excitatory neurotransmitter glutamate some of which binds to N-methyl-D-aspartate (NMDA) receptors in interneurons that contain neuronal nitric oxide synthase (nNOS). This causes an influx of Ca^{2+} which in turn leads to the release of nitric oxide (NO) which dilates arterioles to increase blood flow. Glutamate can also bind to metabotropic glutamate receptors (mGluR) in astrocytes which also leads to an influx of Ca^{2+} in astrocytes and causes the activation of Ca^{2+} activated K^+ channels, referred to as K_{Ca} channels. This in turn releases K^+ ions that dilate local arterioles, through hyperpolarisation of smooth muscle cells by means of inward rectifier K^+ channels (K_{ir}). The influx of Ca^{2+} ions in astrocytes can also lead to the activation of phospholipase A_2 (PLA_2) which causes the production of arachidonic acid (AA). AA can directly control vascular tone but its build up also leads to the release of a number of different metabolites which cause dilation of local arterioles; prostaglandins (PGs) and epoxyeicosatrienoic acids (EETs).

The feed-forward mechanism also implicates the roles of pericytes in neurovascular coupling, which has been a recent discovery. To recap, pericytes are cells that line the capillaries at regular intervals and it has been suggested that they are affected by the release of neurotransmitters which can cause local constriction or dilation of capillaries thereby regulating vascular supply at the capillary level .

Lastly, the feed-forward mechanism also implicates the role of pericytes in neurovascular coupling which has been a recent discovery. Pericytes are cells that line the capillaries at regular intervals and it has been suggested that they are affected by the release of neurotransmitters, thereby leading to local constriction or dilation of capillaries and hence can control/regulate vascular supply at the capillary level (Shepro and Morel, 1993; Puro, 2007; Peppiatt et al., 2006b).

1.3 Functional Near-Infrared Spectroscopy

Functional Magnetic Resonance Imaging (fMRI) and fNIRS are two neuroimaging techniques that measure the oxygen delivery component of functional hyperemia. fMRI measures changes in blood oxygenation levels while fNIRS is a non-invasive technique that uses light in the near-infrared region (NIR) of the electromagnetic spectrum to measure changes in cerebral blood oxygenation levels occurring in response to neuronal activation. Typically, the technique provides measures of oxygenated haemoglobin (HbO_2) and deoxygenated haemoglobin (HHb). Figure 1.6 shows the "classical" haemodynamic response to functional hyperemia in an adult brain where an increase in the concentration of HbO_2 ($\Delta[HbO_2]$) and a decrease in the concentration of deoxygenated haemoglobin ($\Delta[HHb]$) is observed in response to stimulation. Simply put, this can be understood as if a stimulus leads to the activation of specific cortical areas of the brain which leads to an increase in oxygen demand by the neurons, thereby causing an increase in regional cerebral blood flow whereby deoxygenated blood is rapidly replaced by oxygenated blood from which oxygen and glucose are extracted for energy generation. The increase in metabolic demand leads to an overcompensatory increase in oxygenated blood and this large increase is what is then measured by fNIRS and provides a measure of the oxygen delivery component of neurovascular coupling.
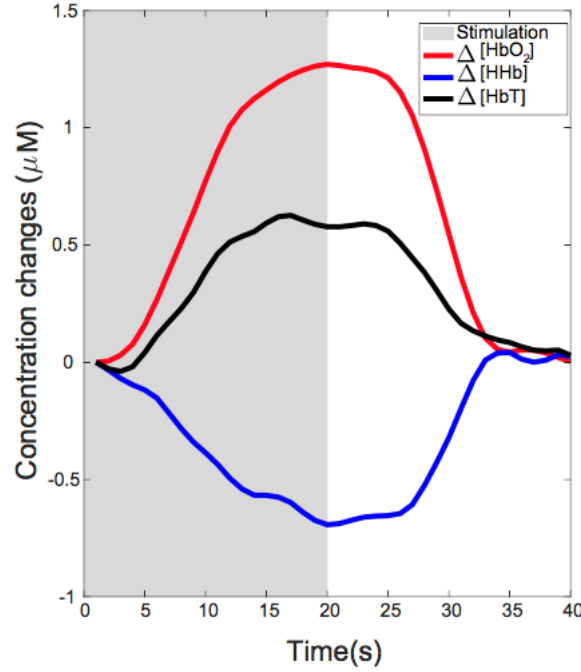
Figure 1.6: The classical haemodynamic response to stimulation as measured by fNIRS, displaying an increase the concentration of oxygenated haemoglobin (red trace), a decrease in the concentration of deoxygenated haemoglobin (blue trace) and an increase in the concentration of total haemoglobin (black trace). This figure was reproduced from (Phan, 2018) with permission.

Broadband NIRS is a type of NIRS that may be used to obtain measurements of cellular oxygen consumption and energy metabolism through the measurement of the oxidation status of mitochondrial ETC enzyme cytochrome-c-oxidase (Δ[oxCCO]), alongside measuring changes in Δ[HbO$_2$] and Δ[HHb]. This can provide a more direct marker of neural activity as it informs on cellular changes occurring within the neurovascular coupling pathway as opposed to changes in oxygen delivery. CCO measurements using NIRS will be described in later sections.

1.3.1 The haemodynamic response in the developing brain

More work has been done to understand the functional hyperemia response in adults than in infants. In adults the observed changes in Δ[HbO$_2$] and Δ[HHb] are immediate as both vasculature and neurovascular coupling mechanisms are fully developed and extensive

neuronal networks have already formed for information processing. In infants however, many of these processing are under rapid development. Further, neurovascular coupling, where a number of different biological pathways are at a complex interplay, may be different in the developing brain. There is evidence from developmental studies indicating that both neural circuitry and cerebral vasculature are under ongoing maturation during development. Moreover, neuronal networks involved in the processing of various stimuli are also under development, for example Watanabe et al (2012a) used NIRS in an infant study and reported activation (i.e. an increase in $\Delta[HbO_2]$ and a decrease in $\Delta[HHb]$) to black and white checkerboard stimuli and a deactivation to unpatterned luminance stimuli (i.e. a decrease in $\Delta[HbO_2]$ and an increase in $\Delta[HHb]$). This led the authors to postulate that the brain networks involved in the processing of the unpatterned stimuli were underdeveloped. A combination of these factors is likely to lead to variability in the haemodynamic response function (HRF) which has been reported in many studies, with some studies describing an observed increase in $\Delta[HbO_2]$ and a decrease $\Delta[HHb]$ in response to the stimuli while others report the opposite pattern. This makes it challenging to interpret results and forms part of the motivation for this PhD thesis. In the following sections an overview is provided of the different studies that have reported variability in the HRF in infancy, categorised by brain region which include occipital, temporal and posterior temporo-parietal.

1.3.1.1 Occipital Lobe

Meek et al (1998) measured changes in $\Delta[HbO_2]$ and $\Delta[HHb]$ over the occipital cortex in response to visual stimulation which consisted of a black and white inverting checkerboard, in infants aged between 2 days to 3-months-old. Heterogeneity was observed in the haemodynamic response with half the infants displaying an increase in $\Delta[HHb]$ and a decrease in $\Delta[HbO_2]$ while half of the infants displayed the classical response (i.e. an increase in $\Delta[HbO_2]$ and a decrease in $\Delta[HHb]$ in response to the stimulus), regardless of the age of the infants. Another study also measured NIRS responses over the occipital and frontal areas in response to a reversing checkerboard and to a face-like pattern with blinking eyes, in infants aged between 2-4-months-old (Taga et al., 2003). While the checkerboard pattern elicited the classical response, a decrease in $\Delta[HbO_2]$ and an increase in $\Delta[HHb]$ was ob-

served in response to the face-like pattern in the occipital lobe. Furthermore, Watanabe et al (2012a) also demonstrated differences in the occipital region in the response to a black and white reversing checkerboard in comparison to a high luminance unpatterned stimulus which led to a decrease in $\Delta[HbO_2]$ and in increase in $\Delta[HHb]$, in 6-month-old infants using a high density NIRS system. Moreover, a NIRS study measured responses over the occipital cortex to faces and visual noise in 4-month-old infants and adults and reported that the face stimuli produced a decrease in $\Delta[HbO_2]$ in the infants (Csibra et al., 2004). The results from these studies are in contrast with previous work where visual stimuli with varying features (included colour, shape, movement and orientation) demonstrated the classical haemodynamic response (Bortfeld et al., 2007; Wilcox et al., 2005b; Taga et al., 2004; Watanabe et al., 2008; Wilcox et al., 2008; Watanabe et al., 2010). In addition to fNIRS studies, a number of fMRI studies have also reported inverted BOLD responses to visual stimulation in infants (Yamada et al., 1997; Born et al., 2002; Yamada et al., 2000; Born et al., 2000; Martin et al., 1999a).

1.3.1.2 Temporal and Parietal Lobes

A study measuring NIRS responses to auditory stimulation (music) in newborns over the temporal and frontal cortical regions demonstrated heterogeneity of the haemodynamic response with 60% of the infants displaying an increase in $\Delta[HHb]$ and the remainder displaying a decrease in $\Delta[HHb]$ (Sakatani et al., 1999a). Wagner et al (2011) conducted an investigation with two groups (aged 7 and 9-months) and measured NIRS responses over the left and right lateral regions of the brain, in response to complex speech stimuli. The stimuli elicited both the classical response as well as inverted responses. More specifically, a developmental shift was observed with the 7-month-old infants displaying a decrease in $\Delta[HHb]$ and an increase in $\Delta[HbO_2]$ while the 9-month-old infants showed the opposite pattern of responses to the same stimuli. Other studies involving neonates investigating language processing (Abboub et al., 2016; Issard and Gervain, 2017) and the processing of auditory stimuli (Telkemeyer et al., 2009) reported differences in responses between conditions as well as across participants. A study of 5-to-8-month-old infants reported both classical and inverted responses (i.e. an increase in $\Delta[HHb]$ and a decrease

in $\Delta[HbO_2]$ in response to the stimulus) to visual stimuli consisting of faces and vegetables (Kobayashi et al., 2011). Despite the diversity in responses observed in these studies, the classical haemodynamic response is observed in the temporal cortex increasingly often from 3 months onwards (Lloyd-Fox et al., 2009), even in infants born preterm (Emberson et al., 2017). In fact, Lloyd-Fox et al (2017) demonstrated, with the use of auditory and visual stimuli to measure responses over the posterior temporo-parietal region in infants from birth till 24-months of age, in a cohort of Gambian infants, that the classical haemodynamic response was present in early infancy (although delayed) and that the response became faster across development, these responses are shown in Figure 1.7 charting the haemodynamic responses from birth to 24-months-old.
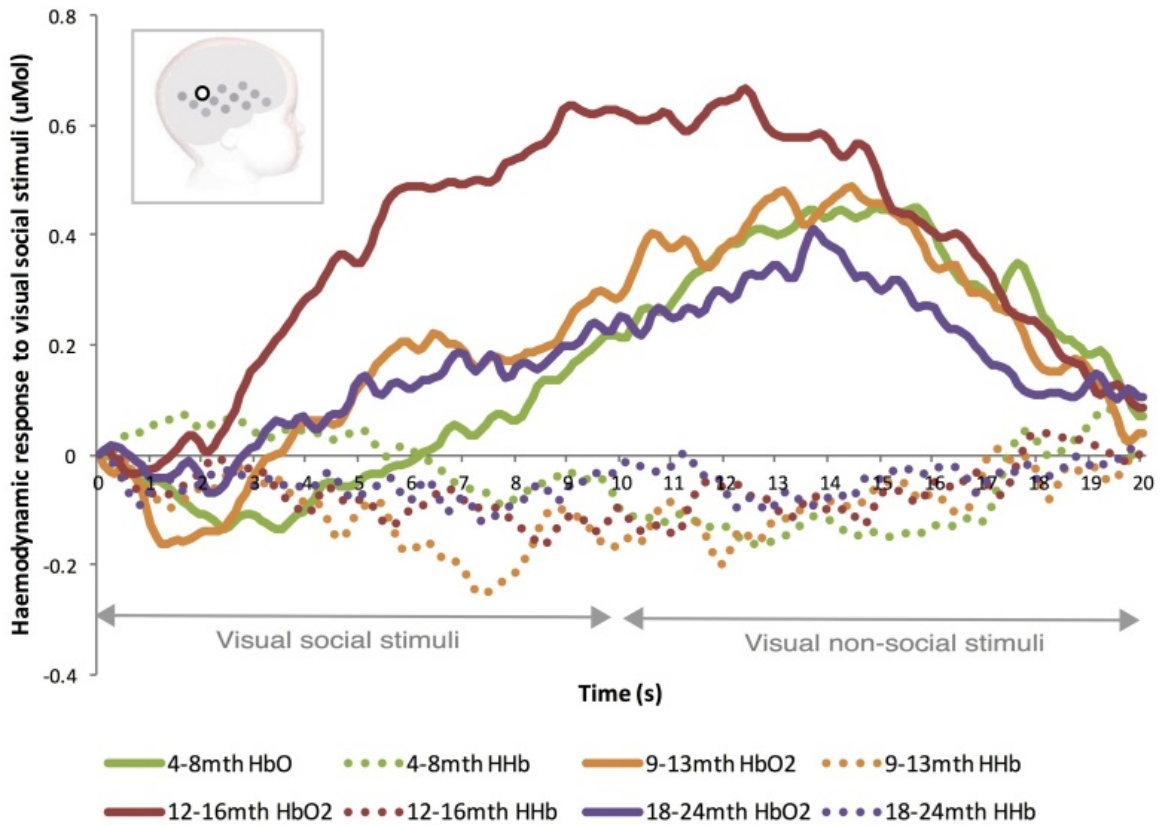
Figure 1.7: Changes in the haemodynamic response to visual social and non-social stimuli from birth till 24 months of age. This figure was reproduced from (Lloyd-Fox et al., 2017) with permission. The solid lines indicate $\Delta[HbO_2]$ and the dotted lines indicate $\Delta[HHb]$ over time which is in seconds.

More invasive work has been performed in rats[1] using optical imaging methods to measure changes in $\Delta[HbO_2]$ and $\Delta[HHb]$ during somatosensory stimulation by Kozberg and colleagues (2013a). This work charts the development of the haemodynamic response across development from birth to adulthood and has shown that at P12-13 (equivalent to the human newborn) the rats displayed an inverted response to the stimulus. Figure 1.8 shows the development of the haemodynamic response from days P12-13 to adulthood, from this study, There is a clear transition of the response from increasing $\Delta[HHb]$ to increasing $\Delta[HbO_2]$ as the rats age. Further work by the same group using a different type of imaging method (wide-field optical imaging of both neural activity and haemodynamics) again using somatosensory stimulation in mice from birth to adulthood (Kozberg and Hillman, 2016b) demonstrated that in P7 mice strong localised neural activity was present while functional hyperemia developed more gradually. They further showed that this development occurred alongside the development of neural circuitry. Moreover, Zehendner et al (2013) used somatosensory stimulation in postnatal mice P7 and P30, using laser-Doppler-flowmetry to measure changes in regional cerebral blood flow (rCBF) alongside multi-electrode recordings to record neural activity. They demonstrated a decrease in rCBF in P7 mice which was associated with neural fatigue while an increase in rCBF was observed in the adult mice. The responses are not charted across development however. Additionally, it must be noted, as the authors have stated, that brain development in mice is yet to be extensively mapped to human brain development and the observation of strong inverted responses particularly in P7 mice, may be the human equivalent of the fetal brain with early human infancy falling in between the transition from inverted responses to classical responses leading to the observed variability in the haemodynamic response.

---

[1]The approximate correspondence between stages of human and rodent brain development may be taken as follows; rats and mice postnatal day 7 (P7) to P35 corresponds to from birth to approximately 18 years of age (Lenroot and Giedd, 2006; Pujol et al., 1993), P30 - P42 maps onto human adolescence (Spear and Brake, 1983) and the rodent brain is considered as adult by P60.
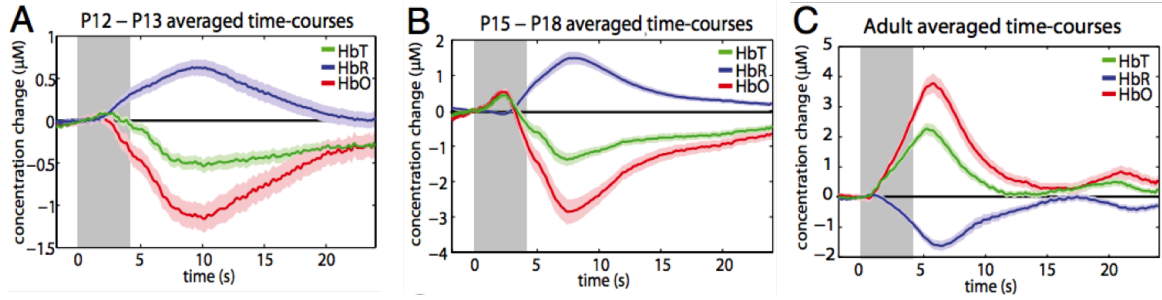
Figure 1.8: Changes in the haemodynamic response from P12-13 to adulthood in rats. This figure was reproduced from (Kozberg et al., 2013a) with permission.

While many infant studies report the presence of an increase in $\Delta[HbO_2]$ and a decrease in $\Delta[HHb]$ to various stimuli during functional activation starting from early infancy (Wilcox et al., 2013; Ichikawa et al., 2013; Grossmann et al., 2008; Hyde et al., 2010; Minagawa-Kawai et al., 2007, 2008; Homae et al., 2006; Wilcox et al., 2005a; Lloyd-Fox et al., 2009) indicating that neurovascular coupling is intact in the developing brain, the results from the studies discussed here demonstrate that variability is present in the observed responses across development and cortical regions. In particular, the human infant studies suggest that the occipital cortex displays the most variability while the temporal cortex starts to display the classical haemodynamic response earlier and shows a clearer developmental trajectory. There may be multi-factorial reasons leading to the observed heterogeneity in the HRF (Issard and Gervain, 2018). These may well include developmental vascular and structural changes occurring within the brain but the effect of stimulus complexity and experimental design may also play an important role. The studies presented in this thesis (particularly in the latter half) explore these factors but a particular emphasis is placed on exploring changes occurring at a neurobiological level through the use of broadband NIRS to measure changes in cellular energy metabolism alongside haemodynamic changes, simultaneously with EEG. This allows the measurement of three different components of the neurovascular coupling mechanism and the exploration of their relationship in the developing human brain. These three components include; (i) *neural activity* (occurring as a result of the presentation of an experimental stimulus and measured by EEG), (ii) *cerebral oxygen utilisation and energy metabolism* (caused by increased neural activity and measured

by Δ[oxCCO]) and (iii) *cerebral haemodynamic changes* (that occur as a consequence of increased neuronal activity and measured by Δ[HbO$_2$] and Δ[HHb]).

The use of broadband NIRS simultaneously with EEG can also allow investigation of early differences in neurovascular related metabolic pathways in atypical brain development. Recent work in the field of autism has demonstrated differences in neural processing in the ASD brain (Jung et al., 2016; Kita et al., 2011; Zhu et al., 2014; Chien et al., 2015) and evidence of neurophysiological differences in the ASD brain are emerging (Belger et al., 2011b; Chauhan et al., 2011; Gu et al., 2013; Anitha et al., 2012). In particular, in the search for precursory biomarkers that associate to the onset of ASD symptoms later in life (Johnson et al., 2015), recent longitudinal studies of infants at high-risk for autism have reported early differences in neural processing (Lloyd-Fox et al., 2013; Blasi et al., 2015; Braukmann et al., 2018; Jones et al., 2014a; Zwaigenbaum et al., 2007a; Szatmari et al., 2016; Lloyd-Fox et al., 2009). Therefore another motivation of this PhD is to explore these differences.

The following section provides an overview of neurovascular coupling mechanisms in the developing brain and a review of the evidence of ongoing maturation of vasculature and neural circuitry is provided; both in typical an atypical brain development.

1.3.1.3 Neurovascular coupling in the developing brain

1.3.1.3.1 Development of neural vasculature and the NVU

1.3.1.3.1.1 *Cerebral blood flow* Previous studies provide evidence of differences in rCBF, regional cerebral metabolic rate of oxygen consumption (rCMRO$_2$) and the regional oxygen extraction fraction (rOEF) using single-photon emission computed tomography (SPECT) (Chiron et al., 1992) and positron-emission tomography (PET) (Takahashi et al., 1999). The studies demonstrated that rCBF and rCMRO$_2$ were significantly lower in early infancy in comparison to adults and increased over development until the age of 7 and then declined to adult values, a pattern that is similar to that of neural synapse formation and elimination (Kozberg and Hillman, 2016a).

1.3.1.3.1.2 *Capillaries and Arteries*   Only recently has the role of capillaries been implicated in neurovascular coupling, with studies hypothesising a potential mechanism involving capillaries. This hypothesis postulates that neurovascular coupling is initiated in the capillary bed (Hall et al., 2014; Hamilton, 2010; Hill et al., 2015) and that in fact capillaries are able to regulate blood flow through the actions of pericytes and smooth muscle cells on the capillary wall (Hill et al., 2015; Iadecola, 2017). Once initiated in the capillaries, functional hyperemia is thought to then spread to arterioles (Tian et al., 2010) and finally reaches larger pial arteries that are located on the surface of the brain (Chen et al., 2011, 2014). These studies indicate that capillaries play a critical role in the generation of a response to stimulation and work investigating the development of cerebral microvasculature in rats (Rowan and Maxwell, 1981) and humans (Norman and O'Kusky, 1986) has demonstrated extensive postnatal structural changes that occur within cerebral vasculature which includes the growth, extension and proliferation of new blood vessels and blood vessel density. Further, the results from the rat study (Rowan and Maxwell, 1981) additionally exhibited a relationship between development of vasculature and an increase in cerebral metabolic activity. Moreover, work in mice by (Kozberg et al., 2013b) (which I have discussed previously) showed that initial local functional hyperemia was present in P15-18 mice only at the capillary and arteriole level and further exploration revealed that this early increase in oxygenation was predominantly in veins. In adults however, the initial hyperemia is strongly observed in pial arteries. This suggests that the recruitment of pial arteries during neurovascular coupling is also a developmental mechanism.

Moreover, the work by Rowan and Maxwell (1981) also demonstrated that it is only postnatally that arteries start to acquire unique characteristics. This may imply that vascular reactivity (i.e. change in vascular tone; vasoconstriction and vasodilation) may change over development. It was discussed previously that NO is synthesised by NOS. NOS has many isoforms one of which is endothelial NOS (eNOS) primarily responsible for the generation of NO in vascular endothelium. In a study of rats by Bustamante et al (2008) eNOS expression was shown to be 85% lower in the 1-month-old brain in comparison to the 14-month-old brain and Chen et al (2014) showed that an intact endothelium was required in order to back propagate the neurovascular response from capillary bed to pial arteries.

Previous studies have also shown an underdevelopment of endothelium and arteries in the developing brain (Zehendner et al., 2013). This work would be in line with the evidence provided by previously discussed work (Kozberg et al., 2013a) where the functional hyperemia was restricted to the capillary bed and arterioles (or brain parenchyma).

These studies highlight that the underdeveloped state of cerebral vasculature can have a significant effect on the neurovascular coupling mechanism in the developing brain.

1.3.1.3.1.3 *Pericytes* The role of pericytes in neurovascular coupling has only recently been reported and they have been shown to be important regulators of blood flow by being able to have a direct effect on capillaries (Hall et al., 2014; Armulik, 2005; Attwell et al., 2016). Previous work suggests that pericytes are underdeveloped postnatally (Kozberg and Hillman, 2016a; Fujimoto, 1995).

1.3.1.3.1.4 *Astrocytes* The importance of astrocytes in neurovascular coupling has already been discussed in previous sections. Similarly to pericytes, astrocytes have been shown to be undergoing maturation in P21 rats and do not reach adult levels until P50, this includes the size, number, connectivity and branching of the astrocytes (Seregi et al., 1987; Stichel et al., 1991; Kozberg and Hillman, 2016b). Furthermore, the pathways involving astrocytes may be altered in development particularly as mGluR5 receptor has been shown to be differentially expressed regionally (Van Den Pol et al., 1995) and across development (Romano et al., 1995). More specifically, it is up-regulated early in life, decreases by the first postnatal week and by postnatal week 3 it is undetectable (Sun et al., 2013) while mGluR3 is expressed in astrocytes across all developmental stages and is known to be employed in adult signaling pathways. Therefore, in comparison to the adult brain, neuron-glial signaling may be performed in a different manner during brain development.

1.3.1.3.2 Development of neural structures and circuitry

1.3.1.3.2.1 *Synaptogenesis and synapse pruning* The importance of synapses has been discussed in previous sections. Synaptogenesis refers to the process through which synapses form between neurons. It is well known that synapse formation begins during

gestation (Huttenlocher and Dabholkar, 1997; Bianchi et al., 2013) and synaptic density continues to increase rapidly reaching its peak in the first year of life (Tierney and Nelson, 2009). Regional differences in peaking of synaptogenesis have been reported with areas such as the visual cortex peaking around the 4-8 months postnatally (Garey and de Courten, 1983) while the prefrontal cortex continues to peak until around 15 months (Tierney and Nelson, 2009). Following the overproduction of synapses, synaptic pruning takes place in order to decrease synaptic density and is largely driven by experience. Pruning has also been shown to occur at different times in different cortical regions (Huttenlocher and Dabholkar, 1997; Tierney and Nelson, 2009; Garey and de Courten, 1983; Harris et al., 2011).

1.3.1.3.2.2 *GABAergic neurons, synapses and inhibition* Another important component in the development of neural circuitry is the refinement and maturation of the GABAergic system, which has been shown to undergo development from birth until adulthood (Harris et al., 2011; Ben-Ari, 2002a) and occurs at different times across different brain regions (Le Magueresse and Monyer, 2013). The inhibition of GABAergic interneurons, which are known to have an important role in neurovascular coupling mechanisms (Iadecola, 2017; Cauli, 2004), is particularly important as it has been suggested to modulate neural firing in contrast to glutamatergic neurons that provide a mode of fast communication of neural information through excitation (Andersen et al., 1963; Buhl et al., 1994; Miles and Wong, 1984). The balance between excitation and inhibition (E/I) therefore, is particularly critical for the development of neural circuitry and networks in the brain (Akerman and Cline, 2007). Moreover, it has been hypothesised that the E/I balance in the developing brain is different to that in adults with GABAergic neurons in early infancy being excitatory rather than inhibitory (Ben-Ari, 2002b; Yamada et al., 2004; Rivera et al., 1999; Ganguly et al., 2001) which is thought to be due to the effect of a potassium chloride co-transporter not being fully active, preventing the influx of Cl- ions when necessary. Therefore, this leads GABAergic neurons to cause depolarisation rather than hyperpolarisation and therefore being excitatory rather than inhibitory. Previous work in mice has shown that GABA undergoes a transition from being excitatory to inhibitory after the first week postnatally

(which would be the equivalent of early infancy in humans), thereby affecting the E/I balance in the developing brain which would in turn affect neurovascular coupling.

1.3.1.3.2.3 *Neuronal migration*   Neuronal migration is the process by which neurons locomote from their place of birth in deeper layers of the brain to their intended locations. There a number of mechanisms through which this cell migration takes place which include radial migration (Nadarajah et al., 2001), tangential migration (Rourke et al., 1995) and multipolar migration (Tabata and Nakajima, 2003). Recent work on infant postmortem brain tissue has demonstrated that this process continues to occur for at least a few months postnatally in the frontal lobe where the neurons then continue to proliferate, differentiate and eventually integrate into neural circuitry (Paredes et al., 2016). The study further found that the migrating cells were specifically inhibitory neurons, an increase of which postnatally would affect the excitation/inhibition balance of the brain. Other studies have further demonstrated that neuronal migration of certain cell types continues into adulthood (Spalding et al., 2013).

1.3.1.3.2.4 *Amine system development*   As discussed previously, a specific class of neurotransmitters are composed of amino acid precursors. The importance of these neurotransmitters in cognitive development (attention in particular) has emerged (Frederick and Stanwood, 2009; Harris et al., 2011; Ansorge et al., 2004; Rebello et al., 2014; Page et al., 2009) and previous studies have shown postnatal increase in the development of these neurotransmitter systems (Lambe et al., 2000; Murrin et al., 2007) which vary across different brain regions thereby influencing functional development across cortical regions (Levitt et al., 1997).

1.3.1.3.3 Development of metabolic environment   PET work in infants has shown lower cerebral metabolic rate of oxygen consumption ($CMRO_2$) which progressively increases until late childhood (Chugani et al., 1987). Moreover, work in rats (Kozberg and Hillman, 2016b) has demonstrated that although large neural responses were present in response to somatosensory stimulation, there was an absence in functional hyperemia until P23 and additionally that there was a lower rate of oxygen metabolism, in comparison to adults,

which gradually increases with age. This work might suggest that oxidative metabolism in the developing brain also undergoes maturational changes and some studies hypothesis that there may be a mechanism of anaerobic energy generation in place during development (Kozberg and Hillman, 2016b; Bilger and Nehlig, 1991; Bonavita et al., 1962; Booth et al., 1980).

Figure 1.9 summarises the developmental vascular and neural circuitry changes that were discussed here, occurring from childhood to adulthood.
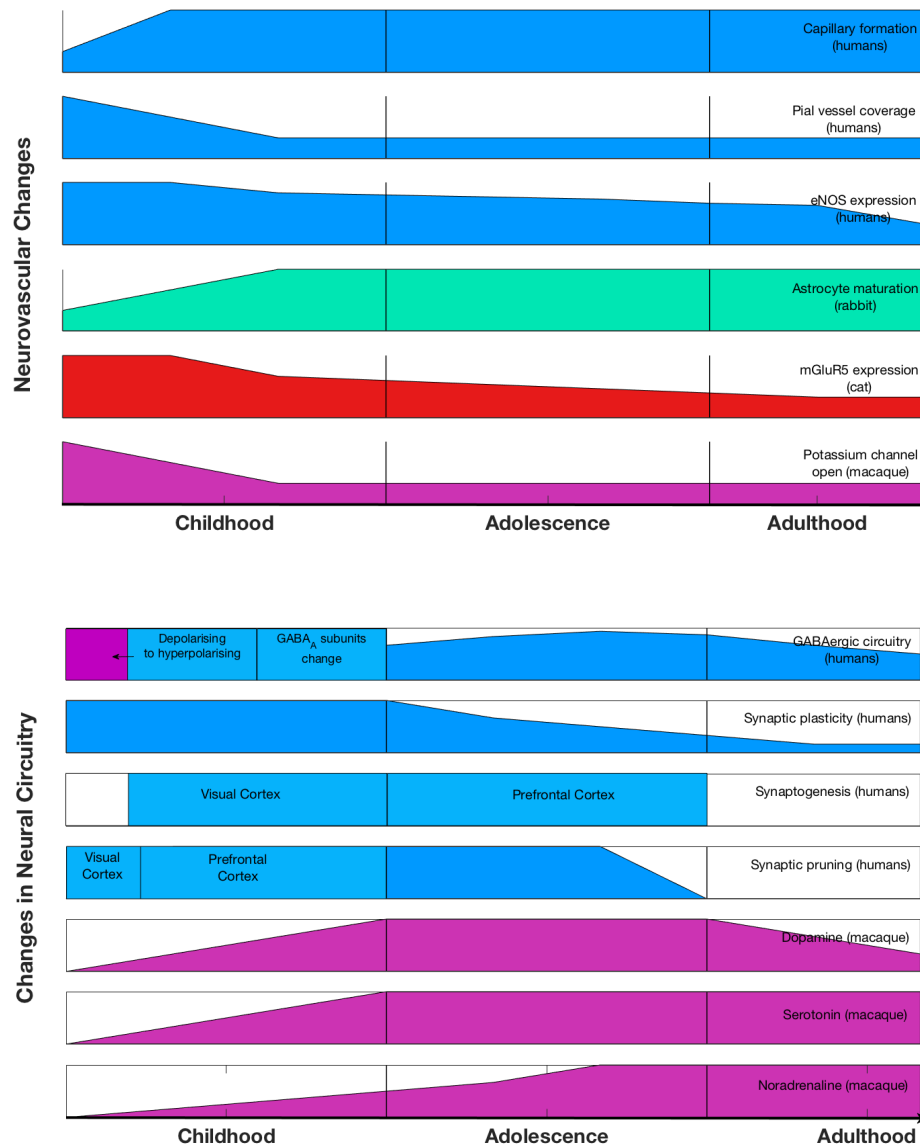
Figure 1.9: Summary of the developmental vascular and neural circuitry changes that occur from childhood to adulthood. This figure was adapted from (Harris et al., 2011).

1.3.1.4 Neurovascular coupling in autism

ASD is classified by the Diagnostic and Statistical Manual of Mental Disorders (DSM-5) (2013) as a group of neurodevelopment disorders which include Asperger's syndrome, autistic disorder, childhood disintegrative disorder and pervasive developmental disorder ASD is diagnosed based on behavioural observations which include repetitive behaviours, diminished verbal and non-verbal communication and impaired social interaction which are thought to be a result of atypical brain development. Much work has been done to explore differences in neuronal activity between ASD and non-ASD groups and while these studies explore differences in neural processing (typically measured through techniques such as EEG, fNIRS and fMRI). More specifically, recent work by Lloyd-Fox et al (Lloyd-Fox et al., 2018, 2013) which was replicated by others (Braukmann et al., 2018) demonstrated significant differences between infants (aged 6-months-old) with low familial risk of autism and high familial risk of autism in the processing of social stimuli in the temporal cortex using fNIRS, particularly in infants that later went on to receive an autism diagnosis at 3 years of age. These results indicate that the NIRS can be a useful tool in investigating atypical brain development and in potentially identifying early markers of autism. Less work has been done to investigate how alterations in oxygen consumption, energy metabolism and the neurovascular coupling mechanisms may lead to apparent differences in neural processing. It is clear that neurovascular coupling is a highly complex mechanism involving numerous neuronal and glial pathways that may not necessarily have linear relationships. Small alterations in any of these pathways may therefore result in observed differences in neural activity. Broadband NIRS provides the opportunity to investigate any potential differences in the neurovascular coupling that may be occurring in atypical brain development through measurement of oxygen consumption. In this section, a review of the existing evidence on neurovascular coupling in autism is provided.

1.3.1.4.1 Neural vasculature

1.3.1.4.1.1 *Vasoactive mediators* NO is a key vasoactive mediator that is responsible for vasoconstriction and vasodilation of blood vessels and has previously been implicated

in ASD (Sogut et al., 2003; Sweeten et al., 2004; Chauhan and Chauhan, 2006; Akyol et al., 2004). Previous work measuring nitrate levels in plasma of children with autism (Zoroglu et al., 2003) has reported an up-regulation of NOS in the group with autism, in comparison to controls. Furthermore, work by Fatemi and colleagues (2000) used a mouse model of autism to demonstrate that there was an increased expression of NOS in anterior brain regions. Given that NO plays an important role in neurovascular coupling, any abnormalities in the production or activity of it may affect neurovascular coupling mechanisms.

1.3.1.4.1.2 *Astrocytes* While in the typical population mGluR5 receptors have increased expression in astrocytes during infancy which reduces in adulthood (Sun et al., 2013), previous studies have demonstrated that children with autism display an even larger increase in expression of astrocytic mGluR5 in comparison to controls (Fatemi and Folsom, 2011; Fatemi et al., 2011; Zoghbi and Bear, 2012). To recap, mGluR5 receptors are activated by glutamate that is released during synaptic signaling and causes the production of vasoactive messengers leading to vasoconstriction or dilation thereby regulating blood flow (Attwell et al., 2010b). Differences in the expression of mGluR5 may therefore affect the relationship between synaptic activity and the observed haemodynamic response in children (Harris et al., 2011).

1.3.1.4.2 Neural circuitry

1.3.1.4.2.1 *GABAergic function* There is evidence that there is an increased expression of enzymes that synthesise GABA while the $GABA_A$ and $GABA_B$ receptors are down-regulated in the ASD brain (Fatemi et al., 2002a, 2009, 2010). This would imply that in autism, there would be an overall reduction in the basal activity of GABA receptors while excess GABA was being synthesised, thereby leading to an overall decrease in inhibition and an increase in neuronal excitation and hence neural activity. Increased neural activity may (i) lead to increased cerebral metabolic demand (Weiss et al., 2008) and (ii) cause increased glutamate release thereby triggering vasodilators and increasing blood flow. Both of these factors could potentially lead to observed differences in haemodynamic changes

measured through fNIRS or fMRI. It would also affect the E/I balance of the brain, an imbalance of which has been postulated in autism (Lee et al., 2017; Rubenstein and Merzenich, 2003; Snijders et al., 2013; Selten et al., 2018; Gogolla et al., 2009) and includes many signaling pathways in the brain. This discussion is beyond the scope of this chapter.

1.3.1.4.2.2 *Amine system*   One of the more important amine system neurotransmitters is serotonin which, as I described previously, has an important role in cognitive development but also in neural developmental processes such as cell proliferation, differentiation and migration (Riccio et al., 2009; Muller et al., 2016; Fujimiya et al., 1986). Cohen et al (1997) have hypothesised that serotonin may also play a role in regulating cerebral microcirculation through vasoconstriction. In studies of children with autism using PET, reduced serotonin synthesis has been demonstrated in comparison to controls (Chugani et al., 1999a; Nakamura et al., 2010), meanwhile studies using SPECT have shown that there may potentially be a reduced re-uptake of serotonin after synaptic transmission (Makkonen et al., 2008). An increase or decrease in serotonergic activity could therefore affect brain responses. The reader is referred to a review by Muller et al (Muller et al., 2016) for a detailed review on serotonin signaling abnormalities in ASD.

1.3.1.4.3   Metabolism

1.3.1.4.3.1 *Mitochondrial dysfunction*   In 1985, Coleman and Blass hypothesised that mitochondrial dysfunction was an underlying comorbidity of autism (Coleman and Blass, 1985). Recent work in post-mortem brain tissue of children with ASD has demonstrated reduced expression of ETC genes (Ginsberg et al., 2012; Anitha et al., 2012; Gu et al., 2013) in the autism group in comparison to controls, in addition to regional differences (i.e. an increase in some regions and a decrease in others) in ETC complexes (Chauhan et al., 2011; Tang et al., 2013; Goldenthal et al., 2015). Whole genome gene expression analysis studies have also reported differences in ETC complex gene expression in ASD individuals (Anitha et al., 2012; Chen et al., 2015). These studies provide evidence of altered oxidative phosphorylation in the ASD brain which may imply that greater levels of oxygen and glucose may be required in order to meet the metabolic demands of the brain.

1.3.1.4.3.2 *Oxygen consumption and glucose utilisation* Following on from mitochondrial dysfunction, previous studies in adults with autism (Rumsey et al., 1985) have provided evidence of increased glucose uptake while others have suggested altered energy metabolism (Chugani et al., 1999b; Friedman et al., 2003). Weiss and colleagues in studies of Eker rats (rat model of autism) (2007; 2008; 2012) have demonstrated an increase in the basal consumption of oxygen in the rats with autism in comparison to controls. In line with the idea of impaired energy metabolism in ASD, increased oxygen and glucose consumption would make sense if the process of cerebral energy metabolism was unable to meet the metabolic demands of the brain. An imbalance between metabolic demand and supply would result in alterations in neurovascular coupling and could potentially be observed in the responses measured by fNIRS. As discussed earlier, previous studies have suggested that an increase in energy demand in autism may be due to reduced activity of GABA receptors leading to an overall increase in excitation and therefore neural activity leading to an increase in energy demand.

Table 1.1 shows a summary of the evidences of altered neurovascular coupling in autism.

1.3.2 Metabolic marker of brain activity

1.3.2.1 Broadband NIRS

As described previously, NIRS is a non-invasive technique that allows measurement of changes occurring within biological tissue. Typically NIRS systems use dual-wavelength systems in order to provide information about cerebral blood oxygenation, i.e. changes in $\Delta[HbO_2]$ and $\Delta[HHb]$. However, measures of changes in cerebral cellular oxygen metabolism can also be obtained using a different type of NIRS, referred to as broadband NIRS, through measurement of changes in $\Delta[oxCCO]$. Broadband NIRS uses multiple wavelengths of light in order to obtain changes in $\Delta[HbO_2]$, $\Delta[HHb]$ and $\Delta[oxCCO]$. Previously, commercial systems with narrow bandwiths have been developed (Brazy et al., 1985; Zaramella et al., 2001a). Recently, the Biomedical Optics Research Laboratory (BORL) at University College London (UCL) and other research groups (Nosrati et al., 2016a; Rajaram et al., 2018; Wang et al., 2016) have recently been developing novel broadband NIRS systems in order

Mediator	Phenotype	Model	Method	Reference
Vasoactive mediators	Increase NO production	Human	Measurement of nitrite levels in plasma	(Zoroglu et al., 2003; Sweeten et al., 2004)
	Increased expression of nNOS	Mouse model of autism	Gel electrophoresis and Western blotting	(Fatemi et al., 2000)
Astroctyes	Increase levels of mGluR5	Human	Western blotting	(Fatemi and Folsom, 2011; Fatemi et al., 2011; Zoghbi and Bear, 2012; Lee et al., 2017)
GABAergic signalling	Reduced expression of enzymes that synthesise GABA	Human	Western blotting	(Fatemi et al., 2002b)
	Downregulation of GABA$_A$ and GABA$_B$ receptors	Human	Western blotting	(Fatemi et al., 2009, 2010)
	Excitation/Inhibition balance	N/A	N/A	(Lee et al., 2017; Rubenstein and Merzenich, 2003; Snijders et al., 2013; Gogolla et al., 2009)
Serotonin	Reduced serotonin synthesis	Human	PET, high pressure liquid chromatography	(Chugani et al., 1999a; Nakamura et al., 2010; Connors et al., 2006)
	Reduced re-uptake of serotonin post synaptic signalling	Human	SPECT	(Makkonen et al., 2008)
Oxygen/Glucose consumption	Increased glucose utilisation	Human	PET	(Rumsey et al., 1985)
	Increased basal consumption of oxygen	Rat model of autism	Cryomicrospectrophotometry	(Weiss et al., 2007, 2008, 2012)
	Altered energy metabolism	Human	Plasma lactate levels	(Chugani et al., 1999b; Friedman et al., 2003)
Mitochondrial function	Abnormal markers of mitochondrial function	Human	^{31}P MRS	(Minshew et al., 1993)
	Abnormal ETC complex activity	Human	Western blotting	(Chauhan et al., 2011; Tang et al., 2013; Goldenthal et al., 2015)
	Mitochondrial DNA over replication and deletions	Human	Quantification of gene expression (q-PCR)	(Giulivi et al., 2010)
	Decreased ETC complex gene expression	Human	Whole genome gene expression analysis	(Ginsberg et al., 2012; Gu et al., 2013)

Table 1.1: Summary of the studies providing evidence of altered components of neurovascular coupling in autism.

to measure changes in oxCCO. To date, there has been significant interest in obtaining these measurements primarily in a clinical setting and there are only a few reports of functional activation studies. This section provides an overview of the studies that have so far used NIRS to measure changes in oxCCO.

1.3.2.2   Clinical studies

Over recent years, there has been an increase in interest to measure oxCCO in order to obtain a new marker for metabolic function for use as a non-invasive, bedside, clinical monitoring technique. oxCCO has been shown to be more brain specific than haemoglobins (de Roever et al., 2016) and has shown to correlate more strongly with Phosphorus Magnetic Resonance Spectroscopy (^{31}P MRS) markers of mitochondrial function (Bainbridge et al., 2014). It is therefore appealing as a unique biomarker of cerebral metabolic activity particularly in conditions such as hypoxia, stroke and brain injury where energy failure may take place or there might be mitochondrial impairment. In particular, the alternative to using NIRS is either MRI or MRS both of which require the use of a scanner and are not only expensive, but cannot be used as early as the first day of life in some clinical populations. NIRS on the other hand is an inexpensive, portable and non-invasive alternative.

1.3.2.2.1   Neonates/Infants   Over the years there have been a number of studies using oxCCO in the hospital to monitor neonates. One of the earliest reports used NIRS to monitor preterm neonates was in 1985 by Jöbsis's group (Brazy et al., 1985) using a three-wavelength system where a decrease in Δ[oxCCO] was reported in response to spontaneous oxygen desaturations in three preterm infants. It is worth noting that the original target for Jöbsis's work in 1977 (Jobsis, 1977) was oxCCO. Neurological deficits can lead to mortality after cardiac procedures and it has been suggested that they could be caused by cerebral hypoxia, which is the condition during which brain tissue is deprived of oxygen, occurring during the surgery (Nollert et al., 1998). A previous study by Plessis et al (1995) used a commercial system to monitor cerebral hypoxia or brain injury that may occur during infant cardiac surgery and reported a decrease in Δ[oxCCO] during the part of the surgery where deep hypothermic circulatory arrest was administered. This is a technique

used during surgery that involves cooling the body in order to suspend blood circulation and brain function for up to 30 minutes. Many adult studies have used NIRS in a similar context as a neuro-monitoring technique during cardiac surgery (Kakihana et al., 2002; Nollert et al., 1998) and brain injury (Tisdall et al., 2008; Highton et al., 2014) however for the purposes of keeping this overview relevant these are not discussed here. Moreover, a recent study involving investigation of neonatal stroke using broadband NIRS found asymmetrical cerebral metabolic function as early as the first day of life (Mitra et al., 2016), demonstrating that not only does oxCCO provide a measure of cerebral metabolic function but predictive assessment using NIRS can be done earlier than MRI. Recent interest has gathered in investigating neonatal brain injury and hypoxia ischaemia encephalopathy (HIE), which is defined as a class of brain injury occurring when the neonate's brain tissue does not receive adequate oxygen supply. A study investigated neonatal encephalopathy (NE; brain damage) using a broadband NIRS system over the frontal lobe and left and right hemispheres (Bale et al., 2014) in conjunction with Proton MRS (^{1}H MRS) and found that oxCCO was significantly correlated with the ^{1}H MRS biomarkers of NE. Further studies have been performed by the same group with larger sample sizes in new borns with acute brain injury and demonstrated that oxCCO along with systemic measurements could be used to predict severity of injury while haemodynamic responses could not (Bale et al., 2016b). The most recent study using the same system in HIE neonates also showed the oxCCO correlated with the outcome and it was possible to perform this measurement prior to the use of an MRS scanner which is the gold standard marker for outcome of HIE (Bale et al., 2018).

1.3.2.2.2 Piglets Studies have also been performed in piglets using ^{31}P MRS and broadband NIRS where HI was induced in piglets by surgically isolating the carotid artery (Bainbridge et al., 2014). There, the authors reported that oxCCO correlated with MRS markers of mitochondrial function and in addition to this, the outcome of the piglet at 48 hours was related to the recovery of the ratios of oxCCO and MRS biomarkers after the HI insult.

These studies demonstrate that oxCCO is a useful marker of metabolic function that can be obtained non-invasively using NIRS in the clinic. For a more detailed review of

clinical applications, the reader is referred to a recent review by Bale et al (2016a).

1.3.2.3 Functional activation studies

1.3.2.3.1 Adults Broadband NIRS has been used in a number of different adult studies to measure changes in oxCCO alongside changes in HbO_2 and HHb. Heekeren et al used visual stimulation in the form of an inverting red/green checkerboard while measuring responses over the visual cortex, using an in-house built broadband NIRS system (Heekeren et al., 1999a). The authors reported an increase in $\Delta[oxCCO]$ in response to the stimulus. An inverted checkerboard was also used in another study measuring $\Delta[oxCCO]$, $\Delta[HbO_2]$ and $\Delta[HHb]$ over the occipital lobe (Phan et al., 2016a) which also reported increases in $\Delta[oxCCO]$ and $\Delta[HbO_2]$ in response to the stimulus and additionally demonstrated distinct spatial localisation of each of the chromophores. Previous studies have also used anagram solving tasks over the prefrontal region (Kolyva et al., 2012; de Roever et al., 2017; Ghosh et al., 2012) reporting majority of the responses observed to be increases in $\Delta[oxCCO]$ and $\Delta[HbO_2]$ in response to the task however some heterogeneity was observed in the oxCCO response. A study using a driving simulation task (Nosrati et al., 2016b) measured responses over the prefrontal cortex using an in-house built broadband NIRS system and demonstrated differences in task-related responses in $\Delta[oxCCO]$ which were consistent with changes in $\Delta[HbO_2]$.

1.3.2.3.2 Infants There is only one reported study of the use of NIRS to measure $\Delta[oxCCO]$ in functional activation in infants. Zaramella et al (2001b) used a commercial NIRS system and measured $\Delta[oxCCO]$, $\Delta[HbO_2]$ and $\Delta[HHb]$ over the left and right temporal regions in response to auditory stimulation in newborns. While the authors reported heterogeneity in the haemodynamic response (i.e. some infants displaying an increase in $\Delta[HbO_2]$ in response to the stimulus and some displaying a decrease), no changes were observed in $\Delta[oxCCO]$. The only other published use of this technique in infants during functional activation is by the first study presented in this thesis, described in Chapter 4.

Table 1.2 provides a summary of the studies which were discussed in this section.

Type of study	Participants	Methods	Pathology	Stimulus	Reference
Clinical	Neonates	NIRS	Preterm neonates	-	Brazy 1985
	Infants	NIRS, Systemic measurements	Cerebral hypoxia during cardiac surgery	-	Plessis 1995
	Adults	NIRS, Systemic measurements	Cerebral hypoxia during cardiac surgery	-	Kakikhana 2002, Nollert 1998
		NIRS	Brain injury	-	Tisdall
		NIRS	Brain haemorrhage	-	Highton, 2014
	Neonates	NIRS	Stroke	-	Mitra, 2016
	Neonates	NIRS, ^{1}H MRS	NE	-	Bale, 2014
	Neonates	NIRS, Systemic measurements	Acute brain injury	-	Bale, 2016
	Neonates	NIRS	HIE	-	Bale, 2018
	Piglets	NIRS, ^{31}P MRS	HIE	-	Bainbridge, 2014
Functional Activation	Adults	NIRS	-	Visual stimulation	Heerken, Phan 2016
	Adults	NIRS	-	Anagram solving task	Kolyva, Roever, Ghosh
	Adults	NIRS	-	Driving simulation task	Nosrati, 2016
	Infants	NIRS	-	Auditory stimulation	Zaramella et al
	Infants	NIRS	-	Visual and auditory stimulation	Siddiqui et al, 2017

Table 1.2: Summary of studies measuring oxCCO in adults, neonates, infants and piglets.

1.3.2.4 oxCCO during functional activation - why measure it?

oxCCO provides a unique marker that, as previous studies have shown, correlates with biomarkers of energy metabolism and mitochondrial function. Therefore in the context of infants where neurovascular coupling mechanisms and neurometabolic pathways are not very well understood, measuring oxCCO could potentially provide an intermediate measure of metabolic activity which can further aid our understanding of human brain development. It can also be useful in investigating neurodevelopmental disorders such as autism where many components of the neurovascular coupling pathway including mitochondrial function have been implicated. Not only this, but measuring oxCCO may be particularly useful in atypical populations such as infants at high genetic risk of autism, where studies have been performed to search for early biomarkers.

1.3.3 Summary

This thesis presents research on the application of broadband near-infrared spectroscopy (NIRS), simultaneously with electroencephalography (EEG), in order to gain a better understand of neurovascular coupling mechanisms and metabolic pathways in typical and

atypical brain development. This PhD pioneered the use of broadband NIRS to measure changes in cellular energy metabolism in awake infants and therefore many methodological challenges needed to be overcome.

Chapter 2 provides an overview of both NIRS and EEG techniques. It outlines the basic principles of light propagation in tissue and discusses the different types of NIRS instrumentation in order to help the reader understand how broadband NIRS systems differ from dual-wavelength commercial NIRS systems and how they can be used to obtain cellular measurements of the change in oxidation state of mitochondrial enzyme cytochrome-c-oxidase (oxCCO). The chapter also details the neural basis of the EEG signal and provides a description of the EEG equipment that is used in the studies presented in Chapters 4, 5 and 6. Finally, data processing streams for both NIRS and EEG are described in detail.

An important aspect of my research has been to develop 3-dimensionally (3-D) printed headgear for use with broadband NIRS systems, particularly for use simultaneously with EEG. **Chapter 3** discusses the various designs that were developed and used during the studies presented in this thesis.

Chapter 4 presents the first study of this PhD work that involved using only NIRS to measure haemodynamic changes and changes in oxCCO during functional activation in typically developing infants, using social dynamic auditory and visual stimuli that have been used previously for many NIRS studies (Lloyd-Fox et al., 2014a, 2009). A single channel miniature broadband NIRS system was used for this study and while the results provided limited information about metabolic processes in the developing infant brain, it was an important methodological milestone demonstrating that broadband NIRS could be used to measure cellular changes resulting from brain activation in early infancy.

While the overall aim of my PhD has been to investigate neuronal functional in infants, **Chapter 5** presents the second study which used simultaneous multi-channel broadband NIRS and EEG during a visual checkerboard paradigm, in adults. This was a necessary step prior to carrying out this work in infants as a number of methodological developments needed to be made. These included development of headgear, experimental paradigms and data analysis methods. All of these are described in detail in this chapter and influenced subsequent work presented in Chapters 6 and 7.

Chapter 6 details the first part of the third study which involved simultaneous multi-channel NIRS and EEG in typically developing infants. This study follows up from work presented in Chapter 4, by measuring brain activity over the temporal cortex in response to dynamic social and non-social auditory and visual stimuli. The results shed a light on the status of neurovascular coupling in infants.

The study presented in **Chapter 7** was performed in the same session as that of Chapter 6 however this study follows on from work presented in Chapter 5 and measured brain activity in response to visual stimuli over the occipital cortex. The study showed differences in neurovascular coupling in comparison to adults and regional differences between temporal and occipital cortices were observed. The study was therefore extended to investigate neurovascular coupling in atypical brain development.

The final study of this PhD is described in **Chapter 8** where the same experimental procedures and paradigms were used to investigate neurovascular coupling in infants at-risk for developing autism spectrum disorders. While the study was a preliminary one and had very few subjects, potentially interesting patterns of atypical neurovascular coupling mechanisms have emerged.

Chapter 9 presents a general discussion, conclusions from this thesis and future directions.

Chapter 2

TECHNIQUES FOR INFANT BRAIN IMAGING: THEORY, FUNDAMENTALS AND INSTRUMENTATION

This chapter discusses the various techniques that are currently used for functional neuroimaging in infants. Near-infrared spectroscopy (NIRS) and electroencephalography (EEG) were the two modalities that were used for the studies presented in this thesis therefore the fundamentals of NIRS, including light propagation in tissue are described in detail, and an overview of different types of NIRS instrumentation is provided with a particular focus on broadband NIRS. The principles of EEG are also discussed and a general overview of data analysis of both NIRS and EEG data is provided.

2.1   Fundamentals of NIRS

Near-infrared spectroscopy is a non-invasive technique first described by Jobsis in 1977 (1977) and that takes advantage of the translucency of tissue to in the near-infrared (NIR) region of the electromagnetic spectrum (650 - 1000 nm), in order to assess changes in

haemodynamics and metabolism. Continuous-wave (CW) NIRS was used for the work presented in this thesis which allows for monitoring of changes in the concentration of at least three chromophores present in tissue; oxygenated haemoglobin (HbO$_2$), deoxygenated haemoglobin (HHb) and the oxidation state of cytochrome-c-oxidase (oxCCO). Compounds that absorb light in the spectral region of interest are known as chromophores. The absorption of light by these chromophores depends upon whether they are carrying oxygen and the propagation of light in tissue is affected by the scattering and absorption of the illuminated tissue. In order to understand and interpret NIRS measures, light transport in tissue needs to be discussed in detail.

2.1.1 Light Transport in Tissue

Light transport is dependent upon two phenomenon which attenuate light as it passes through tissue - absorption and scattering and these are influenced by chromophores, the wavelength of light used, absorbing compounds present in the tissue as well as the structure of the tissue. Both of these processes are described in detail in the following sections.

2.1.1.1 Absorption

The absorption of light traveling through a non-scattering, homogenous medium was described by Bouger in 1729 as the fraction of the light intensity I, incident upon successive layers of equivalent thickness in a non-scattering medium, being absorbed in equal measures. In 1760, Lambert transcribed this relationship into a mathematical equation:

$$\frac{\delta I}{I} = -\mu_a.\delta d \tag{2.1}$$

where δd is the thickness of the absorbing medium, μ_a (cm^{-1}) is referred to as its absorption coefficient and defined as the probability that a photon is absorbed in the medium per unit length travelled. $\frac{\delta I}{I}$ represents the fraction of incident light that gets absorbed by the medium. Equation 2.1 can be alternatively expressed as:

$$I = I_0 e^{-\mu_a.d} \tag{2.2}$$

where I is the transmitted light intensity after the incident light intensity I_0 travels through a non-scattering medium of thickness d (cm) (alternatively referred to as the optical pathlength) that has absorption coefficient μ_a. In 1852, Beer expressed the relationship between the absorption coefficient μ_a and the concentration of c, the absorbing compound in a non-absorbing solution as the following:

$$\mu_a = \alpha.c \tag{2.3}$$

where α is referred to as the specific absorption coefficient $(molar^{-1}.cm^{-1})$. The Lambert-law and the Bouger-law can be combined to derive the Beer-Lambert law which describes the absorption of light intensity in a non-scattering medium. The law states that the absorbance of a compound in a non-absorbing medium is proportional to its concentration c in the solution, its specific absorption coefficient μ_a and the optical pathlength d. This can be derived from combining equations 2.2 and 2.3 to form Equation 2.4 and is shown in Figure 2.1:

$$I = I_0 e^{-\alpha.c.d} \tag{2.4}$$
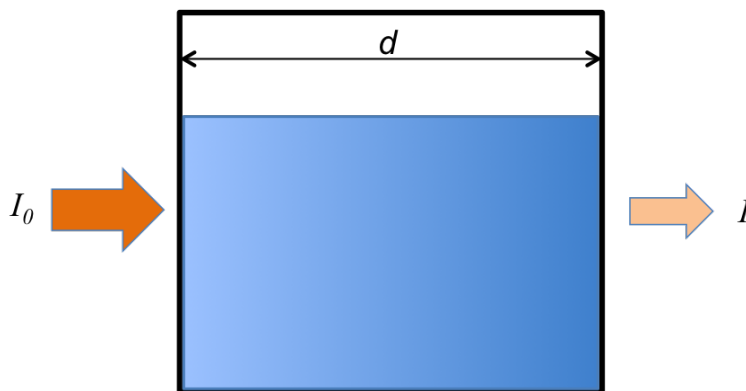
Figure 2.1: Model for Beer-Lambert Law in a non-absorbing medium with incident light intensity I_0, transmitted light intensity I and pathlength d.

A non-absorbing medium may contain multiple absorbing compounds therefore the absorbance of the medium can be described as the sum of the contributions of each compound, c_1, c_2,...,c_n. Equation 2.4 can be further expanded to include this:

$$I = I_0 e^{-(\alpha.c_1 + \alpha.c_2 + ... + \alpha.c_n).d} \tag{2.5}$$

2.1.1.2 NIRS chromophores in biological tissue

Compounds that absorb light in the spectral region of interest are known as chromophores. Biological tissue consists of several principal chromophores, each with an individual absorption spectrum (describing the level of absorption at each wavelength) and concentration. Figure 2.2 shows the absorption spectra for different chromophores in biological tissue from 100 to 10,000 nm. In near-infrared spectroscopy, the chromophores that are of interest are those whose absorption spectra vary with their oxygenation status. These chromophores are discussed in the following sections.
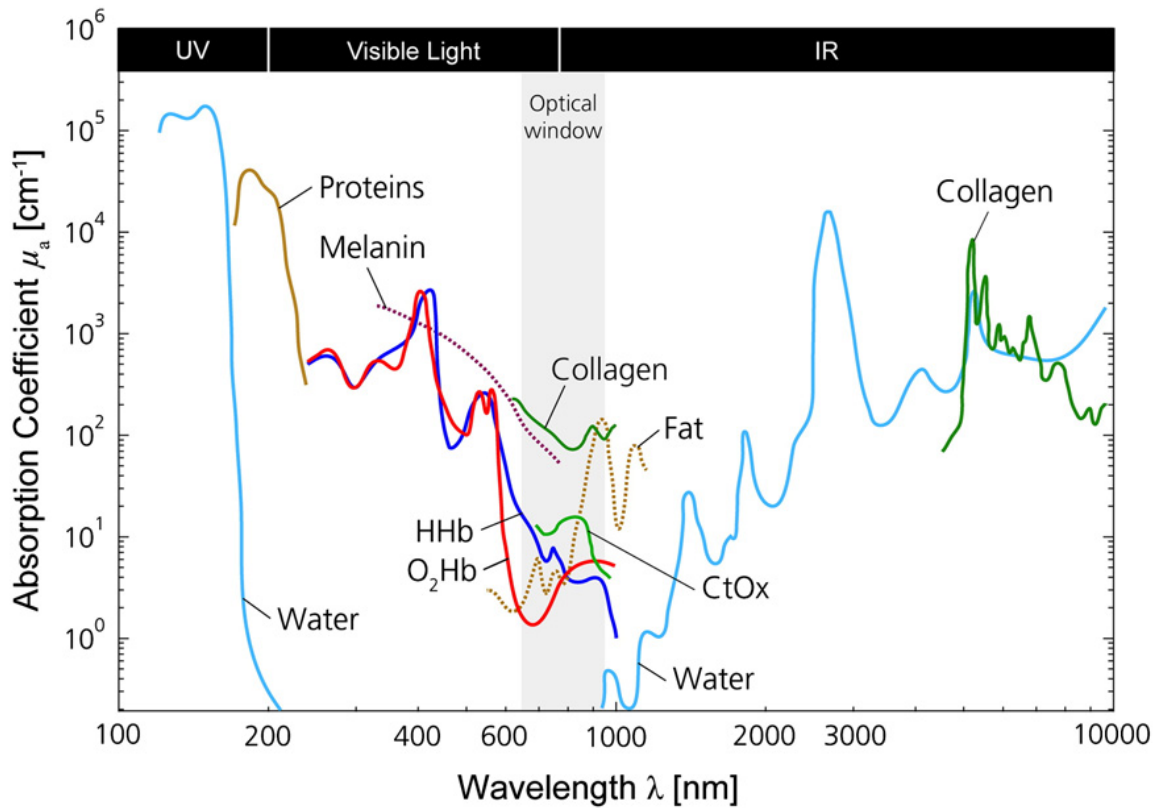
Figure 2.2: Absorption spectra of different chromophores in biological tissue shown between 100 to 10,000 nm. Figure reproduced from (Scholkmann et al., 2014) with permission.

Water 60 - 90% of the adult human body is composed of water which is one of the major chromophores found in biological tissue. As shown in Figure 2.2, the absorption of water is relatively low in the region 200 - 900 nm, with a sharp increase beyond 900 nm which continues to increase with increasing wavelength of light. The high concentration and absorption of water in tissue limits the tissue thickness that light can penetrate and therefore, the window for spectroscopic work is defined based on the region where the absorption of light by water is relatively low; 650 - 900 nm presents a window of transparency for near-infrared spectroscopy measurements.

Lipids Lipids can be considered as a fixed constant absorber of light. While the absorption of light by is thought to be similar to that of water, the concentration of lipids in the brain is relatively low. Therefore for brain functional activation measurements, lipids do not contribute greatly to the attenuation of light.

Haemoglobin Haemoglobin is one of the most important absorbers of light in the near-infrared region and therefore for NIRS measurements. Oxygen binds reversibly to haemoglobin causing a conformational change in the molecular structure of haemoglobin resulting in two species namely oxygenated haemoglobin (HbO_2) and deoxygenated haemoglobin (HHb), both of which have distinct absorption spectra in the NIR region, shown in Figure 2.3. The differences in the spectra allow for quantification of the contribution of each of these species to the attenuation of light.
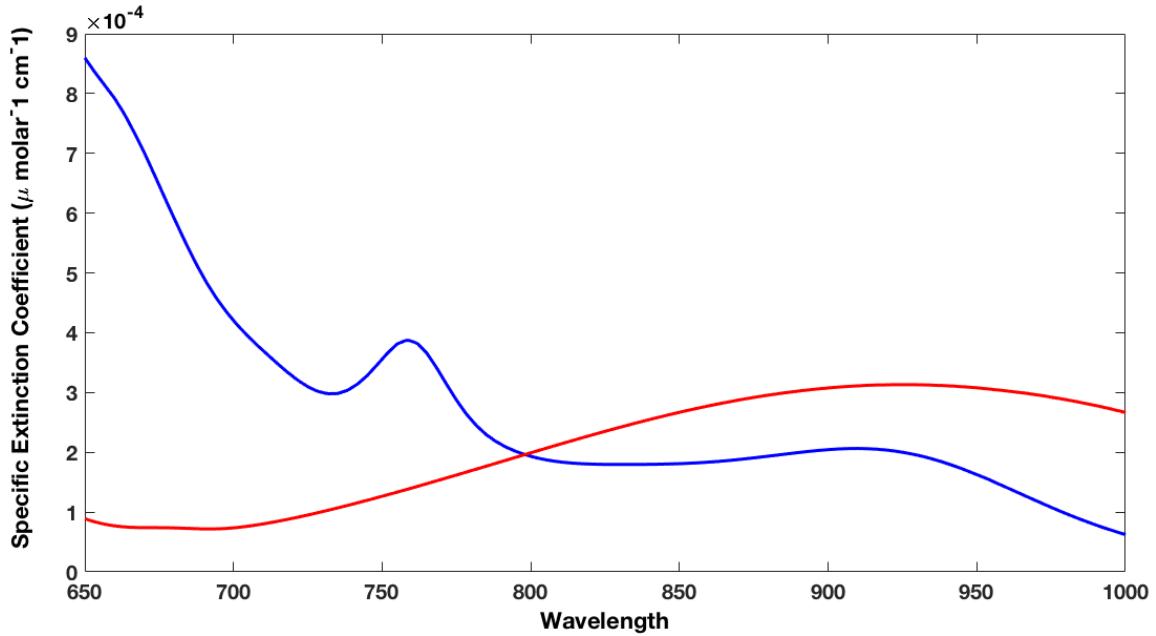
Figure 2.3: Specific extinction spectrum of oxygenated haemoglobin (HbO$_2$) and deoxygenated haemoglobin (HHb) between 650 - 1000 nm.

Cytochrome-c-oxidase   Cytochrome-c-oxidase (CCO) is a mitochondrial enzyme involved in the electron transport chain and is responsible for 95% of oxygen metabolism in the cell. The role of CCO in energy generation has already been discussed in detail in Chapter 1. From a structural perspective, CCO has four redox centres - two copper centres CuA and CuB and two haem groups - a and a_3. CuA is the main absorber of NIR light in CCO. CuB and haem a_3 form a binuclear unit which forms the oxygen binding site of CCO. This binuclear unit receives electrons from the CuA and haem a group and donates electrons to oxygen to generate ATP. This transfer of electrons that occurs between redox centres through a series of oxidation and reduction reactions (also referred to as redox reactions) leads to changes in the optical property of CCO, with the enzyme having different absorption spectra in its oxidized and reduced forms. Figure 2.4 shows these spectra of CCO and the distinct peak of CCO in its oxidized peak can be seen around 840 nm (Jobsis, 1977). The difference between the two spectra can be used to obtain changes in the oxidation status of CCO (oxCCO) which provides a measure of its redox state and reflects the balance between energy supply and demand (Jobsis, 1977). Figure 2.4 also shows the oxidized minus reduced CCO spectrum, which is used for NIRS measurements. The oxidized minus

reduced CCO spectrum is used because unlike the haemoglobin species, it is assumed that the absolute concentration of CCO does not change during the measurement.
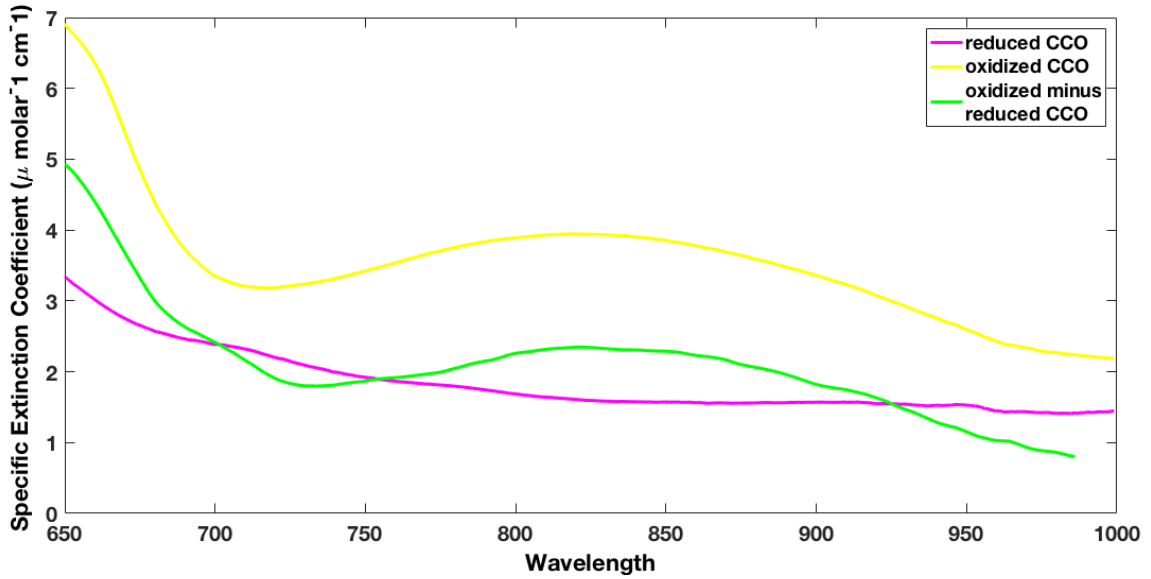
Figure 2.4: Specific extinction spectrum of CCO in its oxidized form (yellow), reduced form (magenta) and the difference between the oxidized and reduced spectrum (green) between 650 - 1000 nm.

2.1.1.3 Scattering

Next to absorption, the other phenomenon that majorly effects the propagation of light is called scattering and accounts for most of the light attenuation that occurs in biological tissue (Elwell, 1995). Scattering is the process whereby the direction of the photons (composing the incident light) is altered upon collision with matter but no energy loss occurs, unlike in absorption. Similar to absorption however, scattering in a medium is also influenced by the wavelength of the incident light. Figure 2.5 shows the model for this occurring in a scattering medium and Equation 2.6 describes a relationship to estimate the attenuation of light in a scattering medium due to scattering:

$$I = I_0 e^{-\mu_s . d} \tag{2.6}$$

where I is the transmitted light, I_0 is the incident light, $-\mu_s$ refers to the scattering coefficient (mm^{-1}) which represents the probability that per unit length travelled in a scat-

tering medium, a photon will be scattered. This equation is valid for a scattering medium containing only a single type of scattering particle and cannot be used to describe light attenuation occurring due to multiple scattering events. However, given the complex nature of the human brain multiple scattering does occur but is challenging to estimate. As a result of this, it is difficult to obtain an estimate of the total attenuation of light that occurs due to scattering and therefore the quantification of the absolute concentration of chromophores in tissue is a complicated matter which is not discussed here. The next section discusses how the attenuation of light in tissue can be quantified using the Modified Beer-Lambert law, taking into account both absorption and scattering in tissue.
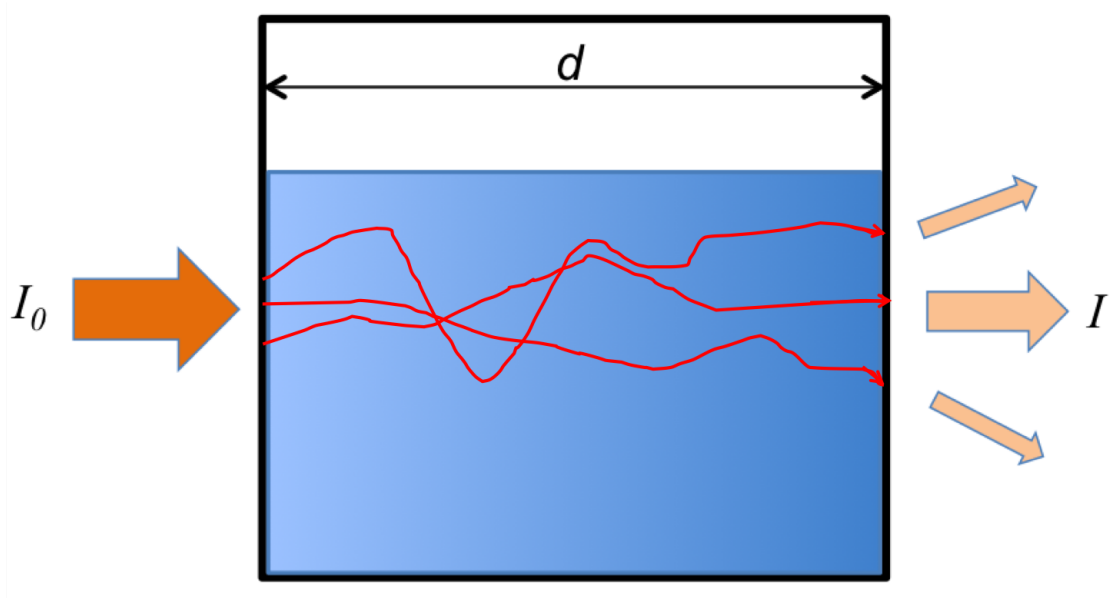
Figure 2.5: Model for light scattering in a scattering medium where I_0 is the incident light, I is the transmitted light and d is the optical pathlength. The red trajectories indicate the path that the light takes in a scattering medium.

2.1.2 Light attenuation

As light travels through tissue, a loss in light intensity referred to as attenuation occurs as a result of the phenomena described in the previous sections, namely absorption and scattering. If the light attenuation needed to be estimated for an absorption-only medium, Equation 2.7 (derived from Beer-Lambert Law) would be sufficient:

$$A = log_{10} \left(\frac{I_0}{I} \right) = \epsilon.c.d \tag{2.7}$$

where A is the attenuation, ϵ is the specific extinction coefficient $(molar^{-1}.cm^{-1})$, c is the concentration of the absorbing compound in the medium and d is the optical pathlength. Given, however, the complex and highly scattering nature of biological tissue, scattering effects need to be taken into account in order to accurately estimate the attenuation of light in tissue. Delpy et. al (1988) developed the Modified Beer-Lambert Law (MBLL) which takes into account loss of light intensity due to absorption and scattering as well as the increased pathlength of the photons due to scattering and is expressed in the following equation:

$$A = log_{10} \left(\frac{I_0}{I} \right) = (\epsilon.c.d.B) + G \tag{2.8}$$

where A is the attenuation, ϵ is the extinction coefficient of the absorbing compound, d is the optical pathlength and B is the differential pathlength factor (DPF). The DPF refers to the increased distance that the photons travel in the medium due to scattering. The product $d.B$ is the differential pathlength (cm) and G is the loss of light intensity occurring due to scattering and other boundary losses. G is difficult to estimate, as mentioned previously estimating total attenuation of light due to scattering is challenging matter. However, if this factor remains constant throughout a measurement, the change attenuation can be used to quantify the change in concentration of chromophores. This is sufficient for brain functional activation studies and can be compared across different brain regions and stimuli.

2.1.2.1 Differential Pathlength Factor

The MBLL requires estimation of the DPF in order to estimate the attenuation of light. DPF is strongly influenced by light scattering and absorption in tissue and somewhat by wavelength of the incident light (Duncan et al., 1995) and it can be challenging to approximate, particularly as it can be variable across participants. There are number of methods that can be used to estimate DPF and Duncan et al. (1995) used an intensity modulated optical spectrometer to estimate the DPF in adults and reported the approximate value in adult

head to be 6.26 ± 14.1%. Previous studies of neonates and infants (Benaron et al., 1995) and Duncan et al. (1995) showed that the DPF was effected by age, head size and wavelengths and emphasized the importance of the selection of the DPF which directly relates to the quantification of change in the concentration of chromophores in tissue. An age-dependent formula was later devised (Duncan et al., 1995) to estimate the DPF for an age group. The infant work presented in this thesis uses an estimated DPF of 5.13 while the adult work uses 6.26.

2.1.3 Differential spectroscopy

The modified Beer-Lambert law has been discussed in detail in the previous section and it has been established that the total change in attenuation in a scattering medium is difficult to estimate. Therefore, the *change* in concentration in chromophores can quantified using the *change* in light attenuation in tissue, for a number of wavelengths. This forms the basis for differential spectroscopy and is important to discuss here as the main focus of this PhD has been to use broadband near-infrared spectroscopy which is based on differential spectroscopy, to estimate changes in concentrations of HbO_2, HHb and oxCCO. Broadband near-infrared spectroscopy instrumentation and the UCLn algorithm will be described in the following sections. Here, I discuss how differential spectroscopy uses the MBLL to estimate chromophore concentration changes using changes in attenuation of light at multiple wavelengths.

Given that we are interested in observing the changes in concentration, consider a scattering medium with only one chromophore with concentration c_1 at time t_1 and concentration c_2 at time t_2. Applying MBLL from Equation 2.8 we would obtain:

$$A_1 = \epsilon.c_1.d.DPF + G \tag{2.9}$$

$$A_2 = \epsilon.c_2.d.DPF + G \tag{2.10}$$

The change in the attenuation $\Delta A = A_2 - A_1$ allows us to obtain

$$\Delta A = \epsilon.\Delta c.d.DPF \tag{2.11}$$

where $\Delta c = (c_2 - c_1)$.

Equation 2.11 can be extended to obtain change in attenuation for n chromophores

$$\Delta A = \sum_n \epsilon_n.\Delta c_n.d.DPF \tag{2.12}$$

This can then be translated to obtain change in attenuation for i wavelengths λ_i, which forms the basis of differential spectroscopy

$$\Delta A_{\lambda_i} = \sum_{n,\lambda_i} \epsilon_{n,\lambda_i}.\Delta c_n.d.DPF \tag{2.13}$$

Typically, most commercial CW NIRS systems use two wavelengths of light to resolve for changes in concentrations of HbO_2 and HHb and the change in attenuation for this scenario with two wavelengths is given by:

$$\begin{bmatrix} \Delta A_{\lambda_1} \\ \Delta A_{\lambda_2} \end{bmatrix} = \begin{bmatrix} \epsilon_{HbO_2,\lambda_1} & \epsilon_{HHb,\lambda_1} \\ \epsilon_{HbO_2,\lambda_2} & \epsilon_{HHb,\lambda_2} \end{bmatrix} \begin{bmatrix} \Delta c_{HbO_2} \\ \Delta c_{HHb} \end{bmatrix}.d.DPF \tag{2.14}$$

Solving Equation 2.14 for the change in concentration gives

$$\begin{bmatrix} \Delta c_{HbO_2} \\ \Delta c_{HHb} \end{bmatrix} = \frac{1}{d.DPF} \begin{bmatrix} \epsilon_{HbO_2,\lambda_1} & \epsilon_{HHb,\lambda_1} \\ \epsilon_{HbO_2,\lambda_2} & \epsilon_{HHb,\lambda_2} \end{bmatrix}^{-1} \begin{bmatrix} \Delta A_{\lambda_1} \\ \Delta A_{\lambda_2} \end{bmatrix} \tag{2.15}$$

2.1.3.1 UCLn algorithm

Broadband near-infrared spectroscopy uses a range of wavelengths in the NIR window, for example the work presented in this thesis uses 120 wavelengths between 780 - 900 nm. The instrumentation for this is described in the following section. The quantification of the changes in the concentrations of HbO_2, HHb and oxCCO using the UCLn algorithm is discussed here.

The UCLn algorithm (Equation 2.16) is based on the principles of differential spectroscopy described in the previous section and can be used resolve for changes in the con-

centration of HbO$_2$, HHb and oxCCO, at n different wavelengths. This is given by:

$$
\begin{bmatrix} \Delta c_{HbO_2} \\ \Delta c_{HHb} \\ \Delta c_{oxCCO} \end{bmatrix} = \frac{1}{d.DPF} \begin{bmatrix} \epsilon_{HbO_2,\lambda_1} & \epsilon_{HHb,\lambda_1} & \epsilon_{oxCCO,\lambda_1} \\ \epsilon_{HbO_2,\lambda_2} & \epsilon_{HHb,\lambda_2} & \epsilon_{oxCCO,\lambda_2} \\ \vdots & \vdots & \vdots \\ \epsilon_{HbO_2,\lambda_n} & \epsilon_{HHb,\lambda_n} & \epsilon_{oxCCO,\lambda_n} \end{bmatrix}^{-1} \begin{bmatrix} \Delta A_{\lambda_1} \\ \Delta A_{\lambda_2} \\ \vdots \\ \Delta A_{\lambda_n} \end{bmatrix}
\tag{2.16}
$$

From a theoretical perspective, the UCLn algorithm could be used with three wavelengths to resolve for changes in the three chromophores of interest. However, previous work (Matcher et al., 1995) has shown that using several different wavelengths produces more accurate measurements, minimizes residual errors from the algorithm and is essential for CCO measurements as the absorption spectra of CCO is similar to that of the haemoglobin species. The concentration of CCO is almost an order of magnitude less in comparison to HbO$_2$and HHb thereby making it more challenging to measure. This may also lead to the question whether the observed CCO signal may be cross-talk (Uludag et al., 2004; Cooper and Springett, 1997; Cooper et al., 1999; Uludag et al., 2002). Typically, therefore, the measurement of Δ[oxCCO] is obtained using a broadband spectroscopy system which measures the changes in light attenuation over a continuous portion of the NIR spectrum. The infant work presented in Chapter 3 uses residual analysis to explore the possibility of the measured oxCCO signal being cross-talk and a more detailed discussion is provided there.

2.1.4 NIRS instrumentation

There are a number of different types of NIRS instrumentation that use a variety of techniques to measure either changes in light attenuation in tissue or total attenuation of light. The most commonly employed are continuous wave (CW), frequency domain (FD) and time-resolved (TR), these are illustrated in Figure 2.6. Briefly, CW NIRS uses light that is emitted at a constant intensity and then the change in light intensity or the attenuation change is measured once the light has passed through tissue. FD NIRS uses light at a modulated intensity and constant frequency and then measures the intensity of the detected light along with a phase-shift. TD NIRS uses short pulses of light and measures the time

taken for the photons to emerge from the tissue.
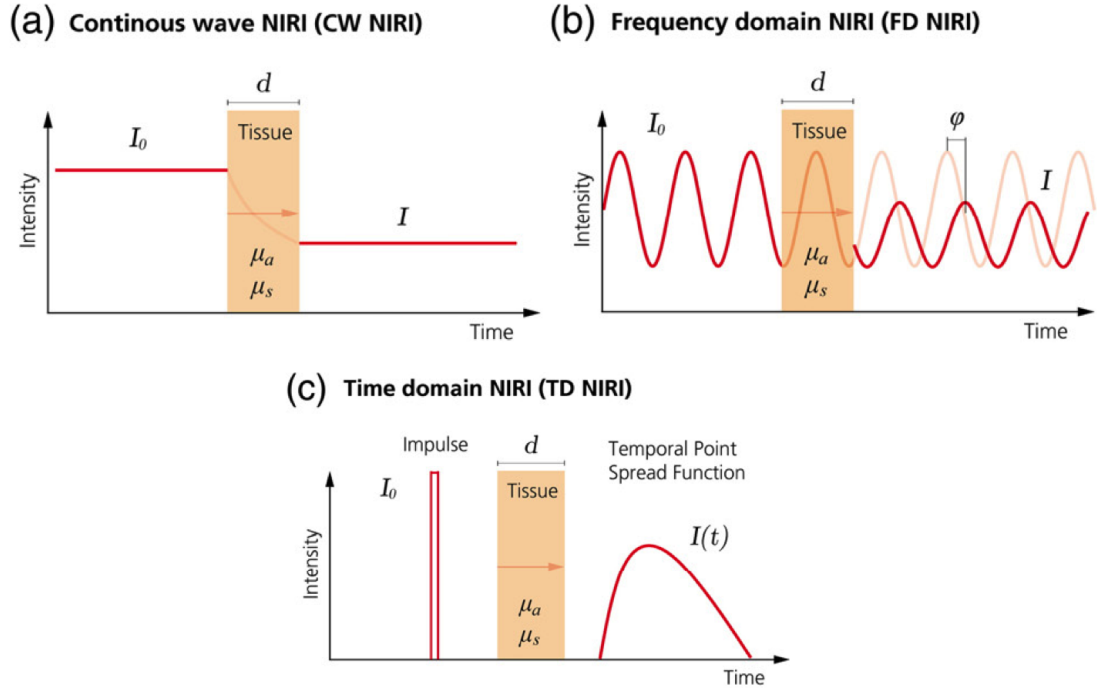
Figure 2.6: The different types of NIRS systems; (a) Continuous Wave (CW) NIRS (b) Frequency Domain (FW) NIRS and (c) Time Domain (TD) NIRS. Image reproduced from (Scholkmann et al., 2014) with permission.

2.1.4.1 Time domain and Frequency-domain

TR NIRS systems emit extremely short impulses of light (of the order of picoseconds) to tissue and measure the time taken for photons to pass through tissue, also referred to as time of flight. This allows the pathlength of the photons to be measured and therefore provides the possibility of obtaining a measure of total attenuation of light and therefore the quantification of the absolute values of haemoglobin. FD systems also provide the opportunity of measuring the absolute concentration of chromophores in tissue using time of flight, through a different principle. The system delivers light to tissue that is modulated at a specific frequency and intensity and then measures the intensity of the detected light and the phase-shift in the frequency which corresponds to the time of flight of the photons.

2.1.4.2 Continuous-wave (CW)

CW systems are discussed in more detail here as they form the basis of the systems used in the studies presented in this thesis. Infant functional activation studies most commonly employ the use of CW NIRS as they are less complex and less expensive in comparison to FD and TR systems. Many commercial CW systems have now been developed to measure brain activity across multiple regions simultaneously (Scholkmann et al., 2014) and typically use two wavelengths of light generated either by laser diodes (LDs) or light emitting diodes (LEDs) to resolve for changes in the concentrations of HbO_2 and HHb. Arrays are formed composing of specific orientations of sources and detectors which are placed on the head, with sources emitting the light and detectors measuring the change in attenuation of light as it passes through tissue, from neighboring light sources. This requires the identification of the source associated with a detected signal and this is done by encoding and decoding the illuminated light sources while the detectors acquire data continuously. This involves modulating the intensity of each individual light source at a specific frequency. The light that is detected at the detector can then be analysed in the frequency domain in order to determine the contribution of each light source to the detected light and therefore identify the associated light source with the detected light signal.

One of the most challenging aspects of CW, particularly for use with infants, is designing appropriate headgear to maintain source-detector coupling as well as coupling of the array with the participant's head as any CW systems are highly sensitive to any changes in either of these. Different headgear designs were developed for each of the studies presented in this thesis and are discussed in Chapter 3. The following section discusses the instrumentation of CW NIRS systems, including broadband systems which are also CW.

2.1.4.3 Instrumentation

There are three main components that form part of a CW NIRS system - light sources to emit light, photodetectors to detect the light that has passed through tissue, optical fibres to transport light from the source to the tissue and from tissue to the photodetector. The components of a broadband NIRS system are briefly described here but as two different

broadband systems were used in this thesis, the systems and their hardware are discussed in more detail in Chapters 4, 5 and 6.

2.1.4.3.1 *Light source* CW systems use either LEDs or LDs as sources to emit light at specific wavelengths and most commercial instruments typically use a combination of two or three wavelengths to measure changes in the concentration of HbO_2 and HHb. Table 2.1 provides a comparison of a variety of commercial NIRS devices and the different wavelengths they use. The selection of wavelengths is an important technical aspect of CW NIRS instruments that can significantly impact the signal to noise ratio of the NIRS measurement and a number different methods have been developed to select the optimum wavelengths, a detailed discussion on this can be found in a review by Scholkmann et al. (Scholkmann et al., 2014). Additionally, the type of light source used i.e. either LEDs or LDs also determines the wavelength selection as LDs have a narrow spectral resolution with limited choice of wavelengths while LEDs have a larger bandwidth of ~35 nm. Broadband NIRS systems require a continuous spectrum between 695 - 900 nm which is achieved through the use of a white light source that offers a wider bandwidth. For all the studies presented in this thesis, chromophore concentration changes were calculated using the UCLn algorithm using 120 wavelengths between 780 - 900 nm.

Device	Manufacturer	No. of wave-lengths	Wavelengths used (nm)
NTS Optical Imaging System	Gowerlabs, UK	2	780, 850
FOIRE-3000	Shimadzu, Japan	3	780, 805, 830
NIRO-200NX	Hamamatsu, Japan	3	735, 810, 850
ETG-4000	Hitachi, Japan	2	695, 830
ETG-7100	Hitachi, Japan	2	695, 830
WOTb	Hitachi, Japan	2	705, 830
OxyMon	Artinis, Netherlands	2	760, 850
PortaLite	Artinis, Netherlands	2	760, 850
NIRSport	NIRx, USA	2	760, 850
NIRScout	NIRx, USA	2 or 4	LED: 760, 850 or Laser; 685, 780, 808, 830

Table 2.1: Comparison of different commercial NIRS systems and their choice of wavelengths.

2.1.4.3.2 *Medium to transport light from the source to the tissue and from the tissue to the detector*   In order to transport the light to the tissue and back from the tissue to the detector, two methods may be employed. The first is by placing the sources and detectors directly in contact the skin (Bozkurt et al., 2005; Muehlemann et al., 2008) and second, by using a transporting medium such as optical fibres to transport the light. The latter is most commonly used by commercial NIRS systems for brain measurements while the former is used by fibreless wearable systems such as the PortaMon (Artinis, Netherlands) and the UCL fibreless Diffuse Optical Tomography (DOT) system (University College London, UK) (Chitnis et al., 2016). The broadband NIRS systems used in this PhD thesis use optical fibres to transport the light from the source to tissue and tissue to photodetector. The studies presented in Chapters 3, 4 and 5 each used a different set of optical fibres the specifications of which are described within each chapter. Appropriate headgear needs to be designed in order to affix the sources and detectors on a participants head. Headgear design is also discussed in more detail in Chapters 3, 4 and 5.

2.1.4.3.3 *Photodetector to detect the light that has passed through the tissue*   Photodetectors employ the use of the photoelectric effect (Scholkmann et al., 2014) which converts light into an electrical signal and there are a number of different types photodetectors - photodiodes (PDs), avalanche photodiodes (APTs), photomultiplier tubes (PMTs) and charge-coupling devices (CCDs). Most commercial CW NIRS systems use PDs and APTs while broadband systems require recording of continuous spectrum (Cope et al., 1988) which is achieved through the use of a CCD, in combination with a spectrometer and a series of lenses. The incoming light is detected at the spectrometer and directed to a diffraction grating which disperses the light. The CCD is then able to spatially separate the spectral components of light to obtain the continuous spectrum (Cope et al., 1988).

2.2   EEG

The neural origin of the EEG signal is discussed here and the specification of the system used for studies in this thesis is described in more detail.

2.2.1 Neural basis of EEG

EEG is a non-invasive technique that is used to record electrical activity of the brain. A neuron propagates electrical signals to other neurons in a two step process which involves transmitting an electrical signal along the cell by means of an action potential and between cells by means of a synapse through chemical neurotransmitters. Both of these processes have already been described in detail in Chapter 1. To recap, the chemical neurotransmitter at the synapse between neurons can either excite or inhibit the postsynaptic neuron resulting in either an excitatory postsynaptic potential (EPSP) or an inhibitory postsynaptic potential (IPSP). Figure 2.7 depicts this process. The arrival of an EPSP at the postsynaptic neuron causes it to become depolarized temporarily and this change in the postsynaptic membrane potential causes an influx of positively charged ions Na^+ and Ca^{2+} causes a change in the voltage deflection inside the neuron with respect to the outside, thereby leading to the formation of extracellular sinks and sources. This causes a current to flow referred to as a dipole, between the extracellular sink and source in order to balance out the difference in voltage between sink and source. This process is shown in Figure 2.8. The voltage potential of the dipole decreases with increasing distance (Buzsáki et al., 2012) and is what can be detected by EEG electrodes placed on the scalp. More specifically, it is thought that pyramidal neurons of the cortex generate the strongest EEG signals as the neurons are spatially aligned and their activity is synchronized. Therefore, the measured EEG signal results from the combined activity of a large number of similarly orientated pyramidal neurons and reflects the summation of the postsynaptic potentials of large populations of neurons which contribute to the local field potential (LFP) (Buzsáki et al., 2012) which can be detected by EEG sensors that are placed on the scalp.
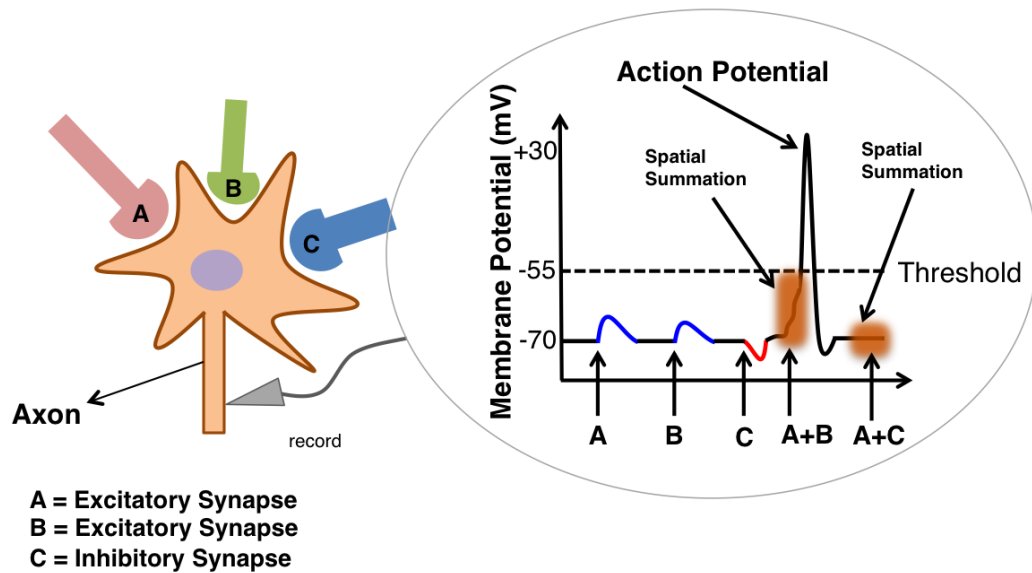
Figure 2.7: Generation of a excitatory postsynaptic potential (EPSP) as a result of the summation of all presynaptic inputs
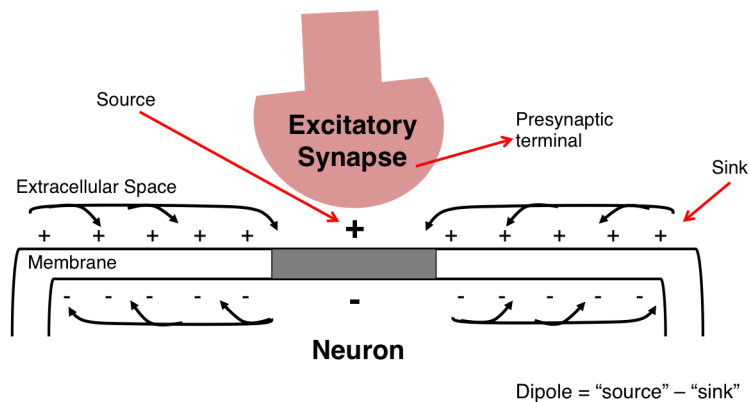
Figure 2.8: Ionic flow across the membrane leads to the flow of current from the extracellular source to the sink. A dipole is generated as a result of the difference in voltage between the source and the sink and this difference is what can be measured using EEG.

2.2.2   Neuroelectrics Enobio EEG System

The first experimental study presented in this thesis (Chapter 3) did not involve acquiring EEG data. However, the remaining chapters - Chapters 4, 5 and 6 involved simultaneous acquisition of NIRS and EEG. Therefore, the EEG system is described here and is applicable

to those chapters.

2.2.2.1 Hardware

The Enobio 32 wireless EEG system (Neuroelectrics, Spain) was used to acquire EEG data. There are a number of components that form part of the EEG system and these include:

1. Electrodes that are referred to as "geltrodes" and are placed into the neoprene cap on the subject's head and are filled with a highly conductive gel - Signagel (Parker Labs, USA) and are shown in Figure 2.9a.

2. The EEG wires which are clipped on top of the geltrodes and are shown in Figures 2.9b and 2.9c and are plugged into a wireless transmitter also referred to as the amplifier.

3. The wireless transmitter also known as the "necbox" is shown in Figure 2.9d. The necbox amplifies the difference between the voltage at each individual electrode site and the reference, which is placed on the mastoid behind the ear. Therefore, the voltage was measured relative to the reference site and is amplified. The sampling rate of the system was 500 Hz. The sampling bandwidth was 0 - 125 Hz.
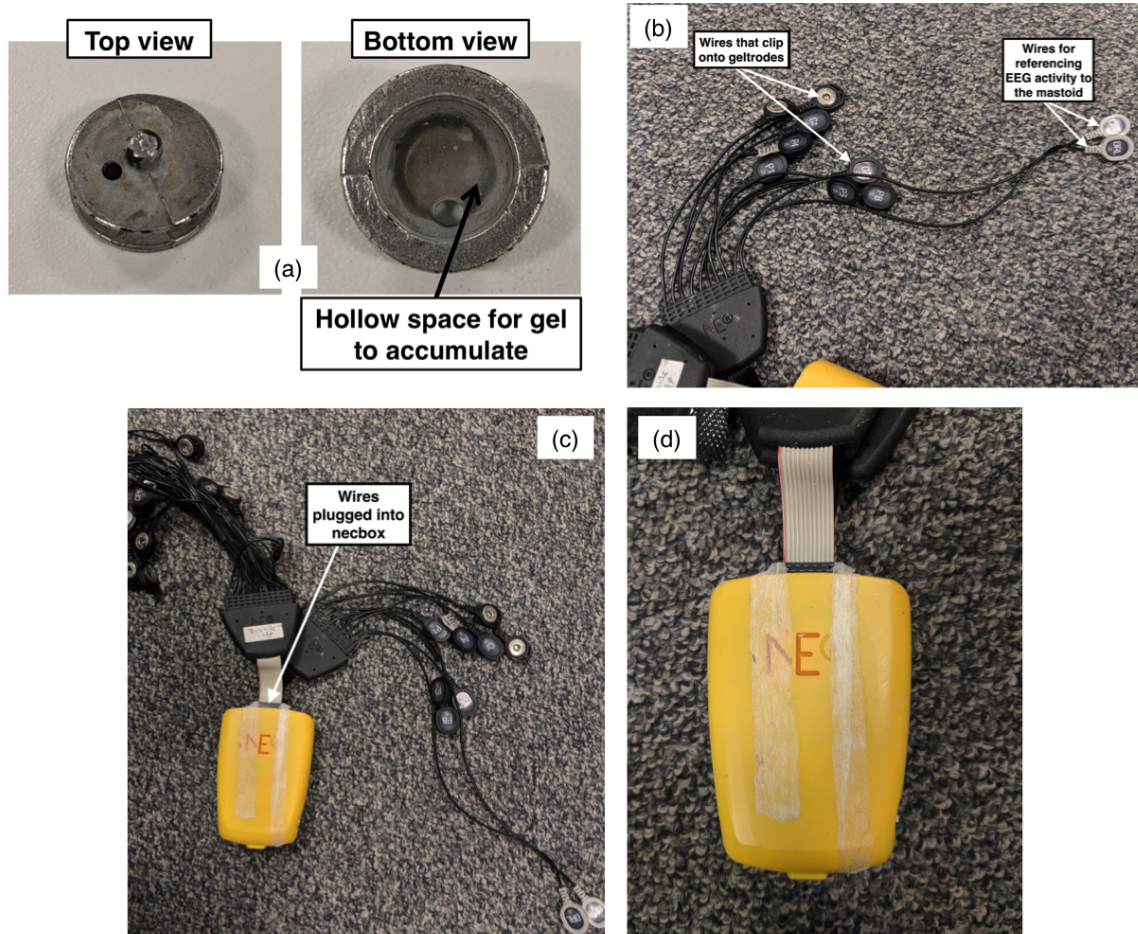
Figure 2.9: Enobio EEG components formed by (a) Geltrodes used inside the EEG headcap (b) EEG wires clipped on top of geltrodes (c) EEG wires plugged into the wireless amplifier, also referred to as the necbox and (d) the wireless amplifier or necbox.

The Enobio System allows measurement from 32 electrode sites located on the head according to the standard International 10/20 system. The electrodes were placed in different orientations on the head in each of the studies presented and the exact EEG montage used will be discussed in each of the relevant chapters.

2.2.2.2 Software

The necbox uses wireless technology to connect to Neuroelectrics Instrument Controller (NIC) Software via Bluetooth. Figure 2.10 shows the front panel of the NIC Software where the EEG signal from each of the electrode sites can be visualised.
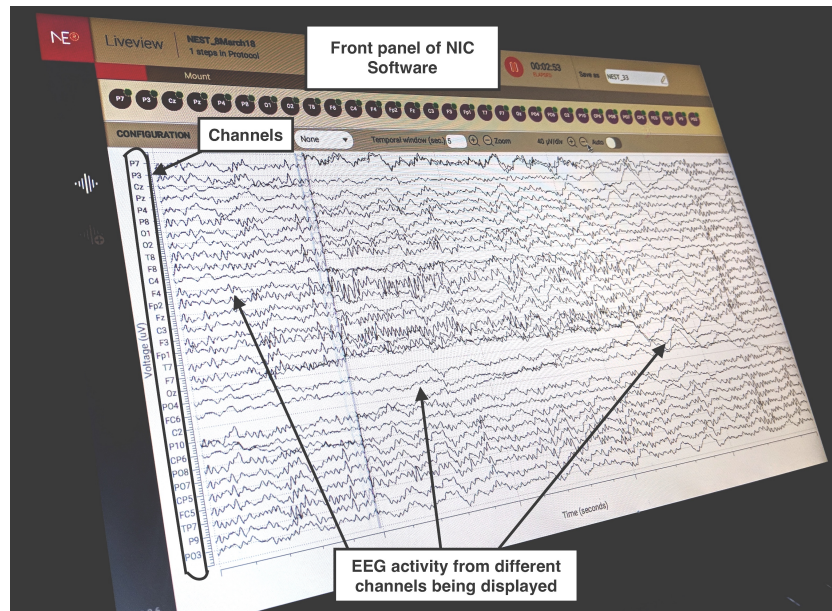
Figure 2.10: NIC software front panel displaying quality of EEG signals from each electrode

2.3   Data Analysis

2.3.1   NIRS

All NIRS data were analysed in Matlab 2014a (Mathworks, USA). The conversion to concentration changes from attenuation data was performed using a program that was written by Dr Ilias Tachtsidis and Dr Phong Phan and all subsequent analyses that were performed were using scripts that I wrote.

2.3.1.1   Preprocessing

In general, the pipeline to process the NIRS data presented in this thesis was the same in each chapter, with some steps not being applicable to the adult data presented in Chapter 5. Figure 2.11 shows main steps involved and each of them are detailed in the following sections.
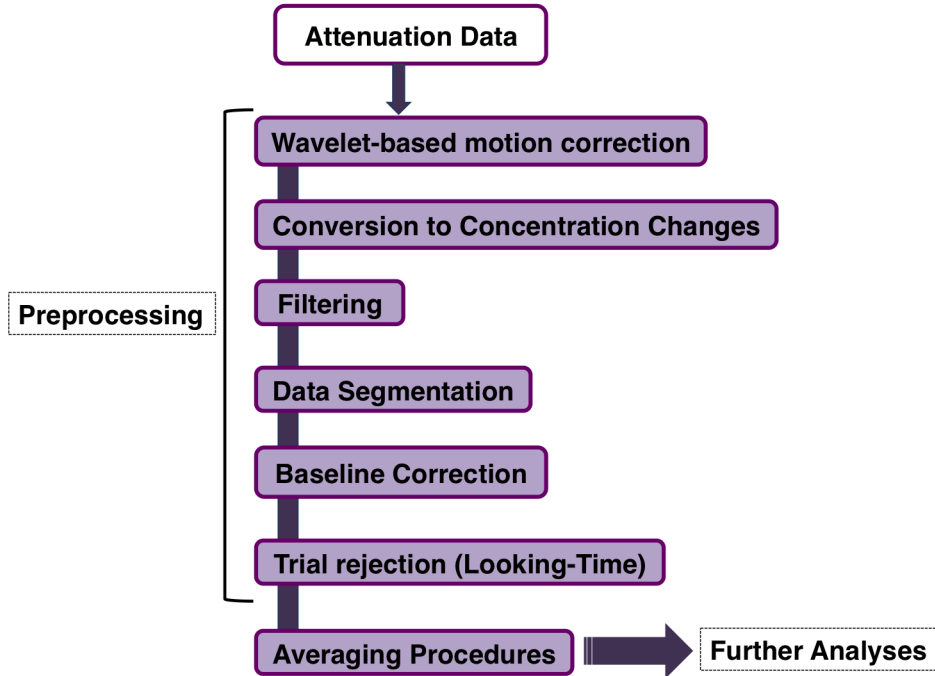
Figure 2.11: NIRS general data analysis pipeline. Trial rejection based on looking-time is only applicable to the infant data presented in Chapters 4, 6, 7 and 8 and is introduced and discussed in Chapter 4.

2.3.1.1.1 *Wavelet-based Motion Correction* Wavelet-based motion correction (Molavi and Dumont, 2012) was used to remove artifacts in the data due to movement. This step is particularly important for infant data as the infants are relatively free to move in their parent's lap and therefore, they are more likely to move or make sharp head movements, especially younger infants who don't have strong neck control. The algorithm was applied to the attenuation signal of each participant across all wavelengths between 780 - 900 nm. It calculates wavelet coefficients for the attenuation data using the discrete wavelet transform and the coefficients that are identified as outliers are marked as movement artifacts and corrected. The tuning parameter alpha controls the trade-off between the intensity of the artifact attenuation and the level of distortion introduced into the NIRS signal. Whilst a high tuning parameter can effectively remove artifacts, it may change the shape of the haemodynamic response and cause the signal to become dampened. Conversely, a low tuning parameter retains the true shape of the haemodynamic response but may not remove artifacts effectively. Different tuning parameters were used in the different studies

and will be discussed in each relevant chapter. Figure 2.12 shows an example of the attenuation signal from a single participant at wavelength equal to 830 nm and how the motion correction algorithm acts to correct portions of the data where motion artifacts are present. Recent work (unpublished, in preparation) by colleagues at the Centre for Brain and Cognitive Development (CBCD) and in the Netherlands have verified that this technique is most successful in correcting motion artifacts present in infant data.
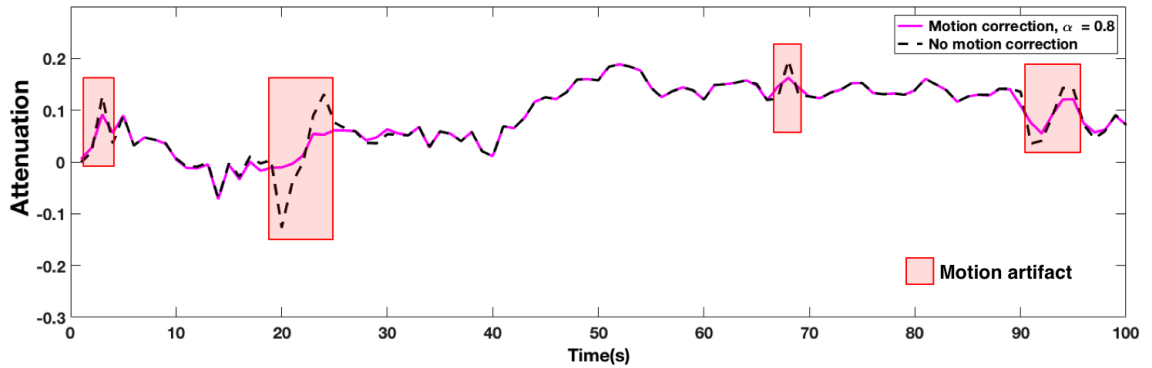
Figure 2.12: Attenuation data from a single participant at wavelength = 830 nm. The wavelet-based motion correction algorithm detects motion artifacts in the attenuation signal and these are highlighted in red and visible as spikes in the signal where the algorithm has not been applied.

2.3.1.1.2 *Calculation of chromophore concentration changes* Once the motion correction had been applied to the attenuation data, the chromophore concentration changes were calculated using the UCLn algorithm which has been discussed earlier. A wavelength-dependent DPF of 5.13 was used for the infant studies presented in Chapters 3, 5 and 6 which is suitable for infants of the age range and 6.26 was used for the adult studies (Duncan et al., 1995).

2.3.1.1.3 *Filtering* Following the conversion from attenuation data to concentration changes, the data was filtered using a order Butterworth bandpass filter. The filters used for each of the studies were different and will be discussed in each chapter.

2.3.1.1.4 *Data segmentation* After filtering, the data were segmented into epochs around the onset of the stimulus and typically included around 4 seconds of the baseline prior

to the onset of the experimental condition, the experimental condition and the entire following baseline period. The lengths of experimental stimuli in each of the studies were different, therefore data segmentation will be discussed in more detail in each chapter.

2.3.1.1.5 *Baseline correction*   The segmentation procedure yielded blocks of data and baseline correction was applied in order to ensure that the HRF reflected a response to the experimental condition versus background activity. This step does not alter the signal but shifts the waveform such that the pre-stimulus activity is reduced to zero. Different methods of baseline correction were used in each of the studies, therefore baseline correction will discussed in more detail in each chapter.

2.3.1.1.6 *Rejection criteria*   Data can be removed from the study due to various rejection criteria which can include poor signal-to-noise ratio as well as behaviour of the participant. For infant data, trials were rejected based on looking-time and as this only applies to the studies presented in Chapters 4, 6, 7 and 8 it is introduced and discussed in Chapter 4. The rejection criteria for each study differed and more information about the exact criteria can be found in the relevant chapter.

2.3.1.1.7 *Averaging Procedures*   The $\Delta[HbO_2]$, $\Delta[HHb]$ and $\Delta[oxCCO]$ responses for each participant were averaged across valid blocks to obtain an average response for an experimental condition, for each of the chromophores, for each participant. The average responses for each participant were then averaged together to obtain a grand mean time course for each of the chromophores. The averaging procedure for the adult study presented in Chapter 5 was slightly different and this will be discussed there.

2.3.1.2   Further Analyses

2.3.1.2.1 *Cross-correlations*   Cross-correlations can be used to determine the similarities between two time-series, particularly if one time-series may be related to past lags of the other time-series. Typically it is used in functional connectivity to explore the relationship between neural activity observed in one area of the brain in relation to activity in another

area of the brain. Here, it was used to investigate the relationship between each of the NIRS chromophores, particularly oxCCO and its relation to the haemoglobins as they represent different components of the neurovascular coupling pathway which may not be correlated exactly temporally.

The cross-correlation, for two time-series $x(t)$ and $y(t)$ where $t = 0, 1, 2, ..., N - 1$, is given by the following formula with time-lag (or time delay) equal to d:

$$r = \frac{\Sigma_t\left[(x(t) - \bar{x}) \times (y(t - d) - \bar{y})\right]}{\sqrt{\Sigma_t(x(t) - \bar{x})^2}\sqrt{\Sigma_i(y(t - d) - \bar{y})^2}} \tag{2.17}$$

where $\bar{x}$ and $\bar{y}$ are the means of each of the time-series.

Equation 2.17 can be used to obtain the cross-correlation at every time delay $d = 0, 1, 2, ..., N - 1$:

$$r(d) = \frac{\Sigma_t\left[(x(t) - \bar{x}) \times (y(t - d) - \bar{y})\right]}{\sqrt{\Sigma_t(x(t) - \bar{x})^2}\sqrt{\Sigma_i(y(t - d) - \bar{y})^2}} \tag{2.18}$$

Essentially, the cross-correlation provides a measure of similarity between the time series by determining cross-correlations between the time-series at every time-point and identifying the time-delay at which the correlation is maximised. Here, it was calculated on a trial-by-trial basis for each participant and then averaged to obtain mean cross-correlations between (1) HbO_2 and HHb, (2) HHb and oxCCO and (3) oxCCO and HbO_2, for each participant. These were then averaged across the participants to obtain grand averaged cross-correlations.

2.3.2   EEG

All EEG data were analysed in Matlab 2017a (Mathworks, USA) using the EEGLab Toolbox (Schwartz Centre for Computational Neuroscience, UC San Diego, USA) and scripts that I wrote.

2.3.2.1 Preprocessing

The same pipeline was used for preprocessing all the EEG data presented in this thesis. Figure 2.13 shows the main preprocessing steps and each of the stages shown is discussed in more detail in the following sections.
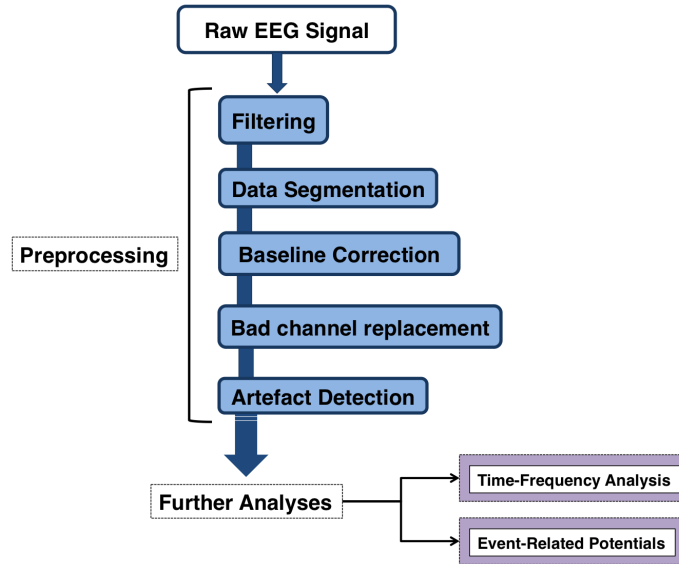
Figure 2.13: EEG data analysis pipeline

2.3.2.1.1 *Filtering*   EEG is sensitive to skin and movement potentials and may also be effected by electrical noise from surrounding equipment. For the studies presented in this thesis, a 5th order Butterworth filter of 0.1 - 100 Hz was applied to all EEG data offline to remove skin and movement potentials (0.1 Hz) and to remove any other activity not considered to be brain activity (100 Hz) that may have arisen due to artifacts. Typically, studies employ the use of a more narrow range for bandpass filtering, particularly if the objective of the study was to investigate event-related potentials or oscillatory activity associated with lower frequency bands such as theta and alpha. For the studies reported here, higher frequency oscillatory activity (i.e. gamma activity) was of interest therefore the bandpass filter was chosen to include a wide range of frequencies in the data.

2.3.2.1.2 *Segmentation*   Once filtering was performed, the data were segmented around the onset of the experimental stimulus. The adult data presented in Chapter 5 were seg-

mented into epochs of 700 milliseconds consisting of 200 milliseconds of baseline preceding the onset of the stimulus and 500 milliseconds after the stimulus onset. The infant data presented in Chapters 6, 7 and 8 were segmented into epochs of 1 s consisting of 200 milliseconds of baseline preceding the stimulus and 800 milliseconds after the onset of the stimulus. Segmenting the data in this way allows stimulus-evoked neural activity to be isolated.

2.3.2.1.3 *Baseline correction*   Segmented epochs were baseline corrected by taking the average of the 200 milliseconds of baseline prior to the onset of the stimulus and subtracting it from the entire epoch. This is done in order to ensure that the activity reflects a response to the experimental stimulus and does not include any other activity occurring in the brain.

2.3.2.1.4 *Artifact detection and removal*   EEG data is particularly sensitive to artifacts and there are few different types of artifacts which can affect the data. These include oculomotor motor activity, large movement potentials, electromyography (EMG) (or muscle noise) and alpha activity. Figure 2.13 shows a few examples of these artifacts present in the data. Alpha activity is commonly seen when participants are tired and occurs around 10 Hz in adults and around 7 Hz in infants and is characterized by its sine morphology. Steps can be taken to reduce alpha contamination by ensuring that participants are well-rested prior to the testing session. EMG or muscle noise typically occurs in bursts around 20 - 40 Hz and can affect the data particularly if the intention is to investigate oscillatory activity above 15 Hz (Cohen, 2014). Oculomotor activity includes eye blinks and eye movements which can be seen in frontal channels and is more prevalent in adult EEG data than in infant data. To remove these artifacts, two levels of detection were performed. The first involved using an automatic detection tool in EEGLab which identified and removed segments of the data where the signal amplitude exceeded a pre-determined threshold. For the adult data presented in Chapter 5, the threshold was set to ±100 mV while for the infant data presented in Chapters 6, 7 and 8 the threshold was set to ±200 mV, in accordance with previous studies (Jones et al., 2015). This removed any large artifacts from the

data due to movement, drifts or any other issues which causes large changes in the signal (for example temporary loss of connection between the amplifier and software or movement of the reference electrode). While the artifact detection tool was useful in identifying large changes in the signal, it did not successfully remove EMG noise, alpha activity or eye blinks. Therefore, the next level of artifact removal involved visually inspecting the signal at each electrode on a trial by trial basis and segments that contained artifacts that were not successfully detected in the previous step were identified and removed.

EMG noise **Alpha activity** **Eye blinks**
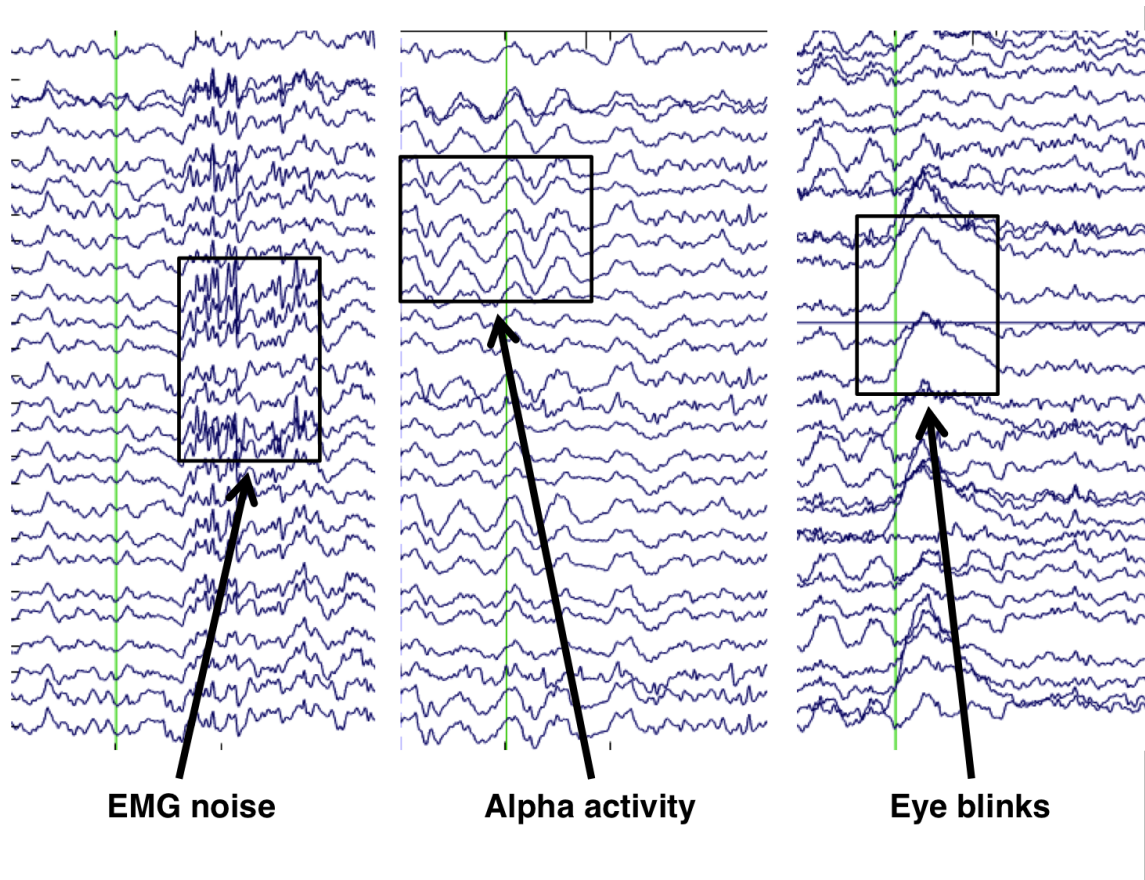
Figure 2.14: Different types of artifacts affecting EEG data. The data used here is from an adult volunteer.

2.3.2.1.5 *Bad channel interpolation* When visually inspecting the data to remove artifacts, if the EEG signal at individual channels appeared to be noisy in comparison to other surrounding electrodes, i.e. the noise was not due to an artifact, the channel was replaced with an average voltage of the nearby channels. This is common practice in EEG studies that use high density EEG (Cohen, 2014). Due to the fact that adults generally sit still when

instructed to do so and more time can be taken to position the cap, gel the electrodes and ensure a good signal was being obtained from all electrodes, the EEG signal quality for the adult studies was better. As a result, bad channel interpolation was not required for any of the datasets in the adult work presented in Chapter 5 and was limited to the infant studies performed in Chapters 6, 7 and 8.

2.3.2.1.6 *Rejection criteria*   In all the EEG studies presented in this thesis, a participant was removed from the study if they did not have at least 5 valid epochs after the preprocessing steps were performed.

2.3.2.2 Further Analyses

EEG activity can be analysed in two domains:

1. Time domain by means of computing event-related potentials

2. Time-Frequency domain by means of decomposing the EEG signal into underlying oscillations

Both methods are discussed in the following section and are used to analyse the EEG data presented in Chapters 4, 5 and 6.

2.3.2.2.1 *Event-related potentials*   Event-related potentials (ERPs) are changes in the EEG that are time-locked to sensory, motor or cognitive events and are small voltages generated in the brain in response to specific stimuli (Blackwood and Muir, 1990). ERPs are obtained at each channel by averaging the segments of the EEG signal free from artifacts and noise. Averaging is performed across epochs to obtain an average ERP for each participant which represents the neural response that is time-locked to the presentation of the stimulus. The averaging process reduces background EEG activity and isolates the neural activity that is related to the stimulus. The number of valid trials required depends on the experiment being conducted and typically depends on the expected size of effect (Luck, 2005). For adult ERP studies this can vary from 20 trials to 200 trials. Following averaging across trials for each participant, averaging across participants is performed to obtain the

grand average waveform. There are different components of an ERP, the most notable of which are the P1 (or P100) and N1 (or N100) peaks which are defined as the positive (P) or negative (N) voltage deflections occurring around 100 ms post-stimulus onset. Earlier components such as the P1 and N1 are termed sensory as they depend on physical features of the stimulus being presented while later components that occur between 300 - 600 ms are termed cognitive as they are deemed to reflect information processing. Figure 2.15 shows an example of an ERP with different components indicated.
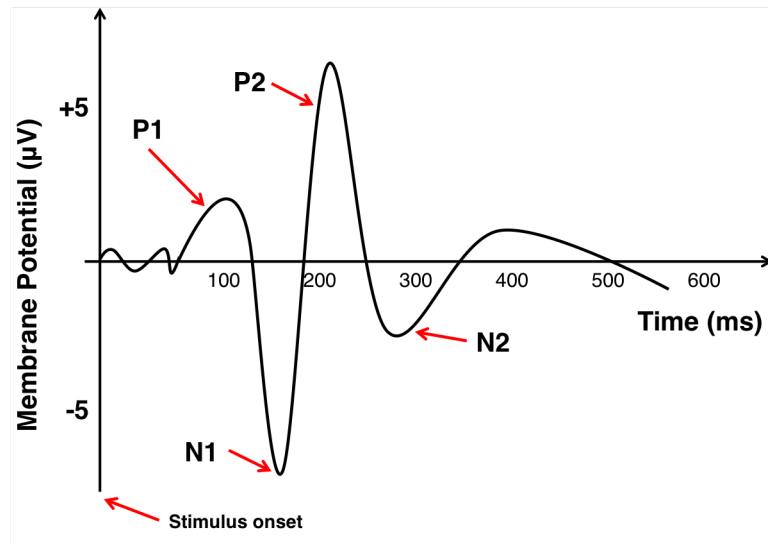
Figure 2.15: Event-related potential with different visual-evoked components identified.

2.3.2.2.2 *Time-Frequency analyses*   While ERPs have a very high temporal precision and accuracy, they are limited to one dimension (time) and many of the neural dynamics contained within EEG data cannot be represented in an ERP. Furthermore, the underlying physiological mechanisms that produce an ERP are not as well understood as other representations of EEG data such as oscillations (Buzsáki et al., 2012; Buzsáki and Wang, 2012) which are in the time-frequency domain. EEG data encapsulates rhythmic activity which reflects neural oscillations occurring due to fluctuations in electrical activity of large populations of neurons that are synchronously active. An oscillation is formed by three key pieces of information which include *(a) frequency* which is defined as the speed of the oscillation with units hertz (Hz) *(b) phase* which is defined as the position at a specific time point on a waveform (sine wave here) and is measured in radians or degrees *(c) power* which is

the square amplitude of the oscillation and represents the amount of energy in a particular frequency band. Figure 2.16 shows the frequency, power and phase that compose the oscillation at one particular electrode.
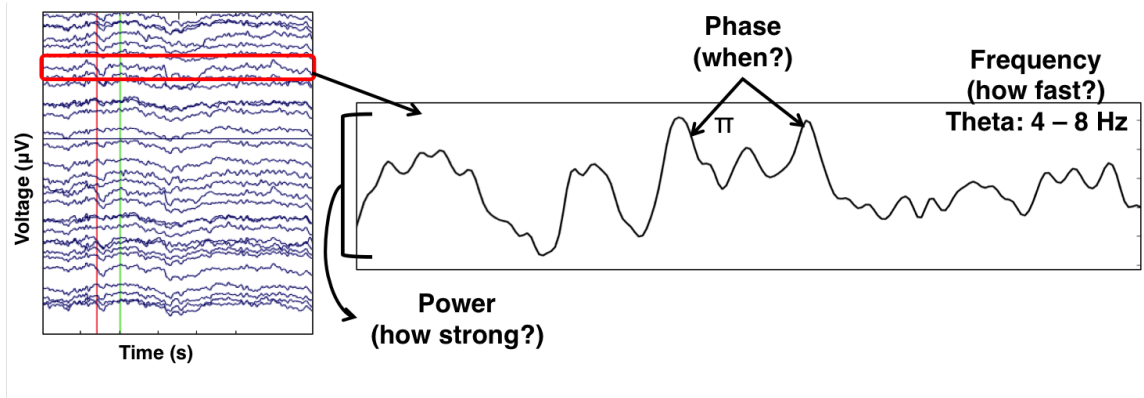
Figure 2.16: Components of an oscillation; phase, frequency and power identified on the EEG signal from one electrode. The data used in this figure is my own and the idea for the figure has been adapted from (Cohen, 2014).

Oscillations appear to reflect fundamental neural mechanisms (Cohen, 2014) and have been linked to physiological events Buzsáki 2006; Engel et al. 2001; Herrmann et al. 2010; Kistler et al. 2000; Klimesch et al. 2008. Neural oscillations are grouped into different frequency bands which are defined as delta, theta, alpha, beta and gamma, each of which have been associated with various cognitive functions. The bands are defined based on the age of the participant and the borders differ between infants and adults. Table 2.2 shows the different frequency bands in both adults and infants.

Frequency Band	Adults	Infants
Delta	1 - 4 Hz	1 - 3 Hz
Theta	4 - 8 Hz	3 - 6 Hz (Saby and Marshall, 2012)
Alpha	8 - 12 Hz	6 - 9 Hz (Jones et al., 2015)
Beta	13 - 30 Hz	10 - 25 Hz (Saby and Marshall, 2012)
Gamma	30 - 100 Hz	20 - 60 Hz (Saby and Marshall, 2012)

Table 2.2: Different frequency bands for adults and infants.

The phase and power of an oscillation are generally considered to be independent of one another and capture different neural dynamics. For the work presented in this thesis, I will be focusing on power-frequency analyses therefore phase is not discussed here. Ob-

taining the time-frequency representation of the EEG data involves transforming it from the time domain (one-dimensional) which involves transforming change in the voltage across time into the time-frequency domain (three-dimensional) consisting of the power of different frequencies being represented in time, frequency and space where space refers to the spatial location of the electrodes. It is important to note that the time-frequency representation produces many more dimensions but for the purposes of this PhD work we consider only the 3-D representation. Figure 2.17 illustrates this representation as a "3-D cube" and how different information measures reflecting neural dynamics can be obtained from the time-frequency decomposition. These measures are:

1. Power-frequency (Figure 2.17A) which represents the power of each frequency in the EEG signal. Note that time is not represented here.

2. Power-time (Figure 2.17B) which represents how the power of **one** frequency changes over time. Note that multiple frequencies cannot be visualised simultaneously here.

3. Space (Figure 2.17C) which shows the data at **one** time-frequency point to visualise the topographical distribution of the power.

4. Time-Frequency (Figure 2.17D) which represents how the power of a frequency changes across time. Note that in general the time-frequency representation can reflect many features of the EEG data such as power, phase clustering, connectivity or correlation coefficient. For the purposes of this work, we are only interested in the representation of power in the time-frequency domain.
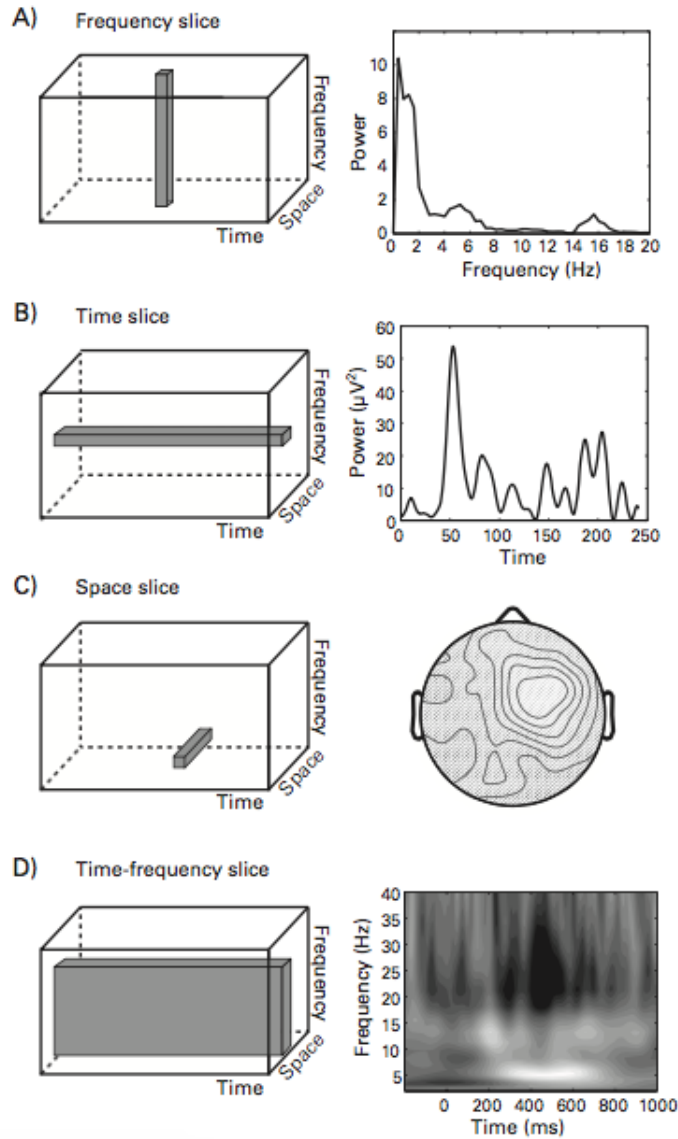
Figure 2.17: Different representations of the 3-D time-frequency "cube" and the measures that can be extracted from it. This figure has been reproduced from (Cohen, 2014).

2.3.2.2.2.1 Discrete Fourier Transform   The Fourier Transform (FT) is a power signal-processing tool that can be used to transform the EEG data from the time domain to the time-frequency domain. The principle of the FT is that all time-series signals can be decomposed into the sum of sine and cosine waves (shown in Figure 2.18), both of which are periodic functions with a difference in phase of $\pi/2$ (radians) or $90°$ and can be represented mathematically as shown in Equations 2.17 and 2.18
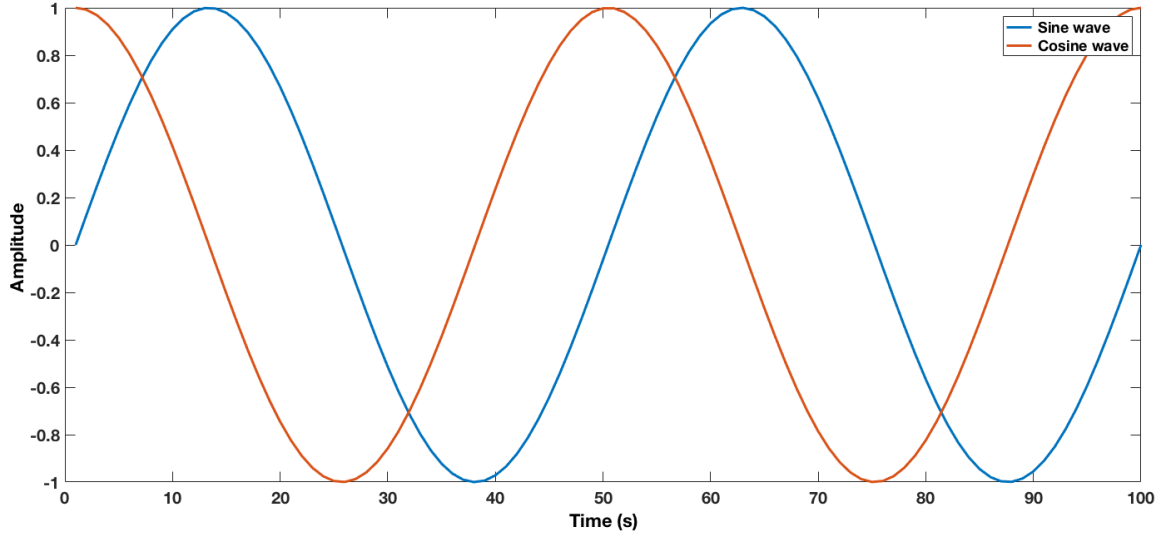
Figure 2.18: Sine (blue) and Cosine waves (orange)

$$A \sin(2\pi f t + \phi) \tag{2.19}$$

$$A \cos(2\pi f t + \phi) \tag{2.20}$$

where A is the amplitude of the sine wave, f is the frequency and t is the time and ϕ is the offset of the phase which is related to the time point $t = 0$. The DFT involves computing the dot product between a sine wave and the time-series data at a specific frequency at each time point in the data. The dot product D is defined in Equation 2.19, between two elements m and n where k is the number of elements in m (or n, both must have the same number of elements):

$$D_{mn} = \sum_{i=1}^{k} m_i n_i \tag{2.21}$$

The sine wave is referred to as the kernel which is multiplied with the time-series signal. Equations 2.17, 2.18 and 2.19 can be combined to transform the EEG signal from the time domain to the frequency domain to obtain the formula for DFT which is given by Equation 2.20:

$$X_f = \sum_{k=1}^{n} x_k e^{(-2\pi i f (k-1) n^{-1})} \tag{2.22}$$

where X is the "complex-valued" Fourier coefficient (computed at frequency f) of the time-series variable x where n is the number of data points and i is the imaginary operator. An imaginary number (or "complex" number) refers to a number having the form $a + ib$, where a is the real component and b is the imaginary component. The real and imaginary components of the Fourier coefficients contain information about the amplitude, power and phase of the EEG signal for different frequencies. The reader is referred to (Cohen, 2014) for the detailed mathematical derivation of Equation 2.20 and discussion of the DFT. The signal in the frequency domain can be transformed into the time domain using the Inverse Fourier Transform (IFT):

$$x_k = \sum_{k=1}^{n} X_f\, e^{(2\pi i f (k-1) n^{-1})} \tag{2.23}$$

Conceptually, the DFT is useful to understand the principle behind the transformation from time domain to frequency domain. Its practical implication however, is computationally expensive and slow. For this purpose the Fast Fourier Transform (FFT) is used in all toolboxes for the time-frequency transformation. The FFT is used to estimate the Power Spectral Density (PSD) which is one of the measures used to estimate the power of the EEG data in the studies presented in this thesis. It is discussed in the next section. An important assumption of the FT is that the time-series signal in question is stationary over time (i.e. there is no change in mean, variance and frequency of the signal). This is an assumption that is likely to be violated in real data as neurophysiological activity is non-stationary and changes over time particularly in response to different stimuli or tasks. Therefore the FT may be a more suitable choice for resting state or sleep studies. Additionally, the FT does not provide any temporal representation of the frequencies. Alternative methods may therefore be employed to obtain the time-frequency decomposition such as the wavelet-based decomposition which is used in this PhD work and is discussed in the following section.

2.3.2.2.2.2 Power Spectral Density   If the temporal representation of the frequencies is not of interest, then the short-time Fourier Transform (STFT) may be used when segments are shorter, during which the signal is likely to remain stationary (Cohen, 2014). This can then be used to calculate the PSD which is obtained by squaring the Fourier coefficient to obtain the distribution of the power of the different frequencies. It can be represented topographically as well.

2.3.2.2.2.3 Wavelet Convolution   Wavelet-based decomposition or wavelet convolution can be used alternatively to the FT if the stationarity assumption is likely to be violated. It has the added advantage of providing temporal information about the signal thereby allowing visualisation of changes in power of frequencies over time, although it must be noted that the time-frequency representation provides a trade-off between the temporal and frequency precision. The reason why the FT is unable to provide any temporal representation is because the kernel used for the dot product is a sine wave which continuously fluctuates over time and in order to obtain temporal characteristics of the frequencies, the dot product between the sine wave and the time-series signal needs to be computed at specific time windows. This can be done by convolving (taking the dot product) between the sine wave with a Gaussian window which is given by Equation 2.22

$$G = ae^{-(t)^2/(2\sigma^2)} \tag{2.24}$$

where G is the Gaussian window, a is the amplitude of the Gaussian curve, t is the time and σ is the width (or standard deviation) of the Gaussian and σ is given by

$$\sigma = \frac{n}{2\pi f} \tag{2.25}$$

where f is the frequency and n is the number of wavelet cycles. n is a non-trivial parameter that determines the trade-off between frequency and temporal precision and needs to be selected carefully based on the data. For the data presented in Chapters 4, 5 and 6 where wavelet convolution is used, $n = 3$ was used. The convolution of sine wave with the Gaussian window provides the Morlet Wavelet (Cohen, 2014) and Figure 2.19 shows an ex-

ample of a sine wave and a Gaussian wave and the resulting convolution. Morlet wavelets are useful in evaluating the temporal features of the frequency structure of the EEG signal. Additionally, wavelet convolution requires the signal to be stationary only during the time window in which the wavelet resembles the sine wave (Cohen, 2014), thereby providing a more reasonable assumption that is less likely to be violated (Cohen, 2014; Florian and Pfurtscheller, 1995; Jaeseung Jeong et al., 2002).
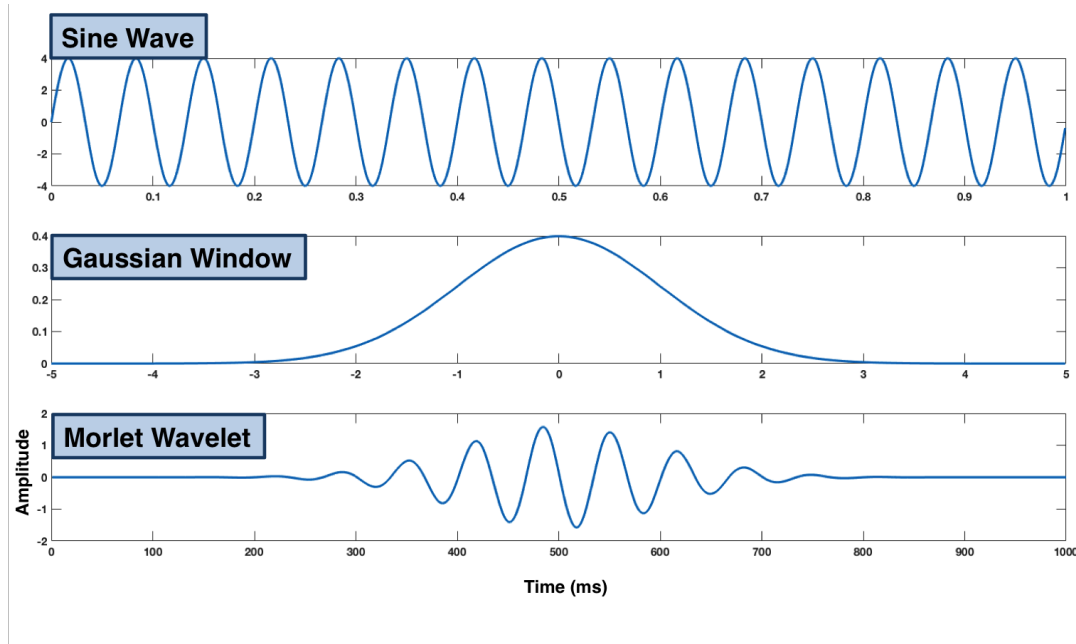
Figure 2.19: Example of how a Gaussian window can be convolved with a sine way to obtain the Morlet wavelet.

As I mentioned earlier, in analysing the EEG data presented in this thesis, obtaining the power of the underlying frequencies in the EEG data is of particular interest. In order to extract the power, complex Morlet wavelets need to be used. Similar to the DFT or FFT, the EEG signal is convolved using the dot product with the complex Morlet wavelet and the resulting complex-valued function can be used to extract information about the time, power and phase. The reader is referred to (Cohen, 2014) for a more detailed discussion and fuller mathematical description of complex Morlet wavelets.

2.3.2.2.2.4 Event-related spectral pertubation   In the analyses presented in this thesis, wavelet convolution was used to obtain the time-frequency representation of the EEG

signal. This representation is referred to as the event-related spectral pertubation (Makeig, 1993) which is computed by obtaining the spectral information on a trial-by-trial basis for each participant which is then averaged to obtain an average ERSP for each participant. This can then be averaged across participants to obtain a grand ERSP.

2.3.3   Summary

In this chapter, the fundamentals of NIRS and EEG techniques were described in detail which included theory as well as instrumentation. The data processing pipelines for each technique were also discussed in detail, which will be used to analyse the data presented in Chapters 4 - 8. While Chapter 4 describes a study that used only broadband NIRS, all subsequent chapters (5 - 8) utilised NIRS simultaneously with EEG.

The following chapter discusses the process of developing headgear for the various studies presented in this thesis.

Chapter 3

DEVELOPMENT OF HEADGEAR

FOR INFANT STUDIES

3.1 Introduction

As outlined in Chapter 1, the purpose of the work presented in this thesis was to utilise broadband NIRS for the non-invasive measurement of cerebral energy metabolism during brain development and further, to use this measure to investigate neurometabolic pathways in the developing infant brain. Specifically for the latter aim, broadband NIRS was required to be used simultaneously with EEG. While extensive work has been carried out by Dr Sarah Lloyd-Fox at the Centre for Brain and Cognitive Development (CBCD) to successfully develop handcrafted headgear for NIRS infant studies, particularly for the work presented in the latter half of this thesis, more adaptable designs were required for use with EEG. Additionally, each of the studies that I carried out during this PhD work had a range of different requirements which are discussed in the following sections. 3-dimensional (3-D) printing presents a good option to prototype more complex designs of the optode holder. This chapter therefore, details the development of 3-D printed headgear for each of the studies presented in this thesis.

3.2 Development of 3-D printed headgear for infant studies

This section discusses the translation from handcrafted arrays to 3-D printed headgear which was used for the first infant study presented in Chapter 4, that utilised a single channel broadband NIRS system referred to as the mini-CYRIL. The system was composed of a single light source and detector.

3.2.1 Optical fibres

It is important to understand the shape of the optical fibre as this greatly influences the design of the headgear. For the first infant study, identical optical fibres were used for both light source and spectrometer and were made of glass, manufactured by Loptek (Loptek, Germany). Each fibre had an inner core diameter of 2.3 mm. The subject-end of the fibres was flat-ended with the optode head at right angles to the optical fibre as shown in Figure 3.1a. Right-angled fibres are commonly used for infant studies as they lie flush against the head and can easily be secured into place without needing to apply extra pressure, thereby making them more comfortable. Additionally, there is no added gravitational pull causing the fibres to lift off the head, as is common in some adult fibres. This is discussed further in Section 3.3. Figure 3.1b shows the subject-end of the optical fibres.
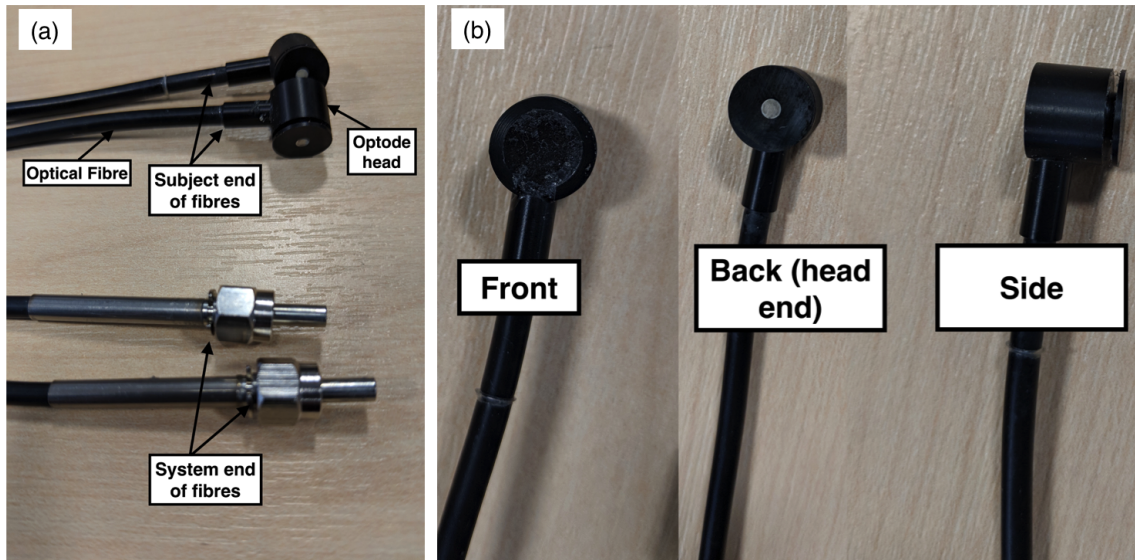
Figure 3.1: Optical fibres forming part of the mini-CYRIL system.

3.2.2 Probe design

3.2.2.1 Existing headgear designs

An extensive amount of work has been done by Dr Sarah Lloyd-Fox at the CBCD, to design infant NIRS headgear that is now used by neurodevelopmental research groups using functional NIRS (fNIRS). The existing NIRS headgear consists of two components:

1. Optode holder which is formed of

   (a) Plastic washers to hold individual fibres

   (b) Pad to hold all the fibres

2. Silicone headband which is used to keep the optode holder in place on the infant's head.

Figures 3.2a, b and c show the optode holder and headband respectively and Figure 3.2d shows the headgear on an infant.
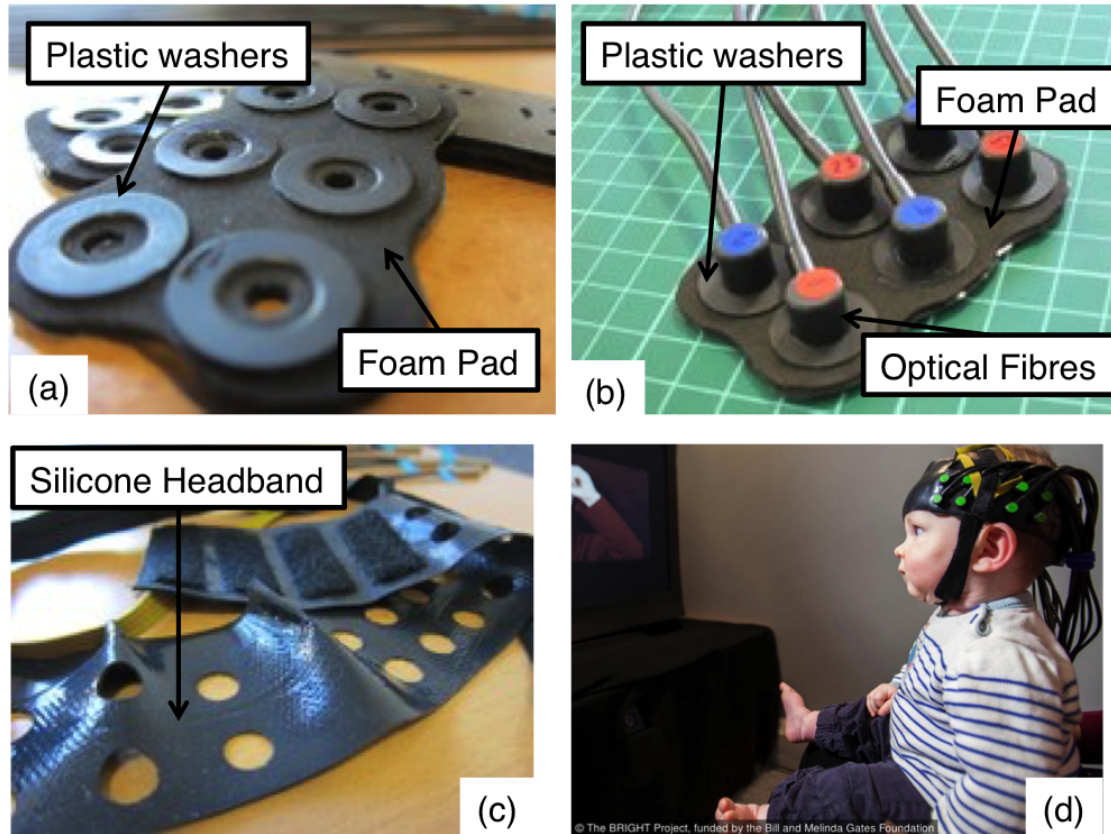
Figure 3.2: Existing NIRS headgear components individually with (a) and (b) showing the optode holder composed of plastic washers and foam pad to hold individual fibres, (c) the silicone headband used to hold the optode holder in place on the infant's head and (d) the headgear positioned on an infant. The images used in (a), (b) and (c) were reproduced from http://cbcd.bbk.ac.uk/node/165 and the image used in (d) is courtesy the Bill and Melinda Gates Foundation.

As I discussed previously, the existing handcrafted headgear works well for infant studies. However, more adaptable designs were required for the studies presented in Chapters 5 - 8 which could be easily designed and tested through 3-D printing. For the study presented in Chapter 4, a simple 3-D printed optode holder was designed for use in conjunction with the NIRS headband developed by Dr Sarah Lloyd-Fox which could then be adapted and modified for use in later studies.

3.2.2.2 3-D printed designs

A number of 3-D printed designs were created and trialed for use in infant NIRS studies. The first design involved reproducing the current handcrafted optode holder design in 3-

D space using AutoCAD; a commercial computer aided design software (Autodesk, USA). The second design was similar to the first with a few varying features and was used for this study. The third design was used for subsequent NIRS studies and will discussed in more detail in Chapter 5.

Design 1

The first design developed is shown in Figure 3.3. It was 3-D printed in three layers; 1) Rigid washers 2) Medium soft rubber material to support washers and 3) Soft rubber pad. The base material used for each of the components was TangoBlack (Stratasys, USA) which is a soft rubber that can be have varying rigidity from the most rigid version used for the washers to the least rigid version used for the soft rubber pad. A PolyJet Objet Connex 500 (Stratasys, USA) printer was used to print the design in layers. During the first attempt to translate the infant optode holder into a 3-D printed model (Design 1), a number of problems were encountered which included:

1. The material for the washers was too rigid and caused the washers to snap when fibres were clipped in and out.

2. The difference in the density of the materials (between the rigid washers and the flexible rubber pad) caused breakages at different points along the optode holder.

For this reason, a second design was developed to improve upon on these problems and this was used for the study presented in Chapter 4.
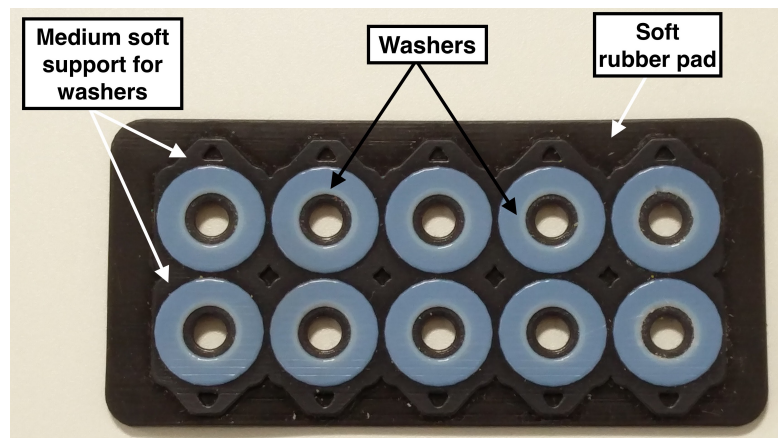
Figure 3.3: Optode holder design 1, with different components indicated.

Design 2

The second design that was developed was printed in two layers; 1) Rigid washers embedded inside the soft rubber 2) Soft rubber pad, as shown in Figure 3.4. These were made of the same material as for Design 1. A shorter version of this design, which is shown in Figure 3.5, was used in conjunction with the silicon headband for this study. The short version of Design 2 was satisfactory and did not break as easily as the washers were embedded but did have some apparent cracks after approximately 30 uses. Additionally, this design was challenging to create as embedding the washers into the rubber pad required advanced AutoCAD skills. Therefore, it was not easy to adapt the optode holder for different array designs and would not work well for future studies. For this purpose, further designs were developed which are discussed in Section 3.4.
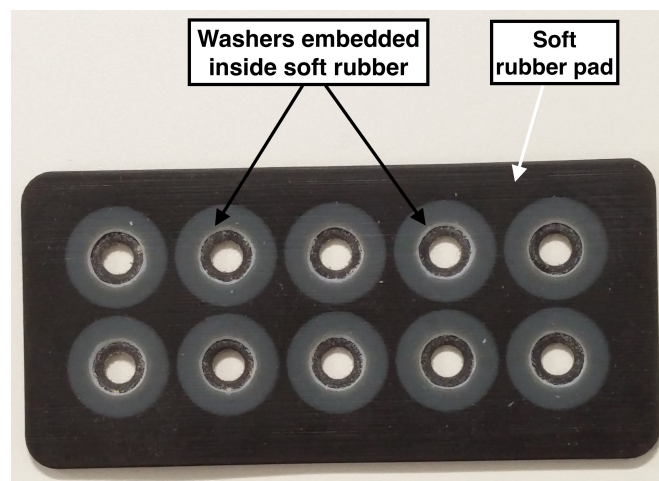
Figure 3.4: Optode holder design 2, with different components indicated.

Figure 3.5: Shorter version of Optode holder design 2 which was used for the study presented in this chapter, with fibres clipped in. The fibres are clipped in for the purposes of the image, the spacing between source and detector was maintained at 2.8 cm for all participants, during the study.

3.3 Development of combined NIRS-EEG headgear for use with adults

While the focus of this PhD work was on infant brain development, the second study in thesis (presented in Chapter 5) utilised multi-channel broadband NIRS simultaneously with EEG in adults. This is because prior to using a combined NIRS and EEG protocol in infants, a number of methodological aspects needed to be developed which could only be done through first performing the studies in adult. The study used visual stimulation and NIRS responses were measured over the occipital cortex. One of the main challenges of simultaneous NIRS and EEG is the design and development of appropriate headgear to accommodate both NIRS optodes and EEG electrodes on the head. This section discusses how the combined NIRS-EEG headgear was created for the adult study prior to extension for use with infants. The work presented here was carried out in collaboration with Mr Andrew Levy of the Wellcome Trust Centre for Neuroimaging, Functional Imaging Laboratory, UCL.

3.3.1 Optical fibres

The system is described in detail in Chapter 5 and was composed of four light sources and 10 detectors which provided a total of 16 measurement channels. The optical fibres used in this study were made of glass and were custom-builty by Loptek (Loptek, Germany).

The diameter of the light source of each individual light source fibre at the subject-end was 3.2 mm. These fibres are shown in Figure 3.6a. Each bundle of the detector fibres had a diameter of 1.5mm and each individual detector fibre within the bundle had a diameter of 70μm. The detector fibre bundle is shown in Figure 3.6b. The system had two detectors for tissue oxygenation index (TOI) measurements which were not used in this study.
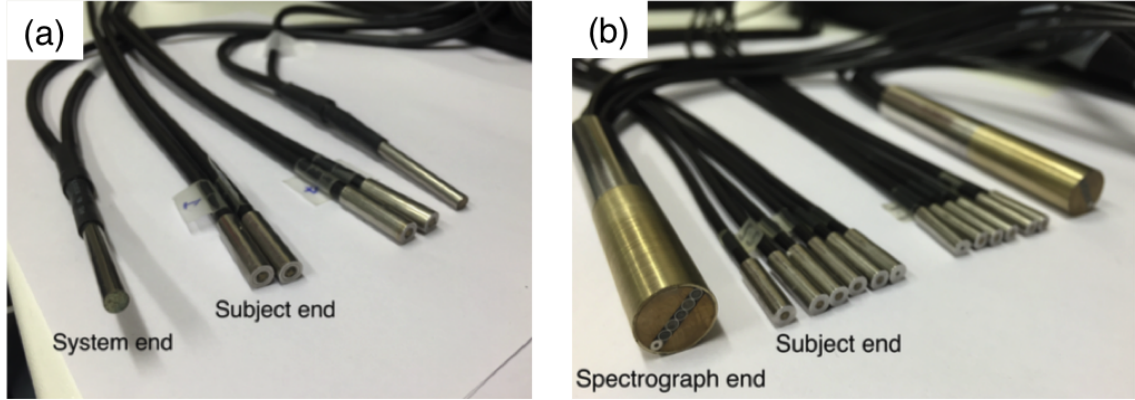
Figure 3.6: Optical fibres forming the source fibres and detector fibres with (a) the system and subject ends of the light source fibres and (b) the system and subject ends of the detector fibres. All photos were reproduced from (Phan, 2018) with permission.

3.3.2   EEG

As this study was performed concurrently with EEG, the EEG montage is described here. The system has already been described in detail in Chapter 2. Twenty-six EEG channels were used with five channels positioned over the occipital lobe (Oz, O1, O2, O9 and O10) and twenty-one channels were distributed over the rest of the participant's head (AF3, AF4, Fz, F3, F4, FC1, FC2, FC5, FC6, Cz, C3, C4, CP1, CP2, Pz, P3, P4, P7, P8, PO3 and PO4). Figure 3.7 shows the EEG montage with all the channels indicated in purple circles.
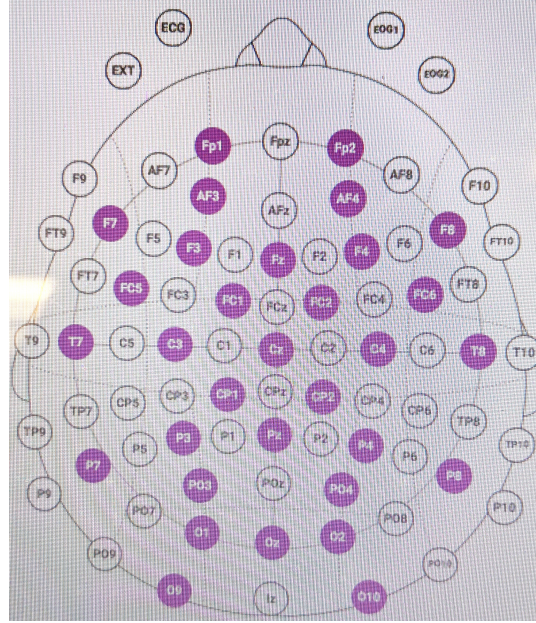
Figure 3.7: EEG montage showing the locations of the 26 channels.

3.3.3 NIRS Probe Design

The orientation of the sources and detectors was kept the same as in previous studies (Phan et al., 2016a) that also used visual stimulation and measured responses over the occipital cortex. While their study used a number of different source-detector separation distances for the purpose of performing image reconstruction, the separation in this study was maintained at 3 cm for all source-detector pairs which has been previously shown to be ideal for adult functional activation studies measuring changes in oxCCO (Phan et al., 2016b). Figure 3.8 shows the schematic for the array which was centred around Oz of the International 10/20 system.
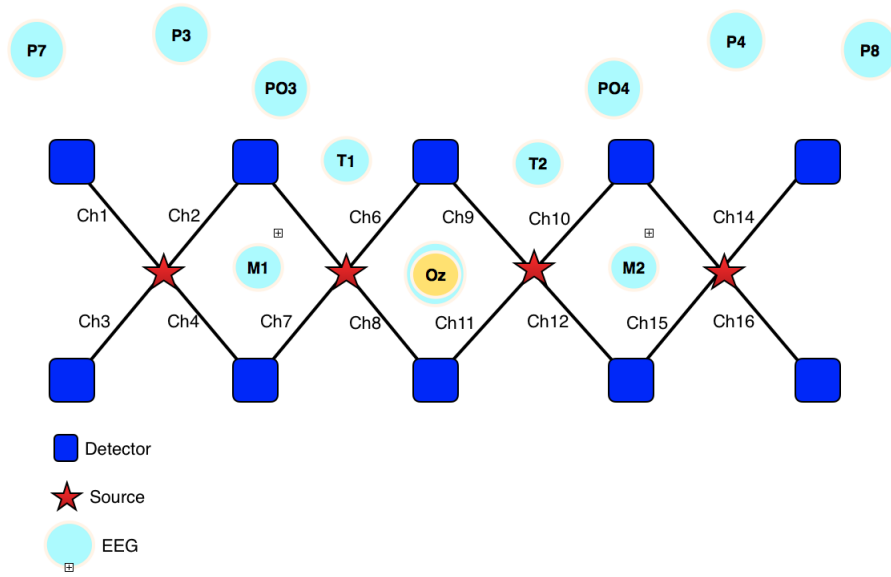
Figure 3.8: A schematic diagram of the NIRS array showing the positions of the sources and detectors and EEG electrodes, with blue squares indicating detectors, red stars indicating sources and cyan circles indicating EEG channels over the occipital cortex. The black lines represent channels that are formed between sources and detectors.

3.3.3.1 Challenges

Although visual stimuli produce strong functional changes and previous work has demonstrated that the cytochrome signal is more localised than haemoglobin (Phan et al., 2016a), designing the headgear for a visual paradigm can be challenging particularly for use simultaneously with EEG. While the temporal resolution of EEG is much better than NIRS, its spatial resolution is poor. In contrast, NIRS provides good spatial resolution and the measured signals are more sensitive to the location of the optodes on the head. Therefore, well-designed headgear design is particularly important for NIRS measurements in order to ensure that the optodes lie over the region of interest and additionally to achieve good coupling between the optical fibres and the head which greatly influences the signal-to-noise ratio. There were a number of factors that needed to be kept in mind when designing the headgear, these included:

1. The occipital cortex is the area of the head where the scalp is the thickest and also

most variable among participants, therefore a solution needed to be devised that would work for all participants.

2. The fibres forming part of the multi-channel broadband system were straight-end fibres that were prone to lifting off the scalp (due to gravitational pull) and therefore failing to maintain good coupling with the head.

3. The EEG necbox and wires added weight to the headgear leading to an additional downward force causing the fibres to further lift off the head. Therefore, a solution was required that would counteract the downward pull on the fibres and allow them to be tightened on the head independently.

The initial focus of this study therefore was to develop appropriate headgear for simultaneous NIRS and EEG measurements over the occipital cortex. The first iteration of the headgear involved using 3-D printed designs by Dr Phong Phan, with some variations. The NIRS headband and EEG cap were developed separately to allow meet the individual requirements of each technique independently.

3.3.3.2   Iteration 1

The NIRS headgear involves a number of components:

1. 3-D printed holders for the source fibres, shown in Figures 3.9a and 3.9b. Figure 3.9a is a conceptual drawing in AutoCAD showing the design in 3-D space prior to printing and Figure 3.9b shows the printed holders with the source fibres plugged in.

2. 3-D printed holders for the detector fibres, shown in Figures 3.9c and 3.9d. Figure 3.9c is a conceptual drawing in AutoCAD and Figure 3.9d shows the printed holders with the detector fibres plugged in.

3. 3-D printed optode couplers (also referred to as washers) that would allow the holders to be secured into the cap, shown in Figure 3.9e, which is a conceptual drawing in AutoCAD.

4. Headband to position holders and couplers on the head.

5. Neoprene fasteners to allow tightening of the headband to the head.
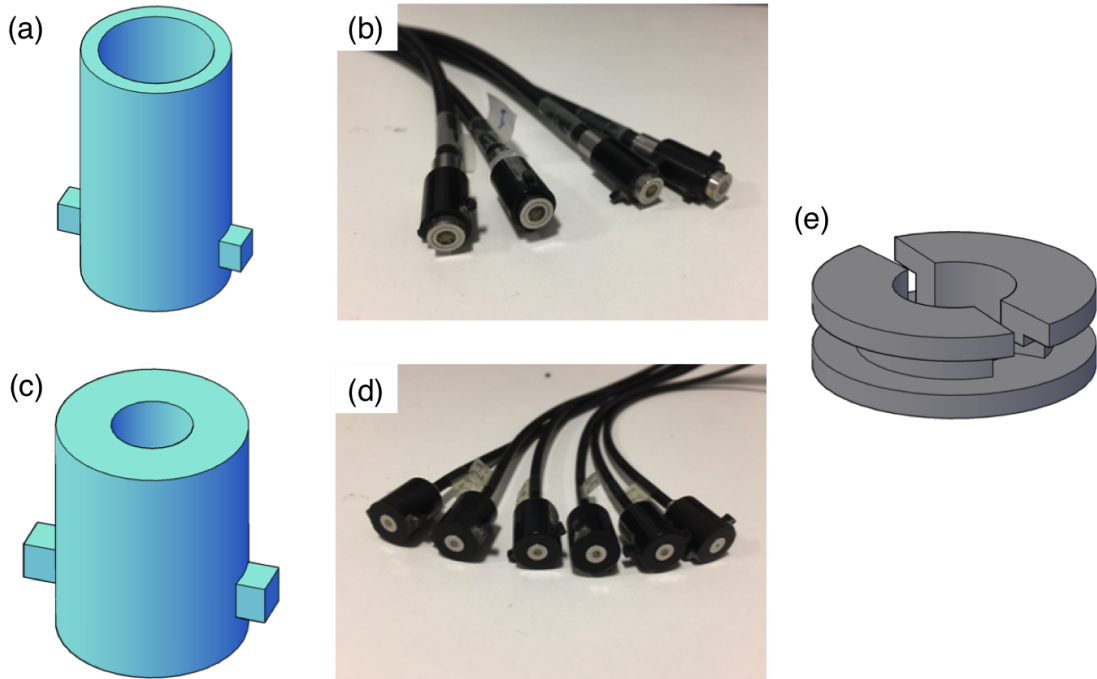
Figure 3.9: Components required to hold optical fibres in place for visual cortex measurements. (a) conceptual design of 3-D printed holder for the source fibres and (b) source fibres shown plugged into the 3-D printed holder, photo courtesy Dr Phong Phan (c) conceptual design of 3-D printed holder for the detector fibres (d) detector fibres shown plugged into the 3-D printed detector holders, photo courtesy Dr Phong Phan and (e) conceptual design of 3-D printed optode coupler to hold optical fibres on the head

The first iteration of the headgear involved creating a headband made of neoprene material, shown in Figure 3.10. This headband was made by creating holes for the optode couplers in the neoprene material. The couplers were then glued into the material using silicone, in order to fix them into place to ensure that the source - detector separation was maintained. The back of the neoprene material was coated with silicon to provide friction and ensure that the headband did not slip down during measurements. Finally, neoprene fasteners were stitched on in order to tighten the headband on the head.
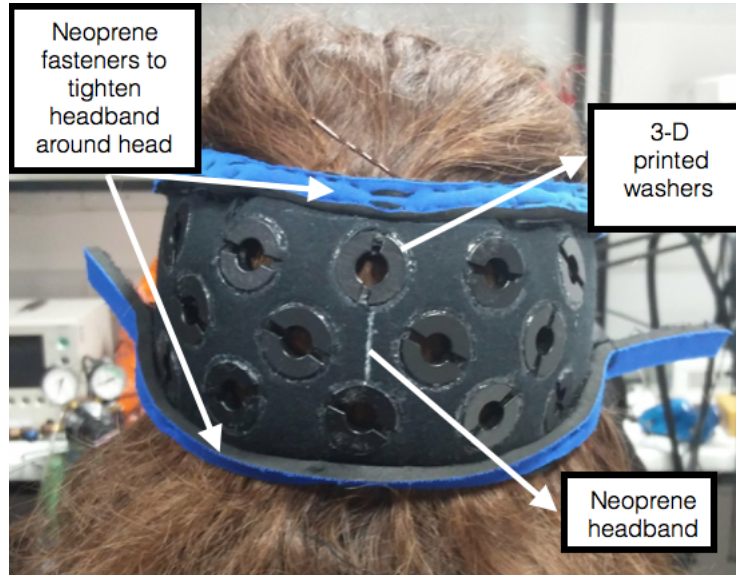
Figure 3.10: The iteration of the NIRS headband for measurements over the occipital cortex, on a participant. The headgear consisted of a neoprene headband, with the washers for the optical fibres glued in to the band. Neoprene fasteners were stitched on to allow tightening of the headband to the front of the head.

3.3.3.2.1 Problems The first iteration of the headband proved to be unsuccessful and a number of issues were encountered, particularly in ensuring that all optical fibres maintained good contact with the head. These included:

1. The silicone used to line the neoprene headband was too thick and not only did it cause the headband to become heavy but also made it stiff. This meant that the headband did not mould very well to the shape of the head and caused rifts where certain parts of the array would make good contact with the head while other parts would lift off. In particular, the most important channels centered around the primary visual cortex were most affected.

2. The neoprene fasteners allowed tightening of the headband but this led to headaches and pulsating sensations at the front of the participant's head. Additionally as the fasteners were made of a thicker type of neoprene they tended to lift off the head rather than provide the tightening effect required at the back of the head.

3. The optode couplers glued into the headband using silicone led to decreased flexibility of the headgear.

4. The neoprene material used for the headband was a rectangular piece of material that was not designed with the shape of the average adult head in mind and therefore did not mould to the participant's head.

Figure 3.11 illustrates the various issues encountered with the first iteration of the headgear. A second iteration of the headband was developed in order to overcome these issues.

Headband not moulding to shape of the head and lifting off, allowing external light in

Thick neoprene fasteners lifting off the head instead of providing tightening of headband to the head

Rifts in headgear leading to poor contact of optical fibre and scalp
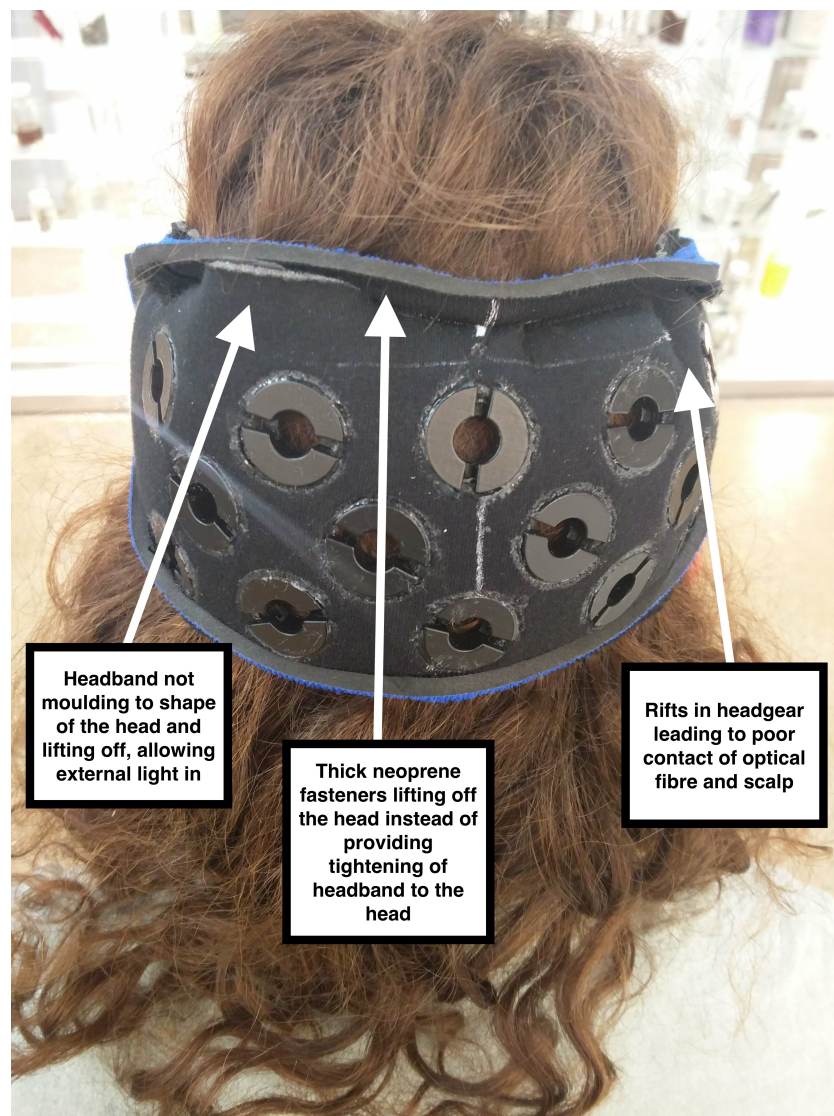
Figure 3.11: Iteration 1 of the headband on a participant indicating some of the issues that arose with this headgear.

3.3.3.3   Iteration 2

For the second iteration, it was necessary to re-design most aspects of the headgear. There were two main issues with first iteration:

1. Inability to mould to the head shape of the average adult.

2. Failure provide enough support and tightness to ensure good optical coupling between the fibres and the head.

These issues were addressed in a two-step improvement process.

3.3.3.3.1   *Issue #1*

- **Headband**

Neoprene was used again to create the headband, however a softer type of neoprene was used. A model head was used for pattern cutting to ensure that the headband had curvature built-in to mould to the shape of an adult head. Figure 3.12 shows an image of the second iteration of the headband.

Figure 3.12: Second iteration of the NIRS headband which was specifically developed to mould to the shape of an adult head.

- **3-D printed flexible grid**

In the previous version of the headgear, the couplers were glued in which led to decreased flexibility of the headgear. Therefore, in this iteration the couplers were not glued in and a different method of ensuring source - detector separation was devised. A flexible grid, shown in Figure 3.13a was designed and 3-D printed using plasticized copolyamide thermoplastic elastomer (PCTPE) (Taulman3D, USA) which is a type of nylon. Due to the flexibility of this material, when attached to the underside of the neoprene headband shown in Figure 3.13b and positioned on the head, the grid gained curvature which aided the overall ability of the headgear to mould to the shape of the head.
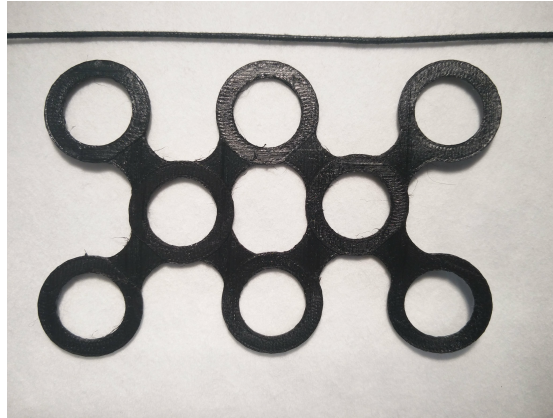
(a) The underside of the headband with the flexible 3-D printed grid indicated.
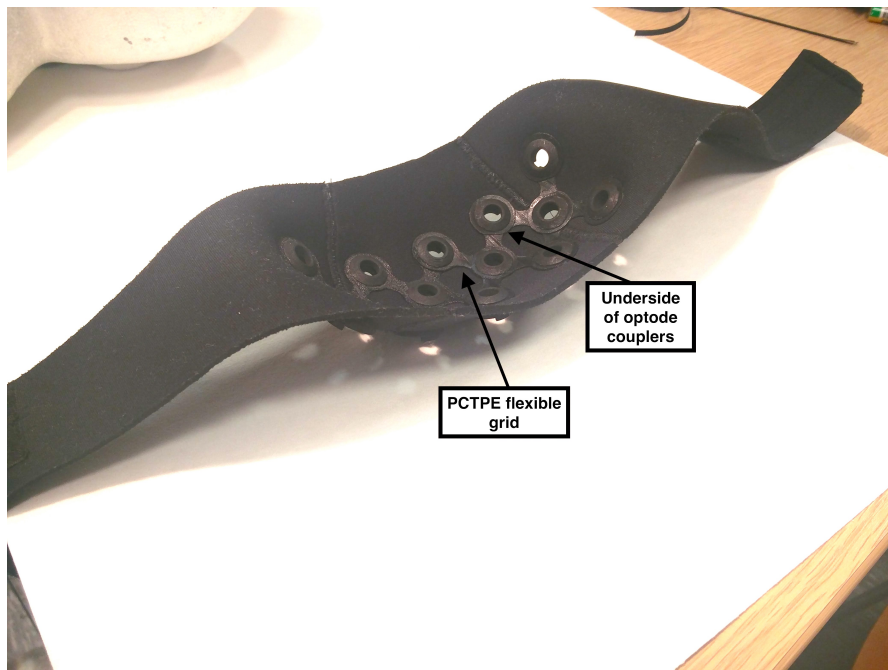
(b) The underside of the headband with the flexible 3-D printed grid indicated.

Figure 3.13: Flexible grid 3-D printed grid to maintain source - detector separation of 3cm.

3.3.3.3.2 *Issue #2*

- **Optode couplers**

The previous design of the 3-D printed optode couplers worked well for NIRS functional activation studies. However, when used in conjunction with EEG, where added weight (due to the electrodes and the wireless transmitter), led to additional downward forces on

the optical fibres. Due to this, the current couplers were unable to satisfactorily support the fibres, often leading to poor coupling with the scalp. The couplers were therefore re-designed in AutoCAD to include additional components to allow further tightening of the fibres on the scalp. The holders for the source and detector fibres were kept the same as in the previous design. Figure 3.14 shows a picture of the new 3-D printed couplers. The couplers were altered in the following ways:

1. Loop holes were added to the top of the coupler in order to feed string through to attach to a buckle pulley system at the front of the head.

2. The bottom half of the coupler was modified to have an upward conical shape in order to ensure that the flexible grid and neoprene did not slip out.
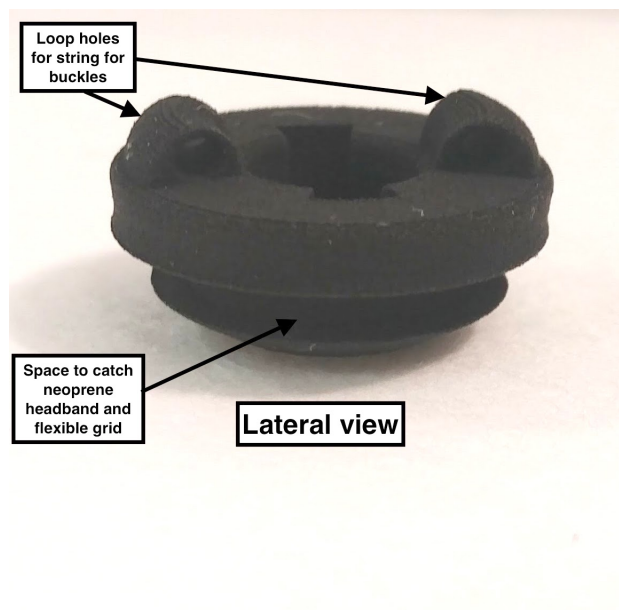
Figure 3.14: Optode couplers re-designed to optimise tighter coupling of optical fibres and the head.

- **Buckle pulley system**

The string that was fed through the loops on top of the optode couplers would be attached to ribbon forming part of a buckle pulley system, shown in Figure 3.15. This allowed

the opportunity to further tighten the fibres on the head, independent of tightening the headband.
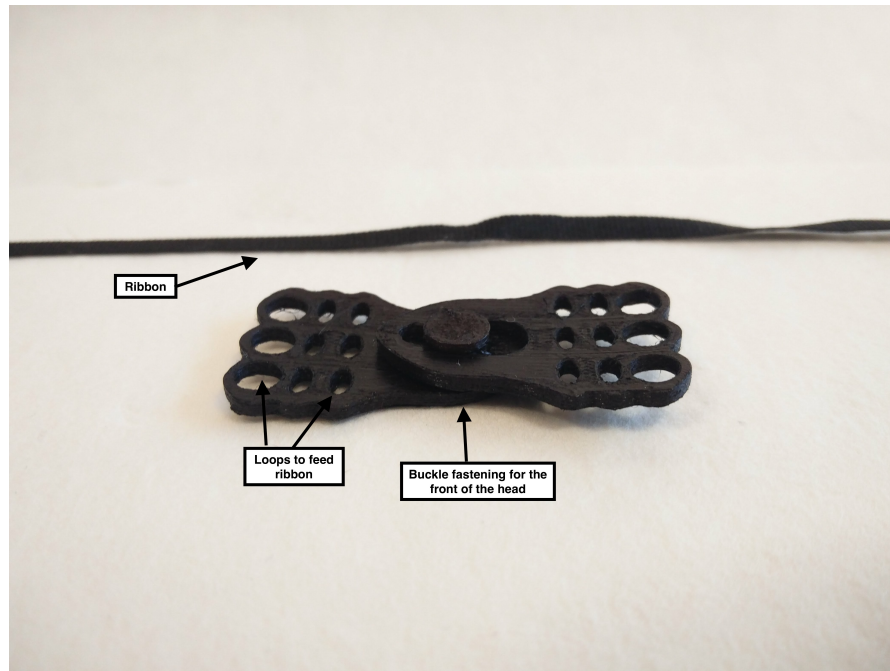
Figure 3.15: Buckle pulley system used to tighten the fibres on the head.

Final Headband

Figures 3.16a-c show the front, side and back views of the headband positioned on a participant.
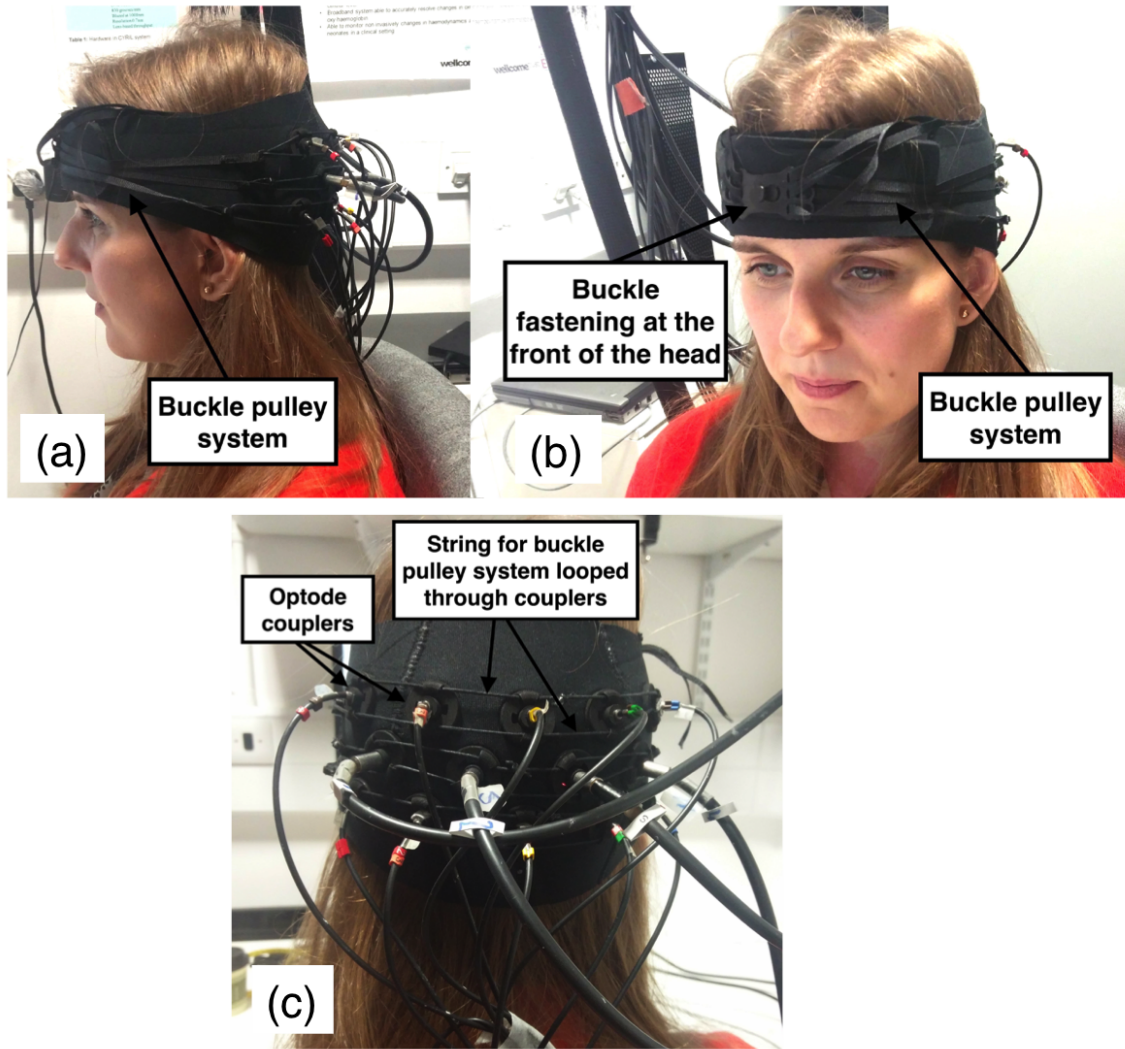
Figure 3.16: (a) Front, (b) side and (c) back views of the headband on a participant. Permission was obtained from the participant for their image to be included here.

3.3.3.4 Combined NIRS-EEG headgear

Preliminary testing showed that the new headband fulfilled all the previously discussed requirements of a functional and comfortable NIRS headband. In order to create a combined NIRS-EEG headgear, the NIRS headband was used in conjunction with the Neuroelectrics Neoprene Headcap (Neuroelectrics, Spain), shown in Figure 3.17. A window was cut out from the back of headcap where the NIRS array could be placed. The two independent systems were then attached with velcro strips which is shown in Figure 3.18.

Figure 3.17: Neuroelectrics Neoprene Headcap used for EEG, image reproduced from www.neuroelectrics.com.

Figure 3.18: Image showing how the NIRS headband and EEG headcap were attached (a) side view and (b) back view, on a participant.

3.4 Development of combined NIRS-EEG headgear for use with infants

The third study in this thesis (presented in Chapter 6 & 7) extended on work from the single channel infant study from Chapter 4 as well as the multi-channel broadband NIRS

and EEG study from Chapter 5. The study used the same multi-channel broadband NIRS system simultaneously with EEG and measured activity over the right temporal cortex and occipital cortex. This section details how the knowledge and processes from the adult headgear development were extended to create the combined NIRS and EEG headgear for use with infants.

3.4.1 Optical fibres

The optical fibres for the infant study differed from those used for the adult study. While the NIRS system used was the same, the infant modification allowed for the incorporation of four extra detectors forming a total of 4 light sources and 14 detectors which provided 19 measurement channels. The optical fibres were similar to those used in the first infant study and the subject-end of the fibres were right-angled. The fibres were made of glass and were custom-built by Loptek (Loptek, Germany), each with a diameter of 30μm. The diameter of each of the individual light source fibres at the subject-end was 5 mm while each detector had a diameter of 1 mm. The subject-end of the detector fibres are shown in Figure 3.19a and b and the light source fibres are shown in Figure 3.19c and d.
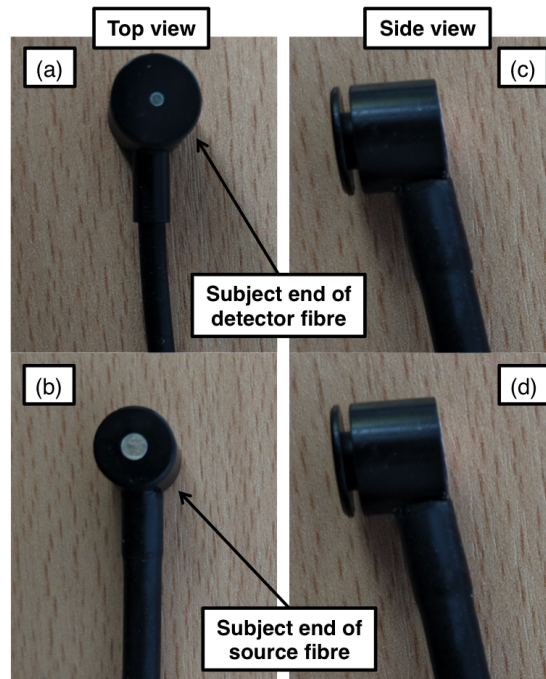
Figure 3.19: Subject end of the source and detector fibres with (a) the top view of the detector fibres (b) side view of the detector fibres (c) top view of the source fibres and (d) side view of the source fibres

3.4.2 EEG

The same EEG system was used as for the adult work. For this study, thirty-two EEG channels were used and these are indicated in purple circles in Figure 3.20 and were distributed equally over the participant's head (FP1, FP2, F7, F3, Fz, F4, F8, FC5, FC6, T7, C3, Cz, C2, C4, T8, TP7, CP5, CP6, P9, P7, P3, Pz, P4, P8, P10, PO7, PO3, PO4, O1, Oz, O2).
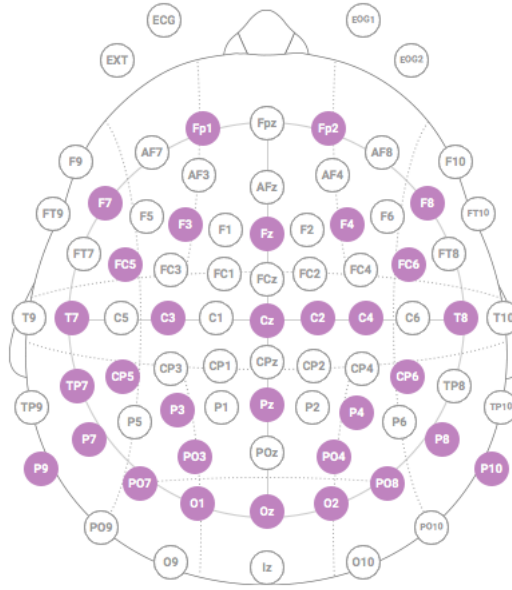
Figure 3.20: EEG Montage for infant study showing the locations of the 32 channels

3.4.3 Headgear Design

The requirements for the headgear for this infant study differed from the adult study in a number of ways:

1. The optical fibres used for the study presented here were flat-ended with a similar design to that described in Section 3.1 and had a gap for a clipping mechanism. Therefore, the headgear did not require 3-D printed holders for source and detector fibres and the optode coupler needed to have a design similar to that presented in Section 3.1.

2. When performing adult studies, there were not as many constraints as with infants. For example, adults can be instructed to sit still while the headgear is being positioned and time can be taken to ensure that a good coupling is achieved between the optical fibres and the head of the participant. On the other hand, infant studies require headgear that is easy to position and tighten within the space of a few minutes. Therefore, while adult studies could have a separate NIRS headband and an EEG headcap, such a solution would not be feasible for infant studies and a single headgear item was required that simultaneously incorporated both NIRS optodes

and EEG electrodes.

The Enobio EEG headcap for infants was used (shown in Figure 3.21a and b) for combined NIRS-EEG measurements. While the EEG electrodes could be plugged straight into the cap, a more sophisticated NIRS array design was required which would also fit into the cap. The next section details the development of the NIRS array for combined NIRS-EEG measurements in infants.

Figure 3.21: Enobio EEG headcap

3.4.3.1 NIRS array design

In Section 3.1, I described how the hand-crafted NIRS arrays (or optode holders) were translated into 3-D printed designs that were used for the first study presented in this thesis. The requirement of the optode holder for this infant study presented remains mostly the same with one additional specification - the washers that held the NIRS fibres in place needed to have a groove similar to that of the EEG geltrodes so that they could be held in place in the headcap. To recap, an optode holder needed to have 1) washers to hold individual fibres and 2) a pad to hold the washers and the fibres. Here, I will be resuming the discussion on how the designs presented in Section 3.1 were improved upon to create the final design used for the combined NIRS-EEG infant studies. Figure 3.22 shows the schematic for the arrays used for this study. The array for the occipital channels was cen-

tred around Oz while that for the temporal channels was centred around CP6. The source - detector separation for all channels here was 2.5 cm, except occipital channels 3 and 6 which had a longer source - detector separation of 2.90 cm.
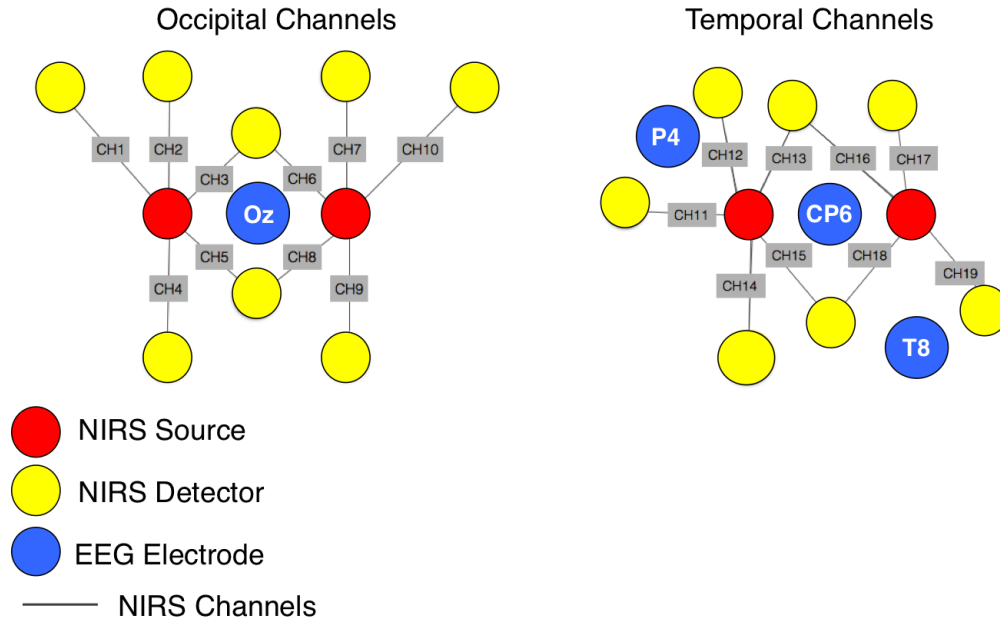
Figure 3.22: Schematic diagram of the NIRS occipital and temporal arrays showing the positions sources, detectors and EEG electrodes. The red and yellow circles represent the sources and detectors respectively while the blue circle indicate nearby EEG electrodes. The black lines represent channels that are formed between sources and detectors.

3.4.3.1.1 Washers

3.4.3.1.1.1 New design for NIRS-only studies Washers are also referred to as optode couplers and both terms are used interchangeably here. Design 2, used for the studies in Chapter 4, failed to fulfill the requirements of the NIRS headgear for long-term and more demanding infant studies. A multi-method approach was required to create 3-D printed designs that were more durable and long-lasting. The primary problem encountered was with the washers, which were printed using an FDM printer which only allows printing in different strengths of the same material - a type of rubber referred to as TangoBlack. Therefore to create stronger washers, an integrated approach utilising different 3-D print-

ing techniques and materials was adopted in order to redesign the optode holder. Additionally, once the array had been used for an extended period of time, the fibres were not held in place in the optode as strongly anymore. The design of the washer was therefore also altered. The following changes were incorporated:

1. The washer design was adapted to have a sliding mechanism rather than a clipping mechanism. Additionally, "pins" were included at the bottom of the washer. The sliding design was created by Mr Simon Scott of the Department of Medical Physics and Biomedical Engineering, University College London.

2. A Selective Laser Sintering (SLS) printer was used to print the washers (independently of the pad) using a tough nylon material.

3. The optode holder pad was printed in three layers on the FDM printer; a) Soft pad at the bottom b) Medium soft portion in the middle c) Rigid rings at the top where the independently printed washers would be glued. The rings had receiving "holes" for the "pins" at the bottom of the washers for ease when gluing.

The washers and the pad were therefore printed separately and glued together after printing. Figure 3.23a shows a conceptual image (in AutoCAD) of the new washer design with the sliding mechanism and the "pins" included at the bottom are also indicated. Figure 3.23b conceptualises the slotting mechanism where. Figure 3.24a and b provide an illustration of the final pad with one washer slotted into place and 3.25 shows the 3-D printed version of the design. This design has been successfully used by longitudinal studies running in Cambridge and the Gambia indicating that this design is durable and can be used for long-term studies as a possible alternative to the hand-crafted NIRS arrays.
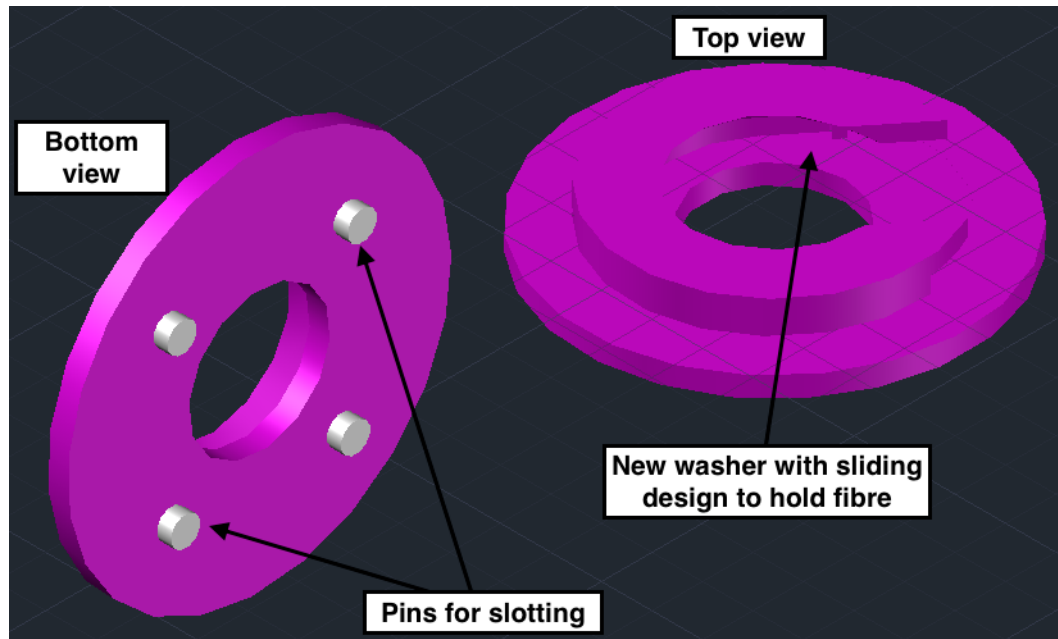
(a) Top and bottom (rotated) conceptual views of the new sliding washer made of nylon, with pins at the bottom.
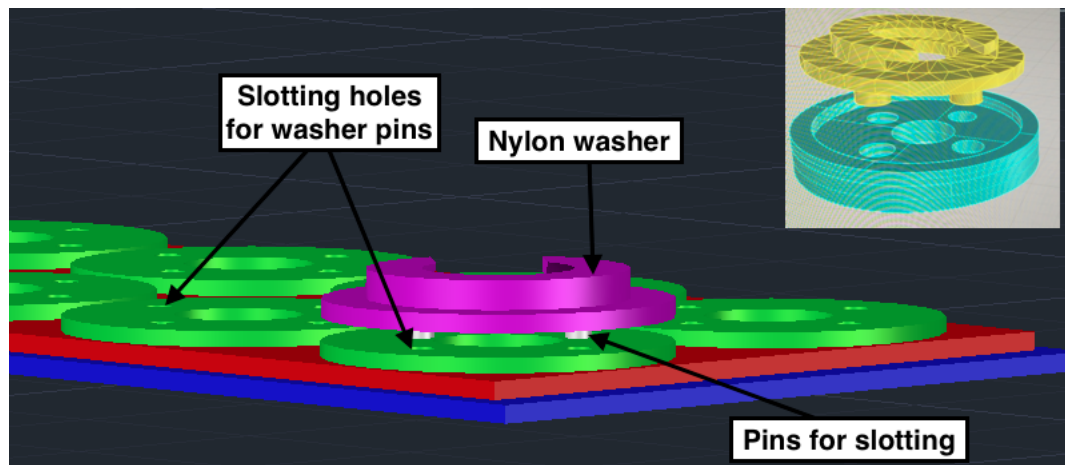
(b) Image conceptualising the slotting mechanism of the washer into the receiving holes in the rigid rings. Top right corner shows a clearer view of the slotting mechanism.

Figure 3.23: Conceptual images in AutoCAD showing the new design of the washer.
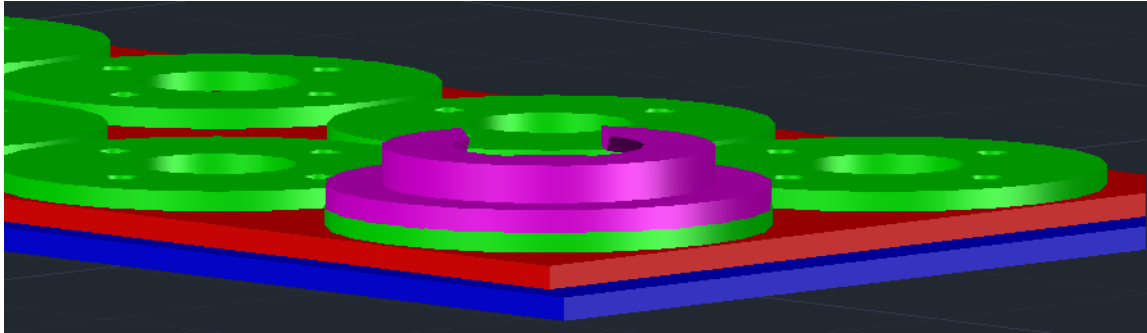
(a) Conceptual image after the washer has slotted into the right position on the rigid rings.
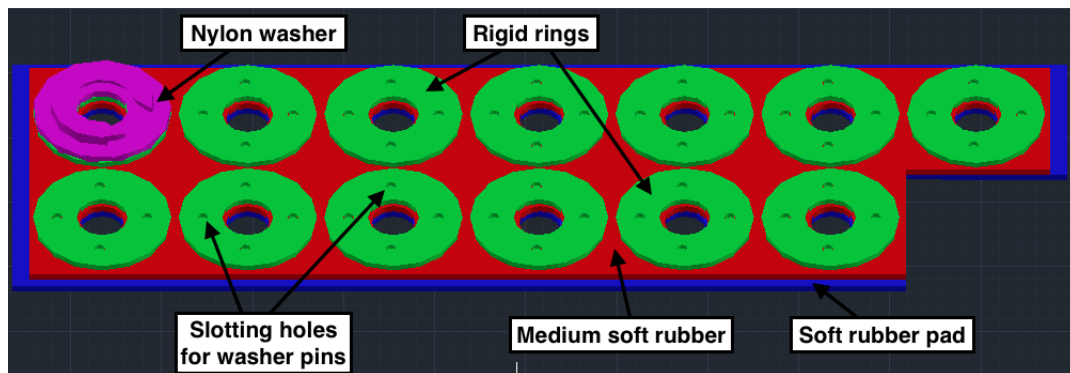
(b) Top view of a conceptual image of the final 3-D pad, with one washer attached.

Figure 3.24: Conceptual images in AutoCAD showing the new design of the array.
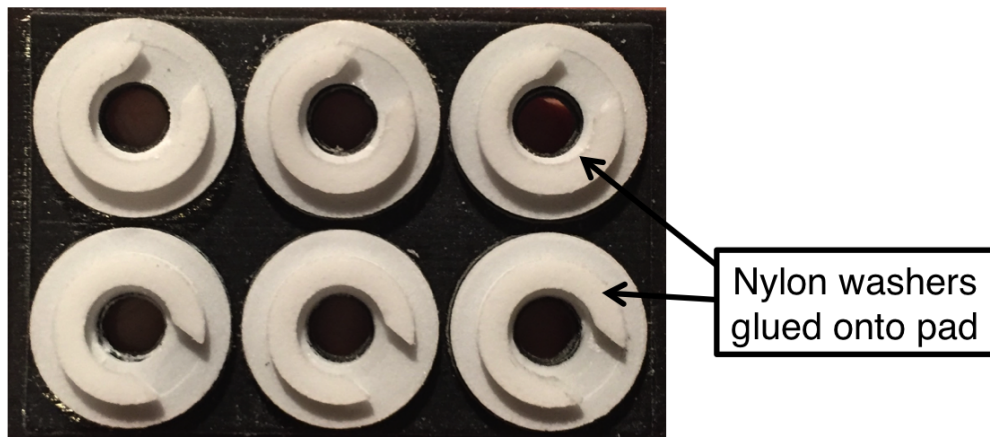
Figure 3.25: 3-D printed version

3.4.3.1.1.2 NIRS-EEG washers While the design presented in the previous section worked well for NIRS-only infant studies, the washer needed to be modified to include a groove in order to be used for the combined NIRS-EEG study presented here. The multi-

method approach used to create the pad was kept the same.

Design 1   A number of different designs were developed, the simplest one is shown in Figure 3.26. A drawback of using an SLS printer was that in comparison to the FDM printer, the 3-D printed object could not have very fine detail. Therefore, designing the clipping space accurately in the washer was a challenging task (often being too tight) which caused difficulty in retrieving the fibre once it had been clipped in.
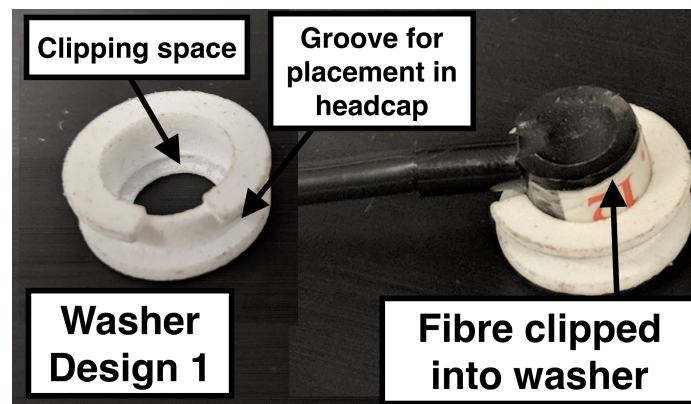
Figure 3.26: NIRS-EEG optode coupler design 1

Designs 2, 3 and 4   Designs 2, 3 and 4 were developed to include "appendages" which held the fibre in place without relying on a clipping space for the fibre. Figure 3.27a shows the conceptual images of these designs in AutoCAD, each design had a slightly different shape and size of the appendage. Figure 3.27b shows the 3-D printed version of Design 3 and while this worked well and held the fibres in place firmly, it resulted in a bulky washer that stuck out approximately 1 - 2 cm outside of the headcap and was not ideal for use with infants as the appendages were slightly pointed.
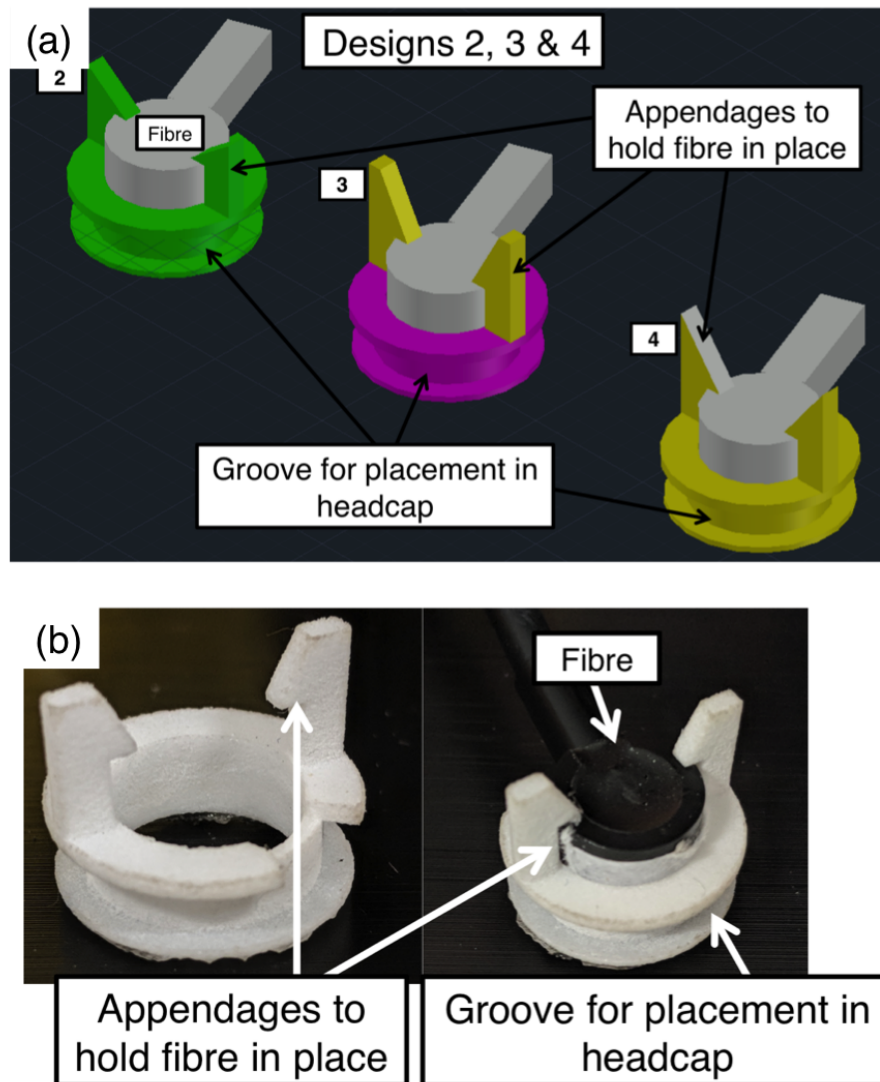
Figure 3.27: NIRS-EEG optode coupler designs 2, 3 and 4 with (a) conceptual images in shown in AutoCAD and (b) 3-D printed version with fibre clipped in.

Final Design Given that the previous designs with appendages did not work well, I reverted back to designing a washer with the clipping mechanism for the fibres. In this iteration however, I created a large opening for the fibre as well as a flat flexible appendage with gaps and a groove which, because the nylon was tough but flexible, allowed the fibres to be retrieved easily in comparison to Design 1. Figure 3.28 illustrates the final design in AutoCAD and Figure 3.29 shows the 3-D printed version of the washer and an image of

the washer glued onto the optode holder pad.

Top view | Top-Side view | Top-Front view

Groove for placement in headcap

Opening for fibre

Flexible appendage for easy retrieval of fibre
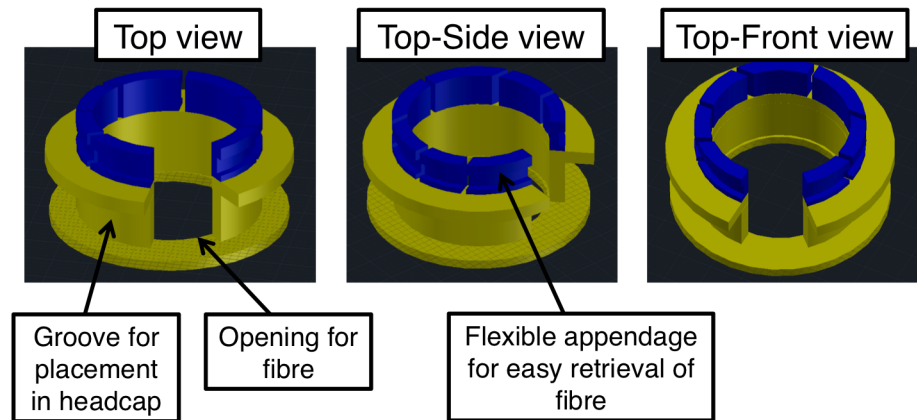
Figure 3.28: Conceptual image of final NIRS-EEG optode coupler, in AutoCAD

Final washer design

Fibre clipped into washer

Final washer design glued on top of soft flexible pad
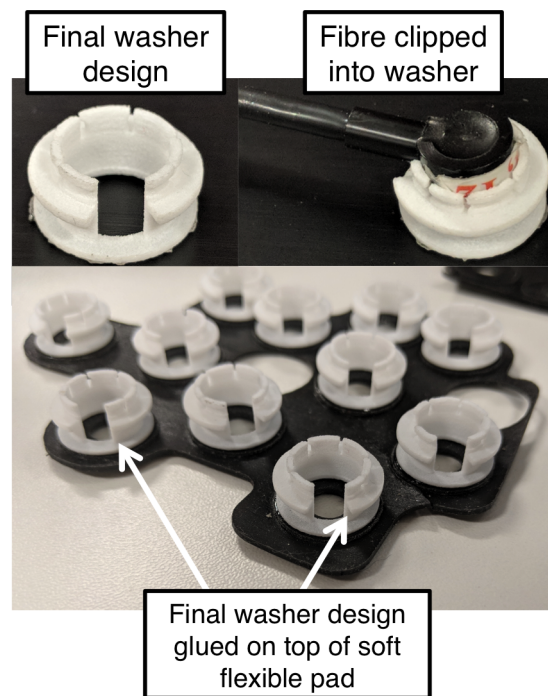
Figure 3.29: 3-D printed version of the final optode coupler design (top left) with fibre clipped in top (right) and glued on top of the flexible pad (bottom)

3.4.3.2 Optode holder pad

As there were two areas of interest for NIRS-EEG measurements (the occipital lobe and the right temporal lobe), therefore two separate optode holder pads were designed for each region. These were 3-D printed in the same way as described previously with a layer of soft flexible rubber at the bottom and medium soft rings on top onto which the nylon washers were glued. Figure 3.30 shows both the conceptual and 3-D printed versions of the temporal and occipital pads with the image on the bottom left showing the temporal pad with the washers glued on top. Figure 3.31 shows both temporal and occipital pads positioned in the headcap on an infant.
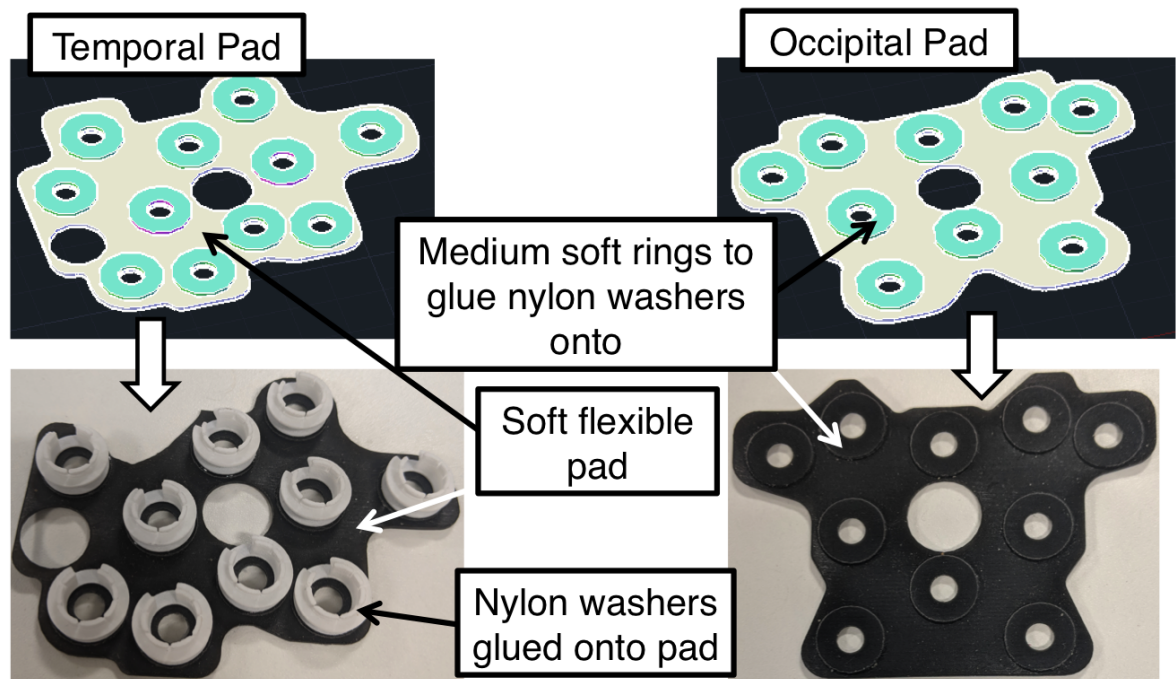
Figure 3.30: (Top) conceptual images of the flexible temporal and occipital pads with medium soft rings to glue the nylon washers (Bottom) 3-D printed versions of the temporal and occipital pads with temporal
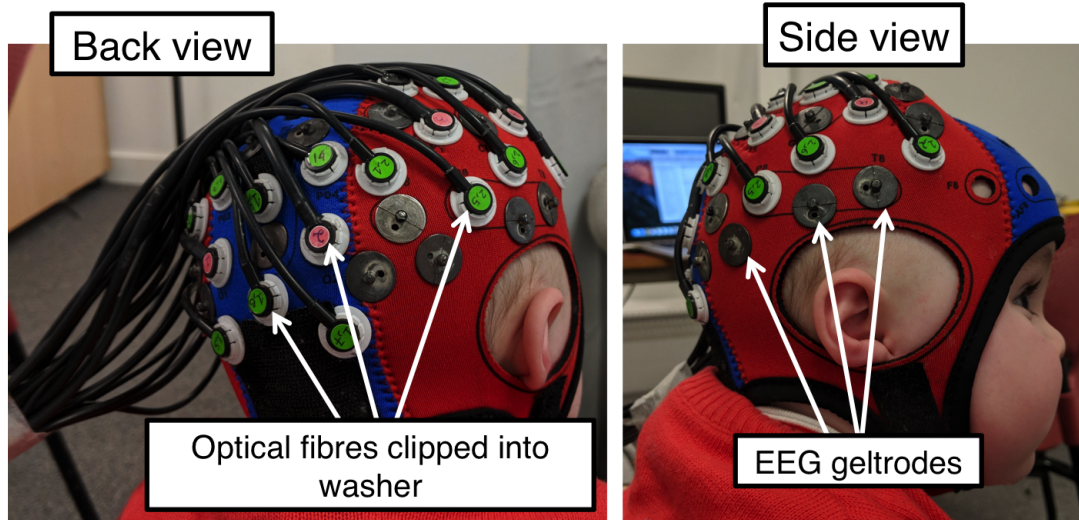
Figure 3.31: NIRS occipital and temporal pads positioned in their respective locations in the headcap. The groove in the optode couplers allowed them to be held in place, the flexible pad is on the underside of the cap and not visible.

3.4.3.3 Combined NIRS-EEG headgear

Once the NIRS arrays had been designed and could positioned into the headcap, there was only one extra component that was required to complete the combined NIRS-EEG headgear, which was the silicone headband. Figure 3.32 and 3.33 show the full headgear and set-up with the silicone headband (which was discussed in Chapter 3) being fed through the NIRS optodes and EEG electrodes. This was tightened at the front of the head and prevented the cap from slipping backwards during the experiment and additionally held the NIRS arrays firmly against the infant's head.
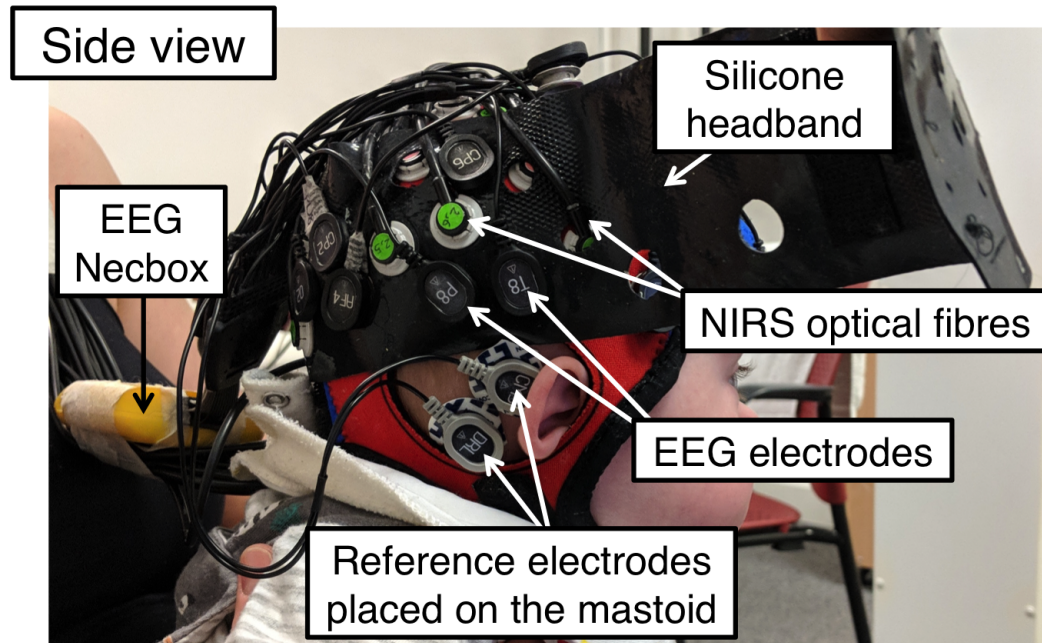
Figure 3.32: Side-view of the full NIRS-EEG set-up on an infant with the NIRS optodes and EEG necbox and electrodes indicated
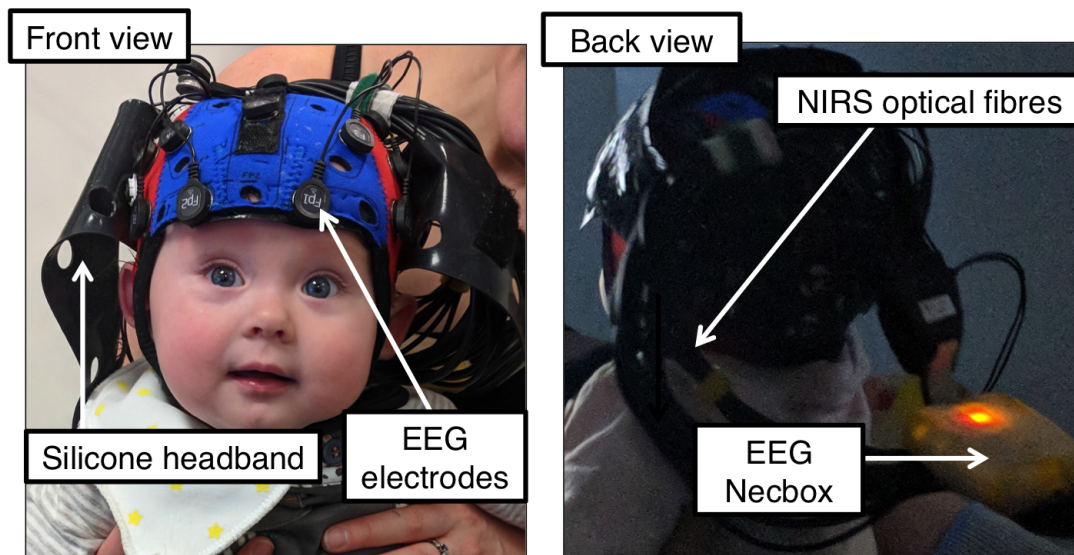
Figure 3.33: Front and back-view of the full NIRS-EEG set-up on an infant with the NIRS optodes and EEG necbox and electrodes indicated

3.5 Summary

Table 3.1 provides a summary of the headgear specifications for each of the studies presented in this thesis.

Study	mini-CYRIL (Study 1)	NIRS-EEG Adults (Study 2)	NIRS-EEG Infants (Study 3)	(Study 3)
Publication	Siddiqui et al., (2017)	-	-	-
System	Single channel broadband NIRS	Multi-channel broadband NIRS	Multi-channel broadband NIRS	Multi-channel broadband NIRS
No. of sources	1	4	4	4
No. of detectors	1	10	15	15
No. of channels	1	16	19	19
Type of fibres	Flat-ended (Right-angled fibres)	Straight-ended fibres	Flat-ended (Right-angled fibres)	Flat-ended (Right-angled fibres)
Cortical region of interest	Temporal	Occipital	Occipital & Temporal	Occipital & Temporal
No. of conditions	1	4	6	6
No. of valid participants	24	5		
Proportion of excluded participants (%)	27%	61%	23%	33%

Table 3.1: A summary of the headgear specifications for each study and the proportions of valid participants.

The following chapter will intrude the first experimental study utilising broadband NIRS during functional activation in infants.

Chapter 4

NON-INVASIVE METABOLIC MARKER OF INFANT BRAIN ACTIVITY

4.1 Introduction

NIRS based haemodynamic measures provide useful markers of brain function and previous work (Lloyd-Fox et al., 2009) illustrates the usefulness of NIRS as a neurodevelopmental research tool that can be used to tease apart differences in typical and atypical brain development occurring early in life. However, the underlying physiological processes giving rise to the haemodynamic response function (HRF) and neurovascular coupling in particular, are not fully understood in the developing human brain. The HRF in infants does not always follow a standard profile and can often differ across brain regions and the time taken to reach the maximum amplitude of the HRF has been shown to change across development, with increasing age (Yamada et al., 2000; Martin et al., 1999a). Furthermore, previous infant NIRS (Kusaka et al., 2004; Telkemeyer et al., 2009; Sakatani et al., 1999b; Issard and Gervain, 2018), fMRI studies (Yamada et al., 2000; Martin et al., 1999a) and work in mice (Kozberg and Hillman, 2016b) report observing an "inverted" response, displaying a decrease in activation in response to an experimental stimulus. It has been hypothesised

that the variability in the HRF may be due to ongoing neuronal development alongside brain blood flow maturation as well as maturation of the neurovascular coupling process itself (Arichi et al., 2012; Kozberg and Hillman, 2016a,b; Cauli and Hamel, 2010b; Harris et al., 2011). In particular, cerebral blood flow (CBF) and the cerebral metabolic rate of oxygen consumption ($CMRO_2$) are known to affect the HRF (Arichi et al., 2012; Chen and Pike, 2009; Roche-Labarbe et al., 2012) and previous work exploring developmental changes in CBF and $CMRO_2$ show that $CMRO_2$ in newborns is well below the threshold in comparison with adults and increases significantly up until early childhood (Takahashi et al., 1999). These multi-factorial physiological reasons can lead to the observed variability in the haemodynamic response in infants thereby making it difficult to interpret results. Furthermore, they highlight the need to further investigate the neurovascular coupling pathway in infants and to improve on the current understanding of the physiological processes that give rise to the HRF. Moreover, it should be remembered that oxygenated and deoxygenated haemoglobin measures are surrogate markers of brain activity informing on the oxygen delivery component of the neurovascular coupling pathway. A more direct measure of the metabolic consequences of neural activity may elucidate mechanisms underlying typical and atypical function.

Broadband NIRS provides the opportunity to obtain a cellular measure by measuring changes in the oxidation state of a mitochondrial enzyme cytochrome-c-oxidase Δ[oxCCO]. A study by Bainbridge et al. (Bainbridge et al., 2014) used phosphorus magnetic resonance spectroscopy (^{31}P MRS) in conjunction with NIRS and found a significant correlation between ^{31}P MRS biomarkers of cerebral energy metabolism and NIRS oxCCO measure, thereby demonstrating its use as a marker of intracellular oxygen metabolism and consequently providing insight into cellular oxygen utilization and oxygen metabolism. Kolyva et al. (Kolyva et al., 2014) have demonstrated in adults that oxCCO is a more brain-specific signal than haemoglobin. Therefore, being a more direct marker of neuronal activity, measurements of changes in the oxidation state of cytochrome have the potential to help further our understanding of neurovascular coupling and to understand the relationship between the NIRS measures and the underlying neural mechanisms.

Previous work by Adolphs et al (2009) has identified a network of brain regions that

are involved in the processing of social information that are collectively referred to as the "social brain". These brain regions include a number of areas such as the inferior frontal gyrus (IFG), the amygdala, the orbitofrontal cortex and the anterior and posterior temporal lobes. Many experimental paradigms have been developed to explore social processing during brain development and a number of NIRS studies have utilised social/non-social paradigms to measure responses over the temporal cortex in typically developing infants (Lloyd-Fox et al., 2014a, 2017, 2009; Grossmann et al., 2008).

The aim of the study presented in this chapter, therefore, was to use a broadband NIRS system to measure changes in oxygenated haemoglobin, deoxygenated haemoglobin and cytochrome-c-oxidase over the temporal cortex in response to functional activation, in infants. As this study was one of the first to measure cytochrome-c-oxidase changes during functional activation, a miniature single channel broadband NIRS system was used. The single channel system was feasible as the use of a social/non-social paradigm was employed and the NIRS haemodynamic response over the temporal cortex using this paradigm has been well documented.

4.2   Methods

4.2.1   Participants

Thirty-three 4-to-6-month-old healthy infants participated in the study (14 males, 19 females mean age: 159 days SD: 25). All parents volunteered to participate and provided informed, written consent prior to the study. The Birkbeck Psychology Ethics Committee approved the study protocol and all procedures performed were within the regulations of the Ethics Committee. Participating infants were from varied ethnic backgrounds and had varying skin and hair colour, but neither of these was used as exclusion criteria to screen participants. All infants who participated were healthy with no known developmental disorders and were born at term (37-40 weeks gestation).

4.2.2 Stimuli design

The experimental stimuli were designed using Psychtoolbox in Matlab (Mathworks, USA). A social/non-social experimental paradigm, which has been demonstrated to produce stimulus-selective haemodynamic response (increase in oxygenated haemoglobin and decrease in deoxygenated haemoglobin) in previous infant NIRS studies (Grossmann et al., 2008; Lloyd-Fox et al., 2009) was chosen. For this study, an experimental stimulus was required that would induce a maximal haemodynamic response allowing the identification of the presence or absence of an accompanying response in oxCC. Hence, an enhanced social stimulus was developed which consisted of a social visual component and a social auditory component. The visual component was composed of a variety of dynamic social movies which consisted of video clips involving biological motion where women performed "peek-a-boo" and "incy-wincy". The video clips also had an auditory component consisting of human vocal sounds such as laughter, crying and coughing. The auditory component of the stimulus was presented at a range between 20-55dB. The social condition was presented for a duration varying between 9 - 12s and was followed by a baseline condition which consisted of full-colour static transport images, for example cars, trucks and helicopters. The images were presented randomly for a pseudorandom duration of 1 - 3s each, for a total of 9 - 12s. Figure 4.1 shows the experimental and baseline conditions and the order in which they were presented.
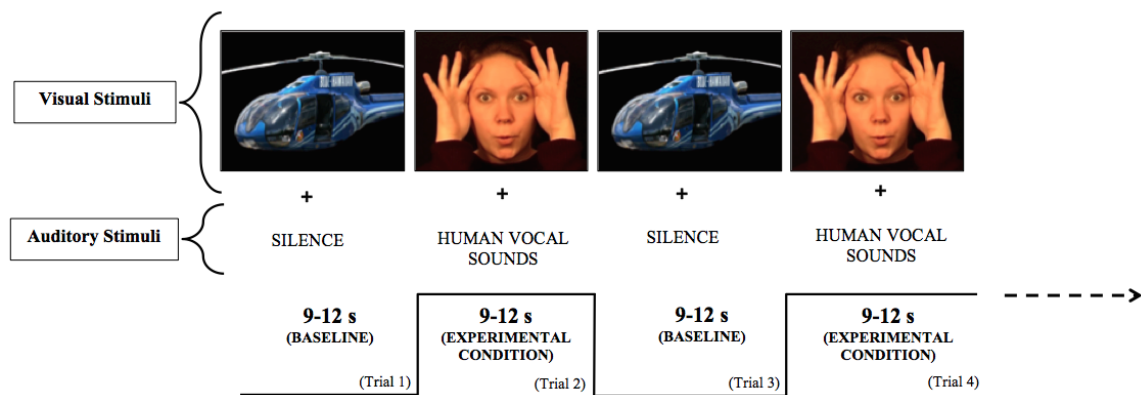
Figure 4.1: Order of stimulus presentation

4.2.3 Data acquisition

4.2.3.1 Mini-CYRIL

The Miniature-Cytochrome Research Instrument and appLicaton or Mini-CYRIL is a single channel multi-wavelength broadband NIRS system developed at UCL Department of Medical Physics and Biomedical Engineering by Dr Pardis Kaynezhad and Dr Ilias Tachtsidis and was used to collect the data presented in this chapter. The system consists of a single white light source, a single miniature spectrometer, two optical fibres and a laptop to run the software (Kaynezhad et al., 2016). These components are described in more detail in the following sections.

4.2.3.1.1 Hardware

4.2.3.1.1.1 *Light source and spectrometer* The mini-CYRIL system is composed of a white light source and a spectrometer. The light source (HL-2000-HP) uses an Ocean Optics 20 W Tungsten Halogen lamp. It produces light between 360 nm - 2400 nm and has an integrated filter in order to remove UV exposure and heating effects. The light source is operated independently by an external on/off switch and is shown in Figure 4.2a. The spectrometer that forms part of the system is a miniature Ventana VIS-NIR spectrometer by Ocean Optics (USA) and is shown in Figure 4.2b. The spectrometer is internally attached to a Hamamatsu S10420-1006 Black-thinned charged coupled device (CCD) and has a spectral range of 430 nm to 1100 nm. The acquisition rate of the system is 1s. Both light source and spectrometer have a SubMiniature version A (SMA) connector for attachment of the optical fibre. The optical fibres used for this study are described in the next section.
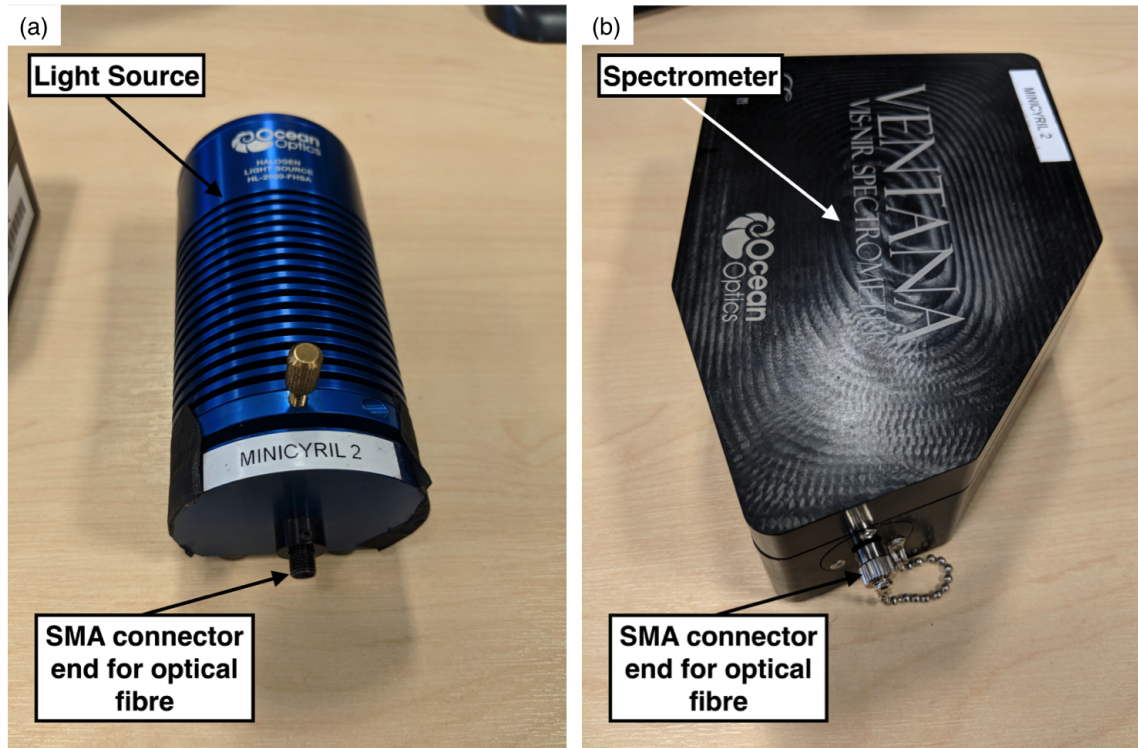
Figure 4.2: Components that comprise the mini-CYRIL system; (a) light source and (b) spectrometer

4.2.3.1.1.2 *Optical fibres*   Both light source and spectrometer have an identical optical fibre each made of glass that are manufactured by Loptek (Loptek, Germany) and have an inner core diameter of 2.3 mm. The system-end of the fibres have an SMA connector while the subject-end is flat-ended with the optode head at right angles to the optical fibre, as shown in Figure 4.3a. Right-angled fibres are commonly used for infant studies as they lie flush against the head and can easily be secured into place without needing to apply extra pressure, thereby making them more comfortable. Additionally, there is no added gravitational pull causing the fibres to lift off the head, as is common in some adult fibres. This is discussed further in Chapter 6. Figure 4.3b shows the subject-end of the optical fibres. Figure 4.4 shows the set-up on a doll with fibres attached to the spectrometer and the light source.
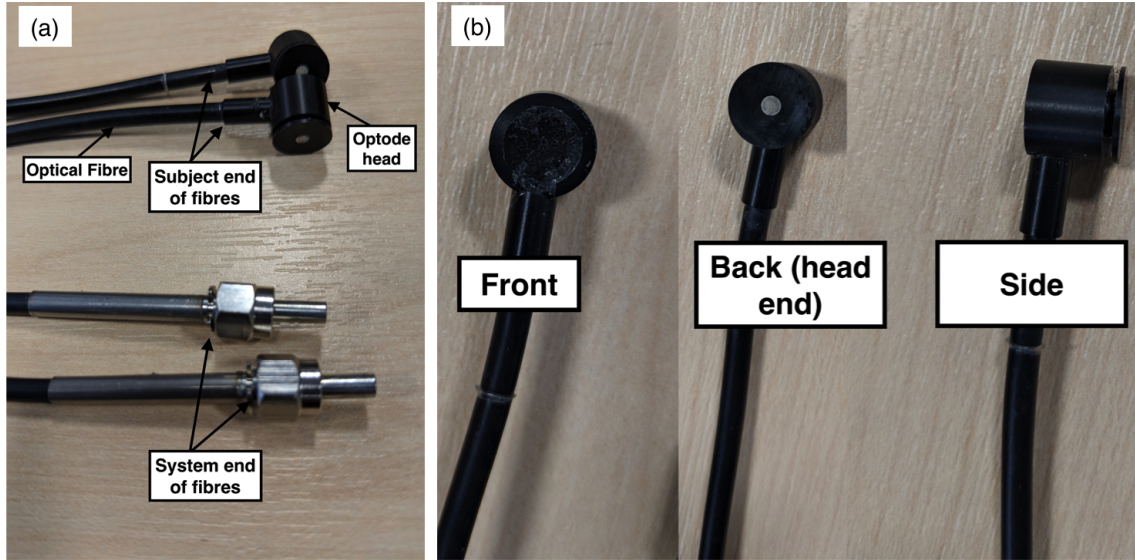
Figure 4.3: Optical fibres forming part of the mini-CYRIL system.
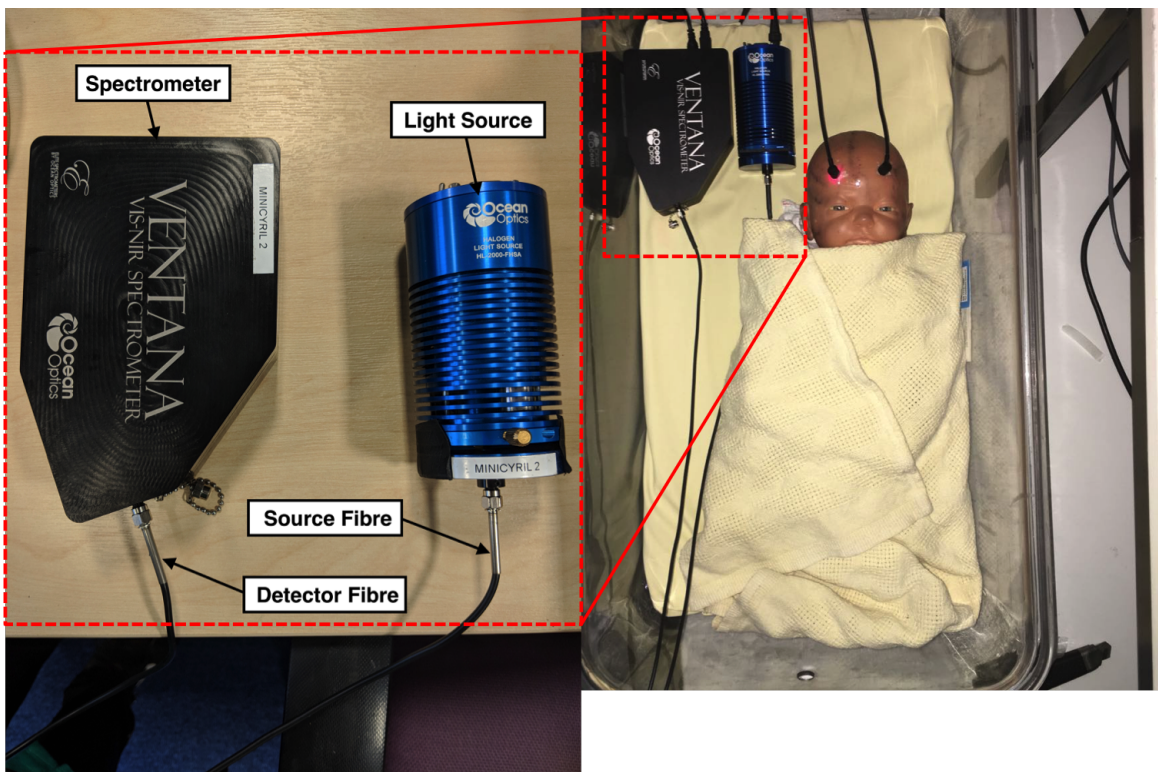
Figure 4.4: Mini-CYRIL set-up with spectrometer and light source connected to optical fibres on a doll head, taken from (Kaynezhad et al., 2016)

4.2.3.1.2 Software   The spectrometer connects to a laptop via USB connection and its operation is controlled through a program written by Dr Pardis Kaynezhad in Matlab 2013 (Mathworks, USA), which uses the Matlab Instrument Control Toolbox. Figure 4.5 shows the full set-up on a phantom with spectrometer connected to the laptop. The software program is used to start acquiring intensity spectra at wavelengths between 780 - 900 nm from the detector fibre. The software converts intensity spectra to chromophore concentration changes using the UCLn algorithm (Bale et al., 2016a) and a differential pathlength factor of 5.13 (Matcher et al., 1995). The bottom figure in Figure 4.5 shows the panel where chromophore concentration changes are displayed during data acquisition. The UCLn algorithm was used to convert the attenuation change signal to the chromophore concentration changes and this has been discussed previously in Section 2.1.3.1 of Chapter 2.
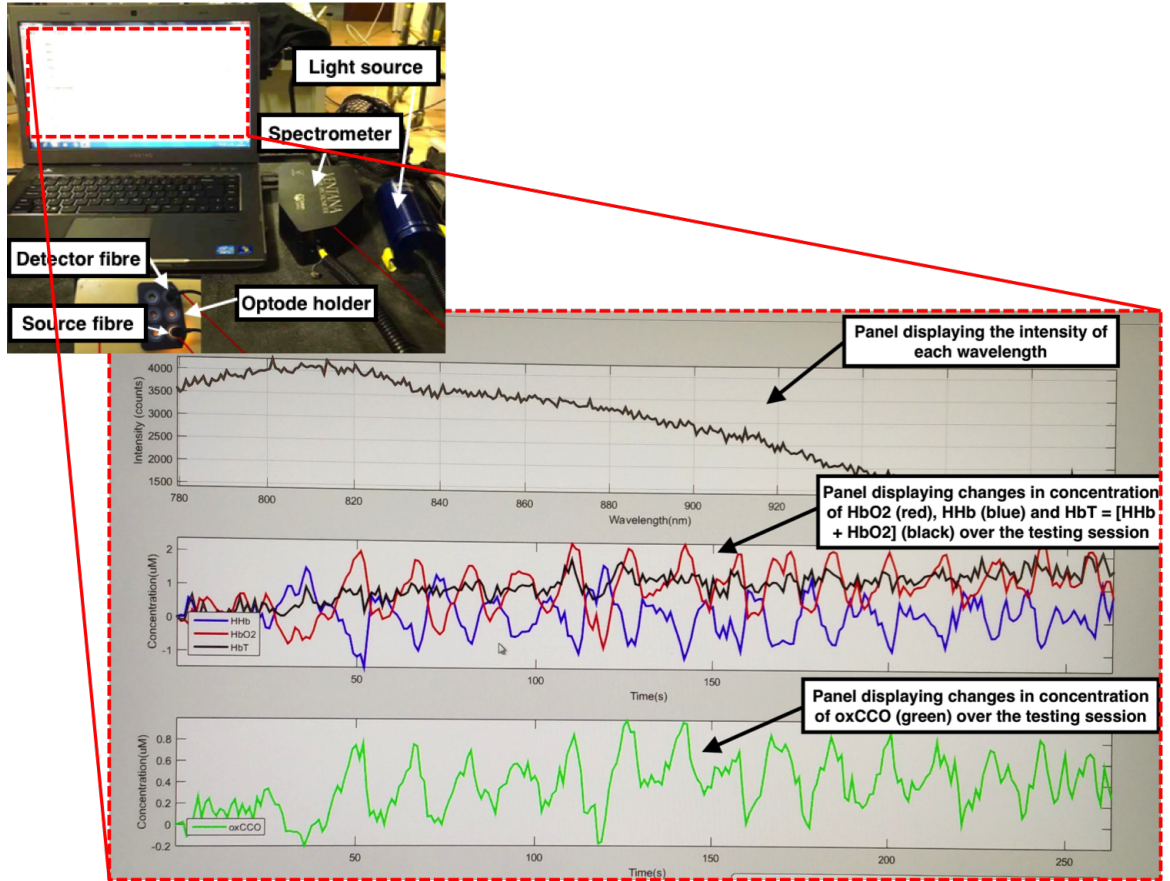
Figure 4.5: (Top) Mini-CYRIL set-up with computer (Bottom) Output from the software during acquisition. The top panel displays the intensity counts of each wavelength between 780 - 900nm. The middle panel displays $\Delta[HbO_2]$ in red, $\Delta[HHb]$ in blue and $\Delta[HbT]$ = $\Delta[HbO_2]$ + $\Delta[HHb]$ in black while the bottom panel displays $\Delta[oxCCO]$ in green, occurring over time across the testing session.

4.2.3.2 Probe design

The headgear design for this study has already been discussed in detail in Chapter 3. Figure 4.6 shows the optode holder that was developed and used for the study presented in this chapter.

Figure 4.6: Optode holder that was used for the study presented in this chapter, with fibres clipped in. The fibres are clipped in for the purposes of the image, the spacing between source and detector was maintained at 2.8 cm for all participants, during the study.

4.2.3.3 Preliminary testing - Cuff Occlusion

Prior to use with infants, preliminary testing was performed on one adult using the mini-CYRIL. This was done to assess mini-CYRIL's capability for measuring in-vivo changes occurring in chromophore concentrations, particularly to resolve changes in the oxidation state of cytochrome. While it is not performed on the head and does not interrogate brain tissue, forearm ischaemia or the cuff-occlusion test was used and is a common validation experiment carried out to assess the performance of NIRS systems (Shadgan et al., 2009; Matcher et al., 1995; Lange et al., 2017; Haensse et al., 2005). During this test, the arteries in the forearm of a volunteer are occluded using a pneumatic blood pressure cuff and chromophore concentration changes are monitored in real-time. The occlusion causes the the total blood volume to remain relatively constant, but arterial blood flow to cease. During the ischaemia, desaturation occurs causing a sharp increase in Δ[HHb] and an almost equivalent decrease in Δ[HbO$_2$] (Matcher et al., 1995). If Δ[oxCCO] is also being measured, then only a small delayed reduction in oxCCO is seen as there is a large oxygen reserve bound to muscle myoglobin and low oxygen consumption is expected in resting muscle (Matcher et al., 1995; Honig et al., 1992). During this preliminary testing, the pneumatic blood pressure cuff was positioned loosely around the left arm of the volunteer while the forearm was laid on the table. The optical fibres were placed on the forearm muscle with a source - detector separation of 4 cm and baseline was recorded while a black cloth was wrapped around the arm and fibres to eliminate light pollution. Baseline was recorded for one minute and the blood pressure cuff was rapidly inflated to 200 - 220 mmHg to prevent

venous blood back flow and to stop arterial blood inflow to the forearm for around 3 - 4 minutes, while ensuring that the volunteer was not experiencing any discomfort. After 3.5 minutes, the blood pressure cuff was deflated and the arm was kept still for a resting state measurement post-ischaemia. Figure 4.7 demonstrates the changes that occurred in Δ [HbO$_2$], Δ [HHb] and Δ [oxCCO] during this study. During the period of ischaemia, Δ [HbO$_2$] decreased to a minimum of -6.4μM while Δ [HHb] increased to a maximum of +8.4 μM. The Δ [oxCCO] changes were much smaller in comparison to oxy-haemoglobin and deoxy-haemoglobin, indicating a gradual decrease to -0.5μM just before the pressure cuff was deflated, which is in accordance with previous studies (Lange et al., 2017). The results from this experiment demonstrate mini-CYRIL's capability to successfully measure haemodynamic changes as well as changes in the oxidation state of cytochrome in the forearm muscle and this indicates that the system should be able to resolve for these changes in the human brain tissue as well.
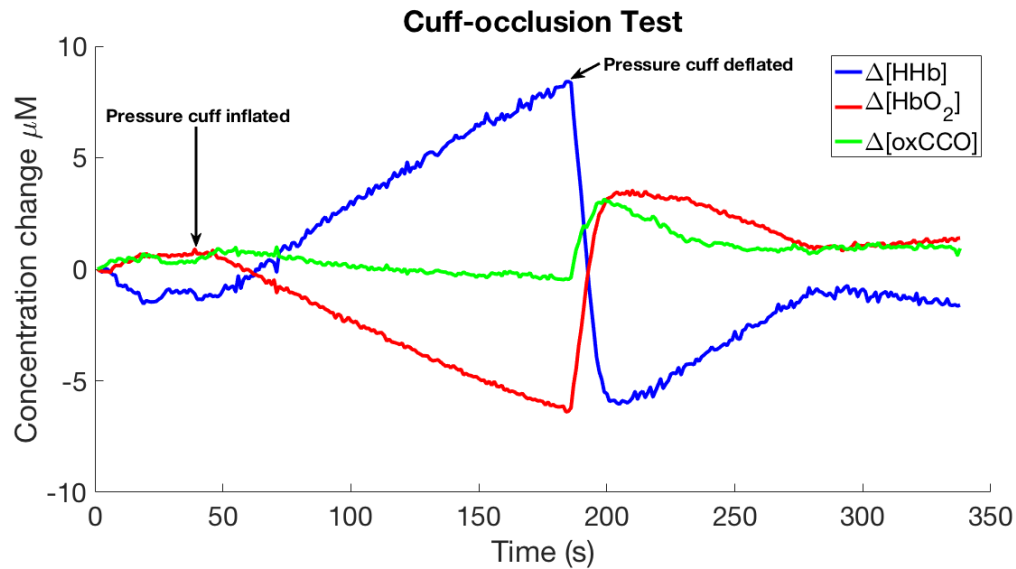
Figure 4.7: Chromophore concentration changes in the forearm in response to cuff occlusion

4.2.4 Infant Study

4.2.4.1 Experimental Procedure

Once written consent was obtained from the parent, the infant's head measurements were taken. These included measuring the head circumference, the central semi-circumference from ear-vertex-ear and the lateral semi-circumference from ear-nasion-ear. Following this, the parent was seated in front of a 46-inch plasma screen at approximately 1m viewing distance with the infant in their lap. The headgear was then positioned on their head as shown in Figure 4.8. Due to the fact that there was only one channel, the array had to be positioned carefully in order to ensure the correct brain region for the stimuli being presented was being targeted. The array was positioned over the right hemisphere. Previous studies involving similar social/non-social stimuli and co-registration work by Lloyd-Fox and colleagues (Lloyd-Fox et al., 2014a) have identified the maximal response to the social stimuli occurring in the superior temporal sulcus - temporo-parietal region (STS - TPJ). The standardised scalp map generated by this co-registration work was used to identify the optimal location of the single source-detector pair headgear developed for this study. This indicated that the yellow marking on the headband (see Figure 4.8) would need to be aligned with the the right pre-auricular point which is defined as "a point of the posterior root of the zygomatic arch lying immediately in front of the upper end of the tragus", for the channel formed between the source and detector to lie over the STS - TPJ region.
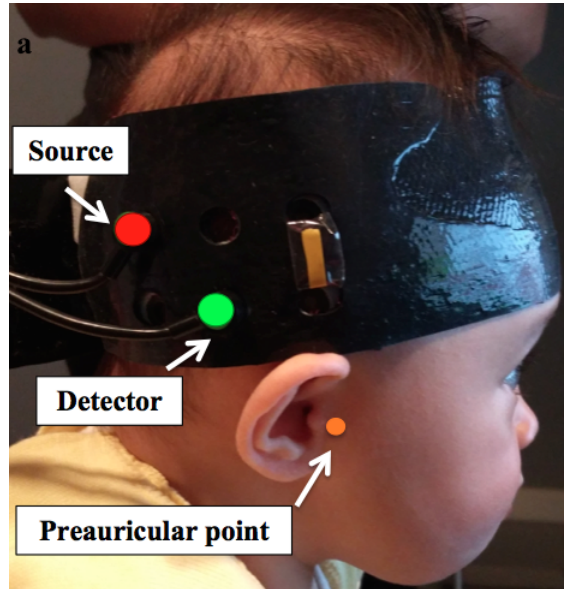
Figure 4.8: Image of a participant wearing the NIRS headgear.

Previous studies (Taga et al., 2007; Gervain et al., 2011) have explored varying source - detector separation distances, between 2 - 4 cm, in order to identify the ideal separation for infant studies. However, most infant functional activation studies typically use a separation of 2 cm (Wilcox et al., 2005a; Lloyd-Fox et al., 2009). Previous adult work undertaken by Phan et al. (Phan et al., 2016b) compared the changes in concentration of cytochrome-c-oxidase using varying source - detector separations between 2 cm - 4 cm. The results from the work indicate 3 cm as being the ideal source - detector separation distance to functional activation driven changes in cytochrome, in adults. Therefore, for this infant study a source - detector separation of 2.8 cm was chosen.

The study began with a rest period (20 s minimum) to draw the infant's attention towards the screen, during which the infant was shown shapes in four corners of the screen. Following this, the baseline and experimental trials (each 9 - 12 s long) were alternated for a pseudorandom duration until the infants became bored or fussy. The order of the stimulus presentation has been shown previously in Figure 4.1. Occasionally, alerting sounds were played during the baseline stimulus to draw the infant's attention back to the screen.

4.2.5 Data analysis

The data were analysed in Matlab 2014a (Mathworks, USA) and the data analysis pipeline has already been described in detail in Section 2.3.1.1 of Chapter 2. At the end of each recording session the mini-CYRIL software provided the concentration changes for each chromophore, calculated from change in attenuation, using the UCLn algorithm. However as described previously, the wavelet-based motion correction had to be applied to the attenuation signal of each infant rather than the concentration changes, to correct for motion artifacts in the data occurring due to motion. Therefore, first, motion correction was applied to the attenuation data and then the UCLn algorithm was used to calculate the chromophore concentration changes.

4.2.5.1 Motion correction

Wavelet-based motion correction, developed by Molavi et al. (Molavi and Dumont, 2012) was used to remove artifacts in the data due to infant movement. This step is critical for infant data as the infants are relatively free to move in their parent's lap, therefore, they are likely to move or make sharp head movements, particularly younger infants who don't have strong neck control. The algorithm has been discussed in detail in Section 2.3.1.1. of Chapter 2. A tuning parameter α of 1.5 was used for this study.

4.2.5.2 Calculation of concentration changes

Once motion correction had been applied, the concentration changes were re-calculated using the UCLn algorithm with a wavelength-dependent DPF of 5.13 - suitable for infants of this age range (Matcher et al., 1995). Following this, the concentration changes for each chromophore were filtered using a 5th order Butterworth filter between 0.01 - 0.45 Hz. The concentration changes were segmented into blocks consisting of 4 seconds of the baseline period prior to the onset of the experimental condition, the experimental condition (9 - 12 s) and the entire following baseline period (9 - 12 s). The average block length was 24 s. Baseline correction was applied to each block of data by subtracting the concentration change value of the chromophore at the start of the experimental condition (i.e. at t = 0)

from the entire signal, for each chromophore.

4.2.5.3 Looking-time coding

Once the other pre-processing steps were complete and the epochs of the data were created, trials were rejected based on looking time. During the study, each infant was recorded for the entire duration of the study in order to code for looking-time offline. The videos from each infant were studied offline and any trials were removed where the infants had been looking away from the screen for more than 6 seconds (approximately 50%) during the baseline condition or had looked away from the screen more than 40% of the experimental condition.

4.2.5.4 Rejection criteria

An infant was included in the study if they had a minimum of six valid trials after coding for looking-time and was also only included in the study if they exhibited the expected "typical" haemodynamic response which is defined as being an increase in oxy-haemoglobin and a decrease or no change in deoxy-haemoglobin, in response to the stimulus. This was done through visual inspection and although not a common practice, for this first study of measuring changes in cytochrome in response to functional activation, it was decided that cytochrome responses would be looked at only in the presence of the "typical" haemodynamic response as defined earlier. "Inverted" responses or an increase in deoxy-haemoglobin and decrease in oxy-haemoglobin are sometimes reported in infant research and are not fully understood with some studies suggesting that an inverted response represents a deactivation to the experimental stimulus (Watanabe et al., 2012a) while others have hypothesised that it is due to underdeveloped cerebral vasculature (Kozberg et al., 2013a). For this first study of cytochrome, it was better to observe cytochrome responses in the context of a response that is more commonly investigated and is better understood. However, investigation of inverted responses is of interest in future studies.

Following these criteria, the valid blocks for each infant were averaged together and time courses of mean Δ[HbO2], Δ[HHb] and Δ[oxCCO] obtained and data from twenty-four out of the thirty-three participants were included. Three infants were excluded for

failing to look at the required minimum number of trials, one infant was excluded due to incorrect placement of the array on the infant's head and five infants were excluded as they showed an increase in Δ[HHb] and a decrease in Δ[HbO2] in response to the stimulus, i.e. an "inverted" response. The averaged haemodynamic response for each of the twenty-four infants was then averaged to obtain a grand average for the the group.

4.2.5.5   Statistical analysis

Statistical analysis was performed on the grand averaged response, at the group level. A time window was selected between 10 and 18 s post-experimental stimulus onset, which has been previously demonstrated to be sufficient to include the range of maximum concentration changes across infants (Lloyd-Fox et al., 2009). A one-sample Students t-test was then performed during this window to statistically compare the maximum concentration change of each chromophore, in response to the experimental stimulus versus the baseline. A normality test was performed on the data to ensure that the data were normally distributed and met the normality assumption. An equivalent non-parametric t-test was also performed - Wilcoxons signed rank test was conducted on the group data. A paired sample t-test was conducted to compare if there was a significant difference between the maximum change in concentration of oxCCO and HbO_2. For this, the maximum concentration change for both chromophores was normalized prior to performing the pairwise t-test. Additionally, time-to-peak analysis was performed to assess whether there was a difference in the time taken for oxCCO and HbO_2 to reach the maximum change in concentration. This involved comparing the time taken for both oxy-haemoglobin and cytochrome to reach their maximum values in response the experimental stimulus.

4.2.5.6   Residual analysis

Due to the concentration of CCO in the brain being much lower than that of oxygenated and deoxygenated haemoglobin, measuring changes in the oxidation state of CCO can be challenging. This leads to the possibility that the measurement of Δ[oxCCO] could be the result of cross-talk. Cross-talk is defined as a genuine change in the concentration of one chromophore inducing spurious change in concentration of another chromophore (Bale

et al., 2016a). Therefore, it is important to analyse residual errors produced when converting the attenuation data into chromophore concentration changes in order to determine whether $\Delta[oxCCO]$ are accounted for in the attenuation change spectrum. The UCLn algorithm was used here to perform residual analysis which involved using the algorithm in order to back-calculate the attenuation change spectra for HHb, HbO_2 and oxCCO from the calculated concentration changes and comparing these to the measured change in attenuation occurring within a trial in different participants. First, the 2-component fit was calculated where only HbO_2 and HHb attenuation change spectra are calculated and followed by the 3-component fit where the HbO_2, HHb and oxCCO attenuation change spectra were calculated. The residuals from these two fits were compared to the oxidized-minus reduced CCO spectrum, using the relevant specific extinction coefficient.

4.3 Results

4.3.1 *Single participant data*

Figure 4.9a displays the changes in concentration of HbO_2, HHb and oxCCO from a single infant (chosen at random), across seven trials and Figure 4.9b displays the changes in concentration of oxCCO from the same infant, across seven trials, with the y-axis rescaled.
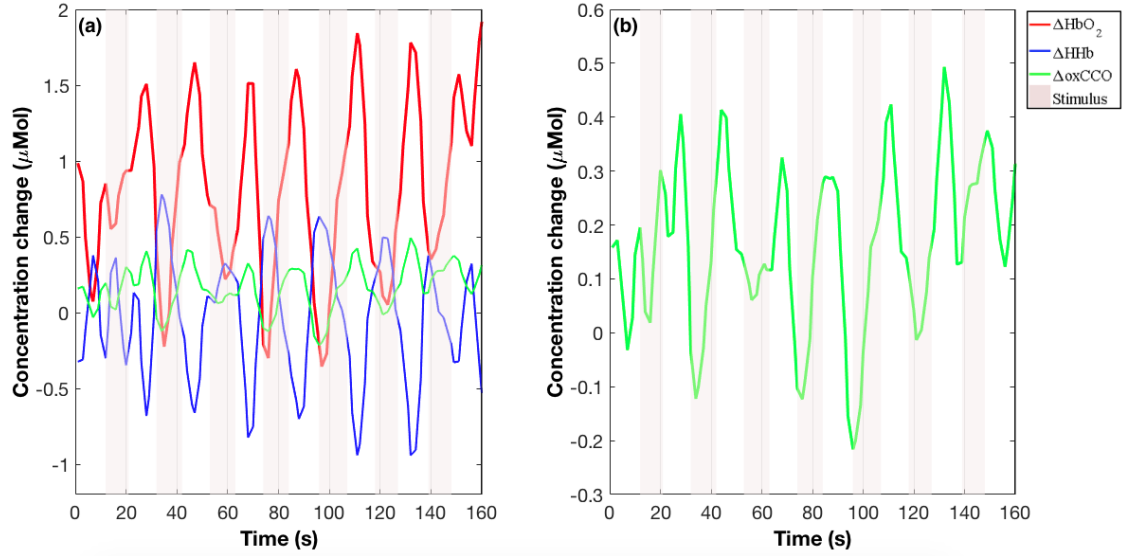
Figure 4.9: Observed chromophore concentration changes. (a) Changes in concentration in HbO2, HHb and oxCCO from one participant, across 7 trials, after filtering and applying motion correction. (b) Changes in concentration in oxCCO from the same participant, with y-axis re-scaled.

4.3.2 *Group data*

Figure 4.10 shows the grand averaged concentration changes for each of the chromophores, averaged across twenty-four participants. The one-sample t-test conducted on the group data showed a significant increase from baseline in oxCCO and HbO_2 but not HHb - ($t_{oxCCO} = 5.710$, $p_{oxCCO} = 0.000008$, $t_{HbO_2} = 4.387$ $p_{HbO_2} = 0.000174$, $t_{HHb} = -0.892$, $p_{HHb} = 0.382$, df = 23). An equivalent non-parametric t-test, Wilcoxons signed rank test was additionally conducted on the group data. The results were consistent with the t-test in showing that there was a significant increase in oxCCO and HbO_2 in response to the stimulus ($z_{oxCCO} = 3.80$, $p_{oxCCO} = 0.000147$, $z_{HbO_2} = 3.2286$ $p_{HbO_2} = 0.0012$, $z_{HHb} = -1.2086$, $p_{HHb} = 0.3037$). The maximum change occurring in oxCCO was 0.238μMol, 0.61μMol in HbO_2 and 0.39μMol in HHb.
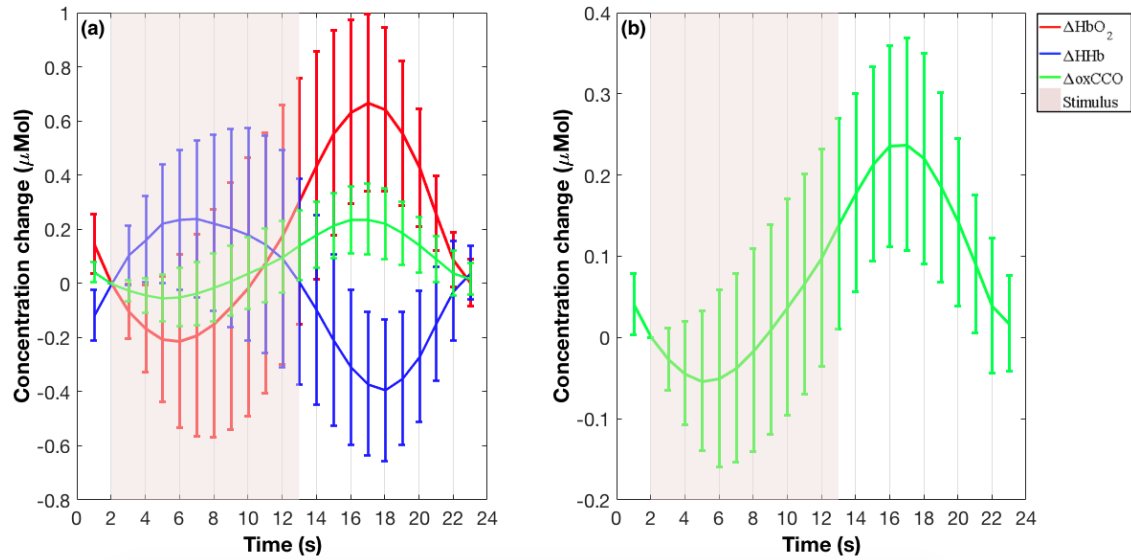
Figure 4.10: Grand averaged time course of concentration changes in HbO_2, HHb and oxCCO, across 24 participants. (d) Grand averaged time course of concentration change in oxCCO, with y-axis re-scaled. The error bars represent standard deviations.

4.3.2.1 *Comparison of oxCCO and HbO_2*

The paired t-test that was conducted to assess whether there was a statistically significant difference between oxCCO and HbO_2 showed that there was no significant difference between the chromophores. The time to peak analysis showed that the time taken to reach the maximum concentration change for both chromophores was similar (approximately 16 s post-stimulus onset) and no significant difference was observed.

4.3.3 Residual analysis

Figure 4.11 presents the results from the residual analysis for four participants, chosen at random from the twenty-four included in the study. The residual analysis indicates that the difference between the 2-component fit and the 3-component is approximately the shape of the oxidized minus reduced spectrum of cytochrome-c-oxidase.
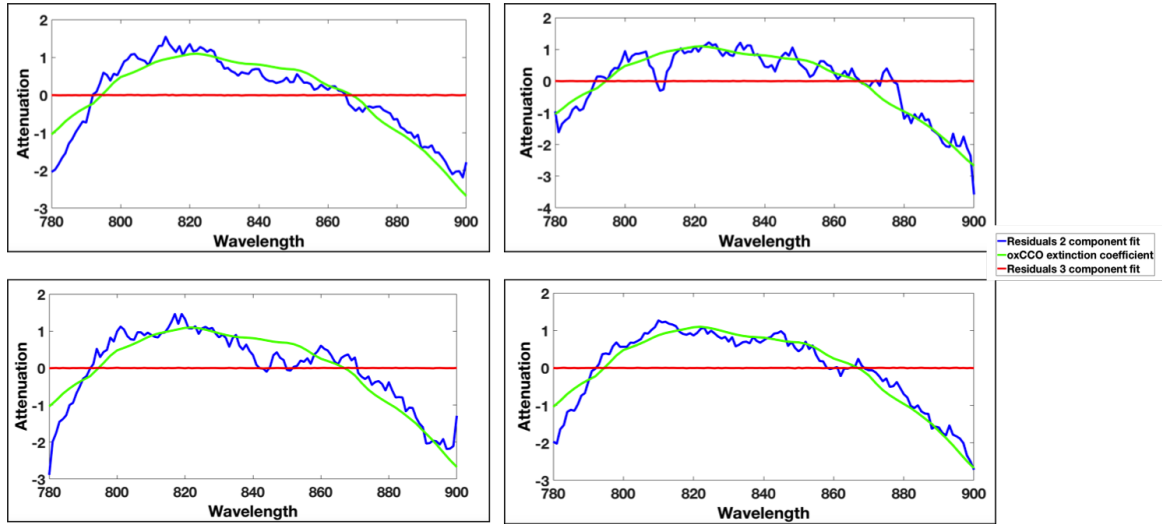
Figure 4.11: Difference between the 3-component and 2-component fit from four participants chosen at random.

4.4   Discussion

In this chapter, a novel study was presented utilizing a miniature broadband NIRS system to measure changes in cellular oxygen metabolism - through measurement of changes in the oxidation state of the mitochondrial enzyme cytochrome-c-oxidase - in infants aged between four-to-six months during functional brain activation. A social visual plus auditory paradigm was utilised which has previously been demonstrated to induce reliable functional activation-related changes over the STS - TPJ region in this age of infants (Lloyd-Fox et al., 2014a, 2009). Broadband NIRS instrumentation, which has shown to be appropriate to measure changes in the redox state of CCO (Bale et al., 2014), was used to detect a significant increase in Δ[oxCCO], alongside concurrent significant changes in HbO_2 and HHb. A residual analysis demonstrated that the observed changes during functional activation could not be solely attributed to HbO_2 and HHb, therefore the observed oxCCO signal was the result of true functional activation as opposed to the influence of cross-talk. These novel findings are important as a previous study (Zaramella et al., 2001a), which used a different multi-wavelength system to measure changes in the oxidation state of cytochrome in response to an auditory stimulus in infants did not observe significant changes in Δ[oxCCO] in the presence of significant Δ[HbO_2] changes. It is possible that the choice of broader

range of wavelengths of the current NIRS system allowed greater sensitivity to the oxCCO signal in relation to the narrower resolution of the system that had previously been used with infants. The current results demonstrate that by using broadband NIRS, it is possible to measure $\Delta[\text{oxCCO}]$ in response to functional activation which could potentially yield critical insights into cellular oxygen utilization and metabolism. The opportunity to non-invasively detect changes at a cellular level associated with active neural tissue holds great potential to further our understanding of physiological processes occurring in the developing human brain and particularly to investigate neurovascular coupling in typical and atypical brain development.

The group data shows that the measured changes in $\Delta[\text{HbO}_2]$ are in accordance with previous infant functional activation studies (Meek et al., 1998; Wilcox et al., 2005a; Taga and Asakawa, 2007; Lloyd-Fox et al., 2009) and the oxCCO response is strongly coupled with HbO_2. The time to peak analysis showed that both chromophores attained their maximum change in concentration with a similar time to peak, approximately 16 s post-experimental stimulus onset. Previous work in adults (Phan et al., 2016b; Kolyva et al., 2014) has shown that the oxCCO response is a more direct marker of brain activation as it is more spatially sensitive and while haemoglobin can be confounded by extra-cranial contamination (Tachtsidis and Scholkmann, 2016), oxCCO is more depth resolved (de Roever et al., 2016; Kolyva et al., 2014) and therefore a more brain specific signal. A prior study of brain injured patients (Highton et al., 2016) suggests that an increase in oxygen consumption is more localized than an increase in blood flow. While this single channel study demonstrates that it is possible to obtain measures of changes in cellular oxygen metabolism, the null results when comparing chromophores shows a limitation of this study, namely that a single channel system was used and responses were measured over one brain region. As such the oxCCO response measured here does not provide any clear additional information to HbO_2 and HHb. A multi-channel approach is required in order to measure oxCCO across different brain regions to investigate the spatial specificity of cytochrome in infants, its relation to the underlying neural activity and to improve our understanding of neurovascular coupling.

To address this, the studies that followed this one (presented in Chapters 5, 6, 7 and

8) employed the use of a multi-channel broadband NIRS system simultaneously with EEG in order to investigate the relationship between blood flow changes, changes in cellular oxygen consumption as well as the neural mechanisms that give rise to the HRF.

Chapter 5

ADULT NIRS STUDY OF CYTOCHROME WITH EEG

5.1 Introduction

The study presented in the previous chapter was useful in validating whether broadband NIRS could be used to measure functional activation driven changes in cellular energy metabolism in infants, alongside haemodynamic changes. However, there is a limit to what could be inferred regarding the relationship between cerebral metabolic activity and haemodynamics using a single channel broadband NIRS system. In order to investigate neurometabolic pathways in the brain, a multi-channel approach is required. This is because multi-channel system allows measurement of responses over multiple brain regions, thereby allowing us to localise the brain area of activation. Furthermore, previous work in adults (Phan et al., 2016b) has shown that measurement of CCO provides a more localised measure of activation. The study presented in this chapter therefore, used multi-channel channel broadband NIRS concurrently with EEG in order to better understand how neural activity relates to NIRS measures and whether CCO could provide a unique marker of brain activity that further informs on this relationship. While the focus of my PhD was to investigate infant brain development, the simultaneous NIRS and EEG work presented in this chapter was first performed in adults before being extended to infants (presented in subsequent chapters). This was due to a number of reasons. Firstly, to my knowledge,

this was the first study using broadband NIRS alongside EEG and therefore a number of methodological developments were required which included creating combined headgear to accommodate both NIRS optodes and EEG electrodes on the head, designing an appropriate experimental paradigm which was sufficient for both techniques and testing a data analysis pipeline in order to combine NIRS and EEG data. Infant studies using a single modality, for example only NIRS or EEG, can be challenging to perform and it would not have been possible to successfully address all methodological aspects that required development. Secondly, it was important to first explore the relationship between neuronal activation related changes in cerebral energy metabolism and haemodynamics in the developed adult brain prior to investigating this relation in the developing brain. As I discussed previously, many studies report variability in the infant HRF during functional activation which can be attributed to both stimulus complexity and the ongoing development of cerebral vasculature and neural circuitry. The adult HRF has been more extensively investigated and does not present with the same irregularities as infant data. Furthermore, EEG is particularly affected by movement artifacts and as adults can be instructed to sit still for longer periods of time, adult EEG data is of higher quality in comparison to infant EEG data. Therefore, performing the concurrent NIRS and EEG work in adults first provided the opportunity to (1) to explore the fundamental processes underlying neurovascular coupling in a context where the data were less variable and noisy and (2) successfully address all methodological aspects of a simultaneous NIRS and EEG study that required development.

In humans, the anatomical structure and functions of the visual cortex have been extensively mapped through invasive electrical and anatomical studies (Spalding, 1952; Harding et al., 1991) and in early fMRI and PET validation work, activations of the visual cortex were used as brain mapping tools (Belliveau et al., 1991; Engel et al., 1997; Fox et al., 1986). Previous work, in adults (Zeff et al., 2007) using high density diffuse optical tomography has shown that visual stimuli can be used to detect changes in the concentration of HbO_2 and HHb over the occipital cortex. A study conducted in adults by Heekeren at al. (1999b) demonstrated that visual stimuli produce measurable changes in oxCCO in the visual cortex, alongside changes in HbO_2 and HHb. More recently, work by Phan et al. (2016a) using

broadband NIRS in healthy adults indicated differences in the spatial localisation of ox-CCO and the haemodynamic signals in response to visual stimulation in the occipital cortex. Moreover, the primary visual cortex receives input from the lateral geniculate nucleus (LGN) in the thalamus. In humans, the LGN has different layers of cells; magnocellular and parvocellular cells which form the magnocellular and parvocellular pathways serving the dorsal and ventral streams respectively. Previous work in cats (Wong-Riley, 1979) and in humans (Wong-Riley et al., 1993) has demonstrated that there is a difference in the concentration of cytochrome-c-oxidase in these two pathways with the parvocellular pathway having a greater concentration of CCO in comparison to the magnocellular. This may reflect differing metabolic demands of the pathways which activate to different aspects of visual stimuli with the parvocellular pathway sensitising more to low contrast, colour and form and the magnocellular pathway being more sensitive to high contrast, motion and orientation (Shapley et al., 1981). Previous fMRI studies (Liu et al., 2006; Denison et al., 2014) have reported differences in the BOLD response in the visual cortex using functional stimuli targeting the two pathways. This may indicate that using visual stimulation that activates either magnocellular or parvocellular pathways may produce differential changes in oxCCO which can be measured using NIRS. The use of such stimuli should therefore provide a good context to investigate how the different components of the neurovascular coupling pathway being measured by NIRS and EEG relate to one another.

The study presented in this chapter therefore, uses a multi-channel broadband NIRS system simultaneously with EEG to measure changes in $\Delta[HbO_2]$, $\Delta[HHb]$, $\Delta[oxCCO]$ as well as changes in the electrical activity of the brain in response to visual stimulation differentially activating the magnocellular and parvocellular pathways of the visual cortex, in adults. The process of developing the combined NIRS and EEG headgear was discussed in Chapter 2.

5.2 Methods

5.2.1 Participants

Thirteen healthy adults participated in the study (9 males and 4 females; aged between 23 to 40 years old). All participants volunteered and gave written, informed consent to take part in the study. The study was approved by the UCL Ethics Committee and all procedures performed were in accordance with the regulations of the Ethics Committee. The participants were from varied ethnic backgrounds and therefore had varying skin and hair colour. Skin colour was not used as an exclusion criteria for participants. One of the limitations of NIRS is that small amounts of hair obstructing the light from the fibre can lead to a poor signal to noise ratio, therefore prior to being recruited for the study, participants were screened for hair colour, thickness and length. While this is not standard procedure for NIRS studies in adults, given the type of developments that needed to be made to optimise simultaneous NIRS - EEG data collection, it was easier to perform the studies on adults without thick, long hair, which added another level/source of poor signal-to-noise ratio in the data. However, as the participants were of varying ethnicity and skin colour, the sample was representative of the general population.

5.2.2 Data acquisition

5.2.2.1 Multi-channel broadband system

For this study and for the studies presented in Chapter 5 - 8, a multi-channel broadband system was used which has been developed at the UCL Department of Medical Physics and Biomedical Engineering by Dr Ilias Tachtsidis and Dr Phong Phan (Phan et al., 2016b). The various components that compose the system are described in the following sections. An overview of the system is shown in Figure 5.1.
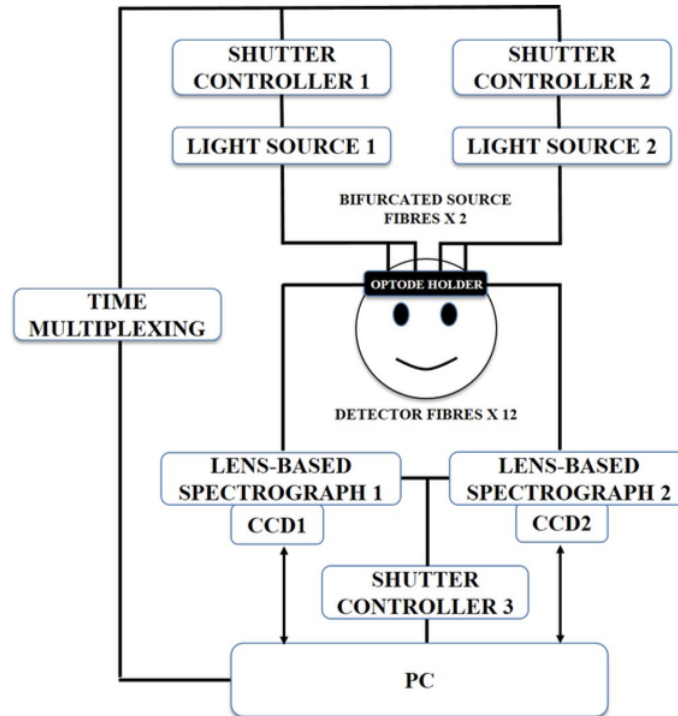
Figure 5.1: Schematic diagram providing an overview of the broadband NIRS system which is composed of two light sources and two spectrographs that are controlled by an electronic shutter. The light from the light sources is directed to the head of participant by means of bifurcated optical fibres, forming four source fibres at the subject end. The detected light from the head of the subject is collected using detector fibres which are connected to two spectrographs and CCD cameras. LabVIEW software is used to control the system from a PC. This picture was reproduced from (Phan, 2018) with permission from the author.

5.2.2.1.1 Hardware

5.2.2.1.1.1 *Light sources and spectrograph* The system is composed of two light sources and two charge-coupled devices (CCD) cameras which have been discussed in Section 2.1.4 of Chapter 2. The light sources (shown in Figure 5.2) each have a 50 W halogen light bulb (Phillips) with an axial filament which is needed to emit a broadband near-infrared enhanced spectrum. The spectrum output by the light source is filtered in order to reduce UV exposure and remove heating effects. The filter removes wavelengths below 504 nm and above 1068 nm. Light is directed to the subject from the light source through a customised bifurcated optical fibre (Loptek, Germany). The bifurcation allows each light source to split into two pairs of light sources. The opening and closing of light sources

are controlled by shutters and a time multiplexing mechanism is used whereby one light source from the pair of light sources is on every 1.4 s.
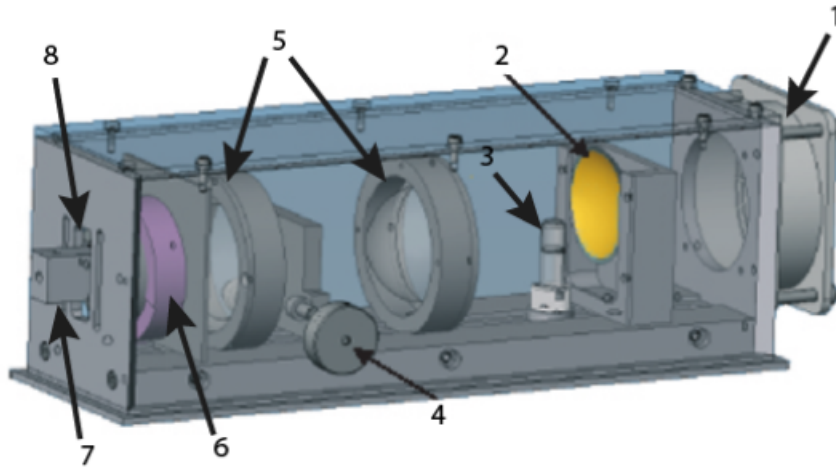
Figure 5.2: Light source forming part of the broadband NIRS system. It is composed of: 1) Ventilator 2) Gold-plated concave mirror 3) 50W halogen light bulb 4) Metal plate for cooling 5) Lenses 6) Magnetic shutter 7) Entrance for source fibre and 8) Filter. This picture was reproduced from (Gramer, 2007).

The light that travels through the tissue is then received by two customised lens-based spectrographs that are connected to the CCD cameras. This is shown in Figure 5.3a. The CCD camera (PIXIS: 512f, Princeton Instruments) detects the light spectrum and is shown in Figure 5.3b. Each spectrograph is connected to a detector fibre bundle which divides into six individual fibres. Only five of the six fibres were used for this study as one of the fibres from each fibre bundle was for tissue oxygenation index measurements which were not required for this work. Therefore in total, the instrument provided 4 light sources and 10 detectors in total to form 16 measurement channels. The following section discusses the optical fibres in more detail.
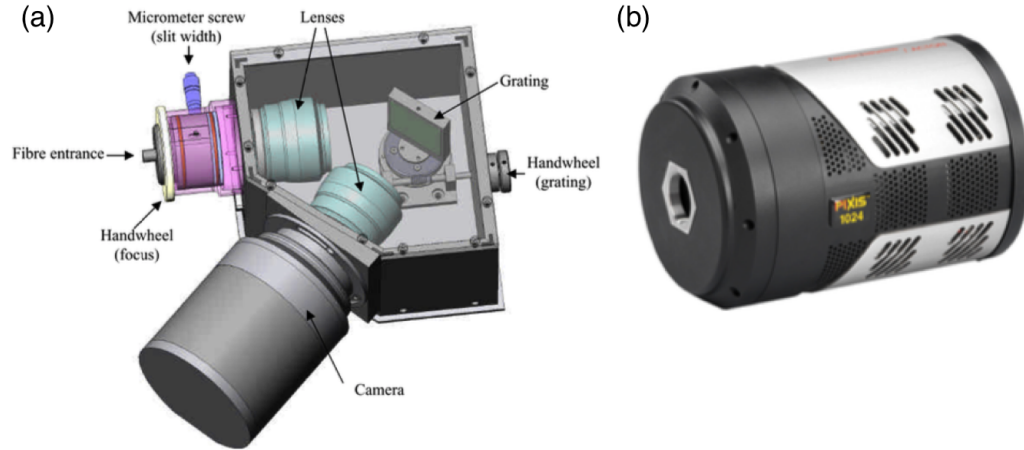
Figure 5.3: (a) Schematic drawing of a spectrograph and CCD camera forming part of the broadband NIRS system. This picture was reproduced from (Gramer, 2007) (b) CCD Camera by Pixis, Princeton Instruments. This picture was reproduced from (Phan, 2018)

5.2.2.1.1.2 *Optical fibres*   The optical fibres are made of glass and were custom-built by Loptek (Glasfasertechnik GmbH, Germany) and each fibre in the optical fibre bundle of detectors has a diameter of 70μm. The system has two sets of light sources which further split into two pairs at the subject end, these bifurcated fibres are shown in Figure 5.4a. The diameter of the light source bundle at the system end is 4.5mm while the diameter of the individual source fibre at the subject-end is 3.2mm. These fibres are shown in Figure 5.4b. The system has six detector fibres at the subject-end which form one detector fibre bundle at the spectrograph-end. The detector fibres are shown in Figure 5.4c and d.
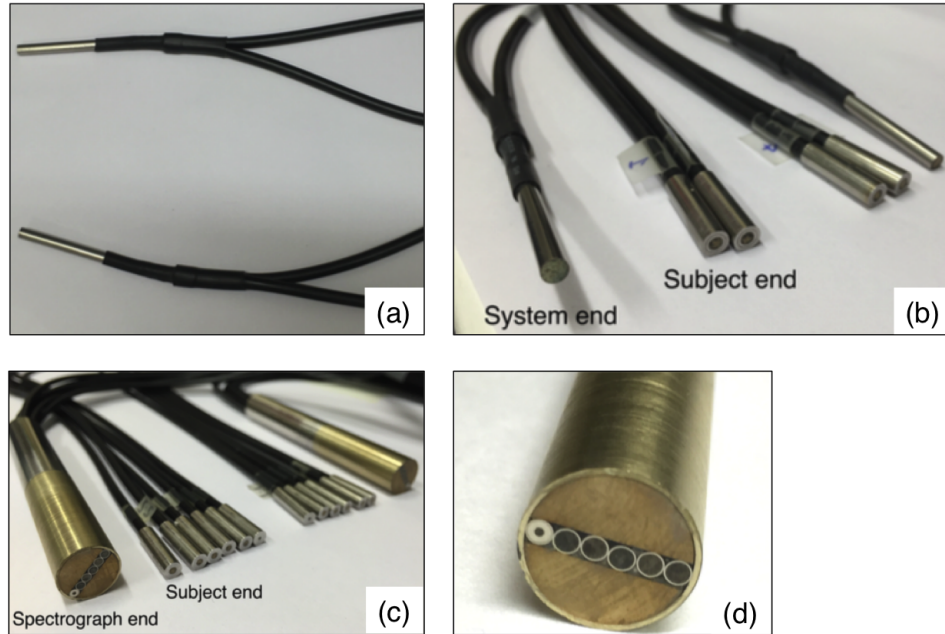
Figure 5.4: Optical fibres forming the source fibres and detector fibres with (a) the bifurcated light source fibres (b) the system and subject ends of the light source fibres (c) system and subject ends of the detector fibres and (d) close-up of the system end of the detector fibres with each of the circles representing a detector. All photos were reproduced from (Phan, 2018) with permission.

5.2.2.1.2 *Software*   The spectrographs are connected to a PC running LabVIEW software which is used to control and operate the system. Figure 5.5a shows the front interface of the software with the settings for CCD2 displayed. Figure 5.5b shows the raw spectrum indicating the photon counts being received at each detector of CCD2. This panel is used to identify the quality of the data when the headgear is positioned on a participant's head. The photon counts (or intensity counts) at each detector represent the number of photons that have passed from the light source, through the tissue and arrived at each detector and can provide an indication of the expected signal-to-noise ratio of the data. The minimum number of counts for good signal-to-noise ratio is approximately 2000 counts as the noise level of the system is around 500 counts and the intensity counts being received at the detector must be at least 4 times above the noise level in order to obtain a good signal-to-noise ratio. The noise level of the system refers to a combination of thermal noise from the

CCD and dark noise which is measured by the closing the shutter of the spectrometer so no light is being received at the spectrometer.
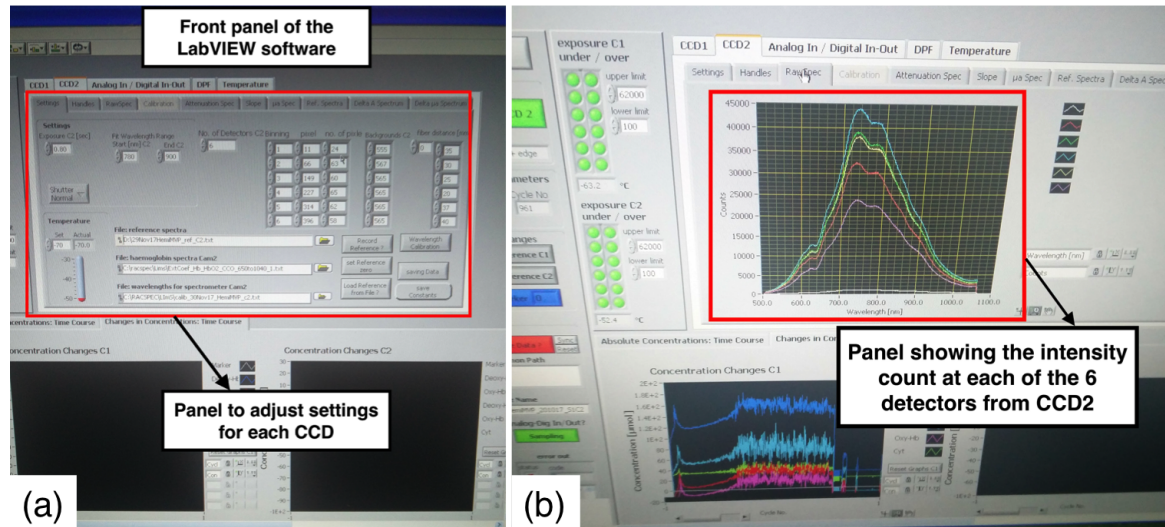
Figure 5.5: LabVIEW software that controls the system with (a) front panel in the LabVIEW software showing settings for the system. Each CCD has an identical tab for settings. and (b) Panel displaying the intensity counts, i.e. the number of photons at each detector. Each coloured line represents a detector from one CCD camera. There are identical tabs for each CCD camera.

5.2.2.2 Enobio EEG

The EEG system used for this study has already been described in Chapter 2, Section 2.3.2. For this study, twenty-six EEG channels were used with five channels positioned over the occipital lobe (Oz, O1, O2, O9 and O10) and twenty-one channels were distributed over the rest of the participant's head (AF3, AF4, Fz, F3, F4, FC1, FC2, FC5, FC6, Cz, C3, C4, CP1, CP2, Pz, P3, P4, P7, P8, PO3 and PO4). Figure 5.6a shows the EEG montage with all the channels indicated in purple circles. Figure 5.6b shows the front-panel of the NIC software with the EEG activity being displayed from all the different channels in real-time.
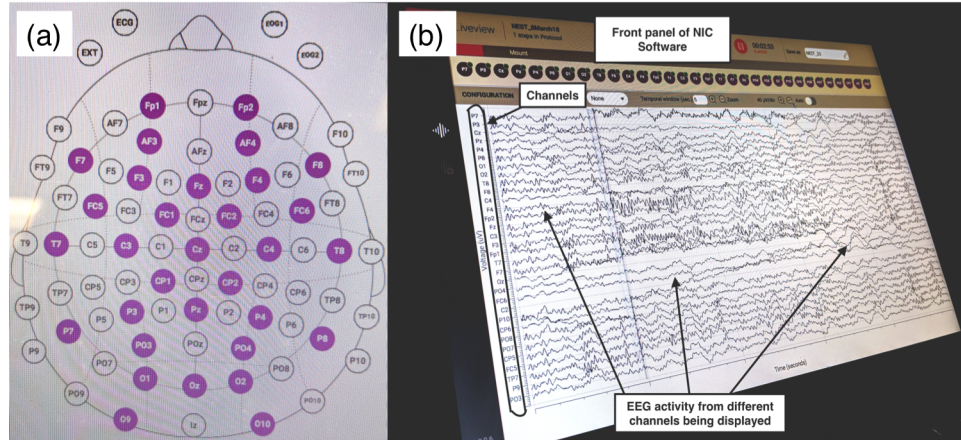
Figure 5.6: (a) EEG montage showing the locations of the 26 channels and (b) NIC software front panel displaying quality of EEG signals from each electrode

5.2.3 NIRS Probe Design

Previous work by Phan et al (2016a) used the same multi-channel broadband system with a visual stimulation experimental paradigm to demonstrate the spatial selectivity of the cytochrome response in the visual cortex. Keeping in line with their work, the orientation of the sources and detectors in this study was kept the same. While their study used varying source-detector separation distances to perform image reconstruction, the separation in this study was maintained at 3 cm for all the source-detector pairs. This separation distance has previously been demonstrated to be ideal for adult functional activation studies measuring changes in oxCCO (Phan et al., 2016b). Figure 5.7 shows the schematic for the array which was centred around Oz of the International 10/20 system.
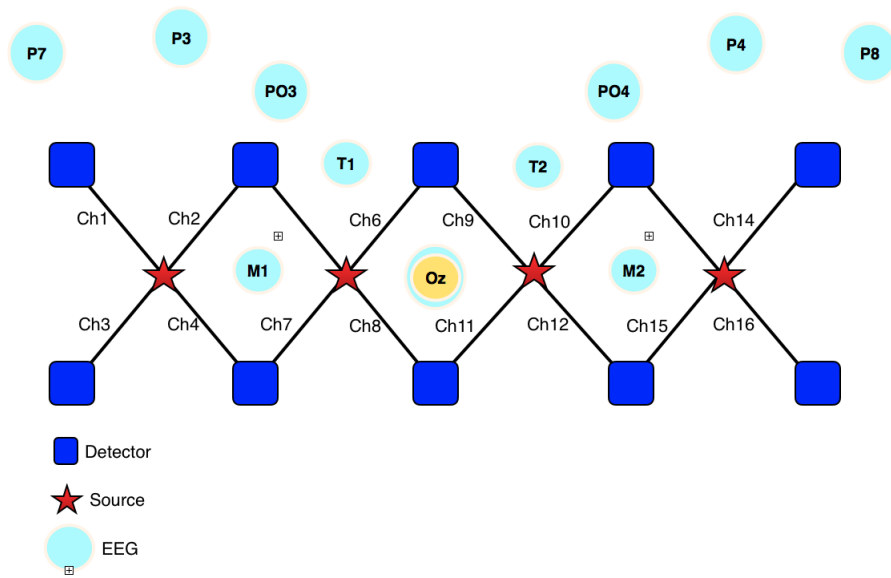
Figure 5.7: A schematic diagram of the NIRS array showing the positions of the sources and detectors and EEG electrodes, with blue squares indicating detectors, red stars indicating sources and cyan circles indicating EEG channels over the occipital cortex. The black lines represent channels that are formed between sources and detectors.

The procedure for designing the NIRS headband has already been described in detail in Chapter 3 and Figures 5.8a-c show the front, side and back views of the headband positioned on a participant to remind the reader of how the NIRS headgear looks.
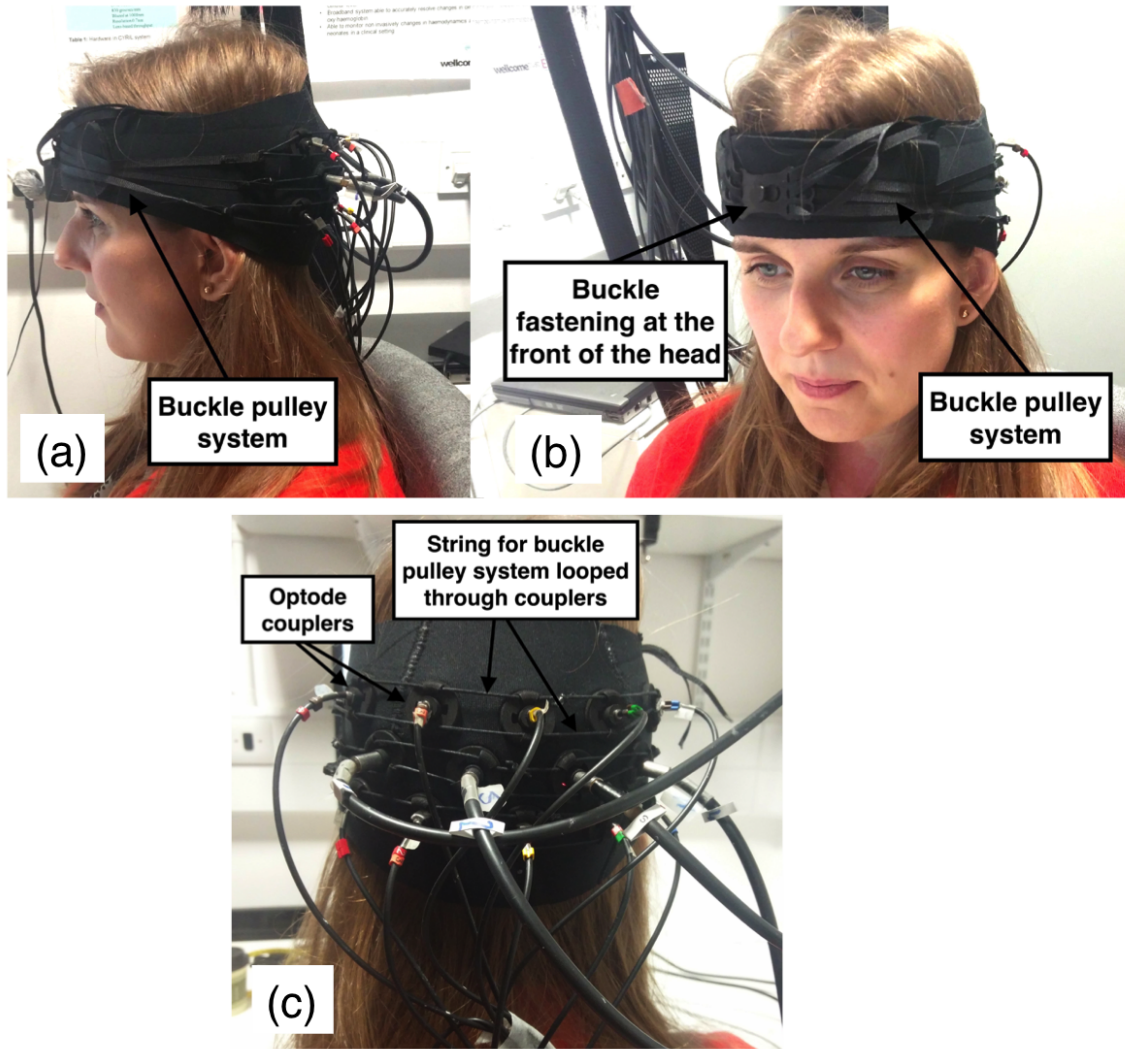
Figure 5.8: (a) Front, (b) side and (c) back views of the headband on a participant. Permission was obtained from the participant for their image to be included here.

Figure 5.9 shows the combined NIRS-EEG headgear positioned on a participant.
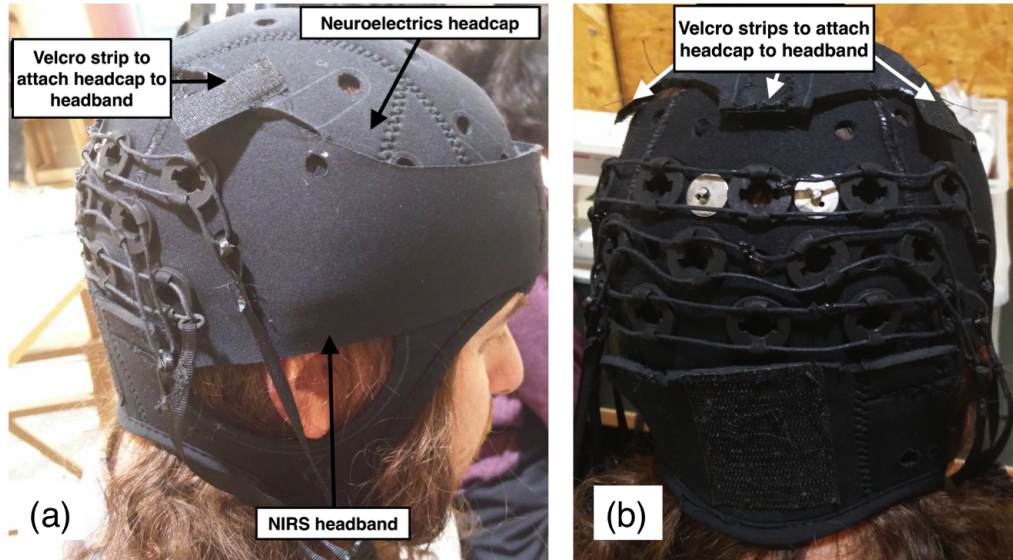
Figure 5.9: Image showing how the NIRS headband and EEG headcap were attached (a) side view and (b) back view, on a participant.

5.2.4 Experimental Stimuli

As discussed in the introduction of this chapter, experimental stimuli were designed to activate the magnocellular and parvocellular pathways of the visual cortex. Given the difference in the concentration of CCO in the two pathways, these stimuli theoretically provide a good context to study the relationship between haemodynamics, cytochrome and the underlying neural activity as they should elicit a differential response in oxCCO. The magnocellular pathway is thought to be activated by high contrast, motion and orientation while the parvocellular pathway is deemed to be more sensitive to low contrast, colour and form (Derrington and Lennie, 1984; Hicks et al., 1983; Shapley et al., 1981). The stimuli used in this study were created by Mr Andrew Levy of the Wellcome Trust Centre for Neuroimaging, Functional Imaging Laboratory, UCL. Circular hemifield checkerboards were designed using Psychtoolbox (Matlab, USA) using the Retinotopy Toolbox developed at the Vision Imaging Science and Technology Lab (Stanford University, USA). There were two contrast conditions with varying colour, spatial and temporal frequency. The spatial frequency of a checkerboard is defined as the number of squares subtended per degree of visual angle on the retina and is indicated by checksize. Large, coarse stimuli with fewer

number of squares are said to have a low spatial frequency whereas stimuli with a higher number of squares are said to have a high spatial frequency. Temporal frequency is measured in Hertz refers to the speed at which the checkerboard alternates, a low temporal frequency refers to a slower alternation while a high temporal frequency refers to a faster alternation. There two conditions were:

1. A high contrast black and white circular checkerboard with low spatial frequency (checksize 2°) and high temporal frequency (15 Hz).

2. A high luminance red and green circular checkerboard with high spatial frequency (checksize 0.25°) and low temporal frequency (2 Hz).

Each of these stimuli were presented in the left and right hemifield followed by baseline which was a blank grey screen. All stimuli had a central fixation point which the participants were instructed to look at throughout the experiment. Figure 5.10a and b show both experimental stimuli.
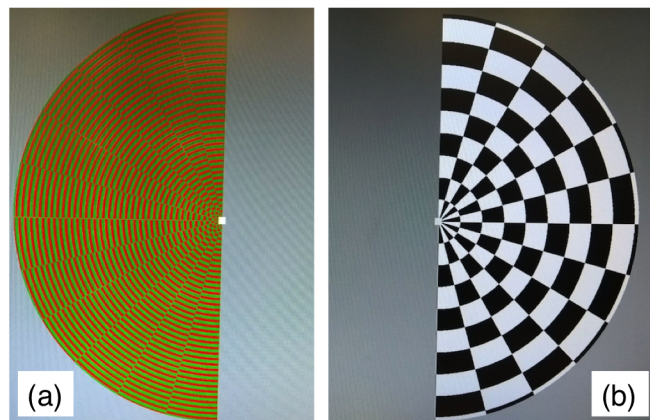
Figure 5.10: Experimental stimuli with (a) High luminance red and green circular checkerboard and (b) High contrast black and white circular checkerboard.

These experimental stimuli worked well with adults as they could be instructed to look at the fixation cross at the centre of the screen. However, hemifield checkerboards do not work well with infants. Further, adults could watch the stimuli for a long time and block design and event related design variations of the task could be used. Infants however, have a shorter attention span and tire more quickly, therefore making it impractical to

have two separate versions of the experiment. An infant-friendly version of this paradigm was developed to explore if a block design format could be used for future studies. This experiment is detailed in the appendix.

5.2.4.1 Experimental Procedure

The data collection was performed in collaboration with Mr Andrew Levy (Wellcome Trust Centre for Neuroimaging, Functional Imaging Laboratory, UCL). Written, informed consent was obtained from each participant following which head measurements were obtained. The measurement from the nasion point (defined as the depressed area in between the eyes, above the bridge of the nose) to the inion (defined as the bony structure at the base of the skull) was obtained and other 10/20 locations along the midline such as Cz, Pz and Oz were calculated using this measurement. The combined headgear was positioned on top of the participant's head such that the NIRS headband was positioned first, with the centre of the row of sources (marked as Oz in Figure 5.7) positioned over Oz. Following this, the holes indicated on the EEG headcap were then carefully aligned with the true Cz, Pz and Oz locations on the participant's head and the headgear was secured. Once the headgear was in place, the locations of the NIRS optodes and EEG electrodes were digitised using the Polhemus (Polhemus, USA) and Brainstorm Software (University of Southern California, USA) was used to visualise these locations on an averaged Colin adult brain template (Collins et al., 1998) to ensure that the headgear was placed accurately, with all optodes and electrodes in the intended locations. Next, the EEG electrodes inside the headcap were filled with gel using a syringe and the wires were clipped on. The participant was then positioned in front of the screen at an approximate viewing distance of 60 cm and the EEG wires were plugged into the necbox which was secured to an arm supporting the NIRS fibres, above the top of the participant's head. Figure 5.11 shows the full set-up on a participant. Once all aspects of the EEG set up had been completed, additional steps were performed to ensure that a good signal-to-noise ratio would be obtained from the NIRS system. This involved clearing hair prior to the insertion of the optical fibres into the optode couplers. Hair was moved out of the way of each optical fibre using plastic cable ties in order to ensure that hair did not obstruct the light from the fibre and a good

signal-to-noise-ratio was obtained. Following this, the buckle-pulley system was used to further tighten the optical fibres to scalp. Occasionally, the optode couplers were rotated to add an extra level of tightness of the fibres with the head. Each participant was then presented with two versions of the same stimuli; a block design version and an event-related version.
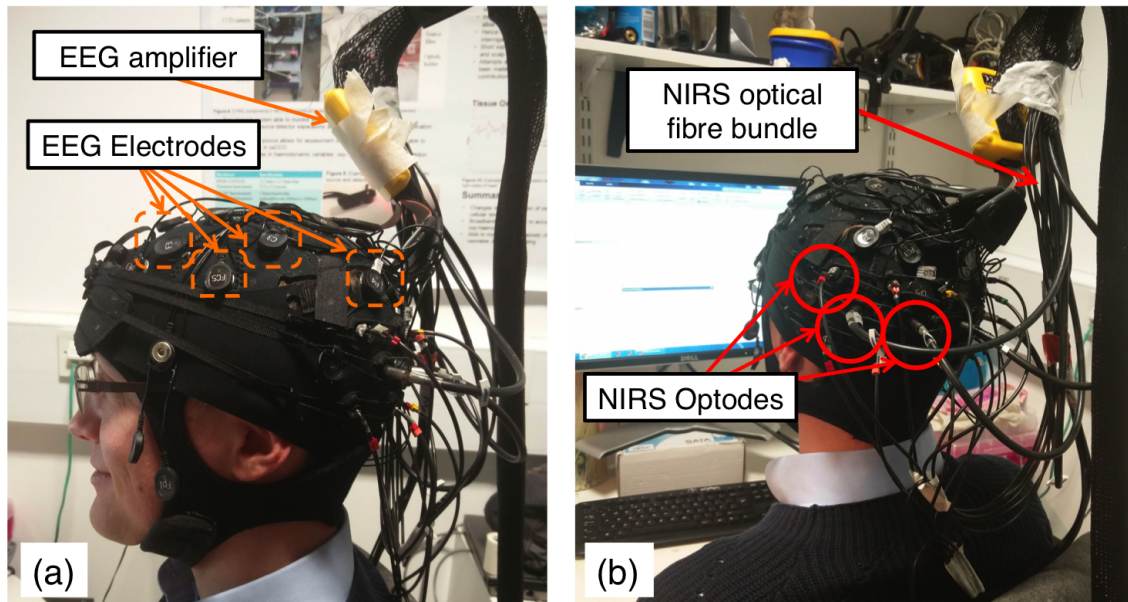
Figure 5.11: NIRS-EEG set-up on a participant (a) side view and (b) back view with NIRS optodes and EEG electrodes indicated.

One of the challenges of a simultaneous NIRS-EEG study is headgear development and this has already been discussed in detail in Chapter 3. Another important aspect to consider is developing a suitable experimental paradigm which is ideal for both techniques. Typically, NIRS functional activation studies use experimental paradigms where the stimuli are presented in blocks of 10 - 20 s. This is because the haemodynamic response is slow and block presentation allows the response to reach its maximum value and then return to baseline before the presentation of the following experimental condition. On the other hand, EEG studies use an event-related design where stimuli are presented many times for a short duration (between 100 ms to 2000 ms) as neural activity is much faster than the haemodynamic response and can be reliably detected 100 ms post-experimental stimulus onset (Luck, 2005). As the purpose of this adult work was to develop all aspects of a

simultaneous NIRS-EEG study to apply to the infant studies, it was necessary to explore varying designs for an experimental paradigm that worked for both techniques. As a starting point, both block design and event-related designs were used to collect simultaneous NIRS-EEG data. In the block design variation, the stimuli were presented for 18 s each followed by 18 s of baseline which consisted of a black grey screen and this was presented eight times to each participant. This is in accordance with previous adult NIRS visual functional activation studies have used similar presentation lengths (Phan et al., 2016b). In the event-related variation, the stimuli were presented in short blocks such that each block consisted of 4 presentations of the same stimulus (e.g. black/white checkerboard presented in the left hemifield) for 2.5 s each with an inter-stimulus interval of 2 s followed by a baseline period of 8 s which consisted of a blank grey screen. Each block was repeated eight times for each participant, amounting to a total of 32 presentations of each condition. As mentioned earlier, in event-related designs stimulus presentation is much shorter and a presentation duration of 2.5 s was used in this study which is consistent with event-related designs and provides sufficient time for a response to be detected (Luck, 2005).

5.2.5 Data analysis

5.2.5.1 NIRS

The NIRS data was analysed only from the block design task. The data was analysed in Matlab 2014a (Mathworks, USA) using a program developed by Dr Ilias Tachtsidis and Dr Phong Phan at UCL. The time multiplexing mechanism of the system allowed each detector to receive two intensity spectra of light from source 1 at one cycle and source 2 in the next cycle. Therefore, the intensity spectra collected at each detector needed to be separated into the corresponding channels. The distances between the channels resulted in differences in the intensity spectra which were to be used to identify the operating light source at each time point. Using these differences, the intensity spectra were then correctly allocated to the appropriate channels. These were then used to calculate the change in attenuation and consequently the changes in the concentrations of each of the chromophores by using the Modified Beer Lambert Law using the UCLn algorithm (Bale et al., 2016a), at

120 wavelengths of light between 780 - 900 nm. Once the concentration changes were calculated, the data were interpolated to 1s and bandpass filtered using a 5th order Butterworth filter from 0.01 - 0.4 Hz, in accordance with previous studies (Phan et al., 2016b). The data were then converted into blocks such that each block consisted of 9 s of the baseline period preceding the experimental condition, the experimental condition and the entire following baseline. The blocks for each condition were averaged to obtain an averaged response for each participant. The averaged responses were then used to create contralateral and ipsilateral conditions. This was done by averaging between channels positioned either side of the midline, for example for the contralateral condition, for the black and white circular checkerboard presented in the right hemifield, the channnels positioned over the left visual cortex were averaged with channels over the right visual cortex when the black and white circular checkerboard was presented in the left hemifield. The contralateral and ipsilateral conditions were then averaged across participants to obtain grand averaged contralateral and ipsilateral responses. Therefore for the contralateral and ipsilateral analysis, there are 8 channels formed by collapsing the 16 contralateral and ipsilateral channels. I chose to analyse the data in this way as it allowed clearer distinction between the haemodynamic responses to the two experimental stimuli.

From this point onwards, the condition referred to as "Magno" refers to the black and white circular checkerboard whereas the condition referred to as "Parvo" refers to the red and green circular checkerboard. Statistical comparisons were performed to compare the maximum change in HbO_2, HHb and oxCCO during a time window of 10 to 20 s post-experimental stimulus onset, to include the range of responses across participants, between contralateral vs ipsilateral responses for both Magno and Parvo conditions. Comparisons were also performed between the contralateral Magno vs Parvo conditions and the ipsilateral Magno vs Parvo. No correction for multiple comparisons was applied in this study. Figure 5.12 shows how the original 16 channels were collapsed to form contralateral and ipsilateral channels with the dashed lines showing the labels of the new channels.
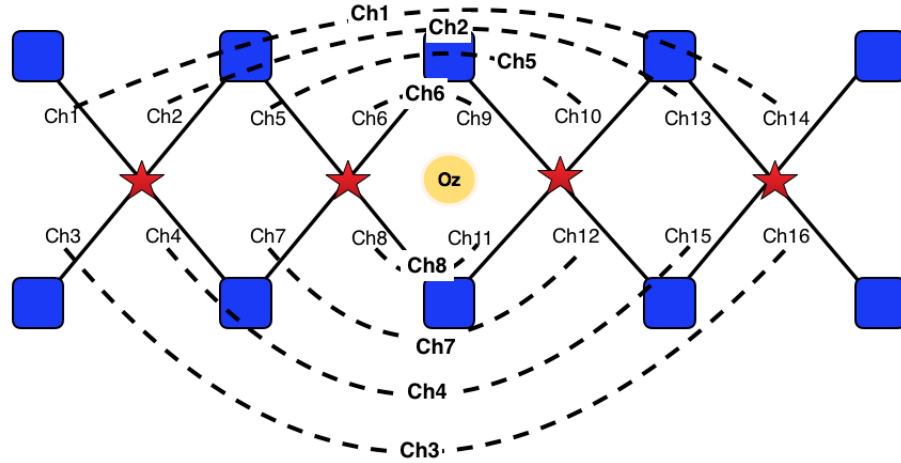
Figure 5.12: Contralateral and Ipsilateral channels created by collapsing over channels across hemispheres. The dashed lines show the labels of the new channels formed.

5.2.5.2 EEG

The EEG data were analysed from both block and event-related tasks. However, due to a small number of participants and trials in the EEG data of the block design task, the combined NIRS-EEG analysis was performed on the NIRS data from the block design task with the EEG data from event related task. All EEG data were analysed using the EEGLab Toolbox (Schwartz Centre for Computational Neuroscience, UC San Diego, USA) in Matlab2017a (Mathworks, USA). For both tasks, the data were bandpass filtered from 0.1-100 Hz and a notch filter of 50 Hz was applied to remove electrical noise and then segmented into 800 ms epochs around the onset of the experimental stimulus. The epoched data were cleaned manually to remove any trials that were contaminated with artifacts such as eye blinks, muscle noise and movement. A similar approach to the NIRS data was followed in order to obtain contralateral and ipsilateral conditions, Figure 5.13 shows how the channels were collapsed to obtain contralateral and ipsilateral conditions. The solid lines between channels show the new labels for the channels. A number of different analyses were performed on the EEG data for contralateral and ipsilateral conditions for both Magno and Parvo:

1. Event related potentials (ERPs) waveforms were generated for the five channels over the occipital cortex.

2. Wavelet-based decomposition was performed to obtain the evoked oscillations for time-frequency analysis, for each channel.

3. Topographical maps of spectral power were generated at specific frequency bands and latencies.

Similar to the NIRS data analysis, statistical comparisons were performed on the maximum amplitude change of the P100 of the ERPs to compare contralateral and ipsilateral conditions for both Magno and Parvo. This is in accordance with previous work investigating the magnocellular and parvocellular pathways using visually evoked potentials (Benedek et al., 2016). The contralateral condition for Magno was compared to Parvo and ipsilateral condition for Magno was compared to Parvo.
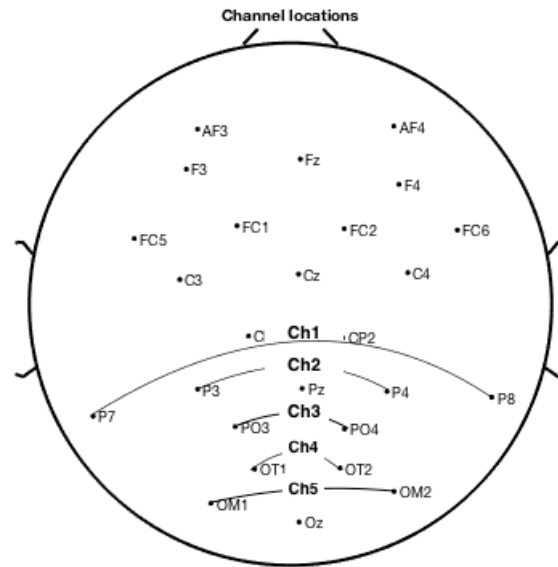
Figure 5.13: Contralateral and Ipsilateral channels created by collapsing over channels across hemispheres. The solid lines between channels show the new labels for the channels.

Figure 5.14 shows a topographical map of both EEG (left) and NIRS (right) channels which were collapsed to create contralateral and ipsilateral channels.
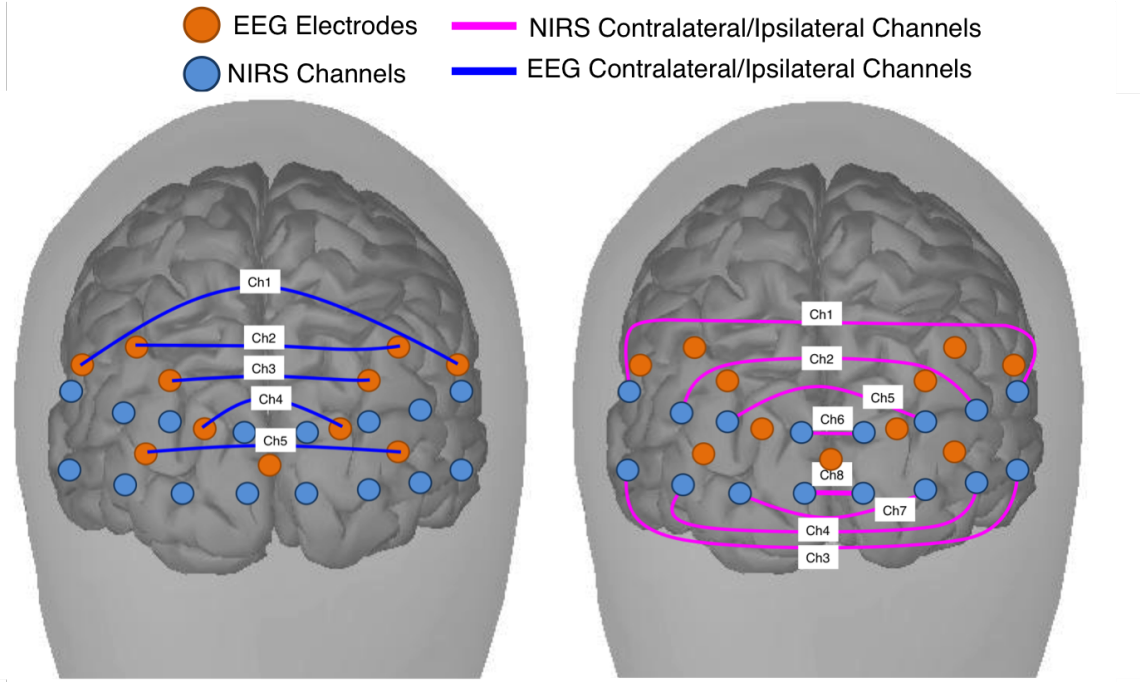
Figure 5.14: Contralateral and Ipsilateral channels for both (left) EEG indicated in blue and (right) NIRS indicated in magenta.

5.2.5.3 Combined NIRS-EEG

For the combined NIRS-EEG analysis, EEG data from the event-related design task were combined with the NIRS data from the block design task. As a result, the combined data analysis was not performed on the concurrently recorded NIRS and EEG however, owing to the small number of subjects and trials in the EEG data from the block design task, it was not meaningful to perform this analysis on the block task. For the infant work presented in Chapter 5 however, variations were made to the experimental stimuli so that simultaneously recorded data could be analysed.

In order to combine the NIRS and EEG, two main types of analyses were performed:

1. **The maximum amplitude of the P100 of the ERP was correlated with the maximum change in concentration of HbO$_2$ and oxCCO.**

    This was done for two contrasts:

    (1) Contralateral vs ipsilateral (for Magno and Parvo conditions)

(2) Magno vs Parvo (for contralateral and ipsilateral conditions)

For both contrasts, a subtraction was performed prior to the correlations which involved subtracting the amplitudes of the P100 of the ERP and the maximum amplitude of the HbO_2 and oxCCO responses of one condition from the other. For example, when comparing the contralateral versus the ipsilateral (i.e. contrast (1) above) the P100 amplitude of the ERP and the maximum amplitude of the HbO_2 and oxCCO responses of the ipsilateral condition were subtracted from the contralateral condition. A similar subtraction was performed for contrast (2) but for this the P100 amplitude of the ERP and the maximum amplitude of the HbO_2 and oxCCO responses of the Parvo condition were subtracted from the Magno. Following this, the data were $z-$scored in order to obtain normalised measures. Pearson's correlation was then calculated between the P100 amplitude and the maximum change in $\Delta[HbO_2]$ and $\Delta[oxCCO]$ for each of the five EEG channels over the occipital cortex and all eight of the NIRS channels.

2. **The power spectral density (PSD) was correlated with the maximum change in concentration of HbO_2 and oxCCO.**

   The PSD of different frequency bands (alpha, beta and gamma) were calculated. Following this, similarly to the analysis described in (1), subtractions were performed for each contrast measure and the data were $z-$scored in order to obtain normalised measures. Pearson's correlation was then calculated between the power of each frequency band and the maximum change in $\Delta[HbO_2]$ and $\Delta[oxCCO]$ for each of the five EEG channels over the occipital cortex and all eight of the NIRS channels.

As a first step EEG data was correlated only with measures of HbO_2 and oxCCO and not HHb.

5.3 Results

5.3.1 NIRS

Out of 13 subjects, 5 were included in the final analysis. Subjects were excluded from the study if they had a poor signal-to-noise ratio, which was determined by the intensity counts of the photons returning at each detector. Low intensity counts were observed for a number of subjects and there are various factors which can contribute to this including hair, variability in the thickness of the scalp as well as anatomical differences.

5.3.1.1 Contralateral vs Ipsilateral

5.3.1.1.1 Magnocellular

Figure 5.15 (upper panel) shows the changes in concentration of HbO_2, (red) HHb (blue) and oxCCO (green) for both contralateral (solid lines) and ipsilateral conditions (dashed lines) for the Magno condition. The coloured boxes indicate channels with a significant difference in the contralateral and ipsilateral conditions for $\Delta[HbO_2]$ (red boxes), $\Delta[oxCCO]$ (green boxes) and $\Delta[HHb]$ (blue boxes). Figure 5.15 (bottom panel) shows the oxCCO responses with y-axis rescaled.

The paired t-test conducted between contralateral and ipsilateral conditions indicated significant differences in HbO_2 in channels 5 ($t = 7.158$, $p = 0.002$), 6 ($t = 2.980$, $p = 0.041$), 7 ($t = 3.040$, $p = 0.038$) and 8 ($t = 3.473$, $p = 0.026$), in HHb in channels 2 ($t = -2.825$,$p = 0.048$), 5 ($t = 4.435$, $p = 0.011$), 6 ($t = 3.213$, $p = 0.033$), 7 ($t = 6.876$, $p = 0.015$) and 8 ($t = 6.876$, $p = 0.002$) and in oxCCO in channels 5 ($t = 4.853$, $p = 0.008$), 6 ($t = 5.692$, $p = 0.005$), 7 ($t = 5.314$, $p = 0.006$) and 8 ($t = 5.559$, $p = 0.005$). The table containing the statistics for each of the chromophores for each channel can be found in the appendix. The channels located over the primary visual cortex show greater responses to the contralateral in comparison to the ipsilateral, as expected.
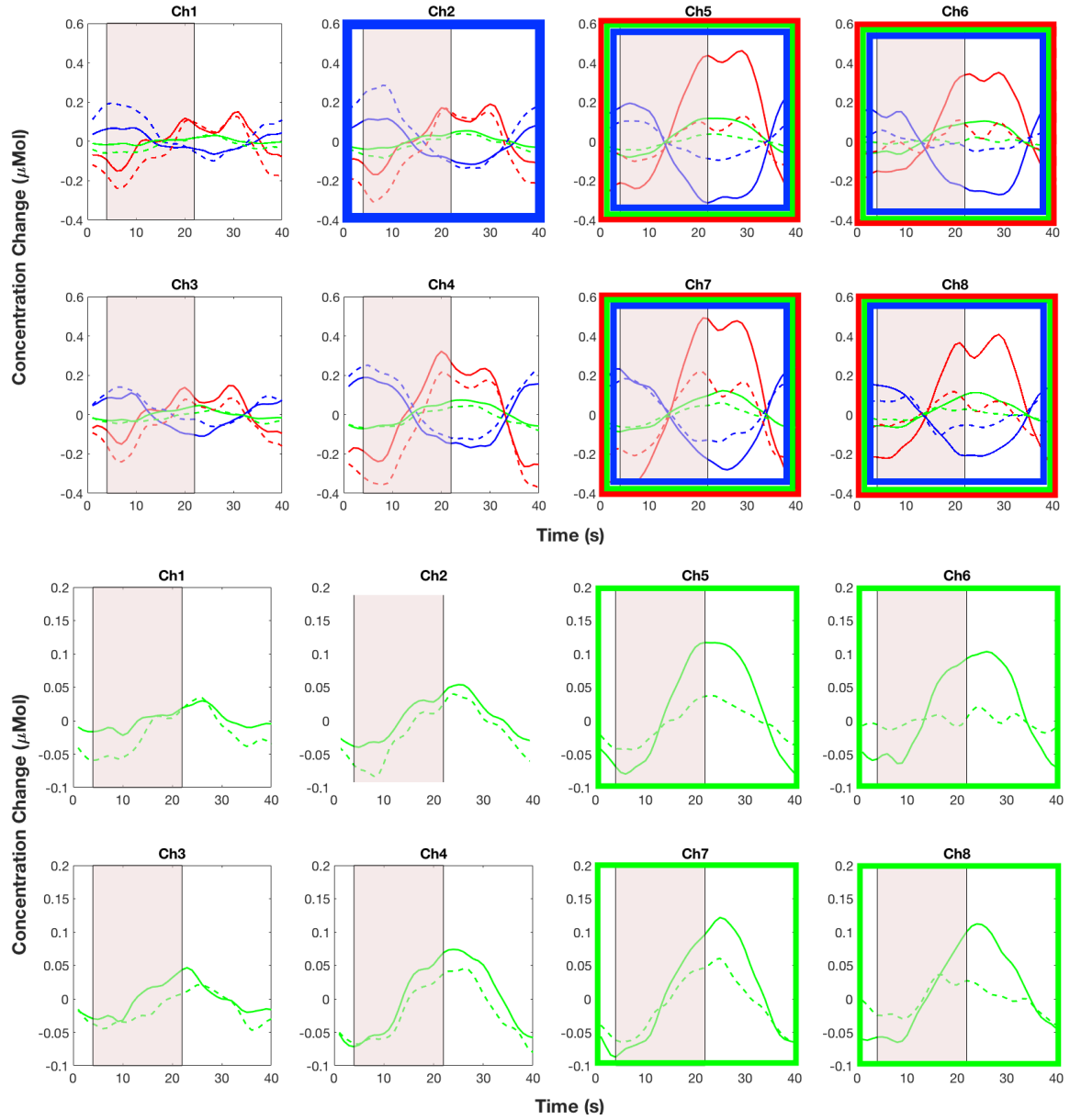
Figure 5.15: Observed changes in concentration of $\Delta[HbO_2]$ (red), $\Delta[HHb]$ (blue) and $\Delta[oxCCO]$ (green) with (upper panel) oxCCO magnified (x2.5) and (bottom panel) oxCCO prior to magnification, for the Magno condition. Both contralateral (solid lines) and ipsilateral (dashed lines) conditions are shown and channels with a significant difference between contra and ipsi conditions are indicated with boxes (red for HbO_2, green for oxCCO and blue for HHb).

5.3.1.1.2   Parvocellular   Figure 5.16 (upper panel) shows the changes in concentration of HbO_2, (red) HHb (blue) and oxCCO (green) for both contralateral (solid lines) and ipsilat-

eral conditions (dashed lines) for the Parvo condition. The coloured boxes indicate channels with a significant difference in the contralateral and ipsilateral conditions for $\Delta[\text{HbO}_2]$ (red boxes), $\Delta[\text{oxCCO}]$ (green boxes) and $\Delta[\text{HHb}]$ (blue boxes). Figure 5.16 (bottom panel) shows the oxCCO responses with y-axis rescaled.

The paired t-test conducted between contralateral and ipsilateral conditions indicated significant differences in HbO_2 in channels 4 ($t = -2.949$, $p = 0.04$), 6 ($t = 3.004$, $p = 0.04$), 7 ($t = 3.992$, $p = 0.016$) and 8 ($t = 3.374$, $p = 0.028$), in HHb in channels 4 ($t = -7.141$, $p = 0.002$), 5 ($t = 5.346$, $p = 0.006$), 6 ($t = 5.882$, $p = 0.004$), and 7 ($t = 8.181$, $p = 0.001$) and in oxCCO in all channels except channel 1 (the t and p values for oxCCO can be found in the appendix). The table containing the statistics for each of the chromophores for each channel can be found in the appendix. The channels located over the primary visual cortex show greater responses to the contralateral in comparison to the ipsilateral, as expected.
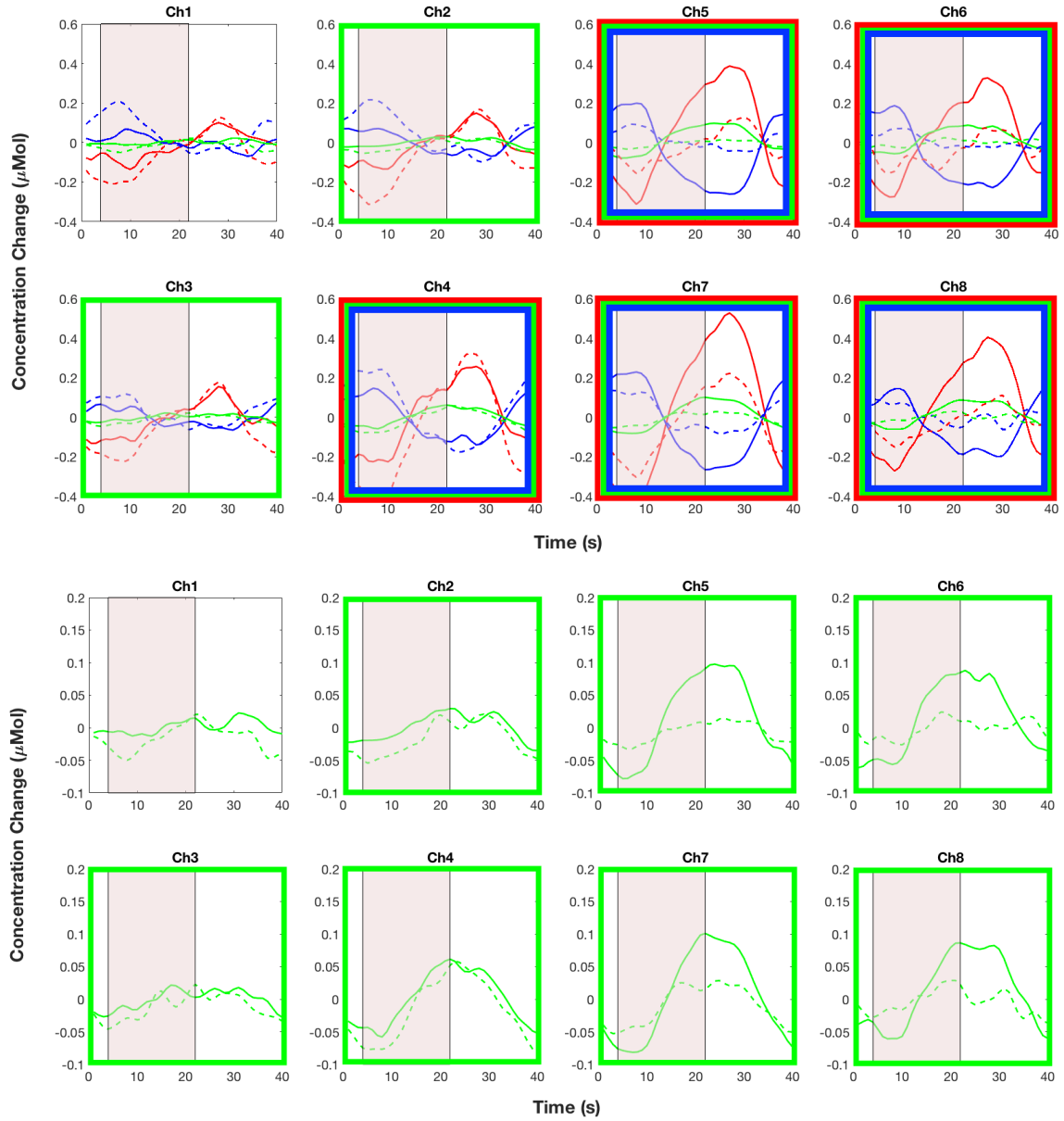
Figure 5.16: Observed changes in concentration of $\Delta[HbO_2]$ (red), $\Delta[HHb]$ (blue) and $\Delta[oxCCO]$ (green) with (upper panel) oxCCO magnified (x2.5) and (bottom panel) oxCCO prior to magnification, for the Parvo condition. Both contralateral (solid lines) and ipsilateral (dashed lines) conditions are shown and channels with a significant difference between contra and ipsi conditions are indicated with boxes (red for HbO_2, green for oxCCO and blue for HHB).

5.3.1.2 Magno vs Parvo

5.3.1.2.1 Contralateral Pairwise t-tests between the Magno and Parvo conditions for the contralateral condition indicated significant differences in HbO_2 in channels 1 ($t = 3.384$, $p = 0.028$) and 5 ($t = 6.462$, $p = 0.003$), HHb in channel 4 ($t = 13.04$, $p < 0.001$) and in oxCCO channels 5 ($t = 3.927$, $p = 0.017$) and 8 ($t = 3.741$, $p = 0.02$). The table with the statistics for each of the chromophores for each channel can be found in Appendix A.

Figure 5.17 shows, for oxCCO (green) and HbO_2 (red), the difference between the maximum concentration change for Magno and Parvo (i.e. Magno minus Parvo) for each channel. Each circle indicates a subject and the channels indicated by the highlighted asterisk show the channels with a significant difference between Magno and Parvo.
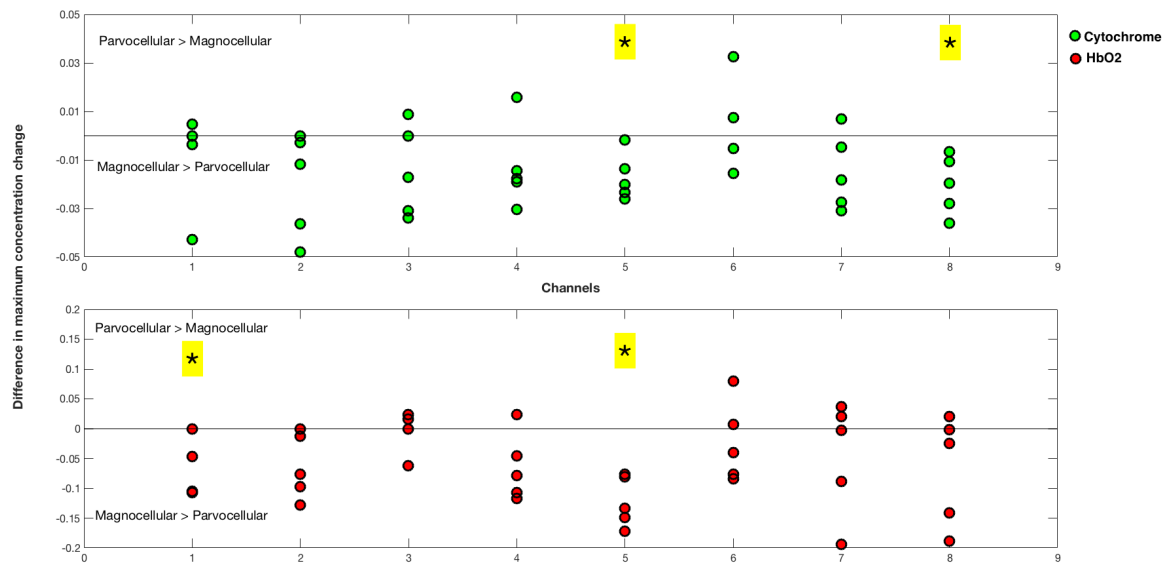
Figure 5.17: Difference between maximum concentration change for contralateral Parvo minus Magno for oxCCO (green) and HbO_2 (red). Channels with a significant difference between contralateral Parvo and Magno conditions are indicated with an asterisk.

5.3.1.2.2 Ipsilateral There were no channels for any of the chromophores with significant differences between Magno and Parvo for the ipsilateral condition.

5.3.1.3 Cross correlations

Cross-correlations were calculated between each of the chromophores, i.e. between (i) HbO_2 and oxCCO (ii) HHb and oxCCO and (iii) HbO_2 and oxCCO for the contralateral Magno and Parvo conditions for all channels and then averaged across channels to obtain the average cross-correlations. These can be seen in Figure 5.18. As ipsilateral displayed the same pattern of results and can be found in Appendix A. Negative correlations were observed between HbO_2 and HHb ($r = -0.78$) and HHb and oxCCO ($r = -0.95$), as expected, and positive correlations were seen between HbO_2 and oxCCO ($r = 0.63$), all around zero time-lag.
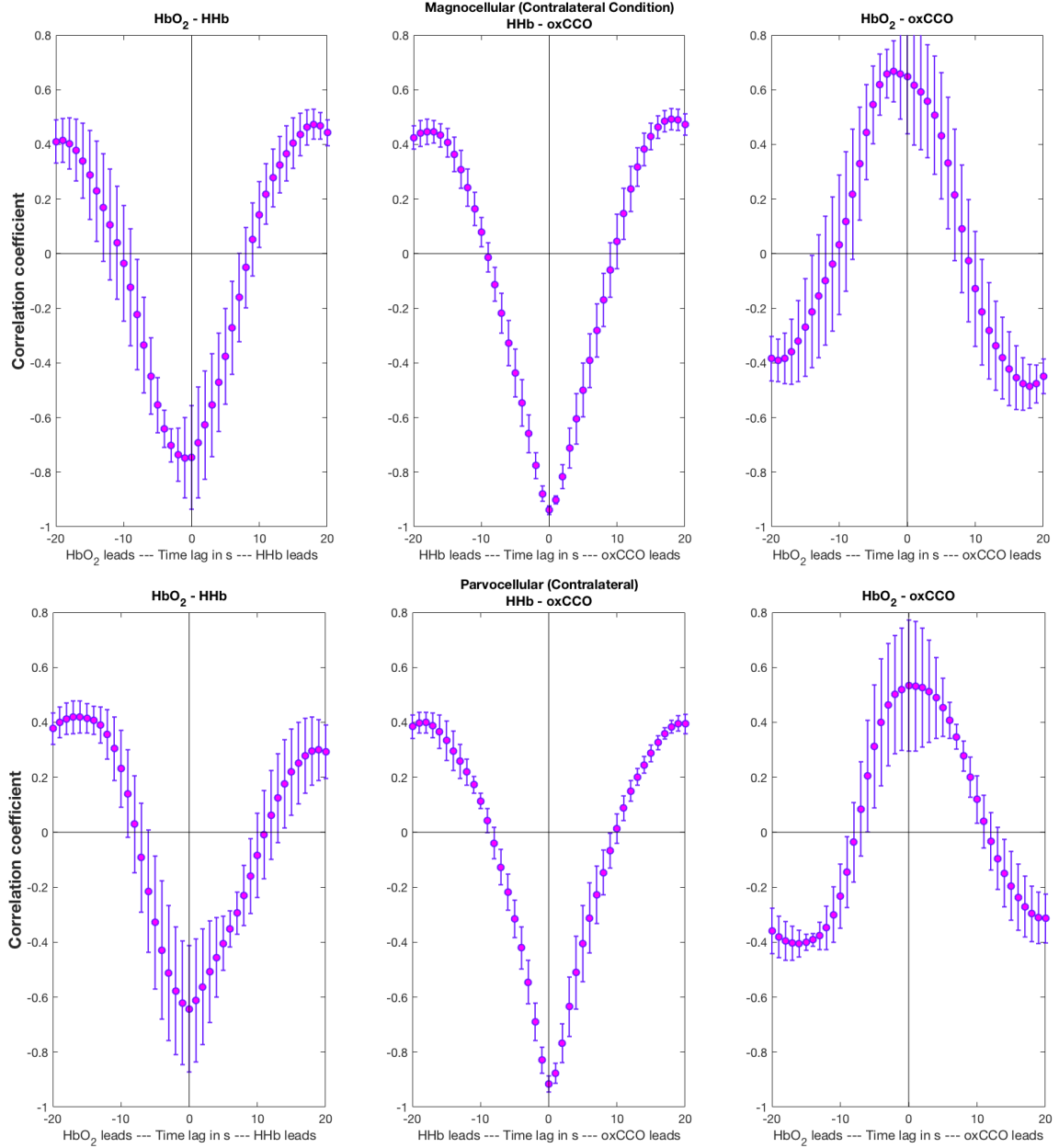
Figure 5.18: Average of the cross-correlation across all occipital channels for the contralateral Magno condition (upper panel) and contralateral Parvo condition (bottom panel).

5.3.1.4 EEG (Event Related Design Task)

5.3.1.4.1 *Event Related Potentials*

5.3.1.4.1.1 Contralateral vs Ipsilateral

Magno

Figure 5.19 shows the ERPs for both contralateral (solid lines) and ipsilateral conditions (dashed lines) for Magno. Pairwise t-tests between the amplitude of the P100 of the contralateral and ipsilateral conditions for Magno indicated a significant difference between contralateral and ipsilateral at channels 1 ($t = 5.098$, $p = 0.001$), 2 ($t = -1.76097$, $p = 0.005$) and 5 ($t = 4.88552$, $p = 0.002$). The table with the statistics from all channels can be found in the appendix.
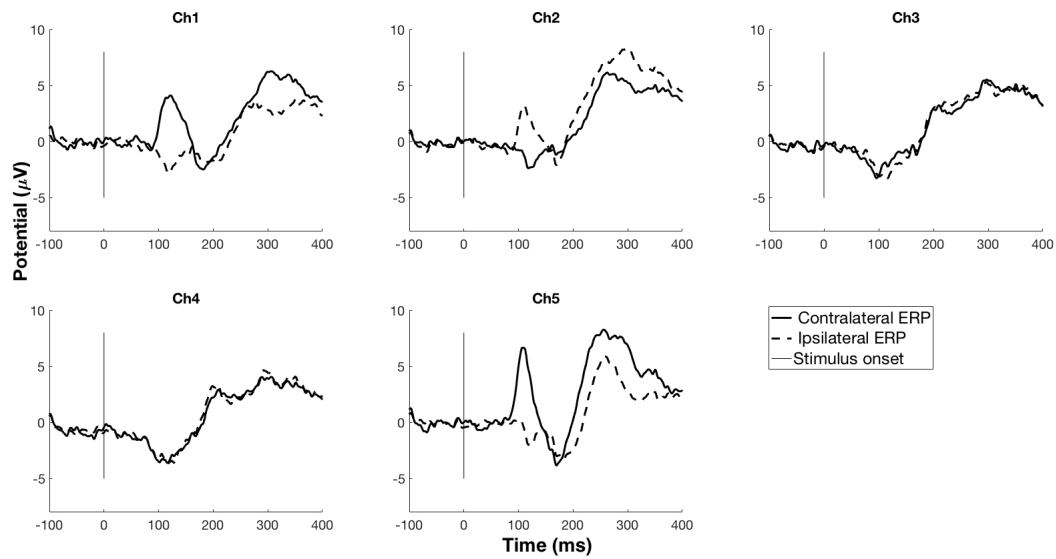
Figure 5.19: Contralateral (solid lines) and Ipsilateral (dashed) event related potentials for Magno condition for channels over the occipital cortex

Parvo

Figure 5.20 shows the ERPs for both contralateral (solid lines) and ipsilateral conditions (dashed lines) for Parvo. Pairwise t-tests between the maximum amplitude of the P100 of the contralateral and ipsilateral conditions for Parvo indicated a significant difference between contralateral and ipsilateral at channels 1 ($t = 5.325$, $p = 0.001$), 2 ($t = -3.911$, $p = 0.004$) and 5 ($t = 3.016$, $p = 0.017$). The table with the statistics from all channels can be found in the appendix.
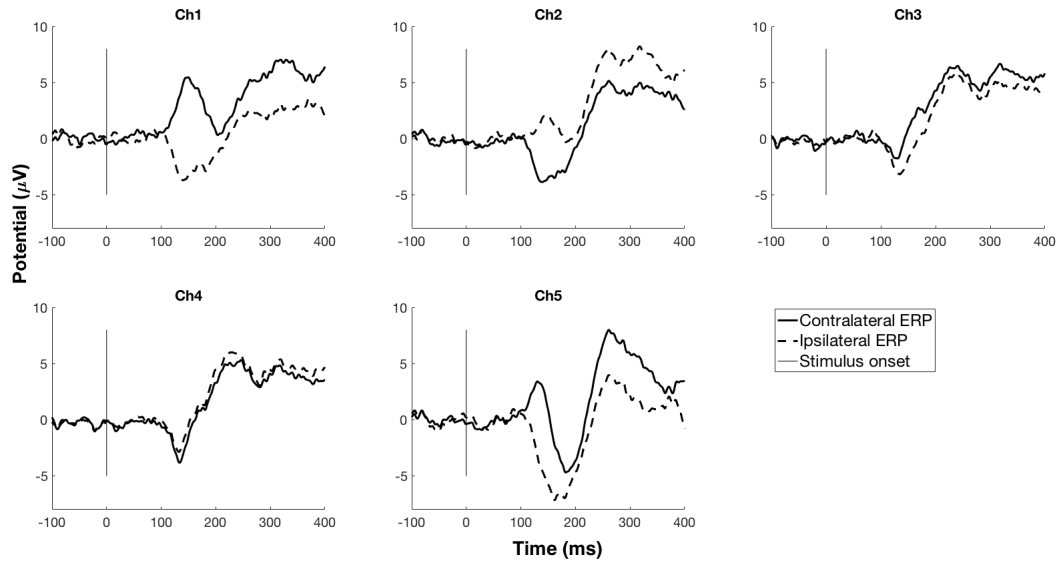
Figure 5.20: Contralateral (solid lines) and Ipsilateral (dashed lines) event related potentials for Parvo condition for channels over the occipital cortex

5.3.1.4.1.2 Magno vs Parvo Pairwise t-tests between the maximum amplitude of the P100 for Magno vs Parvo did not show any significant difference in any of the channels for either contralateral or ipsilateral condition. Figure 5.21 shows the contralateral (solid) and ipsilateral (dashed) Magno (black) and Parvo (red) ERPs plotted on the same figure, for each of the five channels over the occipital cortex. While no significant differences were found between Magno and Parvo, there appears to be a difference in the latency of the P100 amplitude for the contralateral Magno vs Parvo, with the Parvo P100 occurring later than the Magno P100 in channels 1 and 5.
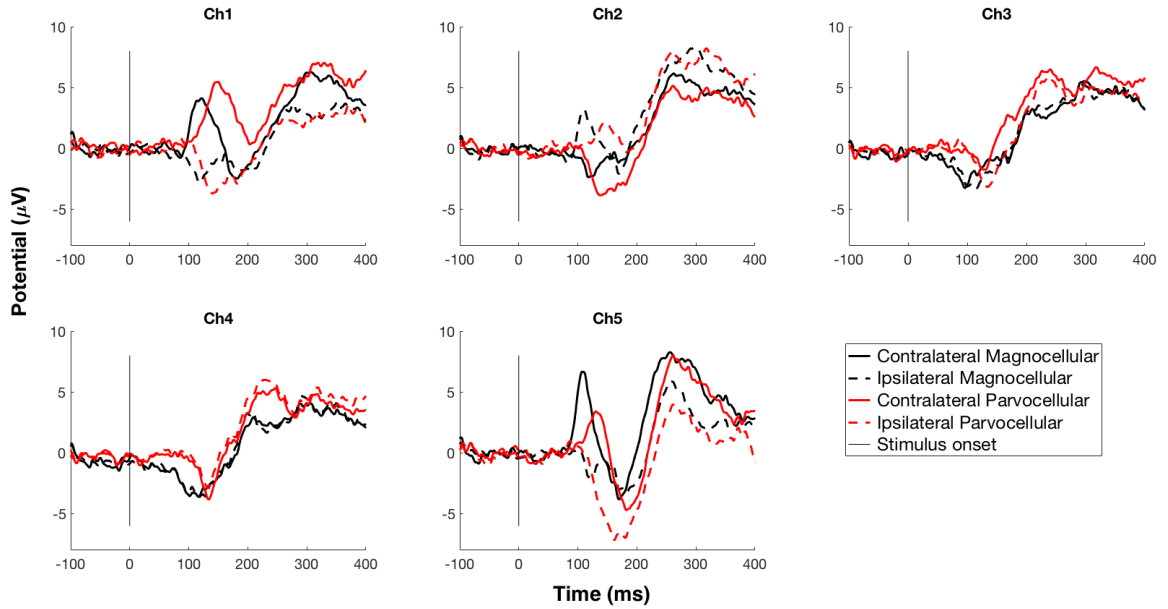
Figure 5.21: Contralateral (solid lines) and Ipsilateral (dashed lines) event related potentials for both Magno (black) and Parvo (red) conditions for channels over the occipital cortex

5.3.1.4.2 *Topographical Maps* Topographical maps of the power of different frequency bands at specified latencies were obtained. These were not for contralateral and ipsilateral conditions but for the original hemifield checkerboards as contralateral and ipsilateral conditions cannot be topographically represented. ML refers to Magno presented in the left hemifield, MR refers to Magno presented in the right hemifield, PL refers to Parvo presented in the left hemifield and PR refers to Parvo presented in the right hemifield. The topographical maps are shown in Figures 5.22 - 5.24. The frequency bands specified here were alpha (8-12 Hz), beta (15-22 Hz) and low gamma (30-40 Hz) and are shown at latencies of 100 ms and 135 ms.

An increase in occipital oscillatory activity is seen in the alpha and beta frequency bands in the contralateral hemisphere at 100 ms for both ML and MR and at 135 ms for PL and PR and for the gamma band at 100 ms for both ML and MR and 122 ms for PL and PR.

Alpha
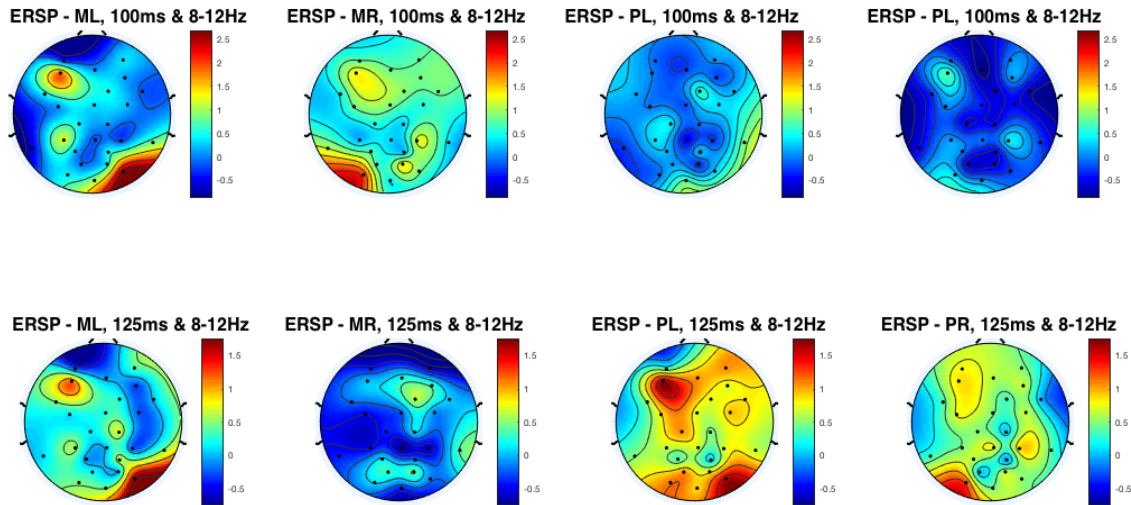
Figure 5.22: Topographical maps at latency of (upper panel) 100 ms and (bottom panel) 135 ms for the alpha band.

Beta
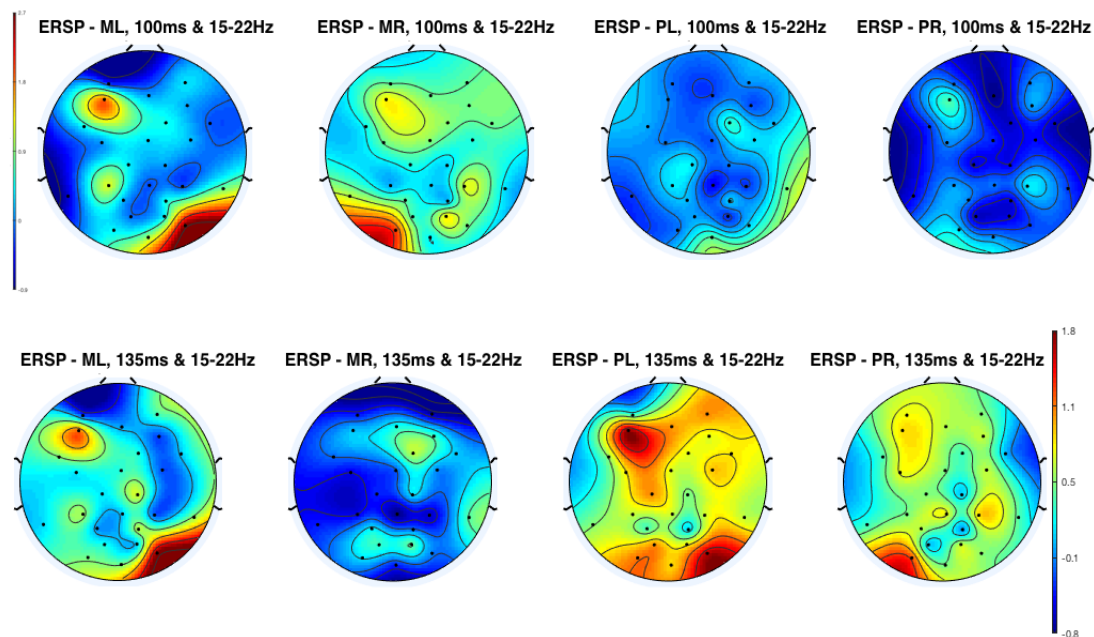
Figure 5.23: Topographical maps at latency of (upper panel) 100 ms and (bottom panel) 135 ms for the beta band.

Gamma
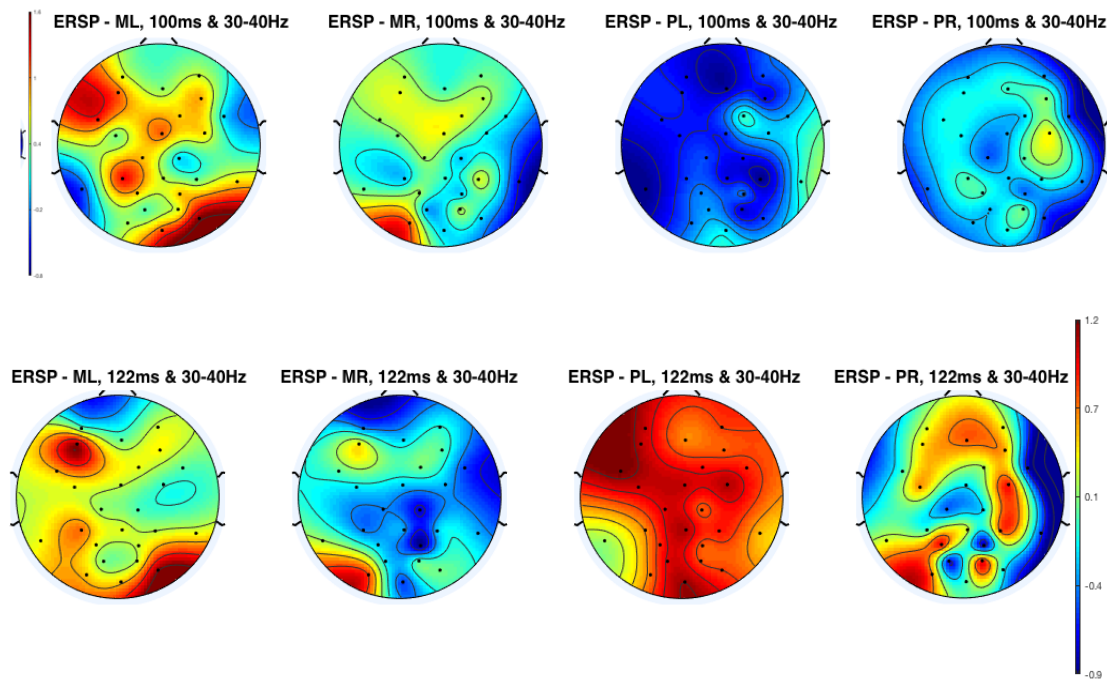
Figure 5.24: Topographical maps at latency of (upper panel) 100 ms and (bottom panel) 122 ms for the gamma band.

5.3.1.4.3 *Time-Frequency* Wavelet-based decomposition, which has been described in detail in Section 2.3.2.2 of Chapter 2, was used to obtain the evoked oscillations for the contralateral condition for both Magno and Parvo conditions. The results of the time-frequency decomposition are shown in Figures 5.25 for Magno condition in the upper panel and the Parvo condition in the bottom panel. An increase in stimulus-evoked alpha band activity can be seen in all channels, particularly in channels 1 and 5. Channels 1 and 5 additionally show an increase in beta band activity which appears to be stronger for the Magno condition in comparison to the Parvo.
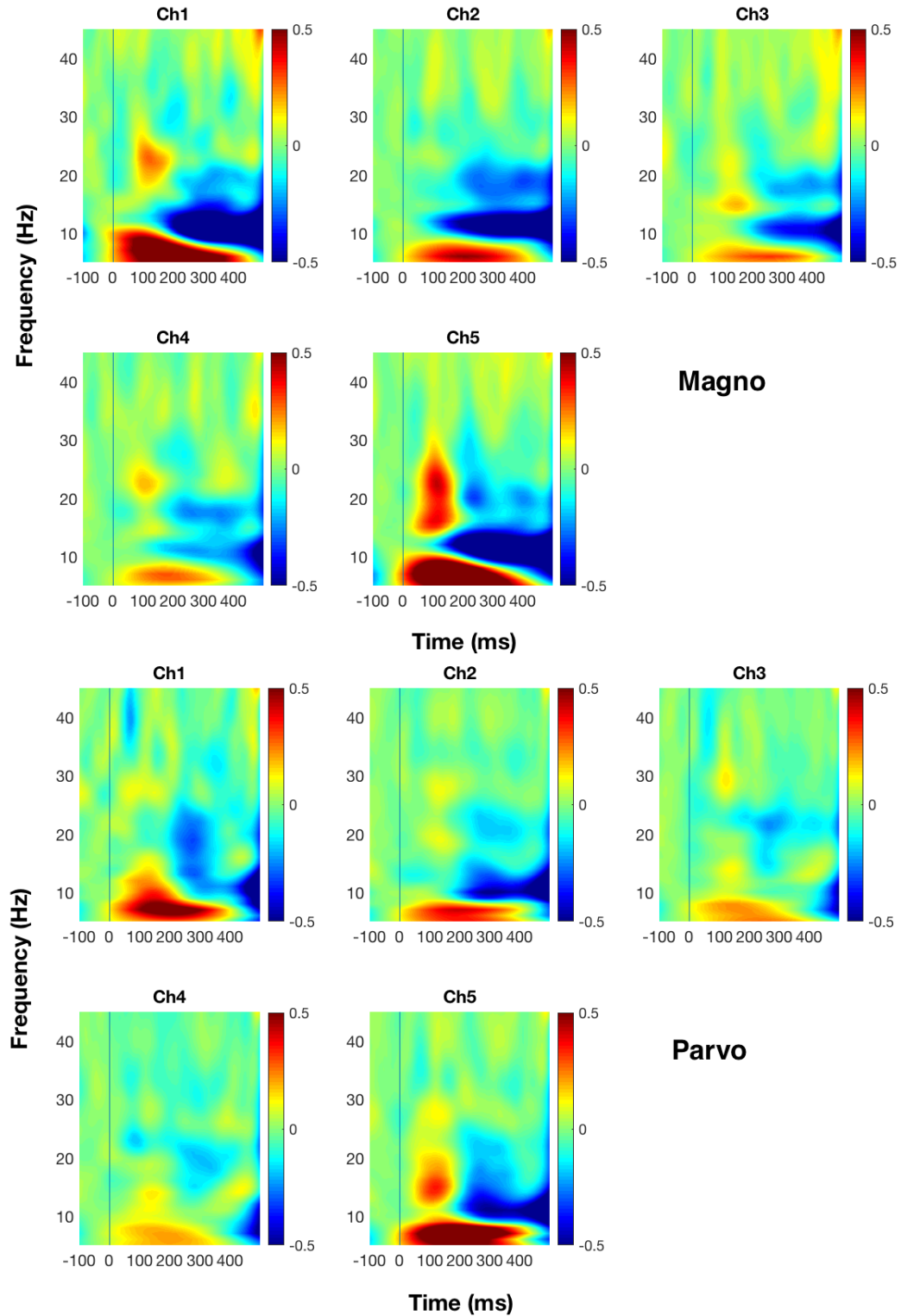
Figure 5.25: Time-frequency plot of each of the five channels over the occipital cortex for contralateral condition for both (upper panel) Magno and (bottom panel) Parvo conditions.

5.3.1.5   EEG (Block Design Task)

5.3.1.5.1   *Event Related Potentials*

5.3.1.5.1.1   Contralateral vs Ipsilateral

Magno

Figure 5.26 shows the event related potentials (ERPs) for both contralateral and ipsilateral conditions for Magno. Pairwise t-tests between the maximum amplitude of the P100 of the contralateral and ipsilateral conditions for Magno indicated a significant difference between contralateral and ipsilateral at channels 1 ($t = 5.098$, $p = 0.001$), 2 ($t = -1.76097$, $p = 0.005$) and 5 ($t = 4.88552$, $p = 0.002$). The table with the statistics from all channels can be found in the appendix. Similarly to the event-related design task, the contralateral ERP is stronger in Channel 5 in comparison to the ipsilateral. Channel 1 was excluded from the analysis for both conditions due to poor signal quality in majority of participants.
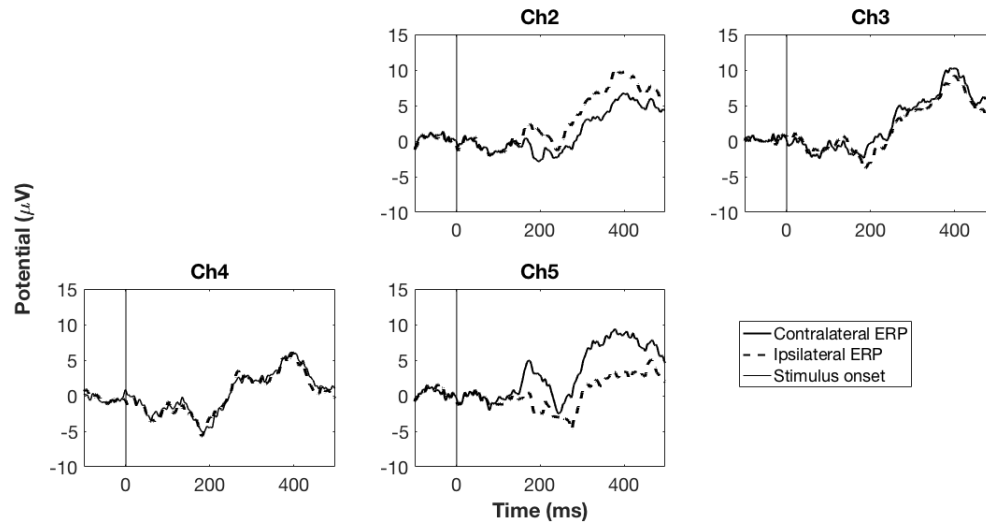
Figure 5.26: Contralateral (solid lines) and Ipsilateral (dashed lines) event related potentials for Magno condition for channels over the occipital cortex

Parvo

Figure 5.27 shows the event related potentials (ERPs) for both contralateral and ipsilateral conditions for Parvo. Pairwise t-tests between the maximum amplitude of the P100 of the contralateral and ipsilateral conditions for Parvo indicated a significant difference between contralateral and ipsilateral at channels 1 ($t = 5.325$, $p = 0.001$), 2 ($t = -3.911$, $p = 0.004$) and 5 ($t = 3.016$, $p = 0.017$). The table with the statistics from all channels can be found in the appendix. Similarly to the event-related design task, the contralateral ERP is stronger in Channel 5 in comparison to the ipsilateral.
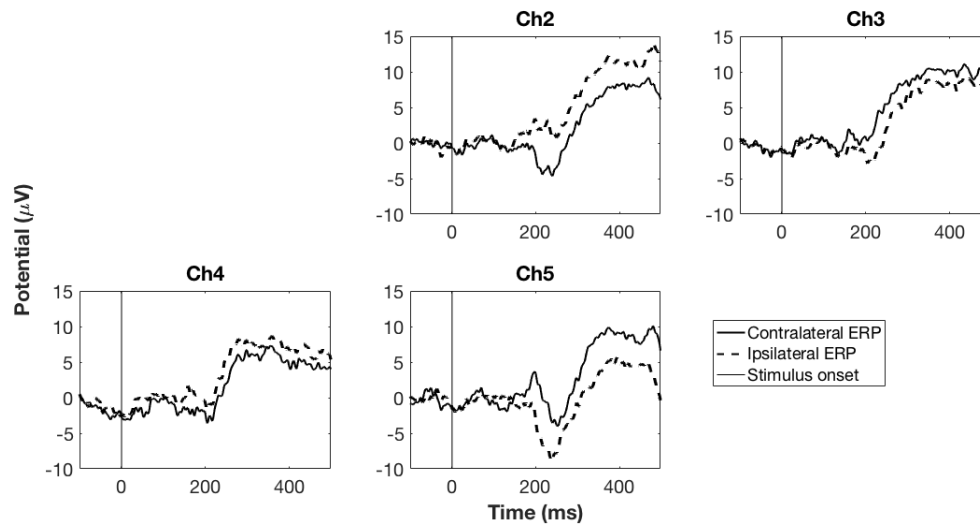
Figure 5.27: Contralateral and Ipsilateral event related potentials for Parvo condition for channels over the occipital cortex

Magno vs Parvo

Pairwise t-tests between the maximum amplitude of the P100 for Magno vs Parvo did not show any significant difference in any of the channels for either contralateral or ipsilateral condition. Figure 5.28 shows the contralateral and ipsilateral Magno and Parvo ERPs plotted on the same figure, for each of the five channels over the occipital cortex. No significant differences were found between Magno and Parvo.
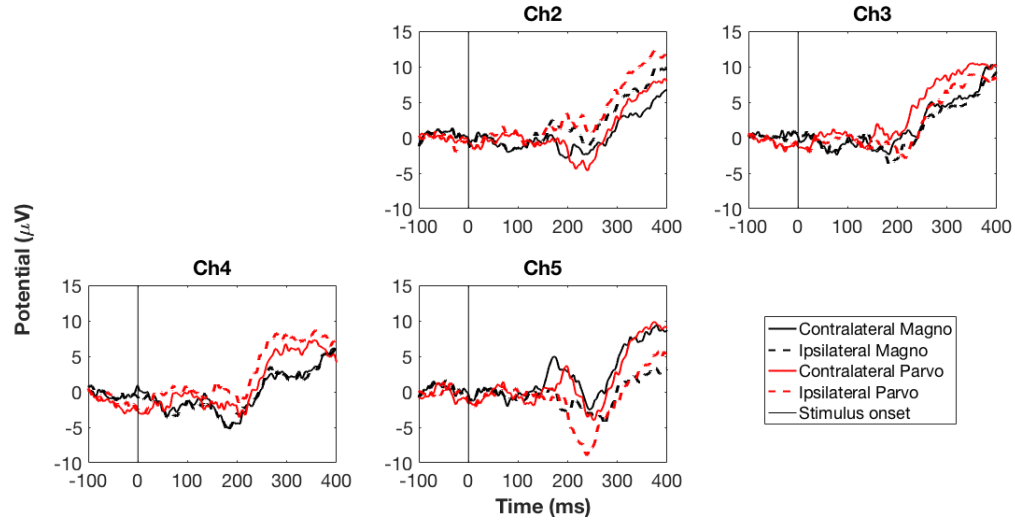
Figure 5.28: Contralateral (solid lines) and Ipsilateral (dashed lines) event related potentials for both Magno (black) and Parvo (red) conditions for channels over the occipital cortex

5.3.1.5.2 *Time-Frequency* Similar to the event-related task design, wavelet decomposition was used to obtain the evoked oscillations for the contralateral condition for both Magno and Parvo conditions. The results of the time-frequency decomposition are shown in Figures 5.29 for Magno (upper panel) and Parvo (bottom panel). Similarly to the event-related design task, an increase in stimulus-evoked alpha band activity was seen in all the channels. Additionally, an increase in beta band activity was seen in Channel 5 which was stronger for the Magno condition, similarly to the event-related design task. While the results show comparable results with event-related design task, the data is much noisier in comparison due to small number of trials.
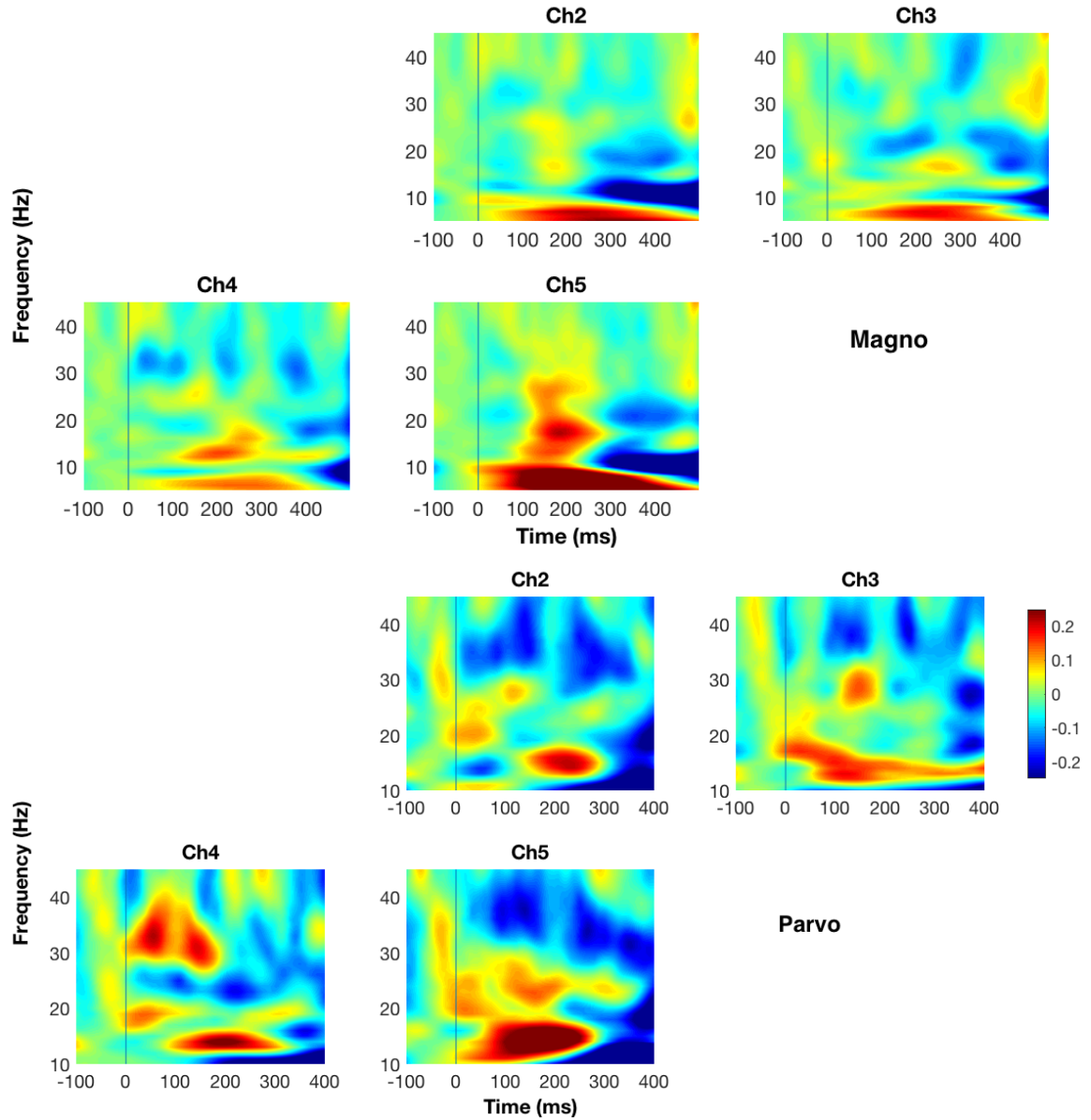
Figure 5.29: Time-frequency plot of each of the five channels over the occipital cortex for (upper panel) contralateral condition for Magno (bottom panel) contralateral condition for Parvo.

5.3.1.6 Combined NIRS-EEG

Figure 5.30 shows the contralateral and ipsilateral channels for both EEG (left) and NIRS (right) indicated by blue and magenta lines respectively, in order to remind the reader of the topographical location of the channels. The channels of interest, lying above the

primary visual cortex, are indicated in yellow.
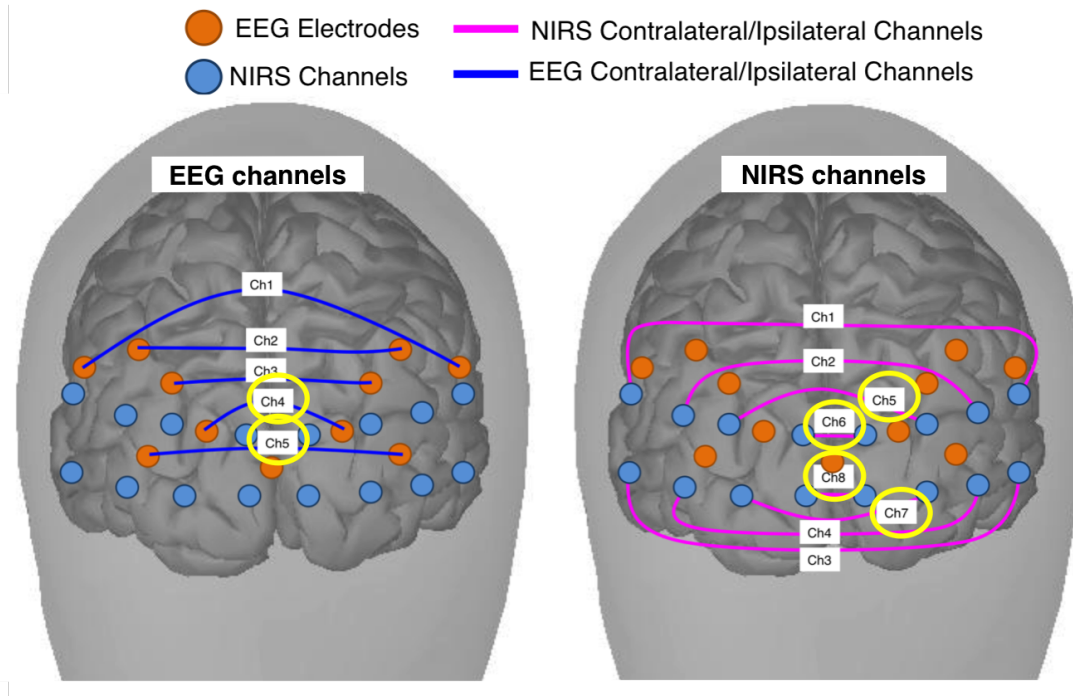
Figure 5.30: Contralateral and Ipsilateral channels for both (left) EEG indicated in blue and (right) NIRS indicated in magenta. The channels of interest are indicated in yellow.

For all conditions, the correlations between NIRS and EEG channels are shown in the form of a heatmap with the colourbar indicating the strength of the correlation, with positive correlations being yellow or green and negative correlations being blue. Channels 4 and 5 of the EEG and Channels 5, 6, 7 and 8 (indicated in yellow in 5.30) correspond to areas over the primary visual cortex and the correlations between them are focused on. These are are indicated by means of red boxes in the figures in the following sections.

5.3.1.6.1 Correlation of P100 with NIRS maximum concentration change

5.3.1.6.1.1 *Contralateral vs Ipsilateral* Figure 5.31 shows a heatmap of the correlations between the maximum P100 amplitude and maximum concentration change of HbO_2 and oxCCO, for the five occipital EEG channels and eight NIRS channels, for the contralateral vs ipsilateral comparison for both Magno (left) and Parvo (right) conditions. None of

the correlations were significant due to a small sample size (n=5).
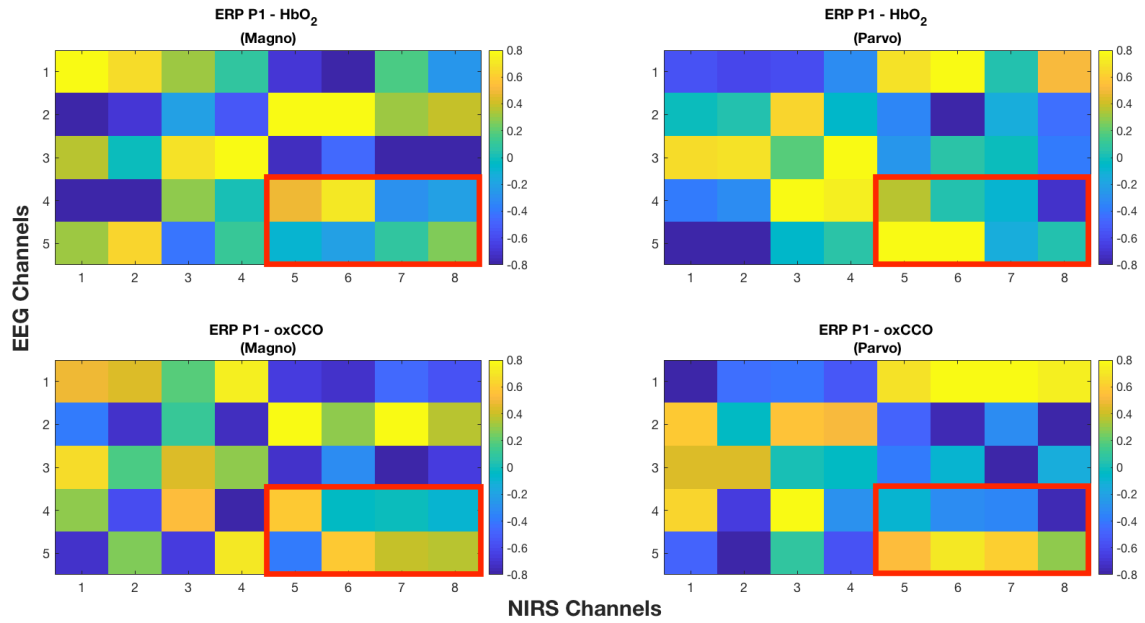
Figure 5.31: Heatmap of the correlations between P100 amplitude and NIRS chromophores HbO$_2$ and oxCCO for the contralateral versus ipsilateral comparison, for both Magno (left) and Parvo (right) conditions. The colourbar indicates the strength of the correlation with yellow indicating positive correlations and blue negative correlations.

Magno vs Parvo

Figure 5.32 shows a heatmap of the correlations between the maximum P100 amplitude and maximum concentration change of HbO$_2$ and oxCCO, for the five occipital EEG channels and eight NIRS channels, for the Magno versus Parvo comparison for both contralateral (left) and ipsilateral (right) conditions. None of the correlations were significant due to a small sample size (n=5). The colourbar represents the strength of the correlation with positive correlations being yellow or green and negative correlations being blue.
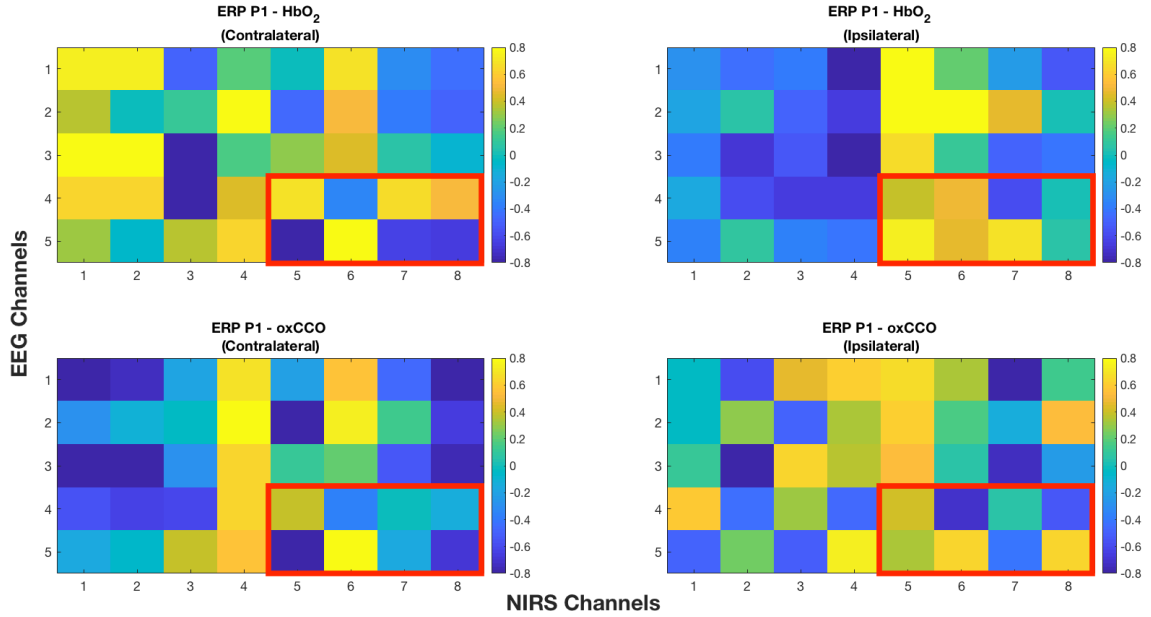
Figure 5.32: Heatmap of the correlations between P100 amplitude and NIRS chromophores HbO$_2$ and oxCCO for the Magno versus Parvo comparison, for both contralateral (left) and ipsilateral (right) conditions. The colourbar indicates the strength of the correlation with yellow indicating positive correlations and blue negative correlations.

5.3.1.6.2 Correlation of PSD with NIRS maximum concentration change

5.3.1.6.2.1 *Contralateral vs Ipsilateral*

1. Magno

Figure 5.33 shows heatmaps of the correlations between the PSD of each of the frequency bands and the maximum concentration change in HbO$_2$and oxCCO for each of the NIRS and EEG channels, for the contralateral versus ipsilateral comparison, for the Magno condition.
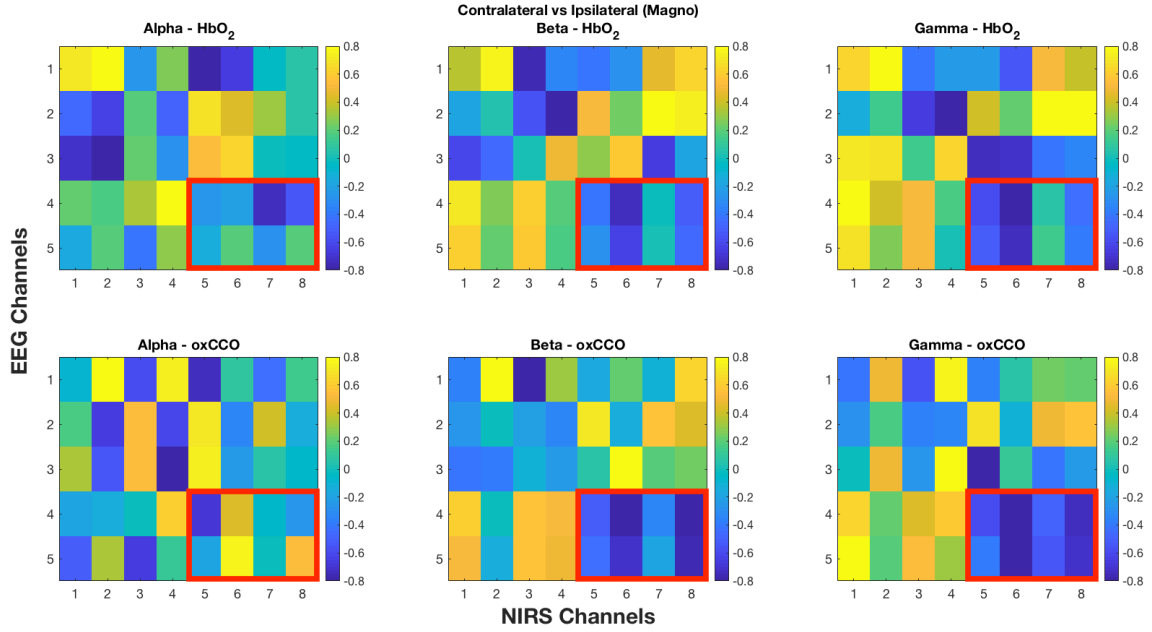
Figure 5.33: Heatmap of the correlations between the PSD of alpha, beta and gamma frequency bands and NIRS chromophores HbO_2 and oxCCO for the contralateral versus ipsilateral comparison, for the Magno condition. The colourbar indicates the strength of the correlation with yellow indicating positive correlations and blue negative correlations.

2. Parvo

Figure 5.34 shows heatmaps of the correlations between the PSD of each of the frequency bands and the maximum concentration change in HbO_2 and oxCCO for each of the NIRS and EEG channels, for the contralateral versus ipsilateral comparison, for the Parvo condition.
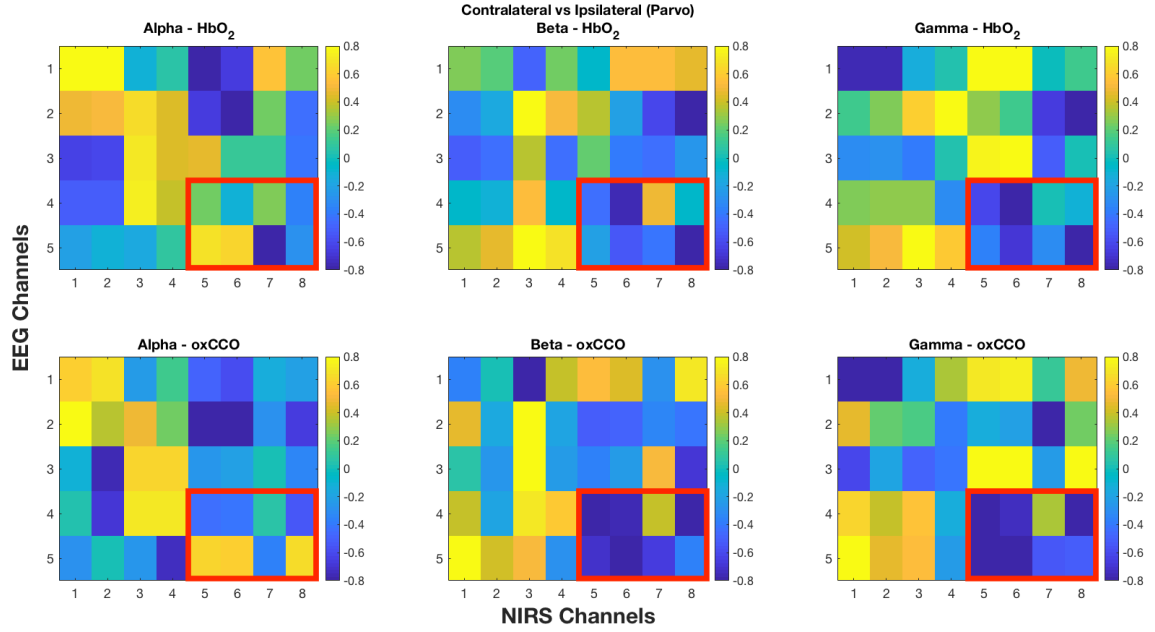
Figure 5.34: Heatmap of the correlations between the PSD of alpha, beta and gamma frequency bands and NIRS chromophores HbO_2 and oxCCO for the contralateral versus ipsilateral comparison, for the Parvo condition. The colourbar indicates the strength of the correlation with yellow indicating positive correlations and blue negative correlations.

Magno vs Parvo

1. Contralateral

Figure 5.35 shows heatmaps of the correlations between the PSD of each of the frequency bands and the maximum concentration change in HbO_2 and oxCCO for each of the NIRS and EEG channels, for the Magno versus Parvo comparison, for the contralateral condition.
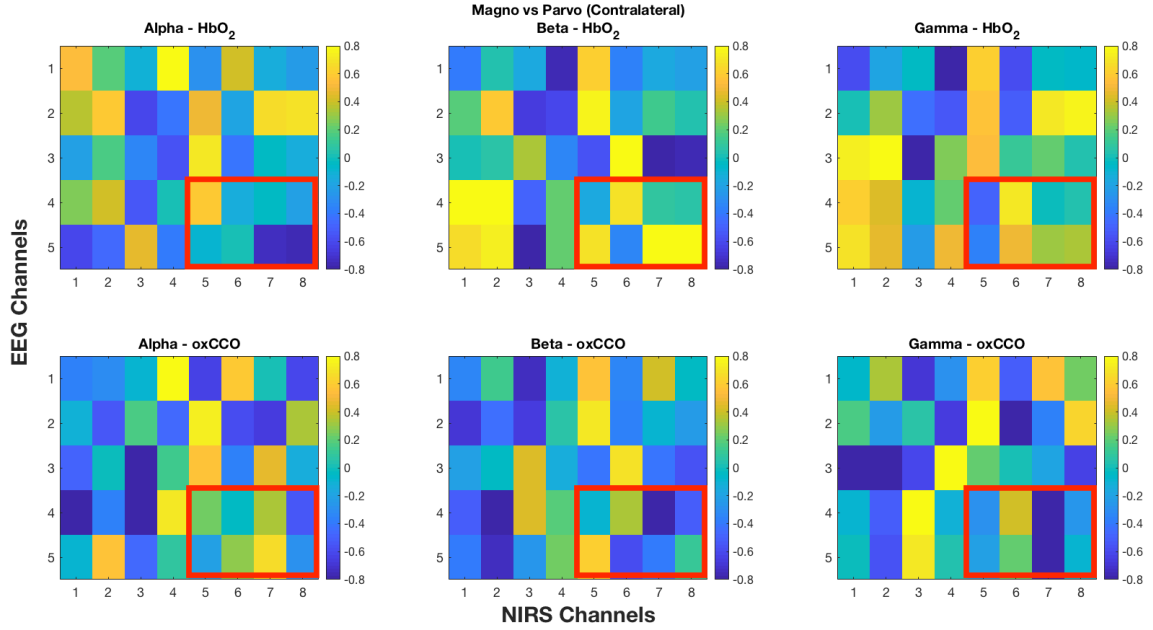
Figure 5.35: Heatmap of the correlations between the PSD of alpha, beta and gamma frequency bands and NIRS chromophores HbO_2 and oxCCO for the Magno versus Parvo comparison, for the contralateral condition. The colourbar indicates the strength of the correlation with yellow indicating positive correlations and blue negative correlations.

1. Ipsilateral

Figure 5.36 shows heatmaps of the correlations between the PSD of each of the frequency bands and the maximum concentration change in HbO_2 and oxCCO for each of the NIRS and EEG channels, for the Magno versus Parvo comparison, for the ipsilateral condition.
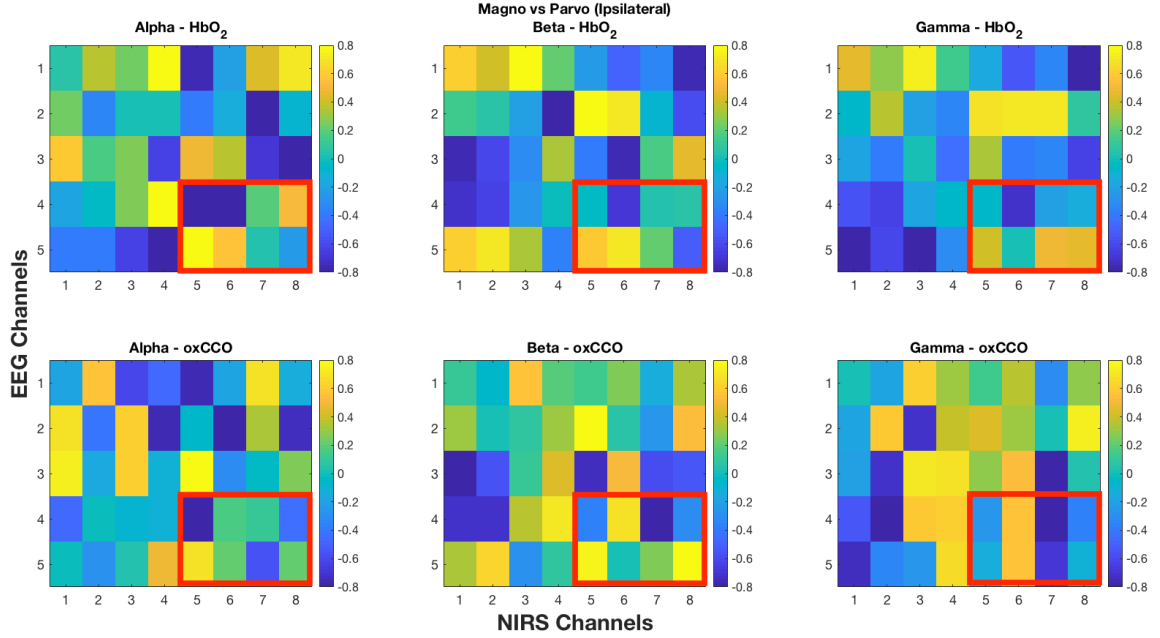
Figure 5.36: Heatmap of the correlations between the PSD of alpha, beta and gamma frequency bands and NIRS chromophores HbO_2 and oxCCO for the Magno versus Parvo comparison, for the ipsilateral condition. The colourbar indicates the strength of the correlation with yellow indicating positive correlations and blue negative correlations.

5.4 Discussion

In this chapter, I used multi-channel broadband NIRS to simultaneously measure changes in the concentrations of oxygenated and deoxygenated haemoglobin alongside changes in cellular oxygen metabolism with EEG, in adults during visual stimulation. Two of the main methodological challenges of this study included developing combined NIRS and EEG headgear and designing an appropriate experimental paradigm for both techniques, the former of these was discussed in Chapter 2 of this thesis. These methodological developments were particularly important as the purpose of the adult work was to optimise concurrent NIRS and EEG data collection which could be extended to infants.

The NIRS changes in concentration of $\Delta[HbO_2]$, $\Delta[HHb]$ and $\Delta[oxCCO]$ indicate a significant difference between contralateral and ipsilateral for both Magno and Parvo conditions for all three chromophores, in the channels located closest to the primary visual cortex. For the Magno condition, all of the same channels showed a significant difference between contralateral and ipsilateral for each of the chromophores while for the Parvocel-

lular condition, oxCCO showed a significant difference in all channels except one. This may perhaps be a reflection of the greater concentration of CCO in the parvocellular pathway. Furthermore, a significant difference was also observed between contralateral Magno and Parvo conditions for all three chromophores. Interestingly, oxCCO was the only chromophore where a significant difference between contralateral Magno and Parvo could be seen in a channel over the primary visual cortex. This may potentially provide evidence of the higher spatial sensitivity of oxCCO in comparison to the haemoglobins, as previous studies have reported (Phan et al., 2016a). Although it must be noted that the response was greater for the Magno condition and not the Parvo, despite the high concentration of CCO in the parvocellular pathway. This could perhaps be due to the fact that cells in the magnocellular pathway are known to be larger and size and may therefore have a greater number of mitochondria present inside the cells.

The ERP analysis from the event-related task demonstrated a strong contralateral P100 in response to both Magno and Parvo conditions, over the primary visual cortex which appeared to be stronger for the Magno condition, although no statistically significant differences could be found between the two conditions. This was perhaps due to the small number of subjects and trials included in the analysis. Through visual inspection of the ERPs and the topographical maps however, it is evident that the response for the Parvo condition has a longer latency, around 130 ms, in comparison to the Magno condition which has latency around 100 ms. The differences in the magnitude and latency of both the NIRS responses and the ERPs may be the reflection of the histological differences between magnocellular and parvocellular pathways and such differences have been reported in previous studies (Schmolesky et al., 1998; Mohamed et al., 2006; Liu et al., 2006). Similar differences are also observed in the EEG time-frequency decomposition where, in the channel located over the primary visual cortex, has an increase in stimulus-evoked alpha, beta and low gamma band activity which is stronger for the Magno condition in comparison to the Parvo. In Parvo condition, the stimulus-evoked activity is contained to the alpha frequency band (8 - 12 Hz) and low beta (13 - 20 Hz) which is in accordance with previous work (Fründ et al., 2007; Sewards and Sewards, 1999) which has demonstrated that stimuli with high spatial frequency (Parvo condition) elicit stronger alpha activity while

stimuli with low spatial frequency (Magno condition) produce stronger gamma activity. Although, the gamma activity is not strongly visible and a higher number of trial and participants might be required in order to observe this effect. This result is further highlighted in the combined NIRS and EEG analysis that was performed to correlate the PSD of alpha, beta and gamma frequency bands with the maximum change in concentration of HbO_2 and oxCCO. That is, in comparing the contralateral Magno and Parvo conditions, in the channels located closest to the primary visual cortex, a positive relationship was observed between HbO_2 and beta and gamma band oscillations for the Magno condition and an inverse relationship between HbO_2 and alpha band activity. The correlations between oxCCO and the frequency bands (gamma band in particular) were not as strong. For the ipsilateral comparison between Magno and Parvo however, stronger correlations were observed between oxCCO and beta and gamma frequency bands. This may be provide evidence in line with previous research that has demonstrated that extrastriate visual regions contain representations of the entire visual field (Tootell et al., 1998).

Moreover, in the combined NIRS and EEG analysis comparing contralateral and ipsilateral for both Magno and Parvo conditions showed stronger correlations between NIRS and EEG channels over the primary visual cortex with a positive relationship between alpha band activity and oxCCO and an inverse relationship with beta and gamma band oscillations. This was an interesting pattern and previous studies have provided evidence of differing neural mechanisms giving rise to low and high frequency oscillations and therefore relating to blood oxygenation levels differently (Scheeringa et al., 2011a, 2016).

The results from this study provide indication of differences in the magnocellular and parvocellular pathways observed in both NIRS responses and neural activity measured by EEG and the combined data analysis provides potential emerging evidence of the link between neuronal activation, energy metabolism and haemodynamics. More importantly however, the feasibility of concurrent broadband NIRS and EEG data collection was demonstrated through the work presented in this chapter which is a milestone in itself. The combined headgear was developed successfully allowing both NIRS optodes and EEG electrodes to be positioned on the head and could be translated for use with infants. There were however, a number of limitations to this study. Firstly, a small number of subjects

were included which can severely impact results. Additionally, for EEG from both event-related and block design tasks, the number of trials was quite small. The average number of trials included in the event-related task was thirty which seems to be lower than what is common for adult EEG studies (Luck, 2005; Cohen, 2014). This could be easily rectified for future studies by decreasing the baseline line period of 8 s which is longer than what is used for most studies and having a shorter baseline period would allow a higher number of presentations of the stimulus, thereby yielding more trials. The small number of trials in the block design task (due to a long stimulus presentation duration of 18 s) meant that concurrently recorded NIRS and EEG data could not be analysed to obtain reliable and meaningful results, thereby limiting the inferences that could be made when correlating the NIRS and EEG data. Another limitation of this study was that no correction for multiple comparisons was applied. The work presented in the following chapter therefore, details the simultaneous NIRS and EEG study in infants and how the current work was improved upon by increasing the sample size and refining the experimental paradigm to have one design that would work for both techniques.

Chapter 6

INFANT NIRS STUDY OF CYTOCHROME WITH EEG - TEMPORAL CORTEX

6.1 Introduction

The work presented in the previous chapter detailed the developments that were necessary to use multi-channel broadband NIRS simultaneously with EEG in order explore the relationship between neural activity, energy metabolism and haemodynamics. While the study measured changes in the concentration of NIRS chromophores only over the occipital cortex in response to visual stimuli, the results indicated that in adults, stimuli that produced differential responses in haemodynamic and metabolic activity do relate differently to associated neural activity. Moreover, HbO_2 and oxCCO related to neural activity differently as well. Yet there were many limitations to the study, most notably the small sample size and the small number of trials. Additionally, only two types of stimuli were presented and the relationship between EEG and NIRS may need to be explored in the context of many different types of stimuli in order to the establish the relationship between the signals. Moreover, the purpose of performing the adult study was to first develop a protocol for simultaneous NIRS and EEG measurements as well as a data analysis pipeline.

From the discussion in the introduction chapter, it is also clear that neurometabolic pathways in the infant brain are under ongoing maturation in comparison to the adult brain. It was therefore important to perform this work first in adults where the neurovascular coupling pathway is fully developed and it would hence be easier to discern the relationships between neural activity and haemodynamic changes in a context where the data had less variability and was better understood than infant data. Having successfully established a protocol and an analysis pipeline, this chapter focuses on the description of the simultaneous NIRS and EEG study in infants. The adult study allowed me to improve a number of aspects of the combined NIRS-EEG protocol. These included an increased sample size, reduction in the length of stimulus durations thereby yielding higher number of individual trials and most importantly the addition of new stimuli to enable the relationship of interest to be investigated in different contexts.

As discussed previously in Chapter 4, one of the limitations of using a single channel broadband NIRS system was that it provided little spatial information and the purpose of moving to a multi-channel broadband NIRS system was to measure spatially resolved changes in Δ[oxCCO] and to observe whether the oxCCO signal was more spatially specific than haemodynamic responses in HbO_2 and HHb. The results from the study presented in Chapter 4 demonstrated that the use of a social experimental stimulus over the STS - TPJ region in the temporal cortex produced not only measurable changes in the concentration of HbO_2 and HHb, but also in oxCCO. Therefore, in the infant NIRS-EEG study, a social/non-social experimental paradigm was developed in order to investigate the spatial specificity of cytochrome and its relation to haemodynamic changes and neural activity.

As mentioned earlier, it was important to use different types of stimuli in order to interrogate the relationship of interest in different contexts, especially to establish any regional differences in the association between NIRS and EEG measures. Hence, visual stimuli similar to those in Chapter 5 were also designed to measure responses over the occipital cortex. All infants were therefore presented with the same combination of social and visual stimuli. This chapter details the use of multi-channel broadband NIRS system introduced in Chapter 4 simultaneously with EEG to measure changes in Δ[HbO_2], Δ[HHb], Δ[oxCCO] as well as neuronal activity of the brain in response to social stimuli, in infants while the

visual stimuli are discussed in Chapter 7.

6.2 Methods

6.2.1 Participants

Forty-two 4-to-7-month-old healthy infants participated in the study (22 males and 20 females, mean age: 179 ± 16 days). All parents volunteered to participate in the study and provided written, informed consent. The study protocol was approved by the Birkbeck Psychology Ethics Committee and all procedures were performed in accordance with the regulations of the Ethics Committee. Infants from varying ethnic backgrounds participated in the study and neither hair color nor skin colour was used as an exclusion criteria to screen participants. All infants who participated were healthy with no known developmental disorders and were born at term between 37 - 40 weeks gestation.

6.2.2 Data acquisition

6.2.2.1 Multi-channel broadband system

The multi-channel broadband NIRS system described in the previous chapter was used to acquire the infant NIRS data presented in this chapter. The hardware of the system was the same as described previously consisting of two light sources and two spectrographs connected to CCD cameras, with a change only in the optical fibres being used. The new optical fibres that were used for the infant studies are described in the following section.

6.2.2.1.1 *Optical fibres* Similar to the adult set-up, there were two sets of light sources each of which further split into two pairs at the subject end, forming bifurcated fibres. The fibres were made of glass and were custom-built by Loptek (Glasfasertechnik GmbH, Germany). The detector fibre bundle had detectors each with a diameter of 30μm. The diameter of the light source bundle at the system end was 10mm while the diameter of the individual source fibres at the subject-end was 5mm. The system-end of the light source fibres are shown in Figure 6.1(a) and (b). While the adult set-up of the system had six

detector fibres at the subject end, the infant modification allowed for seven detector fibres, each with a diameter of 1mm forming a detector fibre bundle at the spectrograph-end. The system-end of the fibres are shown in Figure 6.1(c) and (d).
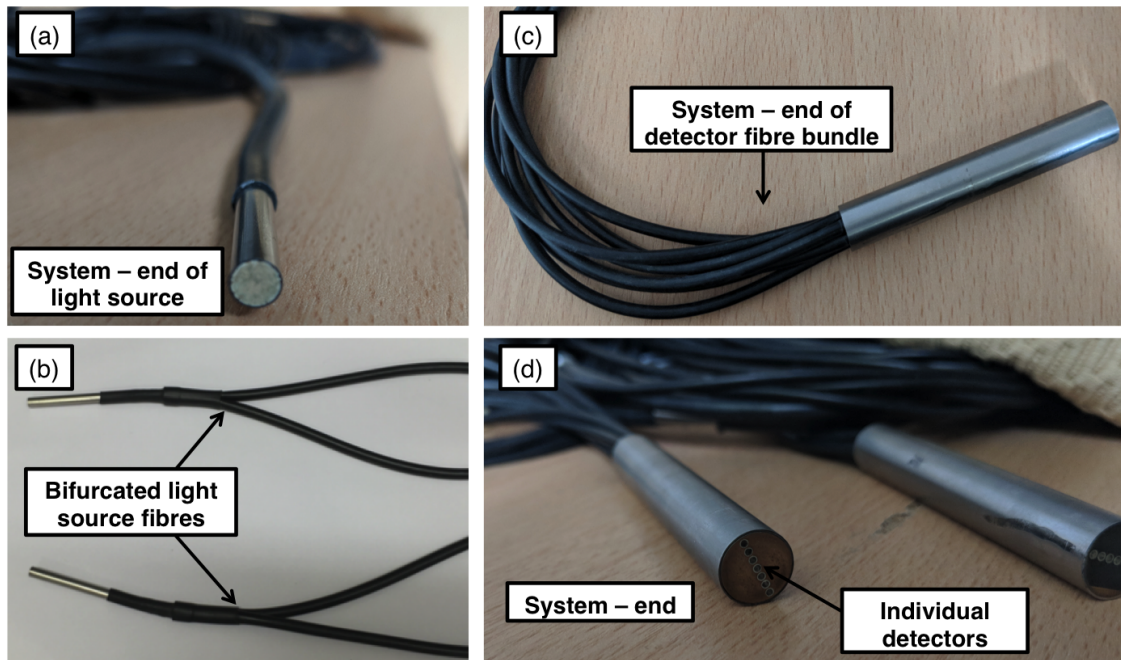
Figure 6.1: System end of the source and detector fibres with (a) the system-end of the bifurcated light source fibres (b) bifurcated light source fibres (c) the system-end of the detector fibres and (d) spectrograph end of the detector fibres with the individual detectors indicated

The subject end of the optical fibres are shown in Figure 6.2 with the top and side views of the detector fibres being shown in Figure 6.2(a) and (c) while the source fibres are shown in Figure 6.2(b) and (d).
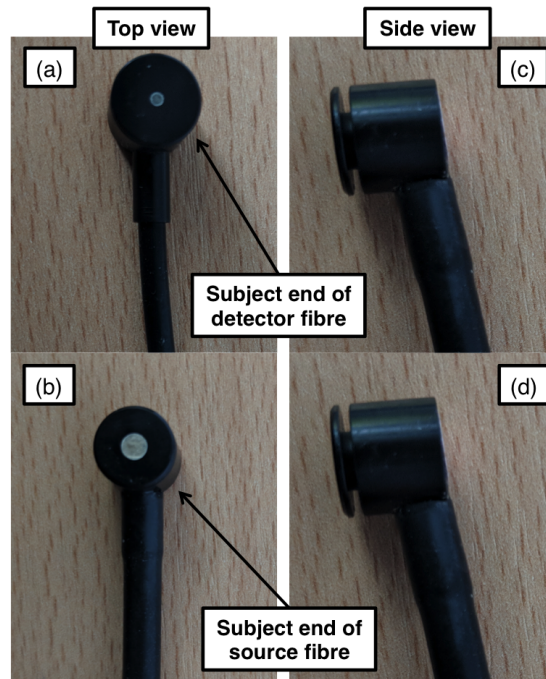
Figure 6.2: Subject end of the source and detector fibres with (a) the top view of the detector fibres (b) side view of the detector fibres (c) top view of the source fibres and (d) side view of the source fibres

6.2.2.1.2 *Software Modification*   LabVIEW software was used again to control and operate the system. Due to the fact that the number of detectors was changed from six to seven, significant modifications were made to the software in order to incorporate and collect data from the extra detector. The details of these modifications can be found in Appendix B.

6.2.2.2 Enobio EEG

The Enobio EEG system used for this study has been described previously in Section 2.3.2 of Chapter 2. For this study, thirty-two EEG channels were used and these are indicated in purple circles in Figure 6.3 and were distributed equally over the participant's head (FP1, FP2, F7, F3, Fz, F4, F8, FC5, FC6, T7, C3, Cz, C2, C4, T8, TP7, CP5, CP6, P9, P7, P3, Pz, P4, P8, P10, PO7, PO3, PO4, O1, Oz, O2).
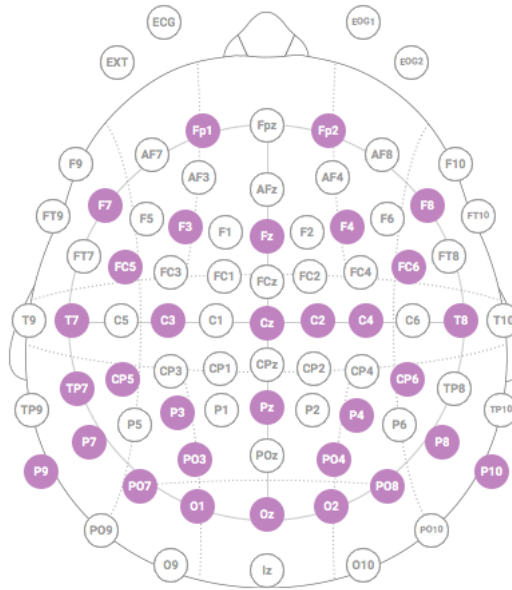
Figure 6.3: EEG Montage for infant study showing the locations of the 32 channels

6.2.2.3   NIRS array design

The procedures for designing the NIRS arrays and the combined NIRS and EEG headgear for this study have already been discussed in detail in Chapter 3. The schematic for the arrays is shown again here in Figure 6.4. The array for the occipital channels was centred around Oz while that for the temporal channels was centred around CP6. The source - detector separation for all channels here was 2.5 cm, except occipital channels 3 and 6 which had a longer source - detector separation of 2.90 cm.
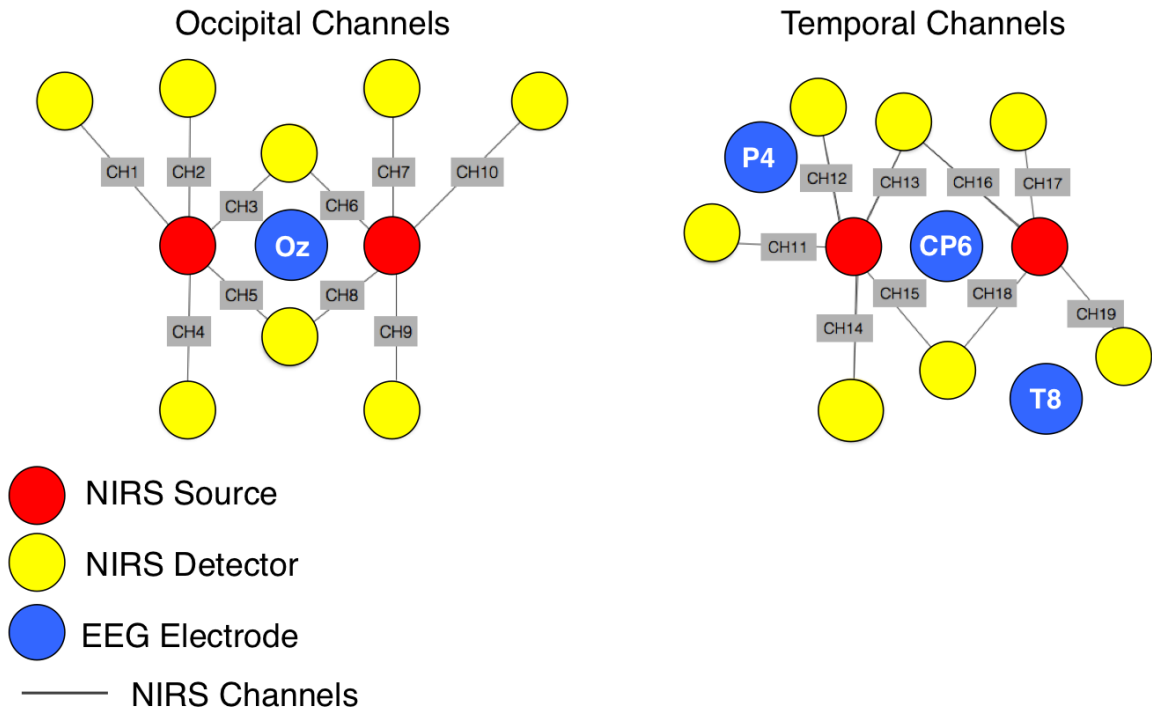
Figure 6.4: Schematic diagram of the NIRS occipital and temporal arrays showing positions of the sources, detectors and EEG electrodes. The red and yellow circles represent the sources and detectors respectively while the blue circle indicate nearby EEG electrodes. The black lines represent channels that are formed between sources and detectors.

Figure 6.5 shows the full headgear and set-up with the silicone headband being fed through the NIRS optodes and EEG electrodes. This was tightened at the front of the head and prevented the cap from slipping backwards during the experiment and additionally held the NIRS arrays firmly against the infant's head.
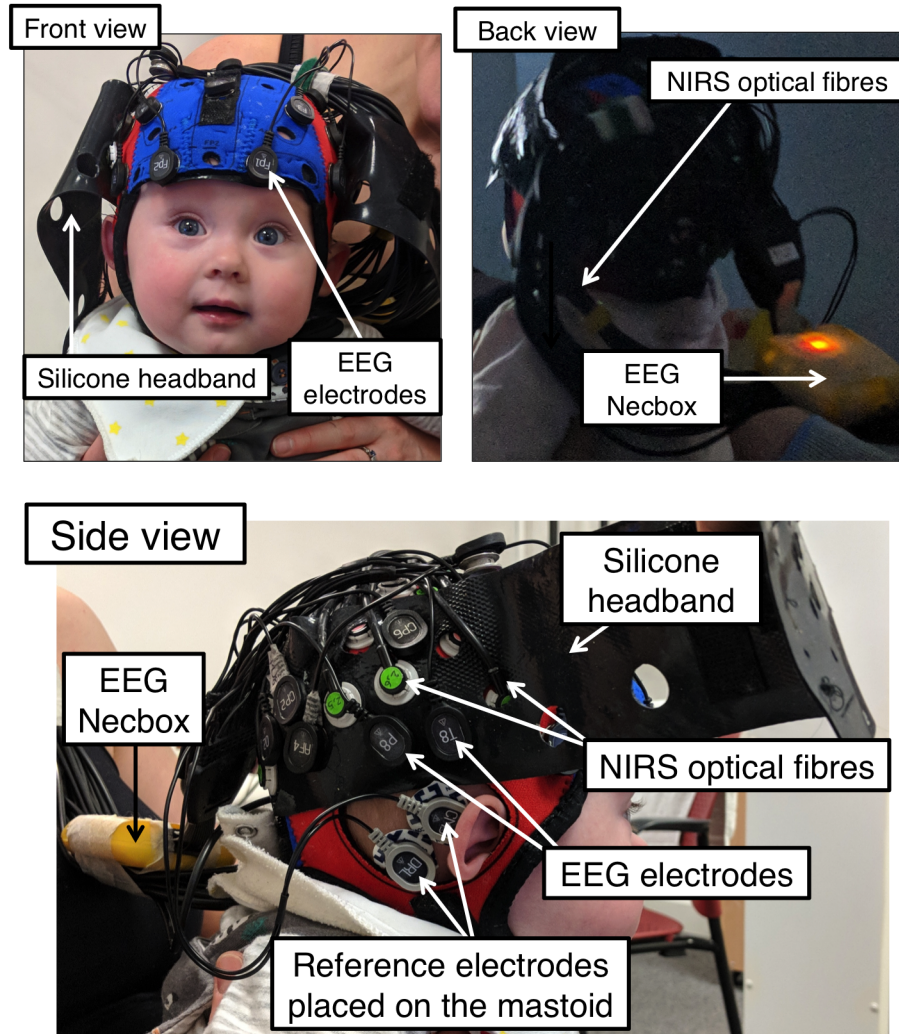
Figure 6.5: Full NIRS-EEG set-up on an infant with NIRS optodes and EEG electrodes indicated; (Top left panel) Front view (Top right panel) Back view (Bottom panel) Side view

6.2.3 Experimental Stimuli

All experimental stimuli were designed using Psychtoolbox in Matlab (Mathworks, USA). As I discussed in the introduction of this chapter, there were three different sets of conditions with two contrasts each that were presented to each of the infants. The first set included social and non-social stimuli which will be discussed in the following section while the other two sets were stimuli to target the visual cortex, consisting of checkerboard patterns and gratings, which will be discussed in the next chapter. The social/non-social stimuli are referred to as "block 1" , the checkerboard stimuli as "block 2" and the gratings

stimuli as "block 3". While the stimuli to target the visual cortex are not discussed in this chapter, the order of their presentation is shown.

6.2.3.1 Social and Non-social Block

The social/non-social block (block 1) had two contrast conditions:

1. The social condition consisted of a variety of dynamic videos where women sang different nursery rhymes such as "incy-wincy" and "wheels on the bus" which have been used in previous EEG studies (Jones et al., 2015). In contrast to the stimulus used in Chapter 4, the auditory component was matched to the visual component of the video.

2. The non-social condition consisted dynamic videos of moving mechanical toys which have been used in previous infant NIRS studies (Lloyd-Fox et al., 2009) and provide a good contrast to biological motion.

Both social and non-social videos were presented for a varying duration between 8 - 12 s and were followed by a baseline condition consisting of full-colour transport images of cars, trucks and helicopters (identical to the baseline used in the study in Chapter 4). The images were presented randomly for a pseudorandom duration of 1 - 3 s each, for a total of 8 s following which a fixation cross in the shape of a ball or a flower appeared in the centre of the screen to draw the infant's attention back to the screen in case they had become bored during the baseline period. I moved on to the next experimental condition only once the infant was looking at the fixation cross. Figure 6.6 shows the order of stimulus presentation for the social/non-social block. After one presentation of each of the social and non-social condition (i.e. after one full presentation of block 1), the stimuli for block 2 were presented followed by block 3. Stimuli from blocks 2 and 3 are discussed in the next chapter.
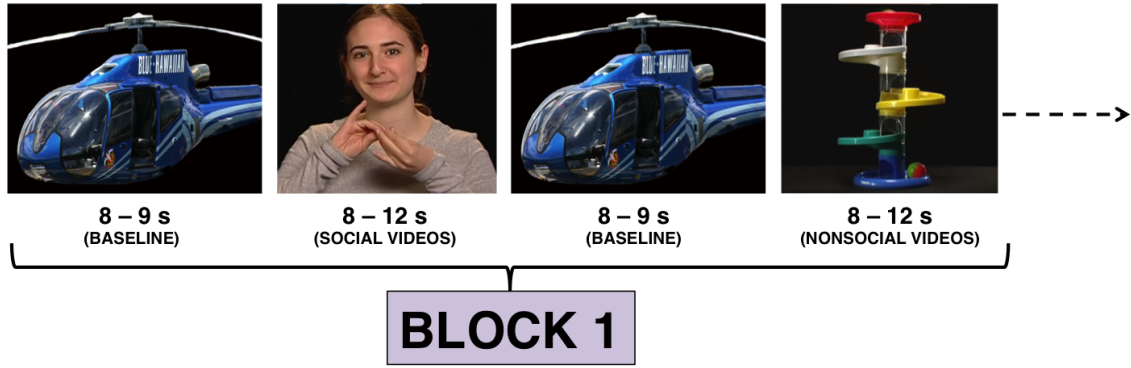
Figure 6.6: Social/Non-social stimuli

6.2.4 Experimental Procedure

Prior to the family's arrival, both the NIRS fibres and the EEG electrodes were clipped into place at their relevant locations in the headcap. The EEG wires were plugged into the necbox (wireless transmitter) which was attached to an arm holding the optical fibres, in order to prevent the headgear from being excessively heavy for the infant. Once the study and procedures had been explained to the parent, written consent was obtained following which the infant's head measurements were obtained. These have been previously described in Chapter 4. The inion (which is defined as the bony structure at the base of the skull) was also identified. In the adult study, the geltrodes were filled with gel using a syringe once the cap had been positioned on the participant's head. For the infant studies however, this was not possible. Instead, gel was inserted directly into the hollow space on the underside of each geltrode (shown in Figure 2.9a in Chapter 2) from inside the headcap, prior to the placement of the cap on the infant's head, while the infant sat in the parent's lap. The headcap had locations from the International 10/20 system marked and the "FPz" location (which should be placed above the nasion as shown in the image on the left in Figure 6.7) was used as the landmark to position the cap. Using one landmark position to place the headgear was sufficient as the 10/20 locations are all marked relative to one another. Once the cap was positioned, the electrodes to reference the EEG activity were placed on the infant's right mastoid (which is defined as the bony area behind the ear), this is shown in the bottom panel in Figure 6.5. Previous NIRS studies measuring haemodynamic responses over the temporal lobe have identified that the maximal responses to

social stimuli occur in the superior temporal sulcus - temporo-parietal region (STS - TPJ) (Lloyd-Fox et al., 2014a) and a map resulting from co-registration work (Lloyd-Fox et al., 2014b) indicated that for this headgear, the optode circled in red in Figure 6.7 would need to be aligned with the right pre-auricular point in order to target the STS-TPJ region. If the infant was compliant, I checked if the NIRS optode that was immediately to the right of the EEG electrode labelled "T8" (circled in red in the image shown on the right in Figure 6.7) was in line with the right pre-auricular point which is defined as "a point of the posterior root of the zygomatic arch lying immediately in front of the upper end of the tragus". However this check was not possible in the majority of infants until the end of the study as sometimes placing the headgear and attaching the reference electrodes behind the ear resulted in the infants becoming bored or fussy and the study therefore had to be started quickly.
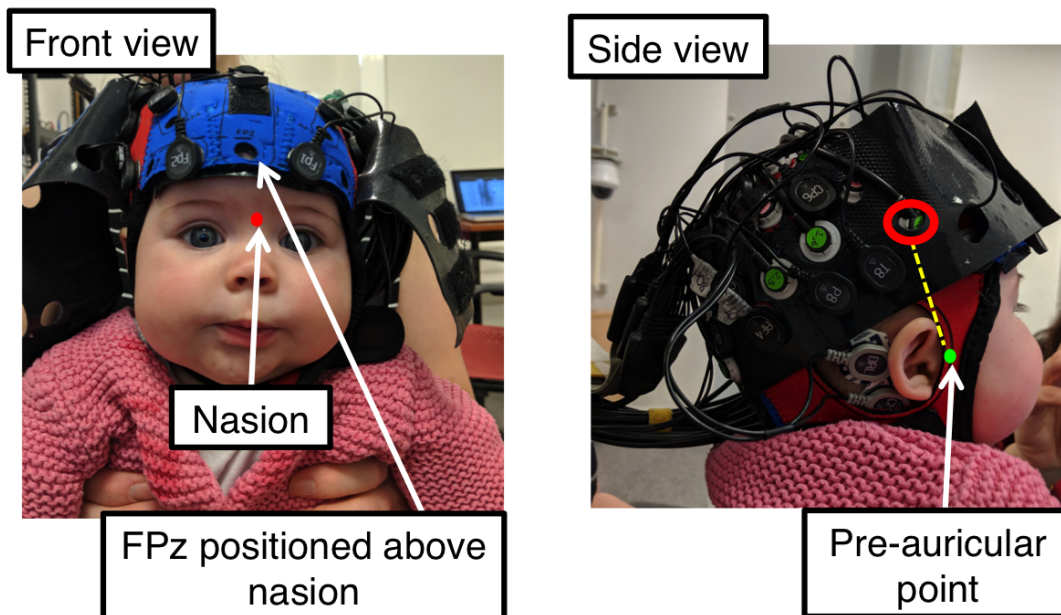
Figure 6.7: Image of a participant wearing the NIRS headgear.

After the headgear was positioned, the infant and parent were seated at a viewing distance of approximately 60 cm from the screen. The study began with a rest period (10 s minimum) to draw the infant's attention towards the screen, during which the infant was shown shapes in the four corners of the screen. Following this, each of the blocks discussed

in Section 6.2.3 were alternated as shown in Figure 6.8 until the infants became bored or fussy. Alerting sounds were occasionally played during the baseline stimulus in order to draw the infant's attention back towards the screen.
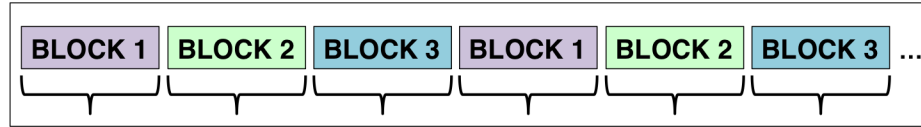
Figure 6.8: Order of stimulus presentation

6.2.5 Data analysis

6.2.5.1 NIRS

6.2.5.1.1 Pre-processing A general overview of the processing pipeline has been given in Chapter 2 and Figure 2.11 shows the steps that are involved. The NIRS data was analysed in Matlab 2014a (Mathworks, USA) using the same programs that were used to analyse the adult data in the previous chapter. The details of how the concentration changes were calculated from the attenuation change spectra have been provided in Section 4.2.5.1 of Chapter 4. Motion artifact detection has been described in detail in Section 2.3.1.1 of Chapter 2 and prior to the conversion to concentration changes in HbO_2, HHb and oxCCO, was applied to the attenuation signal of each participant across all wavelengths between 780 - 900 nm, in order to remove motion artifacts from the data. Following motion correction, the UCLn algorithm was used with a DPF value of 5.13 to calculate $\Delta[HbO_2]$, $\Delta[HHb]$, $\Delta[oxCCO]$ at 120 wavelengths between 780 - 900 nm. A 4th order Butterworth filter from 0.01 - 0.4 Hz was used to filter the data, following which the data were segmented to create trials (or blocks) which consisted of 4 s of the baseline period prior to the start of the experimental stimulus, the entire duration of the experimental condition and the following baseline. Video recordings of the testing session were used to code for looking-time offline. This involves identifying periods of the study where the infant was not looking at the experimental stimulus for a sufficient amount of time and removing those segments from the data. The criteria for this study was the same as described in Section 4.2.5.3 of Chapter 4 - that if an infant did not look at the stimulus for at least 60% of the experimental trial, the trial was removed. An infant was removed from the study if they had fewer than two

trials for any given experimental condition. Once looking-time coding and rejection had been performed, baseline correction was applied to the segmented data. The procedure for this has been described in Section 2.3.1.1 of Chapter 2.

6.2.5.1.1.1 *Additional rejection criteria* Figure 5.5b shown in Section 5.2.2.1.2 of Chapter 5 shows the raw spectrum depicting the photon counts at each detector of the CCD camera. The photon counts (or intensity counts) that can be seen at each individual detector represent the number of photons that pass from the source fibre, through the tissue and then are received at the detector and therefore provide an indication of the signal-to-noise ratio of the data being collected. The intensity counts for each measurement at each detector should be approximately above 2000 and below 60,000. This is because the noise level of the system (consisting of thermal noise from the CCD and dark noise) is approximately 500 counts and the intensity counts need to be roughly 4 times the noise level in order to have a good signal-to-noise ratio, allowing the HRF to be detected. Counts above 60,000 indicate that the detectors are receiving too much light and have become saturated. This is usually due to effects such as *light piping* where light from the source fibre reaches the detector directly without passing through the tissue. This can occur due to poor coupling between the fibres and the participant's head. In the case of simultaneous NIRS-EEG measurements, it can also occur if the EEG gel has seeped from the geltrodes and formed a bridge between the source and detector fibre, providing a medium for light to pass directly between the source and detector rather than through tissue. Light piping is obvious if very high intensity counts are observed at any of the detectors but can also be identified offline if after chromophore concentration changes have been calculated a strong positive correlation is seen between $\Delta[\text{HbO}_2]$ and $\Delta[\text{HHb}]$ where the time series of both chromophores strongly mimic one another. For each infant, the intensity counts from each of the detectors for each wavelength were plotted offline. If any detectors had counts lower than 2000 or higher than 40,000, the corresponding channel was excluded. While 60,000 indicates that a detector is saturated, counts upwards of 40,000 are also unlikely to be genuine therefore 40,000 was used as the threshold here. The Pearson correlation coefficient between the oxy-haemoglobin and deoxy-haemoglobin for the whole time series was additionally cal-

culated and any channels that had *r* value greater than 0.4 were also excluded. An infant was removed from the study if they had more than 40% channels excluded. Some channels were found to contain poor quality signal across the majority of infants and were therefore removed entirely from the analysis. These included Channel 6 (rejected in 76% of babies), Channel 8 (rejected in 62% of babies), Channel 10 (rejected in 57% of babies) and Channel 19 (rejected in 100% of babies). Channel 19 was most likely a broken fibre which resulted in the corresponding detector always having very low counts (approximately 500 counts).

Following rejection of poor quality signal channels, for each experimental condition, the concentration changes were averaged across valid trials, for each participant in order to obtain an average time course response for each chromophore. The averaged responses for valid participants were then averaged across participants to obtain a grand averaged group time course for each chromophore.

6.2.5.1.2 Further analysis

Analysis that is relevant only to the social and non-social conditions is discussed here and the checkerboards and gratings will be discussed in the next chapter.

6.2.5.1.2.1 *Statistical analysis*

Two levels of statistical analyses were conducted for each condition. Prior to determining whether there was a statistically significant difference between conditions, the maximum response for each chromophore, for each condition was compared to the baseline using t-tests. For HbO_2 and oxCCO this was the maximum increase and for HHb it was the maximum decrease or "dip" in response to the stimulus. Following this, pairwise t-tests were used to establish whether there was a statistically significant difference between conditions. A statistical time window of interest was defined to identify the maximum response for each of the conditions and this was then used for statistical analysis and subsequent analyses. For the social/non-social conditions, a time-window of 10 - 18 s post-stimulus onset was selected (similar to the work presented in Chapter 4 and that is frequently used for stimuli of this type (Siddiqui et al., 2017; Lloyd-Fox et al., 2009). This time window includes the range of maximum changes observed across infants for all three chromophores. The false discovery rate (FDR) procedure using

the Benjamin and Hochberg method (Benjamini and Hochberg, 1995) was also performed to correct for multiple comparisons. FDR corrected p values are also shown in each of the tables.

6.2.5.1.2.2 *Difference scores*   Difference scores were calculated for each block between conditions by subtracting the maximum response for each chromophore (in the chosen time window for statistical analysis) from one condition with the other. For example, difference scores for the social/non-social block involved subtracting the maximum response of each chromophore of the non-social block from the social block. The differences were then plotted in a topographical map and depicted in a bar chart to visualise the channels that displayed a greater response to one of the two conditions.

6.2.5.1.2.3 *Time to peak*   The time to peak (TTP) was calculated by determining the time taken for each chromophore to reach the maximum change in concentration in response to the experimental condition, in the time window chosen for statistical analysis.

6.2.5.1.2.4 *Cross-correlations*   Cross-correlations can be used to determine the similarities between two time-series, particularly if one time-series may be related to past lags of the other time-series. Typically it is used in functional connectivity to explore the relationship between neural activity observed in one area of the brain in relation to activity in another area of the brain. Here, it was used to investigate the relationship between each of the NIRS chromophores, particularly oxCCO and its relation to the haemoglobins as they represent different components of the neurovascular coupling pathway which may not be correlated exactly temporally. Here, it was calculated on a trial-by-trial basis for each infant and then averaged to obtain mean cross-correlations between chromophores for each infant. These were then averaged across the infants to obtain grand averaged cross-correlations. The method of calculating cross-correlations has already been described in Chapter 2.

6.2.5.2 EEG

6.2.5.2.1 Pre-processing All EEG data were analysed using Matlab 2017a (Mathworks, USA) and the EEGLab Toolbox (Schwartz Centre for Computational Neuroscience, UC San Diego, USA). Figure 2.13 in Section 2.3.2.1 of Chapter 2 shows the pipeline for pre-processing the EEG data and the procedures have been discussed in detail there, except segmentation which was performed differently for each of the experimental conditions and the social/non-social conditions will be discussed in more detail in the following section while segmentation of data from the visual conditions will be discussed in the next chapter. Based on previous work (Jones et al., 2015), if an infant had fewer than 5 trials per condition after artifact detection and removal, they were removed from the study.

6.2.5.2.1.1 *Segmentation* The EEG data from the social and non-social experimental condition were segmented into 1 s segments such that each 8 - 12 s long social or nonsocial trial resulted in 8 - 12 epochs. This method of segmentation is consistent with previous work (Jones et al., 2015) exploring changes in induced power occurring in response to social and nonsocial videos in infants aged 6 months and 12 months.

6.2.5.2.2 Further Analyses Topographical maps of spectral power were generated for the *theta* (3 - 6 Hz) and *alpha* (7 - 9 Hz) frequency bands. These bands were of interest based on previous work (Jones et al., 2015). No ERP analysis was performed on the infant data as ERP analysis is more appropriate for experimental paradigms that have an event-related design.

6.2.5.2.3 Statistical Analysis For the social/non-social conditions, pairwise t-tests were used to determine whether there was a significant difference in the mean alpha and theta power for both conditions, over temporal and frontal channels.

6.3 Results

Results from the social/non-social conditions are shown here and results from the visual conditions are shown in the next chapter.

6.3.1 NIRS

Out of forty-two subjects, thirty-two were included in the final analysis for NIRS. The exclusion criteria for participants has been discussed previously in Section 6.2.6.1. 7 infants were excluded due to having more than 40% of channels with poor data quality, 2 infants were excluded due to poor signal-to-noise ratio and low intensity counts and 1 infant was excluded due to an insufficient number of trials for any of the conditions.

6.3.1.1 Social

The upper panel of Figure 6.9 displays the grand averaged changes in concentration of HbO_2 (red), HHb (blue) and oxCCO (green) in all channels, across 32 participants, in response to the social stimulus. oxCCO has been magnified (x2.5) and the bottom panel shows the concentration changes in only oxCCO, prior to magnification. The experimental stimuli were presented in a jittered design with the social stimulus varying between 8 - 12 s and this has been indicated in the grand average figures by means of the pink and purple box. The pink box shows the minimum time period during which the stimulus was being presented (8 s for the social stimulus) while the purple box extends up to maximum period (12 s).

Prior to comparison between conditions i.e. social versus non-social, t-tests were performed to assess whether there were statistically significant responses in $\Delta[HbO_2]$, $\Delta[HHb]$ and $\Delta[oxCCO]$ versus the baseline, in each channel. This was done in order to determine whether there was response to the stimulus occurring in any of the channels. Tables 6.1 - 6.3 show the mean maximum changes in $\Delta[HbO_2]$, $\Delta[HHb]$ and $\Delta[oxCCO]$ respectively along with their t and p values and FDR-correct p values. A significant increase in $\Delta[HbO_2]$ and $\Delta[oxCCO]$ from baseline was seen in all channels, with temporal channels 14 and 15 displaying the largest responses for $\Delta[HbO_2]$ and channels 11 and 14 for $\Delta[oxCCO]$. Over the visual cortex, channels 4, 7 and 9 also display large responses for $\Delta[HbO_2]$ while majority of occipital channels display an increase for $\Delta[oxCCO]$. $\Delta[HHb]$ shows statistically significant responses in 9 out of 15 channels with channels 11, 14 and 15 displaying the largest responses over the temporal cortex and channels 5 and 9 over the occipital cortex.
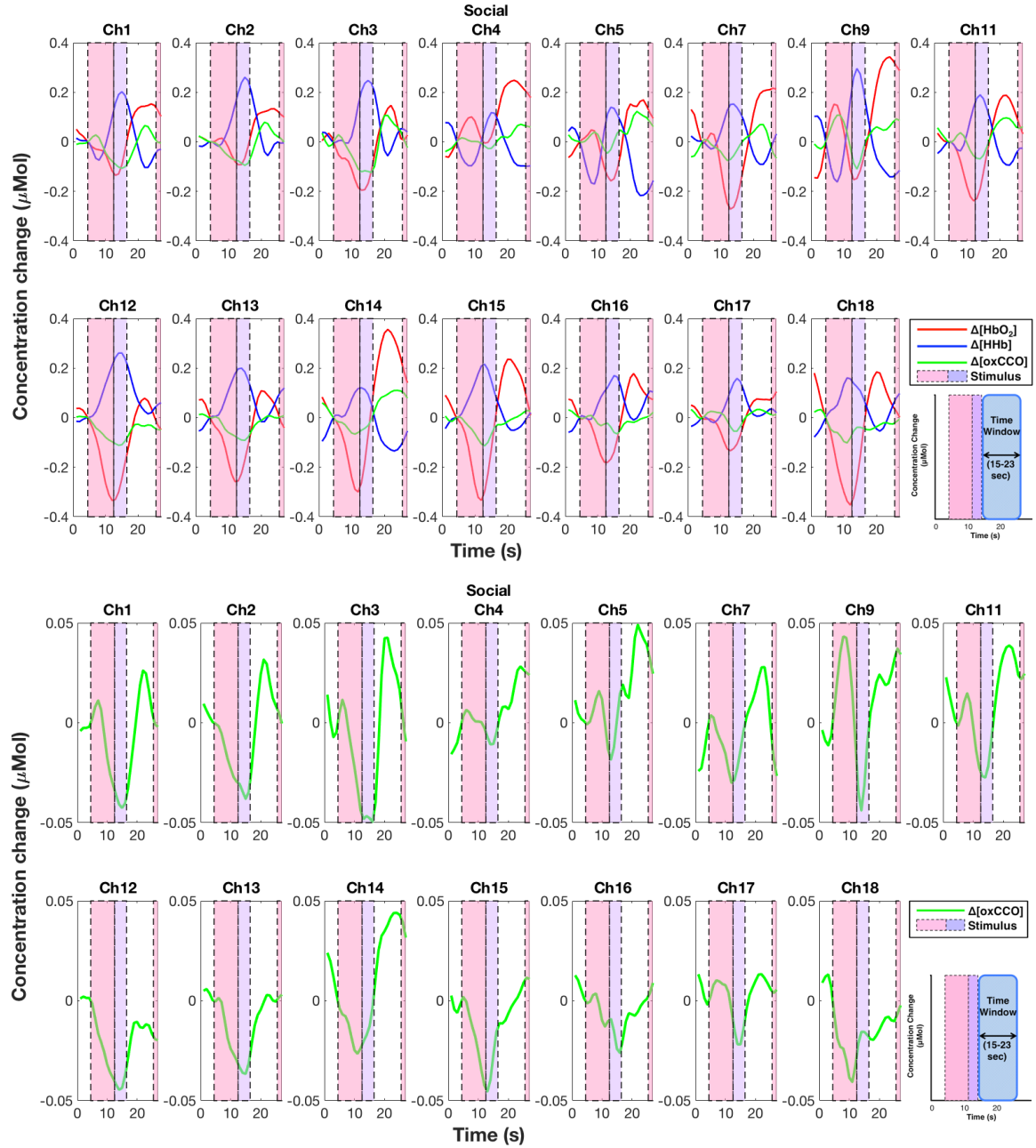
Figure 6.9: Observed chromophore concentration changes in HbO_2, HHb and oxCCO in response to the social stimulus with oxCCO magnified x2.5 and oxCCO not magnified (Bottom panel). The statistical time window of 10-18 s post-stimulus onset is indicated.

Channel	$\Delta[HbO_2]$ Mean Maximum Change	t_{HbO_2}	p_{HbO_2}	FDR corrected p_{HbO_2}
1	0.2873	3.2724	0.0028	0.0033*
2	0.2714	3.8381	$p < 0.001$	0.0011*
3	0.2748	3.5735	0.0019	0.0026*
4	0.4105	4.8306	$p < 0.001$	$p < 0.001$*
5	0.3211	3.9784	$p < 0.001$	$p < 0.001$*
7	0.2854	2.2423	0.0395	0.0395*
9	0.4681	3.9391	$p < 0.001$	0.0011*
11	0.3459	4.7805	$p < 0.001$	$p < 0.001$*
12	0.1912	3.2526	0.0029	0.0033*
13	0.2345	4.4642	$p < 0.001$	$p < 0.001$*
14	0.4601	6.0463	$p < 0.001$	$p < 0.001$*
15	0.3761	4.5972	$p < 0.001$	$p < 0.001$*
16	0.2936	4.4267	$p < 0.001$	$p < 0.001$*
17	0.2096	3.2012	0.0036	0.0038*
18	0.3534	4.1130	$p < 0.001$	$p < 0.001$*

Table 6.1: Mean maximum change and t and p values for the social condition versus baseline for HbO_2. Channels with a statistically significant increase in $\Delta[HbO_2]$ from baseline are marked with an asterisk.

Channel	Δ[HHb] Mean Maximum Change	t_{HHb}	p_{HHb}	FDR corrected p_{HHb}
1	-0.1838	-3.5183	0.0015	0.0054*
2	-0.1177	-2.1753	0.0389	0.0530
3	-0.1387	-2.0621	0.0524	0.0605
4	-0.1541	-2.6984	0.0115	0.0192*
5	-0.2634	-3.0807	0.0047	0.009*
7	-0.1825	-2.1242	0.0496	0.0605
9	-0.2372	-3.2531	0.0035	0.0088*
11	-0.1726	-3.6356	0.001	0.0051*
12	-0.0763	-1.9284	0.0636	0.0658
13	-0.1256	-3.0457	0.0048	0.009*
14	-0.1967	-4.6417	$p < 0.001$	$p < 0.001$*
15	-0.1372	-3.7293	0.00077	0.0051*
16	-0.1158	-2.1810	0.0374	0.053
17	0.0815	-1.9208	0.0658	0.0658
18	-0.1692	-3.3769	0.0022	0.0065*

Table 6.2: Mean maximum change and t and p values for the social condition versus baseline for HHb. Channels with a statistically significant increase in Δ[HHb] from baseline are marked with an asterisk.

Channel	Δ[oxCCO] Mean Maximum Change	t_{oxCCO}	p_{oxCCO}	FDR corrected p_{oxCCO}
1	0.0566	4.2045	$p < 0.001$	0.0011*
2	0.0593	3.7617	$p < 0.001$	0.0026*
3	0.0786	2.5072	0.0209	0.0237*
4	0.0560	3.1359	0.0039	0.0084*
5	0.1005	4.0603	$p < 0.001$	0.0014*
7	0.0753	2.9288	0.0098	0.0164*
9	0.0723	2.9556	0.0071	0.0133*
11	0.0698	4.8696	$p < 0.001$	$p < 0.001$*
12	0.0224	1.9671	0.0588	0.0588
13	0.0316	2.5315	0.0168	0.0229*
14	0.0715	5.8091	$p < 0.001$	$p < 0.001$*
15	0.0330	3.4162	0.0018	0.0045*
16	0.0387	2.1480	0.0221	0.0237*
17	0.0401	2.5858	0.0157	0.0229*
18	0.0313	2.5055	0.0183	0.0229*

Table 6.3: Mean maximum change and t and p values for the social condition versus baseline for oxCCO. Channels with a statistically significant increase in Δ[oxCCO] from baseline are marked with an asterisk.

6.3.1.2 Non-social

The upper panel of Figure 6.10 displays the grand averaged changes in concentration of HbO$_2$(red), HHb (blue) and oxCCO (green) in all channels, across 32 participants, in response to the non-social stimulus. oxCCO has been magnified (x2.5) and the bottom panel displays the concentration changes in only oxCCO, not magnified. The pink box shows the minimum time period during which the stimulus was being presented (8 s for the social stimulus) while the purple box extends up to maximum period (12 s). Similarly to the social condition, t-tests were performed to establish whether there were statistically significant responses in Δ[HbO$_2$], Δ[HHb] and Δ[oxCCO] versus the baseline, in each channel. FDR was used again to correct for multiple comparisons. Tables 6.4 - 6.6 show the mean maximum changes in Δ[HbO$_2$], Δ[HHb] and Δ[oxCCO] respectively along with their the t

and p values. The significant channels are marked with an asterisk. A significant increase in $\Delta[HbO_2]$ from baseline was seen in channels 12, 13 and 18 while a significant increase in $\Delta[HHb]$ was observed in many channels for example channels 5 and 9 over the occipital. Strong responses were not observed for $\Delta[oxCCO]$.
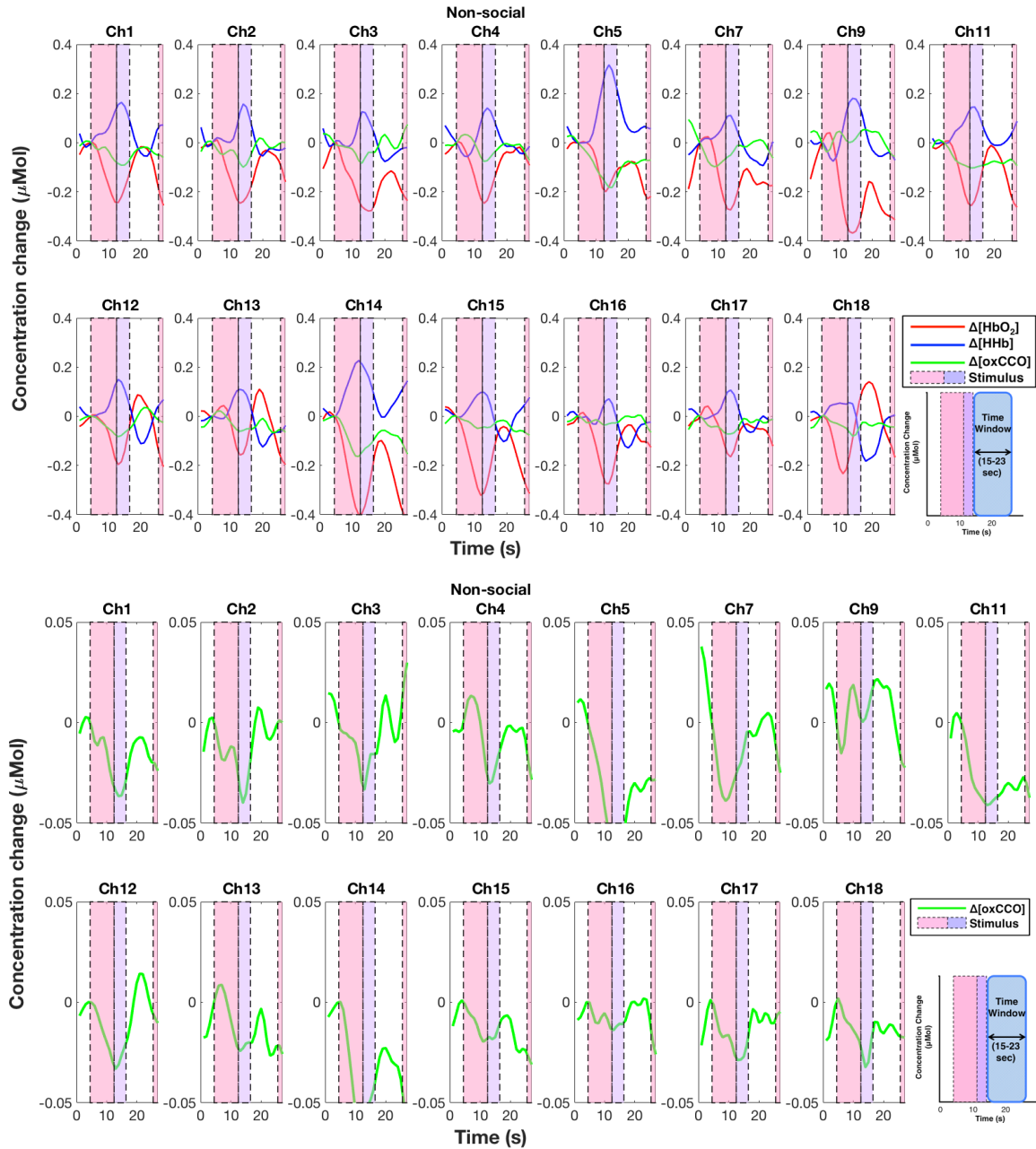
Figure 6.10: Observed chromophore concentration changes in HbO_2, HHb and oxCCO in response to the non-social stimulus with oxCCO magnified x2.5 (Upper panel) and oxCCO not magnified (Bottom panel). The statistical time window of 10-18 s post-stimulus onset is indicated.

Channel	$\Delta[HbO_2]$ Mean Maximum Change	t_{HbO_2}	p_{HbO_2}	FDR corrected p_{HbO_2}
1	0.1133	1.5484	0.1324	0.3315
2	0.0689	1.1776	0.2496	0.3862
3	0.0403	0.6237	0.5398	0.6748
4	0.1198	1.3371	0.1916	0.3592
5	0.1693	1.5880	0.1239	0.3315
7	-0.0198	-0.2125	0.8344	0.9484
9	-0.0067	-0.0654	0.9484	0.9484
11	0.1026	1.4600	0.1547	0.3315
12	0.1770	3.08	0.0045	0.0225*
13	0.2052	3.3864	0.002	0.0150*
14	0.0069	0.0939	0.9258	0.9484
15	0.1009	1.4647	0.1531	0.3315
16	0.0743	1.1552	0.2574	0.3862
17	0.0672	1.0884	0.2864	0.3906
18	0.3217	4.4830	1.13e-04	0.0017*

Table 6.4: Mean maximum change and t and p values for the non-social condition versus baseline for HbO_2. Channels with a statistically significant increase in $\Delta[HbO_2]$ from baseline are marked with an asterisk.

Channel	Δ[HHb] Mean Maximum Change	t_{HHb}	p_{HHb}	FDR corrected p_{HHb}
1	-0.1546	-3.3390	0.0023	0.0039*
2	-0.1493	-3.8003	0.008	0.0017*
3	-0.1993	-3.1807	0.0047	0.0059*
4	-0.1078	-2.4378	0.0211	0.0227*
5	-0.0439	-0.6685	0.5095	0.5095
7	-0.1688	-3.3188	0.0043	0.0059*
9	-0.1846	-2.4951	0.0202	0.0227*
11	-0.1408	-4.0532	0.0003	$p < 0.001$*
12	-0.1907	-5.4270	$p < 0.001$	$p < 0.001$*
13	-0.2203	-4.6895	$p < 0.001$	$p < 0.001$*
14	-0.1052	-3.2610	0.0028	0.0041*
15	-0.1725	-4.9264	$p < 0.001$	0.0041*
16	-0.2212	-5.5518	$p < 0.001$	$p < 0.001$*
17	-0.1247	-3.4339	0.002	0.0038*
18	-0.3015	-5.7540	$p < 0.001$	$p < 0.001$*

Table 6.5: Mean maximum change and t and p values for the non-social condition versus baseline for HHb. Channels with a statistically significant increase in Δ[HHb] from baseline are marked with an asterisk.

Channel	Δ[oxCCO] Mean Maximum Change	t_{oxCCO}	p_{oxCCO}	FDR corrected p_{oxCCO}
1	0.0395	2.8022	0.0089	0.0188*
2	0.0438	4.3190	$p < 0.001$	0.0027*
3	0.0739	3.3474	0.0032	0.0096*
4	0.0318	2.0717	0.0473	0.0645
5	0.0110	0.4211	0.6770	0.6770
7	0.0487	2.2879	0.0361	0.0541
9	0.0790	3.6406	0.0014	0.0051*
11	0.0169	1.2006	0.2393	0.2761
12	0.0466	4.0341	$p < 0.001$	0.0027*
13	0.0250	1.8386	0.0769	0.0949
14	0.0101	0.8647	0.3941	0.4222
15	0.0268	2.7434	0.01	0.0188*
16	0.0426	3.5996	0.0012	0.0051*
17	0.0350	2.4797	0.02	0.0333*
18	0.0345	2.7948	0.0093	0.0188*

Table 6.6: Mean maximum change and t and p values for the social condition versus baseline for oxCCO. Channels with a statistically significant increase in Δ[oxCCO] from baseline are marked with an asterisk.

6.3.1.2.1 Social versus Non-social Based on previous work (Lloyd-Fox et al., 2009), a greater haemodynamic response was expected to the social condition in comparison to the non-social. Pairwise t-tests were performed to determine whether there was a statistically significant difference between responses for the social condition versus the non-social condition. Significant differences were found between the social and non-social conditions for HbO_2 and oxCCO but not HHb with Channels 9 ($t = 2.5432, p = 0.0182$, mean difference $= 0.4747 \mu Mol$), 14 ($t = 3.5049, p = 0.0015$, mean difference $= 0.4532 \mu Mol$), and 15 ($t = 2.1732, p = 0.0375$, mean difference $= 0.2752 \mu Mol$), for HbO_2 and Channels 5 ($t = 2.0607, p = 0.0491$, mean difference $= 0.0895 \mu Mol$), 11 ($t = 2.5774, p = 0.0151$, mean difference $= 0.0529 \mu Mol$), and 14 ($t = 2.8133, p = 0.0086$, mean difference $= 0.0613 \mu Mol$),

for oxCCO. The p values reported here are non-FDR corrected values. The tables including the statistics (t and p values) for each channel and chromophore are included in the appendix. Figure 6.11 indicates the channels where there was a statistically significant difference between social and non-social conditions for $\Delta[HbO_2]$ (red) and $\Delta[oxCCO]$ (green) on a topographical map.
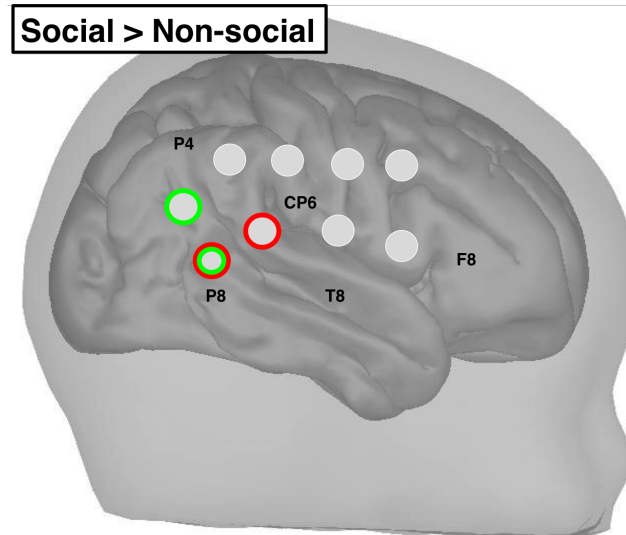
Figure 6.11: Channels with a statistically significant difference between social and non-social conditions indicated on a topographical map. Red circles represent channels with a statistically significant difference in HbO_2 responses and green circles represent channels with a statistically significant difference in oxCCO responses.

Channel 14 showed a statistically significant difference between social and non-social conditions for both HbO_2 and oxCCO, therefore is likely to reflect a cortical region that was involved in the processing of these stimuli. Hence, the observed changes in concentration HbO_2, HHb and oxCCO from this channel are shown in Figure 6.12, for both social and non-social conditions and include the standard deviations.
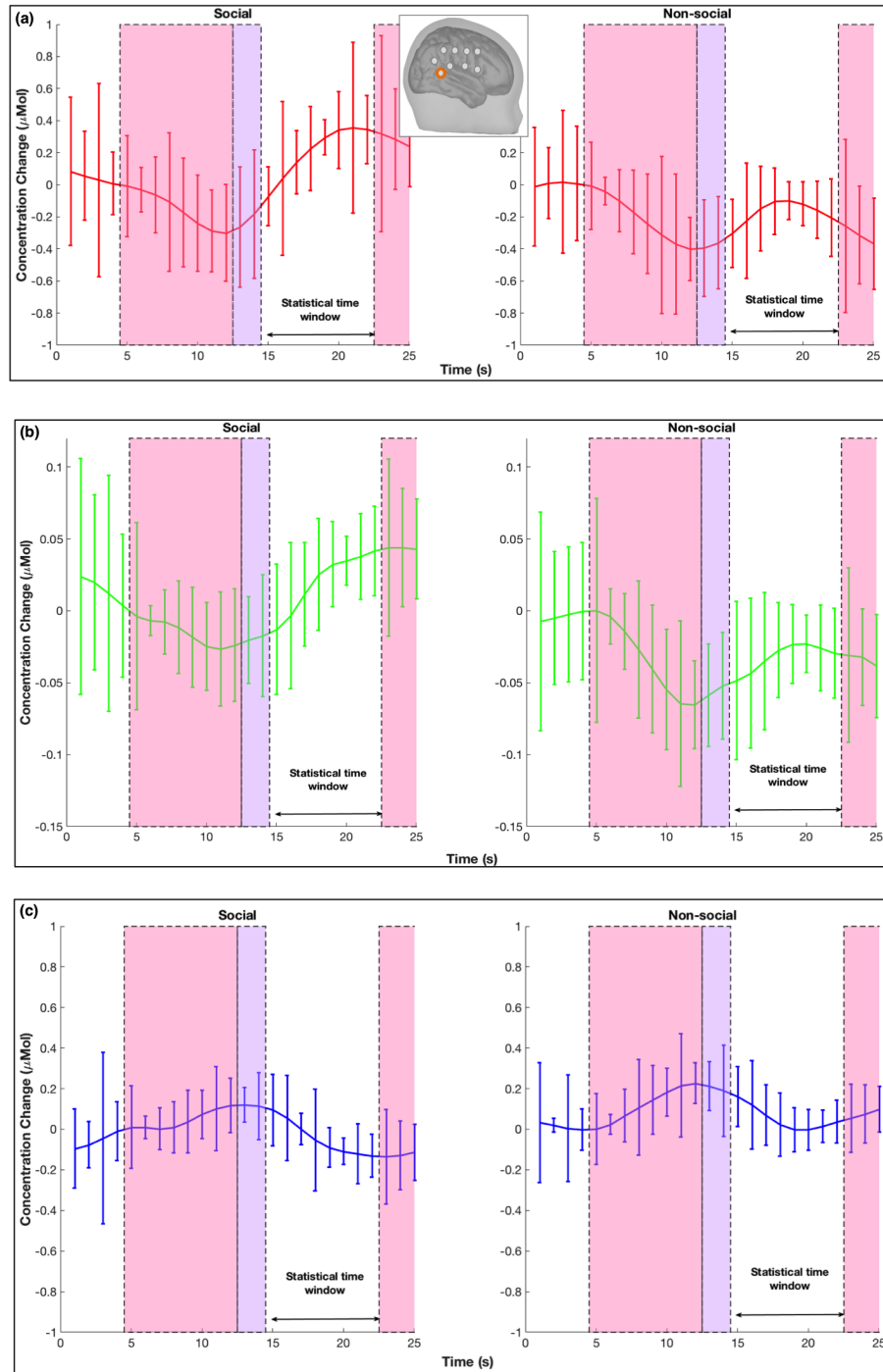
Figure 6.12: Observed changes in the concentration of (a) HbO_2 (b) oxCCO and (c) HHb in response to the social condition (left) and non-social condition (right) in Channel 14. The statistical time window is indicated. The error bars represent standard deviations.

The mean and standard deviations of the maximum responses from each of the tempo-

ral channels are shown in Figure 6.13 with HbO_2in red, HHb in blue and oxCCO in green, for both social and non-social conditions (labelled as "S" and "N" on the x-axis), HbO_2 and HHb are scaled to the y-axis on the left and oxCCO is scaled to the y-axis shown on the right in the figure for each channel. For the social condition, Channels 11, 14, 15, 16 and 18 appear to have the strongest HbO_2 responses while for oxCCO Channels 11 and 14 have the strongest responses. For HHb the non-social condition appears to have the strongest responses (i.e. a strong decrease in HHb) with the exception of Channel 14.
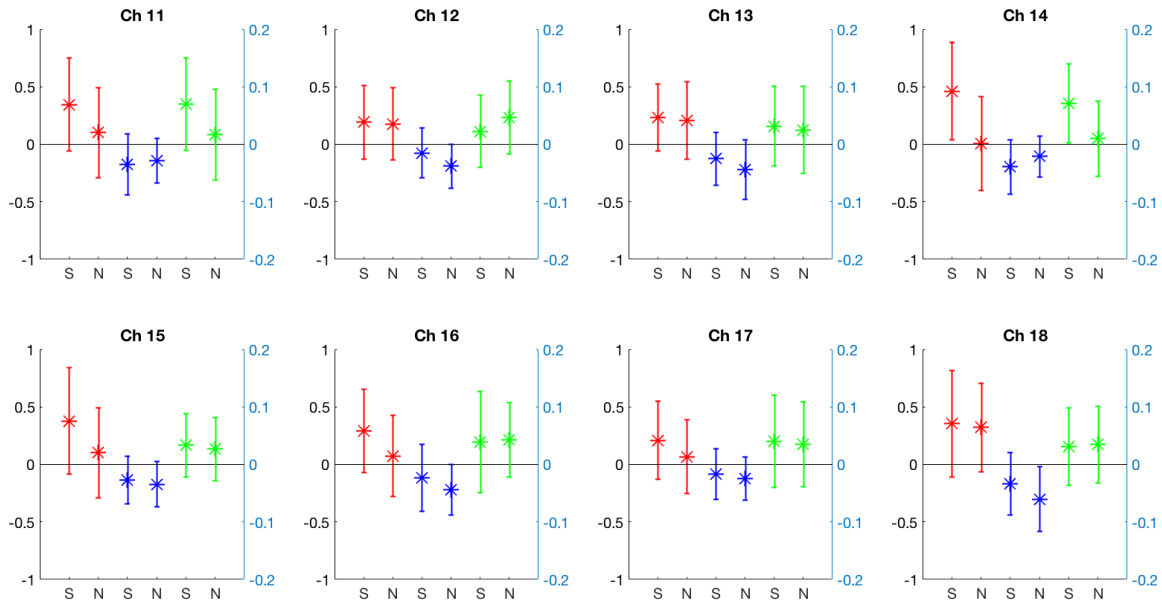
Figure 6.13: Mean and standard deviations of the maximum responses of HbO_2(red), HHb in (blue) and oxCCO (green), for both social and non-social conditions which are labelled as "S" and "N" on the x-axis. The y-axis on the left is for HbO_2 and HHb while the y-axis on the right is for oxCCO.

6.3.1.2.1.1 *Difference scores* The differences in the maximum change in concentration between social and non-social conditions were calculated for each of the 8 channels over the right temporal lobe. Figure 6.14 shows the difference in the maximal response for each chromophore, with each bar in the graph representing a channel over the right temporal lobe. A larger increase in concentration of $\Delta[HbO_2]$ and $\Delta[oxCCO]$ was expected in response to the social condition. Positive values indicate a stronger response to the social condition in comparison to the non-social, while negative values indicate a stronger response to the non-social condition.
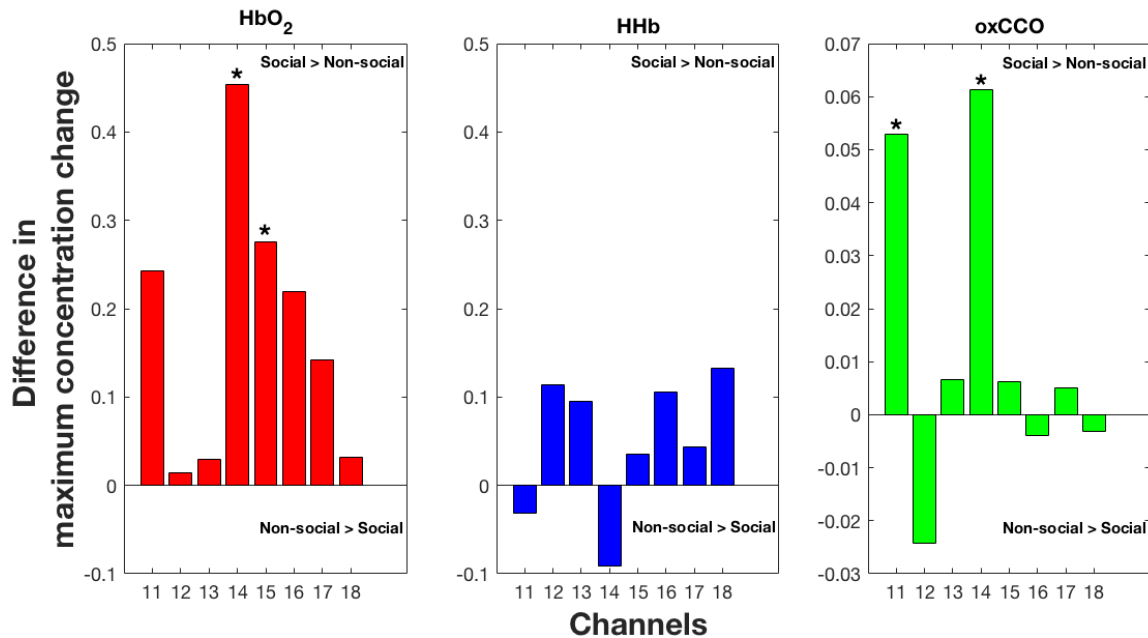
Figure 6.14: Bar graph showing the difference in the mean maximum change, in each chromophore, between social and non-social conditions for the channels over the right temporal lobe. Positive values indicate a greater response to the social condition while negative values indicate a greater response to the non-social condition. Channels with a significant difference between social and non-social conditions are indicated with an asterisk.

6.3.1.2.1.2 *Time to peak*   The TTP was calculated for each chromophore (for both conditions) in the time window chosen for statistical analysis (10 - 18 s post-stimulus onset here). No significant differences were found in the TTP for any of the chromophores and the figures showing this for each of the chromophores and conditions can be found in the appendix.

6.3.1.2.1.3 *Cross-correlations*   Cross-correlations were performed between each of the chromophores, for both social and non-social conditions correlations between (i) HbO_2 and oxCCO (ii) HHb and oxCCO and (iii) HbO_2 and oxCCO for all the channels. This was important as, to my knowledge, this was the first reported use of multi-channel broadband NIRS during functional activation in infants and it was therefore important to explore the relationship between energy metabolism and haemodynamics during brain development.

Figure 6.15 shows the average cross-correlations across the temporal channels for both conditions and the cross-correlations from each of individual channels can be found in the

appendix. For oxCCO and HHb, a negative correlation was seen with $r = -0.46$ and zero time-lag for both conditions. A negative correlation was also seen between HHb and HbO_2 with $r_{social} = -0.23$ and $r_{nonsocial} = -0.22$ and a time-lag of -1 s. oxCCO and HbO_2 showed a weak positive correlation with $r_{social} = 0.16$ and time-lag of -1s and $r_{nonsocial} = 0.13$ with zero time-lag for the non-social condition.
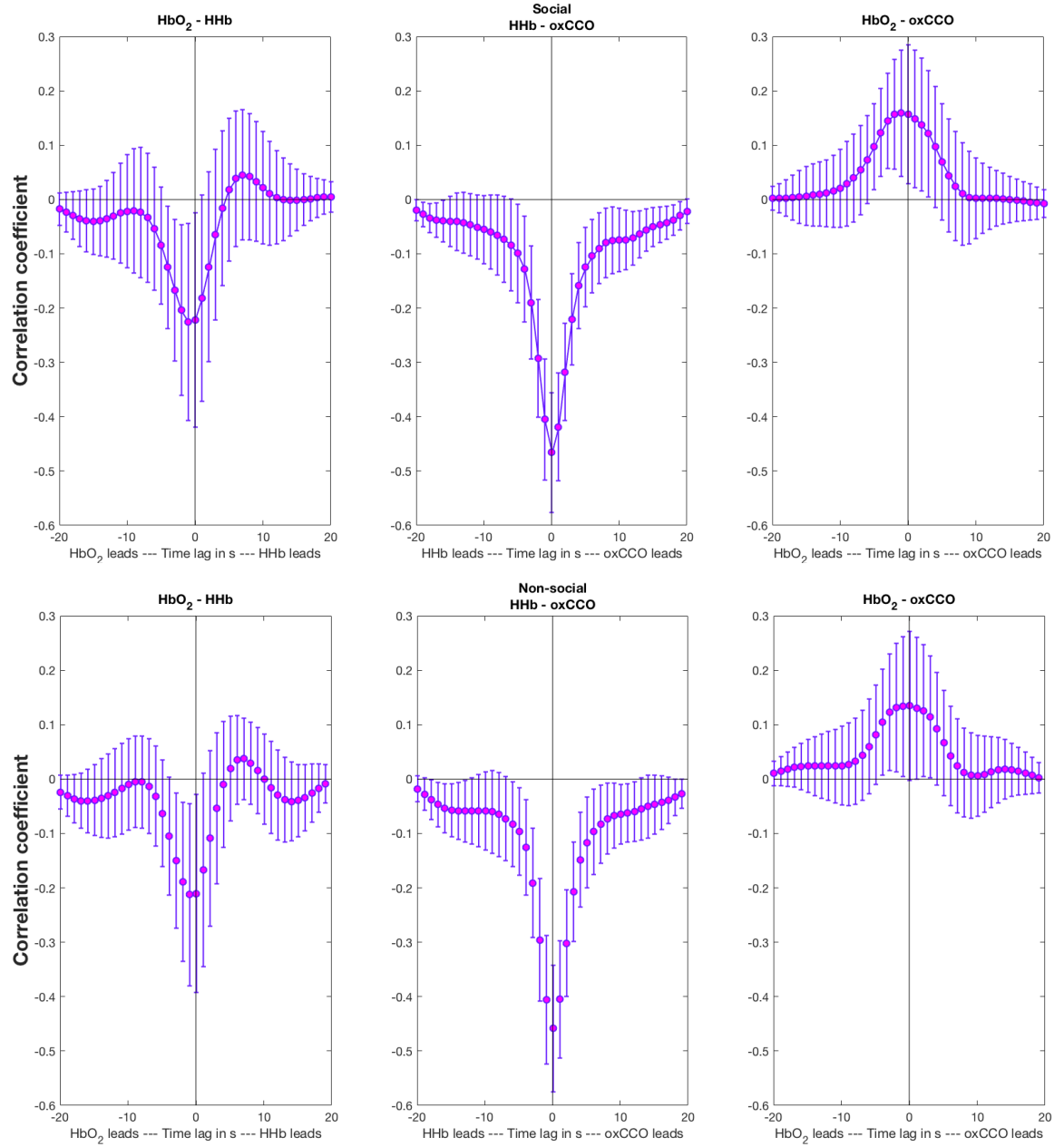
Figure 6.15: Average of the cross-correlation across all temporal channels for the social condition (upper panel) and non-social condition (bottom panel). The error bars represent standard deviations

6.3.2 EEG

For the social condition thirty-nine out of forty-two infants were included in the study and for the non-social condition thirty-six out forty-two infants were included in the study. All of the infants that were excluded were due to poor data quality. Figure 6.16 shows the log power spectral density for the theta and alpha frequency bands for both social and non-social conditions. Based on previous work (Jones et al., 2016b), suppression of theta and alpha activity were expected in response to both conditions. In both frequency bands and stimulus conditions, an overall suppression of alpha and theta is seen which is stronger over the left hemisphere. An increase in both alpha and theta occipital activity is seen in both conditions with alpha frequency band additionally displaying an increase in right temporo-parietal activity to both conditions.
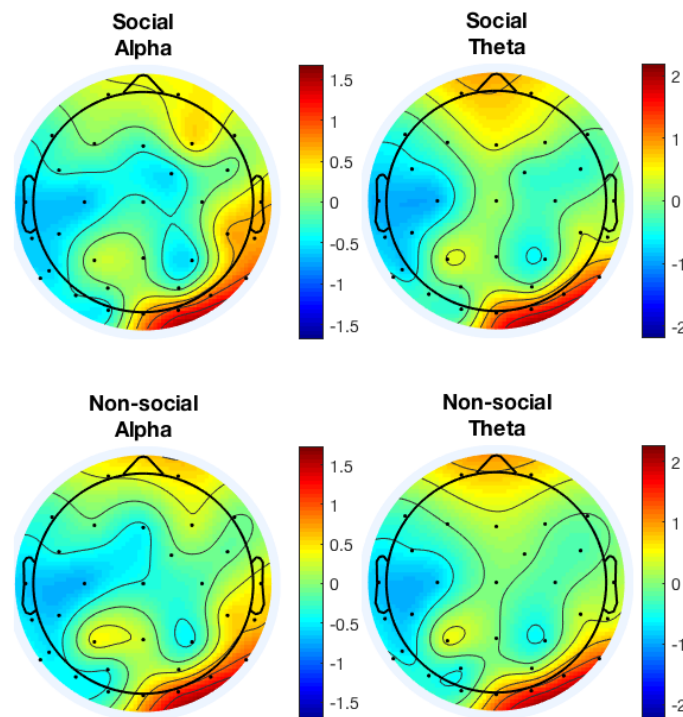
Figure 6.16: Topographical maps of the log power spectral density for the theta and bands for social and non-social conditions.

Figure 6.17 shows the difference in log power spectral density between the social and non-social condition, for the theta and alpha frequency bands. Greater alpha activity is seen in right frontal and temporal channels for the social condition in comparison to the

non-social condition. The occipital channels show greater alpha activity to the non-social condition in comparison to the social condition. Greater theta activity is seen in the occipital channels and frontal-central channels for the social condition in comparison to the non-social condition.
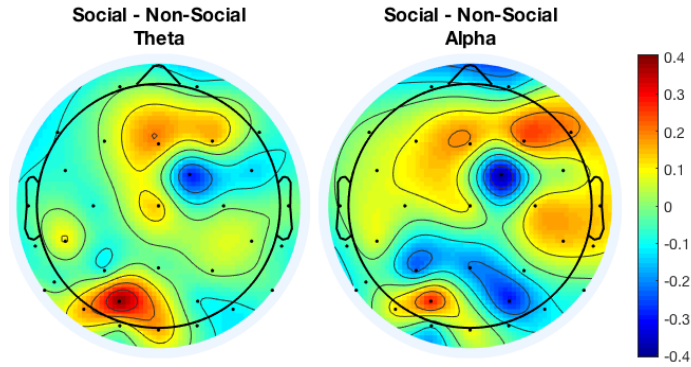
Figure 6.17: Topographical maps of the difference in log power spectral density between social and non-social, for the theta and alpha frequency bands.

6.3.2.1 Statistical analysis

Pairwise t-tests were performed to compare the mean log power of theta and alpha over temporal and frontal channels of the social versus non-social condition revealed no significant differences between the two conditions in either of the frequency bands.

6.3.3 Combined NIRS-EEG Analysis

For the combined analysis only those infants that had both EEG and NIRS data for an experimental condition were included. For the social condition, twenty-nine infants were included and for the non-social condition twenty-eight infants were included (twenty-eight of the same infants had data for both conditions). Correlations were performed for both social and non-social conditions between the mean power spectral density of the alpha and theta frequency bands with the maximum concentration change of $\Delta[HbO_2]$, $\Delta[HHb]$ and $\Delta[oxCCO]$, across the NIRS temporal and EEG right parietal, temporal and frontal channels as the strongest correlations between neural and haemodynamic activity were expected in channels spatially located close to one another. The matrix of the correlations between NIRS and EEG channels was converted into a heatmap which can be seen in Figure 6.19

for the social condition and for the non-social condition in Figure 6.20. The colorbar indicates the strength of the correlation between each channel and the statistically significant correlations ($p < 0.05$) are indicated by red rectangles. No correction for multiple comparisons was applied for these correlations. Figure 6.18 has been included to show the NIRS (blue circles) and EEG channels (orange squares) in order to remind the reader of the spatial locations of each of the channels that are being correlated.
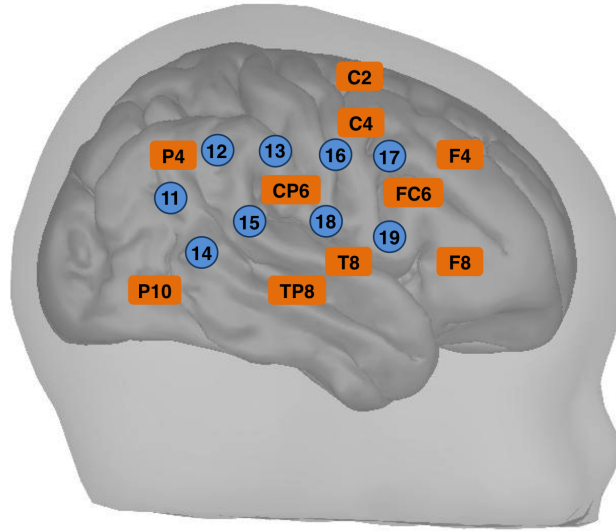
Figure 6.18: Topographical locations of the NIRS channels (blue) and EEG channels (orange rectangles), both have been labelled with their channel labels respectively.

For the social condition, in the alpha band for HbO_2 statistically significant positive correlations are seen between Channel 17 and temporo-parietal EEG channels while moderately significant correlations are observed between Channels 11, 14 and 15 with the temporo-parietal EEG channels. Temporo-parietal EEG channels are where an increase in alpha activity is seen in response to both social and non-social conditions. Channels 11, 14 and 15 are spatially located closest to these EEG channels and display the strongest increase in $\Delta[HbO_2]$ in response to the social condition. An increase in theta activity appears to be restricted to parieto-occipital EEG channels and the theta band shows a similar pattern although fewer statistically significant correlations are observed. Channels 11, 12, 14 and 17 correlate positively with temporo-parietal EEG channels.

For the social condition, in the alpha band for oxCCO, statistically significant correlations are seen between Channel 16 and majority of EEG channels and between Channel 17

frontal and fronto-central channels. Channels 16 and 17 are spatially located close to the fronto-central channels. In the theta band, statistically significant positive correlations are seen between Channels 16 and 17 and specific EEG channels (parietal and frontal) while Channel 15 shows negative correlations with EEG channels, where only a small increase in Δ[oxCCO] is observed. Other than Channels 16 and 17, most NIRS channels located in the posterior temporal cortex correlate negatively in alpha and theta bands.

For the social condition, in the alpha band for HHb, statistically significant negative correlations are observed between Channels 17 and EEG temporo-parietal channels, in the opposite pattern to that of alpha-HbO_2 correlations. In general, most NIRS and EEG channels correlate in the opposite direction to the HbO_2 correlations, as expected.

For the non-social condition, fewer statistically significant correlations are observed and the correlations are, in general, weaker in comparison to the social condition. For HbO_2 and alpha band, Channel 13 correlates positively with EEG Channel P4, which are in close proximity to one another and where an increase in alpha activity is observed for the non-social condition. Among the temporal NIRS channels, Channels 13 and 18 appear to have the largest increase in Δ[HbO_2] in response to the non-social condition but the correlation with Channel 13 is stronger as Channel 18 is not located close to P4. Moreover, in the theta band Channel 13 correlates with temporo-parietal EEG channels (TP8 and T8) and central channels (C4 and FC6). No significant correlations are observed between NIRS and EEG channels for alpha band and oxCCO for the non-social condition. Meanwhile in the theta band, Channel 15 correlates negatively with nearby EEG channels TP8, T8 and CP6.

For the non-social condition, in both theta and alpha bands, Channel 16 correlates negatively with HHb and the same channels are positively correlated for HbO_2. Channel 13 displays strong positive correlations for HbO_2 in both frequency bands, that appear more localised in the theta band. Theta band correlations for oxCCO are stronger with Channel 16 correlating positively with most EEG channels while Channels 14 and 15 correlate negatively, most strongly with temporo-parietal channels.

The analysis was also performed on the difference between social and non-social conditions such that correlations were performed between the difference in mean power spectral
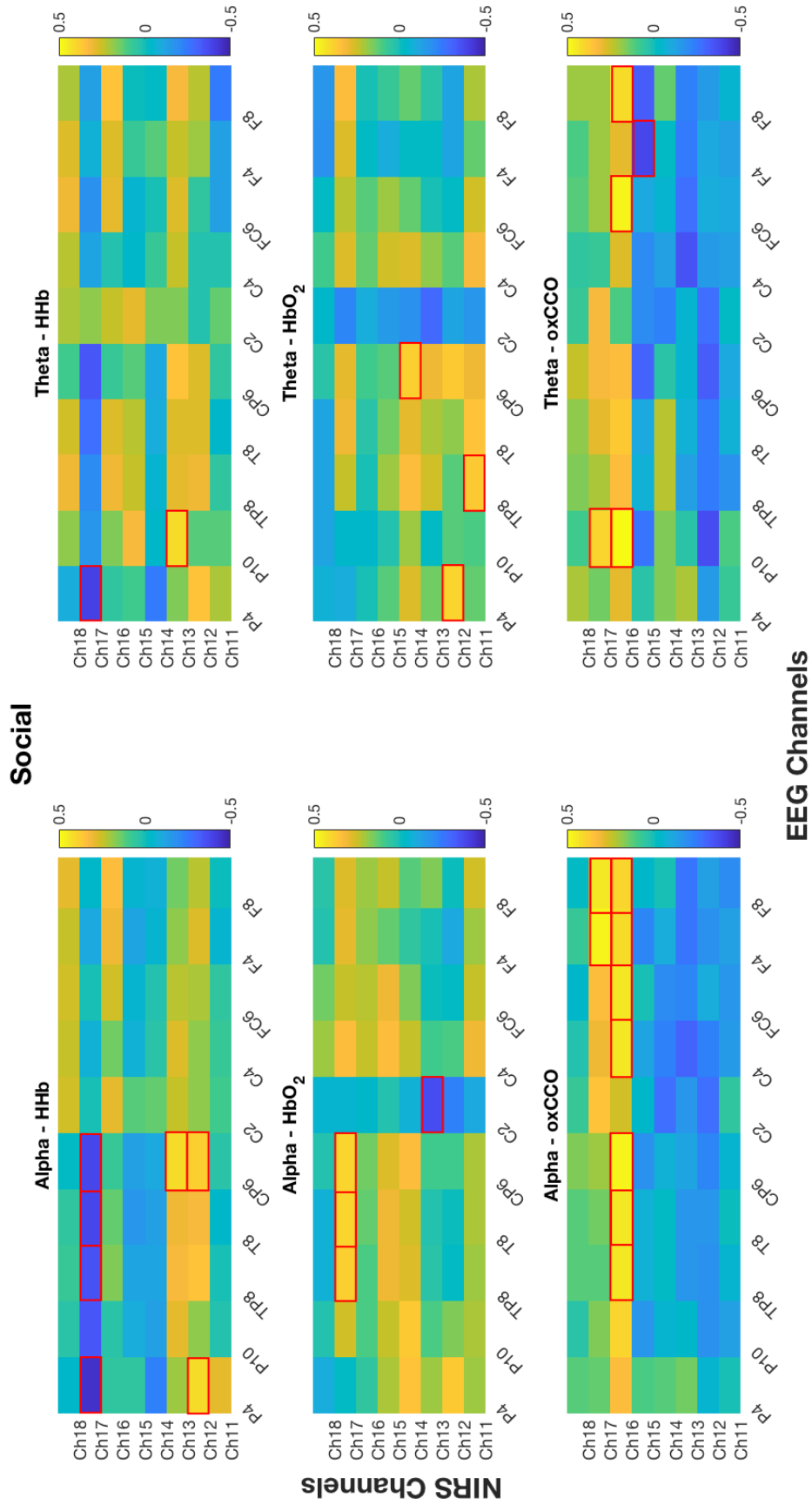
Figure 6.19: Heatmap showing the significant correlations between the mean power spectral density and the maximum change in $\Delta[HbO_2]$, $\Delta[HHb]$ and $\Delta[oxCCO]$, between NIRS temporal channels and EEG channels for the social condition with alpha band (left) and theta band (right). The colour bar indicates the strength of the correlation with yellow showing a positive correlation and blue showing negative. The significant correlations (p value < 0.05) are indicated by red rectangles.
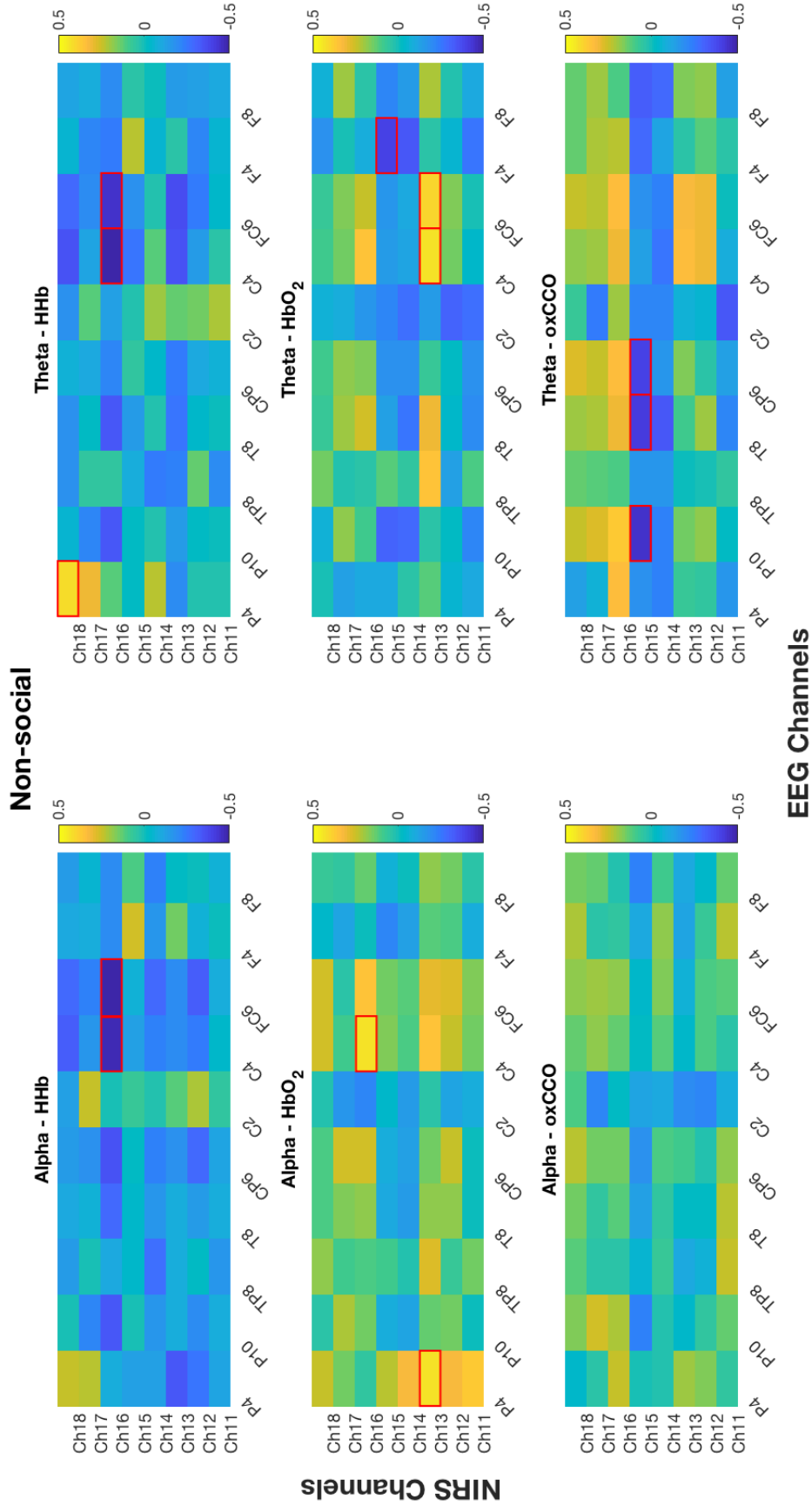
Figure 6.20: Heatmap showing the significant correlations between the mean power spectral density and the maximum change in $\Delta[HbO_2]$, $\Delta[HHb]$ and $\Delta[oxCCO]$, between NIRS temporal channels and EEG channels for the non-social condition with alpha band (left) and theta band (right). The colour bar indicates the strength of the correlation with yellow showing a positive correlation and blue showing negative. The significant correlations (p value < 0.05) are indicated by red rectangles.

density (social minus non-social) and the difference in the maximum change in each of the NIRS chromophores (social minus non-social). These results can be found in the appendix.

6.4 Discussion

Multi-channel broadband NIRS was used simultaneously with EEG in this study with 4-to-7-month old infants to investigate the relationship between haemodynamics, metabolic function and neuronal activation. The NIRS changes in concentration of $\Delta[HbO_2]$ and $\Delta[oxCCO]$ indicate a significant difference in the responses between social and non-social conditions, occurring over the superior temporal sulcus - temporo-parietal junction (STS - TPJ) region, with a stronger response observed for the social condition. This was the first study, to my knowledge, involving the use of multi-channel broadband NIRS during functional activation in infants. Therefore, alongside investigating the relationship between neural activity and subsequent blood oxygenation and metabolic changes, it was equally important to examine how cerebral energy metabolism related to changes in haemodynamics in the developing human brain. This is because, as I discussed previously, many components of the neurovascular coupling pathway are under ongoing maturation in early infancy. This includes development of cerebral vasculature and energy metabolism which may impact the observed changes in concentrations of chromophores measured using NIRS. Two types of analyses were therefore performed on the NIRS data to explore the association between the chromophores. These included time to peak (TTP) analysis and cross-correlation analysis. The TTP analysis showed heterogeneity in the results and no definitive pattern could be established. This is perhaps due to the limitation of the acquisition rate of the broadband system. There may well be temporal differences in the responses however, it might be difficult to discern them with a slow acquisition rate. Moreover, one of the limitations of this analysis is that it only allows comparison of the time taken for the maximum change in concentration across the chromophores as opposed to exploring how the change in concentrations over time (i.e. the shape of the time courses) correlate. Cross-correlations provide the opportunity to investigate this and while it was expected that there would be a stronger coupling between HbO_2 and oxCCO as cerebral blood flow

and blood oxygenation levels have been shown to be correlated with metabolic activity. Here however, stronger negative correlations between oxCCO and HHb were observed in channels over the temporal cortex, in comparison to oxCCO and HbO_2. In general, in channels over the temporal cortex, there is less variability in the correlations between oxCCO and HHb. These results are in contrast to those from the adult cross-correlation analysis presented in Chapter 5, where equally strong correlations were observed between HbO_2 and oxCCO and HHb and oxCCO. This therefore suggests that a stronger relationship exists between HHb and oxCCO while the brain is developing, which may indicate that the coupling between cerebral blood flow and metabolic function may not be fully established during brain development, as previous studies have suggested (Kozberg et al., 2013a; Kozberg and Hillman, 2016b; Arichi et al., 2012). Work by Kozberg and colleagues (2013a; 2016b) has demonstrated that in fact functional hyperemia develops postnatally alongside cortical connectivity while cerebral vasculature undergoes development. For example, they demonstrated that in postnatal rats, an increase in oxygenation in response to somatosensory cortex stimulation was more prominent in veins while in adults the same response is observed in pial arteries. Altered coupling mechanisms may therefore be in place during development in order to meet the metabolic demands of the brain.

The EEG topographical maps of power spectral density show an overall decrease in both alpha and theta activity for both social and non-social conditions which is in line with previous results (Jones et al., 2015). Studies suggest that a reduction in the power of the alpha frequency band is associated with higher cortical activation and greater attention to the stimuli (Orekhova et al., 2006). However, an increase in theta and alpha power was observed in the occipital regions, also in line with previous work and may reflect visual processing (Jones et al., 2015). Alpha is thought to be a reflection of the brain "at rest" or in an "idling" state and has been related to cortical inhibition with an increase in alpha power being observed in task-irrelevant areas and a decrease in task-relevant areas (Klimesch et al., 2007). It has been hypothesised that via this inhibition mechanism alpha oscillations play a role in visual attention and previous studies have demonstrated that alpha power is related to attentional control (Jones et al., 2015). No significant differences were found in either alpha or theta power between social and non-social conditions. A dif-

ference between the results seen here and those by Jones et al (2015) is that their results had a more widespread and stronger suppression of alpha power and a more localised increase in alpha power over the occipital cortex. These differences may be due to the fact that they used a high-density EEG system with 128 channels enabling better coverage while the system used in this study had only 32 EEG channels. Additionally, the EEG system used in this study referenced activity to the right mastoid while their system referenced activity to the vertex or Cz. Moreover, their sample size was also much larger in comparison to that of this study.

For the combined NIRS and EEG analysis performed to investigate how neuronal activation relates to cerebral oxygenation changes and changes in energy metabolism, overall, stronger correlations were observed between NIRS and EEG channels for the social condition and in particular for the alpha band in comparison to the theta band. Significant positive correlations were seen between NIRS channels located over the posterior STS-TPJ region which exhibited the strongest responses in $\Delta[HbO_2]$ and the nearby temporo-parietal EEG channels, where an increase in alpha and theta activity was observed, for HbO_2 while the same channels displayed negative correlations for HHb, in both frequency bands. This would imply that neural activity has a direct relationship with an increase in blood oxygenation, as studies have previously demonstrated (Logothetis et al., 2001a; Logothetis, 2002; Devor et al., 2008; Zehendner et al., 2013). However so far, there have been conflicting results from simultaneous EEG-fMRI work with some studies reporting the observation of an inverse relationship particularly between alpha activity and the BOLD response (Yuan et al., 2010; Stern, 2002; Laufs et al., 2003a), which suggests that an increase in blood oxygenation or $\Delta[HbO_2]$ would be related to a decrease in alpha power. This is not observed here however, for either social or non-social conditions.

For the social condition, a NIRS channel located over the fronto-central region correlated most strongly positively with HbO_2 and oxCCO and negatively with HHb, in the alpha frequency band across majority of EEG channels. As the strongest correlator, the location of this channel may be important in linking neural and haemodynamic activity occurring over the temporal cortex. Although the exact mechanism is unclear here as it is not the channel where the largest changes in concentration of chromophores are ob-

served. Further work involving non-linear analysis and computational modeling might be required to fully comprehend the underlying mechanisms in play.

For oxCCO for this channel, in addition to one located in the central-parietal region, correlated most strongly positively in both theta and alpha bands (stronger than HHb and HbO_2). An interesting observation is that between these two channels there was either a significant correlation between NIRS and EEG channels for HbO_2 (which was weaker for oxCCO) or there was significant correlation for oxCCO (which was weaker for HbO_2). Although both chromophores correlated in the same direction which is in line with previous studies investigating the relationship between neural and metabolic activity have reported that an increase in the haemodynamic response in relation to stimulation correlates with an increase in glucose uptake in response to neuronal activation (Devor et al., 2008). It is unclear why the channels with stronger oxCCO responses did not correlate more strongly with temporo-parietal EEG channels while those with weaker NIRS responses did and the differences in the strength of correlations with oxCCO and HbO_2 are also unclear. This may perhaps be a physiological effect further highlighting the delicate state of neurovascular coupling mechanisms in the developing brain and the potential employment of altered neural coupling mechanisms. It could also possibly reflect that neural activity is more strongly coupled with metabolic activity. This result would be plausible as oxCCO should be more closely linked to neural activity than haemodynamic changes, given its location in the neurovascular coupling pathway.

Further work needs to be done in order to establish a more definitive pattern of results. While this analysis is useful in obtaining a first glance at the relationship between different components of the neurovascular coupling pathway in the developing human brain, it is limited in that it assumes that there is a linear relationship between neural activity, haemodynamic and metabolic changes. In fact, as I discussed in the introduction, the neurovascular coupling mechanism involves numerous metabolic pathways that are at a complex interplay, particularly in early infancy as many of the pathways are under development. Studies have shown that there is a non-linear relationship between electrophysiological activity and the haemodynamic response (Devor et al., 2003) therefore a more sophisticated form of non-linear analysis is required in order to understand the true

relationship between oscillatory activity and NIRS measures. Cross-correlation analysis would be useful in investigating how changes occurring in the time courses of both NIRS chromophores and oscillatory activity relate.

Moreover one of the biggest limitations of this study was that the changes in concentration of HbO_2, HHb and oxCCO were measured only over the right temporal cortex. Therefore, differences in activity occurring in the left and right hemispheres could not be measured. Further studies employing the use of higher density NIRS array with channels over the left and right temporal cortices could further elucidate coupling mechanisms in place during development.

Chapter 7

INFANT NIRS STUDY OF CYTOCHROME WITH EEG - VISUAL CORTEX

7.1   Introduction

The study presented in the previous chapter used social and non-social stimuli to investigate the relationship between neuronal activation, metabolic activity and subsequent blood oxygenation in the temporal cortex. The results provided evidence of the unique metabolic environment of the brain during development. Differences in correlations between chromophores were observed and an interesting result that emerged was that oxCCO coupled more strongly (negatively) with HHb rather than HbO_2, providing evidence of underdeveloped neurovascular coupling mechanisms in early infancy. Moreover, differences in the relationship between neural oscillatory activity and haemodynamic changes and changes in metabolic activity were also observed.

While the study presented in the previous chapter was a logical progression from the work presented in Chapter 4, the study presented in this chapter is a follow-on from that presented in Chapter 5. As I discussed in Chapter 5, the visual stimuli, particularly those with specific characteristics such as colour and form, provide a useful context in which to

investigate the relationship between neural activity and measured NIRS responses. This is because the variation in visual stimuli have been shown to produce differential responses in haemodynamics (Heekeren et al., 1999b) and neuronal activation (Hermes et al., 2017; Jia et al., 2013; Self et al., 2016; Henrie, 2005). Visual stimulation was used in Chapter 5 to measure changes in concentrations of NIRS chromophores simultaneously with EEG, over the occipital cortex. The results indicated that visual stimuli with differing temporal and spatial frequencies and colour do produce differential responses in haemodynamics and metabolic activity which then relate differently to underlying neuronal activity. The stimuli that activated the magnocellular pathway and produced stronger $\Delta[HbO_2]$ and $\Delta[oxCCO]$ responses correlated more strongly with an increase in beta and gamma power in comparison to alpha power. Moreover, differences were also observed in the direction of the correlations between beta and gamma power with oxCCO and HbO_2 with HbO_2 correlating positively and oxCCO correlating negatively. Therefore, the stimuli presented in Chapter 5 were modified for the infant study presented here. Additionally, a second set of visual stimuli were developed which including moving gratings.

Previous studies measuring local field potentials (LFPs) (Hermes et al., 2017) provide evidence that differing characteristics of moving gratings elicit differential oscillatory activity, particularly in the gamma band. Hence, gratings were developed to investigate how differences in neuronal activity affect the haemodynamic response and metabolic function.

The data presented here was acquired in the same testing session as that of the previous chapter. However here, only the results from the stimuli to target the visual cortex are presented. The study presented in this chapter therefore discusses the stimuli that were used to explore the relationship between NIRS and EEG measures over the visual cortex.

7.2   Methods

7.2.1   Participants

Forty-two 4-to-7-month-old healthy infants participated in the study (22 males and 20 females, mean age: 179 ± 16 days). All parents volunteered to participate in the study and provided written, informed consent. The study protocol was approved by the Birkbeck

Psychology Ethics Committee and all procedures were performed in accordance with the regulations of the Ethics Committee. Infants from varying ethnic backgrounds participated in the study and neither hair color nor skin colour was used as an exclusion criteria to screen participants. All infants who participated were healthy with no known developmental disorders and were born at term between 37 - 40 weeks gestation.

As I mentioned in the introduction of this chapter, the study presented in this chapter was carried out in the same testing session as that of the previous chapter. Therefore, the infants were the same.

7.2.2 Data acquisition

7.2.2.1 Multi-channel broadband system

The multi-channel broadband NIRS system, with infant modifications described in the previous chapter, was used for the study here. The Enobio EEG system as used again with thirty-two channels in the same configuration to acquire the EEG data.

7.2.2.2 Headgear

The headgear used for this study was the same as that described in the previous section but for ease of the reader the upper panel of Figure 7.1 shows the NIRS array, consisting of 19 channels with source - detector separation of 2.5 cm, with the exception of occipital Channels 3 and 5 which had source - detector separation of 2.90 cm. The bottom panel of Figure 7.1 shows the configuration of the EEG electrodes.
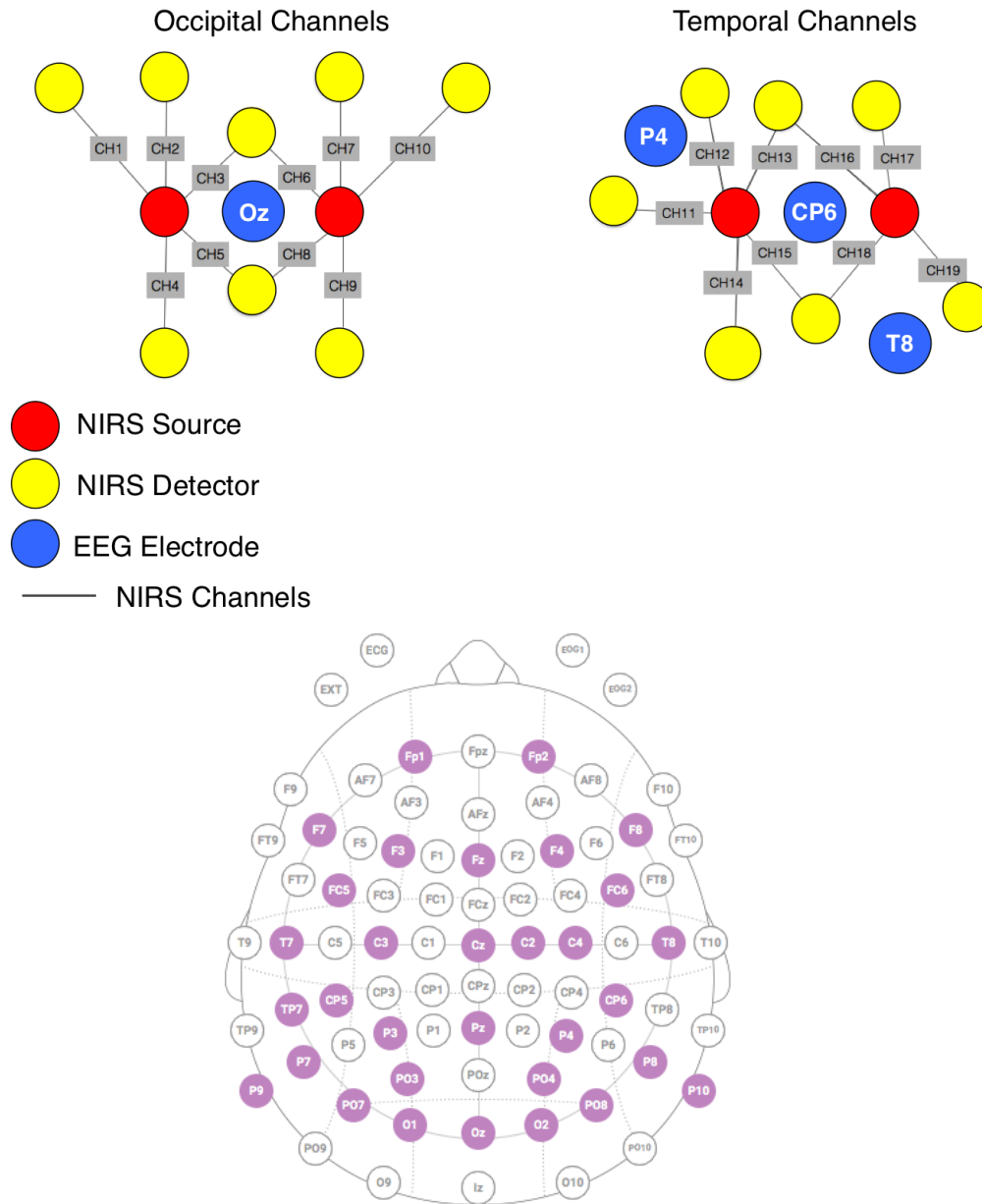
Figure 7.1: (Upper panel) Schematic diagram of the NIRS occipital and temporal arrays showing the positions sources, detectors and EEG electrodes. The red and yellow circles represent the sources and detectors respectively while the blue circle indicate nearby EEG electrodes. The black lines represent channels that are formed between sources and detectors. (Bottom panel) EEG montage used for this study.

7.2.3 Experimental Stimuli

All experimental stimuli were designed using Psychtoolbox in Matlab (Mathworks, USA). After one presentation of the social and non-social condition (i.e. after one full presentation of block 1 as described in the previous chapter), the stimuli for block 2 were presented followed by block 3. These stimuli are described in the next section.

7.2.3.1 Checkerboards

The stimuli from the study in Chapter 5 were modified for the infant study presented here. The modifications included (i) the checkerboards being presented full field rather than hemifield, (ii) they were presented as squares rather than circular checkerboards and (iii) the characteristic that differed between the two types was the colour while the temporal and spatial frequency was kept constant.

The checkerboards (block 2) had two contrast conditions:

1. The black and white checkerboard which consisted of an alternating checkerboard of black and white squares.

2. The red and green checkerboard which consisted of an alternating checkerboard of red and green squares.

Figure 7.2 shows both of the checkerboards which had the same temporal frequency of 1.5 Hz and subtended a visual angle of approximately 3°. Within block 2, the checkerboards were presented pseudorandomly for a varying duration between 6 - 8 s and were followed by the baseline condition which consisted of low contrast videos of animals walking around in a savannah. The baseline was presented for 8 s following which a fixation cross in the shape of a ball or flower appeared in the centre of the screen (identical to the social/non-social block). The fixation cross was particularly important for the visual checkerboard condition and I needed to ensure that the infants were looking at the screen when the next experimental condition was presented. Figure 7.2 shows the order of stimulus presentation for the checkerboards block. After one presentation of each of the black/white and the red/green checkerboards (i.e. after one full presentation of block 2), the stimuli for block 3 were presented which are discussed in the next section.
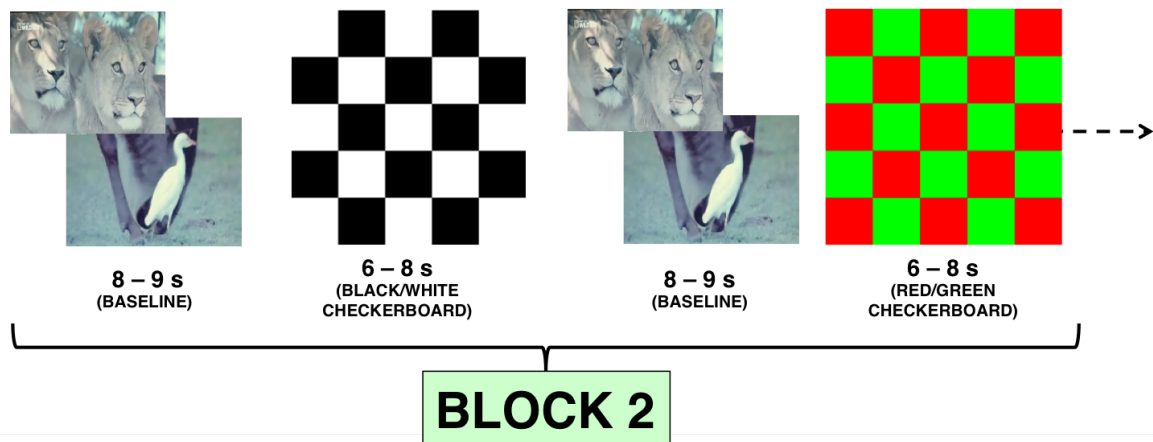
BLOCK 2

Figure 7.2: Checkerboards stimuli

7.2.3.2 Gratings

The gratings block (block 3) had two contrast conditions:

1. A low contrast grating with a low spatial frequency (1 - 2 cycles per degree).

2. A high contrast grating with medium spatial frequency (4 - 6 cycles per degree).

Figure 7.3 shows both of the gratings which drifted at the same temporal frequency of 3 Hz. Within block 3, the gratings were presented pseudorandomly for varying duration between 6 - 8 s and were followed by the identical baseline condition used for the checkerboards condition (block 2). Figure 7.3 shows the order of stimulus presentation for the gratings block. After one presentation of each of the low contrast and high contrast gratings (i.e. after one full presentation of block 3), block 1 was repeated. Figure 7.4 shows the order in which the blocks were presented.
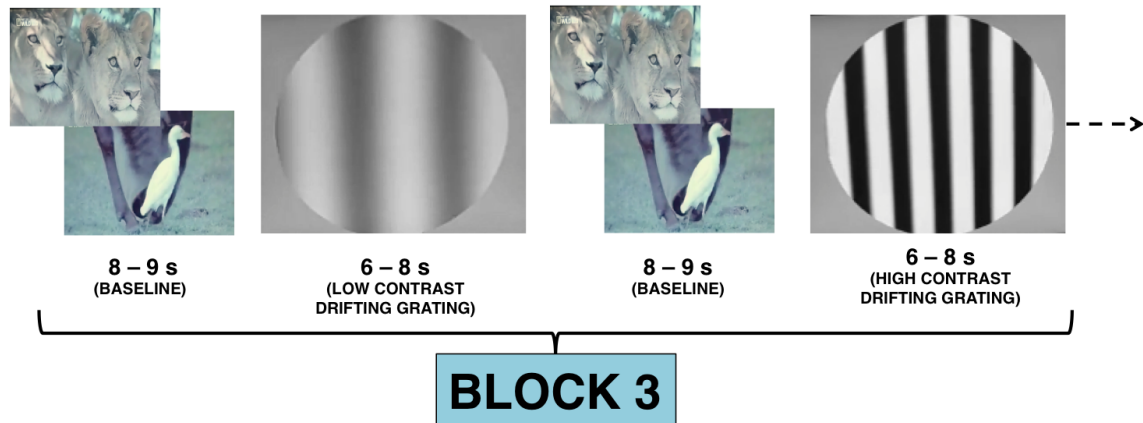
Figure 7.3: Gratings stimuli

7.2.4 Experimental Procedure

As this study was carried out in the same testing session as that presented in the previous chapter, the experimental procedure was the same and has already been described in Section 6.2.4 of Chapter 6. Blocks 1, 2 and 3 were alternated until the infants became bored or fussy and Figure 7.4 shows the order of the stimulus presentation.
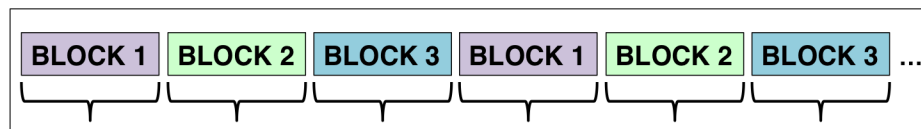
Figure 7.4: Order of stimulus presentation

7.2.5 Data analysis

7.2.5.1 NIRS

7.2.5.1.1 Pre-processing The pre-processing steps have already been described in detail in Section 6.2.5.1 of Chapter 6. The same rejection criteria described therein were used here as well.

7.2.5.1.2 Further analysis

7.2.5.1.2.1 *Statistical analysis* The same statistical analyses, described previously, were performed for each condition. This included using pairwise t-tests to establish whether

there was (i) a statistically significant difference between the condition versus the baseline and (ii) a statistically significant difference between conditions, for example black/white checkerboard versus red/green checkerboard. The statistical time window that was used to identify the maximum response in each chromophore for each condition differed here in comparison to the previous chapter. While a time window of 10 - 18 s post-stimulus onset was selected for the social/non-social conditions, a time window of 4 - 10 s post-stimulus onset was selected here (equivalent to 9 - 15 s of the block). This is much earlier than the window for social/non-social conditions because after visual inspection of the data, I found the responses to the visual stimuli over the occipital cortex followed a different pattern to those seen over the temporal cortex for the social/non-social conditions. The time period of 4 - 10 s post-stimulus onset included the range of responses across infants for the visual conditions. FDR correction was also performed.

7.2.5.1.2.2 *Secondary analyses* Difference scores, TTP analysis and cross-correlation analysis was performed, using the same procedures described in the previous chapter.

7.2.5.2 EEG

7.2.5.2.1 Pre-processing All EEG data were analysed using Matlab 2017a (Mathworks, USA) and the EEGLab Toolbox (Schwartz Centre for Computational Neuroscience, UC San Diego, USA). The EEG pre-processing has already been described in detail previously and the only step that differed here was the segmentation of the data from the visual conditions which will be described in more detail in the following section.

7.2.5.2.1.1 *Segmentation*

Checkerboards Condition The EEG data from each of the checkerboard conditions were segmented over every alternation of the checkerboard such that each 6 - 8 s checkerboard trial resulted in approximately 6 - 8 epochs.

Gratings Condition The EEG data from the gratings condition were segmented over every change in direction of the drifting gratings such that each 6 - 8 s gratings trial resulted

in 2 epochs.

7.2.5.2.2 Further Analyses

Checkerboards and Gratings Condition

1. Wavelet-based decomposition was performed for the channels over the occipital cortex in order to obtain the evoked oscillations occurring in response to the stimuli.

2. Topographical maps of spectral power were generated at specific frequency bands.

7.2.5.2.3 Statistical Analysis

A time-window of interest was selected; 100 - 300 ms post-stimulus onset for the checkerboard conditions and 50 - 400 ms for the gratings conditions. Within these time windows, the mean alpha, beta and gamma power were averaged and pairwise t-tests were performed over occipital, parieto-occipital and parietal channels to assess whether there was significant difference between conditions. The time-windows were chosen after visual inspection of time-frequency results and were thought to include the majority of the stimulus-evoked activity .

7.3 Results

7.3.1 NIRS

As described previously, thirty-two infants, out of forty-two, were included in the final analysis for NIRS. 7 infants were excluded due to having more than 40% of channels with poor data quality, 2 infants were excluded due to poor signal-to-noise ratio and low intensity counts and 1 infant was excluded due to an insufficient number of trials.

7.3.1.1 Checkerboards Task

7.3.1.1.1 Black/white checkerboard

The upper panel of Figure 7.5 displays the grand averaged changes in concentration of HbO_2 (red), HHb (blue) and oxCCO (green) in all channels, across 32 participants, in response to the black/white checkerboard. oxCCO

has been magnified (x2.5) and the bottom panel shows the changes in concentration of oxCCO only, prior to magnification. As I explained previously, the experimental stimuli were presented in a jittered design varying between 6 - 8 s and this has been indicated in the grand average figures by means of the pink and purple boxes. The pink box indicates the minimum time period for the stimulus presentation (6 s) while the purple box extends to the maximum period (8 s).

Prior to comparison between conditions i.e. black/white checkerboard versus red/green, t-tests were performed to assess whether there were statistically significant responses in $\Delta[HbO_2]$, $\Delta[HHb]$ and $\Delta[oxCCO]$ versus the baseline, in each channel. Tables 7.1 - 7.3 show the mean maximum changes in $\Delta[HbO_2]$, $\Delta[HHb]$ and $\Delta[oxCCO]$ respectively along with their t and p values. After FDR-correction, no channels displayed a statistically significant increase in $\Delta[HbO_2]$ from baseline, except Channel 15. Majority of the channels over the temporal cortex displayed a significant increase in $\Delta[oxCCO]$ versus the baseline.
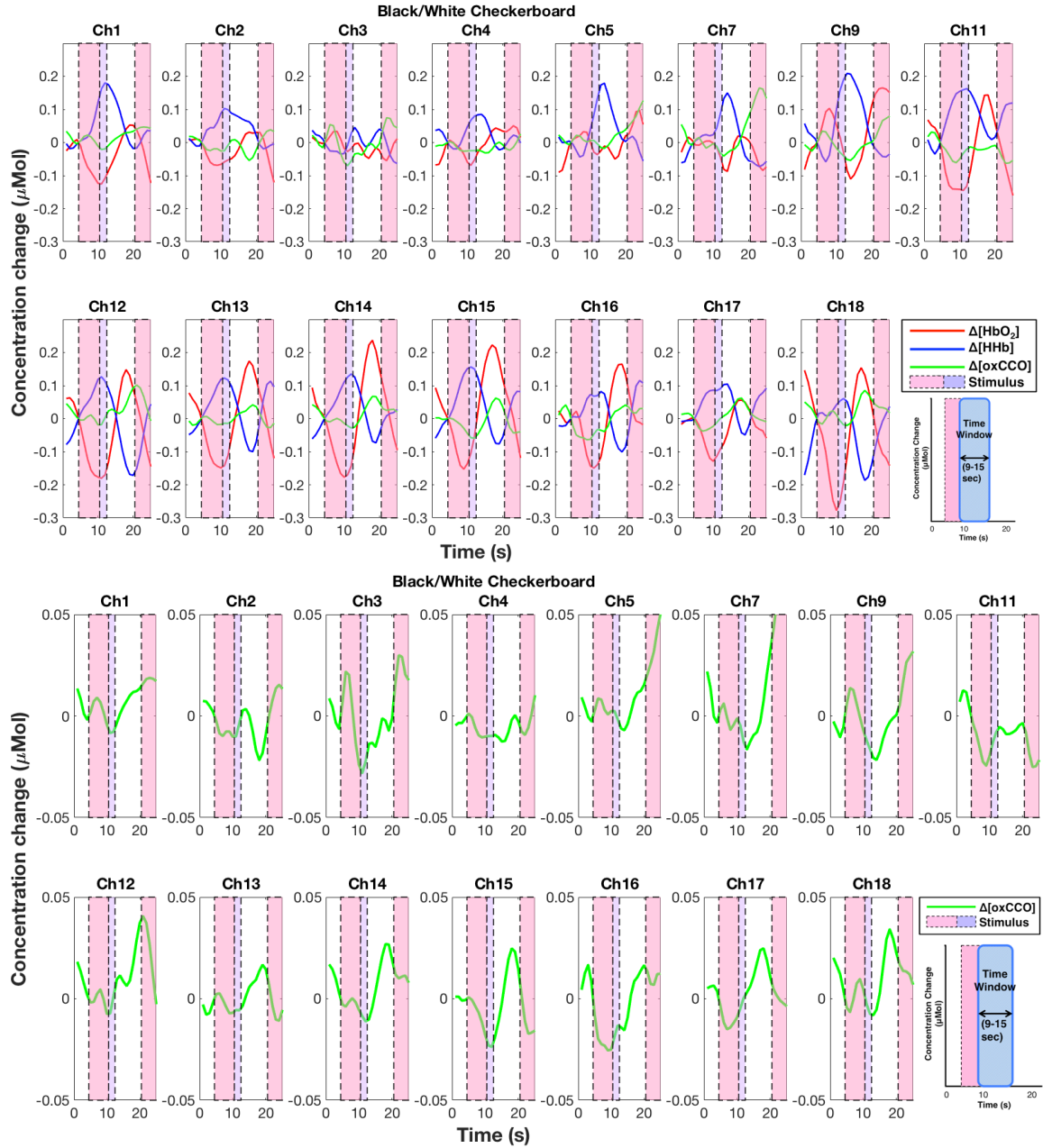
Figure 7.5: Observed chromophore concentration changes in HbO$_2$, HHb and oxCCO in response to the black/white checkerboard condition with oxCCO magnified x2.5 (Upper panel) and oxCCO not magnified (Bottom panel). The statistical time window of 4 - 10 s post-stimulus onset is indicated.

Channel	$\Delta[HbO_2]$ Mean Maximum Change	t_{HbO_2}	p_{HbO_2}	FDR corrected p_{HbO_2}
1	0.0890	1.53	0.1369	0.1633
2	0.1230	2.0117	0.0547	0.0939
3	0.1743	2.6195	0.0164	0.0616
4	0.1247	1.7447	0.0916	0.1323
5	0.1856	2.1574	0.04	0.0858
7	0.1717	3.0389	0.0078	0.0586
9	0.2365	2.7321	0.0119	0.0594
11	0.1234	2.3076	0.0281	0.0764
12	0.0594	1.1511	0.2591	0.2591
13	0.1175	1.7132	0.0970	0.1323
14	0.1458	2.27	0.0306	0.0764
15	0.2113	3.7024	$p < 0.001$	0.0124*
16	0.0839	1.9881	0.0563	0.0939
17	0.0690	1.5164	0.1415	0.1633
18	0.0990	1.4635	0.1545	0.1655

Table 7.1: Mean maximum change, t and p values for the black/white checkerboard condition versus baseline for HbO_2. Channels with a significant response to the condition versus the baseline are indicated with an asterisk, for the FDR corrected p values.

Channel	Δ[HHb] Mean Maximum Change	t_{HHb}	p_{HHb}	FDR corrected p_{HHb}
1	-0.0053	-0.1735	0.8635	0.9251
2	-0.0773	-1.5249	0.1394	0.3007
3	-0.1829	-3.6738	0.0015	0.0226*
4	-0.0393	-1.0556	0.2999	0.4998
5	-0.0851	-1.4943	0.1467	0.3007
7	-0.0565	-0.9914	0.3362	0.5044
9	-0.0671	-1.5828	0.1271	0.3007
11	-0.0029	-0.0525	0.9584	0.9584
12	-0.0476	-1.4913	0.1467	0.3007
13	-0.0525	-1.4394	0.1604	0.3007
14	-0.0137	-0.2790	0.7822	0.9025
15	-0.0218	-0.6232	0.5377	0.6721
16	-0.0646	-1.4806	0.1495	0.3007
17	-0.0211	-0.6595	0.5154	0.6721
18	-0.1283	-2.8082	0.009	0.0673

Table 7.2: Mean maximum change, t and p values for the black/white checkerboard condition versus baseline for HHb. Channels with a significant response to the condition versus the baseline are indicated with an asterisk, for FDR corrected p values.

Channel	Δ[oxCCO] Mean Maximum Change	t_{oxCCO}	p_{oxCCO}	FDR corrected p_{oxCCO}
1	0.0388	4.1070	p < 0.001	0.0045*
2	0.0477	3.1456	0.0041	0.0141*
3	0.0471	2.9721	0.0075	0.0141*
4	0.0242	2.1746	0.038	0.0474*
5	0.0530	2.9782	0.0061	0.0141*
7	0.0323	0.8814	0.3911	0.3911
9	0.0413	2.2639	0.0333	0.0454*
11	0.0305	1.9934	0.0554	0.0593
12	0.0382	2.5662	0.0157	0.0236*
13	0.0348	2.8925	0.0071	0.0141*
14	0.0324	3.2113	0.0031	0.0141*
15	0.0278	2.5876	0.0146	0.0236*
16	0.0232	2.1094	0.0437	0.0504
17	0.0408	3.3108	0.0027	0.0141*
18	0.0496	3.0349	0.0052	0.0141*

Table 7.3: Mean maximum change, t and p values for the black/white checkerboard condition versus baseline for oxCCO. Channels with a significant response to the condition versus the baseline are indicated with an asterisk, for the FDR corrected p values.

7.3.1.1.2 Red/green checkerboard The upper panel of Figure 7.6 displays the grand averaged changes in concentration of HbO_2 (red), HHb (blue) and oxCCO (green) in all channels, across 32 participants, in response to the black/white checkerboard. oxCCO has been magnified (x2.5) and the bottom panel shows the changes in concentration of oxCCO only, prior to magnification.

Prior to comparison between conditions i.e. black/white checkerboard versus red/green, t-tests were performed to assess whether there were statistically significant responses in $\Delta[HbO_2]$, $\Delta[HHb]$ and $\Delta[oxCCO]$ versus the baseline, in each channel. Tables 7.4 - 7.6 show the mean maximum changes in $\Delta[HbO_2]$, $\Delta[HHb]$ and $\Delta[oxCCO]$ respectively along with their t and p values. Strong decreases in $\Delta[HbO_2]$ from baseline were seen in majority of channels over the occipital cortex while an increase in $\Delta[HbO_2]$ was seen in temporal

Channels 14, 15 and 18. An increase in Δ[HHb] was observed in majority of the channels while for Δ[oxCCO] an increase was observed in Channels 1, 4, 9 and 11.
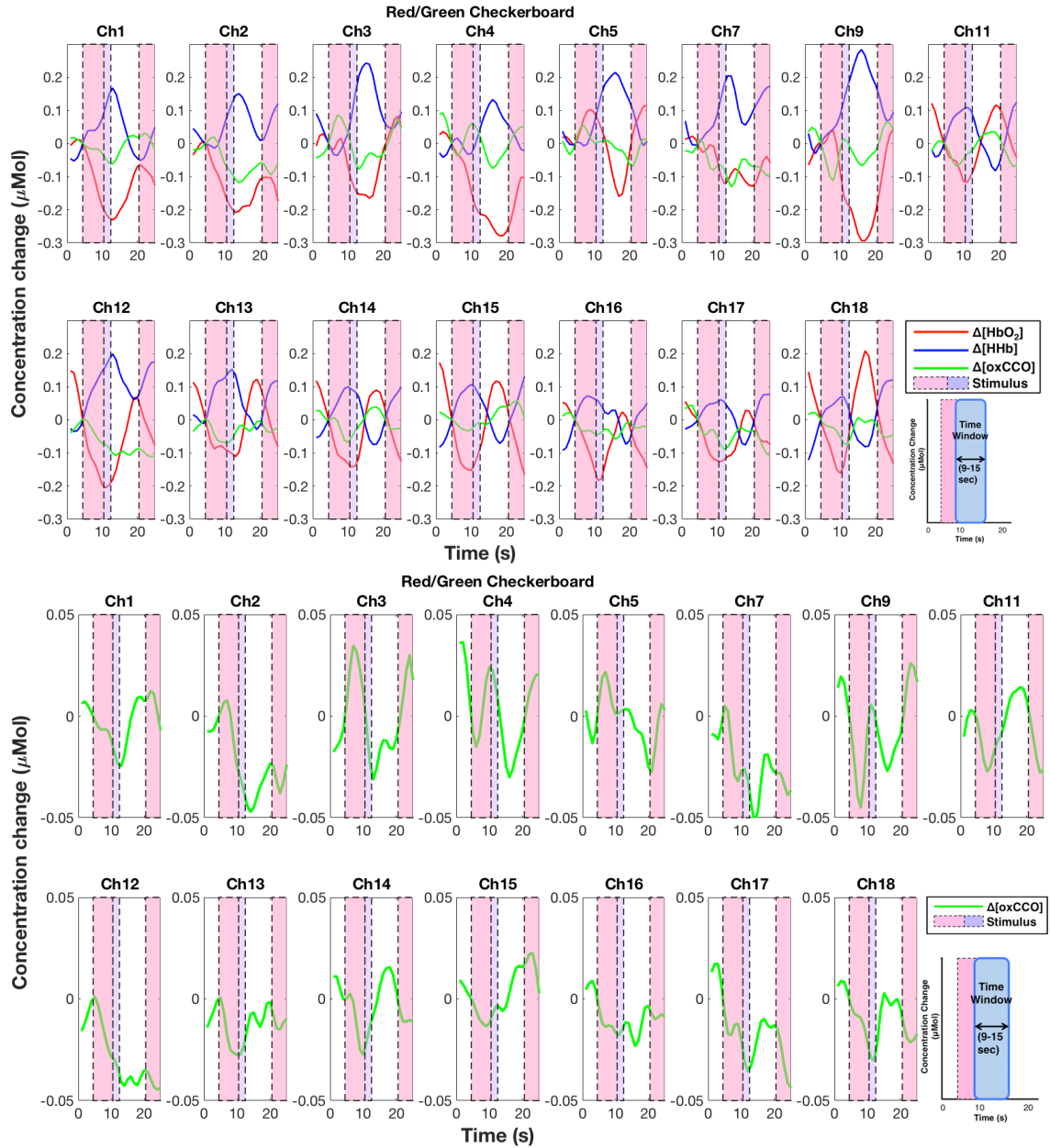
Figure 7.6: Observed chromophore concentration changes in HbO$_2$, HHb and oxCCO in response to the red/green checkerboard stimulus with oxCCO magnified x2.5 (Upper panel) and oxCCO not magnified (Bottom panel). The statistical time window of 4 - 10 s post-stimulus onset is indicated.

Channel	Δ[HbO$_2$] Mean Maximum Change	t_{HbO_2}	p_{HbO_2}	FDR corrected p_{HbO_2}
1	-0.0327	-0.6932	0.4937	0.7405
2	-0.0115	-0.2274	0.8219	0.9299
3	0.0919	2.0340	0.0554	0.2020
4	0.0065	0.1569	0.8764	0.9299
5	0.2721	3.0120	0.0056	0.0418*
7	0.1338	1.9518	0.0687	0.2020
9	0.1165	1.1495	0.2621	0.4369
11	0.0955	1.5909	0.1221	0.2617
12	-0.0041	-0.0887	0.9299	0.9299
13	0.096	1.3485	0.1876	0.3517
14	0.1130	1.8069	0.0808	0.2020
15	0.1358	2.7125	0.0108	0.0540
16	0.0226	0.5391	0.5939	0.7424
17	0.0266	0.6129	0.5453	0.7424
18	0.2244	3.2893	0.0027	0.0407*

Table 7.4: Mean maximum change, t and p values for the red/green checkerboard condition versus baseline for HbO$_2$. Channels with a significant response to the condition versus the baseline are indicated with an asterisk, for the FDR corrected p values.

Channel	Δ[HHb] Mean Maximum Change	t_{HHb}	p_{HHb}	FDR corrected p_{HHb}
1	-0.0448	-0.7745	0.4449	0.5977
2	-0.0465	-0.9856	0.3334	0.5557
3	-0.0760	-1.0474	0.3074	0.5557
4	-0.1265	-2.5303	0.0171	0.1206
5	-0.0406	-0.7159	0.4802	0.5977
7	0.0085	-0.1679	0.8687	0.9308
9	-0.0590	-0.6565	0.5180	0.5977
11	-0.0947	-2.2672	0.0307	0.1206
12	-0.0004	-0.0108	0.9914	0.9914
13	-0.0415	-0.7118	0.4821	0.5977
14	-0.0879	-2.1664	0.0384	0.1206
15	-0.0837	-1.5992	0.1199	0.2998
16	-0.0731	-1.4128	0.1684	0.3608
17	-0.0666	-2.1596	0.0402	0.1206
18	-0.1574	-2.5219	0.0176	0.1206

Table 7.5: Mean maximum change, t and p values for the red/green checkerboard condition versus baseline for HHb. Channels with a significant response to the condition versus the baseline are indicated with an asterisk, for the FDR corrected p values.

Channel	Δ[oxCCO] Mean Maximum Change	t_{oxCCO}	p_{oxCCO}	FDR corrected p_{oxCCO}
1	0.0338	2.5196	0.0175	0.0438*
2	0.0198	1.3763	0.1805	0.2256
3	0.0567	2.4583	0.0232	0.0497*
4	0.0606	4.3608	$p < 0.001$	0.0022*
5	0.0650	2.6578	0.0131	0.0392*
7	0.0203	0.7559	0.4607	0.4936
9	0.636	3.6480	0.0013	0.0067*
11	0.0380	3.6155	0.0011	0.0067*
12	0.0049	0.3941	0.6964	0.6965
13	0.0262	2.1758	0.037	0.0626
14	0.0244	2.0557	0.0486	0.0729
15	0.0279	2.2240	0.0336	0.0626
16	0.0222	1.7721	0.0869	0.1185
17	0.0141	1.2290	0.2301	0.2655
18	0.0348	2.6994	0.0116	0.0392*

Table 7.6: Mean maximum change, t and p values for the red/green checkerboard condition versus baseline for oxCCO. Channels with a significant response to the condition versus the baseline are indicated with an asterisk, for the FDR corrected p values.

7.3.1.1.3 Black/white versus Red/green checkerboard Pairwise t-tests were performed to assess whether there was a statistically significant difference between responses for the black/white versus red/green checkerboards. Given that these stimuli were similar to those used in Chapter 5, in accordance with those results, I expected a greater response to the black/white condition in comparison to the red/green. I was also expecting a differential response in oxCCO given the different metabolic demands of the pathways involved in processing these stimuli, that is the parvocellular pathway (targeted by the red/green checkerboard) is known to have a higher concentration of CCO. Significant differences were found between the two conditions only for oxCCO in Channel 4 ($t = -2.2109, p = 0.0358$, mean difference = 0.0364 μMol) and no significant differences were found in any of the channels for HHb and HbO_2. The p values reported here are

non-FDR corrected values. The tables including the statistics (t and p values) for each channel and chromophore are included in the appendix. Figure 7.7 indicates the channels where there was a statistically significant difference between black/white and red/green conditions for Δ[oxCCO] (green) on a topographical map.
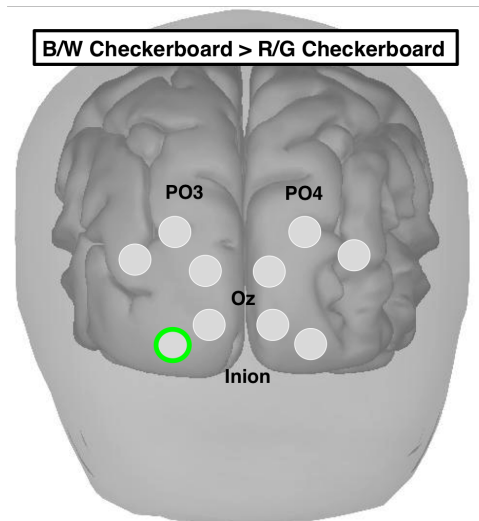
Figure 7.7: Topographical map of the difference in mean maximum change between the two checkerboard conditions. The green circle represents the channel with a statistically significant difference between conditions for oxCCO.

Channel 4 showed a statistically significant difference between the checkerboard conditions for oxCCO. The observed changes in concentration HbO_2, HHb and oxCCO from this channel are shown in Figure 7.8, for both black/white and red/green checkerboards and include the standard deviations.
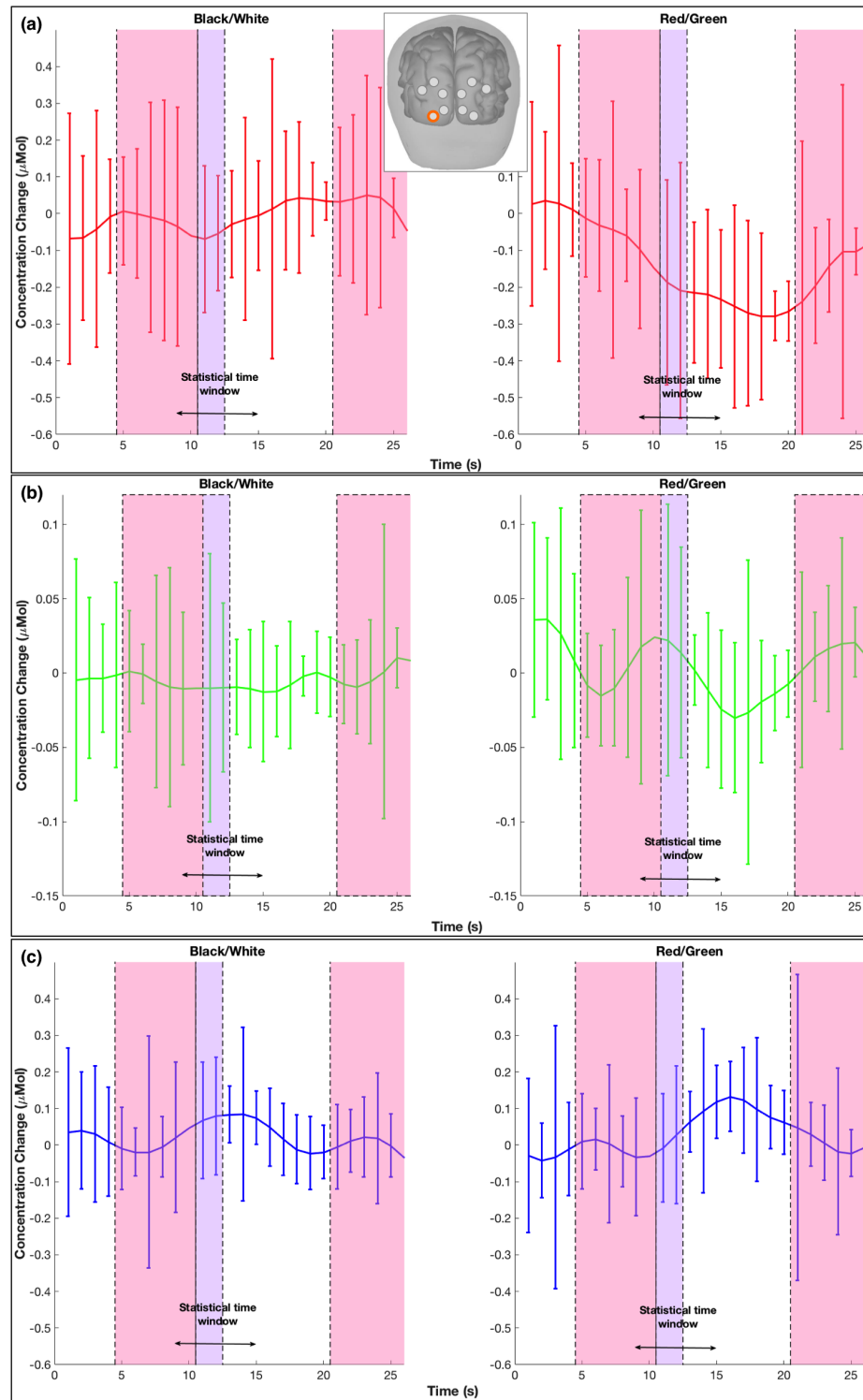
Figure 7.8: Observed changes in the concentration of (a) HbO$_2$ (b) oxCCO and (c) HHb in response to the black/white checkerboard (left) and red/green checkerboard (right) in Channel 4. The statistical time window is indicated. The error bars represent standard deviations.

The mean and standard deviations (represented through error bars) of the maximum responses from each of the occipital channels are shown in Figure 7.8 with HbO_2 in red, HHb in blue and oxCCO in green, for both checkerboard conditions (labelled as "BW" and "RG" on the x-axis), HbO_2 and HHb are scaled to the y-axis on the left and oxCCO is scaled to the y-axis shown on the right in the figure for each channel. The largest increases in Δ[oxCCO] can be seen in Channels 5 and 9 for the black/white condition and Channels 3 and 9 for the red/green condition. Channels 5 and 9 also display the largest responses for both conditions for HbO_2.
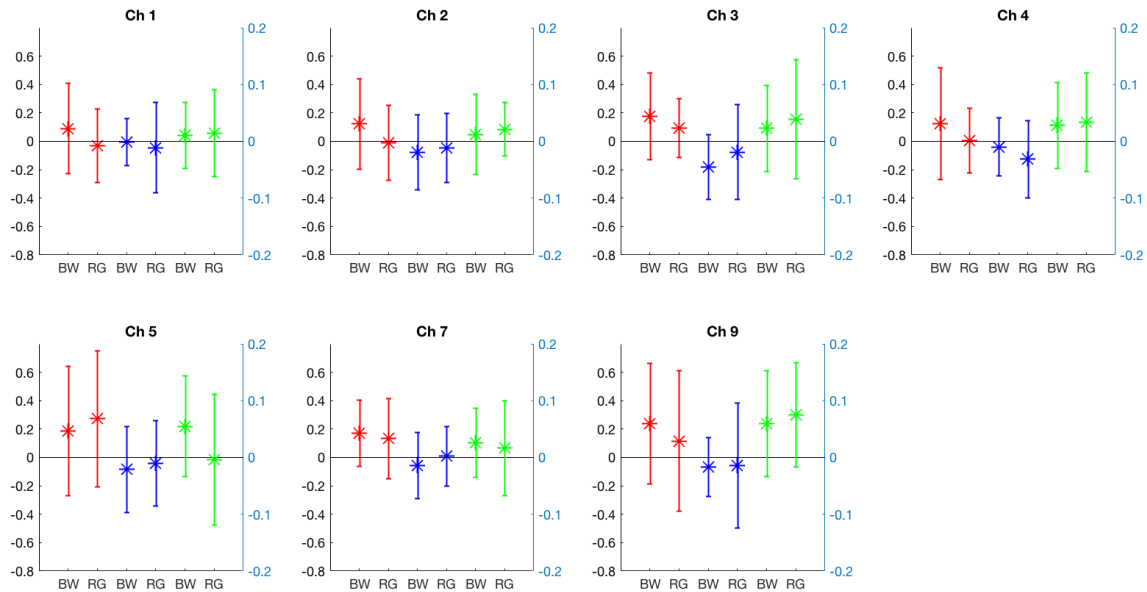
Figure 7.9: Mean and standard deviations of the maximum responses of HbO_2 (red), HHb in (blue) and oxCCO (green), for both black/white and red/green conditions which are labelled as "BW" and "RG" respectively on the x-axis, for channels over the occipital cortex. The y-axis on the left is for HbO_2 and HHb while the y-axis on the right is for oxCCO. The error bars represent standard deviations.

7.3.1.1.3.1 *Difference scores* The differences in the mean maximum change in concentration between the black/white and red/green checkerboard conditions were calculated for each of the channels over the occipital cortex. Figure 7.10 shows the difference in the maximal response for each chromophore, with each bar in the graph representing a channel over the occipital lobe. Positive values indicate a a stronger response to the

black/white condition, while negative values indicate a stronger response to the red/green condition. Channels 6, 8 and 10 appear empty as they were excluded from the analysis due to reasons specified previously. As with the results presented in Chapter 5, a greater response to the black/white condition was expected for HbO_2 and oxCCO in comparison to the red/green condition. Due to the differing metabolic demand of the pathways involved in processing these stimuli, differences in the oxCCO response were expected. For HbO_2 majority of the channels, with the exception of Channel 5, display greater responses to the black/white condition while for oxCCO and HHb, many channels show a greater increase in Δ[oxCCO] and decrease in Δ[HHb] in response to the red/green condition.
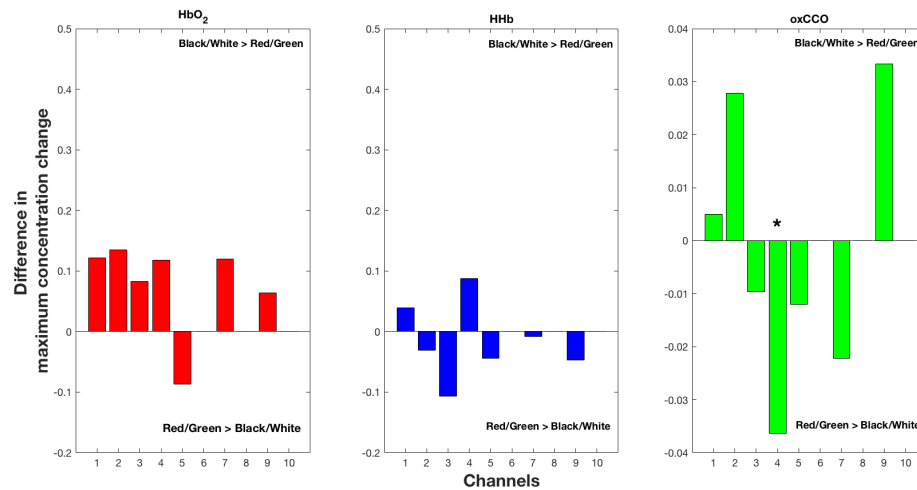
Figure 7.10: Bar graph showing the difference in the mean maximum change, in each chromophore, between the two checkerboard conditions for the channels located over the occipital cortex. Positive values indicate a greater response to the red/green condition while negative values indicate a greater response to the black/white condition. Channels with a significant difference between conditions are indicated with an asterisk.

7.3.1.1.3.2 *Time to peak*   The TTP for each chromophore in response to the checkerboard conditions was calculated, in the chosen time window for statistical analysis (4 - 10 s post-stimulus onset here). Heterogeneity in the TTP was observed. The results from this can be found in the appendix.

7.3.1.1.3.3 *Cross-correlations*   Cross-correlations were performed for both conditions between chromophores in order to observe the relationship between changes in energy metabolism and haemodynamics in occipital cortex. Given that the cross-correlation anal-

ysis from Chapter 6 showed differences in coupling between oxCCO and HbO_2 in the adult and the infant brain, it was important to perform the cross-correlations in the occipital cortex as well. Moreover, these correlations could be directly compared with the adult correlations as they were performed over the same brain region.

The cross-correlations were performed between (i) HbO_2 and oxCCO, (ii) HHb and oxCCO and (iii) HbO_2 and oxCCO for all the channels. Figure 7.11 shows the average cross-correlations across occipital channels, for the black/white checkerboard (upper panel) and red/green checkerboard (bottom panel). The error bars represent standard deviations. For oxCCO and HHb, a strong negative correlation was seen with $r_{BW} = 0.44$ and $r_{RG} = 0.48$ and zero time-lag for both conditions. Weaker correlations were observed between HbO_2 - HHb and HbO_2 - oxCCO for both conditions. The correlations from individual channels can be found in Appendix C.
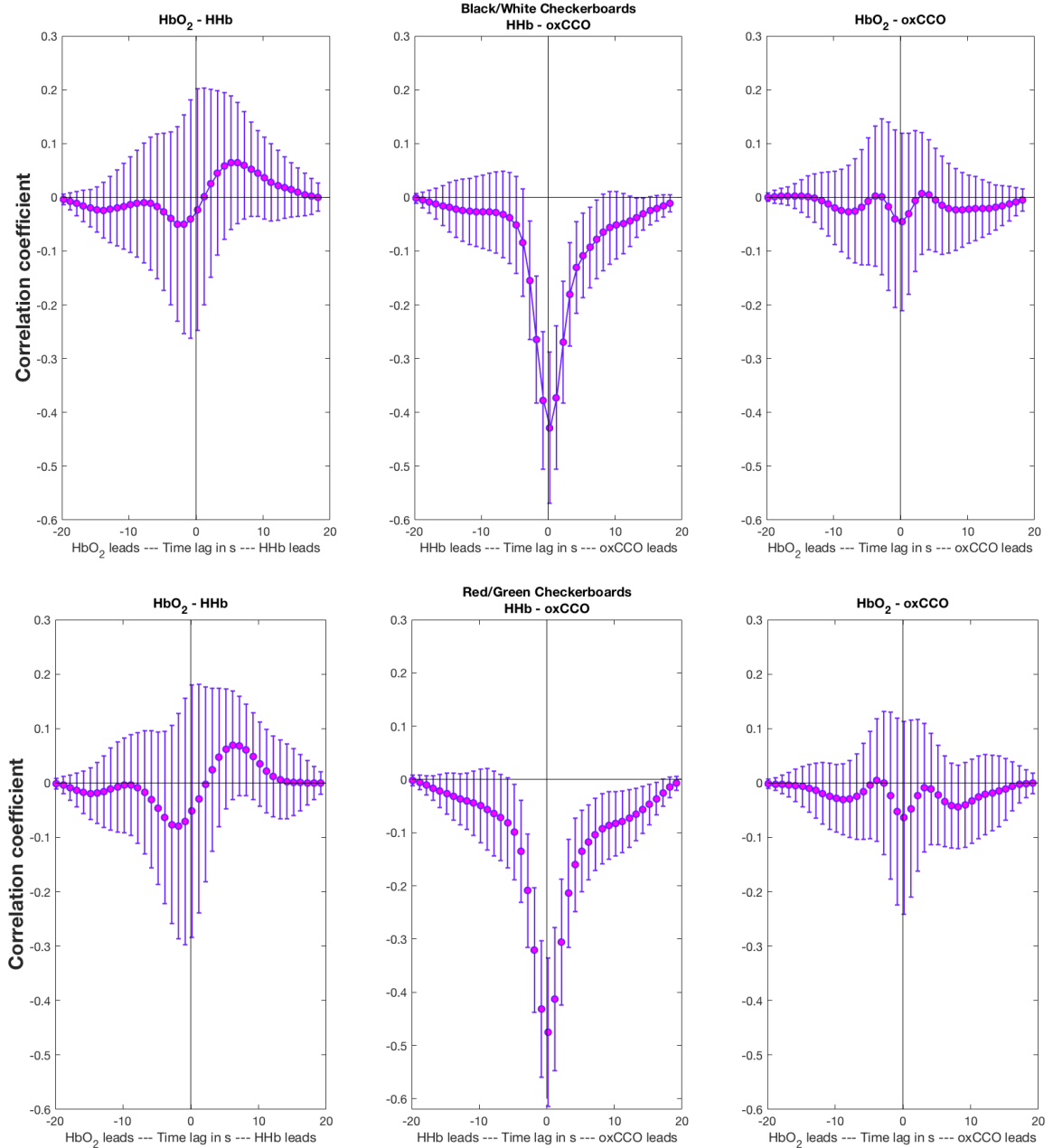
Figure 7.11: Average of the cross-correlation across the occipital channels for the black/white condition (upper panel) and red/green condition (bottom panel). The error bars represent standard deviations

7.3.1.2 Gratings Task

7.3.1.2.1 Low contrast gratings The upper panel of Figure 7.12 displays the grand averaged changes in concentration of HbO_2 (red), HHb (blue) and oxCCO (green) in all channels, across 32 participants, in response to the low contrast gratings. oxCCO has been

magnified (x2.5) and the bottom panel shows the changes in concentration of oxCCO only, prior to magnification.

Prior to comparison between conditions i.e. low contrast gratings versus high contrast, t-tests were performed to assess whether there were statistically significant responses in $\Delta[\text{HbO}_2]$, $\Delta[\text{HHb}]$ and $\Delta[\text{oxCCO}]$ versus the baseline, in each channel. Tables 7.7 - 7.9 show the mean maximum changes in $\Delta[\text{HbO}_2]$, $\Delta[\text{HHb}]$ and $\Delta[\text{oxCCO}]$ respectively along with their t and p values. A significant increase in $\Delta[\text{HbO}_2]$ was observed in occipital channels 2, 3 and 7 and in temporal channels 13, 14, 15 and 18. Channels 3, 4, 5 and 9 displayed a significant increase in $\Delta[\text{HHb}]$ in response to the stimulus versus the baseline. An increase in $\Delta[\text{oxCCO}]$ was seen in occipital Channels 2 and 11 and temporal Channels 13, 16 and 18.
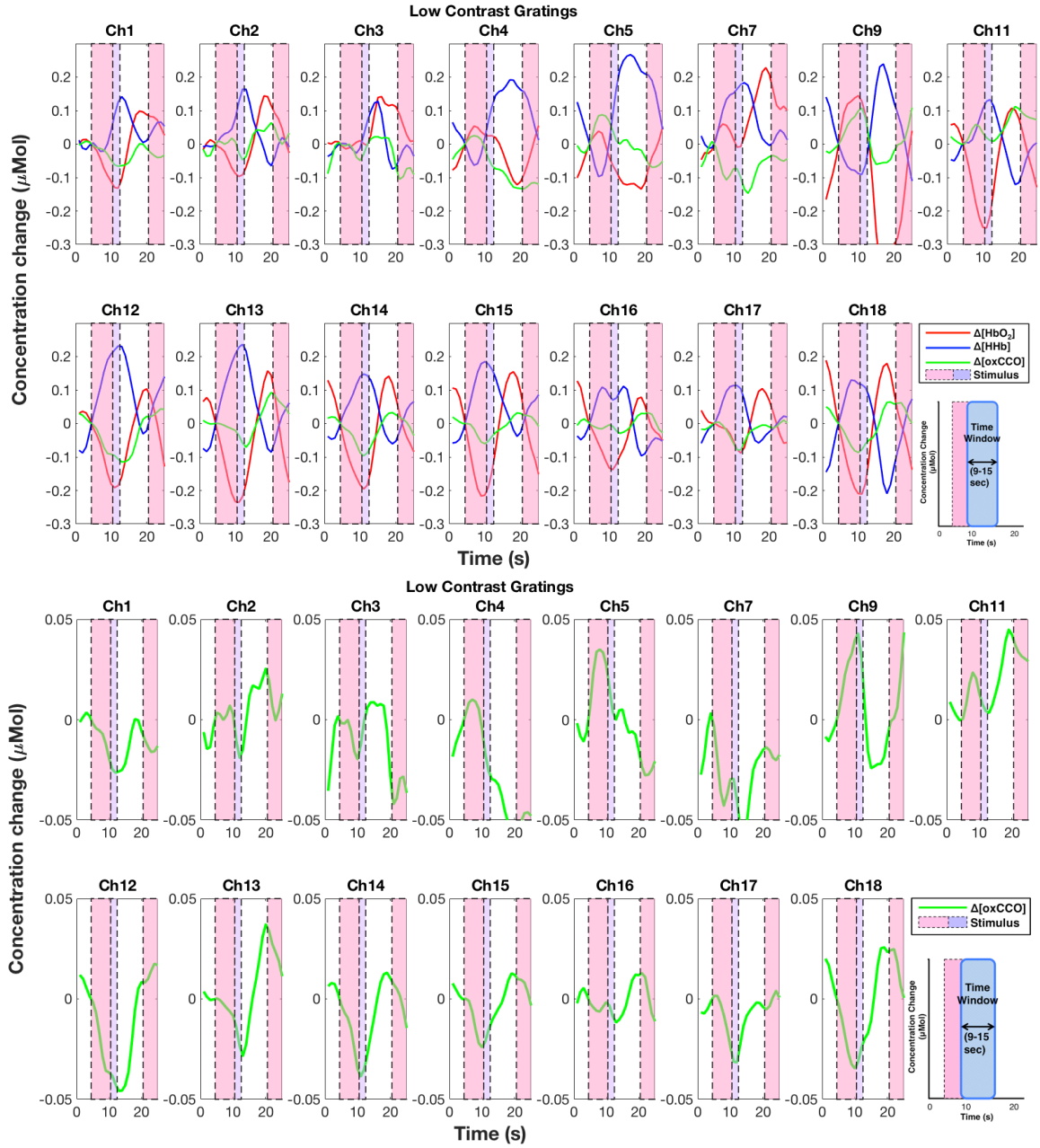
Figure 7.12: Observed chromophore concentration changes in HbO$_2$, HHb and oxCCO in response to the low contrast gratings with oxCCO magnified x2.5 (Upper panel) and oxCCO not magnified (Bottom panel). The statistical time window of 4 - 10 s post-stimulus onset is indicated.

Channel	$\Delta[HbO_2]$ Mean Maximum Change	t_{HbO_2}	p_{HbO_2}	FDR corrected p_{HbO_2}
1	0.1210	1.9124	0.0657	0.0986
2	0.1213	1.9531	0.0616	0.0986
3	0.2466	3.4070	0.0028	0.0210*
4	0.1961	2.8313	0.0083	0.0404*
5	0.1878	2.0666	0.0485	0.0986
7	0.2425	2.7770	0.0135	0.0404*
9	0.2943	3.4637	0.0021	0.0210*
11	0.0835	1.4911	0.1464	0.1689
12	0.0794	1.7022	0.0994	0.1356
13	0.0368	0.6201	0.5399	0.5399
14	0.1082	1.5077	0.1421	0.1689
15	0.1322	1.9739	0.0574	0.0986
16	0.0867	1.4007	0.1719	0.1842
17	0.1335	2.7129	0.0117	0.0404*
18	0.1441	2.0966	0.0452	0.0986

Table 7.7: Mean maximum change, t and p values for the low contrast gratings condition versus baseline for HbO_2. Channels with a significant response to the condition versus the baseline are indicated with an asterisk, for the FDR corrected corrected p values.

Channel	Δ[HHb] Mean Maximum Change	t_{HHb}	p_{HHb}	FDR corrected p_{HHb}
1	-0.0864	-1.9902	0.0561	0.1402
2	-0.0548	-1.5162	0.1415	0.2359
3	-0.1239	-3.1124	0.0055	0.0412*
4	-0.0855	-2.1228	0.0424	0.1273
5	-0.1068	-2.3988	0.0236	0.0886
7	0.0455	0.8686	0.3979	0.4974
9	-0.2406	-3.7588	0.001	0.0153
11	-0.0582	-1.4075	0.1696	0.2543
12	0.0616	1.7215	0.0957	0.2053
13	0.0078	0.2303	0.8195	0.8195
14	-0.0189	-0.7254	0.4738	0.5467
15	-0.0156	-0.4038	0.6892	0.7384
16	-0.0470	-1.0979	0.2813	0.3836
17	-0.0746	-1.6361	0.1139	0.2135
18	-0.1290	-2.7762	0.0097	0.0485*

Table 7.8: Mean maximum change, t and p values for the low contrast gratings condition versus baseline for HHb. Channels with a significant response to the condition versus the baseline are indicated with an asterisk, for the FDR corrected corrected p values.

Channel	Δ[oxCCO] Mean Maximum Change	t_{oxCCO}	p_{oxCCO}	FDR corrected p_{oxCCO}
1	0.0361	2.6697	0.0123	0.0308*
2	0.0545	2.8396	0.0087	0.0260*
3	0.0604	2.2897	0.0330	0.0551
4	0.0301	2.4835	0.019	0.0408*
5	0.0736	3.4526	0.0018	0.0092*
7	0.0021	0.0710	0.9443	0.9443
9	0.0931	5.2934	p < 0.001	p < 0.001*
11	0.0614	4.0663	3.18e-04	0.0024
12	0.0008	0.0733	0.9420	0.9443
13	0.0301	2.9281	0.0065	0.0242*
14	0.0101	0.8852	0.3831	0.4420
15	0.0194	1.7514	0.0898	0.1224
16	0.0308	1.9986	0.0551	0.0827
17	0.0182	1.5070	0.1439	0.1798
18	0.0362	2.4161	0.0225	0.0421*

Table 7.9: Mean maximum change, t and p values for the low contrast gratings condition versus baseline for oxCCO. Channels with a significant response to the condition versus the baseline are indicated with an asterisk, for the FDR corrected corrected p values.

7.3.1.2.2 High contrast gratings

The upper panel of Figure 7.13 displays the grand averaged changes in concentration of HbO_2 (red), HHb (blue) and oxCCO (green) in all channels, across 32 participants, in response to the black/white checkerboard. oxCCO has been magnified (x2.5) and the bottom panel shows the changes in concentration of oxCCO only, prior to magnification.

Prior to comparison between conditions, t-tests were performed to assess whether there were statistically significant responses in Δ[HbO_2], Δ[HHb] and Δ[oxCCO] versus the baseline, in each channel. Tables 7.10 - 7.12 show the mean maximum changes in Δ[HbO_2], Δ[HHb] and Δ[oxCCO] respectively along with their t and p values. An increase in Δ[HbO_2] in response to the stimulus compared to baseline was seen in Channels 5, 12, 13, 15 and 18 while an increase in Δ[HHb] was seen in Channels 4, 7 and 9. A significant increase in

Δ[oxCCO] was seen in occipital Channels 2, 3, 4 and temporal Channels 16 and 18.
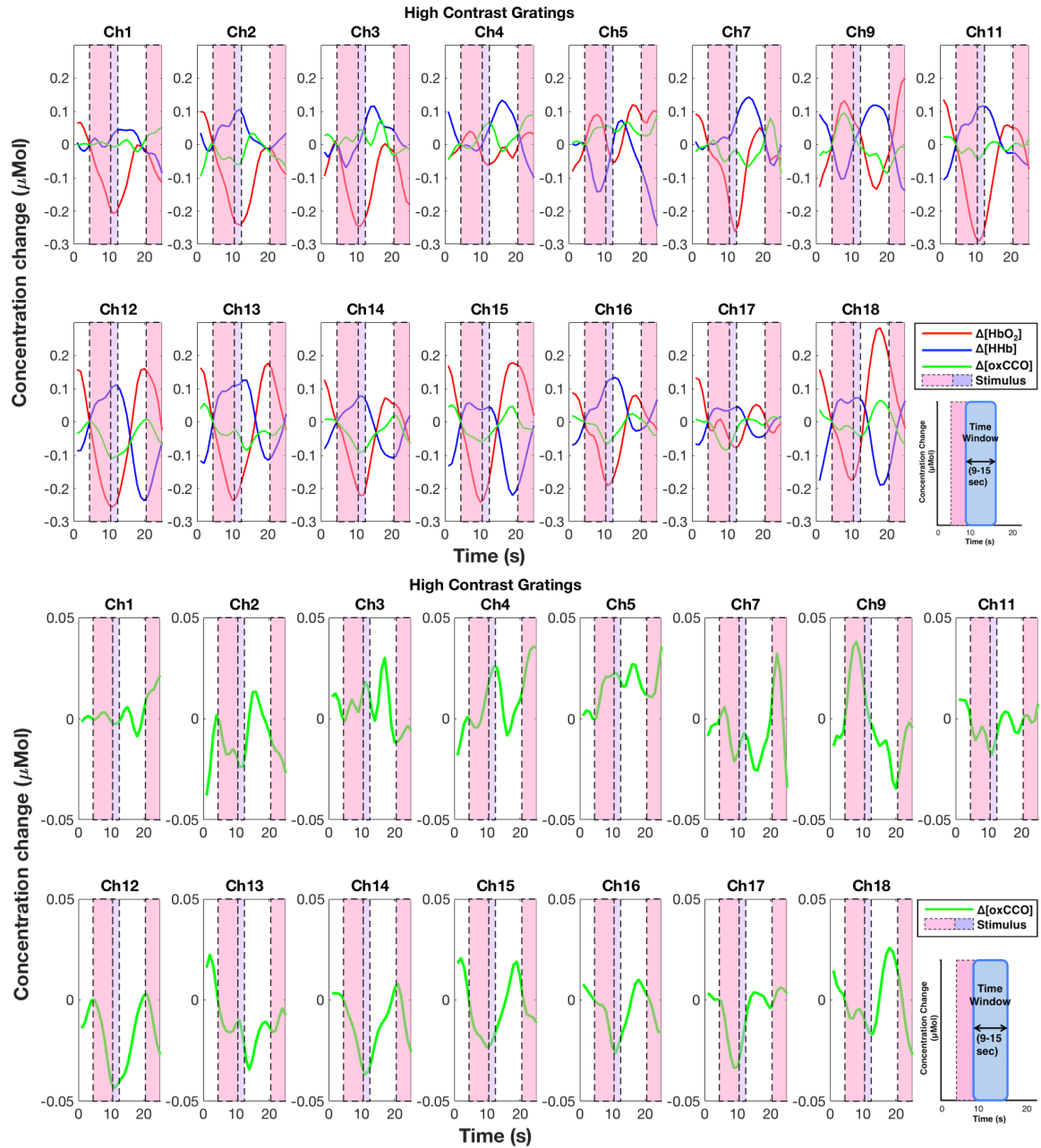
Figure 7.13: Observed chromophore concentration changes in HbO₂, HHb and oxCCO in response to the high contrast gratings with oxCCO magnified x2.5 (Upper panel) and oxCCO not magnified (Bottom panel). The statistical time window of 4 - 10 s post-stimulus onset is indicated.

Channel	$\Delta[HbO_2]$ Mean Maximum Change	t_{HbO_2}	p_{HbO_2}	FDR corrected p_{HbO_2}
1	0.0038	0.07136	0.9436	0.9995
2	-0.027	-0.4123	0.6835	0.9320
3	0.0634	1.0594	0.3020	0.6472
4	0.1374	2.2655	0.0311	0.0934
5	0.2446	2.9145	0.0071	0.0354*
7	0.0137	0.1657	0.8704	0.9995
9	0.2594	3.8898	$p < 0.001$	0.0111*
11	0.0284	0.4342	0.6672	0.9320
12	-0.0001	-0.00061	0.9995	0.9995
13	0.0158	0.2470	0.8065	0.9995
14	0.0529	0.7152	0.48	0.7999
15	0.0868	1.5020	0.1432	0.3580
16	0.0357	0.8224	0.4175	0.7829
17	0.1565	2.445	0.0215	0.0808
18	0.2285	3.5015	0.0016	0.0118*

Table 7.10: Mean maximum change, t and p values for the high contrast gratings condition versus baseline for HbO_2. Channels with a significant response to the condition versus the baseline are indicated with an asterisk, for the FDR corrected corrected p values.

Channel	Δ[HHb] Mean Maximum Change	t_{HHb}	p_{HHb}	FDR corrected p_{HHb}
1	-0.1205	-2.1875	0.0369	0.0791
2	-0.0701	-1.3064	0.2029	0.2938
3	-0.1645	-2.6252	0.0162	0.0606
4	-0.0858	-1.4979	0.1450	0.2417
5	-0.2112	-3.0376	0.0052	0.0262*
7	-0.0494	-0.8362	0.4154	0.4450
9	-0.1825	-3.4364	0.0023	0.0262*
11	-0.0493	-1.2655	0.2154	0.2938
12	-0.0742	-1.1721	0.2507	0.3030
13	-0.0713	-1.1418	0.2626	0.3030
14	-0.1001	-2.2772	0.0301	0.0752
15	-0.1499	-3.0992	0.0041	0.0262*
16	-0.0176	-0.4775	0.6366	0.6366
17	-0.0769	-1.9543	0.0615	0.1153
18	-0.1415	-2.4177	0.0224	0.0671

Table 7.11: Mean maximum change, t and p values for the high contrast gratings condition versus baseline for HHb. Channels with a significant response to the condition versus the baseline are indicated with an asterisk, for the FDR corrected corrected p values.

Channel	Δ[oxCCO] Mean Maximum Change	t_{oxCCO}	p_{oxCCO}	FDR corrected p_{oxCCO}
1	0.0482	3.8216	6.48e-04	0.0032*
2	0.0386	2.6874	0.0124	0.0241*
3	0.0682	4.1297	5.19e-04	0.0032*
4	0.0610	3.1517	0.0038	0.0113*
5	0.0791	3.8690	6.25e-04	0.0032*
7	0.0264	0.8669	0.3988	0.4273
9	0.0710	3.6239	0.0014	0.0053*
11	0.0354	2.6934	0.0115	0.0241*
12	-0.0057	-0.4321	0.6689	0.6689
13	0.0257	2.1196	0.0424	0.0636
14	0.0132	1.2431	0.2235	0.2578
15	0.0245	2.0665	0.0472	0.0644
16	0.0301	2.1895	0.0368	0.0613
17	0.0225	2.0064	0.0553	0.0692
18	0.0439	2.6581	0.0128	0.0241*

Table 7.12: Mean maximum change, t and p values for the high contrast gratings condition versus baseline for oxCCO. Channels with a significant response to the condition versus the baseline are indicated with an asterisk, for the FDR corrected corrected p values.

7.3.1.2.3 Low contrast versus High contrast Pairwise t-tests were performed to assess whether there was a statistically significant difference between responses for the two gratings conditions. Based on previous fMRI studies in adults, I expected there to be a greater HbO_2 response to the high contrast condition in comparison to the low contrast (Heeger et al., 2000; Henriksson et al., 2008). No significant differences between the conditions were found between the two conditions in any of the chromophores. The tables including the statistics for each channel and chromophore are included in the appendix.

The mean and standard deviations (represented through error bars) of the maximum responses from each of the occipital are shown in Figure 7.14 with HbO_2 in red, HHb in blue and oxCCO in green, for both checkerboard conditions (labelled as "HC" and "LC" on the x-axis), for channels over the occipital cortex. HbO_2 and HHb are scaled to the y-

axis on the left and oxCCO is scaled to the y-axis shown on the right in the figure for each channel. The largest increases in $\Delta[HbO_2]$ can be seen in Channels 3, 7 and 9 for the low contrast condition and Channels 5 and 9 for oxCCO.
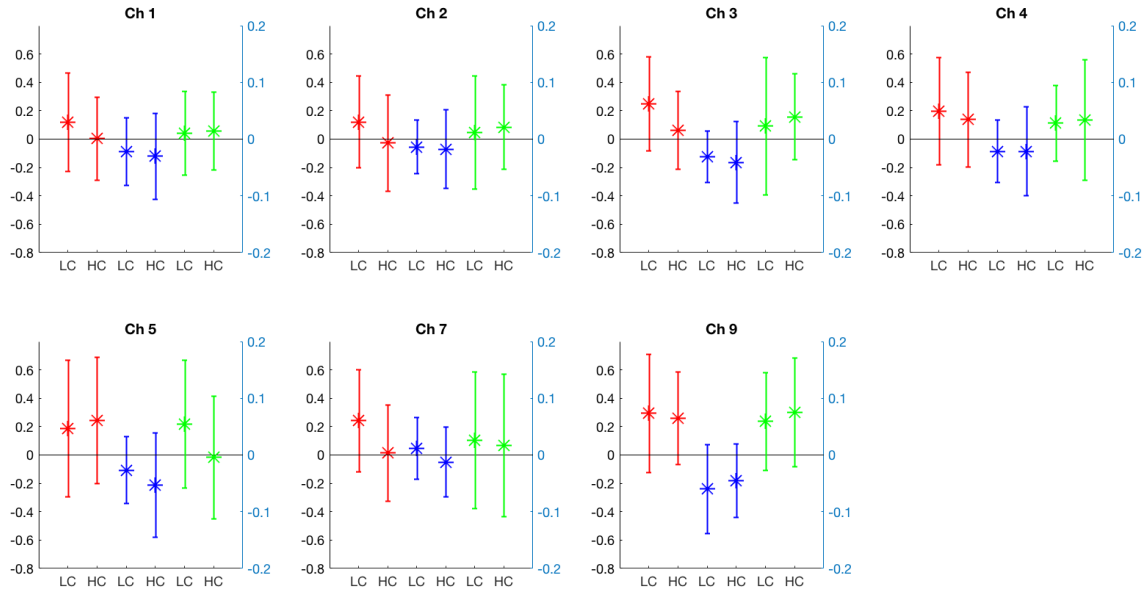
Figure 7.14: Mean and standard deviations of the maximum responses of HbO_2(red), HHb in (blue) and oxCCO (green), for both low contrast and high contrast gratings which are labelled as "LC" and "HC" respectively on the x-axis. The y-axis on the left is for HbO_2 and HHb while the y-axis on the right is for oxCCO. The error bars represent standard deviations.

7.3.1.2.3.1 *Difference scores* Figure 7.15 shows the difference in mean maximum change for each chromophore, with each bar in the graph representing a channel over the occipital lobe. Positive values indicate a stronger response to the low contrast condition while negative values indicate a stronger response to the high contrast condition. Channels 6, 8 and 10 appear empty as they were excluded from the analysis due to reasons specified previously. As I mentioned previously, based on previous fMRI studies, a greater HbO_2 response was expected in response to the high contrast condition. Given that the two stimuli differed in spatial frequency which can also differentially activate magnocellular and parvocellular pathways, differences in the oxCCO response were also expected which would reflect differences in metabolic demand in the two pathways. For HbO_2 and HHb, majority of channels display greater responses to the low contrast condition, with

the exception of Channel 5 for HbO_2 and Channel 9 for HHb. Meanwhile for oxCCO, most channels show greater responses for the high contrast gratings with the exception of Channels 2 and 9.
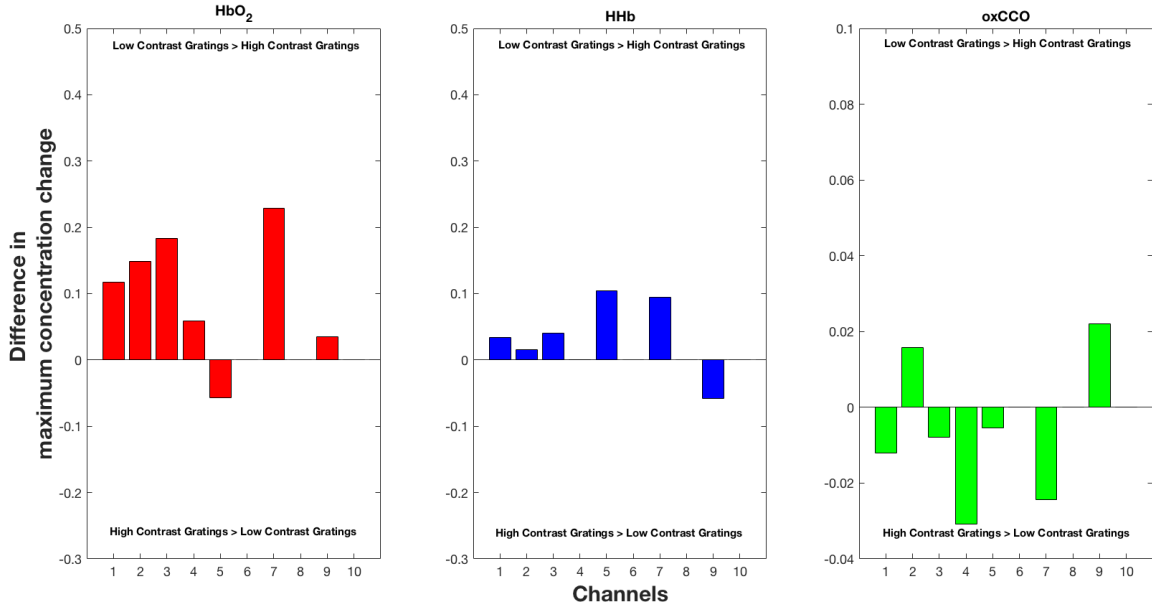
Figure 7.15: Bar graph showing the difference in the mean maximum change, in each chromophore, between the low contrast and high contrast conditions for the channels over the occipital lobe.

7.3.1.2.3.2 *Time to peak* The TTP for each chromophore in response to the checkerboard conditions was calculated, in the chosen time window for statistical analysis (4 - 10 s post-stimulus onset here). Heterogeneity in the TTP was observed. The results from this can be found in the appendix.

7.3.1.2.3.3 *Cross-correlations* Cross-correlations were performed once again to observe the relationship between changes in energy metabolism and haemodynamics in occipital cortex. The cross-correlations were performed between (i) HbO_2 and oxCCO, (ii) HHb and oxCCO and (iii) HbO_2 and HHb for all the channels. Figure 7.16 shows the average cross-correlations across occipital channels, for the low contrast gratings (upper panel) and high contrast gratings (bottom panel). The error bars represent standard deviations. For both high and low contrast conditions, HHb and oxCCO correlated negatively with $r = -0.45$ and zero time-lag. Weaker correlations were observed between HbO_2 - oxCCO

and HbO_2 - HHb. The correlations from individual channels can be found in the appendix.
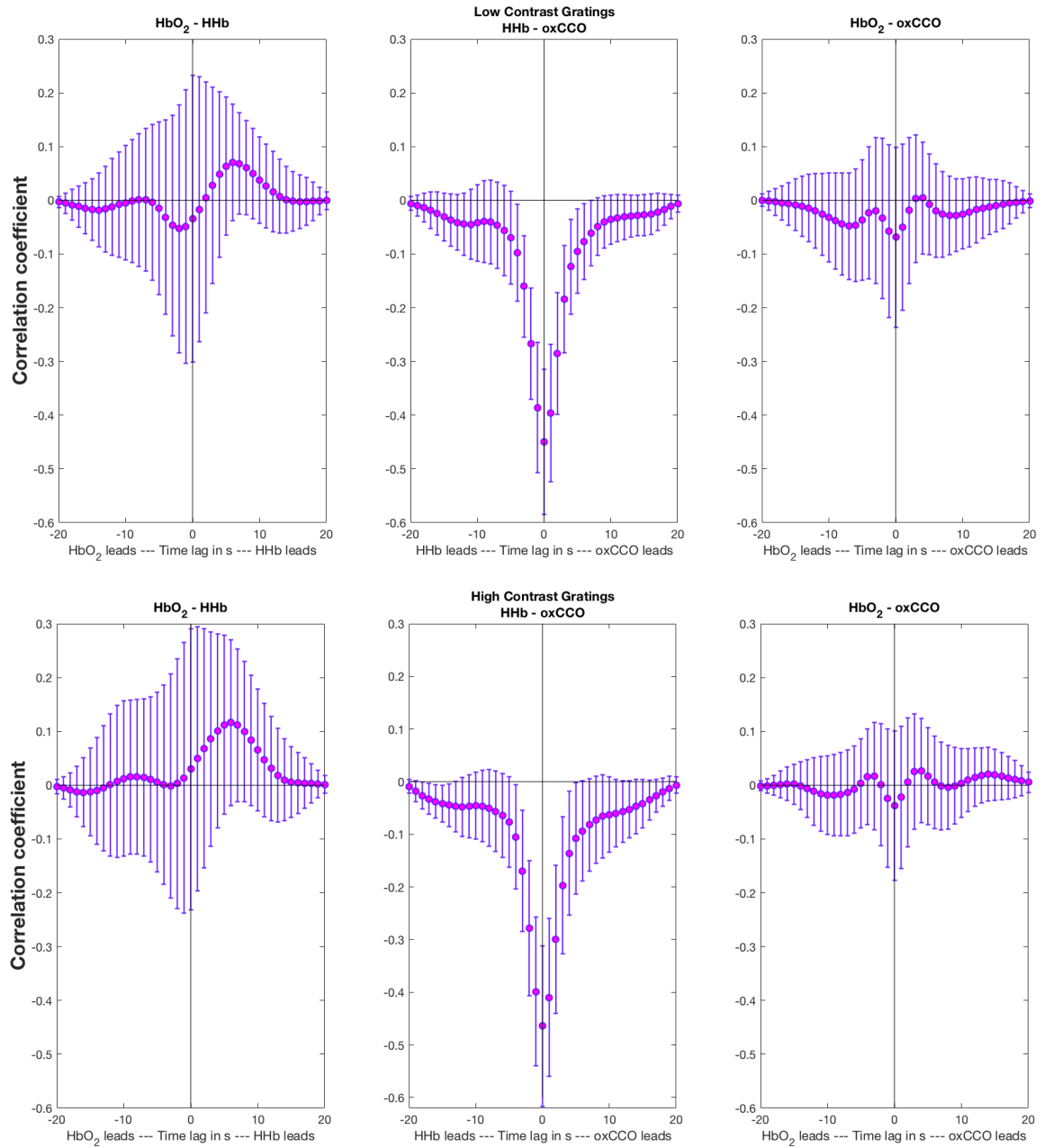
Figure 7.16: Average of the cross-correlation across occipital channels for the low contrast condition (upper panel) and high contrast condition (bottom panel). The error bars represent standard deviations.

7.3.2   EEG

7.3.2.1   Checkerboards Task

For the checkerboards task, thirty-three infants were included in the study for the black/white condition and thirty-four infants were included in the study for the red/green condition. All the infants that were excluded were due to poor data quality.

7.3.2.1.1   Topoplots   Figure 7.17 shows the log power spectral density for the alpha frequency band for both red/green and black/white checkerboard conditions.
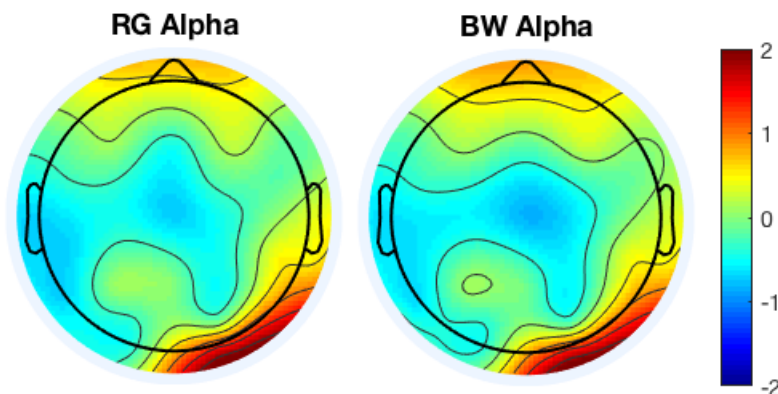
Figure 7.17: Topographical maps of the log power spectral density for the alpha band for the red/green (labelled RG) and black/white (labelled BW) conditions.

Figure 7.18 shows the difference in log power spectral density between the two conditions, for the alpha frequency band. Greater alpha activity was seen in frontal channels for the black/white condition in comparison to the red/green condition while greater alpha activity was seen over the occipital cortex channels for the red/green condition.
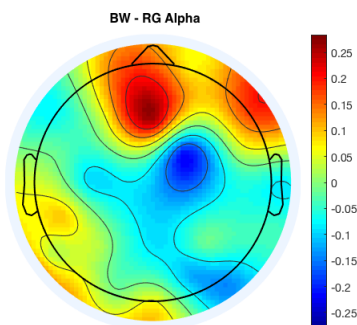
Figure 7.18: Topographical maps of the difference in log power spectral density between the red/green and black/white conditions for the alpha frequency band.

7.3.2.1.1.1 Statistical analysis

7.3.2.1.2 Time-Frequency Figure 7.19 shows the results from the wavelet time-frequency decomposition from the channels located over the visual cortex, for both checkerboard conditions. As with the adults and in accordance with previous studies (Hermes et al., 2017), an increase in stimulus-evoked alpha, beta and gamma was expected in response to both stimuli. For both conditions, alpha, beta and low gamma activity can be seen at Oz, O2 and PO8.
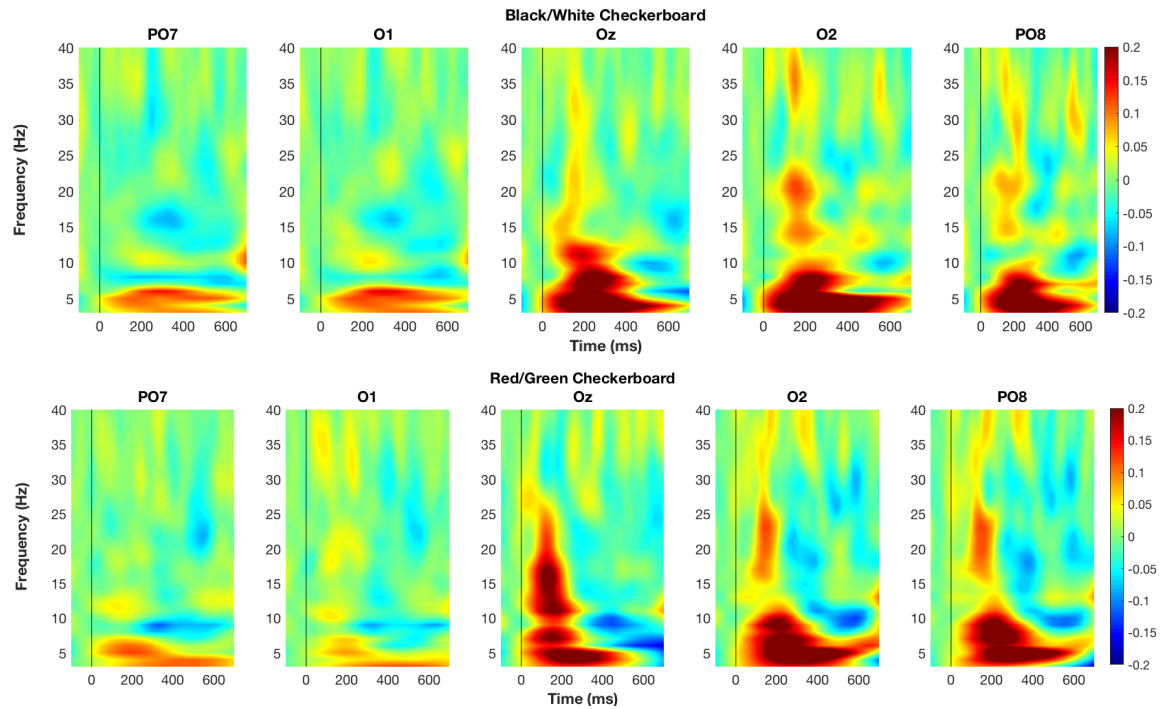
Figure 7.19: Time-frequency decomposition of the channels located over the visual cortex for the black/white checkerboard (top) and red/green checkerboard (bottom)

Figure 7.20 shows the results from the time-frequency decomposition of the difference between the black/white and red/green conditions.
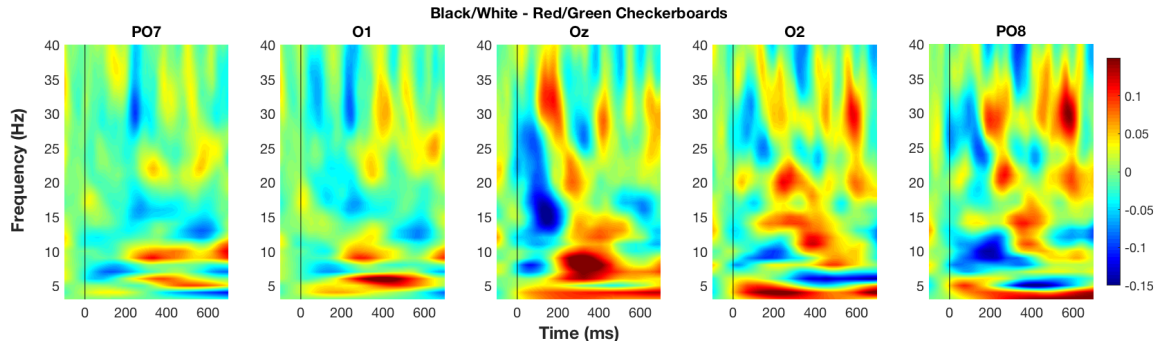
Figure 7.20: Difference between black/white and red/green checkerboard conditions. Red indicates stronger activity for the black/white condition while blue indicates stronger activity for the red/green condition.

7.3.2.1.2.1   Statistical analysis   Pairwise t-tests were performed to compare the mean power of alpha, beta and gamma in a 100 - 300 ms window (post-stimulus onset) between the red/green and black/white checkerboard conditions for channels over the parietal and occipital cortex (these included PO7, PO3, O1, Oz, O2, PO4, PO8 and Pz). No significant differences were found between the two conditions for any of the frequency bands.

7.3.2.2   Gratings

For the gratings condition, twenty-six infants were included in the study for the low contrast condition and twenty-two for the high contrast condition. For the low contrast condition, 5 infants were excluded for not having the minimum number of trials and 11 infants were excluded for having poor data quality. For the high contrast condition, 3 infants were excluded for not having the minimum number of trials and the remainder due to poor data quality.

7.3.2.2.1   Topoplots   Figure 7.21 shows the log power spectral density for the alpha frequency band for both high contrast and low contrast conditions. An increase in alpha power can be seen in the occipital and right temporal channels for both low and high contrast conditions. Increased alpha power is seen in frontal cortex and a decrease in alpha power around Cz, only for the low contrast condition.
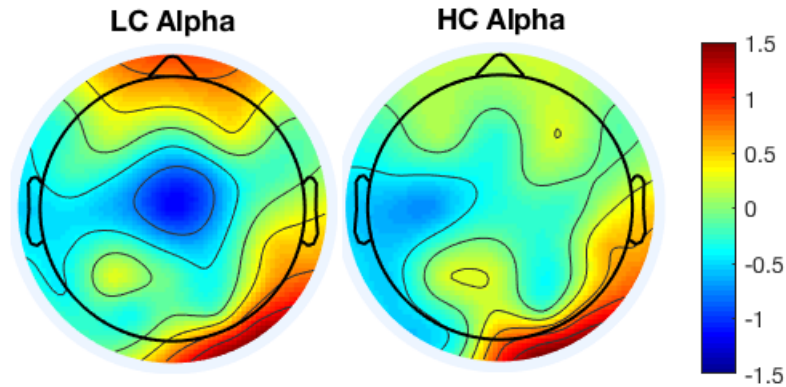
Figure 7.21: Topographical maps of the log power spectral density for the alpha band for the low contrast (labelled LC) and high contrast (labelled HC) conditions.

Figure 7.22 shows the difference in log power spectral density between the two conditions, for the alpha frequency band.
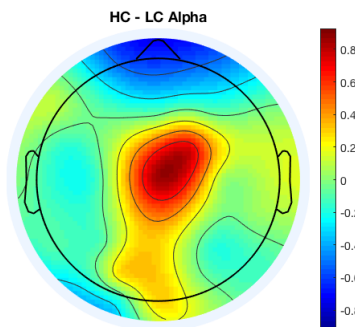
Figure 7.22: Topographical maps of the difference in log power spectral density between the high contrast and low contrast conditions for the *alpha* frequency band.

7.3.2.2.2 Time-Frequency   Figure 7.23 shows the results from the wavelet time-frequency decomposition from the channels located over the visual cortex, for both gratings conditions. Based on previous work (Jia et al., 2013; Self et al., 2016; Henrie, 2005), a greater increase in stimulus-evoked gamma activity was expected in response to the high contrast condition. An increase in alpha and beta power time-locked to the stimulus can be seen at Oz for both high contrast and low contrast conditions. PO7, O1, O2 and PO8 display gamma band activity for both conditions which appears to be stronger for the high contrast condition.
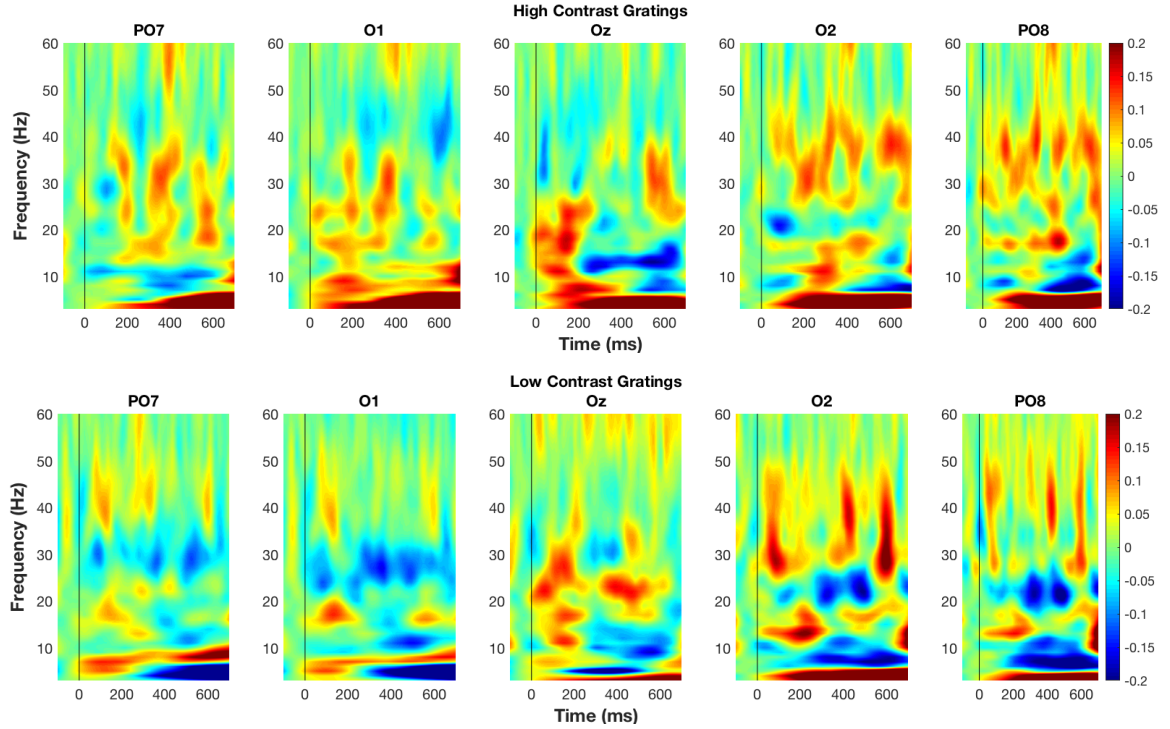
Figure 7.23: Time-frequency decomposition of the channels located over the visual cortex for the high contrast condition (top) and low contrast condition (bottom)

Figure 7.24 shows the results from the time-frequency decomposition of the difference between the two conditions.
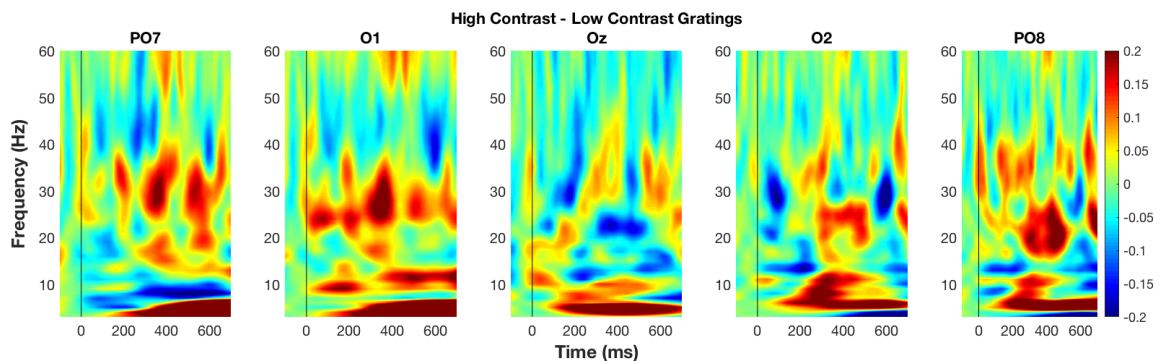
Figure 7.24: Difference between the high contrast and low contrast conditions. Red indicates stronger activity for the high contrast condition while blue indicates stronger activity for the low contrast condition.

7.3.2.2.2.1 Statistical analysis   Pairwise t-tests were performed to compare the mean power of alpha, beta and gamma in a 50 - 400 ms window (post-stimulus onset) between the low contrast and high contrast conditions. No significant differences were found be-

tween the two conditions for any of the three frequency bands.

7.3.3 Combined NIRS-EEG Analysis

7.3.3.1 Checkerboards Task

For the combined analysis, twenty-four infants were included for the black/white condition and twenty-six infants were included for the red/green condition. Correlations were performed for both checkerboard conditions between the mean power spectral density of the alpha, beta and gamma frequency bands with the maximum concentration change of $\Delta[HbO_2]$, $\Delta[HHb]$ and $\Delta[oxCCO]$, across the NIRS occipital and EEG parietal, parieto-occipital and occipital channels. The matrix of the correlations between NIRS and EEG channels was converted into a heatmap which can be seen in Figure 7.26 for the black/white condition and the red/green condition. The colorbar indicates the strength of the correlation between each channel and the map was thresholded to include only the statistically significant correlations ($p < 0.05$) between NIRS and EEG channels. No correction for multiple comparisons was applied for these correlations. Figure 7.25 has been included to show the NIRS (blue circles) and EEG channels (orange squares) in order to remind the reader of the spatial locations of each of the channels that are being correlated.
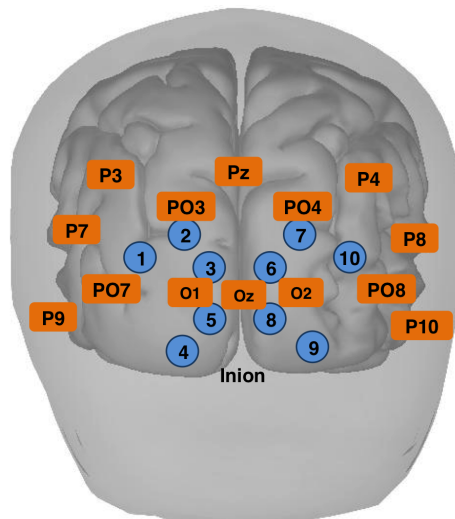
Figure 7.25: Topographical locations of the NIRS channels (blue) and EEG channels (orange rectangles), both have been labelled with their channel labels respectively.

For the black/white condition, many negative correlations were seen between NIRS

and EEG channels for HbO_2 and alpha power, specifically between NIRS Channels 1, 2, 4, 5 and 7 and a number of EEG channels, where an increase in alpha power was observed in response to the black/white condition. Meanwhile, Channels 3 and 9 (where the largest increases in $\Delta[HbO_2]$ were observed) correlated positively with parietal and parieto-occipital EEG channels, in both alpha and beta frequency bands. In the beta band fewer significant correlations were observed in comparison to the alpha band with Channel 7 correlating negatively with nearby parietal EEG channels. No significant correlations were seen between gamma power and HbO_2.

For the black/white condition for oxCCO, NIRS Channel 4 correlated positively for alpha power with many parietal and occipital EEG channels (where an increase in alpha power was observed), while Channel 5 had a significant positive correlation with only one parietal EEG channel. Statistically significant increases in $\Delta[oxCCO]$ were observed at Channels 4 and 5. In the beta band, NIRS Channel 2, where a statistically significant increase in $\Delta[oxCCO]$ was observed, correlated positively with nearby parietal EEG channels P3, P9, PO7. Meanwhile, Channel 7 correlated negatively (as with HbO_2) with parieto-occipital and occipital EEG channels, where an increase in beta activity was observed in response to the stimulus. Similar patterns were observed in the gamma band with Channel 7 once again correlating negatively with parieto-occipital and occipital EEG channels, while Channels 2, 3 and 9 correlated positively (where there were significant increases in $\Delta[oxCCO]$ from the baseline).

Fewer correlations were observed between NIRS and EEG channels for HHb. In the alpha band, Channel 9 correlated negatively with EEG channels while Channel 3 (where the largest change in $\Delta[HHb]$ was observed) correlated positively with a nearby parietal EEG channel. In the beta band, significant correlations were found only for Channel 7 which correlated positively with occipital channels O1 and O2, where an increase in beta power was observed in response to the black/white checkerboard. A similar pattern is observed in the gamma band with Channel 7 correlating positively with O1 and O2 where an increase in (low) gamma power was observed. Meanwhile, Channels 2, 3 and 4 correlated negatively with parietal EEG channels in the gamma band.

A "transition" in correlations was observed from alpha to gamma frequency bands

between chromophores here. That is, for HHb the channels that correlated negatively in the alpha band correlated positively in the beta and gamma frequency bands (and vice versa, for example see Channels 3, 7 and 9 across frequency bands) while in oxCCO the channels that correlated positively in the alpha band became weaker or negative in the beta and gamma frequency bands (for example Channels 4 and 7 across the frequency bands). A similar pattern is not observed for HbO_2 although the correlations appear stronger in the alpha band and become much weaker in the gamma band.

Fewer correlations are seen between NIRS and EEG channels for the red/green condition. For HbO_2, NIRS Channel 2 correlates positively with PO3, which is spatially located next to Channel 2 and Channel 4 correlates positively with nearby EEG electrode P3. While only the correlation between Channel 7 and O1 (where an increase in alpha power in response to the red/green condition is seen) is significant, overall Channel 7 appears to correlate positively with parieto-occipital and occipital EEG channels where an increase in alpha power is observed. In the beta band only Channel 1 correlates positively with P9 which is located nearby. No significant correlations are seen between NIRS and EEG channels for HbO_2 and gamma power.

No significant correlations between channels was observed for oxCCO and alpha power. In the beta band, Channel 5 (with the largest increase in $\Delta[oxCCO]$) correlated negatively with parieto-occipital and occipital EEG channels, where an increase in beta power was observed in response to the red/green condition. Meanwhile, Channels 3 and 4 (also where the largest increases $\Delta[oxCCO]$ were observed) correlated positively with nearby parietal EEG channels and in the gamma band, Channel 3 correlated positively with parieto-occipital and occipital EEG channels where an increase in low gamma was observed.

Significant negative correlations were seen between Channels 3, 4 and 5 in the alpha band for HHb and Channels 3 and 4 in the gamma band, with nearby EEG channels. Of these, Channel 4 displayed a significant decrease in $\Delta[HHb]$ in response to the stimulus.

Figure 7.28 shows a heatmap of the difference between black/white and red/green conditions such that the correlations were performed between the difference in mean power spectral density (black/white minus red/green) and the difference in the maximum change in each of the NIRS chromophores (black/white minus red/green). Overall, the correla-
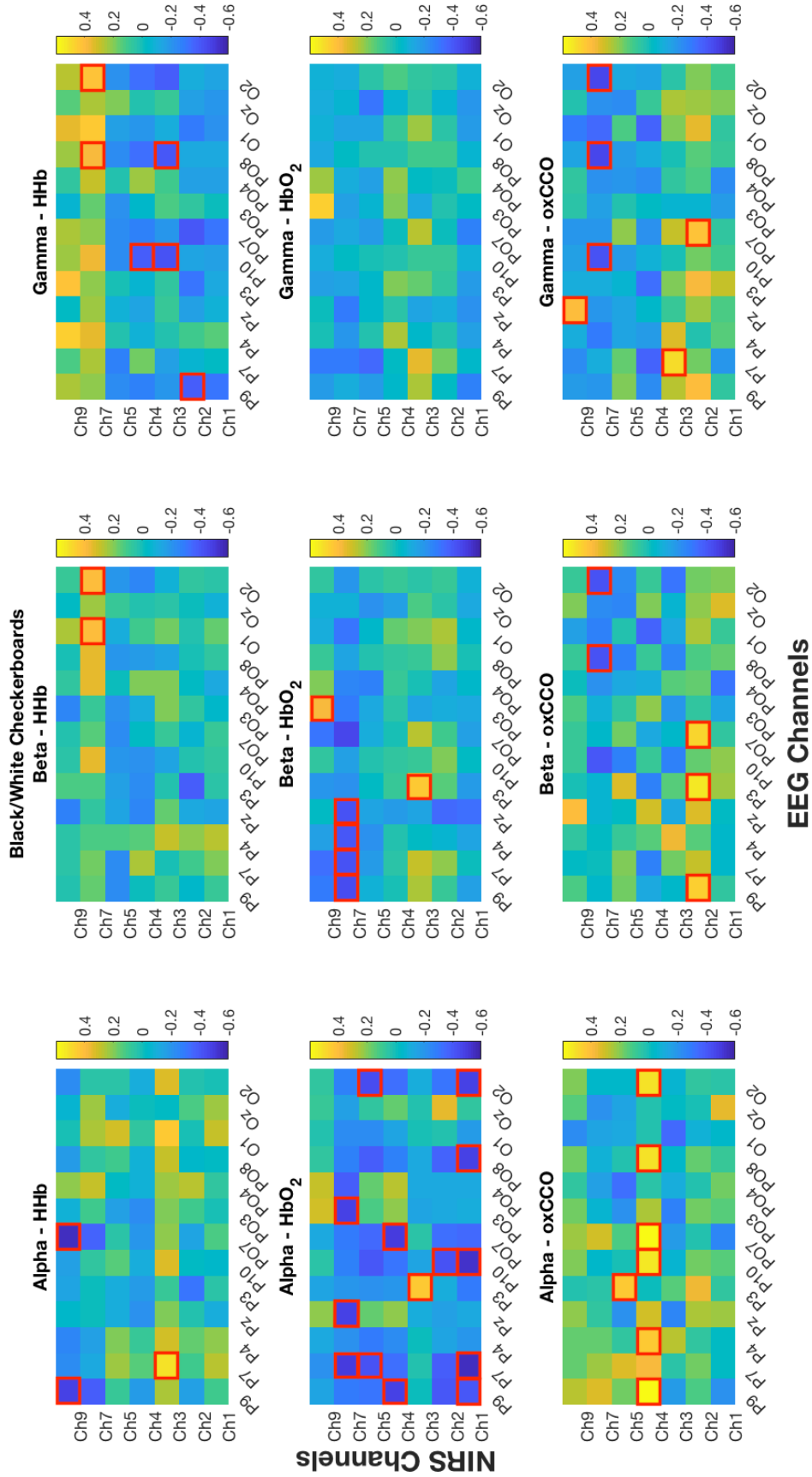
Figure 7.26: Heatmap showing the significant correlations between the mean power spectral density and the maximum change in $\Delta[HbO_2]$, $\Delta[HHb]$ and $\Delta[oxCCO]$, between NIRS occipital channels and EEG channels for the black/white condition.
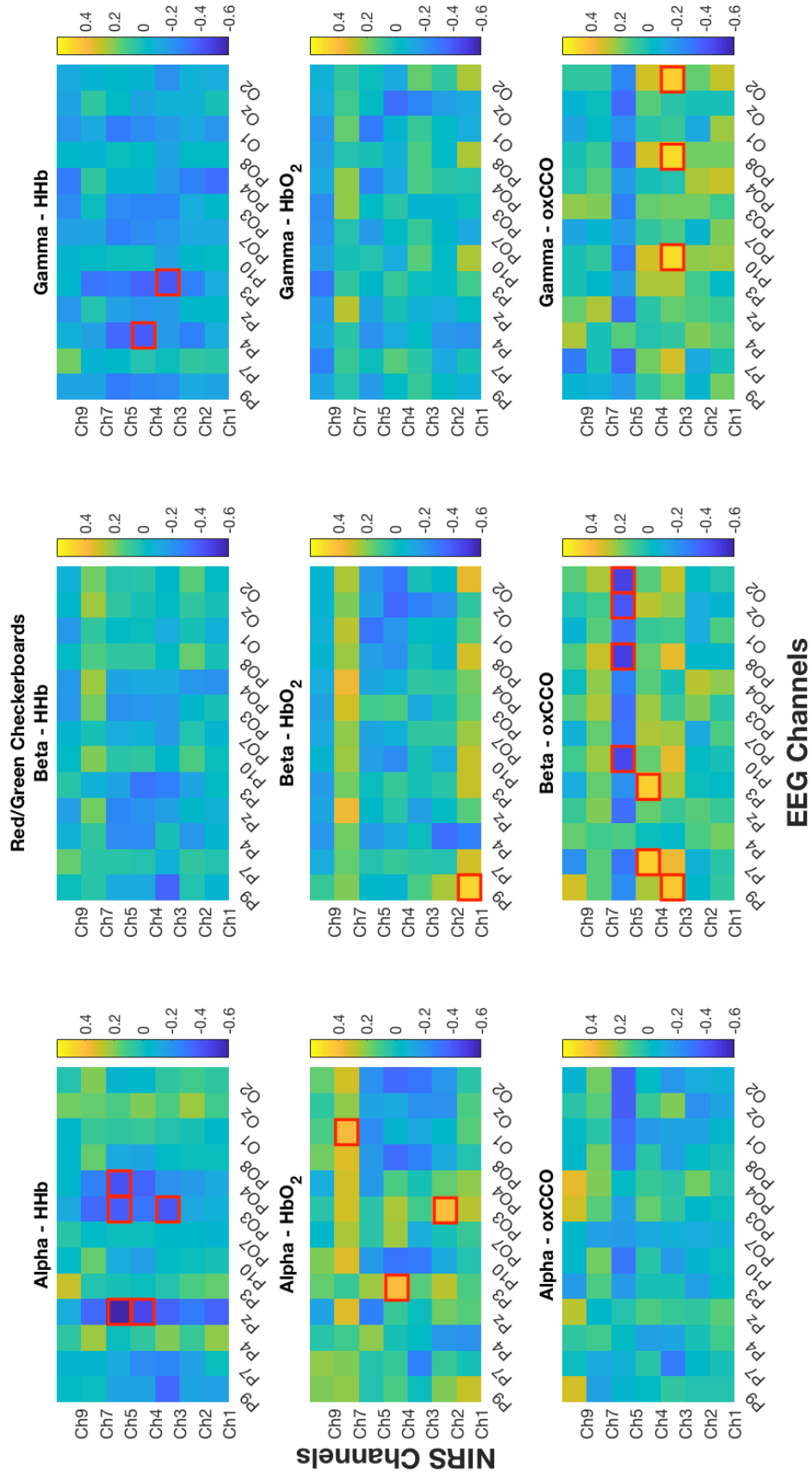
Figure 7.27: Heatmap showing the significant correlations between the mean power spectral density and the maximum change in $\Delta[HbO_2]$, $\Delta[HHb]$ and $\Delta[oxCCO]$, between NIRS occipital channels and EEG channels for the red/green condition.

tions between NIRS and EEG channels across frequency bands for HbO_2 and HHb are stronger for the black/white condition while correlations appear to be stronger for the oxCCO for the red/green condition.

7.3.3.2 Gratings

For the gratings condition, twenty-one infants were included for the low contrast condition and eighteen for the high contrast condition. Correlations were performed for both gratings conditions between the mean power spectral density of the alpha, beta and gamma frequency bands with the maximum concentration change of $\Delta[HbO_2]$, $\Delta[HHb]$ and $\Delta[oxCCO]$, across the NIRS occipital and EEG parietal, parieto-occipital and occipital channels. The matrix of the correlations between NIRS and EEG channels was converted into a heatmap which can be seen in Figure 7.29 for the high contrast condition and low contrast condition. The colorbar indicates the strength of the correlation between each channel and the map was thresholded to include only the statistically significant correlations ($p < 0.05$) between NIRS and EEG channels.

For the high contrast condition, few positive correlations are seen between alpha and beta power and HbO_2, with Channel 7 correlating with parietal EEG channels. The correlations between gamma power and HbO_2 are the strongest with Channels 7 and 9 (with the largest increases in $\Delta[HbO_2]$ are seen) correlating positively, particularly with parieto-occipital and occipital channels where an increase in gamma power is seen in response to the high contrast gratings. Meanwhile Channels 2, 4 and 5 correlate negatively with parietal and occipital EEG channels.

For the high contrast condition for oxCCO, significant positive correlations are seen only between Channel 7 and parieto-occipital and occipital EEG channels where an increase in alpha power was observed. The same channel correlates negatively in the gamma band for oxCCO, across many EEG channels.

For the high contrast condition for HHb, Channels 1, 3 and 4 (of which Channels 1 and 3 show a significant decrease in $\Delta[HHb]$ in response to the stimulus) show significant negative correlations with nearby EEG channels. Fewer correlations are seen in the beta band with Channels 2 and 7 correlating positively with parietal EEG channels. In the gamma
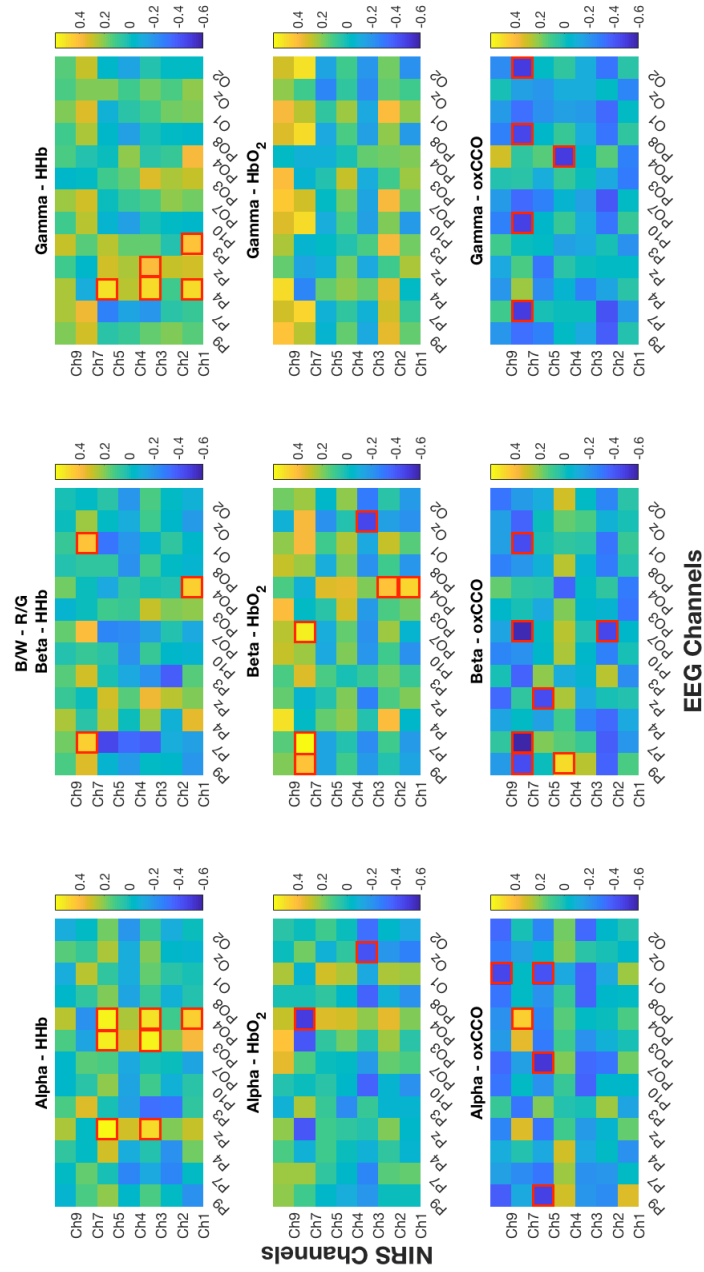
Figure 7.28: Heatmap showing the significant correlations between the difference in mean power spectral density and the difference in maximum change in $\Delta[HbO_2]$, $\Delta[HHb]$ and $\Delta[oxCCO]$ for black/white minus red/green checkerboards.

band, Channel 7 once again correlates positively with the parietal and occipital EEG channels where an increase in gamma power is observed while Channel 3 correlates negatively with nearby parietal EEG channels.

A similar pattern of "transitioning" of correlations as for the checkerboard conditions is observed (for example see Channel 7 across frequency bands for HbO_2, HHb and oxCCO.

For the low contrast condition, Channels 7 and 9 (where the largest increases in $\Delta[HbO_2]$ are observed) correlate specifically with parieto-occipital and occipital EEG channels located over the right hemisphere for HbO_2. No significant correlations are seen in the beta and in the gamma band Channel 1 correlates negatively with nearby EEG electrode P3 and occipital electrode Oz where an increase in low gamma is seen.

For oxCCO, Channel 7 correlates in both alpha and gamma but more strongly in the gamma band with parietal and occipital EEG channels where an increase in gamma power is observed. Channel 4 correlates significantly positively with parietal and occipital EEG channels for both alpha and beta frequency bands.

Figure 7.31 shows a heatmap of the difference between low contrast and high contrast such that the correlations were performed between the difference in mean power spectral density (low contrast minus high contrast) and the difference in the maximum change in each of the NIRS chromophores (low contrast minus high contrast). The strongest correlations are seen between NIRS and EEG channels for beta power and HHb and oxCCO, with HHb correlations being stronger for the low contrast condition while oxCCO correlations are stronger for the high contrast condition.

7.4   Discussion

Multi-channel broadband NIRS was used simultaneously with EEG in 4-to-7-month-old infants to investigate the relationship neurovascular coupling mechanisms, in the visual cortex. Two different sets of visual stimuli which included alternating checkerboards and drifting gratings were used and the results from each of these are discussed in the following sections.
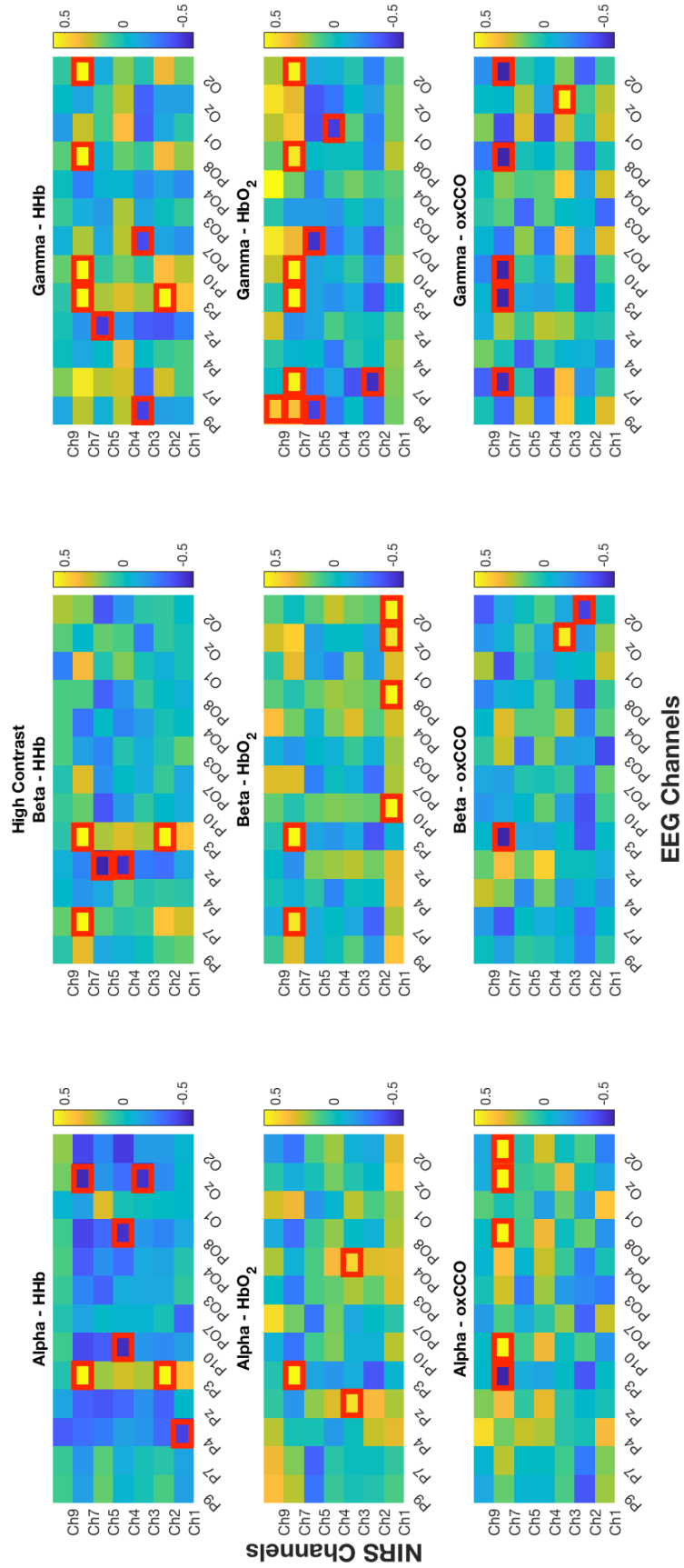
Figure 7.29: Heatmap showing the significant correlations between the mean power spectral density and the maximum change in $\Delta[HbO_2]$, $\Delta[HHb]$ and $\Delta[oxCCO]$, between NIRS occipital channels and EEG channels for the high contrast condition.
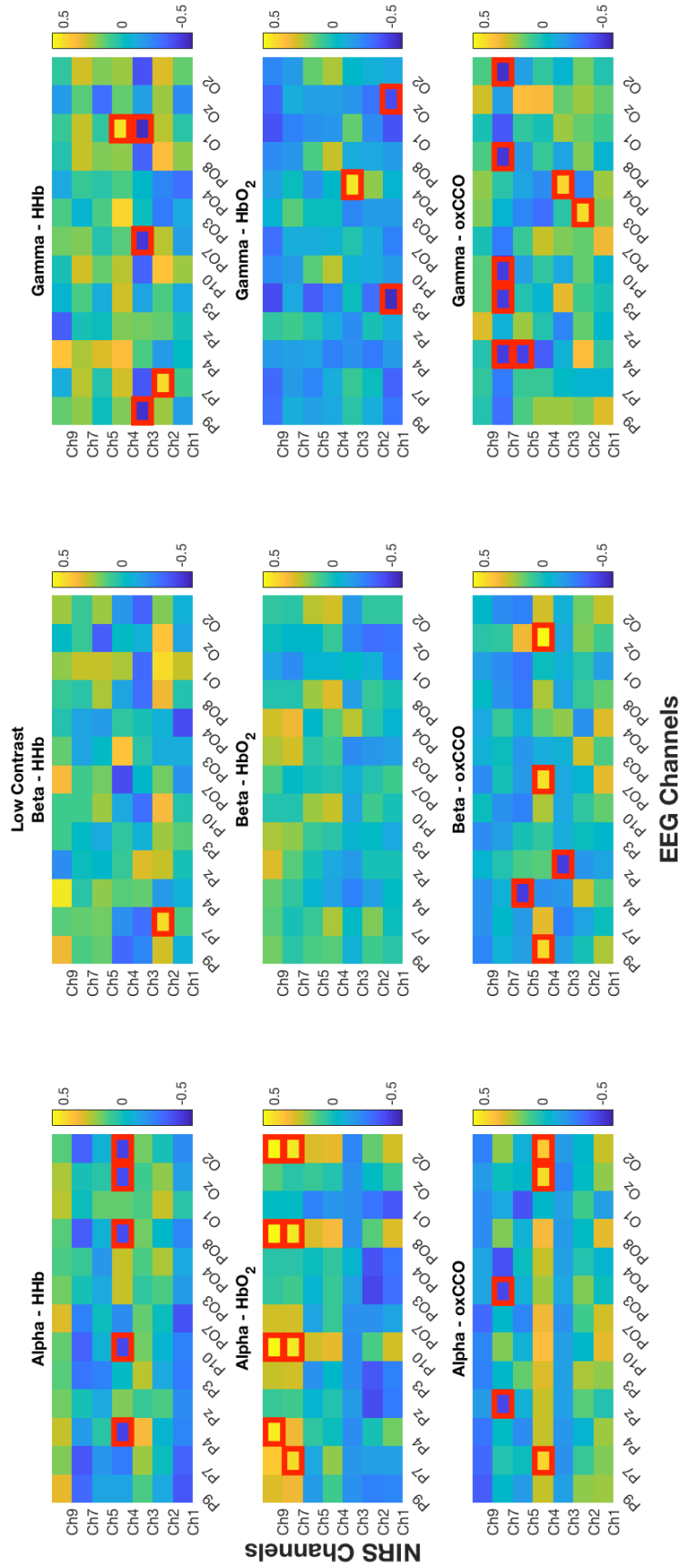
Figure 7.30: Heatmap showing the significant correlations between the mean power spectral density and the maximum change in $\Delta[HbO_2]$, $\Delta[HHb]$ and $\Delta[oxCCO]$, between NIRS occipital channels and EEG channels for the low contrast.
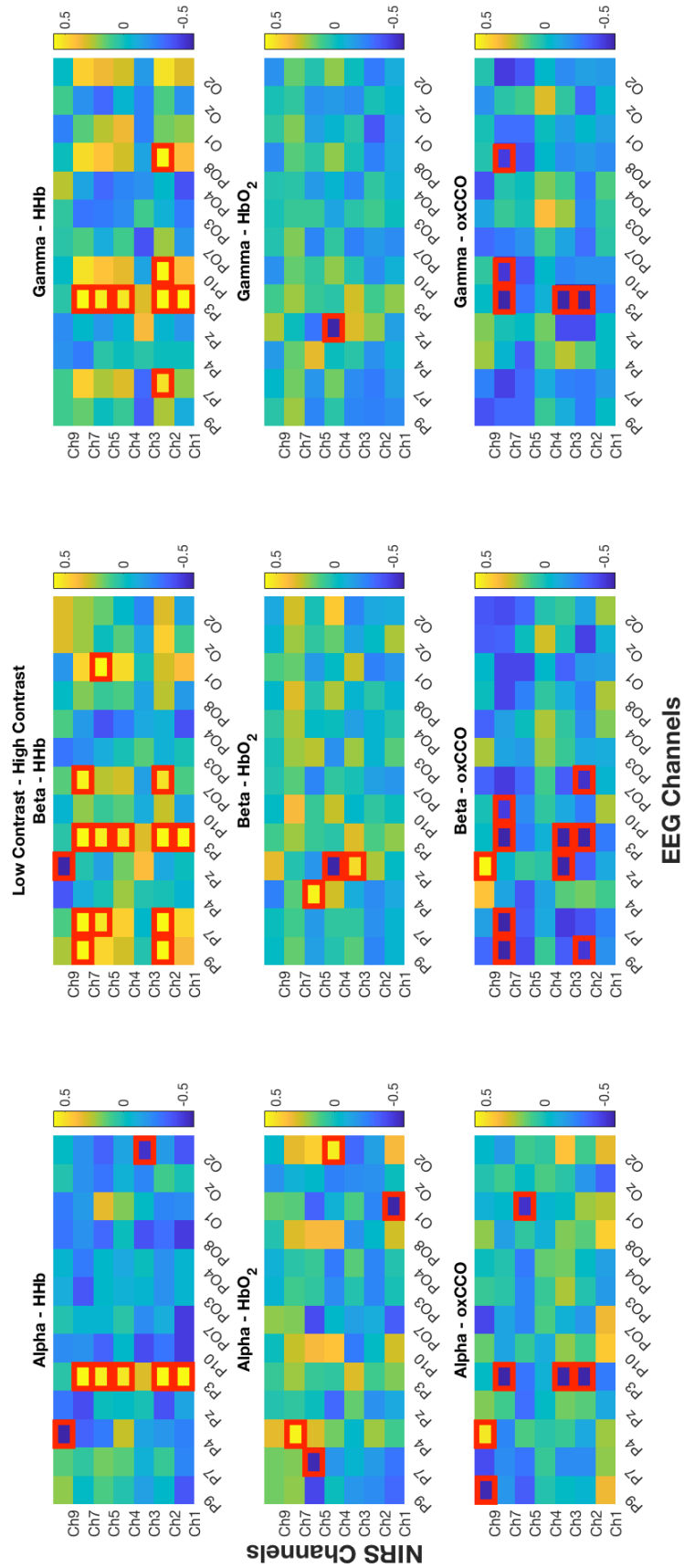
Figure 7.31: Heatmap showing the significant correlations between the difference in mean power spectral density and the difference in maximum change in $\Delta[HbO_2]$, $\Delta[HHb]$ and $\Delta[oxCCO]$ for low contrast minus high contrast gratings.

7.4.1   Checkerboards

The checkerboard stimuli used in the study presented in this chapter were similar to those used in the adult work in Chapter 5. The results from Chapter 5 indicated a statistically significant difference between the black/white (Magno condition) and red/green checkerboards (Parvo condition) with both Δ[oxCCO] and Δ[HbO$_2$] displaying a stronger response to the Magno condition. Therefore, a similar result was expected to be observed in the infants. However, no significant differences were found in the NIRS responses between the two conditions for either HbO$_2$ or HHb. Although, from Figure 7.10 it is obvious, while not statistically significant, that in the majority of channels over the visual cortex, there was greater increase in Δ[HbO$_2$] in response to the black/white condition in accordance with the results from Chapter 5. Meanwhile, the changes in the concentration of Δ[oxCCO] did indicate a significant difference over the primary visual cortex with a stronger response for the red/green condition. This result is not surprising given that the red/green checkerboard was designed to target the parvocellular pathway of the visual cortex which has previously been demonstrated to have a high concentration of cytochrome-c-oxidase. Therefore, a greater response to this condition in Δ[oxCCO] may be a reflection of activity occurring in the parvocellular pathway. In fact, in many of the channels over the visual cortex, as seen from Figure 7.10, a greater response to the red/green condition can be seen in oxCCO. Furthermore, in the channel that exhibited a greater increase in Δ[oxCCO] for the red/green checkerboard displays the opposite pattern of activation for HbO$_2$ and HHb, as seen in Figure 7.8 where an increase in Δ[HHb] and a decrease (or no response) in Δ[HbO$_2$] can be seen in response to the stimulus. This result could be interpreted as a "deactivation" in response to the red/green condition which would support the results by Watanabe et al (2012a) who similarly reported a deactivation to high luminance stimuli, although their stimuli were unpatterned. fMRI work in macaques has demonstrated a hierarchal development of pathways in the visual cortex (Van Grootel et al., 2017; Teller, 1997) which may affect the processing of complex visual stimuli in the developing human brain. Furthermore, a study involving infants aged between 0 to 52 weeks using EEG investigated differences in the latencies of the visual evoked potentials and reported differential maturational

changes between the magnocellular and parvocellular pathways with the former maturing earlier (Hammarrenger et al., 2003). The authors further demonstrated that the time period between 3 to 6 months appeared to be important for the maturation of these pathways, as other previous previous studies have shown (Tremblay et al., 2014).

Cross-correlation analysis was performed once again in order to discern the relationships between chromophores in the visual cortex which may reflect the status of neurovascular coupling during development. As I already discussed in the introduction chapter, there is a period of rapid development of neural circuitry in the visual cortex occurring up until 8 months postnatally (Harris et al., 2011) and this may be reflected in the correlations between chromophores. In strong contrast to the results from the cross-correlations over the temporal cortex, the correlations between HbO_2 and HHb and HbO_2 and oxCCO are highly variable across infants, as seen in Figure 7.11. The correlations between HHb and oxCCO however, are as consistent as they were in the temporal cortex. These results can also be directly compared to the results from the cross-correlations performed in Chapter 5 with the adult data set where equal correlations were observed between all the chromophores. Moreover, the results provide further evidence that coupling mechanisms between cerebral blood flow and metabolic function may not be fully developed in early infancy and that additionally, these mechanisms undergo regional maturation at different rates, with temporal regions of the brain developing earlier than occipital. Chugani et al (1987) reported differences in the cerebral metabolic rate of glucose (CMRG) uptake in different brain regions and found that by 3 months of age the CMRG had increased in the temporal cortex. However, the dorsolateral occipital cortex was slower, showing a maturational increase around 6 - 8 months.

In the results presented in Chapter 5, an increase in stimulus-evoked alpha, beta and gamma was seen in response to both Magno and Parvo conditions and was expected to also be observed in the infants. In accordance with these results, the EEG time-frequency analysis here showed stimulus-evoked increase in alpha, beta and low gamma, over the primary visual cortex; specifically in channels located over the right hemisphere for both conditions, as seen in Figure 7.19. No statistically significant difference was found between the two conditions. This may be due to the fact that the effect size is small and a

larger sample size is needed to discern between these conditions. Furthermore, there was a limitation in the experimental stimulus design particularly with respect to EEG. That is, the segmentation of the EEG data was performed on every alternation of the checkerboard which occurred roughly around every 1.5 s and occurred at least 6 times per presentation of the block. This could result in the observed neural activity being dampened as there was no baseline period prior to each alternation of the checkerboard.

The combined NIRS and EEG analysis showed an inverse relationship between neural activity in the alpha and beta frequency bands and oxygenated haemoglobin for the black/white condition while for the red/green condition some of the same channels displayed a positive relationship. These results are in contrast to those over the temporal cortex where an increase in neural activity correlated with an increase in oxygenated haemoglobin. Previous EEG-fMRI studies have also reported an inverse relationship between neural activity and the BOLD response, particularly in relation to the alpha band (Yuan et al., 2010; Stern, 2002; Laufs et al., 2003a). Moreover, for both conditions, HbO_2 did not correlate as strongly with gamma activity in comparison to oxCCO and HHb. This would be in line with previous studies that have demonstrated that a decoupling between the BOLD response and gamma-band oscillations occurs (Muthukumaraswamy and Singh, 2009; Scheeringa et al., 2011b) and that mitochondrial function and gamma activity are more strongly linked (Kann et al., 2011; Cunningham and Chinnery, 2011). An interesting pattern of results was observed for oxCCO which may provide evidence of its spatial specificity. In the channels located close to the primary visual cortex, a positive relationship between oxCCO and gamma band activity was observed. Meanwhile, channels in the extrastriate cortex displayed the opposite pattern of relationship. It is unclear why this difference in relationship may be occurring but perhaps the neurons in the brain areas involving in processing the visual stimuli (i.e. neurons in the primary visual cortex) have increased oxygen consumption leaving less oxygen for neurons in extrastriate regions to consume. More work is required in order to further investigate these pattern of relationships.

Furthermore, another pattern of differences that emerges between correlations of different frequency bands was the direction of the relationship of the NIRS chromophores with

alpha and gamma oscillatory activity. That is, while oxCCO and HbO_2 correlated negatively with alpha and beta bands, they correlated in the opposite direction with gamma band activity. Previous studies have postulated that different neural mechanisms lead to high and low frequency oscillations (Cardin et al., 2009; Scheeringa et al., 2016, 2011b) and these results may provide evidence of this.

Moreover, the differences in correlations between the red/green and black/white conditions may be due to differences in the processing of stimuli between the magnocellular and parvocellular pathways. It may be that the two pathways develop at different rates, therefore resulting in the observed differences in the correlation between neural activity and blood oxygenation. oxCCO however, displays less heterogeneity, particularly in the gamma band. This may be a consequence of stronger coupling between mitochondrial function and gamma band oscillations (Kann et al., 2011; Cunningham and Chinnery, 2011).

There are clear differences in the processing of these visual stimuli in the developing human brain. However, it is difficult to establish the neural mechanisms that give rise to the differences in the observed responses. As I mentioned in the discussion section of the previous chapter, time-series analyses such as cross-correlations need to be performed in order to understand the true relationship between these mechanisms.

7.4.2 Gratings

Previous fMRI work investigating the effect of a change in stimulus contrast from low to high (Kay et al., 2013; Boynton et al., 1996; Heeger et al., 2000) and in spatial frequency from low to middle spatial frequency (Henriksson et al., 2008; Singh et al., 2000) have reported an increase in the BOLD response to high contrast and middle spatial frequency conditions. Moreover, human studies have also demonstrated that extrastriate regions are more sensitive to contrast in comparison to the primary visual cortex (Tootell et al., 1998). Since the experimental conditions used here were a combination of change in contrast and spatial frequency, I expected there to be stronger changes in $\Delta[oxCCO]$ and $\Delta[HbO_2]$ in response to the high contrast stimulus. No significant differences were seen between the low and high contrast conditions over the primary visual cortex. Although, from Figure

7.15, it can be seen that in the majority of channels over the visual cortex, there was a greater response in $\Delta[HbO_2]$ to the low contrast condition in comparison to the high contrast while the opposite pattern was observed for $\Delta[oxCCO]$. This may be a reflection of differing metabolic demands of the pathways that process these stimuli as changes in spatial frequency can differentially activate the magnocellular and parvocellular pathways. Probably a larger sample size of infants and more trials are required in order to observe the true pattern of differences in the responses between these two conditions. Similarly to the checkerboard conditions, the cross-correlation analysis revealed once more a stronger negative correlation between HHb and oxCCO and weaker correlations between HbO_2 and HHb and HbO_2 and oxCCO which had a high degree of variability across the infants. Therefore providing further evidence of underdeveloped coupling mechanisms between blood flow and metabolic activity in early infancy.

Previous studies of local field potential and multi-unit activity in adults and macaques (Jia et al., 2013; Self et al., 2016; Henrie, 2005) have demonstrated that the high contrast condition leads to an increase in gamma power. Here, stimulus-evoked beta and gamma band activity was observed in response to the high contrast condition which was particularly strong in the channels over the right hemisphere, in accordance with previous studies as seen in Figure 7.23. A similar pattern was observed for the low contrast condition although the channels over the left hemisphere displayed suppression of low gamma activity. No significant differences between conditions were observed for any of the frequency bands. Once again there was a limitation of the experimental design whereby the EEG data segmentation was performed on every reversal of the direction of the gratings, which occurred twice within the presentation of each grating. This not only meant that there was an insufficient baseline but also that there were very few trials for each of the gratings conditions. Moreover, many infants were excluded for poor data quality during these conditions and the final number of infants included in the group data was quite small. A larger sample size with higher number of trials is probably need to discern between oscillatory activity occurring in response to both conditions.

From the combined NIRS-EEG analysis, the results demonstrated that HbO_2 correlates most positively with alpha activity for the low contrast condition and with gamma activity

for the high contrast condition, suggesting that an increase in neural activity has a positive relationship with blood oxygenation. Although the channels located over the primary visual cortex displayed the opposite pattern of relationship once again. Meanwhile oxCCO was found to correlate negatively with gamma activity for both low and high contrast conditions. A similar pattern of differences in the direction of correlations between alpha and gamma frequency bands, as was seen in the checkerboards conditions, was observed here, suggesting once again that different neural mechanisms may give rise to low and high frequency oscillations (Cardin et al., 2009).

7.4.3 General Discussion

In general, the results from this study shed light on neurovascular coupling during brain development. Most interestingly, regional differences were observed where coupling of cerebral blood and metabolic activity appeared to be highly variable across infants in the visual cortex but less so in the temporal cortex. This provides potential evidence of difference in regional cortical development. Differences in the relationship between haemodynamics and low frequency and high frequency oscillatory activity were also observed suggesting that high frequency activity such as gamma coupled in the opposite pattern with blood oxygenation and metabolic activity in comparison to low frequency activity.

There were a number of limitations to this study, some of which I have already discussed. These included stimulus design, sample size and low number of trials particularly for the gratings conditions. A different type of analysis also needs to be conducted to explore the relationships between neural activity, haemodynamics and metabolic activity further.

Chapter 8

NIRS STUDY OF CYTOCHROME WITH EEG IN INFANTS AT-RISK FOR AUTISM

8.1   Introduction

Multi-channel broadband NIRS was used simultaneously with EEG in the previous chapter in order to investigate the relationship between metabolic function, haemodynamics and neuronal activity in the typically developing infants. Changes in the concentration of chromophores were correlated with the oscillatory activity underlying the observed neuronal activity. Analyses were performed to understand the relationship between cerebral blood oxygenation changes and energy metabolism in the infant brain, which was particularly important as many previous studies have reported variability in the HRF in infancy. The results from these analyses highlighted differences in coupling between oxygen delivery and energy metabolism (i.e. the neurovascular coupling pathway) during typical brain development in the occipital and temporal cortices, particularly in comparison with the adult brain.

Furthermore, from a methodological perspective, the study served in demonstrating the feasibility of using broadband NIRS simultaneously with EEG to measure changes in

metabolic activity across multiple brain regions in infants which, to my knowledge, is the first such study in infants to obtain these measurements.

Moving away from the healthy brain, the aim of this chapter is to describe the use of NIRS and EEG in atypical brain development by studying infants at-risk for autism spectrum disorders (ASD).

Autism Spectrum Disorders (ASD) are classified by the Diagnostic and Statistical Manual of Mental Disorders (DSM-5) as a group of neurodevelopmental disorders characterised by the impairment of social communication and interaction, repetitive behaviours as well as atypical sensory responses (2013). While ASD behaviours that are used to diagnose the disorder typically emerge later on in life, studies suggest that atypicalities in neural processing may appear in infancy, prior to the onset of the diagnostic phenotype (Jeste et al., 2015; Jones et al., 2014b). These could be used to identify early biomarkers in order to predict ASD outcome, the severity of symptoms (Johnson et al., 2015) as well as to understand the neural mechanisms that might underlie ASD (Loth et al., 2015; Singh and Rose, 2009). Furthermore, this disorder is highly heritable and younger siblings of children who have been diagnosed with autism are at high-risk (HR) of developing it; approximately 20% of HR infants receive an ASD diagnosis (Ozonoff et al., 2011). There is also evidence from previous studies that suggests that HR infants represent the broader autism phenotype (Constantino et al., 2010; Ozonoff et al., 2011). Therefore combining all these factors, recently, research groups have started investigating early developmental pathways underlying ASD by studying infants at high familial risk for the disorder (Zwaigenbaum et al., 2007b; Jones et al., 2014b; Elsabbagh and Johnson, 2016) in order to identify early differences in brain development as well as to understand the broader autism phenotype.

Adolphs et al (2009) have identified a network of cortical regions that are involved in the processing of social information, collectively termed the "social brain". The brain regions involved include the orbitofrontal cortex, the inferior frontal gyrus (IFG), the amygdala and the anterior and posterior temporal lobes which include regions such as the posterior STS-TPJ. In autism, one of the most common traits is the impairment of social communication and interaction and many of the studies that investigate differences between individuals with ASD and without, use a range of behavioural and neuroimaging techniques

to explore the differences in processing of social stimuli. Moreover, from the perspective of HR infants, there is a wealth of literature on typical development of social processing which allows experimental paradigms to be easily applied to investigate atypical brain development (Elsabbagh and Johnson, 2016).

Previous adult behavioural studies demonstrate (Jemel et al., 2006; Shah et al., 2016) that overall, in individuals with ASD, there is a deficit in the processing of social stimuli such as faces. Moreover, longitudinal studies involving HR-ASD infants report that infants that have an autism diagnosis at 30-36-months-old have a lower inventory of gestures during infancy (Landa et al., 2007; Talbott et al., 2015; Zwaigenbaum et al., 2005; Rozga et al., 2011). Gestures indicate the initiation of social interaction (Jones et al., 2014b) and start to be used by infants to initiate episodes of joint attention (Bates and Dick, 2002; Begus and Southgate, 2012). Furthermore, many longitudinal studies also report that the HR infants, in comparison to the low-risk (LR) infants, orient differently to social stimuli such as faces. For example, (Chawarska et al., 2013) reported that 6-month-old infants with a later diagnosis of autism focused less on faces in naturalistic videos. Consistent with these findings, previous studies report that children who have been diagnosed with ASD orient less towards social stimuli such as faces (Elsabbagh et al., 2013; Ozonoff et al., 2010). Studies have also reported reduced interested in faces in infants who have are later diagnosed with autism (Feldman et al., 2012).

Moreover, similar evidence exists from EEG ERP studies, indicating atypical processing of social stimuli consisting of faces, in both children (Dawson et al., 2004), adolescents and adults (Bailey et al., 2005; McPartland et al., 2004; O'Connor et al., 2005) with autism as well as HR infants (Jones et al., 2016b; Elsabbagh et al., 2009). Furthermore, studies have also explored differences in EEG oscillatory activity which have reported that in children with an autism diagnosis, differences in theta and beta band power exist between HR and LR groups (Coben et al., 2008) as well as in the alpha band (Afifi et al., 2015). Studies involving HR infants display greater variability and previous work by Orekhova et al (2014) found no differences at 14-months in the alpha frequency band between groups.

fMRI has also been used to investigate differences in the social brain in autism. Gervais et al (2004) reported atypical processing of social information in the individuals with ASD

over the STS region. Further, work by Pelphrey et al (2005) showed differences in gaze processing.

More recently, NIRS has been used to explore differences in the neural processing of dynamic social and non-stimuli between HR and LR infants (Braukmann et al., 2018; Lloyd-Fox et al., 2013). These studies demonstrated diminished neural responses in the HR-ASD infants at 5-months-old to the social stimuli in comparison to the LR infants. Further longitudinal work by Lloyd-Fox et al (2018) following up the same infants reported that those infants who were later diagnosed with autism at 36-months showed significantly reduced activation to the social stimuli in the posterior STS-TPJ and IFG regions, in comparison to the infants LR and HR infants who did not receive an autism diagnosis.

The findings from all these behavioural and neuroimaging studies indicate that differences in the processing of social information can be seen in early infancy and it is therefore important to investigate atypical brain development further. While many studies explore differences in neuronal processes and haemodynamics (Goldberg et al., 2011; Pfeifer et al., 2013; Watanabe et al., 2012b; Christakou et al., 2013; Urbain et al., 2016) little work has been done to explore atypicalities that may be occurring within the neurovascular coupling pathway and energy metabolism that may lead to the observed differences in neural activity. Neurophysiological differences in autism may include differences in neural activity which is what most studies characterise. However, it is entirely possible that other biological processes that are associated with neuronal activity such as oxygen consumption are altered (Reynell and Harris, 2013a).

In the introduction of this thesis, I discussed a number of aspects of neurovascular coupling that have been evidenced to be impaired in autism. These can involve a number of different neuronal and glial pathways that lead to the release of vasoactive mediators that can alter the diameter of vessels and increase or restrict blood flow (Attwell et al., 2010b). Any changes that occur in any of the mediators that are controlled by neural activity may significantly impact the relationship between neural activity and haemodynamics. It is therefore important to investigate neurovascular coupling in the atypical brain particularly as recent studies have provided evidence of mitochondrial dysfunction and mitochondrial ETC abnormalities in individuals with ASD (Rossignol and Frye, 2014; Anitha et al., 2012;

Chauhan et al., 2011; Goldenthal et al., 2015; Gu et al., 2013). Many other components of the neurovascular coupling pathway have also been implicated such as the vasodilator nitric oxide in the pathogenesis of autism (Fatemi et al., 2000) and abnormal relationship between synaptic activity and the haemodynamic response in childhood (Fatemi et al., 2011; Sun et al., 2013). There is also evidence of reduced expression of the inhibitory neurotransmitter gamma-Aminobutryic acid (GABA) in ASD as well as the receptors on which GABA acts (Fatemi et al., 2002a). This may lead to an overall decrease in inhibition observed in individuals with ASD, which can be detected using techniques such as fNIRS and fMRI. This is because impaired GABA function would cause more neuronal excitability and firing, leading to more glutamate release causing an increase in blood flow (Attwell et al., 2010b) and thereby impacting the haemodynamic response (Reynell and Harris, 2013a). Table 1.1 provided in the introduction summarises the evidence of altered components of neurovascular coupling in autism.

Given the mounting evidence of many different components of the neurovascular coupling pathway being affected in the ASD brain, it is important to use tools such as multichannel broadband NIRS which allow measurement of oxygen consumption and energy metabolism non-invasively. Particularly when used simultaneously with EEG, it can greatly aid our understanding of the neurovascular coupling pathway in atypical brain development. Moreover, previous work which I discussed (Lloyd-Fox et al., 2018) demonstrates the capability of NIRS to potentially identify early biomarkers of autism, prior to diagnosis. The study presented in this chapter therefore, uses NIRS and EEG simultaneously to investigate brain function in infants at high-risk (HR) for autism. While only 20% of the HR infants are diagnosed with ASD later on in life, studying HR infants allows the opportunity to investigate the broader autism phenotype and to identify early differences in brain development that may occur before the emergence of an ASD diagnosis.

8.2 Methods

8.2.1 Participants

Six infants at high-risk (HR) for autism (having at least one older sibling with a clinical diagnosis in the autism spectrum) of varying ages between 5-to-14 months of age and four low-risk (LR) age-matched controls (with no familial history of autism) participated in the study. It should be noted that the infants studied here are at risk for autism and there is approximately a 26% change that none of the high risk infants will receive a later diagnosis of autism. I recruited the infants by advertising for the study online, on social media and at childrens play groups. Interested parents were then screened for the study and if they were eligible to participate, provided written, informed consent. Birkbeck Psychology Ethics Committee approved the study protocol and all procedures performed were within the regulations of the Ethics Committee. In addition to the simultaneous NIRS and EEG experiment, each infant was also assessed using the Mullen Scales of Early Learning (Mullen, 1995). The MSEL is a standardised measure which consists of five individual scales which include fine motor (FM), expressive language (EL), visual reception (VR), receptive language (RL) and gross motor (GM). Each of these scales combined leads to an Early Learning Composite (ELC) standard score which reflects the overall development of the infant and is categorised as "below average" or "average" for their age range. Table 8.1 details the ages of each of the infants studied along with their ELC scores.

Infant	Group	Age (Months and Days)	ELC standard score
HR-Sib1	HR	6M, 2D	76 (Below Average)
HR-Sib2	HR	10M, 1D	-
HR-Sib3	HR	12M, 29D	-
HR-Sib4	HR	14M, 12D	84 (Below Average)
HR-Sib5	HR	5M, 0D	89 (Average)
HR-Sib6	HR	13M, 1D	83 (Below Average)
Control-Sib7	LR-Control	12M, 11D	-
Control-Sib8	LR-Control	10M, 4D	97 (Average)
Control-Sib9	LR-Control	12M, 5D	-
Control-Sib10	LR-Control	13M, 1 D	77 (Below Average)

Table 8.1: Ages of the LR and HR infants and their ELC standard scores, "-" indicates missing data.

8.2.2 Data acquisition

The multi-channel broadband NIRS system that was described in the previous chapter was used to acquire the data presented here. No further modifications were made to the system prior to its use in this study of HR infants. The Enobio EEG system was used again with thirty-two channels in the same configuration as in the previous chapter, to acquire the EEG data.

8.2.3 Headgear Design

The headgear used for this study was the same as for the previous study and has been described in Chapter 2. The only modification was that an additional NIRS array was designed for use in the older infants (12-to-14-month-olds) as they required the use of a larger sized EEG cap (46 cm) in comparison to the younger 5 and 6-month-old infants.

8.2.4   Experimental Stimuli

The experimental stimuli used for this study were the same as those described in the previous chapter, with a modification in the order of presentation of the stimuli. This was done to prioritize the social/non-social conditions as previous studies have shown atypical patterns of neural activity in response to similar experimental stimuli; in 4-to-7-month-old infants at high-risk for autism (Lloyd-Fox et al., 2013; Braukmann et al., 2018; Lloyd-Fox et al., 2018), using NIRS and additionally in the atypical neural processing of social stimuli such as faces, using EEG (Jones et al., 2016b). Furthermore, we did not have any specific hypotheses about the processing of the occipital targeted visual stimuli during atypical development therefore only the social and non-social conditions were focused on in the present study. Figure 8.1 shows the new order of stimulus presentation which involved "grouping" stimuli together such that the first four trials consisted only of the social/non-social conditions followed by three trials of each of the visual conditions, followed by four presentations of the social/non-social conditions and so on. This ensured that the minimum number of trials were obtained for at least the social/non-social conditions, for each infant.
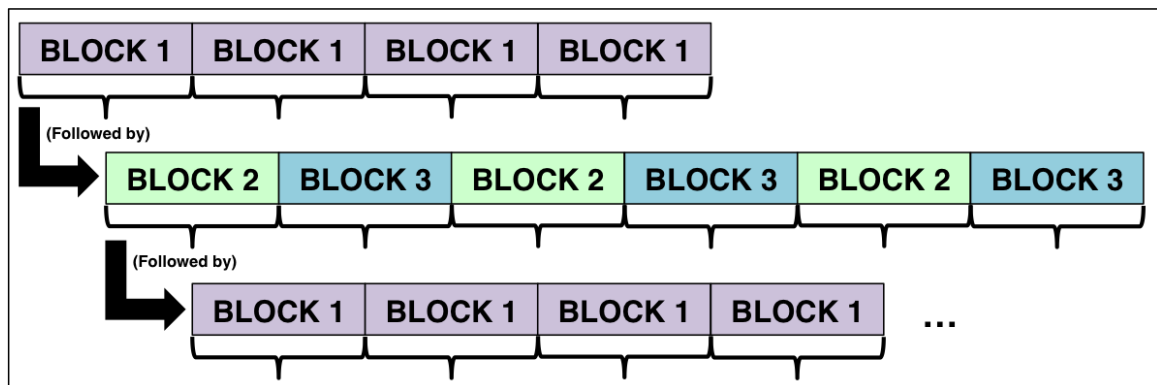
Figure 8.1: Order of stimulus presentation

8.2.5   Experimental Procedure

The same experimental procedure was followed for the NIRS and EEG study as described in the previous chapter. This part of the study was prioritized and once it was complete, each infant was assessed using the Mullen Scales of Early Learning by a trained assessor.

8.2.6   Data analysis

Due to time constraints, only data from the social and non-social conditions were analysed for this study for both EEG and NIRS. Furthermore, as this was a pilot study and there were only six HR infants of varying ages, it was not appropriate to group participants. Therefore, the analysis was performed on an individual level and the results are presented as case studies.

8.2.6.1   NIRS

8.2.6.1.1   Pre-processing The NIRS data was processed in the same way as described in Section 5.2.6.1 of the previous chapter. To recap, these steps included:

1. Performing motion artifact detection and correction with $\alpha = 0.8$

2. Conversion to changes in concentration of $\Delta[HbO_2]$, $\Delta[HHb]$ and $\Delta[oxCCO]$ using the UCLn algorithm with a DPF of 5.13 at 120 wavelengths between 780 - 900nm.

3. Filtering the data using a 4th order Butterworth filter from 0.01 - 0.4 Hz

4. Segmentation of the data into blocks consisting of 4 s of the baseline period prior to the experimental condition, the experimental condition and the entire following baseline period.

5. Rejection of trials based on looking-time coding

6. Rejection of bad channels based on visual inspection, photon counts and correlations between the time courses of $\Delta[HbO_2]$ and $\Delta[HHb]$.

7. Averaging of valid trials to obtain an average time course response for each chromophore, for each infant.

Infants were removed from the study if they did not have a minimum of two trials per experimental condition and/or if more than 40% of channels were bad.

8.2.6.1.2 Further analysis Difference scores, time to peak and cross-correlations were calculated for each HR infant and compared to their age-matched LR control. These calculations have been described previously in Chapters 2 and 6 respectively. Statistical analysis was not performed here as individual infants were being compared.

8.2.6.2 EEG

8.2.6.2.1 Pre-processing All EEG data were pre-processed and analysed using Matlab 2017a (Mathworks, USA) and the EEGLab Toolbox (Schwartz Centre for Computational Neuroscience, UC San Diego, USA), using the same procedures as those described previously in Section 2.3.2.1 of Chapter 2. The segmentation of the data was performed in the same way as described in the previous chapter.

8.2.6.2.2 Further analysis Similarly to the work presented in the previous chapter, topographical maps of spectral power were generated for the theta and alpha frequency bands for each infant.

8.3 Results

As discussed previously, the results from each HR infant are presented as case studies and are compared to their age-matched controls. Out of the six HR infants, three were included in both NIRS and EEG analysis. However, as the pre-processing steps and the rejection criteria for NIRS and EEG are different, the infants included in the NIRS data were not necessarily the same as those included for the EEG. This particularly highlights the differences between the two modalities as the quality of the data from each can be impacted by different factors. For the combined NIRS and EEG analysis, it is required that only the infants with both good NIRS and EEG data be included. Table 8.2 shows which infants were included (of both HR and LR controls) for NIRS, EEG and the combined analysis respectively, along with the reason for exclusion if the infant was not included in the study. For both NIRS and EEG, data from the 5-month-old HR infant was always compared to the data from the previous chapter where the average age of the sample was

5.5 months.

Figure 8.2 shows the NIRS temporal array to remind the reader of the locations of each of the channels over the right temporal cortex and the channels likely to lie over the STS-TPJ region, where the strongest activation to social and non-social stimuli was shown previously, are indicated by the yellow circle.

Figure 8.2: Locations of each of the NIRS channels over the right temporal cortex. The channels likely to lie over the STS-TPJ region are indicated by the yellow circle.

8.3.1 NIRS

8.3.1.1 Social

Figures 8.3 - 8.6 display $\Delta[HbO_2]$ (red), $\Delta[HHb]$ (blue) and $\Delta[oxCCO]$ (green) in the temporal channels for the 5-month-old, 10-month-old and 13-month-old HR infants for the social condition, along with their age-matched controls. For ease of comparison of chromophores here, the y-axis on the left is for HbO_2 and HHb while the y-axis on the right is for oxCCO therefore oxCCO has not been magnified as in the results presented in previous chapters.

The 5-month-old HR infant displays an increase in $\Delta[HHb]$ and $\Delta[oxCCO]$ and no response (or a very small increase in $\Delta[HbO_2]$) in response to the social condition in most channels except Channel 17, while the LR (which is the grand average of the 32 4-to-7-month-old infants tested in the previous chapter) infants do not show the same pattern.

Infant	Group	Age (Months and Days)	EEG (Social)	EEG (Non-social)	NIRS	NIRS-EEG (Social)	NIRS-EEG (Non-social)	Reason for exclusion (NIRS)	Reason for exclusion (EEG)
HR-Sib1	HR	6M, 2D	☑	☑	☒	☒	☒	Technical problems with NIRS system	—
HR-Sib2	HR	10M, 1D	☒	☑	☑	☒	☑		Poor data quality for all social trials
HR-Sib3	HR	12M, 29D	☒	☒	☒	☒	☒	Poor data quality, 70% of channels rejected	Poor data quality throughout testing session
HR-Sib4	HR	14M, 12D	☑	☒	☒	☒	☒	Cap shifted during the recording session, 70% of channels rejected	Poor data quality for all non-social trials
HR-Sib5	HR	5M, 0D	☒	☑	☑	☒	☑	—	Insufficient number of social trials
HR-Sib6	HR	13M, 1D	☑	☒	☑	☑	☒	—	Poor data quality for all non-social trials
Control-Sib7	LR	12M, 11D	☒	☒	☑	☒	☒	—	Technical problems with EEG system
Control-Sib8	LR	10M, 4D	☑	☑	☑	☑	☑	—	—
Control-Sib9	LR	12M, 5D	☒	☒	☒	☒	☒	Non-compliant infant	Non-compliant infant
Control-Sib10	LR	13M, 1 D	☑	☑	☒	☒	☒	Low photon counts, 95% of channels rejected	—

Table 8.2: Details of each HR and LR infant and whether they were included in the NIRS and EEG analysis as well as the reasons for exclusion if they were excluded.

Most notable is the difference in Δ[oxCCO] between the two with the HR infant display-ing a much stronger oxCCO response. In general, the responses in the HR infants seem to be larger and there is a difference in the scale as here data from an individual infant is being compared to a group average. Figure 8.4 shows the data from 2 randomly selected LR 5-month-old infants.
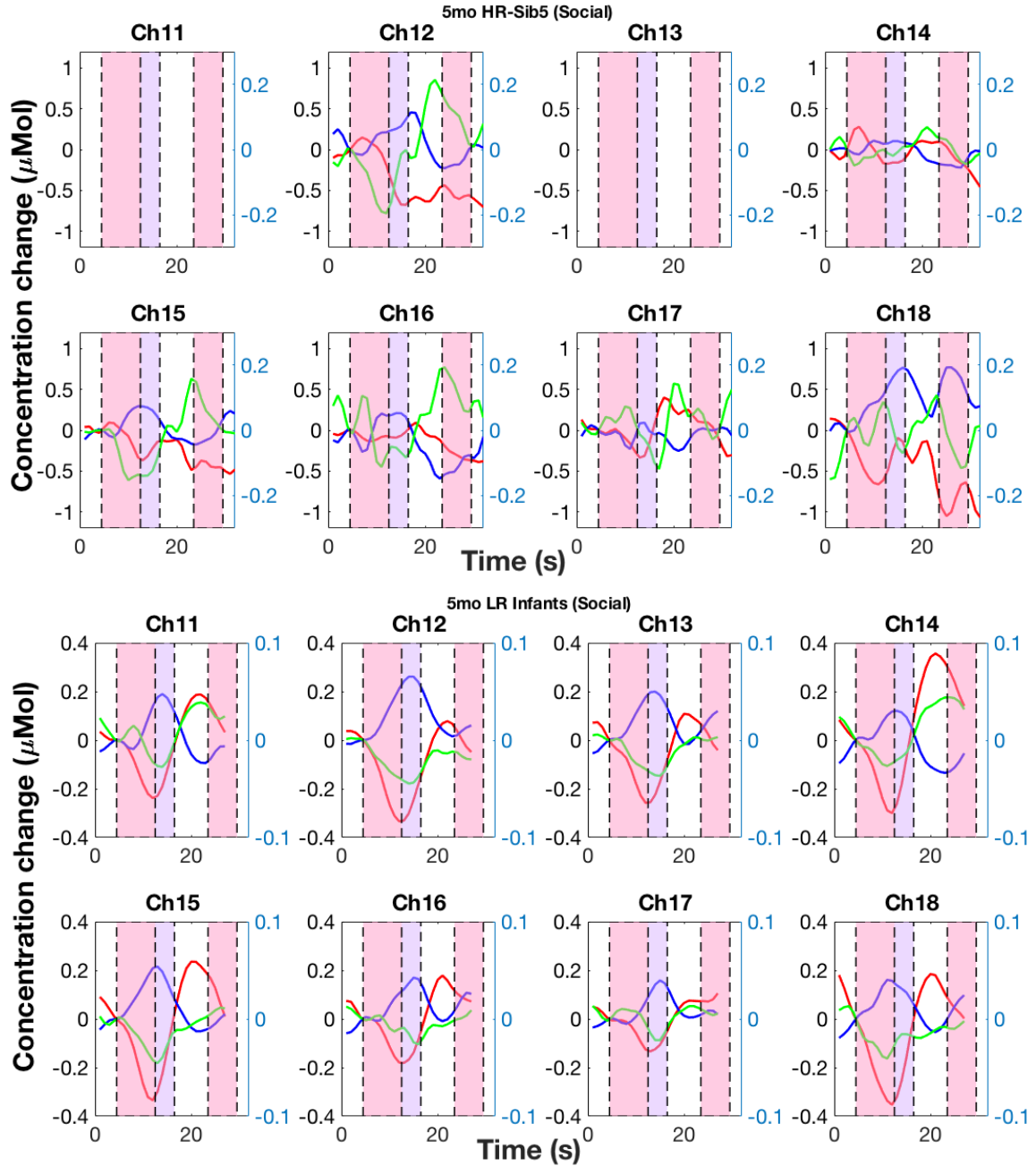
Figure 8.3: Observed changes in concentration of HbO_2 (red), HHb (blue) and oxCCO (green) in temporal channels for the social condition in the 5-month-old HR infant (Upper panel) versus the average of thirty-two 4-to-7-month-old LR infants (Bottom panel). The y-axis on the left is for HbO_2 and HHb and the y-axis on the right is for oxCCO. Empty figures represent missing data where channels were excluded due to poor signal quality.
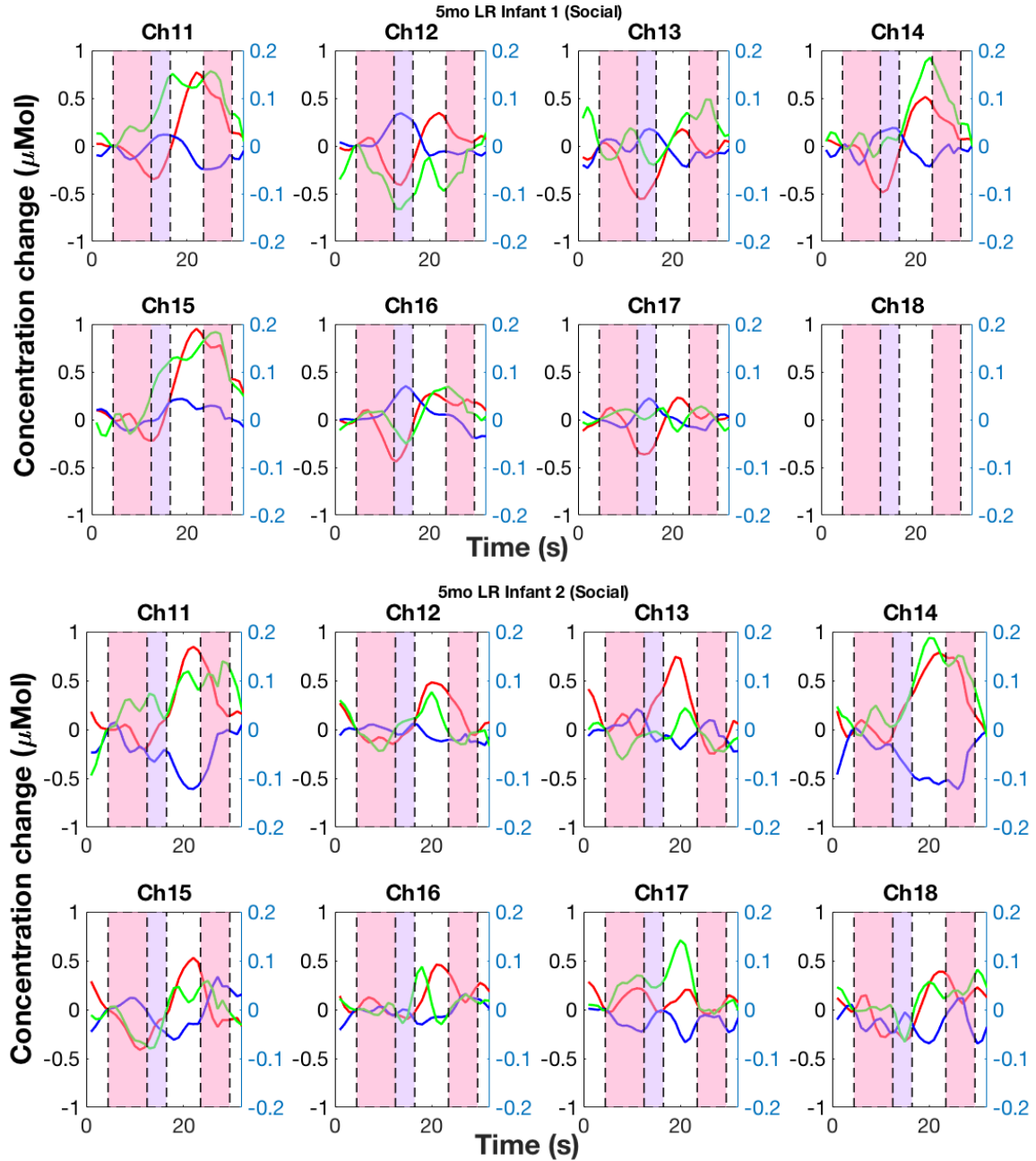
Figure 8.4: Observed changes in concentration of HbO$_2$ (red), HHb (blue) and oxCCO (green) in temporal channels for the social condition in 2 randomly selected LR 5-month-old infants The y-axis on the left is for HbO$_2$ and HHb and the y-axis on the right is for oxCCO. Empty figures represent missing data where channels were excluded due to poor signal quality.

The 10-month-old HR infant displays an increase in Δ[HHb] and a decrease (or no response) in Δ[HbO$_2$] to the social condition in most channels. In comparison, the LR control displays stronger Δ[HbO$_2$] responses.
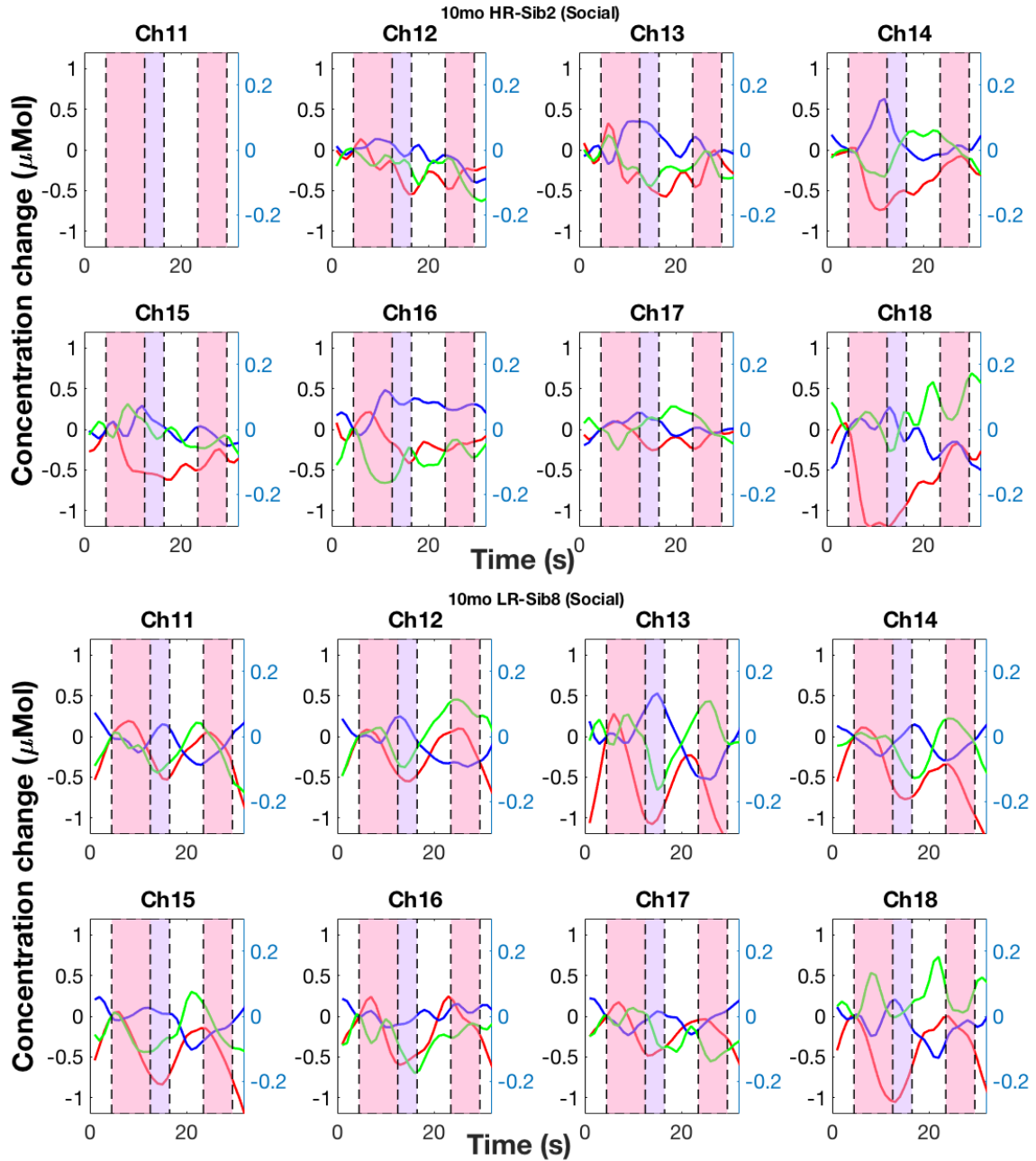
Figure 8.5: Observed changes in concentration of HbO_2 (red), HHb (blue) and oxCCO (green) in temporal channels for the social condition in the 10-month-old HR infant (Upper panel) versus the 10-month-old LR control (Bottom panel). The y-axis on the left is for HbO_2 and HHb and the y-axis on the right is for oxCCO. Empty figures represent missing data where channels were excluded due to poor signal quality.

The 13-month-old HR infant displays variable responses while the LR control displays much stronger responses to the social condition. Most notable here is the difference in the coupling between HbO_2 and oxCCO i.e. there is a strong coupling in the LR infant while

there appears to be a decoupling in the HR infant.
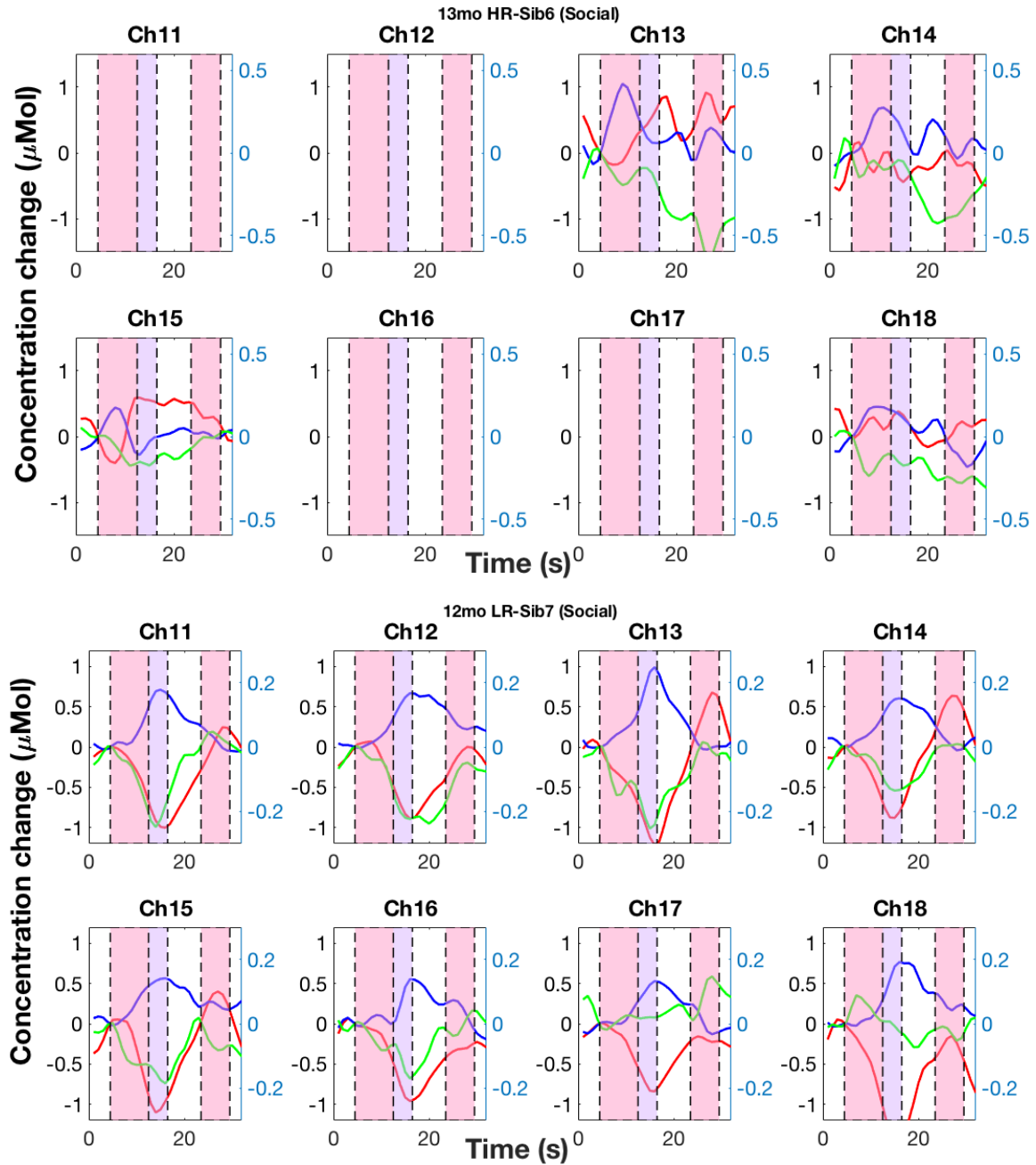
Figure 8.6: Observed changes in concentration of HbO$_2$ (red), HHb (blue) and oxCCO (green) in temporal channels for the social condition in 13-month-old HR infant (Upper panel) versus the 12-month-old LR control (Bottom panel). The y-axis on the left is for HbO$_2$ and HHb and the y-axis on the right is for oxCCO. Empty figures represent missing data where channels were excluded due to poor signal quality.

8.3.1.2 Non-social

Figures 8.7 - 8.10 display $\Delta[HbO_2]$ (red), $\Delta[HHb]$ (blue) and $\Delta[oxCCO]$ (green) in the temporal channels for the 5-month-old, 10-month-old and 13-month-old HR infants for the non-social condition, along with their age-matched controls. For ease of comparison of chromophores here, the y-axis on the left is for HbO_2 and HHb while the y-axis on the right is for oxCCO therefore oxCCO has not been magnified as in the results presented in previous chapters.

The 5-month-old HR infant displays an increase in $\Delta[HbO_2]$ in response to the non-social condition most strongly seen in Channels 12, 15, 16 and 18, although the response is very slow to reach its maximum in comparison to what is seen in typically developing infants. Once again, there appears to be a decoupling between HbO_2 and oxCCO in the HR infants. The strong oxCCO response that was seen in response to the social condition in the HR infant is not seen here. Figure 8.8 shows the data from 2 randomly selected LR 5-month-old infants.
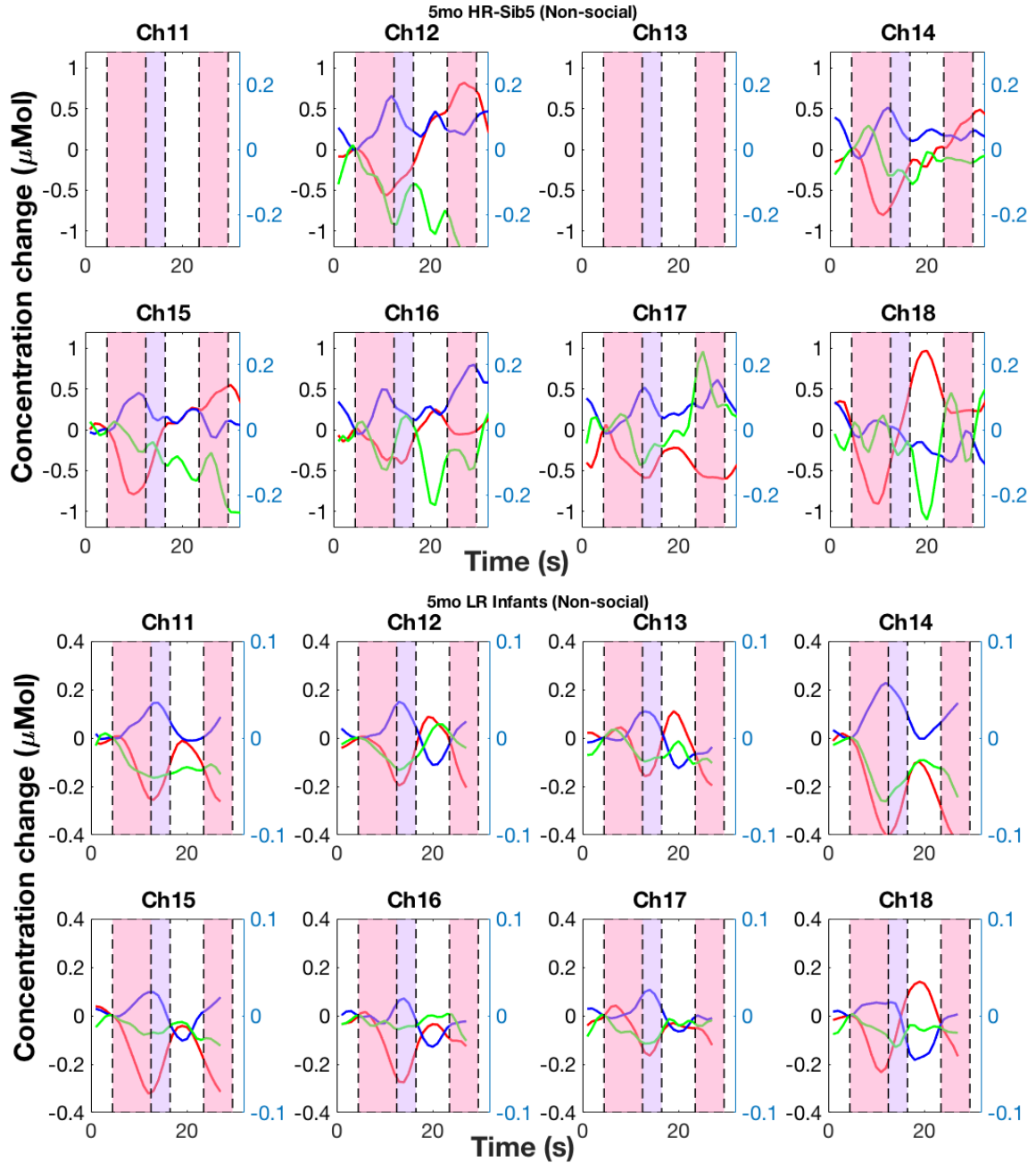
Figure 8.7: Observed changes in concentration of HbO_2 (red), HHb (blue) and oxCCO (green) in temporal channels for the non-social condition in the 5-month-old HR infant (Upper panel) versus the average of thirty-two 4-to-7-month-old LR infants (Bottom panel). The y-axis on the left is for HbO_2 and HHb and the y-axis on the right is for oxCCO. Empty figures represent missing data where channels were excluded due to poor signal quality.
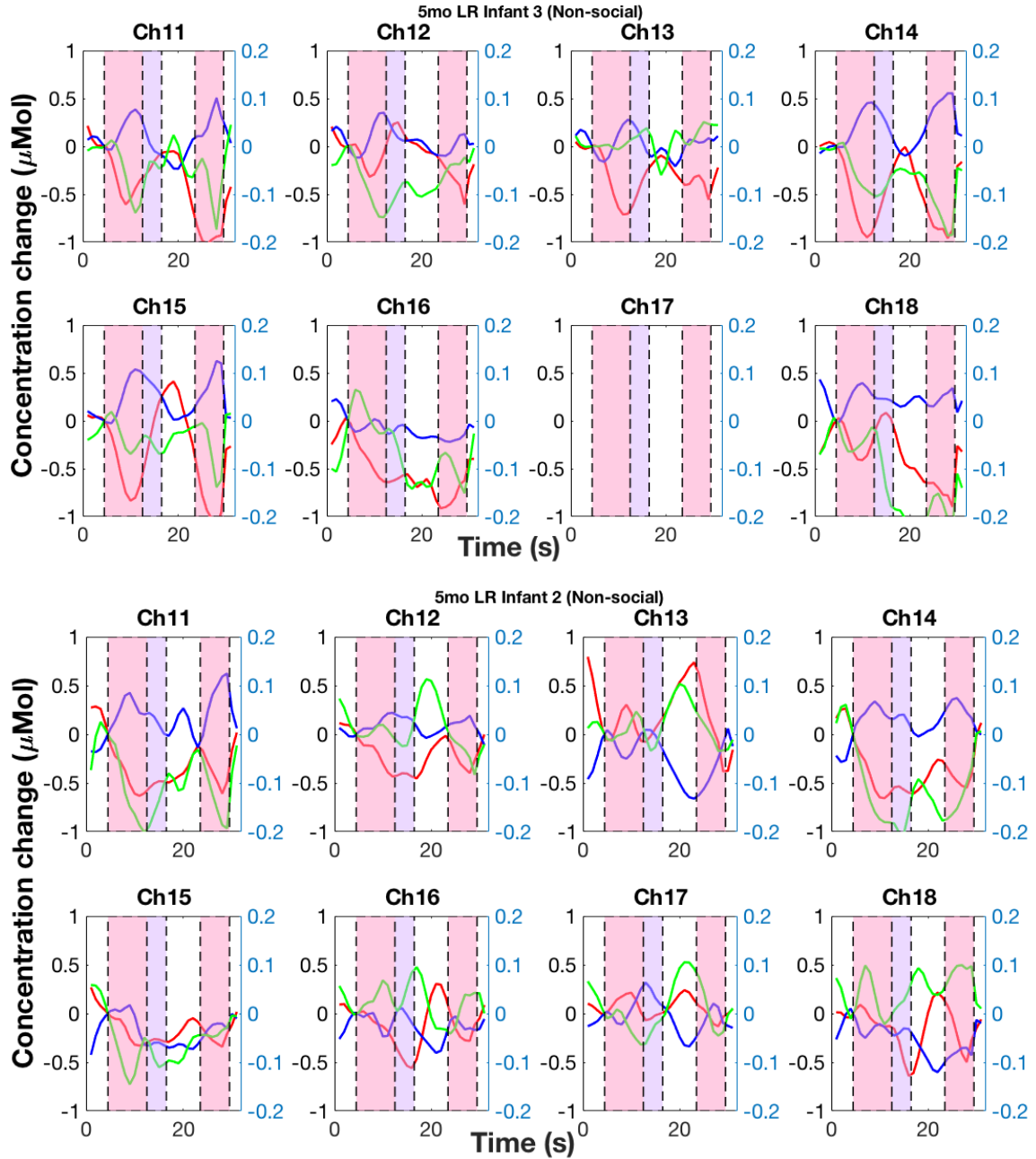
Figure 8.8: Observed changes in concentration of HbO_2 (red), HHb (blue) and oxCCO (green) in temporal channels for the non-social condition in 2 randomly selected LR 5-month-old infants The y-axis on the left is for HbO_2 and HHb and the y-axis on the right is for oxCCO. Empty figures represent missing data where channels were excluded due to poor signal quality.

The 10-month-old HR infant displays very small changes in all chromophores in response to the non-social condition, except in Channels 12 and 15 where an increase in $\Delta[HbO_2]$ and $\Delta[oxCCO]$ can be seen. The LR control displays stronger $\Delta[HbO_2]$ responses

showing an increase in most channels to the non-social condition.
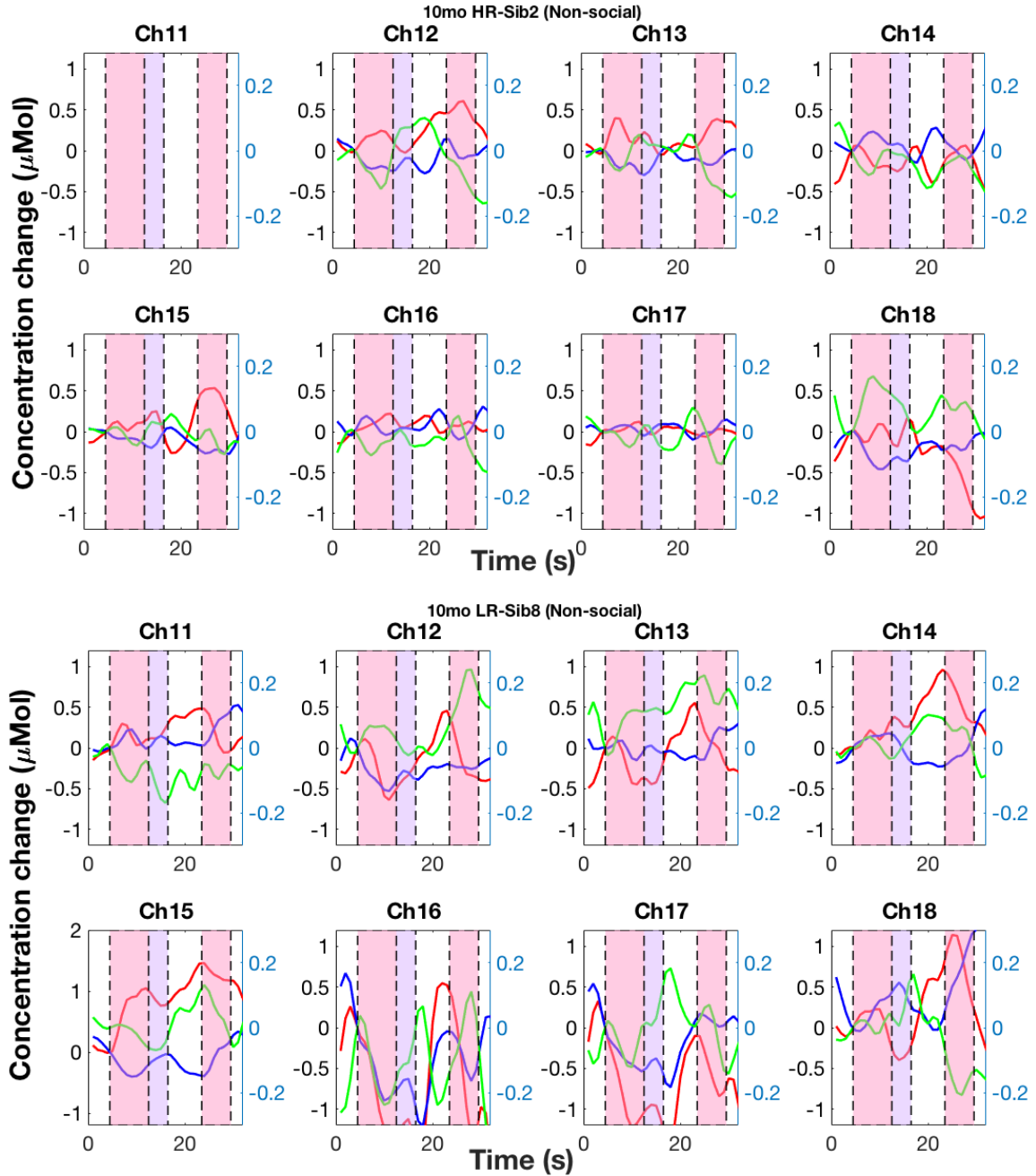
Figure 8.9: Observed changes in concentration of HbO_2 (red), HHb (blue) and oxCCO (green) in temporal channels for the non-social condition in 10-month-old HR infant (Upper panel) versus the 10-month-old LR control (Bottom panel). The y-axis on the left is for HbO_2 and HHb and the y-axis on the right is for oxCCO. Empty figures represent missing data where channels were excluded due to poor signal quality.

The 13-month-old HR infant once again displays variable responses while the LR control displays stronger responses to the non-social condition.
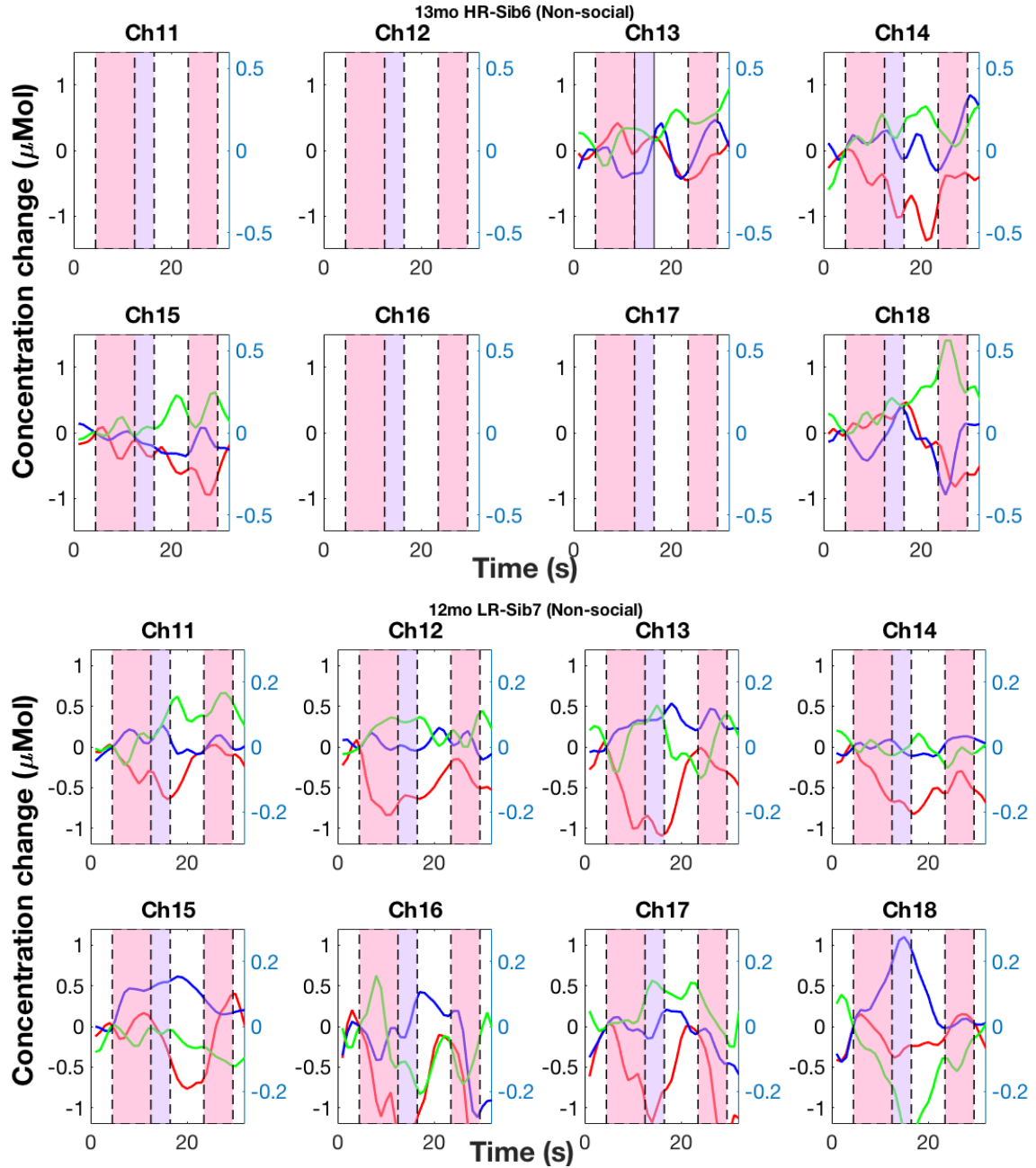
Figure 8.10: Observed changes in concentration of HbO_2 (red), HHb (blue) and oxCCO (green) in temporal channels for the non-social condition in 13-month-old HR infant (Upper panel) versus the 12-month-old LR control (Bottom panel). The y-axis on the left is for HbO_2 and HHb and the y-axis on the right is for oxCCO. Empty figures represent missing data where channels were excluded due to poor signal quality.

8.3.1.2.1 Social versus Non-social

8.3.1.2.1.1 *Time to peak* The TTP was calculated for each chromophore (for both conditions) in the time window chosen for statistical analysis (10 - 18 s post-stimulus onset here) and averaged across temporal channels, for each infant. Figure 8.11 shows the averaged TTP for each chromophore for social and non-social conditions respectively, for the HR infants and their age-matched controls. For the social condition the biggest difference in the time to peak is between the 5-month-old and 13-month-old HR and LR infants for HbO$_2$ and oxCCO, with the LR infants displaying a longer time to attain their maximal response while the HHb time to peak is faster in all the HR infants. In the non-social condition, the oxCCO time to peak is faster in all of the HR infants while the 10-month-old and 13-month-old HR infants display a shorter time to peak for HbO$_2$.
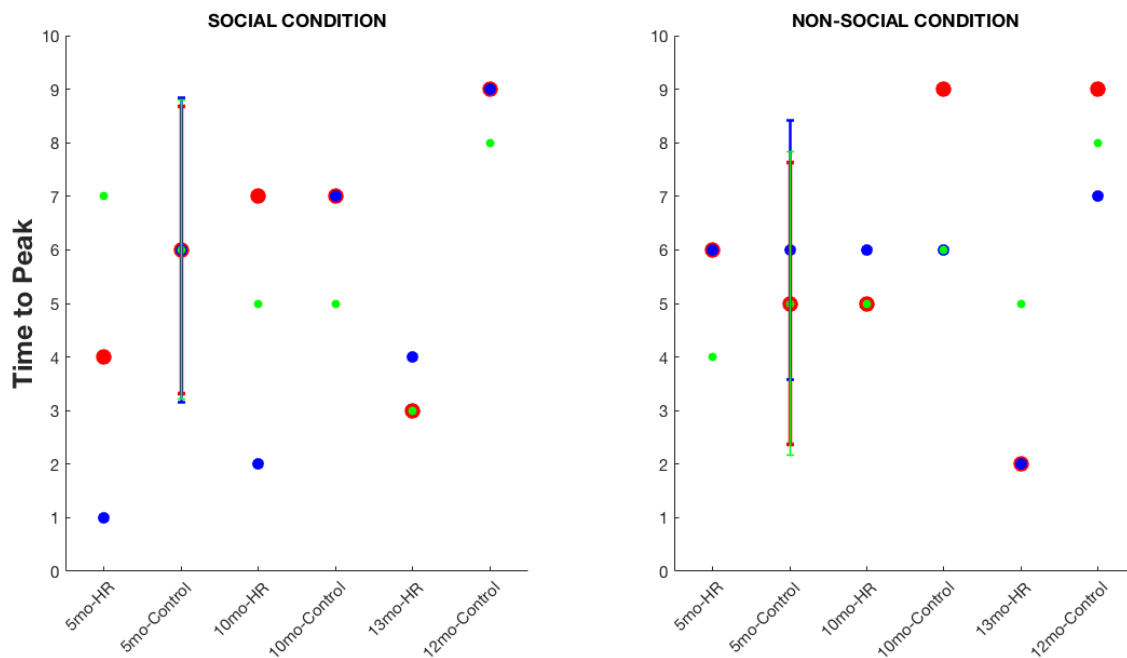
Figure 8.11: The average of the TTP for each chromophore; HbO$_2$ (red), HHb (blue) and oxCCO (green) across temporal channels for the social condition (left) and non-social condition (right) for the HR and LR infants. The error bars for the 5-month-old control infants represent standard deviations.

8.3.1.2.1.2 *Cross-correlations* Cross-correlations were performed between each of the chromophores, for both social and non-social conditions, across all temporal channels. Figures 8.12 - 8.14 show the cross-correlations for each of the HR and LR infants for the social condition. The correlations for the non-social condition followed a similar pattern

and can be found in the appendix. While the correlations between HbO_2 - HHb and HHb - oxCCO are more consistent across HR infants and the controls, the 5-month-old and 13-month-old HR infants display the opposite pattern between HbO_2 and oxCCO in comparison to their age-matched controls. The correlations shown are between (i) HbO_2 and HHb (ii) HHb and oxCCO and (iii) HbO_2 and oxCCO and were averaged across all temporal channels for the social condition. The social and non-social conditions showed a similar pattern therefore the non-social correlations are not shown here and can be found in the appendix.
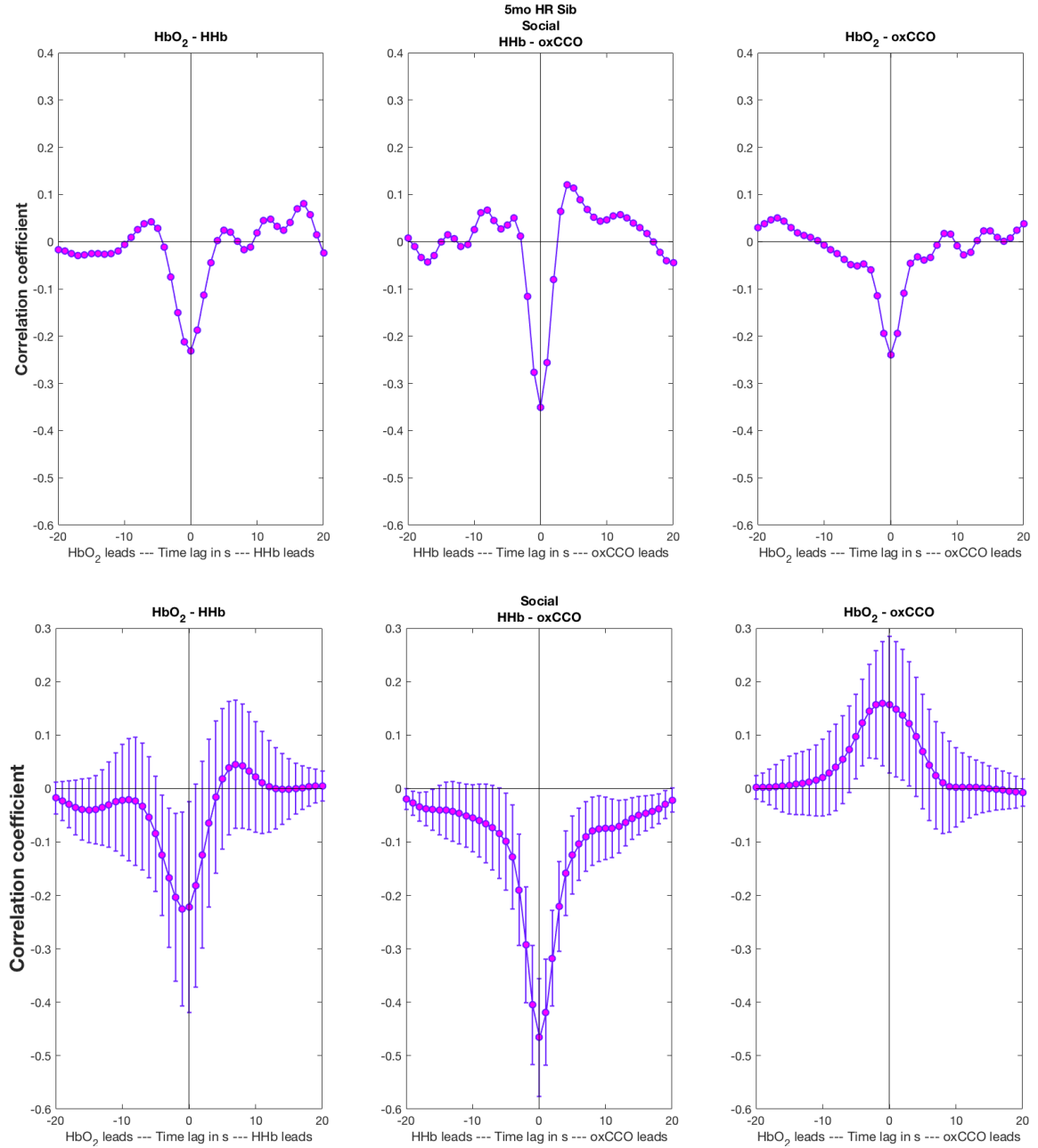
Figure 8.12: The cross-correlations between each of the chromophores, averaged across temporal channels, for the 5-month-old HR infant (upper panel) and 5-month-old controls (bottom panel) for the social condition. The error bars represent standard deviations.
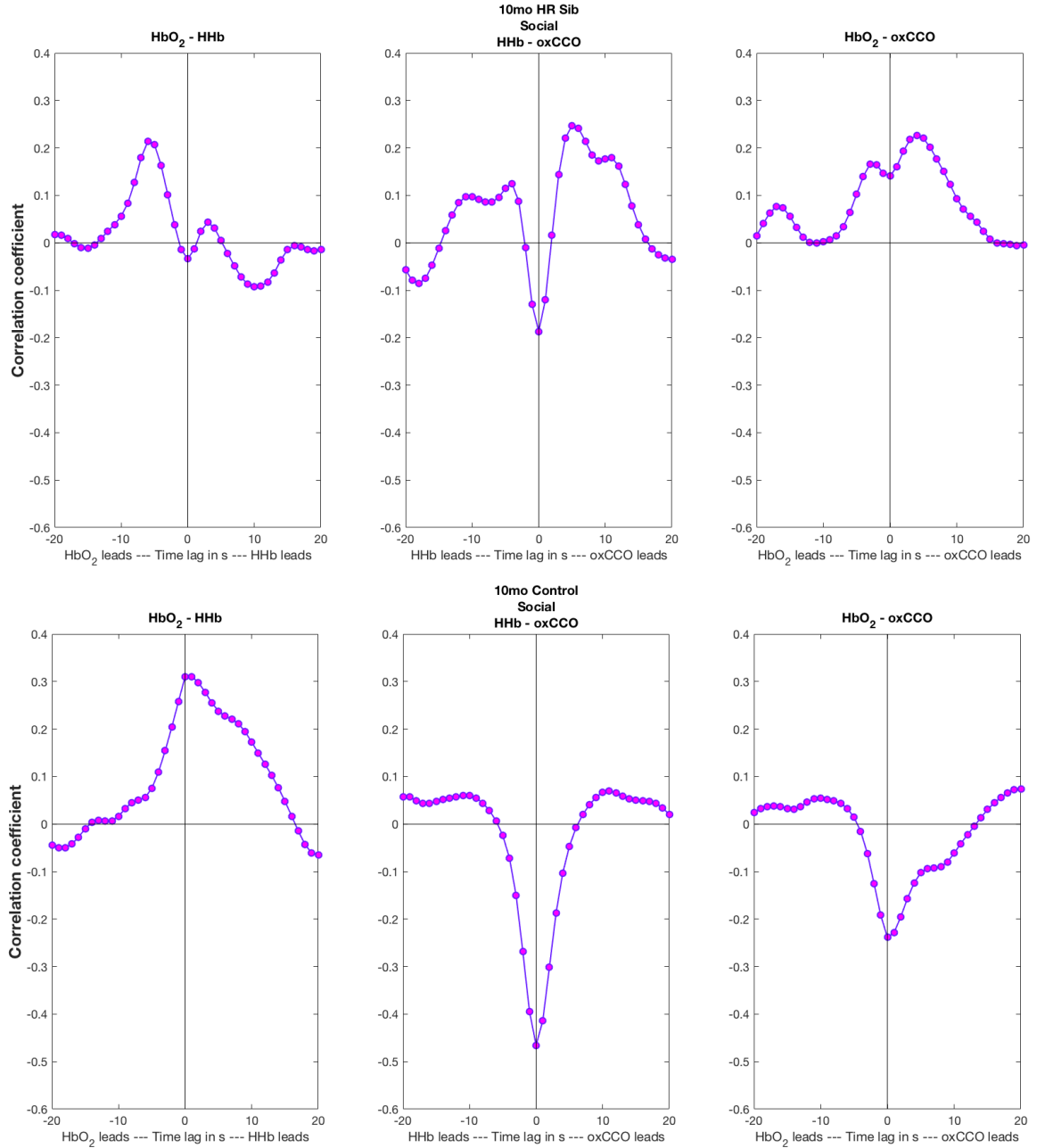
Figure 8.13: The cross-correlations between each of the chromophores, averaged across temporal channels, for the 10-month-old HR infant (upper panel) and 10-month-old LR infant (bottom panel) for the social condition.
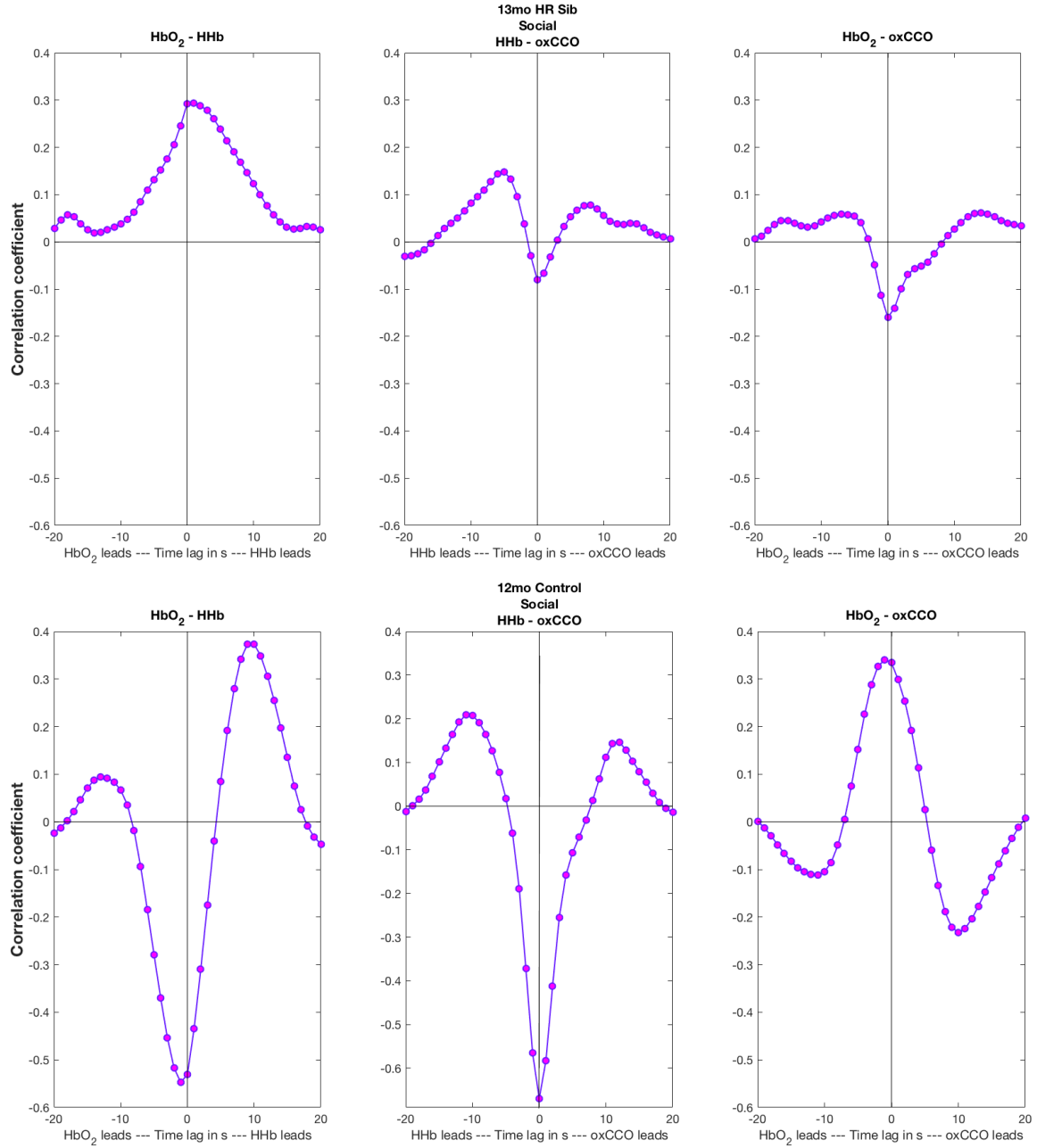
Figure 8.14: The cross-correlations between each of the chromophores, averaged across temporal channels, for the 13-month-old HR infant (upper panel) and 12-month-old control (bottom panel) for the social condition.

8.3.2 EEG

8.3.2.1 Social

Figure 8.15 - 8.17 shows the log power spectral density for the theta and alpha frequency bands for the social condition for the 6-month-old, 13-month-old and 14-month old HR infants and their age matched controls respectively.

In the alpha band, the 6-month-old HR infant displays greater alpha activity over the occipital and right central region. There is also greater alpha suppression in the frontal and temporal regions, where the LR controls display an increase in alpha activity. A similar pattern of theta band activity is seen between the HR and the LR infant, both displaying an increase in alpha activity over the frontal channels and over the occipital channels although, in the HR infant the increase in alpha activity extends from the occipital channels to the occipito-parietal regions.

For the 13-month-old HR infant, in comparison to the LR control, an increase in alpha activity is observed over the left central channels. Meanwhile, the LR 13-month-old infant displays greater frontal alpha activity which is absent in the HR infant. A similar pattern is observed in the theta band where stronger theta activity is seen in the frontal channels in the LR infant while there is increased suppression in the theta band in the HR infant. The theta activity observed in the occipital and left temporal regions is similar in both infants.

Similar patterns are observed when comparing the 14-month-old HR infant to the LR 13-month-old control. In both alpha and theta bands, alpha suppression is observed over the frontal regions in the HR infants and an increase in alpha activity is observed over frontal channels in the LR infant. While the LR infant displays decreased alpha activity over the left temporal and occipital regions (a pattern that is observed in both the 5-month-old LR controls and the 13-month-old control), the HR infant displays greater alpha activity over the right temporal and central channels. In the theta band, an increase in theta activity is observed in the central channels in the HR infant.
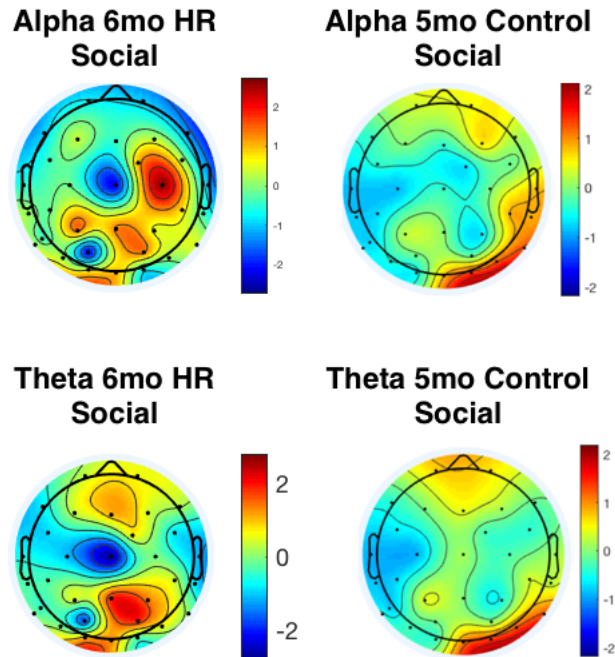
Figure 8.15: Topographical maps of the log power spectral density for the theta and bands for the 6-month-old HR infant and LR controls.
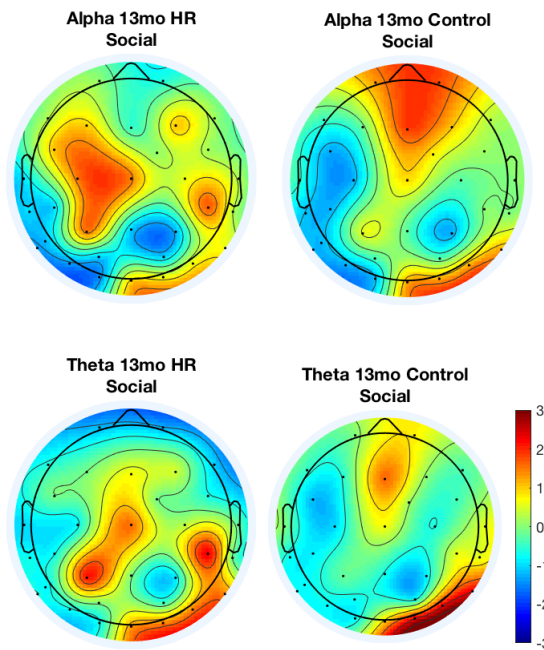
Figure 8.16: Topographical maps of the log power spectral density for the theta and bands for the 13-month-old HR infant and LR control.
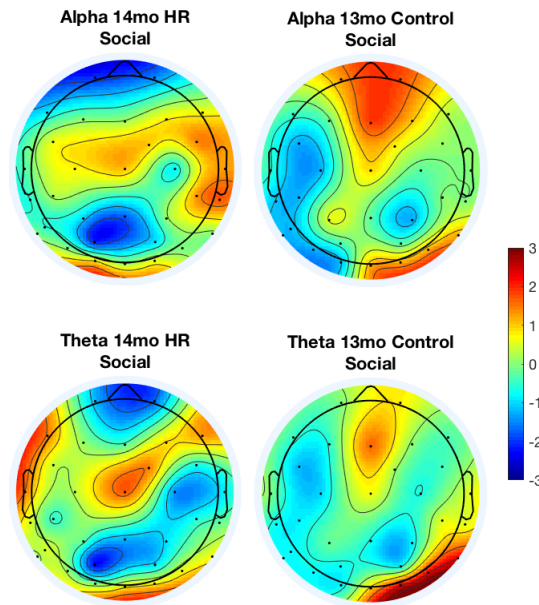
Figure 8.17: Topographical maps of the log power spectral density for the theta and bands for the 14-month-old HR infant and LR control.

8.3.2.2 Non-social

Figure 8.18 - 8.19 shows the log power spectral density for the theta and alpha frequency bands for the non-social condition for the 6-month-old and 10-month-old HR infants and their age matched controls respectively.

For the non-social condition, not many differences are seen in the alpha or theta band between the HR 6-month-old infant and LR controls, with the exception of an increase in alpha activity in the central channels in the HR infant and the absence of theta activity in the frontal channels (which is observed in the LR controls).

For the 10-month-old HR infant an increase in alpha activity is observed in the left central and temporal channels while the LR control infant displays a decrease in alpha activity over the frontal region. In the theta band, differences between the HR and LR infants are observed over the central and occipital channels with the HR displaying an overall decrease in alpha activity over the central channels and the LR displaying an increase in alpha activity in the occipital region which extends to central channels. Additionally, there is an observed increase in frontal theta activity in the HR infant.
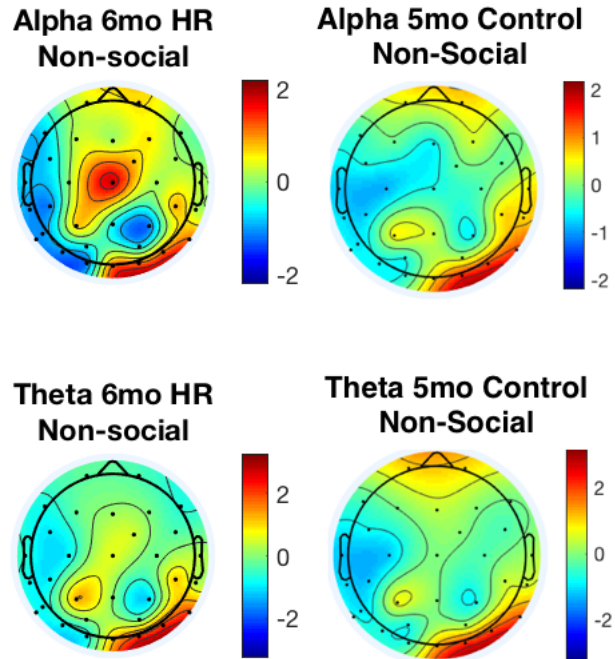
Figure 8.18: Topographical maps of the log power spectral density for the theta and bands for the 6-month-old HR infant and LR controls.
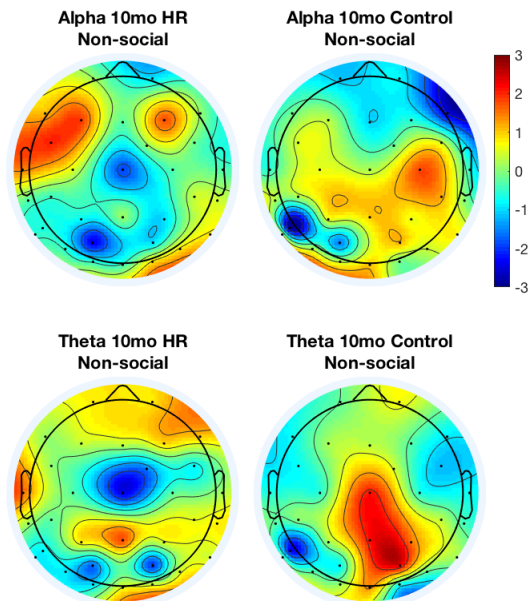
Figure 8.19: Topographical maps of the log power spectral density for the theta and bands for the 10-month-old HR infant and LR control.

8.3.2.3 Social vs Non-social

Figure 8.20 shows the difference in log power spectral density between the social and non-social condition, for the theta and alpha frequency bands, for the 6-month-old HR infant. Data from only one infant is shown as the 6-month-old HR infant was the only one that had good data for both the social and non-social conditions. Both HR and LR infants show greater frontal alpha activity in response to the social condition in comparison to the non-social. The LR controls also show greater temporal alpha activity for the social condition. Over the occipital area, the LR infants display stronger alpha activity for the non-social condition while the opposite is seen in the HR infant where a greater occipital alpha activity is seen for the social condition. Theta band activity between the HR and LR infants is similar with greater frontal theta activity observed for the social condition for both. However, there is greater right temporal (extending to occipital) theta activity for the non-social condition in comparison to the social in the HR infant.
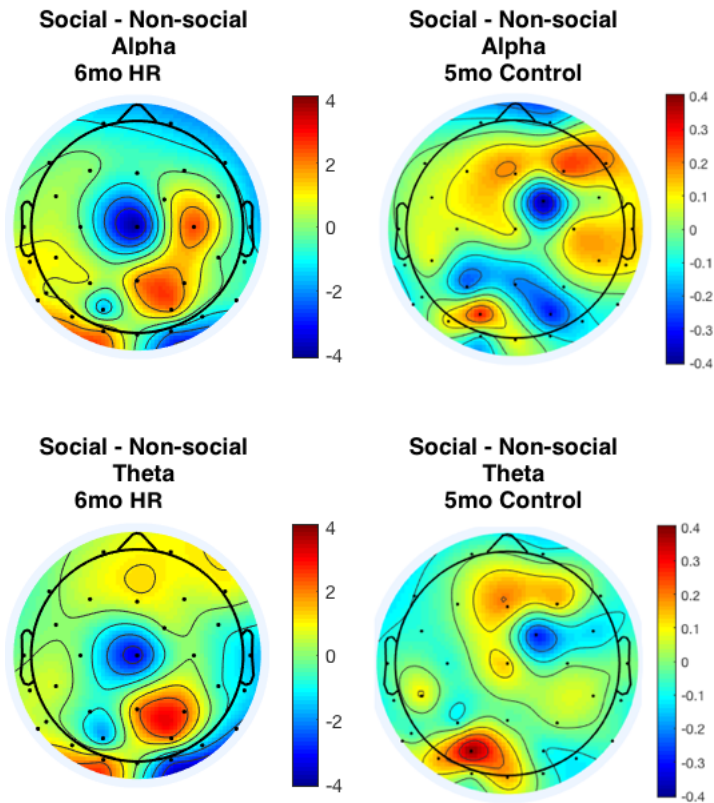
Figure 8.20: Topographical maps of the difference in log power spectral density between social and non-social, for the theta and alpha frequency bands, for the 6-month-old HR infant the LR controls.

8.3.3 Combined NIRS-EEG Analysis

Combined NIRS-EEG analysis was performed by correlating the alpha and theta power to the maximum concentration change occurring in HbO_2, HHb and oxCCO, similar to that in the previous chapter. However here, individual infants were being compared rather than a group of infants and therefore only an overall correlation was obtained between NIRS and EEG channels that were located spatially close to one another over the right temporal cortex. Figure 8.21 shows NIRS and EEG channels to remind the reader of the locations of each of the channels over the right temporal cortex.
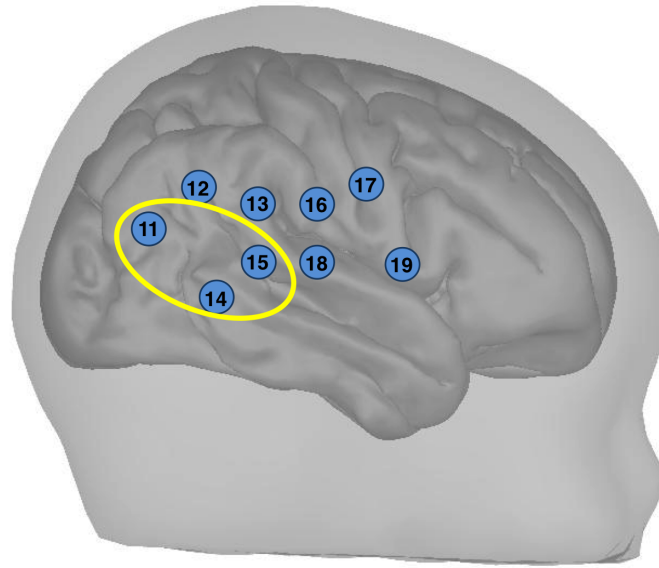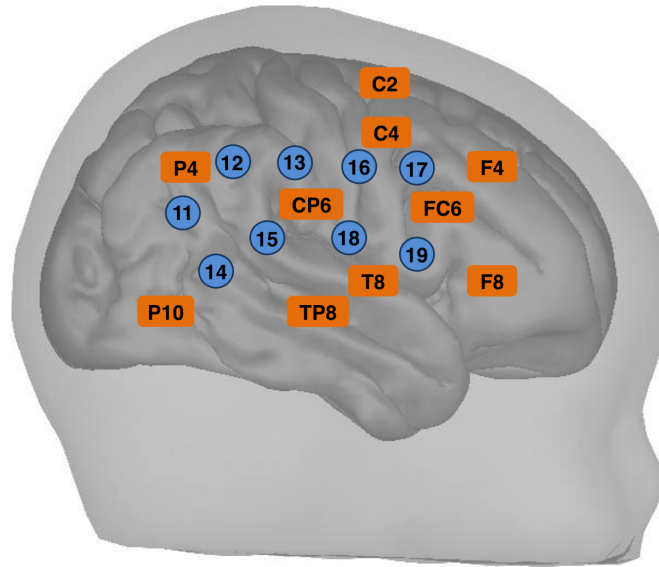
Figure 8.21: Locations of each of the NIRS channels over the right temporal cortex. The channels likely to lie over the STS-TPJ region are indicated by the yellow circle.

Figure 8.22 shows the channels between which correlations were performed and Figure 8.23 represents the average of these channels for each of the infants that were included in this analysis.
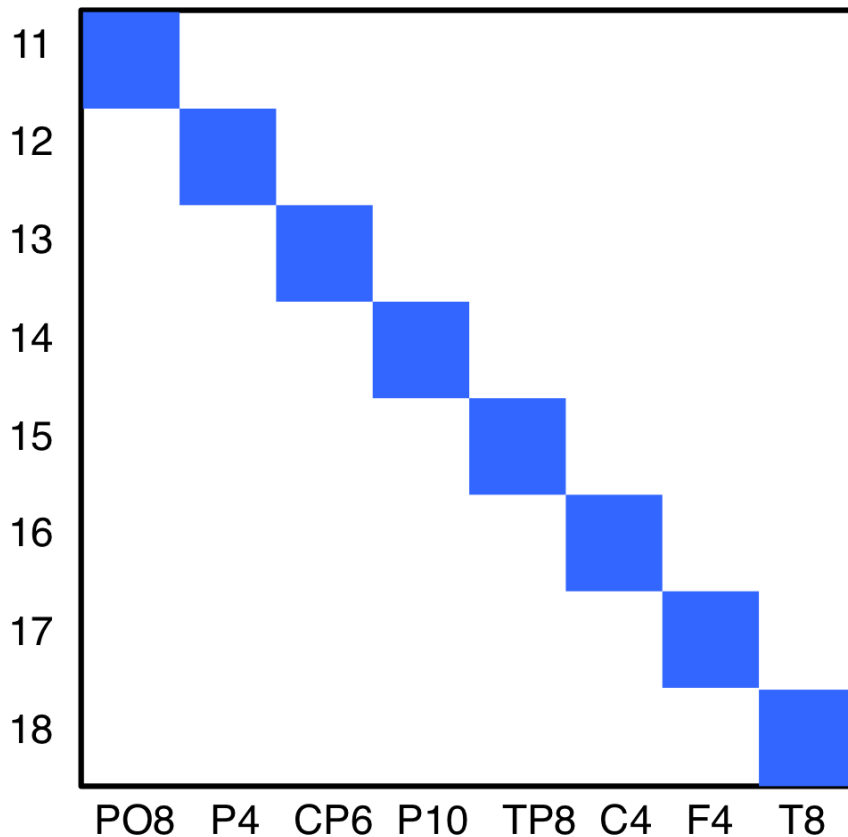
Figure 8.22: Matrix representing the EEG ad NIRS channels between which the correlations were performed (blue squares).

These correlations could only be performed for infants that had both NIRS and EEG data and therefore it is important to note that there is no control infant to compare the correlations for the social condition for 13-month-old HR infant. This is because while the 12-month-old LR control had good NIRS data, it was not included in the EEG analysis and conversely while the 13-month-old LR control had good EEG data it was excluded from the NIRS analysis. The correlations between NIRS and EEG channels seen in Figure 8.23 show, in the 5-month-old HR infant versus the LR controls, the opposite pattern of relationship between neural activity and the NIRS chromophores. That is, the 5-month-old HR infant for the non-social for both theta and alpha power showed a positive relationship between neural activity and HbO_2 and oxCCO while the 5-month-old LR infants showed an inverse relationship between neural activity and HbO_2 and oxCCO. The 10-month-old HR and LR infants displayed the same direction of correlation between alpha and theta power with

HbO$_2$ and HHb (inverse correlation) however a difference between oxCCO was observed with there being a positive relationship between oxCCO and alpha and theta power for the 10-month-old controls and an inverse relationship for the 10-month-old HR infant.
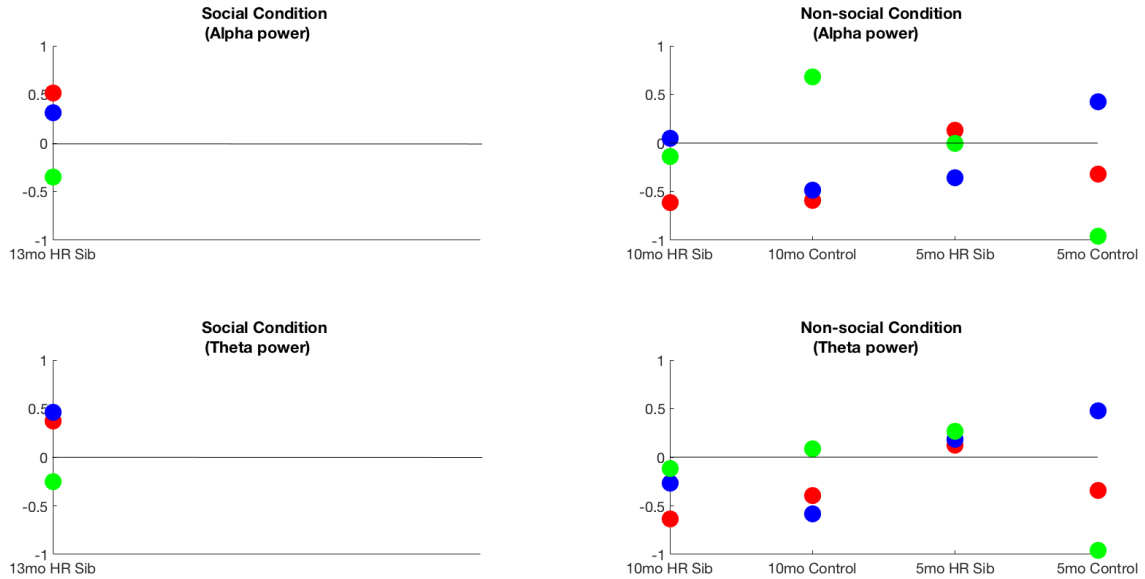
Figure 8.23: Correlations between the mean power spectral density of alpha and theta bands and the maximum change in Δ[HbO$_2$], Δ[HHb] and Δ[oxCCO] for social (left) and non-social conditions (right) between NIRS and EEG channels, for HR and LR infants.

8.4 Discussion

In this chapter, the combined NIRS and EEG protocol that was developed to study typically developing infants in the previous chapter, was used to investigate brain function in infants at-risk for autism. As I discussed in the introduction of this chapter, evidence exists from many previous neuroimaging studies using a variety of techniques such as fMRI, EEG and fNIRS, indicating atypical neural processing of social information in HR-ASD infants and in children, adolescents and adults who have been diagnosed with autism. While much of the work focuses on differences in the measured neural activity, less work has been done to understand the underlying biological mechanisms in the neurovascular coupling pathway that may lead to the observed differences. Broadband NIRS, particularly when used simultaneously with EEG, allows investigation of neurovascular coupling mechanisms but prior to the combined NIRS-EEG protocol being used to establish altered pathways in atypical

brain development, the feasibility of the combined protocol had be demonstrated. To this end, I conducted a proof of principle preliminary study using the combined protocol in six HR-ASD infants varying in age between five and fourteen months, which was presented in this chapter. The feasibility of combining the two techniques to understand atypical brain development was successfully demonstrated which is a milestone in itself and indicates that this protocol can be used on a larger scale to understand biological pathways under-lying autism. Further indicative of this that both HR and LR infants had an average of 6 trials per condition, showing that the HR infants tolerated the study just as well as the LR infants. As a wealth of literature exists investigating the social brain in typical develop-ment, the social and non-social stimuli were focused on. As the infants spanned a wide age range, it was not appropriate to perform analysis on a group level and therefore the results from each of the infants were presented individually.

The NIRS results indicated provisional differences in the HR and LR infants, particu-larly in the 5-month-old infants where an increase in $\Delta[HHb]$ and a diminished response in $\Delta[HbO_2]$ was observed to the social condition in the HR infant, which is in accordance with previous studies (Lloyd-Fox et al., 2013; Braukmann et al., 2018). The opposite pattern was seen in response to the non-social condition. Interestingly however, a decoupling between HbO_2 and oxCCO seemed to occur in many channels, particularly in the 5-month-old and 13-month-old HR infants. That is, while large changes in $\Delta[HbO_2]$ were not present in those channels, there was an increase in $\Delta[oxCCO]$ and often the responses were in op-posite directions in the HR infants. Decoupling of the HbO_2 and oxCCO response was not seen previously in the typically developing infants, which may suggest impaired cou-pling of cerebral blood flow and energy metabolism in atypical brain development which is further supported by the results from the cross-correlation analysis. Impaired or under-developed coupling may be due to a number of reasons. As I have discussed previously, NO and nNOS have been shown to be upregulated in adults (Zoroglu et al., 2003) and in mouse models of autism (Fatemi et al., 2000) which can directly affect the vasoconstric-tion and dilation and therefore affect the oxygen supply to the brain, thereby affecting the observed haemodynamic response.

Furthermore, the HR infants (particularly the 5-month-old HR in the social condition)

showed a greater increase in Δ[oxCCO] in comparison to the LR controls, suggesting that there may possibly be elevated oxygen utilisation and energy metabolism in the HR infants. This would be in line with studies providing evidence of mitochondrial dysfunction and abnormal mitochondrial electron transport chain complexes in individuals with ASD (Rossignol and Frye, 2014; Chauhan et al., 2011; Chauhan and Chauhan, 2006; Gu et al., 2013) which may indicate that oxidative phosphorylation may not be as effective and possibly require more oxygen to meet energy requirements. Furthermore, PET work in adults (Rumsey et al., 1985) has shown increased glucose utilisation in adults with autism. Additionally, studies using an autism animal model in young rats showed an increase in cerebral oxygen consumption (by 50%) in comparison to controls (Weiss et al., 2007). The authors have hypothesised that this may be due to a loss of inhibitory effects of $GABA_A$ (a subclass of GABA receptors) on cerebral metabolic function (Weiss et al., 2008), which are known to have a major effect on cerebral metabolism (Michels and Moss, 2007) particularly in early neuronal development (Jelitai and Madarasz, 2005).

The role of of theta and alpha oscillatory activity has been linked to cognition and memory (Klimesch, 1999) as well as sustained attention (Clayton et al., 2015; Xie et al., 2018) and recent studies have demonstrated impaired theta band modulation in a working memory task (Larrain-Valenzuela et al., 2017) and others have demonstrated impaired sustained attention (Chien et al., 2015; Garretson et al., 1990; Christakou et al., 2013) linked to ASD. Differences were observed in this study both in the theta and alpha bands between HR and LR infants, particularly in the frontal theta activity in the older HR infants. Moreover, differences in temporal and occipital lobe alpha activity were observed as well. However, as I mentioned earlier, more infants are needed to establish a pattern and obtain sufficient evidence of impaired theta and and alpha band modulation in the HR infants.

The combined NIRS and EEG analysis was severely limited as individual infants were being compared and a definitive pattern between oscillatory activity and changes in the concentration of NIRS chromophores over the temporal lobe could not be established. Additionally, due to time constraints, it was only possible to study six infants spanning a wide age range and therefore data could not be collated to obtain more meaningful results. Despite this, the study is a milestone in itself providing the first non-invasive measures of

cerebral energy metabolism using functional neuroimaging, over multiple brain regions, in atypical brain development. Moreover it provides evidence of the feasibility of using combined modalities to investigate brain function in further work in a larger study of HR infants.

Furthermore, there are general limitations to studying HR ASD infants. For example, only on a subset of the infants will receive an autism diagnosis later on in life and therefore many of the HR infants will have a typical developmental trajectory. This is highlighted particularly in the cross-correlations between the 10-month-old HR and LR infants (Figure 8.13) where the HR infant displays the expected correlations between chromophores while the LR infant does not.

Moreover it is also unclear whether those HR infants that are later diagnosed with ASD are representative of the general ASD population and recent work involving simplex (where one family member as autism) and multiplex families (where multiple family members have autism) has suggested that there may be differences in genetic pathways in simplex and multiplex families (Iossifov et al., 2012) and that certain behavioural phenotypes might be more severe in the multiplex families (Taylor et al., 2015). Therefore, it is difficult to ascertain whether the results presented here, particularly the NIRS results, are representative of individuals with ASD and whether they highlight early differences before the emergence of ASD. Further work is required in a larger sample of HR infants and this approach has been adopted by early studies of HR-ASD infants that I discussed in the introduction of this chapter.

Chapter 9

GENERAL DISCUSSION AND CONCLUSIONS

The aim of this PhD work was to use broadband near-infrared spectroscopy to investigate neurometabolic coupling mechanisms during development through measurement of changes in cellular energy metabolism. This thesis has presented many advances in the field of NIRS both in terms of methodological advancements and in understanding typical and atypical brain development. In the following section the experimental findings of this thesis are discussed in relation to the aims that were outlined previously in Chapter 1:

1. *Can broadband NIRS be used to measure changes in cellular oxygen consumption and energy metabolism during functional activation in infancy?*

2. *Can multi-channel broadband NIRS be used in conjunction with EEG successfully to improve our understanding of the status of neurovascular coupling in the infant brain?*

3. *If this is possible, then can the technique be used to help explore the relationship between neuronal activity and cerebral blood oxygenation changes and how does measuring changes in CCO shed a light on this relationship?*

4. *Can differences in regional cortical development be inferred?*

5. *Can this method be applied to understand atypical brain development?*

9.1   Summary of findings

The summary of the main findings from the studies presented in this thesis are presented in Table 9.1.

Chapter	Study	Method	Main Findings (NIRS)	Main Findings (NIRS-EEG)	Methodological advancements
Chapter 3	-	-	-	-	• Development of 3-dimensionally printed NIRS headgear for use with infant studies • Development of headgear for simultaneous NIRS and EEG data acquisition in adults • Development of headgear for simultaneous NIRS and EEG data acquisition in infants
Chapter 4	Non-invasive metabolic marker of infant brain activity	Single channel broadband NIRS in 6-month-old infants (social stimuli)	**NIRS** Increase in cellular metabolic activity over the STS-TPJ region in response to social stimuli	-	-
Chapter 5	NIRS and EEG study of cytochrome in adults	Multi-channel broadband NIRS and EEG in healthy adults (visual stimuli)	**NIRS** • Activation over the visual cortex greater to magnocellular stimuli than parvocellular • CCO displaying highest spatial sensitivity over the visual cortex **EEG** • Greater alpha, beta and gamma band activity and ERPs in response to magnocellular stimuli	• Heterogeneity in relationship between alpha activity and blood oxygenation with some channels displaying an inverse relationship and others positive • Strong inverse relationship between beta and gamma oscillatory activity and blood oxygenation and metabolic activity for both stimuli	• Development of experimental design for simultaneous NIRS and EEG data acquisition in adults

Table 9.1: Summary of findings from each of the studies presented in this thesis.

Chapter	Study	Method	Main Findings (NIRS)	Main Findings (NIRS-EEG)	Methodological advancements
Chapter 6	NIRS and EEG study of cytochrome in infants - Part I	Multi-channel broadband NIRS and EEG in TD 4-to-7-month-old infants (social and non-social stimuli)	**NIRS** • Greater activation to social stimuli than non-social stimuli • Weaker coupling of cerebral blood flow and metabolic activity in comparison to adults **EEG** • Suppression of theta and alpha over left temporal and central regions • Increase in theta and alpha activity over occipital and right temporal cortex	• Positive relationship between alpha oscillatory activity and blood oxygenation • Inverse relationship between alpha activity and oxCCO in majority of channels over STS-TPJ region	• Significant modifications to broadband NIRS system for use with infants
Chapter 7	NIRS and EEG study of cytochrome in infants - Part II	Multi-channel broadband NIRS and EEG in TD 4-to-7-month-old infants (visual stimuli)	**NIRS** • Significant difference in metabolic activity between achromatic and chromatic stimuli with stronger response for chromatic stimulus • CCO much more "active" in the visual cortex • Underdeveloped cerebral blood flow and metabolism coupling in the visual cortex **EEG** • Increase in stimulus-evoked alpha, beta and low gamma activity for both stimuli	• Strong inverse relationship between alpha oscillations and blood oxygenation for achromatic (black/white) stimulus • Heterogeneity of relationship between oscillatory activity and NIRS measures for all other visual stimuli; channels over visual cortex display inverse relationship between alpha and blood oxygenation • Gratings stimuli display strong correlations for gamma oscillatory activity and metabolic activity • CCO strongly correlates with gamma band activity, direction of correlation variable depending on location of channels • Low frequency and high frequency oscillatory activity relate to blood oxygenation and metabolic activity in opposite directions	-
Chapter 8	NIRS and EEG study of cytochrome in infants at-risk for autism	Multi-channel broadband NIRS and EEG in infants at high-risk for autism (social and non-social stimuli)	**NIRS** • Decoupling between oxygenated haemoglobin and CCO observed in some infants • "Inverted" responses to social stimuli observed in some infants	-	-

Table 9.2: Summary of findings from each of the studies presented in this thesis.

Chapter 3 focused on the development of headgear for studies presented in this thesis.

At the onset of this PhD work, handcrafted NIRS arrays were being used for functional activation studies in infants. The studies that were presented in this thesis, particularly simultaneous NIRS and EEG studies, required more adaptable designs that could be easily tailored. The handcrafted NIRS arrays were therefore translated into 3-dimensionally printed arrays which were used in the study described in Chapter 4. The knowledge and development process from this was applied to create the combined NIRS and EEG headgear for use in adults for the study presented in Chapter 5. The final design presented in this chapter was adapted from the designs used in Chapters 4 and 5 to create a final third design for simultaneous NIRS and EEG infant studies which was used in the studies described in Chapters 6, 7 and 8.

At the start of this PhD, there was one reported use of multi-wavelength NIRS in healthy newborns (Zaramella et al., 2001a) to measure changes in cellular energy metabolism alongside haemodynamic changes, in response to auditory stimulation. The authors reported changes in the concentrations of both haemoglobin species but found no changes in the activity of CCO. The first aim of this thesis therefore, was to employ the use of a single channel miniature broadband NIRS system to assess whether functional activation related changes in cellular energy metabolism could be measured in healthy awake infants. For this, an experimental paradigm consisting of social stimuli was designed, that had previously been demonstrated to elicit a robust haemodynamic response to the stimuli (Lloyd-Fox et al., 2017, 2009) over the STS-TPJ region. The results from the study presented in this chapter showed that an increase in oxygenated haemoglobin was coupled with an increase in metabolic activity in response to the experimental stimulus. Furthermore, that the measured increase in metabolic activity was a signal of brain activation as opposed to being the result of cross-talk between haemoglobin species. This motivated all the subsequent work presented in this thesis. The single channel system was useful in validating whether changes in metabolic activity could be measured in the infant brain however, a multi-channel approach measuring responses over multiple brain regions was required in order to understand neurovascular coupling mechanisms and neurometabolic pathways in the developing human brain. The subsequent aims of this thesis therefore were to assess whether multi-channel broadband NIRS could be used in conjunction with EEG to un-

derstand these underlying relationships and whether CCO was a unique marker of brain activity that aided this understanding. Hence, the work presented in Chapter 5 used simultaneous NIRS and EEG in healthy adults during visual stimulation, the motivation for which came from previous studies that demonstrated the robustness of visual paradigms to measure haemodynamic changes in healthy adults (Heekeren et al., 1999b; Phan et al., 2016a; Zeff et al., 2007). The study presented in this chapter had a strong methodological component which enabled the studies presented in Chapters 6 - 8 to be carried out. The results from the study found CCO to be more spatially specific than the haemoglobin species and differential responses were observed over the primary visual cortex, in response to visual stimuli with differing characteristics, providing potential evidence of the different visual processing streams in the visual cortex. These responses related differently to low and high frequency oscillatory activity i.e. low frequency and high frequency activity correlated in opposite directions to haemodynamic and metabolic activity, which has been shown by previous EEG-fMRI work (Scheeringa et al., 2011b, 2016).

Chapter 6 used a similar paradigm to that used in Chapter 4 to measure NIRS and EEG simultaneously over the right temporal cortex in infants. The results from this study were similar to previous results where an increase in oxygenated haemoglobin was accompanied by an increase in metabolic activity over the STS-TPJ region. Low frequency oscillatory activity correlated positively with oxygenated haemoglobin, while CCO related differently, with many channels displaying an inverse relationship between neuronal oscillatory activity and metabolic activity. Furthermore, the results provided potential evidence of the gradual maturation of the relationship between cerebral blood flow and metabolic activity, as shown by previous studies (Kozberg et al., 2013a; Kozberg and Hillman, 2016a). This is because the relationships between chromophores in the temporal cortex were much weaker than those observed in the occipital cortex in adults. With the fifth aim of the thesis in mind, a visual stimulation paradigm that was adapted from the study presented in Chapter 5 was used for NIRS and EEG measurements in infants over the occipital cortex in Chapter 7. Further differences in coupling between energy metabolism and blood flow were observed, even more underdeveloped in the occipital cortex in comparison to the temporal cortex. This therefore suggests differences in regional maturation. Overall, for all

the stimuli, channels located over the primary visual cortex displayed an inverse relationship between low frequency oscillatory activity and changes in oxygenated haemoglobin and oxCCO while peripheral channels showed a different pattern. A similar pattern of decoupling between the relationship of low and high frequency activity with haemodynamic and metabolic changes, as in the adults, was observed.

Having explored the relationship between changes in blood oxygenation and metabolic activity with neural activity in adults and healthy infants, Chapter 8 aimed to explore these relationships in the context of atypical brain development in infants at high-risk for autism. While the results from this study could not provide conclusive evidence of differences between high-risk and low-risk ASD infants due to limited sample size and wide age ranges, a potential emerging result was that a decoupling was occurring between oxygenated haemoglobin and metabolic activity, which was not seen previously in the low-risk infants or adults. This may provide possible evidence of altered mitochondrial function and energy metabolism in the high-risk infants which has been previously implicated in autism (Rossignol and Frye, 2014; Chauhan et al., 2011; Gu et al., 2013; Reynell and Harris, 2013b).

9.2 Theoretical implications

9.2.1 Does the temporal cortex mature more rapidly than the visual cortex?

Differential haemodynamic responses were observed over the temporal and occipital cortices. In the temporal cortex the social stimuli elicited an initial decrease in oxygenated haemoglobin and oxCCO which was followed by a large increase in the concentration of both chromophores. Meanwhile over the visual cortex a different pattern was observed. More specifically, in the responses over the visual cortex a large initial increase in deoxygenated haemoglobin was observed followed by either a small or non increase in oxygenated haemoglobin and oxCCO. While this could be a reflection of differing pathways in place for processing various stimuli, it may also provide evidence of regional differences in the development of neurovascular coupling in early infancy. Particularly as the EEG data suggests that all the stimuli do elicit an increase in stimulus-evoked oscillatory activity. These results are further supported by the fact that there were regional differences

observed in coupling between metabolic activity and blood flow with the temporal cortex displaying a pattern of coupling similar to that observed in the adults while more variability in this coupling was observed over the visual cortex. These results may suggest that there are differences in regional cortical maturation particularly on the vascular side of the neurovascular coupling pathway, thereby affecting the observed haemodynamic responses over the two cortical regions.

The circle of willis is a circulatory anastomosis (ring like arterial connection between blood vessels) which supplies blood to the brain and its surrounding structures. The anterior (ACA), middle (MCA) and posterior cerebral arteries (PCA) branch out from the circle of willis and are responsible for supplying blood to different regions of the brain with the MCA and PCA supplying temporal and occipital lobes respectively. A previous infant study used morphological angiography in order to investigate anatomical differences in the circle of willis in the developing brain (Leijser et al., 2006) and reported an incomplete circle of willis in almost half of the term infants with the most common anatomical variation being in the posterior cerebral vessels in comparison to the anterior vessels. An adult study using the same technique (Krabbe-Hartkamp et al., 1998) reported that 74% of subjects had a complete anterior circle of willis while only 52% had a complete posterior part. Mitchell et al (Mitchell et al., 1989) used color Doppler imaging on term infants to measure blood flow and reported that normal flow in the ACA and MCA were found in all infants but not in the PCA. These differences in regional blood supply to temporal and occipital cortices may play a role in the differences observed in the haemodynamic responses. Furthermore, previous work in humans has reported a significant increase in angiogenesis (the increase in the formation of new capillaries and vessels) during development (Norman and O'Kusky, 1986). The authors from this study hypothesised that during developmental increases in blood vessel density, and therefore the coupling between neuronal activity and cerebral blood flow, may not be as efficient in comparison to when the vasculature is fully developed.

Moreover, CBF and $CMRO_2$ are known to affect the haemodynamic responses directly and previous studies using SPECT (Chiron et al., 1992) and PET (Takahashi et al., 1999) have demonstrated that both rCBF and $rCMRO_2$ are significantly lower in early infancy

and that $CMRO_2$ continues to increase until late childhood (Chugani et al., 1987). The work by Chugani et al (1987) has also demonstrated regional differences in the cerebral metabolic rate of glucose uptake (CMRG) in the occipital and temporal cortices, with the occipital cortex showing a slower maturational increase peaking around 6-8 months post-natally. This is supported by previous rat work (Kozberg et al., 2013a) that demonstrated an absence of functional hyperemia in the presence of large neural responses and a significantly lower rate of oxygen metabolism that gradually increased postnatally. While these results were from the somatosensory cortex, it may provide evidence that oxidative metabolism itself undergoes maturational changes during development particularly when coupled with the idea that CMRG and $CMRO_2$ show regional differences. This may be another reason why regional differences in the haemodynamic response are observed. Lin et al (2013) used frequency-domain NIRS alongside diffuse correlation spectroscopy and additionally demonstrated that CBF, cerebral blood volume (CBV), haemoglobin oxygenation saturation (SO_2) and $CMRO_2$ were greater in temporal and parietal regions in comparison to other regions in newborns.

Postnatal cortical expansion has also been shown to be non-uniform and a study comparing healthy infants and adults using MRI scans has demonstrated that lateral frontal, temporal and parietal regions expand almost twice as much as the insula and medial occipital cortex (Hill et al., 2010). It has been hypothesised that these differences in cortical expansion may reflect postnatal synaptic expansion which has been reported to occur in a heterochronic manner with the visual cortex peaking around 4-8 months postnatally (Garey and de Courten, 1983). Synaptogenesis is followed by a significant period of synaptic pruning which has also been shown to occur at differential rates regionally (Huttenlocher and Dabholkar, 1997; Tierney and Nelson, 2009; Garey and de Courten, 1983; Harris et al., 2011). Developmental changes in synaptic density will affect the observed haemodynamic response, particularly an increase in synaptic density which leads to an increase in metabolic demand (Martin et al., 1999b).

Furthermore, the role of stimulus complexity cannot be overlooked in understanding differences in the observed haemodynamic responses. Previous infant studies using fNIRS (Watanabe et al., 2012a; Taga et al., 2003, 2004; Liao and Tjong, 2010) have used a vari-

ety of stimuli including black and white inverting checkerboards and reported a classical haemodynamic response in the occipital cortex to the stimuli. However, there have also been previous reports of "inverted" responses over the occipital cortex by fNIRS infant studies (Meek et al., 1998; Karen et al., 2008) and a number of fMRI studies that have reported a decrease in blood oxygenation level to visual stimulation (Born et al., 1998, 2000; Martin et al., 1999b; Yamada et al., 1997) with many of the studies reporting "biphasic" responses, i.e. classical responses in some infants and inverted responses in others. The differences in haemodynamic responses in the visual and temporal cortices may provide evidence of an "evolving" haemodynamic response which starts off being similar to the responses observed over the occipital cortex and gradually matures to assume the shape of that observed over the temporal cortex. Previous work in rats (Kozberg et al., 2013a) has demonstrated that in postnatal rats between P15 and P23 the amplitude of the oxygenated haemoglobin in the somatosensory cortex progressively increased with age. The authors therefore hypothesised that intermediate age groups may exhibit a biphasic negative-to-positive change in oxygenated haemoglobin. Infant fMRI work by Arichi et al (2012) have also also postulated a similar hypothesis. Therefore it is possible that the differences observed in the results here might be a representation of the biphasic responses that these authors describe. It would be interesting to investigate individual differences in the data from Chapters 6-8 to see if a pattern of regional differences emerges at that level and whether differences in occipital and temporal responses could be used as a measure of individual developmental trajectory. Deen et al (2017) used faces and naturalistic scenes as stimuli in an infant fMRI study and found that in the visual cortex, the profile of the HRF and pattern of activity varied across visual categories between infants.

Previous fMRI work in adults (Goodyear and Menon, 1998; Marcar et al., 2004b,a) has shown that in the visual cortex, an increasing number of active neurons leads to an increase in oxygen consumption that is not matched by an equal increase in blood flow, resulting in no or a very small change in blood oxygenation levels, as is observed in my results. This may imply that the observed haemodynamic response may critically depend on the amount of neural activity that is evoked by the experimental stimulus (Harris et al., 2011).

9.2.2   Neurovascular coupling in the developing brain

The previous section discussed the differences observed in haemodynamic differences over temporal and visual cortices and the reasons why they might be occurring. Differences were also observed in the coupling between blood flow and energy metabolism between infants and adults with the infant cross-correlation analysis providing potential evidence that coupling mechanisms in the infant brain are not fully developed, particularly in the occipital lobe. Meanwhile, in the results from the adult study presented in Chapter 5 strong relationships between all three chromophores were observed, indicative of fully developed neurovascular coupling mechanisms. This suggests that functional hyperemia is still developing and that as neural circuitry, vasculature and networks expand and are pruned over the first year of life, that the optimised mechanism of oxygen delivery may also be developing. The previous section already discussed a number of factors that might lead to the differences in the observed relationship between haemodynamic and metabolic activity such as ongoing cerebral vascular development, angiogenesis and synaptogenesis. There are also a number of different components of the NVU that are under development that may also affect the observed responses. For instance, astrocytes and pericytes are known to be under ongoing development early on in life (Hall et al., 2014; Seregi et al., 1987; Stichel et al., 1991; Yang et al., 2013) and previous studies have suggested that they undergo a dramatic maturation process (Yang et al., 2013). Moreover, previous work has also demonstrated varying astrocytic density across different cortical regions (Roessmann and Gambetti, 1986). Furthermore, other studies (Chen et al., 2014; Bustamante et al., 2008) have reported a reduced expression of endothelial NOS which is important for cerebral blood flow regulation as NO is an important regulator of vascular tone. Developmental differences in the enzyme that synthesises NO will therefore affect NO-mediated pathways thereby influencing the observed haemodynamic response. Lastly, amine neurotransmitters, which are known to play an important role in cognition (Frederick and Stanwood, 2009; Harris et al., 2011; Ansorge et al., 2004; Rebello et al., 2014; Page et al., 2009) have been shown to be under development and may significantly impact neurovascular coupling (Lambe et al., 2000; Murrin et al., 2007) .

9.2.3 Differences in the relationship of low and high frequency oscillations with haemodynamics and metabolism

While many studies have focussed on exploring the relationship between haemodynamic activity and neuronal oscillations in the gamma frequency band (Logothetis, 2008; Niessing et al., 2005; Logothetis et al., 2001b) others have provided evidence that lower frequency oscillations such as alpha and beta are correlates of the haemodynamic response and that their role in the generation of haemodynamic activity cannot be ignored (Kilner et al., 2005; Laufs et al., 2006; Rosa et al., 2010; Scheeringa et al., 2011b). The results presented in this thesis also provide evidence of differential relationships between neuronal oscillations and haemodynamics that vary depending on the experimental stimulus, the brain region and the location of measurement within brain regions. It has been hypothesised that this may be the result of the employment of different brain networks for different tasks (Mantini et al., 2007; Sumiyoshi et al., 2012). It appeared that during social processing in channels over the temporal cortex, haemodynamic activity was coupled with alpha band activity while during the processing of visual stimuli, an inverse coupling was observed which has been reported more consistently (Scheeringa et al., 2011b; Yuan et al., 2010; Goldman et al., 2002). Although, previous studies (Logothetis, 2008; Niessing et al., 2005; Logothetis et al., 2001b) have also showed a positive relationship between alpha activity and blood oxygenation level. These differing results are not surprising though, given the regional differences that were observed in the coupling between blood flow and energy metabolism between temporal and occipital cortices.

Furthermore, while regional differences exist, the direction of the relationships between low and high frequency bands and NIRS measures also differ. For example, during visual stimulation, inverse relationships were observed between alpha and beta oscillations with oxCCO and HbO_2. Gamma oscillations however, correlated positively. A similar result has been reported in work by Scheeringa et al (2011b) that used simultaneous EEG and fMRI during a visual attention task in adults and reported that low and high frequency oscillations correlated differentially with the BOLD response. Moreover, other studies (Scheeringa et al., 2011a, 2016; Lachaux et al., 2007; Zaehle, 2009; Mulert et al., 2010; Gi-

raud et al., 2007; Mantini et al., 2007) have specifically reported a stronger coupling between gamma oscillations and haemodynamic activity. Although many of the studies only explore correlations in the high gamma frequency range (>60 Hz). It has been postulated that the low and high frequency oscillations may potentially be generated through different mechanisms or through the employment of different cell-types (Scheeringa et al., 2011a) or different layers of the cortex (Scheeringa et al., 2016) during neural synchronisation. A previous study using cell-type-specific optogenetic activation in the somatosensory cortex of adult mice demonstrated that fast-spiking GABAergic interneurons specifically increased the LFP in the gamma band while the rhythmic driving of pyramidal neurons caused an increase in LFP power in lower frequency bands (Cardin et al., 2009). This does not however, imply that these different types of neurons generate oscillations in different frequency bands independently, but are involved in the generation of both low and high frequency oscillations (Börgers and Kopell, 2005; Hasenstaub et al., 2005). While high frequency oscillations correlate positively with haemodynamic and metabolic activity, a number of studies have reported an inverse relationship with alpha and beta frequency bands in a number of tasks over different brain areas (Feige et al., 2005; Laufs et al., 2003b,c; Meltzer et al., 2007; Moosmann et al., 2003; Scheeringa et al., 2009; Yuan et al., 2010) which is in line with the results from the visual stimuli but not the social/non-social stimuli.

Moreover, while coupling between HbO_2 and gamma oscillations is seen in the results, CCO appears to be more tightly coupled with gamma band oscillations. Previous research (Kann et al., 2011; Attwell and Iadecola, 2002) has demonstrated that gamma oscillations are associated with an increase in oxidative metabolism characterised by an increase in oxygen consumption. This may be due to a number of reasons, Gulyas et al (2006) have suggested that GABAergic interneurons which are involved in the generation of gamma oscillations, contain a high number of mitochondria. Other studies suggest that the fast alternating pairs of sources and sinks that are required to generate gamma oscillations may require increased activity of the ETC to restore ionic gradients. Another pattern that is more strongly observed between CCO and frequency bands is that correlations over the specific area of interest (for example primary visual cortex) display a different pattern in comparison to correlations over peripheral areas (for example extrastriate cortex). Specifically in

the gamma band, positive correlations are observed over the primary visual cortex while negative correlations are observed over the extrastriate regions. This might be indicative of the fact that the areas involved in the processing of stimuli have increased consumption in oxygen leading to decreased oxygen availability for the extrastriate regions. For infants, this may be particularly true as there may be a limited influx of oxygenated blood flow and past work in postnatal rats reported the presence of a global vasoconstrictive mechanism in response to activation which the authors suggested might be the a protective mechanism in place in the delicate developing brain in order to limit blood flow (Kozberg et al., 2013a).

9.3   Limitations and Future Directions

The combined NIRS and EEG data presented in this thesis represents one of the first series of studies to utilise simultaneous NIRS and EEG during functional activation in infants and the first to utilise broadband NIRS with EEG in infants. A number of methodological and technical challenges needed to be overcome in order to carry out this work and due to time restrictions only correlation analysis combining NIRS and EEG data were performed. This is one of the major limitations of the combined NIRS and EEG results presented in Chapters 5 - 8. As I have mentioned previously, the correlation analysis performed assumed a linear relationship between neural activity, haemodynamics and energy metabolism when in fact, neurovascular coupling is highly complex involving a number of intermediate pathways. At the first instance, a non-linear approach is required to investigate how the EEG and NIRS time-series correlate with one another using cross-correlation or time-series analysis. Wavelet coherence analysis (Tian et al., 2016) is a technique that can transform time-series into the time-frequency domain using Morlet wavelets to obtain the cross-wavelet transform of the two time-series. This can then yield the wavelet transfer function (similar to the Fourier transform), the modulus of which provides the relative power (gain) between the time-series and the complex argument provides the phase relationship. The cross-wavelet coherence can be obtained using the square of the wavelet transfer function. This technique has been used previously to investigate neurovascular coupling in neonatal encephalopathy (Chalak et al., 2017) and in brain injured patients to assess the relationship between

NIRS variables and physiological parameters (Highton et al., 2015).

A more far reaching aim could be to implement the use of computational modelling in order to more appropriately integrate EEG and NIRS data, for which a number of different models have been proposed (Rosa et al., 2011). Of these, the most innovative is *dynamic causal modelling (DCM)* proposed by Friston et al (2003) which has been used to characterise functional connectivity in adults (Friston, 2011; Schuyler et al., 2010) and recently in infants (Bulgarelli et al., 2018) and can also be used to integrate EEG and fMRI data (Friston et al., 2017). Briefly, the basic idea behind DCM is to model causal interactions either between brain regions or haemodynamic and electrophysiological responses that are mediated by coupling parameters that can be estimated using Bayesian statistics. Another approach may be to use a *psycho-physiological interaction model (PPI)* which estimates interactions between variables (but does not provide directionality or causality) and has been used previously in EEG-fMRI studies to explore the relationship between neuronal oscillations and the BOLD response (Vaudano et al., 2013; Scheeringa et al., 2012; Zotev et al., 2016) and more recently to investigate functional connectivity using fNIRS (Piva et al., 2017). While both these techniques are promising, they require EEG and NIRS data to be integrated into the Statistical Parametric Mapping (SPM) framework (Friston et al., 2007; Tak et al., 2016) which is currently not widely used to process infant NIRS data. This is because it uses general linear modelling (GLM) to model the haemodynamic response based on a pre-specified HRF shape. This may be difficult to implement and to use to accurately interpret results in infants, given the degree of variability that is observed in the amplitude and latency of haemodynamic responses, as seen in particular with the data presented in this thesis. Other models to integrate EEG and fMRI data have also been proposed, which can be extended to fNIRS data, and include *biophysical models* (Sotero and Trujillo-Barreto, 2008) and *models of metabolism* (Shulman et al., 2001; Aubert and Costalat, 2005). These include neural mass models (Babajani and Soltanian-Zadeh, 2006) which are based on physiological principles of cortical microcolumns and their connections and local electrovascular coupling models (Riera et al., 2006).

Furthermore, while interesting relationships between oxygenated haemoglobin and cerebral energy metabolism emerged in the infant brain through the work presented in

this thesis, further work is necessary to understand the physiological parameters that may manifest in the observed underdeveloped coupling of cerebral blood flow and energy metabolism. The BrainSignals model is a biophysical model of cerebral physiology developed to explore the relationships between measured NIRS responses and the key parameters that may give rise to them. This model has been developed for adults (Banaji et al., 2008; Caldwell et al., 2015), neonates (Hapuarachchi, 2015) and piglets (Moroz et al., 2012) and can be modified for infants. Sensitivity analysis can be performed to identify the parameters that each of the measured chromophores would be most sensitive to, thereby allowing a more in-depth investigation of physiological factors that are important during infant brain development and may differ from adult physiology.

Another future direction could possibly be to use broadband NIRS over a range of ages from newborn to 24-months-old in order to explore how the relationship between metabolic and haemodynamic activity evolves across development and at which age it starts to resemble that observed in adults. This methodology could then be further expanded on to investigate developmental trajectories of other brain regions, specifically those that are known to mature more slowly such as the prefrontal cortex (Deen et al., 2017; Tierney and Nelson, 2009). This could potentially be useful in providing a non-invasive method of providing measures of structural brain development.

Lastly, an important future direction is to acquire data in a larger sample of HR infants over a range of ages in order to explore whether there truly is a decoupling that occurs between haemodynamic and metabolic activity. If this is the case, then broadband NIRS could be a promising tool for investigating atypical brain function and may provide a new avenue of non-invasive research in autism. Hitherto, fMRI and NIRS work has provided measures of blood oxygenation levels and the use of broadband NIRS particularly with EEG, allows us to improve our understanding of basic cellular mechanisms in disorders such as autism. Moreover, the studies that have demonstrated mitochondrial dysfunction in children with autism have performed studies on post-mortem brain tissue. Simultaneous broadband NIRS with EEG would allow us to obtain these measurements non-invasively in awake infants relatively easily and would therefore be an invaluable tool in this line of research. Furthermore, studies have reported reduced expression of mi-

tochondrial ETC genes in children with ASD (Gu et al., 2013; Giulivi et al., 2010; Anitha et al., 2012). Thus, it would be interesting to relate mitochondrial DNA expression with observed changes in oxCCO in both low and high-risk infants. In particular, DNA methylation studies may be an interesting future direction as recent evidence from an epigenetic study has emerged implicating abnormal mitochondrial metabolism in autism (Stathopoulos et al., 2018).

9.4   Concluding remarks

With this PhD work, the capability of the use of broadband NIRS in infants to understand the neurometabolic pathways in both typical and atypical brain development has been demonstrated. Through a number of pioneering studies utilising broadband NIRS simultaneously with EEG, made possible by extensive headgear development, I provided evidence that broadband NIRS measures of cellular oxygen metabolism do provide a unique marker of brain activation and can be used to further our understanding of neurovascular coupling mechanisms in the developing brain. Alongside developing methods to perform concurrent NIRS and EEG studies in infants aged between 4-to-14-months of age, I also provided evidence of regional differences in neurovascular coupling and further elucidated the relationships between neural activity, haemodynamics and oxidative metabolism in infancy. Moreover, I showed how NIRS and EEG may be used simultaneously to investigate neurophysiological differences in high-risk ASD infants and while results from this study were not conclusive, this study provides an exciting direction for future research.

Bibliography

Abbott, N. J., Rönnbäck, L., and Hansson, E. (2006). Astrocyte-endothelial interactions at the blood-brain barrier.

Abboub, N., Nazzi, T., and Gervain, J. (2016). Prosodic grouping at birth. *Brain and Language*, 162:46–59.

Adolphs, R. (2009). The Social Brain: Neural Basis of Social Knowledge. *Annual Review of Psychology*.

Afifi, L., Raafat, H., Abdullah, K., Elhabashy, H., and Raafat, O. (2015). Quantitative EEG in autistic children. *The Egyptian Journal of Neurology, Psychiatry and Neurosurgery*, 52(3):176.

Akerman, C. J. and Cline, H. T. (2007). Refining the roles of GABAergic signaling during neural circuit formation. *Trends in Neurosciences*, 30(8):382–389.

Akyol, O., Zoroglu, S. S., Armutcu, F., Sahin, S., and Gurel, A. (2004). Nitric oxide as a physiopathological factor in neuropsychiatric disorders. *In vivo (Athens, Greece)*, 18(3):377–90.

American Psychiatric Association (2013). Diagnostic and Statistical Manual of Mental Disorders, 5th Edition (DSM-5). *Diagnostic and Statistical Manual of Mental Disorders 4th edition TR.*, page 280.

Andersen, P., Eccles, J. C., and Løyning, Y. (1963). Hippocampus of the brain: Recurrent inhibition in the hippocampus with identification of the inhibitory cell and its synapses. *Nature*, 198(4880):540–542.

Anitha, A., Nakamura, K., Thanseem, I., Yamada, K., Iwayama, Y., Toyota, T., Matsuzaki, H., Miyachi, T., Yamada, S., Tsujii, M., Tsuchiya, K. J., Matsumoto, K., Iwata, Y., Suzuki, K., Ichikawa, H., Sugiyama, T., Yoshikawa, T., and Mori, N. (2012). Brain region-specific altered expression and association of mitochondria-related genes in autism. *Molecular autism*, 3(1):12.

Ansorge, M. S., Zhou, M., Lira, A., Hen, R., and Gingrich, J. A. (2004). Early-life blockade of the 5-HT transporter alters emotional behavior in adult mice. *Science*, 306(5697):879–881.

Arichi, T., Fagiolo, G., Varela, M., Melendez-Calderon, A., Allievi, A., Merchant, N., Tusor, N., Counsell, S. J., Burdet, E., Beckmann, C. F., and Edwards, A. D. (2012). Development of BOLD signal hemodynamic responses in the human brain. *NeuroImage*, 63(2):663–673.

Arizona Board of Regents (2012). Neuron Diagram | ASU - Ask A Biologist.

Armulik, A. (2005). Endothelial/Pericyte Interactions. *Circulation Research*, 97(6):512–523.

Attwell, D., Buchan, A. M., Charpak, S., Lauritzen, M., MacVicar, B. A., and Newman, E. A. (2010a). Glial and neuronal control of brain blood flow. *Nature*, 468(7321):232–243.

Attwell, D., Buchan, A. M., Charpak, S., Lauritzen, M., MacVicar, B. A., and Newman, E. A. (2010b). Glial and neuronal control of brain blood flow.

Attwell, D. and Iadecola, C. (2002). The neural basis of functional brain imaging signals. *Trends in Neurosciences*, 25(12):621–625.

Attwell, D., Mishra, A., Hall, C. N., O'Farrell, F. M., and Dalkara, T. (2016). What is a pericyte? *Journal of cerebral blood flow and metabolism : official journal of the International Society of Cerebral Blood Flow and Metabolism*, 36(2):451–5.

Aubert, A. and Costalat, R. (2005). Interaction between astrocytes and neurons studied using a mathematical model of compartmentalized energy metabolism. *Journal of Cerebral Blood Flow and Metabolism*.

Babajani, A. and Soltanian-Zadeh, H. (2006). Integrated MEG/EEG and fMRI model based on neural masses. *IEEE Transactions on Biomedical Engineering*.

Bailey, A. J., Braeutigam, S., Jousmäki, V., and Swithenby, S. J. (2005). Abnormal activation of face processing systems at early and intermediate latency in individuals with autism spectrum disorder: a magnetoencephalographic study. *The European journal of neuroscience*.

Bainbridge, A., Tachtsidis, I., Faulkner, S. D., Price, D., Zhu, T., Baer, E., Broad, K. D., Thomas, D. L., Cady, E. B., Robertson, N. J., and Golay, X. (2014). Brain mitochondrial oxidative metabolism during and after cerebral hypoxia-ischemia studied by simultaneous phosphorus magnetic-resonance and broadband near-infrared spectroscopy.

Bale, G., Elwell, C. E., and Tachtsidis, I. (2016a). From Jöbsis to the present day: a review of clinical near-infrared spectroscopy measurements of cerebral cytochrome-c-oxidase. *Journal of Biomedical Optics*, 21(9):91307.

Bale, G., Mitra, S., de Roever, I., Chan, M., Caicedo-Dorado, A., Meek, J., Robertson, N., and Tachtsidis, I. (2016b). Interrelationship between broadband NIRS measurements of cerebral cytochrome C oxidase and systemic changes indicates injury severity in neonatal encephalopathy. In *Advances in Experimental Medicine and Biology*, volume 923, pages 181–186.

Bale, G., Mitra, S., de Roever, I., Sokolska, M., Price, D., Bainbridge, A., Gunny, R., Uria-Avellanal, C., Kendall, G. S., Meek, J., Robertson, N. J., and Tachtsidis, I. (2018). Oxygen dependency of mitochondrial metabolism indicates outcome of newborn brain injury.

Bale, G., Mitra, S., Meek, J., Robertson, N., and Tachtsidis, I. (2014). A new broadband near-infrared spectroscopy system for in-vivo measurements of cerebral cytochrome-c-oxidase changes in neonatal brain injury. *Biomedical Optics Express*, 5(10):3450.

Banaji, M., Mallet, A., Elwell, C. E., Nicholls, P., and Cooper, C. E. (2008). A model of brain circulation and metabolism: NIRS signal changes during physiological challenges. *PLoS Computational Biology*.

Bates, E. and Dick, F. (2002). Language, gesture, and the developing brain. *Developmental Psychobiology*.

Begus, K. and Southgate, V. (2012). Infant pointing serves an interrogative function. *Developmental Science*.

Belger, A., Carpenter, K. L. H., Yucel, G. H., Cleary, K. M., and Donkers, F. C. L. (2011a). The Neural Circuitry of Autism. *Neurotoxicity Research*, 20(3):201–214.

Belger, A., Carpenter, K. L. H., Yucel, G. H., Cleary, K. M., and Donkers, F. C. L. (2011b). The Neural Circuitry of Autism. *Neurotoxicity Research*, 20(3):201–214.

Belliveau, J. W., Kennedy, D. N., McKinstry, R. C., Buchbinder, B. R., Weisskoff, R. M., Cohen, M. S., Vevea, J. M., Brady, T. J., and Rosen, B. R. (1991). Functional mapping of the human visual cortex by magnetic resonance imaging. *Science*, 254(5032):716–719.

Ben-Ari, Y. (2002a). Excitatory actions of gaba during development: the nature of the nurture. *Nature Reviews Neuroscience*, 3(9):728–739.

Ben-Ari, Y. (2002b). Excitatory actions of GABA during development: The nature of the nurture.

Benaron, D. A., Van Houten, J. P., Cheong, W.-F., Kermit, E. L., and King, R. A. (1995). Early clinical results of time-of-flight optical tomography in a neonatal intensive care unit. volume 2389, pages 582–596. International Society for Optics and Photonics.

Benedek, G., Horváth, G., Kéri, S., Braunitzer, G., and Janáky, M. (2016). The Development and Aging of the Magnocellular and Parvocellular Visual Pathways as Indicated by. *Vision*.

Benjamini, Y. and Hochberg, Y. (1995). Controlling the false discovery rate: a practical and powerful approach to multiple testing. *Journal of the Royal Statistical Society B*, 57:289–300.

Bianchi, S., Stimpson, C. D., Duka, T., Larsen, M. D., Janssen, W. G. M., Collins, Z., Bauernfeind, A. L., Schapiro, S. J., Baze, W. B., McArthur, M. J., Hopkins, W. D., Wildman, D. E., Lipovich, L., Kuzawa, C. W., Jacobs, B., Hof, P. R., and Sherwood, C. C. (2013). Synaptogenesis and development of pyramidal neuron dendritic morphology in the chimpanzee neocortex resembles humans. *Proceedings of the National Academy of Sciences*, 110(Supplement_2):10395–10401.

Bilger, A. and Nehlig, A. (1991). Quantitative histochemical changes in enzymes involved in energy metabolism in the rat brain during postnatal Development. I. Cytochrome oxidase and lactate dehydrogenase. *International Journal of Developmental Neuroscience*, 9(6):545–553.

Biology (2016). #120 Synapses | Biology Notes for A level.

Blackwood, D. H. and Muir, W. J. (1990). Cognitive brain potentials and their application. *The British Journal of Psychiatry*, 157(9):96–101.

Blasi, A., Lloyd-Fox, S., Sethna, V., Brammer, M. J., Mercure, E., Murray, L., Williams, S. C. R., Simmons, A., Murphy, D. G. M., and Johnson, M. H. (2015). Atypical processing of voice sounds in infants at risk for autism spectrum disorder. *Cortex*, 71:122–133.

Bonavita, V., Ponte, F., and Amore, G. (1962). Lactate dehydrogenase isozymes in the developing rat brain. *Nature*, 196(4854):576–577.

Booth, R. F. G., Patel, T. B., and Clark, J. B. (1980). The Development of Enzymes of Energy Metabolism in the Brain of a Precocial (Guinea Pig) and Non-Precocial (Rat) Species. *Journal of Neurochemistry*, 34(1):17–25.

Börgers, C. and Kopell, N. (2005). Effects of noisy drive on rhythms in networks of excitatory and inhibitory neurons. *Neural Computation*.

Born, A. P., Miranda, M. J., Rostrup, E., Toft, P. B., Peitersen, B., Larsson, H. B., and Lou, H. C. (2000). Functional Magnetic Resonance Imaging of the Normal and Abnormal Visual System in Early Life. *Neuropediatrics*, 31(1):24–32.

Born, A. P., Rostrup, E., Miranda, M. J., Larsson, H. B., and Lou, H. C. (2002). Visual cortex reactivity in sedated children examined with perfusion MRI (FAIR). *Magnetic Resonance Imaging*, 20(2):199–205.

Born, P., Leth, H., Miranda, M. J., Rostrup, E., Stensgaard, A., Peitersen, B., Larsson, H. B. W., and Lou, H. C. (1998). Visual Activation in Infants and Young Children Studied by Functional Magnetic Resonance Imaging. *Pediatric Research*, 44(4):578–583.

Bortfeld, H., Wruck, E., and Boas, D. A. (2007). Assessing infants' cortical response to speech using near-infrared spectroscopy. *NeuroImage*, 34(1):407–415.

Boynton, G. M., Engel, S. A., Glover, G. H., and Heeger, D. J. (1996). Linear systems analysis of functional magnetic resonance imaging in human V1. *Journal of Neuroscience*.

Bozkurt, A., Rosen, A., Rosen, H., and Onaral, B. (2005). A portable near infrared spectroscopy system for bedside monitoring of newborn brain. *BioMedical Engineering OnLine*, 4(1):29.

Braukmann, R., Lloyd-Fox, S., Blasi, A., Johnson, M. H., Bekkering, H., Buitelaar, J. K., and Hunnius, S. (2018). Diminished socially selective neural processing in 5-month-old infants at high familial risk of autism. *European Journal of Neuroscience*, 47(6):720–728.

Brazy, J. E., Lewis, D. V., Mitnick, M. H., and vander Vliet, F. F. J. (1985). Noninvasive Monitoring of Cerebral Oxygenation in Preterm Infants: Preliminary Observations. *Pediatrics*, 75(2):217–225.

Buhl, E. H., Halasy, K., and Somogyi, P. (1994). Diverse sources of hippocampal unitary inhibitory postsynaptic potentials and the number of synaptic release sites. *Nature*, 368(6474):823–828.

Bulgarelli, C., Blasi, A., Arridge, S., Powell, S., de Klerk, C. C., Southgate, V., Brigadoi, S., Penny, W., Tak, S., and Hamilton, A. (2018). Dynamic causal modelling on infant fNIRS data: A validation study on a simultaneously recorded fNIRS-fMRI dataset. *NeuroImage*.

Busija, D. W., Bari, F., Domoki, F., Horiguchi, T., and Shimizu, K. (2008). Mechanisms involved in the cerebrovascular dilator effects of cortical spreading depression.

Bustamante, J., Czerniczyniec, A., Cymeryng, C., and Lores-Arnaiz, S. (2008). Age related changes from youth to adulthood in rat brain cortex: Nitric oxide synthase and mito-

chondrial respiratory function. *Neurochemical Research*, 33(7):1216–1223.

Buzsáki, G. (2006). *Rhythms of the Brain*. Oxford University Press.

Buzsáki, G., Anastassiou, C. A., and Koch, C. (2012). The origin of extracellular fields and currents-EEG, ECoG, LFP and spikes.

Buzsáki, G. and Wang, X.-J. (2012). Mechanisms of Gamma Oscillations. *Annual Review of Neuroscience*, 35(1):203–225.

Caldwell, M., Hapuarachchi, T., Highton, D., Elwell, C., Smith, M., and Tachtsidis, I. (2015). BrainSignals revisited: Simplifying a computational model of cerebral physiology. *PLoS ONE*.

Cardin, J. A., Carlén, M., Meletis, K., Knoblich, U., Zhang, F., Deisseroth, K., Tsai, L. H., and Moore, C. I. (2009). Driving fast-spiking cells induces gamma rhythm and controls sensory responses. *Nature*, 459(7247):663–667.

Cauli, B. (2004). Cortical GABA Interneurons in Neurovascular Coupling: Relays for Subcortical Vasoactive Pathways. *Journal of Neuroscience*, 24(41):8940–8949.

Cauli, B. and Hamel, E. (2010a). Revisiting the role of neurons in neurovascular coupling. *Frontiers in Neuroenergetics*, 2:9.

Cauli, B. and Hamel, E. (2010b). Revisiting the role of neurons in neurovascular coupling. *Frontiers in neuroenergetics*, 2:9.

Chalak, L. F., Tian, F., Adams-Huet, B., Vasil, D., Laptook, A., Tarumi, T., and Zhang, R. (2017). Novel Wavelet Real Time Analysis of Neurovascular Coupling in Neonatal Encephalopathy. *Scientific Reports*.

Chauhan, A. and Chauhan, V. (2006). Oxidative stress in autism.

Chauhan, A., Gu, F., Essa, M. M., Wegiel, J., Kaur, K., Brown, W. T., and Chauhan, V. (2011). Brain region-specific deficit in mitochondrial electron transport chain complexes in children with autism. *Journal of Neurochemistry*, 117(2):209–220.

Chawarska, K., Macari, S., and Shic, F. (2013). Decreased spontaneous attention to social scenes in 6-month-old infants later diagnosed with autism spectrum disorders. *Biological Psychiatry*.

Chen, B. R., Bouchard, M. B., McCaslin, A. F., Burgess, S. A., and Hillman, E. M. (2011). High-speed vascular dynamics of the hemodynamic response. *NeuroImage*, 54(2):1021–1030.

Chen, B. R., Kozberg, M. G., Bouchard, M. B., Shaik, M. A., and Hillman, E. M. C. (2014). A Critical Role for the Vascular Endothelium in Functional Neurovascular Coupling in the Brain. *Journal of the American Heart Association*, 3(3):e000787–e000787.

Chen, J. J. and Pike, G. B. (2009). BOLD-specific cerebral blood volume and blood flow changes during neuronal activation in humans. *NMR in Biomedicine*, 22(10):n/a–n/a.

Chen, S., Li, Z., He, Y., Zhang, F., Li, H., Liao, Y., Wei, Z., Wan, G., Xiang, X., Hu, M., Xia, K., Chen, X., and Tang, J. (2015). Elevated mitochondrial DNA copy number in peripheral

blood cells is associated with childhood autism. *BMC psychiatry*, 15:50.

Chien, Y. L., Gau, S. S.-F., Shang, C. Y., Chiu, Y. N., Tsai, W. C., and Wu, Y. Y. (2015). Visual memory and sustained attention impairment in youths with autism spectrum disorders. *Psychological Medicine*, 45(11):2263–2273.

Chiron, C., Raynaud, C., Mazière, B., Zilbovicius, M., Laflamme, L., Masure, M. C., Dulac, O., Bourguignon, M., and Syrota, A. (1992). Changes in regional cerebral blood flow during brain maturation in children and adolescents. *Journal of nuclear medicine*, 33(5):696–703.

Chitnis, D., Cooper, R. J., Dempsey, L., Powell, S., Quaggia, S., Highton, D., Elwell, C., Hebden, J. C., and Everdell, N. L. (2016). Functional imaging of the human brain using a modular, fibre-less, high-density diffuse optical tomography system. *Biomedical optics express*, 7(10):4275–4288.

Christakou, A., Murphy, C. M., Chantiluke, K., Cubillo, A. I., Smith, A. B., Giampietro, V., Daly, E., Ecker, C., Robertson, D., Murphy, D. G., and Rubia, K. (2013). Disorder-specific functional abnormalities during sustained attention in youth with Attention Deficit Hyperactivity Disorder (ADHD) and with Autism. *Molecular Psychiatry*, 18(2):236–244.

Chugani, D. C., Muzik, O., Behen, M., Rothermel, R., Janisse, J. J., Lee, J., and Chugani, H. T. (1999a). Developmental changes in brain serotonin synthesis capacity in autistic and nonautistic children. *Annals of Neurology*, 45(3):287–295.

Chugani, D. C., Sundram, B. S., Behen, M., Lee, M. L., and Moore, G. J. (1999b). Evidence of altered energy metabolism in autistic children.

Chugani, H. T., Phelps, M. E., and Mazziotta, J. C. (1987). Positron emission tomography study of human brain functional development. *Annals of Neurology*, 22(4):487–497.

Clayton, M. S., Yeung, N., and Cohen Kadosh, R. (2015). The roles of cortical oscillations in sustained attention. *Trends in Cognitive Sciences*, 19(4):188–195.

Coben, R., Clarke, A. R., Hudspeth, W., and Barry, R. J. (2008). EEG power and coherence in autistic spectrum disorder. *Clinical Neurophysiology*.

Cohen, M. (2014). *Analyzing Neural Time Series Data*. MIT Press.

Cohen, Z., Molinatti, G., and Hamel, E. (1997). Astroglial and Vascular Interactions of Noradrenaline Terminals in the Rat Cerebral Cortex. *Journal of Cerebral Blood Flow & Metabolism*, 17(8):894–904.

Coleman, M. and Blass, J. P. (1985). Autism and lactic acidosis. *Journal of Autism and Developmental Disorders*, 15(1):1–8.

Collins, D., Zijdenbos, A., Kollokian, V., Sled, J., Kabani, N., Holmes, C., and Evans, A. (1998). Design and construction of a realistic digital brain phantom. *IEEE Transactions on Medical Imaging*, 17(3):463–468.

Connors, S. L., Matteson, K. J., Sega, G. A., Lozzio, C. B., Carroll, R. C., and Zimmerman, A. W. (2006). Plasma Serotonin in Autism. *Pediatric Neurology*, 35(3):182–186.

Constantino, J. N., Zhang, Y., Frazier, T., Abbacchi, A. M., and Law, P. (2010). Sibling recurrence and the genetic epidemiology of autism. *American Journal of Psychiatry*.

Cooper, C. E., Cope, M., Springett, R., Amess, P. N., Penrice, J., Tyszczuk, L., Punwani, S., Ordidge, R., Wyatt, J., and Delpy, D. T. (1999). Use of Mitochondrial Inhibitors to Demonstrate That Cytochrome Oxidase Near-Infrared Spectroscopy Can Measure Mitochondrial Dysfunction Noninvasively in the Brain. *Journal of Cerebral Blood Flow & Metabolism*, 19(1):27–38.

Cooper, C. E. and Springett, R. (1997). Measurement of cytochrome oxidase and mitochondrial energetics by near-infrared spectroscopy. *Philosophical transactions of the Royal Society of London. Series B, Biological sciences*, 352(1354):669–76.

Cope, M., Delpy, D. T., Reynolds, E. O., Wray, S., Wyatt, J., and van der Zee, P. (1988). Methods of quantitating cerebral near infrared spectroscopy data. *Advances in experimental medicine and biology*, 222(July):183–189.

Csibra, G., Henty, J., Volein, A., Elwell, C. E., Tucker, L. T., Meek, J., and Johnson, M. H. (2004). Near infrared spectroscopy reveals neural activation during face perception in infants and adults.

Cunningham, M. O. and Chinnery, P. F. (2011). Mitochondria and cortical gamma oscillations: Food for thought?

Dawson, G., Webb, S. J., Carver, L., Panagiotides, H., and McPartland, J. (2004). Young children with autism show atypical brain responses to fearful versus neutral facial expressions of emotion. *Developmental Science*.

de Roever, I., Bale, G., Cooper, R. J., and Tachtsidis, I. (2016). Cytochrome-C-Oxidase Exhibits Higher Brain-Specificity than Haemoglobin in Functional Activation. In *Biomedical Optics 2016*, page BTh4D.4, Washington, D.C. OSA.

de Roever, I., Bale, G., Cooper, R. J., and Tachtsidis, I. (2017). Functional NIRS measurement of cytochrome-c-oxidase demonstrates a more brain-specific marker of frontal lobe activation compared to the haemoglobins. *Advances in Experimental Medicine and Biology*, 977:141–147.

Deen, B., Richardson, H., Dilks, D. D., Takahashi, A., Keil, B., Wald, L. L., Kanwisher, N., and Saxe, R. (2017). Organization of high-level visual cortex in human infants. *Nature Communications*.

Delpy, D. T., Cope, M., van der Zee, P., Arridge, S., Wray, S., and Wyatt, J. (1988). Estimation of optical pathlength through tissue from direct time of flight measurement. *Physics in Medicine and Biology*, 33(12):1433–1442.

Denison, R. N., Vu, A. T., Yacoub, E., Feinberg, D. A., and Silver, M. A. (2014). Functional mapping of the magnocellular and parvocellular subdivisions of human LGN. *NeuroImage*, 102 Pt 2(0 2):358–69.

Derrington, A. M. and Lennie, P. (1984). Spatial and temporal contrast sensitivities of neurones in lateral geniculate nucleus of macaque. *The Journal of physiology*, 357:219–40.

Devor, A., Dunn, A. K., Andermann, M. L., Ulbert, I., Boas, D. A., and Dale, A. M. (2003).

Coupling of total hemoglobin concentration, oxygenation, and neural activity in rat somatosensory cortex. *Neuron*, 39(2):353–359.

Devor, A., Hillman, E. M. C., Tian, P., Waeber, C., Teng, I. C., Ruvinskaya, L., Shalinsky, M. H., Zhu, H., Haslinger, R. H., Narayanan, S. N., Ulbert, I., Dunn, A. K., Lo, E. H., Rosen, B. R., Dale, A. M., Kleinfeld, D., and Boas, D. A. (2008). Stimulus-Induced Changes in Blood Flow and 2-Deoxyglucose Uptake Dissociate in Ipsilateral Somatosensory Cortex. *Journal of Neuroscience*, 28(53):14347–14357.

Duncan, A., Meek, J., Clemence, M., Elwell, C., Tyszczuk, L., Cope, M., and Delpy, D. (1995). Optical pathlength measurements on adult head, calf and forearm and the head of the newborn infant using phase resolved optical spectroscopy. *Physics in Medicine and Biology*, 40(2):295.

Elsabbagh, M., Gliga, T., Pickles, A., Hudry, K., Charman, T., Johnson, M. H., and BASIS Team (2013). The development of face orienting mechanisms in infants at-risk for autism. *Behavioural Brain Research*, 251:147–154.

Elsabbagh, M. and Johnson, M. H. (2016). Autism and the Social Brain: The First-Year Puzzle.

Elsabbagh, M., Volein, A., Holmboe, K., Tucker, L., Csibra, G., Baron-Cohen, S., Bolton, P., Charman, T., Baird, G., and Johnson, M. H. (2009). Visual orienting in the early broader autism phenotype: Disengagement and facilitation. *Journal of Child Psychology and Psychiatry and Allied Disciplines*.

Elwell, C. (1995). A Practical Users Guide to Near Infrared Spectroscopy. *Hamamatsu Photonics KK: London, UK. (1995).*

Emberson, L. L., Boldin, A. M., Riccio, J. E., Guillet, R., and Aslin, R. N. (2017). Deficits in Top-Down Sensory Prediction in Infants At Risk due to Premature Birth. *Current Biology*, 27(3):431–436.

Engel, A. K., Fries, P., and Singer, W. (2001). Dynamic predictions: Oscillations and synchrony in top-down processing. *Nature Reviews Neuroscience*, 2(10):704–716.

Engel, S. A., Glover, G. H., and Wandell, B. A. (1997). Retinotopic organization in human visual cortex and the spatial precision of functional MRI. *Cerebral cortex (New York, N.Y. : 1991)*, 7(2):181–92.

Fatemi, S. H., Cuadra, a. E., El-Fakahany, E. E., Sidwell, R. W., and Thuras, P. (2000). Prenatal viral infection causes alterations in nNOS expression in developing mouse brains. *Neuroreport*, 11(7):1493–1496.

Fatemi, S. H. and Folsom, T. D. (2011). Dysregulation of fragile X mental retardation protein and metabotropic glutamate receptor 5 in superior frontal cortex of individuals with autism: A postmortem brain study. *Molecular Autism*, 2(1):6.

Fatemi, S. H., Folsom, T. D., Kneeland, R. E., and Liesch, S. B. (2011). Metabotropic glutamate receptor 5 upregulation in children with autism is associated with underexpression of both Fragile X mental retardation protein and GABAA receptor beta 3 in adults with autism. *Anatomical Record (Hoboken)*, 294(10):1635–45.

Fatemi, S. H., Halt, A. R., Stary, J. M., Kanodia, R., Schulz, S. C., and Realmuto, G. R. (2002a). Glutamic acid decarboxylase 65 and 67 kDa proteins are reduced in autistic parietal and cerebellar cortices. *Biological Psychiatry*, 52(8):805–810.

Fatemi, S. H., Halt, A. R., Stary, J. M., Kanodia, R., Schulz, S. C., and Realmuto, G. R. (2002b). Glutamic acid decarboxylase 65 and 67 kDa proteins are reduced in autistic parietal and cerebellar cortices. *Biological psychiatry*, 52(8):805–10.

Fatemi, S. H., Reutiman, T. J., Folsom, T. D., Rooney, R. J., Patel, D. H., and Thuras, P. D. (2010). mRNA and protein levels for GABAAalpha4, alpha5, beta1 and GABABR1 receptors are altered in brains from subjects with autism. *Journal of autism and developmental disorders*, 40(6):743–50.

Fatemi, S. H., Reutiman, T. J., Folsom, T. D., and Thuras, P. D. (2009). GABAA Receptor Downregulation in Brains of Subjects with Autism. *Journal of Autism and Developmental Disorders*, 39(2):223–230.

Feige, B., Scheffler, K., Esposito, F., Di Salle, F., Hennig, J., and Seifritz, E. (2005). Cortical and subcortical correlates of electroencephalographic alpha rhythm modulation. *Journal of neurophysiology*.

Feldman, M. A., Ward, R. A., Savona, D., Regehr, K., Parker, K., Hudson, M., Penning, H., and Holden, J. J. (2012). Development and initial validation of a parent report measure of the behavioral development of infants at risk for autism spectrum disorders. *Journal of Autism and Developmental Disorders*.

Figley, C. R. and Stroman, P. W. (2011). The role(s) of astrocytes and astrocyte activity in neurometabolism, neurovascular coupling, and the production of functional neuroimaging signals.

Filosa, J. A., Bonev, A. D., Straub, S. V., Meredith, A. L., Wilkerson, M. K., Aldrich, R. W., and Nelson, M. T. (2006). Local potassium signaling couples neuronal activity to vasodilation in the brain. *Nature Neuroscience*, 9(11):1397–1403.

Florian, G. and Pfurtscheller, G. (1995). Dynamic spectral analysis of event-related EEG data. *Electroencephalography and Clinical Neurophysiology*, 95(5):393–396.

Fox, P. T., Mintun, M. A., Raichle, M. E., Miezin, F. M., Allman, J. M., and Van Essen, D. C. (1986). Mapping human visual cortex with positron emission tomography. *Nature*, 323(6091):806–809.

Frederick, A. L. and Stanwood, G. D. (2009). Drugs, biogenic amine targets and the developing brain. *Developmental neuroscience*, 31(1-2):7–22.

Friedman, S. D., Shaw, D. W., Artru, a. a., Richards, T. L., Gardner, J., Dawson, G., Posse, S., and Dager, S. R. (2003). Regional brain chemical alterations in young children with autism spectrum disorder. *Neurology*, 60:100–107.

Friston, K., Mattout, J., Trujillo-Barreto, N., Ashburner, J., and Penny, W. (2007). Variational free energy and the Laplace approximation. *NeuroImage*.

Friston, K. J. (2011). Functional and Effective Connectivity: A Review. *Brain Connectivity*.

Friston, K. J., Harrison, L., and Penny, W. (2003). Dynamic causal modelling. *NeuroImage*.

Friston, K. J., Preller, K. H., Mathys, C., Cagnan, H., Heinzle, J., Razi, A., and Zeidman, P. (2017). Dynamic causal modelling revisited.

Fründ, I., Busch, N. A., Körner, U., Schadow, J., and Herrmann, C. S. (2007). EEG oscillations in the gamma and alpha range respond differently to spatial frequency. *Vision Research*, 47(15):2086–2098.

Fujimiya, M., Kimura, H., and Maeda, T. (1986). Postnatal development of serotonin nerve fibers in the somatosensory cortex of mice studied by immunohistochemistry. *The Journal of Comparative Neurology*, 246(2):191–201.

Fujimoto, K. (1995). Pericyte-endothelial gap junctions in developing rat cerebral capillaries: A fine structural study. *The Anatomical Record*, 242(4):562–565.

Ganguly, K., Schinder, A. F., Wong, S. T., and Poo, M. (2001). GABA itself promotes the developmental switch of neuronal GABAergic responses from excitation to inhibition. *Cell*, 105(4):521–32.

Garey, L. and de Courten, C. (1983). Structural development of the lateral geniculate nucleus and visual cortex in monkey and man. *Behavioural Brain Research*, 10(1):3–13.

Garretson, H. B., Fein, D., and Waterhouse, L. (1990). Sustained attention in children with autism. *Journal of Autism and Developmental Disorders*, 20(1):101–114.

Gervain, J., Mehler, J., Werker, J. F., Nelson, C. A., Csibra, G., Lloyd-Fox, S., Shukla, M., and Aslin, R. N. (2011). Near-infrared spectroscopy: A report from the McDonnell infant methodology consortium.

Gervais, H., Belin, P., Boddaert, N., Leboyer, M., Coez, A., Sfaello, I., Barthélémy, C., Brunelle, F., Samson, Y., and Zilbovicius, M. (2004). Abnormal cortical voice processing in autism. *Nature Neuroscience*, 7(8):801–802.

Ghosh, A., Tachtsidis, I., Kolyva, C., Cooper, C. E., Smith, M., and Elwell, C. E. (2012). Use of a hybrid optical spectrometer for the measurement of changes in oxidized cytochrome c oxidase concentration and tissue scattering during functional activation. *Advances in Experimental Medicine and Biology*, 737:119–124.

Ginsberg, M. R., Rubin, R. A., Falcone, T., Ting, A. H., and Natowicz, M. R. (2012). Brain Transcriptional and Epigenetic Associations with Autism. *PLoS ONE*, 7(9).

Giraud, A. L., Kleinschmidt, A., Poeppel, D., Lund, T. E., Frackowiak, R. S., and Laufs, H. (2007). Endogenous Cortical Rhythms Determine Cerebral Specialization for Speech Perception and Production. *Neuron*.

Giulivi, C., Zhang, Y.-F., Omanska-Klusek, A., Ross-Inta, C., Wong, S., Hertz-Picciotto, I., Tassone, F., and Pessah, I. N. (2010). Mitochondrial Dysfunction in Autism. *JAMA*, 304(21):2389.

Gogolla, N., LeBlanc, J. J., Quast, K. B., Südhof, T. C., Fagiolini, M., and Hensch, T. K. (2009). Common circuit defect of excitatory-inhibitory balance in mouse models of autism. *Journal of Neurodevelopmental Disorders*, 1(2):172–181.

Goldberg, M. C., Spinelli, S., Joel, S., Pekar, J. J., Denckla, M. B., and Mostofsky, S. H. (2011). Children with high functioning autism show increased prefrontal and temporal cortex activity during error monitoring. *Developmental Cognitive Neuroscience*, 1(1):47–56.

Goldenthal, M. J., Damle, S., Sheth, S., Shah, N., Melvin, J., Jethva, R., Hardison, H., Marks, H., and Legido, A. (2015). Mitochondrial enzyme dysfunction in autism spectrum disorders; a novel biomarker revealed from buccal swab analysis. *Biomarkers in medicine*, 9(10):957–965.

Goldman, R. I., Stern, J. M., Engel, J., and Cohen, M. S. (2002). Simultaneous EEG and fMRI of the alpha rhythm. *NeuroReport*.

Goodyear, B. G. and Menon, R. S. (1998). Effect of Luminance Contrast on BOLD fMRI Response in Human Primary Visual Areas. *Journal of Neurophysiology*, 79(4):2204–2207.

Gordon, G. R. J., Choi, H. B., Rungta, R. L., Ellis-Davies, G. C. R., and MacVicar, B. A. (2008). Brain metabolism dictates the polarity of astrocyte control over arterioles. *Nature*, 456(7223):745–749.

Gramer, M. (2007). *Further Development and Validation of a Multi-Distance NIR Broadband Spectrometer for Monitoring Brain Tissue Haemodynamics on the Adult Head: Application on Dynamic Phantoms.* PhD thesis, University College London.

Grossmann, T., Johnson, M. H., Lloyd-Fox, S., Blasi, A., Deligianni, F., Elwell, C., and Csibra, G. (2008). Early cortical specialization for face-to-face communication in human infants. *Proceedings. Biological sciences / The Royal Society*, 275(1653):2803–2811.

Gu, F., Chauhan, V., Kaur, K., Brown, W. T., LaFauci, G., Wegiel, J., and Chauhan, A. (2013). Alterations in mitochondrial DNA copy number and the activities of electron transport chain complexes and pyruvate dehydrogenase in the frontal cortex from subjects with autism. *Translational psychiatry*, 3:e299.

Gulyás, A. I., Buzsáki, G., Freund, T. F., and Hirase, H. (2006). Populations of hippocampal inhibitory neurons express different levels of cytochrome <i>c</i>. *European Journal of Neuroscience*, 23(10):2581–2594.

Haensse, D., Szabo, P., Brown, D., Fauchère, J.-C., Niederer, P., Bucher, H.-U., and Wolf, M. (2005). A new multichannel near infrared spectrophotometry system for functional studies of the brain in adults and neonates. *Optics express*, 13(12):4525–38.

Hall, C. N., Reynell, C., Gesslein, B., Hamilton, N. B., Mishra, A., Sutherland, B. A., Oâ Farrell, F. M., Buchan, A. M., Lauritzen, M., and Attwell, D. (2014). Capillary pericytes regulate cerebral blood flow in health and disease. *Nature*, 508(1):55–60.

Hamel, E. (2006). Perivascular nerves and the regulation of cerebrovascular tone. *Journal of Applied Physiology*, 100(3):1059–1064.

Hamilton, N. B. (2010). Pericyte-mediated regulation of capillary diameter: a component of neurovascular coupling in health and disease. *Frontiers in Neuroenergetics*, 2.

Hammarrenger, B., Leporé, F., Lippé, S., Labrosse, M., Guillemot, J. P., and Roy, M. S. (2003). Magnocellular and parvocellular developmental course in infants during the first year of life. *Documenta Ophthalmologica*.

Hapuarachchi, T. (2015). Modelling metabolism in the neonatal brain. *Doctoral thesis, UCL (University College London)*.

Harding, G. F. A., Janday, B., and Armstrong, R. A. (1991). Topographic mapping and source localization of the pattern reversal visual evoked magnetic response. *Brain Topography*, 4(1):47–55.

Harris, J. J., Reynell, C., and Attwell, D. (2011). The physiology of developmental changes in BOLD functional imaging signals. *Developmental Cognitive Neuroscience*, 1(3):199–216.

Hasenstaub, A., Shu, Y., Haider, B., Kraushaar, U., Duque, A., and McCormick, D. A. (2005). Inhibitory postsynaptic potentials carry synchronized frequency information in active cortical networks. *Neuron*.

Heeger, D. J., Huk, A. C., Geisler, W. S., and Albrecht, D. G. (2000). Spikes versus BOLD: What does neuroimaging tell us about neuronal activity?

Heekeren, H. R., Kohl, M., Obrig, H., Wenzel, R., von Pannwitz, W., Matcher, S. J., Dirnagl, U., Cooper, C. E., and Villringer, A. (1999a). Noninvasive assessment of changes in cytochrome-c oxidase oxidation in human subjects during visual stimulation. *Journal of cerebral blood flow and metabolism : official journal of the International Society of Cerebral Blood Flow and Metabolism*, 19(6):592–603.

Heekeren, H. R., Kohl, M., Obrig, H., Wenzel, R., von Pannwitz, W., Matcher, S. J., Dirnagl, U., Cooper, C. E., and Villringer, A. (1999b). Noninvasive assessment of changes in cytochrome-c oxidase oxidation in human subjects during visual stimulation. *J Cereb Blood Flow Metab*, 19(6):592–603.

Henrie, J. A. (2005). LFP Power Spectra in V1 Cortex: The Graded Effect of Stimulus Contrast. *Journal of Neurophysiology*, 94(1):479–490.

Henriksson, L., Nurminen, L., Hyvarinen, A., and Vanni, S. (2008). Spatial frequency tuning in human retinotopic visual areas. *Journal of Vision*.

Hermes, D., Kasteleijn-Nolst Trenité, D. G., and Winawer, J. (2017). Gamma oscillations and photosensitive epilepsy. *Current Biology*, 27(9):R336–R338.

Herrmann, C. S., Fründ, I., and Lenz, D. (2010). Human gamma-band activity: A review on cognitive and behavioral correlates and network models. *Neuroscience & Biobehavioral Reviews*, 34(7):981–992.

Heye, A. K., Culling, R. D., Valdés Hernández, M. D. C., Thrippleton, M. J., and Wardlaw, J. M. (2014). Assessment of blood-brain barrier disruption using dynamic contrast-enhanced MRI. A systematic review. *NeuroImage. Clinical*, 6:262–74.

Hicks, T. P., Lee, B. B., and Vidyasagar, T. R. (1983). The responses of cells in macaque lateral geniculate nucleus to sinusoidal gratings. *The Journal of physiology*, 337:183–200.

Highton, D., Ghosh, A., Tachtsidis, I., Elwell, C., and Smith, M. (2014). Analysis of slow wave oscillations in cerebral haemodynamics and metabolism following subarachnoid haemorrhage. *Advances in Experimental Medicine and Biology*, 812:195–201.

Highton, D., Ghosh, A., Tachtsidis, I., Panovska-Griffiths, J., Elwell, C. E., and Smith, M.

(2015). Monitoring cerebral autoregulation after brain injury: Multimodal assessment of cerebral slow-wave oscillations using near-infrared spectroscopy. *Anesthesia and Analgesia*.

Highton, D., Tachtsidis, I., Tucker, A., Elwell, C., and Smith, M. (2016). Near infrared light scattering changes following acute brain injury. In *Advances in Experimental Medicine and Biology*, volume 876, pages 139–144. Springer, New York, NY.

Hill, J., Inder, T., Neil, J., Dierker, D., Harwell, J., and Van Essen, D. (2010). Similar patterns of cortical expansion during human development and evolution. *Proceedings of the National Academy of Sciences of the United States of America*.

Hill, R., Tong, L., Yuan, P., Murikinati, S., Gupta, S., and Grutzendler, J. (2015). Regional Blood Flow in the Normal and Ischemic Brain Is Controlled by Arteriolar Smooth Muscle Cell Contractility and Not by Capillary Pericytes. *Neuron*, 87(1):95–110.

Homae, F., Watanabe, H., Nakano, T., Asakawa, K., and Taga, G. (2006). The right hemisphere of sleeping infant perceives sentential prosody. *Neuroscience Research*, 54(4):276–280.

Honig, C. R., Connett, R. J., and Gayeski, T. E. (1992). O2 transport and its interaction with metabolism; a systems view of aerobic capacity. *Medicine and science in sports and exercise*, 24(1):47–53.

Huttenlocher, P. R. and Dabholkar, A. S. (1997). Regional differences in synaptogenesis in human cerebral cortex. *The Journal of comparative neurology*, 387(2):167–78.

Hyde, D. C., Boas, D. A., Blair, C., and Carey, S. (2010). Near-infrared spectroscopy shows right parietal specialization for number in pre-verbal infants. *NeuroImage*, 53(2):647–652.

Iadecola, C. (1993). Regulation of the cerebral microcirculation during neural activity: is nitric oxide the missing link? *Trends in Neurosciences*, 16(6):206–214.

Iadecola, C. (2017). The Neurovascular Unit Coming of Age: A Journey through Neurovascular Coupling in Health and Disease. *Neuron*, 96(1):17–42.

Iadecola, C., Zhang, F., Xu, S., Casey, R., and Ross, M. E. (1995). Inducible Nitric Oxide Synthase Gene Expression in Brain following Cerebral Ischemia. *Journal of Cerebral Blood Flow & Metabolism*, 15(3):378–384.

Ichikawa, H., Otsuka, Y., Kanazawa, S., Yamaguchi, M. K., and Kakigi, R. (2013). Contrast reversal of the eyes impairs infants' face processing: A near-infrared spectroscopic study. *Neuropsychologia*, 51(13):2556–2561.

Iossifov, I., Ronemus, M., Levy, D., Wang, Z., Hakker, I., Rosenbaum, J., Yamrom, B., ha Lee, Y., Narzisi, G., Leotta, A., Kendall, J., Grabowska, E., Ma, B., Marks, S., Rodgers, L., Stepansky, A., Troge, J., Andrews, P., Bekritsky, M., Pradhan, K., Ghiban, E., Kramer, M., Parla, J., Demeter, R., Fulton, L. L., Fulton, R. S., Magrini, V. J., Ye, K., Darnell, J. C., Darnell, R. B., Mardis, E. R., Wilson, R. K., Schatz, M. C., McCombie, R. W., and Wigler, M. (2012). De Novo Gene Disruptions in Children on the Autistic Spectrum. *Neuron*.

Issard, C. and Gervain, J. (2017). Adult-like processing of time-compressed speech by newborns: A NIRS study. *Developmental Cognitive Neuroscience*, 25:176–184.

Issard, C. and Gervain, J. (2018). Variability of the hemodynamic response in infants: Influence of experimental design and stimulus complexity.

Jaeseung Jeong, Gore, J., and Peterson, B. (2002). A method for determinism in short time series, and its application to stationary EEG. *IEEE Transactions on Biomedical Engineering*, 49(11):1374–1379.

Jelitai, M. and Madarasz, E. (2005). The Role of GABA in the Early Neuronal Development. *International Review of Neurobiology*, 71:27–62.

Jemel, B., Mottron, L., and Dawson, M. (2006). Impaired Face Processing in Autism: Fact or Artifact? *Journal of Autism and Developmental Disorders*, 36(1):91–106.

Jeste, S. S., Frohlich, J., and Loo, S. K. (2015). Electrophysiological biomarkers of diagnosis and outcome in neurodevelopmental disorders.

Jia, X., Xing, D., and Kohn, A. (2013). No Consistent Relationship between Gamma Power and Peak Frequency in Macaque Primary Visual Cortex. *Journal of Neuroscience*, 33(1):17–25.

Jobsis, F. F. (1977). Noninvasive, infrared monitoring of cerebral and myocardial oxygen sufficiency and circulatory parameters. *Science*, 198(4323):1264 LP – 1267.

Johnson, M. H., Gliga, T., Jones, E., and Charman, T. (2015). Annual research review: Infant development, autism, and ADHD - Early pathways to emerging disorders. *Journal of Child Psychology and Psychiatry and Allied Disciplines*, 56(3):228–247.

Jones, E. J., Gliga, T., Bedford, R., Charman, T., and Johnson, M. H. (2014a). Developmental pathways to autism: A review of prospective studies of infants at risk. *Neuroscience & Biobehavioral Reviews*, 39:1–33.

Jones, E. J., Venema, K., Earl, R., Lowy, R., Barnes, K., Estes, A., Dawson, G., and Webb, S. J. (2016a). Reduced engagement with social stimuli in 6-month-old infants with later autism spectrum disorder: A longitudinal prospective study of infants at high familial risk. *Journal of Neurodevelopmental Disorders*, 8(1):7.

Jones, E. J. H., Gliga, T., Bedford, R., Charman, T., and Johnson, M. H. (2014b). Developmental pathways to autism: a review of prospective studies of infants at risk. *Neuroscience and biobehavioral reviews*, 39(100):1–33.

Jones, E. J. H., Venema, K., Earl, R., Lowy, R., Barnes, K., Estes, A., Dawson, G., and Webb, S. J. (2016b). Reduced engagement with social stimuli in 6-month-old infants with later autism spectrum disorder: a longitudinal prospective study of infants at high familial risk. *Journal of Neurodevelopmental Disorders*, 8(1):7.

Jones, E. J. H., Venema, K., Lowy, R., Earl, R. K., and Webb, S. J. (2015). Developmental changes in infant brain activity during naturalistic social experiences. *Developmental Psychobiology*, 57(7):842–853.

Jung, C. E., Strother, L., Feil-Seifer, D. J., and Hutsler, J. J. (2016). Atypical Asymmetry for Processing Human and Robot Faces in Autism Revealed by fNIRS. *PLOS ONE*, 11(7):e0158804.

Kakihana, Y., Matsunaga, A., Tobo, K., Isowaki, S., Kawakami, M., Tsuneyoshi, I., Kan-mura, Y., and Tamura, M. (2002). Redox behavior of cytochrome oxidase and neurological prognosis in 66 patients who underwent thoracic aortic surgery. *European Journal of Cardio-thoracic Surgery*, 21(3):434–439.

Kann, O., Huchzermeyer, C., Kovács, R., Wirtz, S., and Schuelke, M. (2011). Gamma oscillations in the hippocampus require high complex I gene expression and strong functional performance of mitochondria. *Brain*, 134(2):345–358.

Karen, T., Morren, G., Haensse, D., Bauschatz, A. S., Bucher, H. U., and Wolf, M. (2008). Hemodynamic response to visual stimulation in newborn infants using functional near-infrared spectroscopy. *Human Brain Mapping*, 29(4):453–460.

Kay, K. N., Winawer, J., Rokem, A., Mezer, A., and Wandell, B. A. (2013). A Two-Stage Cascade Model of BOLD Responses in Human Visual Cortex. *PLoS Computational Biology*, 9(5).

Kaynezhad, P., De Roever, I., Bale, G., and Tachtsidis, I. (2016). Optical monitoring of neonatal brain injury: towards the development of compact clinical systems.

Kilner, J. M., Mattout, J., Henson, R., and Friston, K. J. (2005). Hemodynamic correlates of EEG: A heuristic. *NeuroImage*.

Kim, K. J. and Filosa, J. A. (2012). Advanced <i>in vitro</i> approach to study neurovascular coupling mechanisms in the brain microcirculation. *The Journal of Physiology*, 590(7):1757–1770.

Kistler, W. M., van Hemmen, J. L., and De Zeeuw, C. I. (2000). Time window control: a model for cerebellar function based on synchronization, reverberation, and time slicing. *Progress in brain research*, 124:275–97.

Kita, Y., Gunji, A., Inoue, Y., Goto, T., Sakihara, K., Kaga, M., Inagaki, M., and Hosokawa, T. (2011). Self-face recognition in children with autism spectrum disorders: A near-infrared spectroscopy study. *Brain and Development*, 33(6):494–503.

Klimesch, W. (1999). EEG alpha and theta oscillations reflect cognitive and memory performance: a review and analysis. *Brain Research Reviews*, 29(2-3):169–195.

Klimesch, W., Freunberger, R., Sauseng, P., and Gruber, W. (2008). A short review of slow phase synchronization and memory: Evidence for control processes in different memory systems? *Brain Research*, 1235:31–44.

Klimesch, W., Sauseng, P., and Hanslmayr, S. (2007). EEG alpha oscillations: The inhibition-timing hypothesis.

Kobayashi, M., Otsuka, Y., Nakato, E., Kanazawa, S., Yamaguchi, M. K., and Kakigi, R. (2011). Do Infants Represent the Face in a Viewpoint-Invariant Manner? Neural Adaptation Study as Measured by Near-Infrared Spectroscopy. *Frontiers in Human Neuroscience*, 5:153.

Kocharyan, A., Fernandes, P., Tong, X.-K., Vaucher, E., and Hamel, E. (2008). Specific Subtypes of Cortical GABA Interneurons Contribute to the Neurovascular Coupling Response to Basal Forebrain Stimulation. *Journal of Cerebral Blood Flow & Metabolism*,

28(2):221–231.

Kolyva, C., Ghosh, A., Tachtsidis, I., Highton, D., Cooper, C. E., Smith, M., and Elwell, C. E. (2014). Cytochrome c oxidase response to changes in cerebral oxygen delivery in the adult brain shows higher brain-specificity than haemoglobin. *NeuroImage*, 85:234–244.

Kolyva, C., Tachtsidis, I., Ghosh, A., Moroz, T., Cooper, C. E., Smith, M., and Elwell, C. E. (2012). Systematic investigation of changes in oxidized cerebral cytochrome c oxidase concentration during frontal lobe activation in healthy adults. *Biomedical optics express*, 3(10):2550–66.

Kozberg, M. and Hillman, E. (2016a). Neurovascular coupling and energy metabolism in the developing brain. In *Progress in Brain Research*, volume 225, pages 213–242.

Kozberg, M. G., Chen, B. R., DeLeo, S. E., Bouchard, M. B., and Hillman, E. M. C. (2013a). Resolving the transition from negative to positive blood oxygen level-dependent responses in the developing brain. *Proceedings of the National Academy of Sciences*, 110(11):4380–4385.

Kozberg, M. G., Chen, B. R., DeLeo, S. E., Bouchard, M. B., and Hillman, E. M. C. (2013b). Resolving the transition from negative to positive blood oxygen level-dependent responses in the developing brain. *Proceedings of the National Academy of Sciences*, 110(11):4380–4385.

Kozberg, M. G. and Hillman, E. M. C. (2016b). Neurovascular coupling develops alongside neural circuits in the postnatal brain. *Neurogenesis*, 3(1):e1244439.

Krabbe-Hartkamp, M. J., van der Grond, J., de Leeuw, F. E., de Groot, J. C., Algra, A., Hillen, B., Breteler, M. M., and Mali, W. P. (1998). Circle of Willis: morphologic variation on three-dimensional time-of-flight MR angiograms. *Radiology*.

Kusaka, T., Kawada, K., Okubo, K., Nagano, K., Namba, M., Okada, H., Imai, T., Isobe, K., and Itoh, S. (2004). Noninvasive optical imaging in the visual cortex in young infants. *Human Brain Mapping*, 22(2):122–132.

Lachaux, J.-P., Fonlupt, P., Kahane, P., Minotti, L., Hoffmann, D., Bertrand, O., and Baciu, M. (2007). Relationship between task-related gamma oscillations and BOLD signal: New insights from combined fMRI and intracranial EEG. *Human Brain Mapping*, 28(12):1368–1375.

Lambe, E. K., Krimer, L. S., and Goldman-Rakic, P. S. (2000). Differential postnatal development of catecholamine and serotonin inputs to identified neurons in prefrontal cortex of rhesus monkey. *The Journal of neuroscience : the official journal of the Society for Neuroscience*, 20(23):8780–8787.

Landa, R. J., Holman, K. C., and Garrett-Mayer, E. (2007). Social and communication development in toddlers with early and later diagnosis of autism spectrum disorders. *Archives of General Psychiatry*.

Lange, F., Dunne, L., and Tachtsidis, I. (2017). Evaluation of haemoglobin and cytochrome responses during forearm ischaemia using multi-wavelength time domain NIRS. *Ad-*

vances in Experimental Medicine and Biology, 977:67–72.

Larrain-Valenzuela, J., Zamorano, F., Soto-Icaza, P., Carrasco, X., Herrera, C., Daiber, F., Aboitiz, F., and Billeke, P. (2017). Theta and Alpha Oscillation Impairments in Autistic Spectrum Disorder Reflect Working Memory Deficit. *Scientific Reports*, 7(1).

Laufs, H., Holt, J. L., Elfont, R., Krams, M., Paul, J. S., Krakow, K., and Kleinschmidt, A. (2006). Where the BOLD signal goes when alpha EEG leaves. *NeuroImage*.

Laufs, H., Kleinschmidt, A., Beyerle, A., Eger, E., Salek-Haddadi, A., Preibisch, C., and Krakow, K. (2003a). EEG-correlated fMRI of human alpha activity. *NeuroImage*, 19(4):1463–1476.

Laufs, H., Kleinschmidt, A., Beyerle, A., Eger, E., Salek-Haddadi, A., Preibisch, C., and Krakow, K. (2003b). EEG-correlated fMRI of human alpha activity. *NeuroImage*.

Laufs, H., Krakow, K., Sterzer, P., Eger, E., Beyerle, A., Salek-Haddadi, A., and Kleinschmidt, A. (2003c). Electroencephalographic signatures of attentional and cognitive default modes in spontaneous brain activity fluctuations at rest. *Proceedings of the National Academy of Sciences*.

Le Magueresse, C. and Monyer, H. (2013). GABAergic Interneurons Shape the Functional Maturation of the Cortex.

Lee, E., Lee, J., and Kim, E. (2017). Excitation/Inhibition Imbalance in Animal Models of Autism Spectrum Disorders.

Leijser, L., Fitzpatrick, J., Srinivasan, L., Rutherford, M., Dyet, L., Hajnal, J., Cowan, F., Malamateniou, C., Counsell, S., and Allsop, J. (2006). Anatomic variations of the Circle of Willis in neonates: a high resolution MRA study at 3 Tesla. In *Proceedings 14th Scientific Meeting, International Society for Magnetic Resonance in Medicine*, page 3409.

Lenroot, R. K. and Giedd, J. N. (2006). Brain development in children and adolescents: Insights from anatomical magnetic resonance imaging.

Levitt, P., Harvey, J. A., Friedman, E., Simansky, K., and Murphy, H. E. (1997). New evidence for neurotransmitter influences on brain development.

Liao, C. Z. and Tjong, S. C. (2010). Mechanical and Fracture Behaviors of Elastomer-Rich Thermoplastic Polyolefin/ Nanocomposites. *Journal of Nanomaterials*, 2010:1–9.

Lin, P. Y., Roche-Labarbe, N., Dehaes, M., Fenoglio, A., Grant, P. E., and Franceschini, M. A. (2013). Regional and hemispheric asymmetries of cerebral hemodynamic and oxygen metabolism in newborns. *Cerebral Cortex*.

Lindauer, U., Megow, D., Matsuda, H., and Dirnagl, U. (1999). Nitric oxide: a modulator, but not a mediator, of neurovascular coupling in rat somatosensory cortex. *American Journal of Physiology-Heart and Circulatory Physiology*, 277(2):H799–H811.

Liu, C. S. J., Bryan, R. N., Miki, A., Woo, J. H., Liu, G. T., and Elliott, M. A. (2006). Magnocellular and parvocellular visual pathways have different blood oxygen level-dependent signal time courses in human primary visual cortex. *American Journal of Neuroradiology*, 27(8):1628–1634.

Lloyd-Fox, S., Begus, K., Halliday, D., Pirazzoli, L., Blasi, A., Papademetriou, M., Darboe, M. K., Prentice, A. M., Johnson, M. H., Moore, S. E., and Elwell, C. E. (2017). Cortical specialisation to social stimuli from the first days to the second year of life: A rural Gambian cohort. *Developmental Cognitive Neuroscience*, 25:92–104.

Lloyd-Fox, S., Blasi, A., Elwell, C. E., Charman, T., Murphy, D., and Johnson, M. H. (2013). Reduced neural sensitivity to social stimuli in infants at risk for autism. *Proceedings of the Royal Society B: Biological Sciences*, 280(1758):20123026–20123035.

Lloyd-Fox, S., Blasi, A., Pasco, G., Gliga, T., Jones, E. J. H., Murphy, D. G. M., Elwell, C. E., Charman, T., and Johnson, M. H. (2018). Cortical responses before 6 months of life associate with later autism. *European Journal of Neuroscience*, 47(6):736–749.

Lloyd-Fox, S., Blasi, A., Volein, A., Lloyd-Fox, S., Blasi, A., Volein, A., Everdell, N., Elwell, C. E., and Johnson, M. H. (2009). Social perception in infancy: a near infrared spectroscopy study. *Child Development*.

Lloyd-Fox, S., Papademetriou, M., Darboe, M. K., Everdell, N. L., Wegmuller, R., Prentice, A. M., Moore, S. E., and Elwell, C. E. (2014a). Functional near infrared spectroscopy (fNIRS) to assess cognitive function in infants in rural Africa. *Scientific Reports*, 4:4740.

Lloyd-Fox, S., Richards, J. E., Blasi, A., Murphy, D. G. M., Elwell, C. E., and Johnson, M. H. (2014b). Coregistering functional near-infrared spectroscopy with underlying cortical areas in infants. *Neurophotonics*, 1(2):025006.

Logothetis, N. K. (2002). The neural basis of the blood-oxygen-level-dependent functional magnetic resonance imaging signal. *Philosophical Transactions of the Royal Society B: Biological Sciences*.

Logothetis, N. K. (2008). What we can do and what we cannot do with fMRI. *Nature*, 453(7197):869–878.

Logothetis, N. K., Pauls, J., Augath, M., Trinath, T., and Oeltermann, A. (2001a). Neurophysiological investigation of the basis of the fMRI signal. *Nature*, 412(6843):150–157.

Logothetis, N. K., Pauls, J., Augath, M., Trinath, T., and Oeltermann, A. (2001b). Neurophysiological investigation of the basis of the fMRI signal. *Nature*, 412(6843):150–157.

Loth, E., Spooren, W., Ham, L. M., Isaac, M. B., Auriche-Benichou, C., Banaschewski, T., Baron-Cohen, S., Broich, K., Bölte, S., Bourgeron, T., Charman, T., Collier, D., de Andres-Trelles, F., Durston, S., Ecker, C., Elferink, A., Haberkamp, M., Hemmings, R., Johnson, M. H., Jones, E. J. H., Khwaja, O. S., Lenton, S., Mason, L., Mantua, V., Meyer-Lindenberg, A., Lombardo, M. V., O'Dwyer, L., Okamoto, K., Pandina, G. J., Pani, L., Persico, A. M., Simonoff, E., Tauscher-Wisniewski, S., Llinares-Garcia, J., Vamvakas, S., Williams, S., Buitelaar, J. K., and Murphy, D. G. M. (2015). Identification and validation of biomarkers for autism spectrum disorders. *Nature Reviews Drug Discovery*.

Luck, S. J. (2005). An Introduction to the Event-Related Potential Technique. *Monographs of the Society for Research in Child Development*, 78(3):388.

Makeig, S. (1993). Auditory event-related dynamics of the EEG spectrum and effects of exposure to tones. *Electroencephalography and Clinical Neurophysiology*, 86(4):283–293.

Makkonen, I., Riikonen, R., Kokki, H., Airaksinen, M. M., and Kuikka, J. T. (2008). Serotonin and dopamine transporter binding in children with autism determined by SPECT. *Developmental Medicine and Child Neurology*, 50(8):593–597.

Mantini, D., Perrucci, M. G., Del Gratta, C., Romani, G. L., and Corbetta, M. (2007). Electrophysiological signatures of resting state networks in the human brain. *Proceedings of the National Academy of Sciences*, 104(32):13170–13175.

Marcar, V. L., Loenneker, T., Straessle, A., Girard, F., and Martin, E. (2004a). How much luxury is there in 'luxury perfusion'? An analysis of the BOLD response in the visual areas V1 and V2. *Magnetic Resonance Imaging*.

Marcar, V. L., Straessle, A., Girard, F., Loenneker, T., and Martin, E. (2004b). When more means less: A paradox BOLD response in human visual cortex. *Magnetic Resonance Imaging*.

Martin, E., Joeri, P., Loenneker, T., Ekatodramis, D., Vitacco, D., Hennig, J., and Marcar, V. L. (1999a). Visual processing in infants and children studied using functional MRI. *Pediatric Research*, 46(2):135–140.

Martin, E., Joeri, P., Loenneker, T., Ekatodramis, D., Vitacco, D., Hennig, J., and Marcar, V. L. (1999b). Visual Processing in Infants and Children Studied Using Functional MRI. *Pediatric Research*, 46(2):135–140.

Matcher, S., Elwell, C., Cooper, C., Cope, M., and Delpy, D. (1995). Performance Comparison of Several Published Tissue Near-Infrared Spectroscopy Algorithms. *Analytical Biochemistry*, 227(1):54–68.

McPartland, J., Dawson, G., Webb, S. J., Panagiotides, H., and Carver, L. J. (2004). Event-related brain potentials reveal anomalies in temporal processing of faces in autism spectrum disorder. *Journal of Child Psychology and Psychiatry and Allied Disciplines*.

Meek, J. H., Firbank, M., Elwell, C. E., Atkinson, J., Braddick, O., and Wyatt, J. S. (1998). Regional Hemodynamic Responses to Visual Stimulation in Awake Infants. *Pediatric Research*, 43(6):840–843.

Meltzer, J. A., Negishi, M., Mayes, L. C., and Constable, R. T. (2007). Individual differences in EEG theta and alpha dynamics during working memory correlate with fMRI responses across subjects. *Clinical Neurophysiology*.

Metea, M. R. (2006). Glial Cells Dilate and Constrict Blood Vessels: A Mechanism of Neurovascular Coupling. *Journal of Neuroscience*, 26(11):2862–2870.

Michels, G. and Moss, S. J. (2007). GABAA receptors: Properties and trafficking.

Miles, R. and Wong, R. K. (1984). Unitary inhibitory synaptic potentials in the guinea-pig hippocampus in vitro. *The Journal of Physiology*, 356(1):97–113.

Minagawa-Kawai, Y., Mori, K., Hebden, J. C., and Dupoux, E. (2008). Optical imaging of infants' neurocognitive development: Recent advances and perspectives. *Developmental Neurobiology*, 68(6):712–728.

Minagawa-Kawai, Y., Mori, K., Naoi, N., and Kojima, S. (2007). Neural attunement pro-

cesses in infants during the acquisition of a language-specific phonemic contrast. *The Journal of neuroscience : the official journal of the Society for Neuroscience*, 27(2):315–321.

Minshew, N. J., Goldstein, G., Dombrowski, S. M., Panchalingam, K., and Pettegrew, J. W. (1993). A preliminary 31P MRS study of autism: Evidence for undersynthesis and increased degradation of brain membranes. *Biological Psychiatry*, 33(11-12):762–773.

Mitchell, D. G., Merton, D. A., Mirsky, P. J., and Needleman, L. (1989). Circle of Willis in newborns: color Doppler imaging of 53 healthy full-term infants. *Radiology*.

Mitra, S., Bale, G., Meek, J., Mathieson, S., Uria, C., Kendall, G., Robertson, N., and Tachtsidis, I. (2016). *In vivo measurement of cerebral mitochondrial metabolism using broadband near infrared spectroscopy following neonatal stroke*, volume 876.

Mohamed, M. A., Yousem, D. M., Tekes, A., Browner, N. M., Calhoun, V. D., and Elliott, M. (2006). Timing of cortical activation: a latency-resolved event-related functional MR imaging study. *AJNR. American journal of neuroradiology*, 24(10):1967–74.

Molavi, B. and Dumont, G. A. (2012). Wavelet-based motion artifact removal for functional near-infrared spectroscopy. *Physiol. Meas. Physiol. Meas*, 33(33):259–270.

Moosmann, M., Ritter, P., Krastel, I., Brink, A., Thees, S., Blankenburg, F., Taskin, B., Obrig, H., and Villringer, A. (2003). Correlates of alpha rhythm in functional magnetic resonance imaging and near infrared spectroscopy. *NeuroImage*, 20(1):145–158.

Moroz, T., Banaji, M., Robertson, N. J., Cooper, C. E., and Tachtsidis, I. (2012). Computational modelling of the piglet brain to simulate near-infrared spectroscopy and magnetic resonance spectroscopy data collected during oxygen deprivation. *Journal of the Royal Society, Interface / the Royal Society*.

Muehlemann, T., Haensse, D., and Wolf, M. (2008). Wireless miniaturized in-vivo near infrared imaging. *Optics express*, 16(14):10323–30.

Mulert, C., Leicht, G., Hepp, P., Kirsch, V., Karch, S., Pogarell, O., Reiser, M., Hegerl, U., Jäger, L., Moller, H. J., and McCarley, R. W. (2010). Single-trial coupling of the gamma-band response and the corresponding BOLD signal. *NeuroImage*.

Mullen, E. M. (1995). Mullen Scales of Early Learning, AGS Edition: Manual and Item Administrative Books. *American Guidance Services, Inc.*, pages 1–92.

Muller, C. L., Anacker, A. M. J., and Veenstra-VanderWeele, J. (2016). The serotonin system in autism spectrum disorder: From biomarker to animal models. *Neuroscience*, 321:24–41.

Murrin, L. C., Sanders, J. D., and Bylund, D. B. (2007). Comparison of the maturation of the adrenergic and serotonergic neurotransmitter systems in the brain: Implications for differential drug effects on juveniles and adults. *Biochemical Pharmacology*, 73(8):1225–1236.

Muthukumaraswamy, S. D. and Singh, K. D. (2009). Functional decoupling of BOLD and gamma-band amplitudes in human primary visual cortex. *Human Brain Mapping*, 30(7):2000–2007.

Nadarajah, B., Brunstrom, J. E., Grutzendler, J., Wong, R. O. L., and Pearlman, A. L. (2001).

Two modes of radial migration in early development of the cerebral cortex. *Nature Neuroscience*.

Nakamura, K., Sekine, Y., Ouchi, Y., Tsujii, M., Yoshikawa, E., Futatsubashi, M., Tsuchiya, K. J., Sugihara, G., Iwata, Y., Suzuki, K., Matsuzaki, H., Suda, S., Sugiyama, T., Takei, N., and Mori, N. (2010). Brain Serotonin and Dopamine Transporter Bindings in Adults With High-Functioning Autism. *Archives of General Psychiatry*, 67(1):59.

Niessing, J., Ebisch, B., Schmidt, K. E., Niessing, M., Singer, W., and Galuske, R. A. W. (2005). Hemodynamic Signals Correlate Tightly with Synchronized Gamma Oscillations. *Science*, 309(5736):948–951.

Nollert, G., Shin'oka, T., and Jonas, R. A. (1998). Near-infrared spectrophotometry of the brain in cardiovascular surgery.

Norman, M. G. and O'Kusky, J. R. (1986). The growth and development of microvasculature in human cerebral cortex. *Journal of Neuropathology and Experimental Neurology*, 45(3):222–232.

Nosrati, R., Lin, S., Dorian, P., Toronov, V., Dorian, P., Dorian, P., Toronov, V., and Toronov, V. (2016a). Monitoring cerebral oxygenation and metabolism during cardiac arrest and CPR using hyperspectral NIRS. In *Biomedical Optics 2016*, page JW3A.31, Washington, D.C. OSA.

Nosrati, R., Vesely, K., Schweizer, T. A., and Toronov, V. (2016b). Event-related changes of the prefrontal cortex oxygen delivery and metabolism during driving measured by hyperspectral fNIRS. *Biomedical optics express*, 7(4):1323–35.

O'Connor, K., Hamm, J. P., and Kirk, I. J. (2005). The neurophysiological correlates of face processing in adults and children with Asperger's syndrome. *Brain and Cognition*.

Orekhova, E. V., Elsabbagh, M., Jones, E. J., Dawson, G., Charman, T., and Johnson, M. H. (2014). EEG hyper-connectivity in high-risk infants is associated with later autism. *Journal of Neurodevelopmental Disorders*, 6(1):40.

Orekhova, E. V., Stroganova, T. A., Posikera, I. N., and Elam, M. (2006). EEG theta rhythm in infants and preschool children. *Clinical neurophysiology : official journal of the International Federation of Clinical Neurophysiology*, 117(5):1047–62.

Ozonoff, S., Iosif, A.-M., Baguio, F., Cook, I. C., Hill, M. M., Hutman, T., Rogers, S. J., Rozga, A., Sangha, S., Sigman, M., Steinfeld, M. B., and Young, G. S. (2010). A prospective study of the emergence of early behavioral signs of autism. *Journal of the American Academy of Child and Adolescent Psychiatry*, 49(3):256–66.e1–2.

Ozonoff, S., Young, G. S., Carter, A., Messinger, D., Yirmiya, N., Zwaigenbaum, L., Bryson, S., Carver, L. J., Constantino, J. N., Dobkins, K., Hutman, T., Iverson, J. M., Landa, R., Rogers, S. J., Sigman, M., and Stone, W. L. (2011). Recurrence Risk for Autism Spectrum Disorders: A Baby Siblings Research Consortium Study. *Pediatrics*.

Page, D. T., Kuti, O. J., Prestia, C., and Sur, M. (2009). Haploinsufficiency for Pten and Serotonin transporter cooperatively influences brain size and social behavior. *Proceedings of the National Academy of Sciences of the United States of America*, 106(6):1989–94.

Paredes, M. F., James, D., Gil-Perotin, S., Kim, H., Cotter, J. A., Ng, C., Sandoval, K., Rowitch, D. H., Xu, D., McQuillen, P. S., Garcia-Verdugo, J.-M., Huang, E. J., and Alvarez-Buylla, A. (2016). Extensive migration of young neurons into the infant human frontal lobe. *Science (New York, N.Y.)*, 354(6308):aaf7073.

Pelphrey, K. A., Morris, J. P., and McCarthy, G. (2005). Neural basis of eye gaze processing deficits in autism. *Brain*, 128(5):1038–1048.

Peng, X., Carhuapoma, J. R., Bhardwaj, A., Alkayed, N. J., Falck, J. R., Harder, D. R., Traystman, R. J., and Koehler, R. C. (2002). Suppression of cortical functional hyperemia to vibrissal stimulation in the rat by epoxygenase inhibitors. *American Journal of Physiology-Heart and Circulatory Physiology*, 283(5):H2029–H2037.

Peng, X., Zhang, C., Alkayed, N. J., Harder, D. R., and Koehler, R. C. (2004). Dependency of Cortical Functional Hyperemia to Forepaw Stimulation on Epoxygenase and Nitric Oxide Synthase Activities in Rats. *Journal of Cerebral Blood Flow & Metabolism*, 24(5):509–517.

Peppiatt, C. M., Howarth, C., Mobbs, P., and Attwell, D. (2006a). Bidirectional control of CNS capillary diameter by pericytes. *Nature*, 443(7112):700–704.

Peppiatt, C. M., Howarth, C., Mobbs, P., and Attwell, D. (2006b). Bidirectional control of CNS capillary diameter by pericytes. *Nature*, 443(7112):700–704.

Pfeifer, J. H., Merchant, J. S., Colich, N. L., Hernandez, L. M., Rudie, J. D., and Dapretto, M. (2013). Neural and Behavioral Responses During Self-Evaluative Processes Differ in Youth With and Without Autism. *Journal of Autism and Developmental Disorders*, 43(2):272–285.

Phan, P., Highton, D., Brigadoi, S., Tachtsidis, I., Smith, M., and Elwell, C. E. (2016a). Spatial distribution of changes in oxidised cytochrome C oxidase during visual stimulation using broadband near infrared spectroscopy imaging. In *Advances in Experimental Medicine and Biology*, volume 923, pages 195–201. Springer, Cham.

Phan, P., Highton, D., Lai, J., Smith, M., Elwell, C., and Tachtsidis, I. (2016b). Multi-channel multi-distance broadband near- infrared spectroscopy system to measure the spatial response of cellular oxygen metabolism and tissue oxygenation. *BIOMEDICAL OPTICS EXPRESS*, 7(4424).

Phan, P. T. (2018). Development of a multi-distance, multi-channel broadband near-infrared spectroscopy system to investigate the spatial variation in cellular oxygen metabolism in the healthy and injured adult human brains. *Doctoral thesis, UCL (University College London)*.

Piva, M., Zhang, X., Noah, J. A., Chang, S. W. C., and Hirsch, J. (2017). Distributed Neural Activity Patterns during Human-to-Human Competition. *Frontiers in Human Neuroscience*.

Plessis, A. J., Newburger, J., Jonas, R. A., Hickey, P., Naruse, H., Tsuji, M., Walsh, A., Walter, G., Wypij, D., and Volpe, J. J. (1995). Cerebral oxygen supply and utilization during infant cardiac surgery. *Annals of Neurology*, 37(4):488–497.

Porter, J. T. and McCarthy, K. D. (1996). Hippocampal astrocytes in situ respond to glutamate released from synaptic terminals. *The Journal of neuroscience : the official journal of the Society for Neuroscience*, 16(16):5073–81.

Pujol, J., Vendrell, P., Junqué, C., Martí-Vilalta, J. L., and Capdevila, A. (1993). When does human brain development end? Evidence of corpus callosum growth up to adulthood. *Annals of Neurology*, 34(1):71–75.

Puro, D. G. (2007). Physiology and Pathobiology of the Pericyte-Containing Retinal Microvasculature: New Developments. *Microcirculation*, 14(1):1–10.

Rajaram, A., Bale, G., Kewin, M., Morrison, L. B., Tachtsidis, I., St. Lawrence, K., and Diop, M. (2018). Simultaneous monitoring of cerebral perfusion and cytochrome c oxidase by combining broadband near-infrared spectroscopy and diffuse correlation spectroscopy. *Biomedical Optics Express*, 9(6):2588.

Rebello, T. J., Yu, Q., Goodfellow, N. M., Caffrey Cagliostro, M. K., Teissier, A., Morelli, E., Demireva, E. Y., Chemiakine, A., Rosoklija, G. B., Dwork, A. J., Lambe, E. K., Gingrich, J. A., and Ansorge, M. S. (2014). Postnatal Day 2 to 11 Constitutes a 5-HT-Sensitive Period Impacting Adult mPFC Function. *Journal of Neuroscience*, 34(37):12379–12393.

Reynell, C. and Harris, J. J. (2013a). The BOLD signal and neurovascular coupling in autism. *Developmental cognitive neuroscience*, 6(100):72–9.

Reynell, C. and Harris, J. J. (2013b). The BOLD signal and neurovascular coupling in autism. - PubMed - NCBI. *Developmental Cognitive Neuroscience*, 6:72–79.

Riccio, O., Potter, G., Walzer, C., Vallet, P., Szabó, G., Vutskits, L., Kiss, J. Z., and Dayer, A. G. (2009). Excess of serotonin affects embryonic interneuron migration through activation of the serotonin receptor 6. *Molecular Psychiatry*, 14(3):280–290.

Riera, J. J., Wan, X., Jimenez, J. C., and Kawashima, R. (2006). Nonlinear local electrovascular coupling. I: A theoretical model. *Human Brain Mapping*.

Rivera, C., Voipio, J., Payne, J. A., Ruusuvuori, E., Lahtinen, H., Lamsa, K., Pirvola, U., Saarma, M., and Kaila, K. (1999). The K+/Cl- co-transporter KCC2 renders GABA hyperpolarizing during neuronal maturation. *Nature*, 397(6716):251–255.

Roche-Labarbe, N., Fenoglio, A., Aggarwal, A., Dehaes, M., Carp, S. A., Franceschini, M. A., and Grant, P. E. (2012). Near-Infrared Spectroscopy Assessment of Cerebral Oxygen Metabolism in the Developing Premature Brain. *Journal of Cerebral Blood Flow & Metabolism*, 32(3):481–488.

Roessmann, U. and Gambetti, P. (1986). Astrocytes in the developing human brain - An immunohistochemical study. *Acta Neuropathologica*.

Romano, C., Sesma, M. a., McDonald, C. T., O'Malley, K., Van den Pol, a. N., and Olney, J. W. (1995). Distribution of metabotropic glutamate receptor mGluR5 immunoreactivity in rat brain. *The Journal of comparative neurology*, 355(3):455–469.

Rosa, M. J., Kilner, J., Blankenburg, F., Josephs, O., and Penny, W. (2010). Estimating the transfer function from neuronal activity to BOLD using simultaneous EEG-fMRI. *NeuroImage*.

Rosa, M. J., Kilner, J. M., and Penny, W. D. (2011). Bayesian comparison of neurovascular coupling models using EEG-fmRI. *PLoS Computational Biology*.

Rossignol, D. A. and Frye, R. E. (2014). Evidence linking oxidative stress, mitochondrial dysfunction, and inflammation in the brain of individuals with autism.

Rourke, N. A. O., Sullivan, D. P., Kaznowski, C. E., Jacobs, A. A., McConnell, S. K., and O'Rourke, N. A. (1995). Tangential migration of neurons in the developing cerebral cortex. *Development (Cambridge, England)*.

Rowan, R. A. and Maxwell, D. S. (1981). Patterns of vascular sprouting in the postnatal development of the cerebral cortex of the rat. *American Journal of Anatomy*, 160(3):247–255.

Roy, C. S. and Sherrington, C. S. (1890). On the Regulation of the Blood-supply of the Brain. *The Journal of Physiology*, 11(1-2):85–158.

Rozga, A., Hutman, T., Young, G. S., Rogers, S. J., Ozonoff, S., Dapretto, M., and Sigman, M. (2011). Behavioral profiles of affected and unaffected siblings of children with autism: Contribution of measures of mother-infant interaction and nonverbal communication. *Journal of Autism and Developmental Disorders*.

Rubenstein, J. L. R. and Merzenich, M. M. (2003). Model of autism: increased ratio of excitation/inhibition in key neural systems. *Genes, Brain and Behavior*, 2(5):255–267.

Rumsey, J. M., Duara, R., Grady, C., Rapoport, J. L., Margolin, R. A., Rapoport, S. I., and Cutler, N. R. (1985). Brain metabolism in autism. Resting cerebral glucose utilization rates as measured with positron emission tomography. *Arch Gen Psychiatry*, 42(5):448–455.

Saby, J. N. and Marshall, P. J. (2012). The Utility of EEG Band Power Analysis in the Study of Infancy and Early Childhood. *Developmental Neuropsychology*, 37(3):253–273.

Sakatani, K., Chen, S., Lichty, W., Zuo, H., and Wang, Y. P. (1999a). Cerebral blood oxygenation changes induced by auditory stimulation in newborn infants measured by near infrared spectroscopy. *Early human development*, 55(3):229–36.

Sakatani, K., Chen, S., Lichty, W., Zuo, H., and Wang, Y. P. (1999b). Cerebral blood oxygenation changes induced by auditory stimulation in newborn infants measured by near infrared spectroscopy. *Early human development*, 55(3):229–36.

Scheeringa, R., Fries, P., Petersson, K. M., Oostenveld, R., Grothe, I., Norris, D. G., Hagoort, P., and Bastiaansen, M. C. (2011a). Neuronal Dynamics Underlying High- and Low-Frequency EEG Oscillations Contribute Independently to the Human BOLD Signal. *Neuron*.

Scheeringa, R., Fries, P., Petersson, K.-M., Oostenveld, R., Grothe, I., Norris, D. G., Hagoort, P., and Bastiaansen, M. C. (2011b). Neuronal Dynamics Underlying High- and Low-Frequency EEG Oscillations Contribute Independently to the Human BOLD Signal. *Neuron*, 69(3):572–583.

Scheeringa, R., Koopmans, P. J., van Mourik, T., Jensen, O., and Norris, D. G. (2016). The relationship between oscillatory EEG activity and the laminar-specific BOLD signal. *Pro-*

ceedings of the National Academy of Sciences.

Scheeringa, R., Petersson, K. M., Kleinschmidt, A., Jensen, O., and Bastiaansen, M. C. (2012). EEG Alpha Power Modulation of fMRI Resting-State Connectivity. *Brain Connectivity*.

Scheeringa, R., Petersson, K. M., Oostenveld, R., Norris, D. G., Hagoort, P., and Bastiaansen, M. C. (2009). Trial-by-trial coupling between EEG and BOLD identifies networks related to alpha and theta EEG power increases during working memory maintenance. *NeuroImage*, 44(3):1224–1238.

Schmolesky, M. T., Wang, Y., Hanes, D. P., Thompson, K. G., Leutgeb, S., Schall, J. D., and Leventhal, A. G. (1998). Signal Timing Across the Macaque Visual System. *Journal of Neurophysiology*, 79(6):3272–3278.

Scholkmann, F., Kleiser, S., Metz, A. J., Zimmermann, R., Mata Pavia, J., Wolf, U., and Wolf, M. (2014). A review on continuous wave functional near-infrared spectroscopy and imaging instrumentation and methodology.

Schuyler, B., Ollinger, J. M., Oakes, T. R., Johnstone, T., and Davidson, R. J. (2010). Dynamic Causal Modeling applied to fMRI data shows high reliability. *NeuroImage*.

Self, M. W., Peters, J. C., Possel, J. K., Reithler, J., Goebel, R., Ris, P., Jeurissen, D., Reddy, L., Claus, S., Baayen, J. C., and Roelfsema, P. R. (2016). The Effects of Context and Attention on Spiking Activity in Human Early Visual Cortex. *PLoS Biology*, 14(3).

Selten, M., van Bokhoven, H., and Nadif Kasri, N. (2018). Inhibitory control of the excitatory/inhibitory balance in psychiatric disorders. *F1000Research*, 7:23.

Seregi, A., Keller, M., and Hertting, G. (1987). Are cerebral prostanoids of astroglial origin? Studies on the prostanoid forming system in developing rat brain and primary cultures of rat astrocytes. *Brain Research*, 404(1-2):113–120.

Sewards, T. V. and Sewards, M. A. (1999). Alpha-band oscillations in visual cortex: part of the neural correlate of visual awareness? *International journal of psychophysiology : official journal of the International Organization of Psychophysiology*, 32(1):35–45.

Shadgan, B., Reid, W. D., Gharakhanlou, R., Stothers, L., and MacNab, A. J. (2009). Wireless near-infrared spectroscopy of skeletal muscle oxygenation and hemodynamics during exercise and ischemia. *Spectroscopy*, 23(5-6):233–241.

Shah, P., Bird, G., and Cook, R. (2016). Face processing in autism: Reduced integration of cross-feature dynamics. *Cortex*, 75:113–119.

Shapley, R., Kaplan, E., and Soodak, R. (1981). Spatial summation and contrast sensitivity of X and Y cells in the lateral geniculate nucleus of the macaque. *Nature*, 292(5823):543–5.

Shepro, D. and Morel, N. M. (1993). Pericyte physiology. *FASEB journal : official publication of the Federation of American Societies for Experimental Biology*, 7(11):1031–8.

Shulman, R. G., Hyder, F., and Rothman, D. L. (2001). Cerebral energetics and the glycogen shunt: Neurochemical basis of functional imaging. *Proceedings of the National Academy of Sciences*.

Siddiqui, M. F., Lloyd-Fox, S., Kaynezhad, P., Tachtsidis, I., Johnson, M. H., and Elwell, C. E. (2017). Non-invasive measurement of a metabolic marker of infant brain function. *Scientific Reports*, 7(1).

Singh, I. and Rose, N. (2009). Biomarkers in psychiatry.

Singh, K. D., Smith, A. T., and Greenlee, M. W. (2000). Spatiotemporal frequency and direction sensitivities of human visual areas measured using fMRI. *NeuroImage*.

Snijders, T. M., Milivojevic, B., and Kemner, C. (2013). Atypical excitation-inhibition balance in autism captured by the gamma response to contextual modulation. *NeuroImage: Clinical*, 3:65–72.

Sogut, S., Zoroglu, S. S., Ozyurt, H., Yilmaz, H. R., Ozugurlu, F., Sivasli, E., Yetkin, Ö., Yanik, M., Tutkun, H., Savas, H. A., Tarakcioglu, M., and Akyol, O. (2003). Changes in nitric oxide levels and antioxidant enzyme activities may have a role in the pathophysiological mechanisms involved in autism. *Clinica Chimica Acta*, 331(1-2):111–117.

Sotero, R. C. and Trujillo-Barreto, N. J. (2008). Biophysical model for integrating neuronal activity, EEG, fMRI and metabolism. *NeuroImage*.

Spalding, J. M. (1952). Wounds of the visual pathway. Part II. The striate cortex. *Journal of neurology, neurosurgery, and psychiatry*, 15(3):169–183.

Spalding, K., Bergmann, O., Alkass, K., Bernard, S., Salehpour, M., Huttner, H., Boström, E., Westerlund, I., Vial, C., Buchholz, B., Possnert, G., Mash, D., Druid, H., and Frisén, J. (2013). Dynamics of Hippocampal Neurogenesis in Adult Humans. *Cell*.

Spear, L. P. and Brake, S. C. (1983). Periadolescence: Age-dependent behavior and psychopharmacological responsivity in rats. *Developmental Psychobiology*, 16(2):83–109.

Stathopoulos, S., Gaujoux, R., and O'Ryan, C. (2018). Genome-wide DNA methylation patterns in Autism Spectrum Disorder and mitochondrial function. *bioRxiv*, page 310748.

Stern (2002). Simultaneous EEG and fMRI of the alpha rhythm. *NeuroReport*, pages 2487–2492.

Stichel, C. C., Mi¿œller, C. M., and Zilles, K. (1991). Distribution of glial fibrillary acidic protein and vimentin immunoreactivity during rat visual cortex development. *Journal of Neurocytology*, 20(2):97–108.

Sumiyoshi, A., Suzuki, H., Ogawa, T., Riera, J. J., Shimokawa, H., and Kawashima, R. (2012). Coupling between gamma oscillation and fMRI signal in the rat somatosensory cortex: Its dependence on systemic physiological parameters. *NeuroImage*, 60(1):738–746.

Sun, W., McConnell, E., Pare, J. F., Xu, Q., Chen, M., Peng, W., Lovatt, D., Han, X., Smith, Y., and Nedergaard, M. (2013). Glutamate-dependent neuroglial calcium signaling differs between young and adult brain. *Science*, 339(6116):197–200.

Sweeten, T. L., Posey, D. J., Shankar, S., and McDougle, C. J. (2004). High nitric oxide production in autistic disorder: A possible role for interferon-γ. *Biological Psychiatry*, 55(4):434–437.

Szatmari, P., Chawarska, K., Dawson, G., Georgiades, S., Landa, R., Lord, C., Messinger, D. S., Thurm, A., and Halladay, A. (2016). Prospective Longitudinal Studies of Infant Siblings of Children With Autism: Lessons Learned and Future Directions. *Journal of the American Academy of Child & Adolescent Psychiatry*, 55(3):179–187.

Tabata, H. and Nakajima, K. (2003). Multipolar migration: the third mode of radial neuronal migration in the developing cerebral cortex. *The Journal of Neuroscience*.

Tachtsidis, I. and Scholkmann, F. (2016). False positives and false negatives in functional NIRS: issues, challenges and the way forward. *Journal of Biomedical Optics*.

Taga, G. and Asakawa, K. (2007). Selectivity and localization of cortical response to auditory and visual stimulation in awake infants aged 2 to 4 months. *NeuroImage*, 36(4):1246–1252.

Taga, G., Asakawa, K., Hirasawa, K., and Konishi, Y. (2004). Hemodynamic responses to visual stimulation in occipital and frontal cortex of newborn infants: A near-infrared optical topography study. *Pathophysiology*.

Taga, G., Asakawa, K., Maki, A., Konishi, Y., and Koizumi, H. (2003). Brain imaging in awake infants by near-infrared optical topography. *Proceedings of the National Academy of Sciences of the United States of America*, 100(19):10722–7.

Taga, G., Homae, F., and Watanabe, H. (2007). Effects of source-detector distance of near infrared spectroscopy on the measurement of the cortical hemodynamic response in infants. *NeuroImage*, 38(3):452–460.

Tak, S., Uga, M., Flandin, G., Dan, I., and Penny, W. D. (2016). Sensor space group analysis for fNIRS data. *Journal of Neuroscience Methods*.

Takahashi, T., Shirane, R., Sato, S., and Yoshimoto, T. (1999). Developmental Changes of Cerebral Blood Flow and Oxygen Metabolism in Children. *AJNR Am J Neuroradiol*, 20:917–922.

Talbott, M. R., Nelson, C. a., and Tager-Flusberg, H. (2015). Maternal Gesture Use and Language Development in Infant Siblings of Children with Autism Spectrum Disorder. *Journal of Autism and Developmental Disorders*.

Tang, G., Gutierrez Rios, P., Kuo, S. H., Akman, H. O., Rosoklija, G., Tanji, K., Dwork, A., Schon, E. A., DiMauro, S., Goldman, J., and Sulzer, D. (2013). Mitochondrial abnormalities in temporal lobe of autistic brain. *Neurobiology of Disease*, 54:349–361.

Taylor, L. J., Maybery, M. T., Wray, J., Ravine, D., Hunt, A., and Whitehouse, A. J. (2015). Are there differences in the behavioural phenotypes of Autism Spectrum Disorder probands from simplex and multiplex families? *Research in Autism Spectrum Disorders*.

Telkemeyer, S., Rossi, S., Koch, S. P., Nierhaus, T., Steinbrink, J., Poeppel, D., Obrig, H., and Wartenburger, I. (2009). Sensitivity of Newborn Auditory Cortex to the Temporal Structure of Sounds. *Journal of Neuroscience*, 29(47):14726–14733.

Telkemeyer, S., Rossi, S., Nierhaus, T., Steinbrink, J., Obrig, H., and Wartenburger, I. (2011). Acoustic processing of temporally modulated sounds in infants: Evidence from a combined near-infrared spectroscopy and EEG study. *Frontiers in Psychology*, 2(APR).

Teller, D. Y. (1997). First glances: The vision of infants: The Friedenwald lecture. In *Investigative Ophthalmology and Visual Science*.

Tian, F., Tarumi, T., Liu, H., Zhang, R., and Chalak, L. (2016). Wavelet coherence analysis of dynamic cerebral autoregulation in neonatal hypoxic-ischemic encephalopathy. *NeuroImage: Clinical*.

Tian, P., Teng, I. C., May, L. D., Kurz, R., Lu, K., Scadeng, M., Hillman, E. M. C., De Crespigny, A. J., D'Arceuil, H. E., Mandeville, J. B., Marota, J. J. A., Rosen, B. R., Liu, T. T., Boas, D. A., Buxton, R. B., Dale, A. M., and Devor, A. (2010). Cortical depth-specific microvascular dilation underlies laminar differences in blood oxygenation level-dependent functional MRI signal. *Proceedings of the National Academy of Sciences*, 107(34):15246–15251.

Tierney, A. L. H. G. S. o. E. and Nelson, C. A. C. H. B. H. M. S. (2009). Brain Development and the Role of Experience in the Early Years. *Zero Three*, 30(2):9–13.

Tisdall, M. M., Tachtsidis, I., Leung, T. S., Elwell, C. E., and Smith, M. (2008). Increase in cerebral aerobic metabolism by normobaric hyperoxia after traumatic brain injury. *Journal of neurosurgery*, 109(3):424–432.

Tootell, R. B., Hadjikhani, N. K., Vanduffel, W., Liu, A. K., Mendola, J. D., Sereno, M. I., and Dale, A. M. (1998). Functional analysis of primary visual cortex (V1) in humans. *Proceedings of the National Academy of Sciences of the United States of America*, 95(3):811–817.

Tremblay, E., Vannasing, P., Roy, M.-S., Lefebvre, F., Kombate, D., Lassonde, M., Lepore, F., McKerral, M., and Gallagher, A. (2014). Delayed Early Primary Visual Pathway Development in Premature Infants: High Density Electrophysiological Evidence. *PLoS ONE*.

Uludag, K., Kohl, M., Steinbrink, J., Obrig, H., and Villringer, A. (2002). Cross talk in the Lambert-Beer calculation for near-infrared wavelengths estimated by Monte Carlo simulations. *Journal of Biomedical Optics*, 7(1):51.

Uludag, K., Steinbrink, J., Kohl-Bareis, M., Wenzel, R. Ü., Villringer, A., and Obrig, H. (2004). Cytochrome-c-oxidase redox changes during visual stimulation measured by near-infrared spectroscopy cannot be explained by a mere cross talk artefact. *NeuroImage*, 22(1):109–119.

Urbain, C., Vogan, V. M., Ye, A. X., Pang, E. W., Doesburg, S. M., and Taylor, M. J. (2016). Desynchronization of fronto-temporal networks during working memory processing in autism. *Human Brain Mapping*, 37(1):153–164.

Van Den Pol, A. N., Romano, C., and Ghosh, P. (1995). Metabotropic glutamate receptor mGluR5 subcellular distribution and developmental expression in hypothalamus. *Journal of Comparative Neurology*, 362(1):134–150.

Van Grootel, T. J., Meeson, A., Munk, M. H. J., Kourtzi, Z., Movshon, J. A., Logothetis, N. K., and Kiorpes, L. (2017). Development of visual cortical function in infant macaques: A BOLD fMRI study. *PLOS ONE*.

Vaudano, A. E., Avanzini, P., Tassi, L., Ruggieri, A., Cantalupo, G., Benuzzi, F., Nichelli, P.,

Lemieux, L., and Meletti, S. (2013). Causality within the epileptic network: An EEG-fMRI study validated by intracranial EEG. *Frontiers in Neurology*.

Wagner, J. B., Fox, S. E., Tager-Flusberg, H., and Nelson, C. A. (2011). Neural processing of repetition and non-repetition grammars in 7and 9-month-old infants. *Frontiers in Psychology*, 2(JUL):168.

Wang, X., Tian, F., Soni, S. S., Gonzalez-Lima, F., and Liu, H. (2016). Interplay between up-regulation of cytochrome-c-oxidase and hemoglobin oxygenation induced by near-infrared laser. *Scientific reports*, 6:30540.

Watanabe, H., Homae, F., Nakano, T., and Taga, G. (2008). Functional activation in diverse regions of the developing brain of human infants. *NeuroImage*, 43(2):346–357.

Watanabe, H., Homae, F., and Taga, G. (2010). General to specific development of functional activation in the cerebral cortexes of 2- to 3-month-old infants. *NeuroImage*.

Watanabe, H., Homae, F., and Taga, G. (2012a). Activation and deactivation in response to visual stimulation in the occipital cortex of 6-month-old human infants. *Developmental Psychobiology*, 54(1):1–15.

Watanabe, T., Yahata, N., Abe, O., Kuwabara, H., Inoue, H., Takano, Y., Iwashiro, N., Natsubori, T., Aoki, Y., Takao, H., Sasaki, H., Gonoi, W., Murakami, M., Katsura, M., Kunimatsu, A., Kawakubo, Y., Matsuzaki, H., Tsuchiya, K. J., Kato, N., Kano, Y., Miyashita, Y., Kasai, K., and Yamasue, H. (2012b). Diminished Medial Prefrontal Activity behind Autistic Social Judgments of Incongruent Information. *PLoS ONE*, 7(6):e39561.

Weiss, H. R., Liu, X., and Chi, O. Z. (2008). Cerebral O_2consumption in young Eker rats, effects of GABA blockade: implications for autism. *International Journal of Developmental Neuroscience*, 26(5):517–521.

Weiss, H. R., Liu, X., Grewal, P., and Chi, O. Z. (2012). Reduced effect of stimulation of AMPA receptors on cerebral O_2 consumption in a rat model of autism. *Neuropharmacology*, 63(5):837–841.

Weiss, H. R., Liu, X., Zhang, Q., and Chi, O. Z. (2007). Increased cerebral oxygen consumption in Eker rats and effects of N-methyl-D-aspartate blockade: Implications for autism. *Journal of Neuroscience Research*, 85(11):2512–2517.

Wilcox, T., Bortfeld, H., Woods, R., Wruck, E., and Boas, D. A. (2005a). Using near-infrared spectroscopy to assess neural activation during object processing in infants. *Journal of Biomedical Optics*, 10(1):011010.

Wilcox, T., Bortfeld, H., Woods, R., Wruck, E., and Boas, D. A. (2005b). Using near-infrared spectroscopy to assess neural activation during object processing in infants. *Journal of Biomedical Optics*, 10(1):011010.

Wilcox, T., Bortfeld, H., Woods, R., Wruck, E., and Boas, D. A. (2008). Hemodynamic response to featural changes in the occipital and inferior temporal cortex in infants: A preliminary methodological exploration: Paper. *Developmental Science*.

Wilcox, T., Stubbs, J. A., Wheeler, L., and Alexander, G. M. (2013). Infants' scanning of dynamic faces during the first year. *Infant Behavior and Development*, 36(4):513–516.

Wong-Riley, M. (1979). Changes in the visual system of monocularly sutured or enucleated cats demonstrable with cytochrome oxidase histochemistry. *Brain research*, 171(1):11–28.

Wong-Riley, M. T. T., Hevner, R. F., Cutlan, R., Earnest, M., Egan, R., Frost, J., and Nguyen, T. (1993). Cytochrome oxidase in the human visual cortex: Distribution in the developing and the adult brain. *Visual Neuroscience*, 10(01):41.

Xie, W., Mallin, B. M., and Richards, J. E. (2018). Development of infant sustained attention and its relation to EEG oscillations: an EEG and cortical source analysis study. *Developmental Science*, 21(3):e12562.

Yamada, H., Sadato, N., Konishi, Y., Kimura, K., Tanaka, M., Yonekura, Y., and Ishii, Y. (1997). A rapid brain metabolic change in infants detected by fMRI. *NeuroReport*, 8(17):3775–3778.

Yamada, H., Sadato, N., Konishi, Y., Muramoto, S., Kimura, K., Tanaka, M., Yonekura, Y., Ishii, Y., and Itoh, H. (2000). A milestone for normal development of the infantile brain detected by functional MRI. *Neurology*, 55(2):218–23.

Yamada, J., Okabe, A., Toyoda, H., Kilb, W., Luhmann, H. J., and Fukuda, A. (2004). Cl-uptake promoting depolarizing GABA actions in immature rat neocortical neurones is mediated by NKCC1. *The Journal of physiology*, 557(Pt 3):829–41.

Yang, Y., Higashimori, H., and Morel, L. (2013). Developmental maturation of astrocytes and pathogenesis of neurodevelopmental disorders. *Journal of Neurodevelopmental Disorders*.

Yuan, H., Liu, T., Szarkowski, R., Rios, C., Ashe, J., and He, B. (2010). Negative covariation between task-related responses in alpha/beta-band activity and BOLD in human sensorimotor cortex: An EEG and fMRI study of motor imagery and movements. *NeuroImage*, 49(3):2596–2606.

Zaehle, T. (2009). Inter- and intra-individual covariations of hemodynamic and oscillatory gamma responses in the human cortex. *Frontiers in Human Neuroscience*.

Zaramella, P., Freato, F., Amigoni, A., Salvadori, S., Marangoni, P., Suppiej, A., Suppjei, A., Schiavo, B., and Chiandetti, L. (2001a). Brain auditory activation measured by near-infrared spectroscopy (NIRS) in neonates. *Pediatric research*, 49(2):213–9.

Zaramella, P., Freato, F., Amigoni, A., Salvadori, S., Marangoni, P., Suppjei, A., Schiavo, B., and Chiandetti, L. (2001b). Brain auditory activation measured by near-infrared spectroscopy (NIRS) in neonates. *Pediatric Research*, 49(2):213–219.

Zeff, B. W., White, B. R., Dehghani, H., Schlaggar, B. L., and Culver, J. P. (2007). Retinotopic mapping of adult human visual cortex with high-density diffuse optical tomography. *Proceedings of the National Academy of Sciences of the United States of America*, 104(29):12169–12174.

Zehendner, C. M., Tsohataridis, S., Luhmann, H. J., and Yang, J. W. (2013). Developmental switch in neurovascular coupling in the immature rodent barrel cortex. *PLoS ONE*, 8(11):e80749.

Zhu, H., Fan, Y., Guo, H., Huang, D., and He, S. (2014). Reduced interhemispheric func-

tional connectivity of children with autism spectrum disorder: evidence from functional near infrared spectroscopy studies. *Biomedical Optics Express*, 5(4):1262–1274.

Zoghbi, H. Y. and Bear, M. F. (2012). Synaptic dysfunction in neurodevelopmental disorders associated with autism and intellectual disabilities. *Cold Spring Harbor perspectives in biology*, 4(3).

Zonta, M., Angulo, M. C., Gobbo, S., Rosengarten, B., Hossmann, K. A., Pozzan, T., and Carmignoto, G. (2003). Neuron-to-astrocyte signaling is central to the dynamic control of brain microcirculation. *Nature Neuroscience*, 6(1):43–50.

Zoroglu, S. S., Yurekli, M., Meram, I., Sogut, S., Tutkun, H., Yetkin, O., Sivasli, E., Savas, H. A., Yanik, M., Herken, H., and Akyol, O. (2003). Pathophysiological role of nitric oxide and adrenomedullin in autism. *Cell biochemistry and function*, 21(1):55–60.

Zotev, V., Yuan, H., Misaki, M., Phillips, R., Young, K. D., Feldner, M. T., and Bodurka, J. (2016). Correlation between amygdala BOLD activity and frontal EEG asymmetry during real-time fMRI neurofeedback training in patients with depression. *NeuroImage: Clinical*.

Zwaigenbaum, L., Bryson, S., Rogers, T., Roberts, W., Brian, J., and Szatmari, P. (2005). Behavioral manifestations of autism in the first year of life. *International Journal of Developmental Neuroscience*.

Zwaigenbaum, L., Thurm, A., Stone, W., Baranek, G., Bryson, S., Iverson, J., Kau, A., Klin, A., Lord, C., Landa, R., Rogers, S., and Sigman, M. (2007a). Studying the Emergence of Autism Spectrum Disorders in High-risk Infants: Methodological and Practical Issues. *Journal of Autism and Developmental Disorders*, 37(3):466–480.

Zwaigenbaum, L., Thurm, A., Stone, W., Baranek, G., Bryson, S., Iverson, J., Kau, A., Klin, A., Lord, C., Landa, R., Rogers, S., and Sigman, M. (2007b). Studying the Emergence of Autism Spectrum Disorders in High-risk Infants: Methodological and Practical Issues. *Journal of Autism and Developmental Disorders*, 37(3):466–480.

Appendix A

Appendix to Chapter 5

Experiment 2

An infant-friendly variation of the experimental paradigm presented in Chapter 5 was developed to explore a block design format where the stimuli were presented for 10 s followed by 10 s baseline. While it is clear from Experiment 1 that a block design format does not work well for EEG as it yields too few trials, Experiment 2 was built such that each change occurring within a block was considered an event for the EEG. For example, each alternation of the checkerboard was averaged over during the data analysis rather than just the start of the experimental condition. This yields many more trials for the EEG.

Stimuli

All stimuli were developed in Psychtoolbox (Matlab, USA) and consisted of three tasks such that each task had two contrast conditions. Only Task 1 is discussed here, the other tasks will be described in more detail in Chapter 5.

Task 1

The first task was designed to mimic the stimuli in Experiment 1, preferentially activating the magnocellular or parvocellular pathway with

1. A full red and green alternating screen

2. Circular checkerboard

The alternating frequency of both stimuli was 4Hz. The stimuli are shown in Figure A.1.
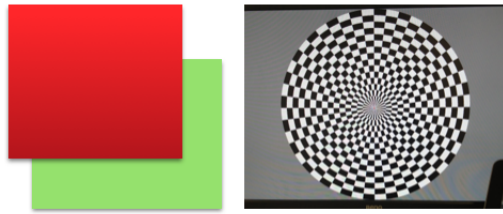
Figure A.1: Stimuli for Task 1, Experiment 2

Experimental Procedure

Due to the time constraints and limited availability of the broadband system, only EEG was used in Experiment 2. As a validating procedure this was fine as Experiment 2 used a block-design format which has been used extensively for NIRS studies so it was more important to investigate its compatibility as an experimental paradigm for EEG. Four adults (4 females, aged between 23 - 28) participated in the study after providing written, informed consent. Head measurements were taken for each participant and the nasion to inion measurement was used to identify the location of Cz on the participant's head. The EEG headcap was positioned with the marked Cz position on the cap aligned with the Cz of the participant. EEG electrodes were filled with gel using a syringe and the wires clipped on top which were then connected to the necbox. The necbox was positioned at the base of the participant's neck. Participants were seated approximately 60cm from the screen. Each stimulus was presented for 10 s followed by 10 s of baseline which consisted of a blank grey screen with a fixation cross at the centre of the screen.

Data analysis

EEG

All EEG data were analysed using the EEGLab Toolbox (Schwartz Centre for Computational Neuroscience, UC San Diego, USA) in Matlab2017a (Mathworks, USA). The data were bandpass filtered from 0.1 - 100 Hz and a notch filter of 50 Hz was applied to remove electrical noise and then segmented into epochs of 800 ms around each event occurring within a block. That is, for the checkerboard the data were segmented over every alternation of the checkerboard and for the red and green condition, the data were segmented over every alternation between red and green. The epoched data were cleaned manually and trials were removed if they were contaminated with artifacts such as eye blinks, muscle noise or movement. Epochs were averaged across trials and ERP waveforms were then

generated for each channel as they provide a good indication of whether the experimental stimulus is appropriate to measure neuronal activation.

Results

Data from only Task 1 was looked at and ERPs generated, as ERPs provide a good indication of whether the experimental condition induces a neural response (Luck, 2005). Figure A.2 shows the ERPs from a single subject at Oz, with the red line corresponding to the ERP generated by the red/green stimulus and the black line corresponding to the ERP generated by the black/white radial checkerboard stimulus. A pairwise t-test indicated a significant difference between the two conditions ($t = 2.33$, $p = 0.019$).
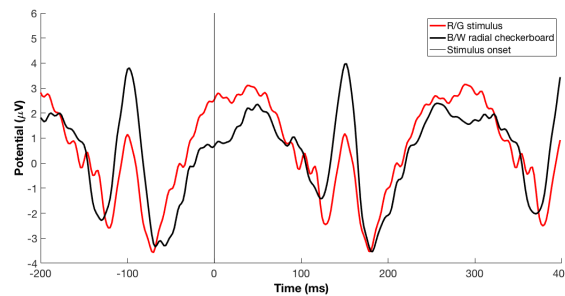
Figure A.2: ERP from one subject from Task 1 of Experiment 2 at Oz. The black and white radial checkerboard ERP is shown in black while the red and green stimulus ERP is shown in red.

Statistical tables results (Experiment 1)

NIRS

Contralateral vs Ipsilateral

Magnocellular

Pair	Δ[HbO$_2$] Mean Maximum Change	Δ[HbO$_2$] Mean difference	t_{HbO_2}	p_{HbO_2}
(Pair 1) Ch1 Contra - Ch1 Ipsi	Contralateral - 0.2302 / Ipsilateral - 0.3180	-0.08785	-1.909	0.129
(Pair 2) Ch2 Contra - Ch2 Ipsi	Contralateral - 0.2774 / Ipsilateral - 0.3635	-0.08611	-1.316	0.258
(Pair 3) Ch3 Contra - Ch3 Ipsi	Contralateral - 0.2356 / Ipsilateral - 0.3389	-0.10325	-1.195	0.298
(Pair 4) Ch4 Contra - Ch4 Ipsi	Contralateral - 0.3824 / Ipsilateral - 0.5613	-0.17892	-1.625	0.179
(Pair 5) Ch5 Contra - Ch5 Ipsi	Contralateral - 0.5694 / Ipsilateral - 0.2705	0.29889	7.158	.002*
(Pair 6) Ch6 Contra - Ch6 Ipsi	Contralateral - 0.4394 / Ipsilateral - 0.2706	0.16880	2.980	.041*
(Pair 7) Ch7 Contra - Ch7 Ipsi	Contralateral - 0.6050 / Ipsilateral - 0.3487	0.25627	3.040	.038*
(Pair 8) Ch8 Contra - Ch8 Ipsi	Contralateral - 0.4956 / Ipsilateral - 0.2193	0.27629	3.473	.026*

Pair	Δ[HHb] Mean Maximum Change	Δ[HHb] Mean difference	t_{HHb}	p_{HHb}
(Pair 1) Ch1 Contra - Ch1 Ipsi	Contralateral - 0.0982 / Ipsilateral - 0.2165	-0.11837	-2.702	0.054
(Pair 2) Ch2 Contra - Ch2 Ipsi	Contralateral - 0.1566 / Ipsilateral - 0.3002	-0.14361	-2.825	0.048*
(Pair 3) Ch3 Contra - Ch3 Ipsi	Contralateral - 0.1318 / Ipsilateral - 0.1621	-0.03027	-1.988	0.118
(Pair 4) Ch4 Contra - Ch4 Ipsi	Contralateral - 0.2334 / Ipsilateral - 0.2884	-0.05502	-2.249	0.088
(Pair 5) Ch5 Contra - Ch5 Ipsi	Contralateral - 0.3211 / Ipsilateral - 0.1490	0.17216	4.435	0.011*
(Pair 6) Ch6 Contra - Ch6 Ipsi	Contralateral - 0.2784 / Ipsilateral - 0.1076	0.17081	3.213	0.033*
(Pair 7) Ch7 Contra - Ch7 Ipsi	Contralateral - 0.2840/ Ipsilateral - 0.2275	0.05643	4.093	0.015*
(Pair 8) Ch8 Contra - Ch8 Ipsi	Contralateral - 0.2214 / Ipsilateral - 0.1521	0.06930	6.876	0.002*

Pair	Δ[oxCCO] Mean Maximum Change	Δ[oxCCO] Mean difference	t_{oxCCO}	p_{oxCCO}
(Pair 1) Ch1 Contra - Ch1 Ipsi	Contralateral - 0.0380 / Ipsilateral - 0.0911	-0.05313	-1.899	.130
(Pair 2) Ch2 Contra - Ch2 Ipsi	Contralateral - 0.0574 / Ipsilateral - 0.0915	-0.03404	-2.605	0.060
(Pair 3) Ch3 Contra - Ch3 Ipsi	Contralateral - 0.0551 / Ipsilateral - 0.0818	-0.02670	-1.101	0.333
(Pair 4) Ch4 Contra - Ch4 Ipsi	Contralateral - 0.0865 / Ipsilateral - 0.1057	-0.01915	-1.416	0.230
(Pair 5) Ch5 Contra - Ch5 Ipsi	Contralateral - 0.1315 / Ipsilateral - 0.0527	0.07889	4.853	0.008*
(Pair 6) Ch6 Contra - Ch6 Ipsi	Contralateral - 0.1123 / Ipsilateral - 0.0445	0.06785	5.692	0.005*
(Pair 7) Ch7 Contra - Ch7 Ipsi	Contralateral - 0.1263 / Ipsilateral - 0.0830	0.04332	5.314	0.006*
(Pair 8) Ch8 Contra - Ch8 Ipsi	Contralateral - 0.1235 / Ipsilateral - 0.0544	0.06914	5.559	0.005*

Table A.1: Mean maximum differences in contralateral and ipsilateral conditions for Magno for HbO$_2$, HHb and oxCCO. The significant p values are indicated with an asterisk.

Parvocellular

Pair	Δ[HbO$_2$] Mean Maximum Change	Δ[HbO$_2$] Mean difference	t_{HbO_2}	p_{HbO_2}
(Pair 1) Ch1 Contra - Ch1 Ipsi	Contralateral - 0.1568 / Ipsilateral - 0.2757	-0.11890	-1.933	0.125
(Pair 2) Ch2 Contra - Ch2 Ipsi	Contralateral - 0.2147 / Ipsilateral - 0.3172	-0.10242	-1.337 -	0.252
(Pair 3) Ch3 Contra - Ch3 Ipsi	Contralateral - 0.2310 / Ipsilateral - 0.3304	-0.09940	1.816	0.144
(Pair 4) Ch4 Contra - Ch4 Ipsi	Contralateral - 0.3175 / Ipsilateral - 0.5025	-0.18504	-2.949	0.042*
(Pair 5) Ch5 Contra - Ch5 Ipsi	Contralateral - 0.4470 / Ipsilateral - 0.2533	0.19368	3.004	0.040*
(Pair 6) Ch6 Contra - Ch6 Ipsi	Contralateral - 0.4166 / Ipsilateral - 0.2583	0.15826	3.349	0.029*
(Pair 7) Ch7 Contra - Ch7 Ipsi	Contralateral - 0.5593 / Ipsilateral - 0.3019	0.25736	3.992	0.016*
(Pair 8) Ch8 Contra - Ch8 Ipsi	Contralateral - 0.4288 / Ipsilateral - 0.1903	0.23848	3.374	0.028*

Pair	Δ[HHb] Mean Maximum Change	Δ[HHb] Mean difference	t_{HHb}	p_{HHb}
(Pair 1) Ch1 Contra - Ch1 Ipsi	Contralateral - 0.1165 / Ipsilateral - 0.2306	-0.11409	-2.495	0.067
(Pair 2) Ch2 Contra - Ch2 Ipsi	Contralateral - 0.1039 / Ipsilateral - 0.2273	-0.12337	-2.322	0.081
(Pair 3) Ch3 Contra - Ch3 Ipsi	Contralateral - 0.1143 / Ipsilateral - 0.1548	-0.04049	-2.411	0.073
(Pair 4) Ch4 Contra - Ch4 Ipsi	Contralateral - 0.1820 / Ipsilateral - 0.2886	-0.10660	-7.141	0.002*
(Pair 5) Ch5 Contra - Ch5 Ipsi	Contralateral - 0.2983 / Ipsilateral - 0.1283	0.17003	5.346	0.006*
(Pair 6) Ch6 Contra - Ch6 Ipsi	Contralateral - 0.2508 / Ipsilateral - 0.1151	0.13569	5.882	0.004*
(Pair 7) Ch7 Contra - Ch7 Ipsi	Contralateral - 0.2738 / Ipsilateral - 0.1730	0.10081	8.181	0.001*
(Pair 8) Ch8 Contra - Ch8 Ipsi	Contralateral - 0.1992 / Ipsilateral - 0.1518	0.04743	1.735	0.158

Pair	Δ[oxCCO] Mean Maximum Change	Δ[oxCCO] Mean difference	t_{oxCCO}	p_{oxCCO}
(Pair 1) Ch1 Contra - Ch1 Ipsi	Contralateral - 0.0296 / Ipsilateral - 0.0695	-0.03996	-2.201	0.093
(Pair 2) Ch2 Contra - Ch2 Ipsi	Contralateral - 0.0377 / Ipsilateral - 0.0817	-0.04396	-2.813	0.048*
(Pair 3) Ch3 Contra - Ch3 Ipsi	Contralateral - 0.0404 / Ipsilateral - 0.0832	-0.04274	-2.929	0.043*
(Pair 4) Ch4 Contra - Ch4 Ipsi	Contralateral - 0.0733 / Ipsilateral - 0.1146	-0.04129	-11.450	0.00033*
(Pair 5) Ch5 Contra - Ch5 Ipsi	Contralateral - 0.1145 / Ipsilateral - 0.0521	0.06247	5.815	0.004*
(Pair 6) Ch6 Contra - Ch6 Ipsi	Contralateral - 0.1130 / Ipsilateral - 0.0463	0.06671	4.419	0.012*
(Pair 7) Ch7 Contra - Ch7 Ipsi	Contralateral - 0.1115 / Ipsilateral - 0.0745	0.03701	6.107	0.004*
(Pair 8) Ch8 Contra - Ch8 Ipsi	Contralateral - 0.1033 / Ipsilateral - 0.0623	0.04099	2.784	0.0496*

Table A.2: Mean maximum differences in contralateral and ipsilateral conditions for Parvo for HbO$_2$, HHb and oxCCO. The significant p values are indicated with an asterisk.

Magno vs Parvo

Contralateral

Pair	$\Delta[HbO_2]$ Mean Maximum Change	$\Delta[HbO_2]$ Mean difference	t_{HbO_2}	p_{HbO_2}
(Pair 1) Ch1 Magno - Ch1 Parvo	Magno - 0.2302 / Parvo 0.1568	0.07339	3.384	0.028*
(Pair 2) Ch2 Magno - Ch2 Parvo	Magno - 0.2774 / Parvo 0.2147	0.06264	2.549	0.063
(Pair 3) Ch3 Magno - Ch3 Parvo	Magno - 0.2356 / Parvo 0.2310	0.00465	0.309	0.773
(Pair 4) Ch4 Magno - Ch4 Parvo	Magno - 0.3824 / Parvo 0.3175	0.06489	2.553	0.063
(Pair 5) Ch5 Magno - Ch5 Parvo	Magno - 0.5694 / Parvo 0.4470	0.12246	6.462	0.003*
(Pair 6) Ch6 Magno - Ch6 Parvo	Magno - 0.4394 / Parvo 0.4166	0.02286	0.757	0.491
(Pair 7) Ch7 Magno - Ch7 Parvo	Magno - 0.6050 / Parvo 0.5593	0.04573	1.063	0.348
(Pair 8) Ch8 Magno - Ch8 Parvo	Magno - 0.4956 / Parvo 0.4288	0.06684	1.623	0.180

Pair	$\Delta[HHb]$ Mean Maximum Change	$\Delta[HHb]$ Mean difference	t_{HHb}	p_{HHb}
(Pair 1) Ch1 Magno - Ch1 Parvo	Magno - 0.0982 / Parvo 0.1165	-0.01832	-1.083	0.340
(Pair 2) Ch2 Magno - Ch2 Parvo	Magno - 0.1566 / Parvo 0.1039	0.05265	2.004	0.116
(Pair 3) Ch3 Magno - Ch3 Parvo	Magno - 0.1318 / Parvo 0.1143	0.01748	0.632	0.562
(Pair 4) Ch4 Magno - Ch4 Parvo	Magno - 0.2334 / Parvo 0.1820	0.05135	13.046	0.000199*
(Pair 5) Ch5 Magno - Ch5 Parvo	Magno - 0.3211 / Parvo 0.2983	0.02285	0.882	0.428
(Pair 6) Ch6 Magno - Ch6 Parvo	Magno - 0.2784 / Parvo 0.2508	0.02757	0.746	0.497
(Pair 7) Ch7 Magno - Ch7 Parvo	Magno - 0.2840 / Parvo 0.2738	0.01014	0.484	0.654
(Pair 8) Ch8 Magno - Ch8 Parvo	Magno - 0.2214 / Parvo 0.1992	0.02216	0.870	0.433

Pair	$\Delta[oxCCO]$ Mean Maximum Change	$\Delta[oxCCO]$ Mean difference	t_{oxCCO}	p_{oxCCO}
(Pair 1) Ch1 Magno - Ch1 Parvo	Magno - 0.0380 / Parvo 0.0296	0.00839	.960	0.392
(Pair 2) Ch2 Magno - Ch2 Parvo	Magno - 0.0574 / Parvo 0.0377	0.01973	2.069	0.107
(Pair 3) Ch3 Magno - Ch3 Parvo	Magno - 0.0551 / Parvo 0.0404	0.01467	1.746	0.156
(Pair 4) Ch4 Magno - Ch4 Parvo	Magno - 0.0865 / Parvo 0.0733	0.01317	1.702	0.164
(Pair 5) Ch5 Magno - Ch5 Parvo	Magno - 0.1315 / Parvo 0.1145	0.01702	3.927	0.017*
(Pair 6) Ch6 Magno - Ch6 Parvo	Magno - 0.1123 / Parvo 0.1130	-0.00072	-.080	0.940
(Pair 7) Ch7 Magno - Ch7 Parvo	Magno - 0.1263 / Parvo 0.1115	0.01484	2.099	0.104
(Pair 8) Ch8 Magno - Ch8 Parvo	Magno - 0.1235 / Parvo 0.1033	0.02021	3.741	0.020*

Table A.3: Mean maximum differences in contralateral and ipsilateral conditions for Parvo for HbO$_2$, HHb and oxCCO. The significant p values are indicated with an asterisk.

NIRS Cross-Correlations (Ipsilateral)
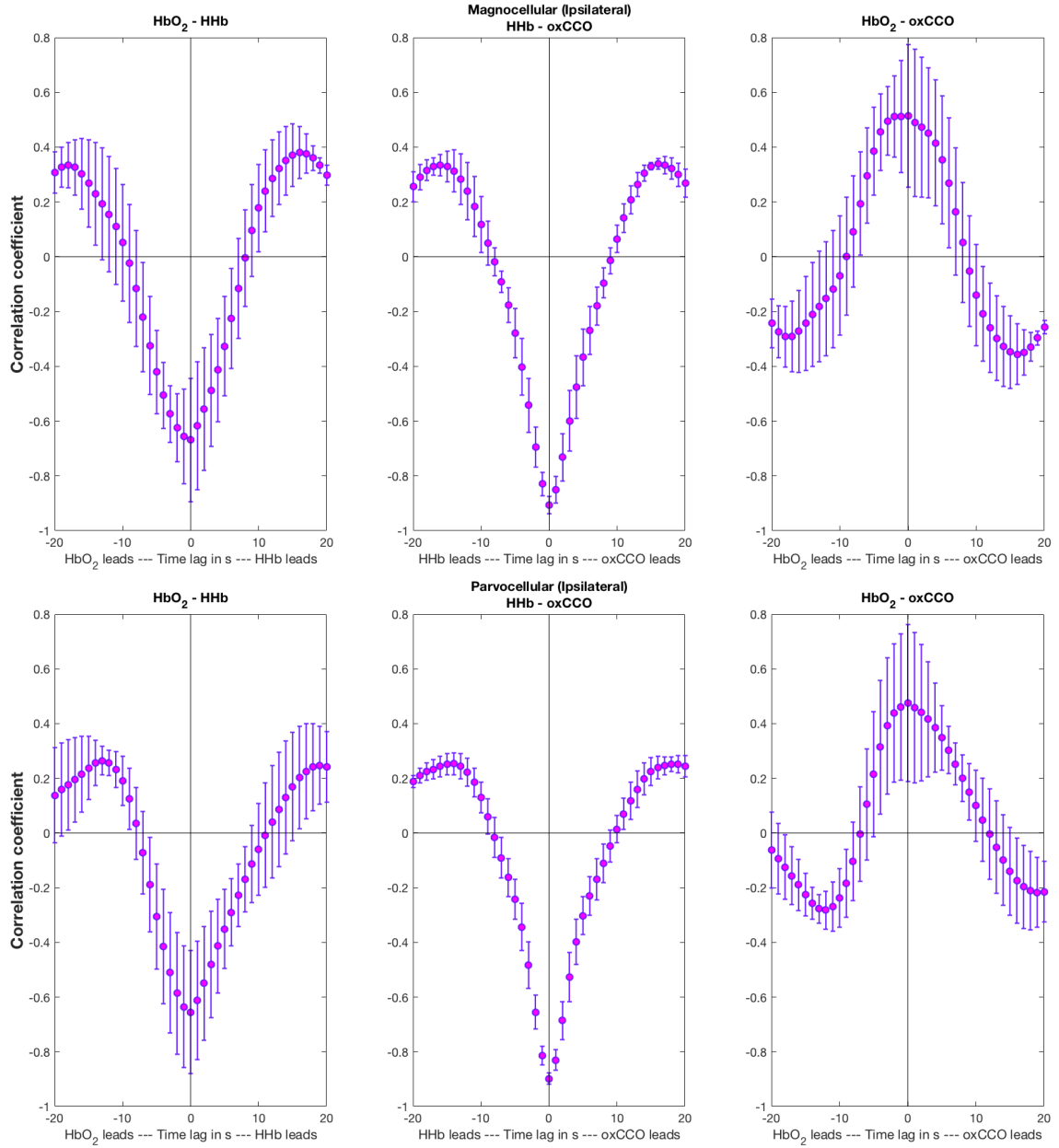
Figure A.3: Average of the cross-correlation across all occipital channels for the ipsilateral Magno condition (upper panel) and ipsilateral Parvo condition (bottom panel).

EEG - Event related design task

Event Related Potentials

Contralateral vs Ipsilateral

Magno

Pair	Mean Maximum Change	Mean difference	t	p
(Pair 1) Ch1 Contra - Ch1 Ipsi	Contra - 6.2226 / Ipsi 1.9795	4.24315	5.098	0.001*
(Pair 2) Ch2 Contra - Ch2 Ipsi	Contra - 3.4979 / Ipsi 5.2588	-1.76097	-3.800	0.005*
(Pair 3) Ch3 Contra - Ch3 Ipsi	Contra - 2.2977 / Ipsi 1.4207	0.87697	1.703	0.127
(Pair 4) Ch4 Contra - Ch4 Ipsi	Contra - 1.4257 / Ipsi 1.7775	-0.3518	-0.908	0.390
(Pair 5) Ch5 Contra- Ch5 Ipsi	Contra - 9.5048 / Ipsi 1.8477	4.88552	4.554	0.002*

Table A.4: Mean maximum differences in contralateral and ipsilateral ERPs for Magno. The significant p values are indicated with an asterisk.

Parvo

Pair	Mean Maximum Change	Mean difference	t	p
(Pair 1) Ch1 Contra - Ch1 Ipsi	Contra - 6.8775 / Ipsi 2.1867	4.69076	5.325	0.001*
(Pair 2) Ch2 Contra - Ch2 Ipsi	Contra - 2.5241 / Ipsi 4.5261	-2.00207	-3.911	0.004*
(Pair 3) Ch3 Contra - Ch3 Ipsi	Contra - 3.2760 / Ipsi 2.4071	0.86887	1.666	0.134
(Pair 4) Ch4 Contra - Ch4 Ipsi	Contra - 2.0008 / Ipsi 2.5822	-0.58139	-1.922	0.091
(Pair 5) Ch5 Contra- Ch5 Ipsi	Contra - 6.2306 / Ipsi 3.0136	3.21702	3.016	0.017*

Table A.5: Mean maximum differences in contralateral and ipsilateral ERPs for Parvo. The significant $p$values are indicated with an asterisk.

EEG - Block design task

Event Related Potentials

Contralateral vs Ipsilateral

Magno

Pair	Mean Maximum Change	Mean difference	t	p
(Pair 1) Ch1 Contra - Ch1 Ipsi	Contra - 6.2226 / Ipsi 1.9795	4.24315	5.098	0.001*
(Pair 2) Ch2 Contra - Ch2 Ipsi	Contra - 3.4979 / Ipsi 5.2588	-1.76097	-3.800	0.005*
(Pair 3) Ch3 Contra - Ch3 Ipsi	Contra - 2.2977 / Ipsi 1.4207	0.87697	1.703	0.127
(Pair 4) Ch4 Contra - Ch4 Ipsi	Contra - 1.4257 / Ipsi 1.7775	-0.3518	-0.908	0.390
(Pair 5) Ch5 Contra- Ch5 Ipsi	Contra - 9.5048 / Ipsi 1.8477	4.88552	4.554	0.002*

Table A.6: Mean maximum differences in contralateral and ipsilateral ERPs for Magno. The significant p values are indicated with an asterisk.

Parvo

Pair	Mean Maximum Change	Mean difference	t	p
(Pair 1) Ch1 Contra - Ch1 Ipsi	Contra - 6.8775 / Ipsi 2.1867	4.69076	5.325	0.001*
(Pair 2) Ch2 Contra - Ch2 Ipsi	Contra - 2.5241 / Ipsi 4.5261	-2.00207	-3.911	0.004*
(Pair 3) Ch3 Contra - Ch3 Ipsi	Contra - 3.2760 / Ipsi 2.4071	0.86887	1.666	0.134
(Pair 4) Ch4 Contra - Ch4 Ipsi	Contra - 2.0008 / Ipsi 2.5822	-0.58139	-1.922	0.091
(Pair 5) Ch5 Contra- Ch5 Ipsi	Contra - 6.2306 / Ipsi 3.0136	3.21702	3.016	0.017*

Table A.7: Mean maximum differences in contralateral and ipsilateral ERPs for Parvo. The significant p values are indicated with an asterisk.

Appendix B

Appendix to Chapter 6

NIRS Broadband System Modifications

The NIRS system that was used for the adult study described in Chapter 5 was used for the studies presented in Chapters 6 - 8. The main modification for the system for use with infants was to include one extra detector per CCD camera, providing a total of 7 detectors per CCD. This required the binning of each CCD camera to be adjusted

   This required modifications to be made to the system software in order to incorporate intensity data from the two extra detectors.

LabVIEW software modification

Figure B.1 shows the settings tab for the adult system configuration as described in Chapter 5 in the upper panel and the modifications for the infant studies in the lower panel, for one of the CCD cameras. An extra detector "Detector 7" has been added. As the CCD chip had 512 pixels, the binning of each pixel needed to be adjusted so that each detector had equal spacing on each CCD chip. The new pixel binning can be seen in the bottom panel of Figure B.1. Figure B.2 shows the allocation of the pixels for each each of the detectors, for one of the CCD cameras.

Figure B.1: LabVIEW settings tab for (Upper panel) adult system configuration and (Bottom panel) infant system modification.
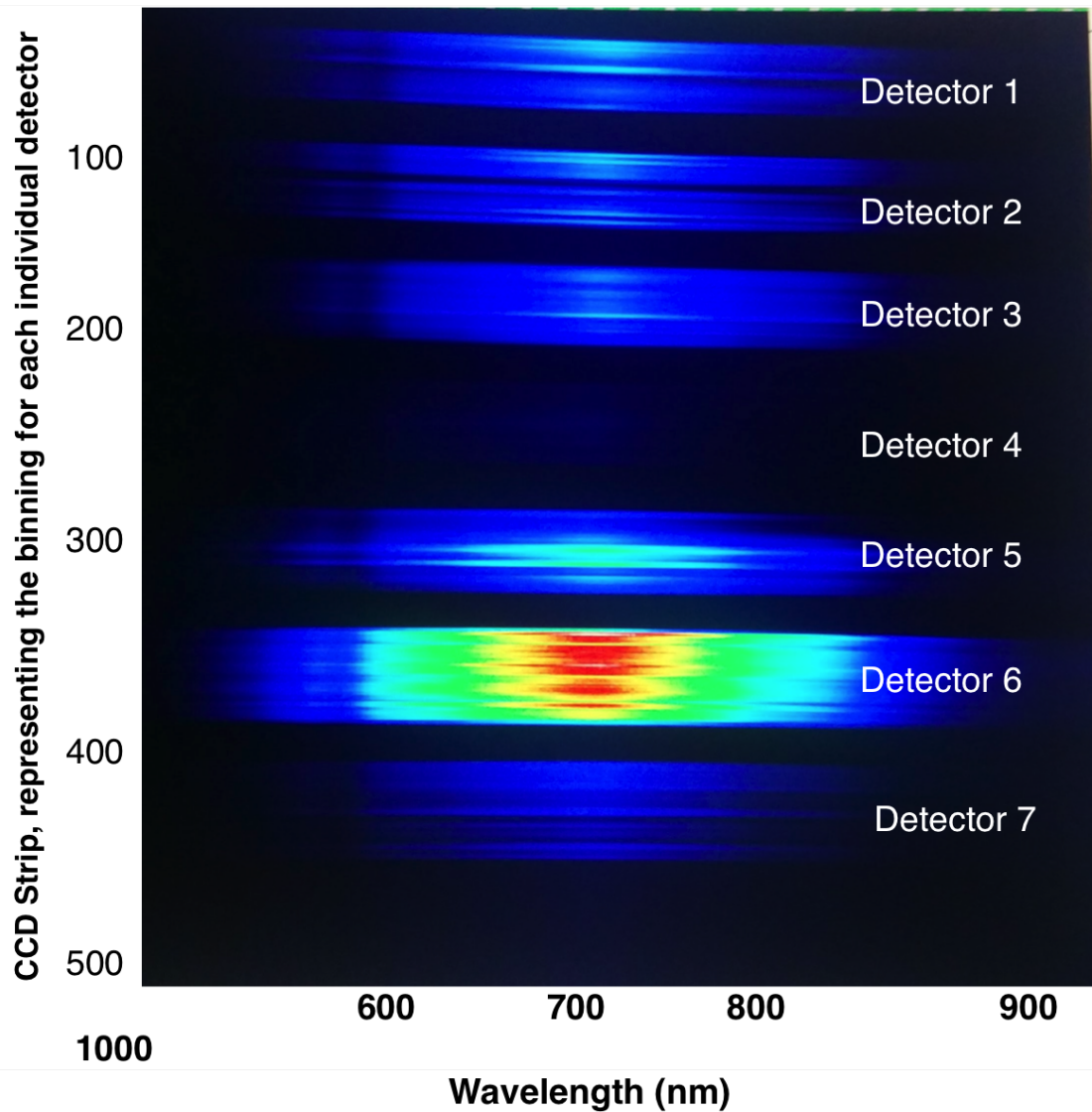
Figure B.2: LabVIEW settings tab for (Upper panel) adult system configuration and (Bottom panel) infant system modification.

NIRS Results

Time to peak analysis

Figure B.3 shows the TTP for each chromophore for social and non-social conditions respectively.
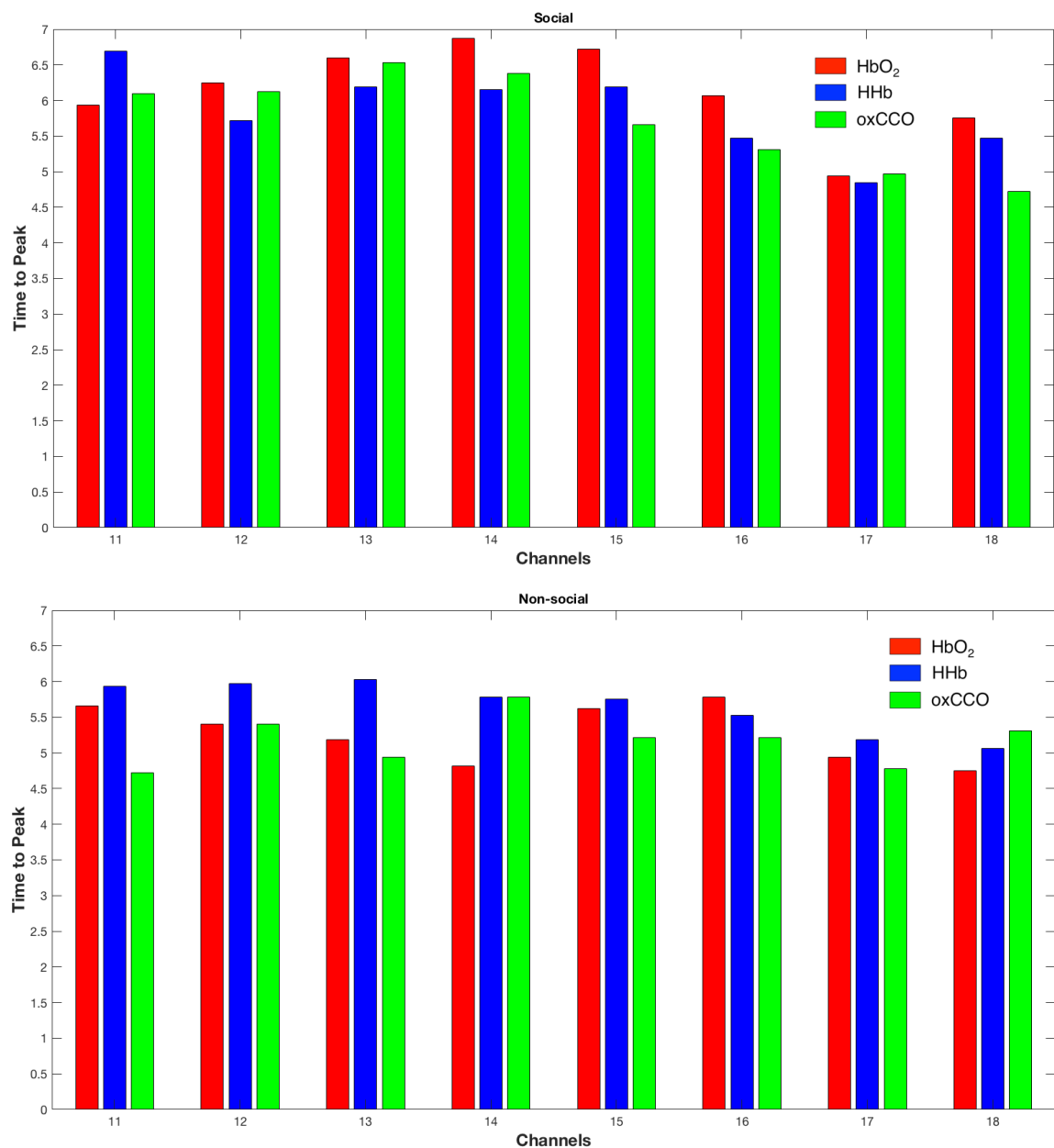
Figure B.3: Bar graph showing the time taken for each of the chromophores to reach their maximal response to the social condition (top) and non-social (bottom) in the statistical time window of 10 - 18 s post-stimulus onset.

Cross-correlation analysis

Figure B.4 shows the cross-correlations between (i) HbO_2 and oxCCO (ii) HHb and oxCCO and (iii) HbO_2 and oxCCO for all the channels (including the channels over the occipital cortex) for the social and non-social conditions.
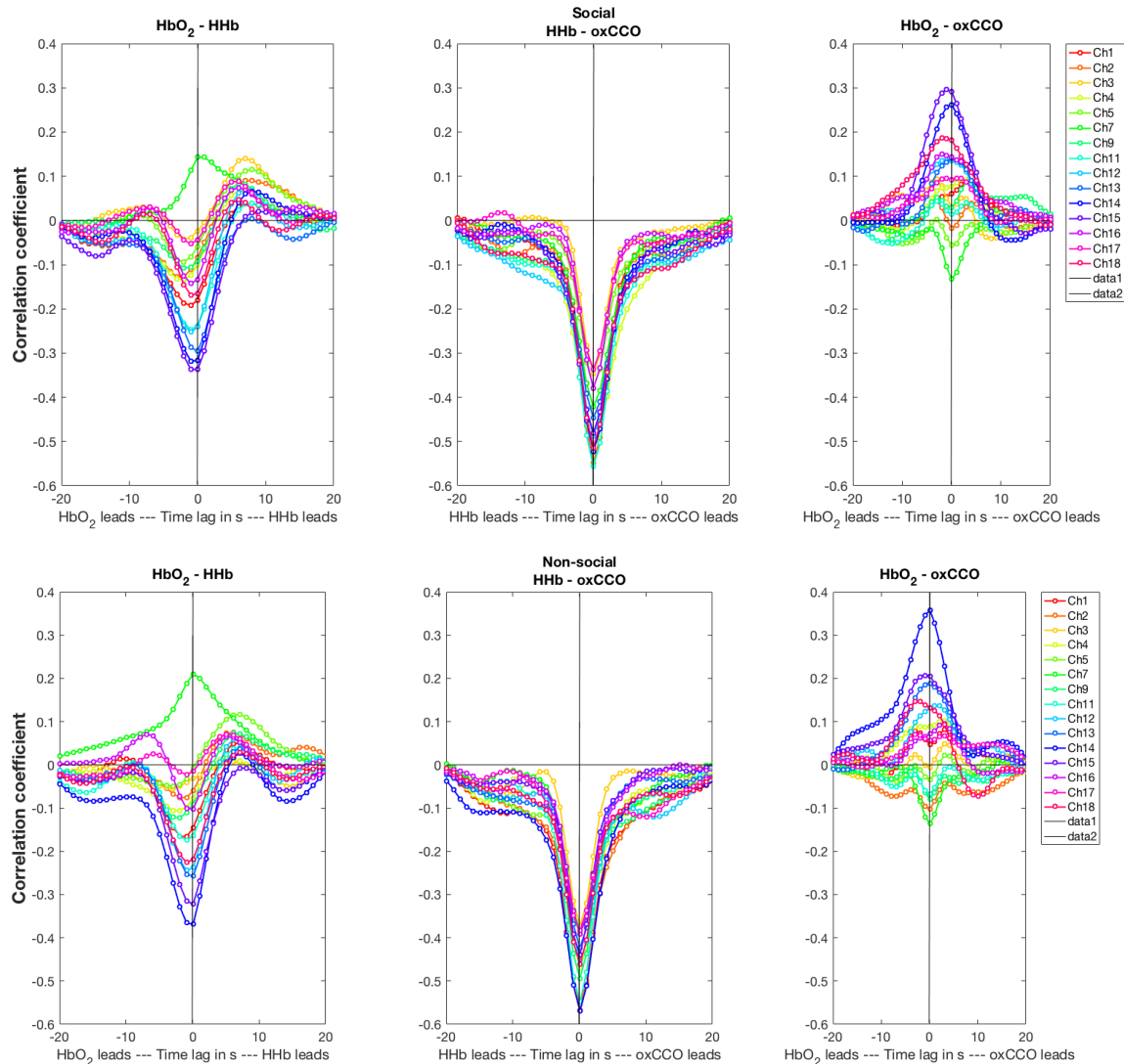
Figure B.4: Cross-correlations between HbO$_2$ and oxCCO (left), HHb and oxCCO (middle) and HbO$_2$ and oxCCO (right) for the social condition (top) and non-social condition (bottom). The x-axis shows the time-lag between the time series while the y-axis shows the correlation coefficient.

Social versus non-social statistical tables

Tables B.1 - B.3 show the mean maximum changes in Δ[HbO$_2$], Δ[HHb] and Δ[oxCCO] respectively with their the t and p values and FDR corrected p values. Significant channels are marked with an asterisk, both for the uncorrected and corrected p values.

Channel	$\Delta[HbO_2]$ Mean Difference (soc - nonsoc)	t_{HbO_2}	p_{HbO_2}	FDR corrected p_{HbO_2}
1	0.1740	1.1984	0.2405	0.3279
2	0.2025	2.0188	0.0539	0.1248
3	0.2346	1.9403	0.0666	0.1248
4	0.2980	2.0314	0.0515	0.1248
5	0.1518	0.9839	0.3339	0.4174
7	0.3051	1.618	0.1251	0.2085
9	0.4747	2.5432	0.0182*	0.1248
11	0.2433	1.9326	0.0628	0.1248
12	0.0143	0.1562	0.8770	0.8770
13	0.0293	0.3448	0.7327	0.8454
14	0.4532	3.5049	0.0015*	0.0219*
15	0.2752	2.1732	0.0375*	0.1248
16	0.2193	1.9528	0.0606	0.1248
17	0.1424	1.3403	0.1917	0.2876
18	0.0317	0.2530	0.8021	0.8594

Table B.1: Mean maximum differences and t and p values for the social versus non-social for HbO_2.

Channel	Δ[HHb] Mean Difference	t_{HHb}	p_{HHb}	FDR corrected p_{HHb}
1	-0.0293	-3.3390	0.7190	0.7704
2	0.0316	-3.8003	0.66570	0.7681
3	0.0605	-3.1807	0.5321	0.7681
4	-0.0463	-2.4378	0.5796	0.7681
5	-0.2195	-0.6685	0.1215	0.4280
7	-0.0137	-3.3188	0.9005	0.9005
9	-0.0526	-2.4951	0.6490	0.7681
11	-0.0318	-4.0532	0.5689	0.7681
12	0.1144	-5.4270	0.0658	0.4280
13	0.0947	-4.6895	0.1509	0.4280
14	-0.0915	-3.2610	0.1465	0.4280
15	0.0353	-4.9264	0.4599	0.7681
16	0.1054	-5.5518	0.1712	0.4280
17	0.0432	-3.4339	0.5118	0.7681
18	0.1323	-5.7540	0.08	0.4280

Table B.2: Mean maximum differences and t and p values for the social versus non-social for HHb.

Channel	Δ[oxCCO] Mean Difference	t_{oxCCO}	p_{oxCCO}	FDR corrected p_{oxCCO}
1	0.0171	0.7791	0.4422	0.8292
2	0.0155	0.9081	0.3721	0.8292
3	0.0047	0.1034	0.9187	0.9187
4	0.0242	1.0946	0.2827	0.8292
5	0.0895	2.0607	0.0491*	0.2454
7	0.0266	0.8185	0.4251	0.8292
9	-0.0067	-0.1932	0.8485	0.9187
11	0.0529	2.5774	0.0151*	0.1134
12	-0.0242	-1.6323	0.1134	0.4253
13	0.0066	0.3261	0.7466	0.9187
14	0.0613	2.8133	0.0086*	0.1134
15	0.0062	0.4078	0.6862	0.9187
16	-0.0039	-0.1654	0.8698	0.9187
17	0.0015	0.2305	0.8195	0.9187
18	-0.0032	-0.1545	0.8784	0.9187

Table B.3: Mean maximum differences and t and p values for the social versus non-social for oxCCO.

Combined NIRS and EEG analysis for social minus non-social

Figure B.5 shows a heatmap of the difference between social and non-social conditions such that the correlations were performed between the difference in mean power spectral density (social minus non-social) and the difference in the maximum change in each of the NIRS chromophores (social minus non-social). The significant correlations ($p < 0.05$) are indicated by red rectangles. Theta band appears to correlate overall more strongly with HHb for the social condition in comparison to the non-social, while more negative correlations are observed between channels for HbO_2. A similar pattern is observed for the alpha band with alpha power and HbO_2 correlating more strongly for social than non-social. In both alpha and theta bands for oxCCO, stronger positive correlations were seen

for the social condition in comparison to the non-social, particularly in Channels 16 and 17. Channel 11 also displayed stronger correlations with temporo-parietal channels for the social condition in comparison to the non-social.
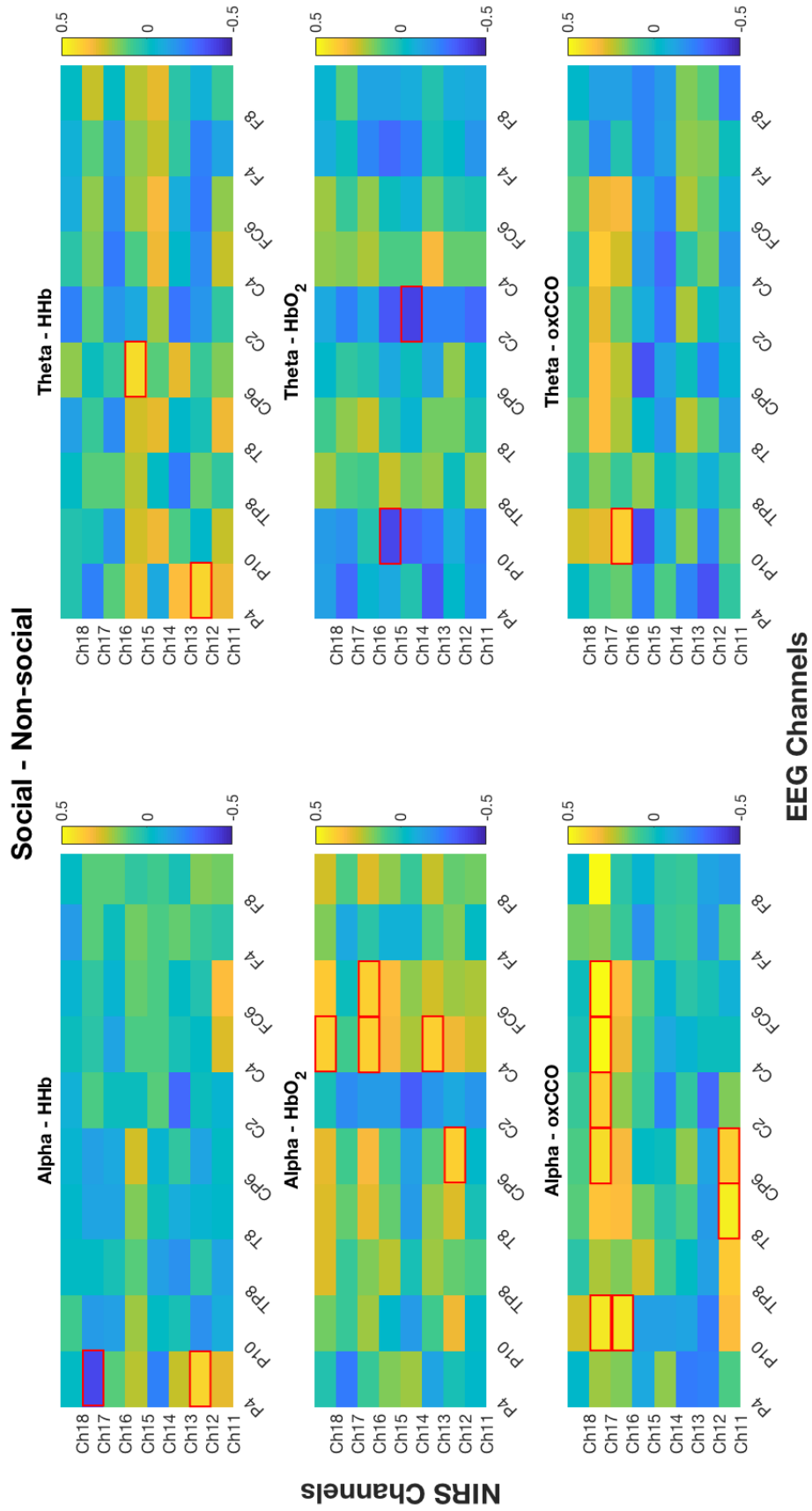
Figure B.5: Heatmap showing the significant correlations between the difference in mean power spectral density and the difference in maximum change in $\Delta[HbO_2]$, $\Delta[HHb]$ and $\Delta[oxCCO]$ for social minus non-social.

Appendix C

Appendix to Chapter 7

NIRS Results - Checkerboard conditions

Time to peak analysis

Figure C.1 shows the TTP for each chromophore for black/white and red/green conditions respectively.
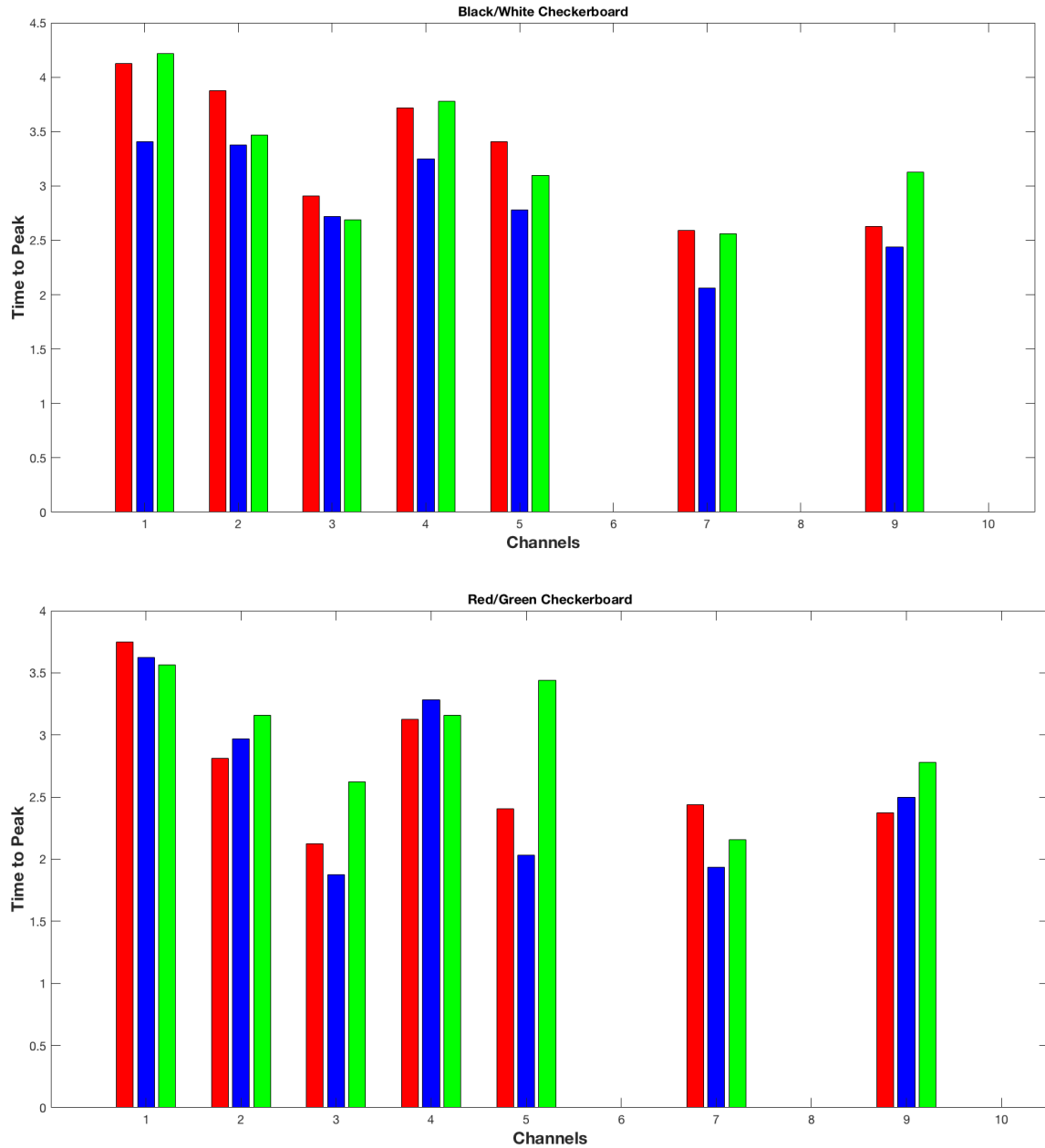
Figure C.1: Bar graph showing the time taken for the response in each of the chromophores to reach its maximum value in response to the black/white (top) and red/green checkerboard (bottom).

Cross-correlation analysis

Figure C.2 shows the cross-correlations between (i) HbO_2 and oxCCO (ii) HHb and oxCCO and (iii) HbO_2 and oxCCO for all the channels (including the channels over the occipital cortex) for the black/white conditions and red/green conditions.
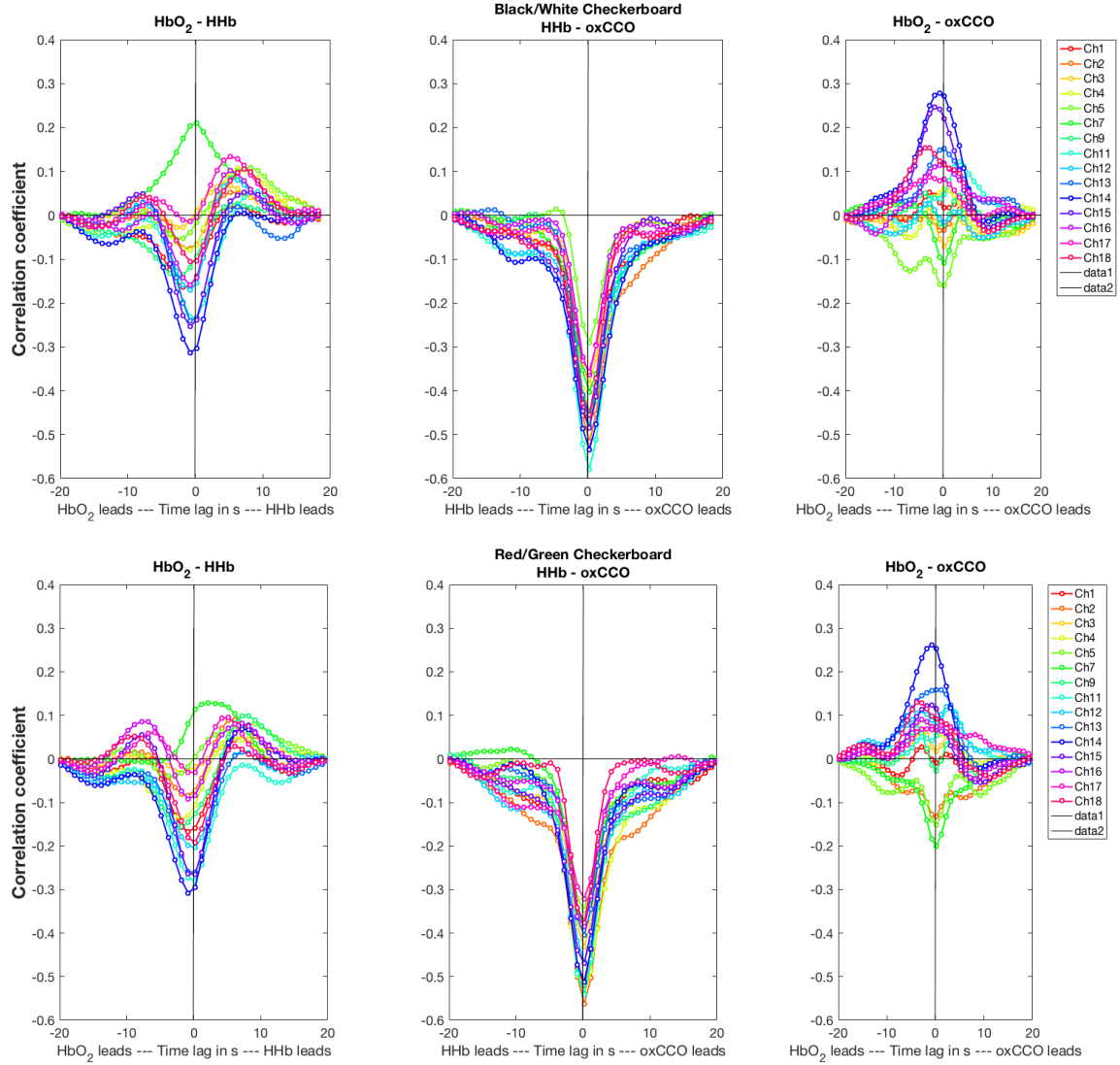
Figure C.2: Cross-correlations between HbO$_2$ and oxCCO (left), HHb and oxCCO (middle) and HbO$_2$ and oxCCO (right) for the black/white condition (top) and red/green condition (bottom). The x-axis shows the time-lag between the time series while the y-axis shows the correlation coefficient.

Black/white versus red/green statistical tables

Tables C.1 - C.3 show the mean maximum changes in Δ[HbO$_2$], Δ[HHb] and Δ[oxCCO] respectively with their the t and p values and FDR corrected p values. Significant channels are marked with an asterisk, both for the uncorrected and corrected p values.

Channel	$\Delta[HbO_2]$ Mean Difference (b/w - r/g)	t_{HbO_2}	p_{HbO_2}	FDR corrected p_{HbO_2}
1	0.1217	1.8068	0.0812	0.5635
2	0.1345	1.6949	0.1020	0.5635
3	0.0824	1.1042	0.2826	0.5635
4	0.1182	1.3249	0.1955	0.5635
5	-0.0865	-0.8707	0.3916	0.5874
7	0.0379	0.6261	0.5401	0.6751
9	0.12	1.0591	0.3005	0.5635
11	0.0279	0.3223	0.7494	0.7995
12	0.0635	0.9234	0.3634	0.5874
13	0.0216	0.2563	0.7995	0.7995
14	0.0329	0.3715	0.7129	0.7995
15	0.0755	1.1096	0.2757	0.5635
16	0.0613	1.1093	0.2764	0.7995
17	0.0424	0.6630	0.5131	0.6751
18	-0.1254	-1.3280	0.1949	0.5635

Table C.1: Mean maximum differences and t and p values for the black/white versus red/green conditions for HbO_2.

Channel	Δ[HHb] Mean Difference (b/w - r/g)	t_{HHb}	p_{HHb}	FDR corrected p_{HHb}
1	0.0395	0.6040	0.5505	0.8131
2	-0.0308	-0.4584	0.6505	0.8131
3	-0.1069	-1.1227	0.2749	0.7501
4	0.0871	1.2859	0.2086	0.7501
5	-0.0445	-0.6758	0.5049	0.8131
7	-0.0650	-1.0055	0.3296	0.7501
9	-0.008	-0.0827	0.9348	0.9348
11	0.0918	1.2051	0.2376	0.7501
12	-0.0472	-0.9206	0.3649	0.7501
13	-0.0110	-0.1457	0.8851	0.9348
14	0.0741	1.1003	0.2800	0.7501
15	0.0618	0.8533	0.4001	0.7501
16	0.0085	0.1156	0.9088	0.9348
17	0.0454	0.9005	0.3761	0.7501
18	0.0291	0.4739	0.6392	0.8131

Table C.2: Mean maximum differences and t and p values for the black/white versus red/green conditions for HHb.

Channel	Δ[oxCCO] Mean Difference (b/w - r/g)	t_{oxCCO}	p_{oxCCO}	FDR corrected p_{oxCCO}
1	0.005	0.3015	0.7652	0.9224
2	0.0279	1.3219	0.1977	0.7414
3	-0.0096	-0.3829	0.7058	0.9224
4	-0.0364	-2.2019	0.0358*	0.5367
5	-0.0120	-0.4045	0.6891	0.9224
7	0.0120	0.2584	0.7994	0.9224
9	-0.0222	-0.9392	0.3574	0.9224
11	-0.0075	-0.3998	0.6921	0.92240
12	0.0333	1.8525	0.0742	0.5562
13	0.0086	0.4423	0.6614	0.9224
14	0.008	0.4966	0.6231	0.9224
15	-0.0000087	-0.0048	0.9962	0.9962
16	0.0011	0.0722	0.9429	0.9962
17	0.0268	1.4544	0.1578	0.7414
18	0.0049	0.2571	0.7990	0.9224

Table C.3: Mean maximum differences and t and p values for the black/white versus red/green conditions for oxCCO.

NIRS Results - Gratings conditions

Time to peak analysis

Figure C.3 shows the TTP for each chromophore for low contrast and high contrast conditions respectively.
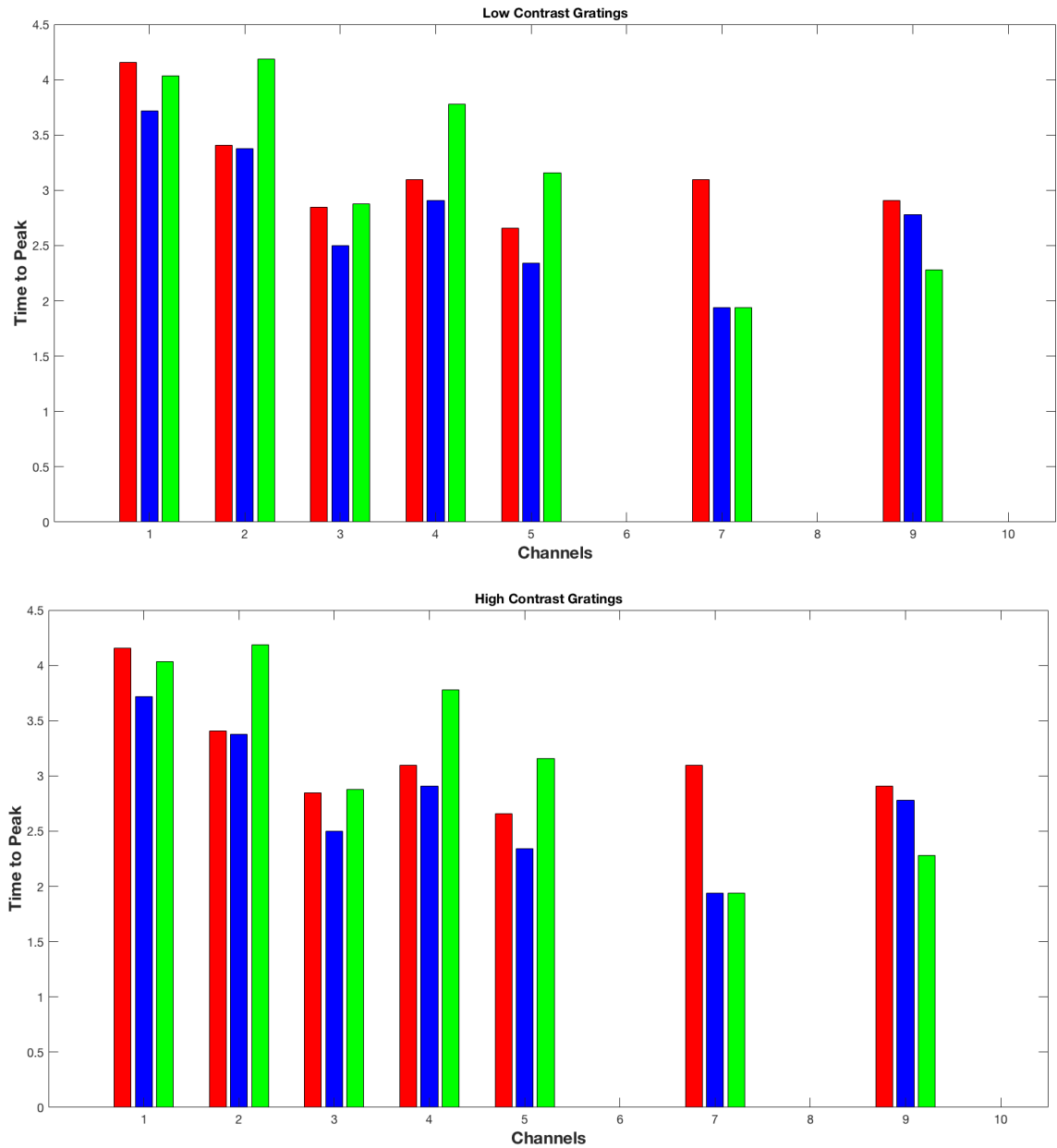
Figure C.3: Bar graph showing the time taken for the response in each of the chromophores to reach its maximum value in response to the low contrast gratings (top) and high contrast gratings (bottom).

Cross-correlation analysis

Figure C.4 shows the cross-correlations between (i) HbO_2 and oxCCO (ii) HHb and oxCCO and (iii) HbO_2 and oxCCO for all the channels (including the channels over the occipital cortex) for the black/white conditions and red/green conditions.
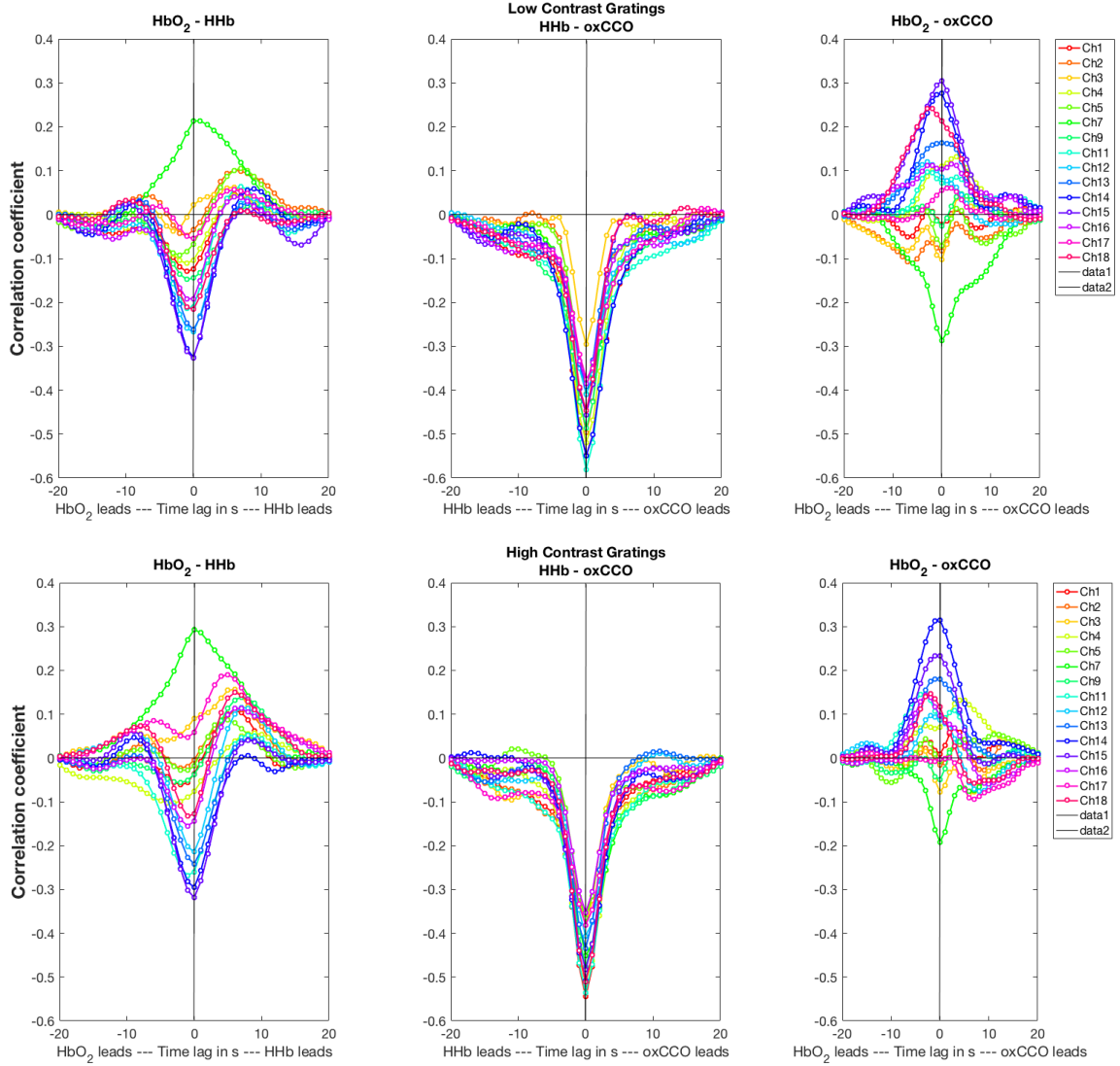
Figure C.4: Cross-correlations between HbO$_2$ and oxCCO (left), HHb and oxCCO (middle) and HbO$_2$ and oxCCO (right) for the low contrast condition (top) and high contrast condition (bottom). The x-axis shows the time-lag between the time series while the y-axis shows the correlation coefficient.

High contrast versus low contrast statistical tables

Tables C.4 - C.6 show the mean maximum changes in $\Delta[HbO_2]$, $\Delta[HHb]$ and $\Delta[oxCCO]$ respectively with their the t and p values and FDR corrected p values. Significant channels are marked with an asterisk, both for the uncorrected and corrected p values.

Channel	$\Delta[HbO_2]$ Mean Difference (hc - lc)	t_{HbO_2}	p_{HbO_2}	FDR corrected p_{HbO_2}
1	0.1172	1.2830	0.2097	0.6290
2	0.1483	1.5945	0.1229	0.4609
3	0.1832	1.9706	0.0628	0.4609
4	0.0587	0.8901	0.3808	0.7573
5	-0.0569	-0.5196	0.6076	0.7573
7	0.2288	1.9159	0.0734	0.4609
9	0.0349	0.3865	0.7027	0.7573
11	0.0551	0.6852	0.4985	0.7573
12	0.0794	1.6731	0.1051	0.4609
13	0.0209	0.3118	0.7573	0.7573
14	0.0553	0.5564	0.5821	0.7573
15	0.0454	0.5037	0.6180	0.7573
16	0.0511	0.6981	0.4907	0.7573
17	-0.0231	-0.3715	0.7133	0.7573
18	-0.0844	-0.9417	0.3544	0.7573

Table C.4: Mean maximum differences and t and p values for the low contrast versus high contrast conditions for HbO_2.

Channel	Δ[HHb] Mean Difference (hc - lc)	t_{HHb}	p_{HHb}	FDR corrected p_{HHb}
1	0.0341	0.5168	0.6092	0.9419
2	0.0154	0.2288	0.8208	0.9954
3	0.0406	0.5002	0.6224	0.9419
4	0.00029	0.0059	0.9954	0.9954
5	0.1045	1.4346	0.1629	0.4886
7	0.0949	1.6646	0.1154	0.4329
9	-0.0582	-0.7935	0.4356	0.9334
11	-0.009	-0.1697	0.8664	0.9954
12	0.1358	1.8504	0.0745	0.4329
13	0.0791	1.1963	0.2409	0.6023
14	0.0812	1.6342	0.1127	0.4329
15	0.1343	2.1619	0.0385	0.4329
16	-0.0293	-0.4898	0.6279	0.9419
17	0.0023	0.0458	0.9638	0.9954
18	0.0125	0.2244	0.8241	0.9954

Table C.5: Mean maximum differences and t and p values for the the low contrast versus high contrast conditions for HHb.

Channel	Δ[oxCCO] Mean Difference (hc - lc)	t_{oxCCO}	p_{oxCCO}	FDR corrected p_{oxCCO}
1	-0.0121	-0.6848	0.4989	0.9101
2	0.0159	0.7222	0.4766	0.9101
3	-0.0079	-0.3582	0.7240	0.9101
4	-0.0309	-1.4530	0.1570	0.9101
5	-0.0055	-0.3080	0.7604	0.9101
7	-0.0243	-0.5597	0.5834	0.9101
9	0.0221	0.8685	0.3941	0.9101
11	0.0260	1.2239	0.2305	0.9101
12	0.0065	0.3719	0.7127	0.9101
13	0.0044	0.3016	0.7650	0.9101
14	-0.0031	-0.1868	0.8531	0.9140
15	-0.0051	-0.3405	0.7358	0.9101
16	0.00074	0.0433	0.9658	0.9658
17	-0.0043	-0.2707	0.7888	0.9101
18	-0.0113	-0.5732	0.5711	0.9101

Table C.6: Mean maximum differences and t and p values for the low contrast versus high contrast conditions for oxCCO.